

BIOINFORMATICS & BIOMEDICAL IMAGING

# Microscopic Image Analysis

*for Life Science Applications*

Jens Rittscher  
Raghu Machiraju  
Stephen T. C. Wong

*editors*



CD-ROM  
Included

# **Microscopic Image Analysis for Life Science Applications**

# Artech House Series

## Bioinformatics & Biomedical Imaging

Series Editors

Stephen T. C. Wong, The Methodist Hospital and Weill Cornell Medical College

Guang-Zhong Yang, Imperial College

*Advances in Diagnostic and Therapeutic Ultrasound Imaging*, Jasjit S. Suri, Chirinjeev Kathuria, Ruey-Feng Chang, Filippo Molinari, and Aaron Fenster, editors

*Biological Database Modeling*, Jake Chen and Amandeep S. Sidhu, editors

*Biomedical Informatics in Translational Research*, Hai Hu, Michael Liebman, and Richard Mural

*Genome Sequencing Technology and Algorithms*, Sun Kim, Haixu Tang, and Elaine R. Mardis, editors

*Life Science Automation Fundamentals and Applications*, Mingjun Zhang, Bradley Nelson, and Robin Felder, editors

*Microscopic Image Analysis for Life Science Applications*, Jens Rittscher, Raghu Machiraju and Stephen T. C. Wong, editors

*Next Generation Artificial Vision Systems: Reverse Engineering the Human Visual System*, Maria Petrou and Anil Bharath, editors

*Systems Bioinformatics: An Engineering Case-Based Approach*, Gil Alterovitz and Marco F. Ramoni, editors

# Microscopic Image Analysis for Life Science Applications

Jens Rittscher  
Raghu Machiraju  
Stephen T. C. Wong

*Editors*



**ARTECH  
HOUSE**

BOSTON | LONDON  
[artechhouse.com](http://artechhouse.com)



**Library of Congress Cataloging-in-Publication Data**

A catalog record for this book is available from the U.S. Library of Congress.

***Disclaimer:***

***This eBook does not include the ancillary media that was packaged with the original printed version of the book.***

**British Library Cataloguing in Publication Data**

A catalogue record for this book is available from the British Library.

ISBN-13: 978-1-59693-236-4

Cover design by Yekaterina Ratner

© 2008 ARTECH HOUSE, INC.

685 Canton Street

Norwood, MA 02062

All rights reserved. Printed and bound in the United States of America. No part of this book may be reproduced or utilized in any form or by any means, electronic or mechanical, including photocopying, recording, or by any information storage and retrieval system, without permission in writing from the publisher.

All terms mentioned in this book that are known to be trademarks or service marks have been appropriately capitalized. Artech House cannot attest to the accuracy of this information. Use of a term in this book should not be regarded as affecting the validity of any trademark or service mark.

**DISCLAIMER OF WARRANTY**

The technical descriptions, procedures, and computer programs in this book have been developed with the greatest of care and they have been useful to the author in a broad range of applications; however, they are provided as is, without warranty of any kind. Artech House, Inc. and the authors and editors of the book titled *Microscopic Image Analysis for Life Science Applications* make no warranties, expressed or implied, that the equations, programs, and procedures in this book or its associated software are free of error, or are consistent with any particular standard of merchantability, or will meet your requirements for any particular application. They should not be relied upon for solving a problem whose incorrect solution could result in injury to a person or loss of property. Any use of the programs or procedures in such a manner is at the user's own risk. The editors, authors, and publisher disclaim all liability for direct, incidental, or consequent damages resulting from use of the programs or procedures in this book or the associated software.

10 9 8 7 6 5 4 3 2 1

# Contents

Foreword	xv
Preface	xvii

## **PART I**

### Introduction

#### **CHAPTER 1**

Introduction to Biological Light Microscopy	1
1.1 Introduction	1
1.2 Need for Microscopy	1
1.3 Image Formation in Transmitted Light Microscopy	2
1.4 Resolution, Magnification, and Contrast in Microscopy	5
1.5 Phase Contrast Microscopy	7
1.6 Dark Field Microscopy	8
1.7 Polarization Microscopy	8
1.8 Differential Interference Contrast Microscopy	9
1.9 Reflected Light Microscopy	10
1.10 Fluorescence Microscopy	12
1.11 Light Microscopy in Biology	12
1.12 Noise and Artifacts in Microscopic Images	14
1.13 Trends in Light Microscopy	16
References	17

#### **CHAPTER 2**

Molecular Probes for Fluorescence Microscopy	19
2.1 Introduction	19
2.2 Basic Characteristics of Fluorophores	21
2.3 Traditional Fluorescent Dyes	25
2.4 Alexa Fluor Dyes	26
2.5 Cyanine Dyes	28
2.6 Fluorescent Environmental Probes	29
2.7 Organelle Probes	32
2.8 Quantum Dots	34
2.9 Fluorescent Proteins	36
2.10 Hybrid Systems	39
2.11 Quenching and Photobleaching	40
2.12 Conclusions	43
References	43
Selected Bibliography	48

**CHAPTER 3**

Overview of Image Analysis Tools and Tasks for Microscopy	49
3.1 Image Analysis Framework	50
3.1.1 Continuous-Domain Image Processing	51
3.1.2 A/D Conversion	54
3.1.3 Discrete-Domain Image Processing	55
3.2 Image Analysis Tools for Microscopy	56
3.2.1 Signal and Image Representations	57
3.2.2 Fourier Analysis	60
3.2.3 Gabor Analysis	61
3.2.4 Multiresolution Analysis	62
3.2.5 Unsupervised, Data-Driven Representation and Analysis Methods	64
3.2.6 Statistical Estimation	67
3.3 Imaging Tasks in Microscopy	68
3.3.1 Intelligent Acquisition	68
3.3.2 Deconvolution, Denoising, and Restoration	69
3.3.3 Registration and Mosaicking	72
3.3.4 Segmentation, Tracing, and Tracking	74
3.3.5 Classification and Clustering	77
3.3.6 Modeling	78
3.4 Conclusions	79
References	79

**CHAPTER 4**

An Introduction to Fluorescence Microscopy: Basic Principles, Challenges, and Opportunities	85
4.1 Fluorescence in Molecular and Cellular Biology	86
4.1.1 The Physical Principles of Fluorescence	86
4.1.2 The Green Revolution	88
4.2 Microscopes and Image Formation	91
4.2.1 The Widefield Microscope	91
4.2.2 The Confocal Scanning Microscope	93
4.2.3 Sample Setup and Aberrations	94
4.3 Detectors	95
4.3.1 Characteristic Parameters of Detection Systems	95
4.3.2 Detection Technologies	96
4.4 Limiting Factors of Fluorescence Imaging	98
4.4.1 Noise Sources	98
4.4.2 Sample-Dependent Limitations	99
4.5 Advanced Experimental Techniques	99
4.5.1 FRET	100
4.5.2 FRAP	101
4.5.3 FLIM	102

4.6	Signal and Image Processing Challenges	103
4.6.1	Data Size and Dimensionality	103
4.6.2	Image Preparation	103
4.6.3	Restoration	104
4.6.4	Registration	105
4.6.5	Segmentation	106
4.6.6	Quantitative Analysis	106
4.7	Current and Future Trends	107
4.7.1	Fluorescent Labels	107
4.7.2	Advanced Microscopy Systems	108
4.7.3	Super-Resolution: Photoactivated Localization- Based Techniques	109
4.8	Conclusions	110
	References	111

## CHAPTER 5

	FARSIGHT: A Divide and Conquer Methodology for Analyzing Complex and Dynamic Biological Microenvironments	115
5.1	Introduction	115
5.2	A Divide-and-Conquer Segmentation Strategy	122
5.3	Computing and Representing Image-Based Measurements	131
5.4	Analysis of Spatio-Temporal Associations	135
5.5	Validation of Automated Image Analysis Results	142
5.6	Summary, Discussion, and Future Directions	146
	References	146

## PART II

### Subcellular Structures and Events

## CHAPTER 6

	MST-Cut: A Minimum Spanning Tree-Based Image Mining Tool and Its Applications in Automatic Clustering of Fruit Fly Embryonic Gene Expression Patterns and Predicting Regulatory Motifs	153
6.1	Introduction	153
6.2	MST	154
6.3	MST-Cut for Clustering of Coexpressed/Coregulated Genes	154
6.3.1	MST-Cut Clustering Algorithm	155
6.3.2	Embryonic Image Clustering	157
6.4	Experiments	160
6.4.1	Performance of MST-Cut on Synthetic Datasets	160
6.4.2	Detection of Coregulated Genes and Regulatory Motifs	163
6.5	Conclusions	166
	References	167
	Selected Bibliography	168

**CHAPTER 7**

Simulation and Estimation of Intracellular Dynamics and Trafficking	169
7.1 Context	169
7.1.1 Introduction to Intracellular Traffic	170
7.1.2 Introduction to Living Cell Microscopy	171
7.2 Modeling and Simulation Framework	172
7.2.1 Intracellular Trafficking Models in Video-Microscopy	172
7.2.2 Intracellular Traffic Simulation	174
7.2.3 Example	177
7.3 Background Estimation in Video-Microscopy	178
7.3.1 Pixel-Wise Estimation	178
7.3.2 Spatial Coherence for Background Estimation	179
7.3.3 Example	181
7.4 Foreground Analysis: Network Tomography	181
7.4.1 Network Tomography Principle	182
7.4.2 Measurements	184
7.4.3 Problem Optimization	185
7.4.4 Experiments	187
7.5 Conclusions	187
References	188

**CHAPTER 8**

Techniques for Cellular and Tissue-Based Image Quantitation of Protein Biomarkers	191
8.1 Current Methods for Histological and Tissue-Based Biomarker	191
8.2 Multiplexing	192
8.2.1 Fluorescence Microscopy	192
8.2.2 Fluorescent Dyes	193
8.2.3 Quantum Dots	193
8.2.4 Photobleaching	194
8.3 Image Analysis	194
8.3.1 Image Preprocessing	195
8.3.2 Image Registration	197
8.3.3 Image Segmentation	199
8.3.4 A Unified Segmentation Algorithm	200
8.3.5 Segmentation of Cytoplasm and Epithelial Regions	202
8.4 Multichannel Segmentation Techniques	202
8.5 Quantitation of Subcellular Biomarkers	203
8.6 Summary	204
References	204

**CHAPTER 9**

Methods for High-Content, High-Throughput, Image-Based Cell Screening	209
9.1 Introduction	209
9.2 Challenges in Image-Based High-Content Screening	210
9.3 Methods	210
9.3.1 Illumination and Staining Correction	210
9.3.2 Segmentation	212
9.3.3 Measurements	214
9.3.4 Spatial Bias Correction	214
9.3.5 Exploration and Inference	215
9.4 Discussion	218
References	219

**PART III****Structure and Dynamics of Cell Populations****CHAPTER 10**

Particle Tracking in 3D+t Biological Imaging	223
10.1 Introduction	223
10.2 Main Tracking Methods	225
10.2.1 Autocorrelation Methods	225
10.2.2 Deterministic Methods	226
10.2.3 Multiple Particle Tracking Methods	226
10.2.4 Bayesian Methods	227
10.3 Analysis of Bayesian Filters	229
10.3.1 The Conceptual Filter	229
10.3.2 The Kalman Filter	231
10.3.3 The Filter Based on a Grid	234
10.3.4 The Extended Kalman Filter	235
10.3.5 The Interacting Multiple Model Filter	238
10.3.6 The Approximated Filter Based on a Grid	242
10.3.7 The Particle Filter	245
10.4 Description of the Main Association Methods	251
10.4.1 The Nearest Neighbor (ML)	253
10.4.2 Multihypothesis Tracking (MHT)	254
10.4.3 The Probabilistic Data Association Filter (PDAF)	256
10.4.4 Joint PDAF (JPDAF)	257
10.5 Particle Tracking: Methods for Biological Imaging	259
10.5.1 Proposed Dynamic Models for the IMM	259
10.5.2 Adaptive Validation Gate	261
10.5.3 Association	265
10.6 Applications	266
10.6.1 Validation on Synthetic Data	266



10.6.2 Applications to Cell Biology	267
10.7 Conclusions	270
References	271
Appendix 10A Pseudocodes for the Algorithms	277

## CHAPTER 11

Automated Analysis of the Mitotic Phases of Human Cells in 3-D Fluorescence Microscopy Image Sequences	283
11.1 Introduction	283
11.2 Methods	284
11.2.1 Image Analysis Workflow	284
11.2.2 Segmentation of Multicell Images	285
11.2.3 Tracking of Mitotic Cell Nuclei	287
11.2.4 Extraction of Static and Dynamic Features	288
11.2.5 Classification	289
11.3 Experimental Results	290
11.3.1 Image Data	290
11.3.2 Classification Results	290
11.4 Discussion and Conclusion	292
References	292

## CHAPTER 12

Automated Spatio-Temporal Cell Cycle Phase Analysis Based on Covert GFP Sensors	295
12.1 Introduction	296
12.2 Biological Background	296
12.2.1 Cell Cycle Phases	296
12.2.2 Cell Cycle Checkpoints	297
12.2.3 Cell Staining	298
12.2.4 Problem Statement	299
12.3 State of the Art	300
12.4 Mathematical Framework: Level Sets	302
12.4.1 Active Contours with Edges	303
12.4.2 Active Contours Without Edges	303
12.5 Spatio-Temporal Cell Cycle Phase Analysis	304
12.5.1 Automatic Seed Placement	305
12.5.2 Shape/Size Constraint for Level Set Segmentation	305
12.5.3 Model-Based Fast Marching Cell Phase Tracking	307
12.6 Results	310
12.6.1 Large-Scale Toxicological Study	310
12.6.2 Algorithmic Validation	310
12.7 A Tool for Cell Cycle Research	311
12.7.1 Research Prototype	312
12.7.2 Visualization	313
12.8 Summary and Future Work	314
References	314

**CHAPTER 13**

Cell Segmentation for Division Rate Estimation in Computerized Video Time-Lapse Microscopy	317
13.1 Introduction	317
13.2 Methodology	319
13.2.1 Cell Detection with AdaBoost	319
13.2.2 Foreground Segmentation	323
13.2.3 Cytoplasm Segmentation Using the Watershed Algorithm	326
13.2.4 Cell Division Rate Estimation	327
13.3 Experiments	328
13.4 Conclusions	329
References	329

**PART IV****Automated Cellular and Tissue Analysis****CHAPTER 14**

Systems Biology and the Digital Fish Project: A Vast New Frontier for Image Analysis	331
14.1 Introduction	331
14.2 Imaging-Based Systems Biology	331
14.2.1 What Is Systems Biology?	331
14.2.2 Imaging in Systems Biology	335
14.3 Example: The Digital Fish Project	338
14.3.1 Goals of Project	338
14.3.2 Why Fish?	340
14.3.3 Imaging	340
14.3.4 Image Analysis	347
14.3.5 Visualization	352
14.3.6 Data Analysis	352
14.3.7 Registration/Integration, Reference Atlas	357
14.4 Bridging the Gap	353
14.4.1 Open Source	353
14.4.2 Traversing the Gap	354
14.5 Conclusions	354
References	355

**CHAPTER 15**

Quantitative Phenotyping Using Microscopic Images	357
15.1 Introduction	357
15.2 Relevant Biomedical Applications	359

15.2.1	Mouse Model Phenotyping Study: Role of the Rb Gene	359
15.2.2	Mouse Model Phenotyping Study: The PTEN Gene and Cancer	359
15.2.3	3-D Reconstruction of Cellular Structure of Zebrafish Embryo	360
15.3	Tissue Segmentation Using <i>N</i> -Point Correlation Functions	361
15.3.1	Introduction to <i>N</i> -Point Correlation Functions	361
15.3.2	Segmentation of Microscopic Images Using <i>N</i> -pcfs	364
15.4	Segmentation of Individual Cells	364
15.4.1	Modality-Dependent Segmentation: Active Contour Models	364
15.4.2	Modality-Independent Segmentation: Using Tessellations	366
15.5	Registration of Large Microscopic Images	371
15.5.1	Rigid Registration	371
15.5.2	Nonrigid Registration	372
15.6	3-D Visualization	375
15.6.1	Mouse Model Phenotyping Study: Role of the Rb Gene	375
15.6.2	Mouse Model Phenotyping Study: Role of the PTEN Gene in Cancer	377
15.6.3	Zebrafish Phenotyping Studies	379
15.7	Quantitative Validation	380
15.7.1	Mouse Placenta Phenotyping Studies	380
15.7.2	Mouse Mammary Gland Phenotyping Study	382
15.8	Summary	384
	References	389

## CHAPTER 16

	Automatic 3-D Morphological Reconstruction of Neuron Cells from Multiphoton Images	389
16.1	Introduction	389
16.2	Materials and Methods	391
16.2.1	Experimental Data	391
16.3	Results	396
16.4	Conclusions	397
	References	398

## CHAPTER 17

	Robust 3-D Reconstruction and Identification of Dendritic Spines	401
17.1	Introduction	401
17.2	Related Work	404
17.3	Image Acquisition and Processing	404
17.3.1	Data-Set	405
17.3.2	Denoising and Resampling	405

17.3.3 Segmenting the Neuron	407
17.3.4 Floating Spine Heads	408
17.4 Neuron Reconstruction and Analysis	409
17.4.1 Surfacing and Surface Fairing	410
17.4.2 Curve Skeletonization	412
17.4.3 Dendrite Tree Model	413
17.4.4 Morphometry and Spine Identification	413
17.5 Results	414
17.6 Conclusion	419
References	419

## **PART V**

### **In Vivo Microscopy**

#### **CHAPTER 18**

Small Critter Imaging	425
18.1 In Vivo Molecular Small Animal Imaging	425
18.1.1 Fluorescence Microscopic Imaging	425
18.1.2 Bioluminescence Imaging	426
18.1.3 Coherent Anti-Stokes Raman Scattering Imaging	426
18.1.4 Fibered In Vivo Imaging	427
18.2 Fluorescence Molecular Imaging (FMT)	427
18.2.1 Fluorescence Scanning	427
18.2.2 FMT Data Processing	428
18.2.3 Multimodality	428
18.3 Registration of 3-D FMT and MicroCT Images	429
18.3.1 Introduction	429
18.3.2 Problem Statement and Formulation	430
18.3.3 Combined Differential Evolution and Simplex Method Optimization	432
18.3.4 A Novel Optimization Method Based on Sequential Monte Carlo	436
18.4 Conclusions	438
References	439

#### **CHAPTER 19**

Processing of In Vivo Fibered Confocal Microscopy Video Sequences	441
19.1 Motivations	441
19.2 Principles of Fibered Confocal Microscopy	443
19.2.1 Confocal Microscopy	443
19.2.2 Distal Scanning Fibered Confocal Microscopy	443
19.2.3 Proximal Scanning Fibered Confocal Microscopy	444
19.3 Real-Time Fiber Pattern Rejection	447
19.3.1 Calibrated Raw Data Acquisition	447

19.3.2 Real-Time Processing	448
19.4 Blood Flow Velocimetry Using Motion Artifacts	450
19.4.1 Imaging of Moving Objects	450
19.4.2 Velocimetry Algorithm	451
19.4.3 Results and Evaluation	453
19.5 Region Tracking for Kinetic Analysis	454
19.5.1 Motion Compensation Algorithm	454
19.5.2 Affine Registration Algorithm	455
19.5.3 Application to Cell Trafficking	456
19.6 Mosaicking: Bridging the Gap Between Microscopic and Macroscopic Scales	457
19.6.1 Overview of the Algorithm	458
19.6.2 Results and Evaluation	460
19.7 Conclusions	461
References	461
About the Editors	465
List of Contributors	467
Index	

# Foreword

Microscopy is one of the oldest biological research techniques, and yet it has lagged behind other methods in adopting the statistical, quantitative, and automated approaches that characterize biology in the age of systems biology. However, work performed over the past dozen years has begun to make biological imaging, especially fluorescence microscopy, a suitable tool for large-scale, systematic, and automated studies of biological processes. The need for computational analysis of biological images is driven in part by the advent of automated, high throughput microscopes, but the significant limitations of visual analysis of biological images is an equally important factor. The goal of the field of bioimaging informatics is to enable the direct extraction of assertions about biological events from images or sets of images so that these assertions can be integrated with those from other biological methods into comprehensive models of biological systems.

The chapters that Jens Rittscher, Raghu Machiraju, and Stephen T. C. Wong have assembled in this book describe the range of methods used in bioimaging informatics and provide the reader with both an introduction to the challenges of the field and the current state of the art in addressing those challenges.

The book begins with four introductory chapters on microscopy, fluorescent probes, and basic image processing. The next 12 chapters review work from the authors' groups in the context of particular goals but from which two broad themes emerge. The first theme is recognizing patterns using both supervised and unsupervised methods from images from sources as varied as high-throughput screen, histochemistry, and whole embryo imaging. The second theme is analyzing spatiotemporal dynamics for processes with time scales as varied as organelle movement and cell cycle progression. The need for approaches to combine analysis results from different methods and channels is also addressed.

The last four chapters of this book focus primarily on a different task: the reconstruction from an image set (which may include images from different modalities) of an adequate model describing the original sample. The first two of these chapters focus on neuronal images, and the last two chapters focus on bridging microscopy with larger-scale imaging modalities such as magnetic resonance imaging.

This book should be valuable both to readers familiar with biology and microscopy, but lacking knowledge of current image informatics methods, and to those familiar with image analysis, but seeking challenging new applications.

The field is in its infancy, but the challenges and opportunities make it one of the most exciting in all of biomedical research. It is hoped that this book



will stimulate the reader to contribute to realizing the potential of bioimage informatics for understanding complex biological processes and behaviors.

*Robert F. Murphy*  
*Ray and Stephanie Lane Professor of Computational Biology*  
*Carnegie Mellon University*  
*Pittsburgh, Pennsylvania*  
*July 2008*

# Preface

Advances in the microscopy of living cells, small organisms, and tissues have changed life science research. Modern microscopy has developed from a convergence of advances in cell manipulation, probe chemistry, solid state physics, electronics, optics, and image analysis. Today, fluorescence markers suitable for live cell imaging are readily available. Not only is it possible to image biological structures in three dimensions by tagging particular proteins, but it is also possible to monitor a variety of biological processes occurring in cells and tissues. State-of-the-art microscopes enable us to record such biological processes at extremely high spatial and temporal resolutions.

Optical microscopy enables the determination of the structure within a cell and the location of specific molecules within a cell. More importantly, these insights are obtained with relatively less sophisticated instrumentation than other forms of microscopy, especially those relying on electron tunneling methods. More recently, certain protocols of optical microscopy provide more than structural information. Various subcellular properties and events, as manifested through the presence and interaction of certain molecules, can also be determined through the use of chemical and biological probes.

Important application areas include cancer research, toxicity screening, digital pathology, and neuroscience research. All of these applications require an in-depth understanding of the biology, the probe chemistry, the underlying imaging physics, and the associated analysis of images. It is clear that new breakthroughs in this rapidly emerging field will only be accomplished through effective interdisciplinary research. Automated state-of-the-art microscopes enable researchers to acquire data that can no longer be analyzed manually. Such data sets pose a number of challenges that are very distinct from conventional clinical imagery in their size and abundance and the detail of relevant features and their statistics. Sophisticated algorithms are necessary to process such imagery and extract biologically relevant measurements.

This book presents an in-depth exploration of issues related to automated image analysis applied to life science applications. The primary aim of this book is to provide a bridge between the biomedical image analysis and bioscience communities. Striking a balance between an entirely self-contained presentation and a review of the state of the art in the field is always challenging. This book is divided into five major parts: Introduction, Subcellular Structures and Events, Structure and Dynamics of Cell Populations, Automated Tissue Analysis, and In Vivo Microscopy. The introduction consists of five chapters that are tutorial chapters. The remaining chapters cover a wide spectrum of examples illustrating the potential of biomedical vision algorithms.

While each of the chapters can be read independently, some of the image analysis concepts that are applied require an understanding of basic concepts such as

image segmentation and visual tracking. Rather than presenting a review of relevant algorithm and image analysis methods, this book presents techniques in a concrete application context. The biological background necessary to understand the specific technical challenges associated to each problem is included in the chapter. The content of each section is briefly described next.

## **Part I: Introduction**

In Chapter 1, Gunjan Agarwal presents a brief but comprehensive overview of light microscopy. The various forms of microscopy, contrast mechanisms, and aspects of sample preparation techniques that are commonly employed for biological light microscopy are introduced.

A key aspect of fluorescence microscopy is molecular probes that enable the targeting of structural components and dynamic processes in living cells and tissues. In Chapter 2 Michael Davidson and his collaborators present a detailed overview of fluorescent probes. Throughout the chapter, the underlying chemical structure of such probes and associated fluorescent mechanisms are discussed.

The remaining three chapters of the introduction provide an overview of the necessary signal processing and image analysis tools that are necessary to examine and quantify acquired fluorescent microscopy images. Jelena Kovacevic and Gustavo K. Rohde present a summary of computer-aided-image analysis tools and tasks for microscopy in Chapter 3. This chapter is structured around mathematical tools and concepts that hold great potential to advance the state of the art for automated artifact removal and information extraction.

Michael Unser and his collaborators present an introduction to fluorescence microscopy in Chapter 4. This chapter puts the current developments into a historical perspective, clearly formulating the main challenges that need to be addressed while highlighting possible future perspectives in this field. In addition, it describes a broad and comprehensive framework for capturing the multitude of geometric structures and their dynamic behavior at both cellular and subcellular levels. It also emphasizes the need to build scalable algorithms, given the ever-increasing size of datasets. These datasets pose a number of challenges that are very distinct from conventional clinical imagery in their size and abundance, the detail of relevant features, and their statistics.

The goal of the FARSIGHT concept, developed by Badri Roysam, is the formulation of a unified approach that captures the richness of such data sets. Chapter 5 presents an overview of this approach and illustrates how computational models can be applied to establish associations among cellular compartments, surfaces, and functional markers.

## **Part II: Subcellular Structures and Events**

The first group of chapters highlighting the application of advance image analysis tools focuses on the analysis and measurement of subcellular structures and events. In Chapter 6, Hanchuan Peng addresses the analysis of in situ gene expression pattern images obtained from the use of specialized mRNA probes. The goal

is to utilize pattern recognition as an important source of information towards understanding the functions of genes required for the development of various organisms. Automated image analysis methods are applied to build image informatics tools that analyze the spatial-temporal patterns of gene expressions during embryogenesis of *Drosophila melanogaster* (fruit fly). The end results of the analysis are appropriate ontological annotations of expression patterns.

Techniques for probing intracellular dynamics in living cells using optical methods are still very crude. The large number of small moving particles complexity of particle interactions pose significant challenges. In Chapter 7 Jérôme Boulanger and his associates present a general estimation and simulation framework that allows the modeling of image sequences depicting the motion of small regions as complex motion patterns that, in turn, are manifestations of intracellular dynamics and trafficking in biology.

Immunofluorescent methods that allow the staining of a single tissue section with an entire set of different protein biomarkers are beginning to emerge. In Chapter 8, Ali Can and his associates review how such a new staining technique enables multiplexing a large number of markers in a single tissue. They illustrate how specialized image analysis methods enable the quantification of the expression levels of different markers. By extracting the expressions in different subcellular compartments, these techniques allow one to gain insight into unexamined relationships between spatial locations and various protein-protein interactions. Preliminary data certainly demonstrates the value of automated fluorescence-based image analysis when used on clinical studies of breast and lung cancers.

Supporting large screenings of RNA interference experiments and small molecule screenings is the focus of Chapter 9. Thouis R. Jones and his associates present methods for automatic image cytometry. Developing methods for illumination normalization, foreground/background separation, and cell segmentation that work robustly on thousands of images acquired with a high-throughput robotic microscope is challenging. The authors describe how the CellProfiler system, which is available as open source software, can be applied for making discoveries about cellular processes, genetic pathways, and drug candidates.

### **Part III: Structure and Dynamics of Cell Populations**

Computerized video time-lapse microscopy enables the monitoring of cell populations over extended periods of time. While some of the introductory chapters have already touched on the subject, Chapters 10 through 13 focus on the analyses of the dynamics of cell populations and cellular functions. In Chapter 10, Auguste Genovesio and Jean-Christophe Olivo-Marin present a detailed introduction to various stochastic methods for cell tracking. Specific examples demonstrate how certain algorithms work thus highlighting their advantages. They demonstrate how these visual tracking methods can be used to automatically track biological particulate material as manifest in 3-D+time sequences. Analyzing such datasets is a major challenge and constitutes a major bottleneck for the full exploitation of multidimensional microscopy sequences that documents studies of biological object dynamics.

Chapters 11 and 12 are closely related as both author groups study the cell cycle of a large cell population on a single cell level. Nathalie Harder and her associates introduce in Chapter 11 a computational scheme to automatically segment, track, and classify cell nuclei into different mitotic phases. This work is carried out within the European Union project MitoCheck, which aims to explore the coordination of mitotic processes in human cells at a molecular level and to contribute towards the revealing of mechanisms of cellular development. The results demonstrate that the proposed analysis system reliably classifies cells into the seven mitotic phases.

Dirk Padfield and collaborators expand on the topic in Chapter 12 by applying automatic image analysis algorithms to extract information on the cell cycle progression through the interphase, which is divided into G1, S, and G2 phases, of each cell using a cell cycle phase marker. Among other applications, this is necessary for studying the effect of inhibitor compounds that are designed to block the replication of cancerous cells. Hence, this technique holds the promise of allowing a more detailed study of the distribution of cell cycle checkpoints and perturbations. Label-free imaging of cellular systems is an important topic and highly relevant for many practical experiments. Many molecular markers that are used as nuclei stains have toxic side effects and consequently perturb the living cells. In Chapter 13, Xiaoxu Wang and his colleagues present algorithms that enable the automatic segmentation and cell counting in phase contrast images. Due to the low contrast that exists in the image intensity across membrane boundaries, this is a very challenging task. More importantly, the proposed methods show how computerized image analysis techniques can eliminate the need for fluorescent markers.

#### **Part IV: Automated Cellular and Tissue Analysis**

Going beyond analyzing individual cells, Chapters 14 through 17 present applications that relate to the structure and organization of tissues. Chapter 14 is the presentation of the Digital Fish Project written by Sean G. Megason. Rather than presenting particular algorithmic approach, this chapter highlights how imaging can play a crucial role in this study of systems biology. The goal is to understand how multiple components of a biological system interact to give rise to the function of that system. These components can include metabolites, genes, proteins, cells, and even whole organisms. Because imaging can provide anatomical landmarks as well as data that is single cell, longitudinal, and quantitative, it can provide salient and key insights that will expand our current understanding of such systems. The subject of the Digital Fish Project is a tropical fish called zebrafish (*Danio rerio*). The embryos and larvae of such fish are transparent, allowing the entire embryo to be imaged with in vivo optical microscopy. The goal of in toto imaging is to image every single cell in a tissue and eventually image the entire embryo as it develops over time. Chapter 14 promotes the concept of open data and interested researchers can access the data and contribute to its analysis.

The main goal of the work presented in Chapter 15 by Kun Huang and his collaborators is the 3-D reconstruction of tissue sections, for example, mouse placenta organ, from a set of histology sections. As it is not possible to acquire such

datasets with confocal microscopy, the challenge of sparse sampling needs to be overcome to reconstruct and analyze such datasets. New algorithms for image segmentation, registration, visualization, and quantization are necessary to address such challenges. This work is part of a mouse model phenotyping, which aims to study the roles of tumor suppressor genes in the regulation of normal cellular processes. This chapter is another example how the increased use of both histology and tagged confocal images and subsequent analyses provide more insight into fundamental mechanisms of developmental and cancer biology. Chapters 16 and 17 are closely related since both author groups study neural morphology which is broadly affected by age, genetic diseases such as Down's Syndrome, and degenerative diseases such as Alzheimer's disease. In Chapter 16, Ioannis A. Kakadiaris and his collaborators present a fully automatic system for the reconstruction of neuronal morphologies from multiphoton microscopy data. The goal of their work is to enable morphological-guided functional imaging and to create an entire library of such neuron morphologies. The proposed methods are general and make no prior assumptions about the shape of tubular structures.

Firdaus Janoos and his colleagues describe the 3-D reconstruction and classification of dendritic spines. The emphasis is on the use of computer graphics techniques that are best used on surface meshes. The advantage of such methods is that they are amenable to verification and validation. The data is obtained from a confocal microscope.

## **Part V: In Vivo Microscopy**

In order to understand the full complexity of biological systems it is desirable to study such systems *in vivo* and *in situ*. Additionally, it is necessary to establish and explain the images that are acquired on a microscopic scale in the context of higher-resolution images that are typically acquired using magnetic resonance imaging, ultrasound, or computed tomography (CT). Both of these requirements pose significant challenges for images acquisition and are the subject of ongoing and future research. Chapters 18 and 19 present examples of such efforts.

In Chapter 18, Zheng Zia and associates presents an approach to *in vivo* molecular small animal imaging. Small animals are often used as surrogates for humans in the study of normal and disease states. As it is now possible to introduce genetic mutations identical to those commonly found in human cancer tissue into the endogenous murine gene locus, the physiological relevance of such small animal models has dramatically improved. This chapter introduces optical imaging methods for small animal studies and describes a new multimodality fusion method that combines 3-D fluorescence molecular tomography and CT images to improve the overall information content.

The principle of fibered confocal microscopy is introduced in Chapter 19. This new imaging technology raises several new image processing and image analysis challenges that cannot readily be addressed by using classical approaches. Tom Vercauteren and colleagues present several tools that increase the relevance and utility of such datasets. One of these tools enables, for example, the analysis of the behavior of blood cells and vessels *in situ*. By applying image sequence mosaicking,



they effectively widen the field of view of the system and bridge the gap between the microscopic and macroscopic scales.

This field is, as Robert F. Murphy concludes in the foreword to this book, still in its infancy. The work presented here demonstrates that biomedical image analysis can enhance our understanding of complex biological processes and behaviors. This book project was initiated by a series of workshops, Microscopic Image Analysis with Applications in Biology (MIAAB). As this is a new and rapidly developing field, there are naturally a number of forums that focus on various aspects of microscopic image analysis and its applications. However, it has become abundantly clear that strong interdisciplinary collaborations are necessary to exploit the potential of image analysis methods. We are already seeing examples of discoveries that otherwise would not have been possible. While algorithm developers need to learn how certain specific application-related challenges can be addressed, it is imperative that researchers in the life sciences develop a good understanding of what advantages these technologies can offer. The goal of this book is to facilitate this exchange and contribute to an increased collaboration between these fields. The presentation of the applications is certainly not complete, and this volume is a presentation of selected examples as opposed to an encyclopedic review of the state of the art, but we hope that this book contributes to achieving this goal.

## Acknowledgments

We would like to express our gratitude to Dimitri Metaxas (Rutgers University), Ross Whitaker (University of Utah), and Stephen Lockett and Terry Yoo (both of NIH) as they have supported the MIAAB workshops in many ways. We are particularly grateful that Wayne Yuhasz, executive acquisitions editor at Artech House, strongly encouraged this book project. His colleagues, Barbara Lovenvirth and Rebecca Allendorf, were instrumental in guiding us to translate the plan into reality. It should be duly noted that, without the contributions of the many authors, we could not have compiled this volume. We owe thanks to all of them for their patience and timely interaction. Finally, we owe thanks to our individual families for letting us spend the time to complete the task of compiling this volume

*Jens Rittscher  
Raghu Machiraju  
Stephen T. C. Wong  
Editors  
July 2008*

# Introduction to Biological Light Microscopy

Gunjan Agarwal

## 1.1 Introduction

The aim of this chapter is to give a quick overview of light microscopy and its applications for biological samples. Our goal is not to give a detailed overview of microscopy and the underlying hardware design, as several excellent texts (cited in the references) are available for this purpose. Instead, we introduce the reader to the various forms of microscopy, contrast mechanisms, and sample preparation techniques commonly employed for biological light microscopy. We conclude with the common sources of artifacts and noise in light microscopy and discuss future trends in biological light microscopy. The reader should note that more details can be found in Chapters 3 and 4.

## 1.2 Need for Microscopy

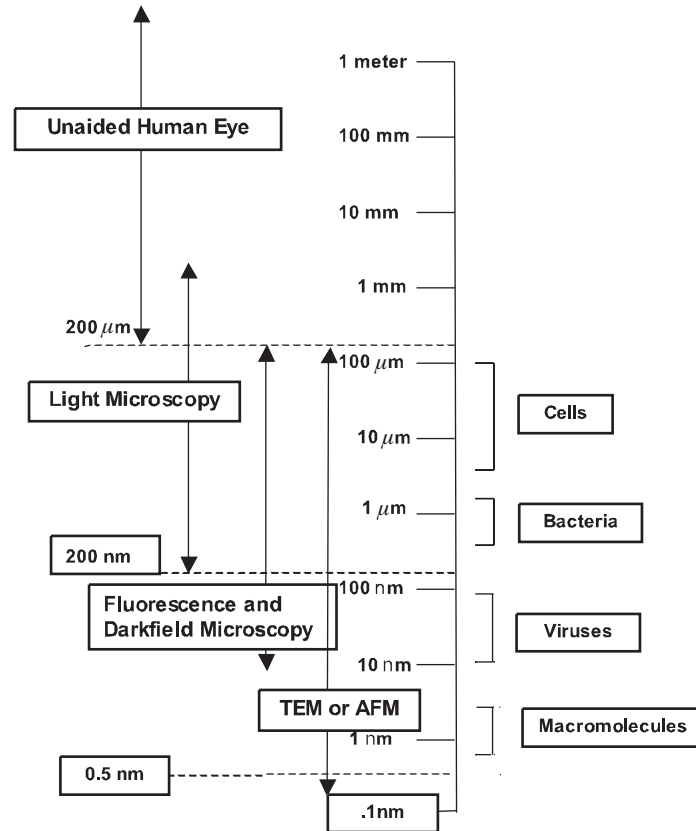
The human eye, though profound in its capacity as a sense organ, is limited in several aspects. It can only detect wavelengths in the visible range, namely 400 to 750 nm, and can perceive contrast, “C,” only as differences in intensity given by:

$$C = \log_{10}(I_1/I_2)$$

where  $I_1$  and  $I_2$  are the intensities of two regions in the image formed. The resolution of the human eye is limited to  $\sim 0.1$  mm, and our eyes are insensitive to the state of polarization or phase differences in light.

The microscope is a device that helps us overcome these limitations of the human eye by enabling us to visualize objects normally not possible by the unaided human eye. Principally, a good microscope achieves this by increased magnification, contrast, and resolution in the image of the object formed.

These days a number of different *probes* can be used to perform microscopy, such as light waves, electron waves, or physical probes as in scanning probe microscopy (SPM) techniques. In addition, these probes can either be used to *scan* the sample, as in scanning microscopy techniques (laser scanning microscopy, scanning electron microscopy, SPM) or, in the case of wavelike probes, be made to *transmit through* the sample, as in transmitted light microscopy or transmitted electron microscopy. These microscopic techniques enable us to visualize and study an entire gamut of micro- and nanoscale objects ranging from tissue sections and cells to single molecules and nanoparticles (Figure 1.1). The past few decades have witnessed a sharp rise in the advancement and application of microscopic techniques for study of biological samples, with innovations in microscope design, sample prepa-

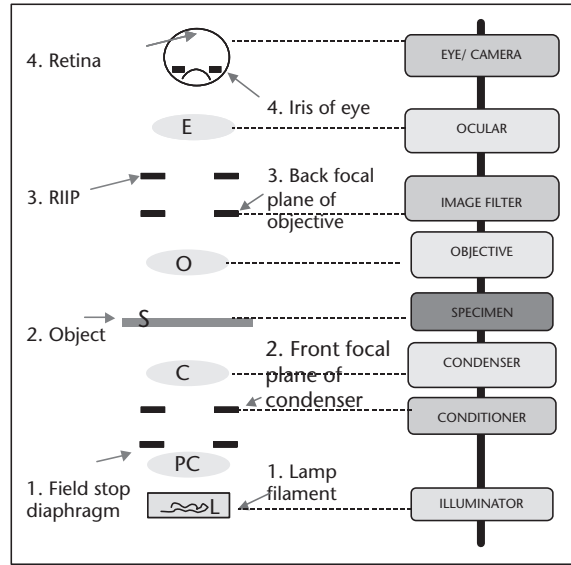


**Figure 1.1** Microscopic techniques enable us to visualize objects such as cells, microorganisms, and macromolecules, which are much beyond the resolution limit of the unaided human eye. (TEM: transmission electron microscopy; AFM: atomic force microscopy.)

ration techniques, and image acquisition. However, to understand microscopy, image formation, and image analysis, it is almost always useful to begin with the very first and most commonly used microscopy technique—transmitted light microscopy.

### 1.3 Image Formation in Transmitted Light Microscopy

Since its origin as a simple microscope (consisting of a single lens) more than five hundred years ago, followed by the development of the compound microscope around 1600 by the Janssen brothers in the Netherlands and Galileo in Italy, light microscopy equipment has come a long way from what is known today as the modern compound microscope [1]. The compound microscope consists of number of elements; the principal ones are the illumination system, condenser, specimen, objective, image filter, eyepiece, and the detection system, as illustrated in Figure 1.2. The microscope is defined by two sets of conjugate planes known as the *field planes* and the *diffraction planes*. Each set of planes needs to be correctly aligned along the microscope axis to ensure proper sample illumination, image



**Figure 1.2** Schematic representation of the elements of a transmitted light microscope: L = lamp, PC = precondenser lens, C = condenser, S = specimen, O = objective, E = eyepiece. The microscope consists of two sets of conjugate planes—the field planes (where the real images are formed) and the diffraction or aperture planes (where diffraction patterns are formed; these are also the places to insert apertures or optical elements for conditioning the illumination light and/or to improve contrast in the diffraction pattern formed). By aligning one set of conjugate planes, the other set automatically gets aligned. The schematic shown represents an *upright* light microscope.

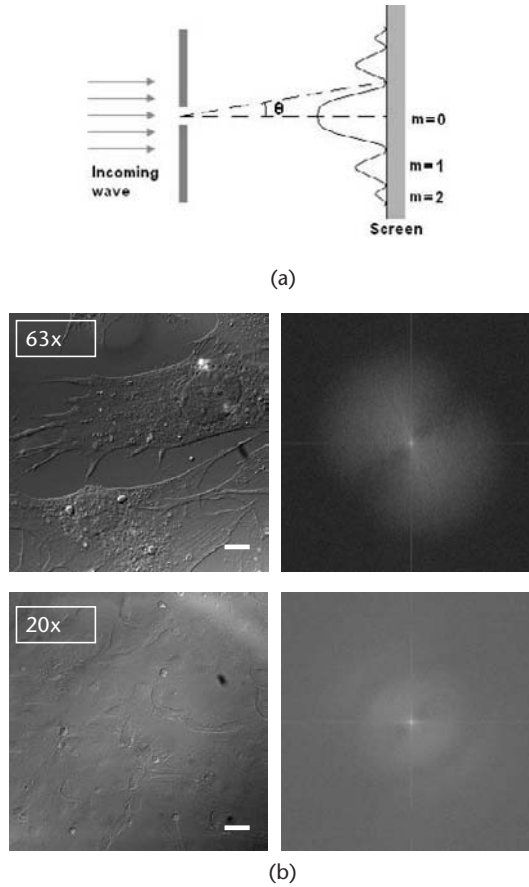
formation, magnification, and contrast. The standard procedure for aligning the light microscope is called Koehler alignment [2].

The physical principle behind image formation for transmitted light microscopy is diffraction. As illustrated in Figure 1.3(a), when light of wavelength  $\lambda$  is incident on an object at an angle  $\theta$ , it can get diffracted if the object consists of features of size  $\sim d$ , defined as:

$$d \sin \theta = m \lambda$$

where  $m$  is the order of diffraction maxima formed. It is the interference or *superposition* of diffraction patterns arising from various features in the object that give rise to contrast in the image. How are the diffraction patterns made to interfere? Here comes the ability of the objective lens, positioned right after the sample, that collects the “nearly parallel” diffracted rays and makes them “interfere” at its back focal plane. So if one looks at the back focal plane of an objective lens, one would indeed find just the diffraction pattern of the object—see Figure 1.3(b). How complex and true the diffraction pattern is will depend on the ability of the objective lens to collect the diffraction pattern of higher orders. This ability of the lens is also called its *numerical aperture* (NA), defined as follows:

$$\text{NA} = n(\sin \alpha)$$



**Figure 1.3** (a) Diffraction of light by a slit of width  $d$  ( $d \leq \lambda$ ) results in a diffraction pattern on a screen characterized by maxima and minima governed by the equation  $d \sin \theta = m\lambda$ , where  $m$  is the “order” of the diffraction maxima. Note that the central undiffracted beam ( $m = 0$ ) has the highest intensity, and the intensity of the diffraction maxima decreases significantly with increasing values of  $m$ . (b) Microscopic images of mouse fibroblast cells acquired using (top) a high NA, 63x and (bottom) a low NA, 20x objective. On the right is the corresponding Fourier transform (FT) of these images. Note the more complex FT for 63x objective as compared to 20x, demonstrating that a larger NA lens can acquire diffraction patterns of even higher orders. This complex diffraction pattern when reconverted to its real image (as on the left) helps in resolving the details in the object.

where  $n$  is the refractive index of the medium of the lens and  $\alpha$  is its half angle of illumination.

That the objective lens collects nearly parallel diffracted rays and makes them interfere underlies the condition of what is called *Fraunhofer diffraction* in wave optics. In this case, the diffraction pattern is the Fourier transform of the object. Concepts like *spatial filtering* can therefore be used on this object diffraction pattern formed at the back focal plane of the objective to select or block certain spatial frequencies in the image formed [3].

Image formation in the microscope results due to progression of light rays from the diffraction maxima (at the back focal plane of the objective) and their interference at the *real intermediate image plane* (RIIP) to form a “real” image of the sample (Figure 1.4). In fact, the interference pattern formed at the RIIP is again a Fourier transform of the diffraction pattern of the object, or in other words a real image conjugate to the object. Therefore the object plane and the RIIP belong to the same set of conjugate field planes as described in Figure 1.2. In transmitted light microscopy, the illumination light is often modified or “conditioned” by means of special optical elements to achieve better contrast. Such conditioning elements are placed at the condenser focus, and their “conjugate” element at the objective focus. The conditioning and the conjugate elements together help in enhancing the “interference pattern” of the diffracted rays, which is further described in Sections 1.4 through 1.7.

## 1.4 Resolution, Magnification, and Contrast in Microscopy

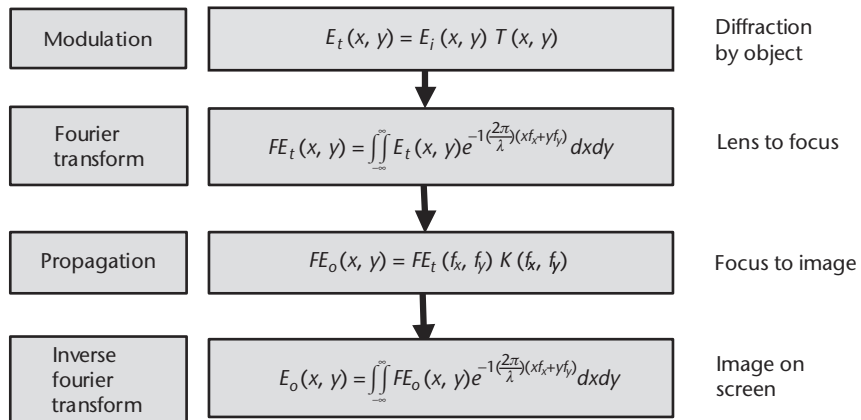
As discussed earlier, while a high NA is essential for generating as true a diffraction pattern as possible, the NA also governs the resolution and contrast in microscopy. The minimum distance  $d$  resolved by a microscope is defined by the Rayleigh’s criterion of *resolution* given by

$$d = 0.61 \lambda / NA$$

when  $NA_{cond} \geq NA_{obj}$  (as in fluorescence or dark field microscopy), and

$$d = 1.221 \lambda / (NA_{cond} + NA_{obj})$$

when  $NA_{cond} < NA_{obj}$  (as in bright field, DIC, or phase contrast microscopy).  $NA_{cond} < NA_{obj}$  are the numerical apertures of the condenser and objective, respectively.



**Figure 1.4** Image formation in transmitted light microscopy occurs by diffraction of light by the specimen, collection of the diffracted rays by the objective, formation of the object diffraction pattern at the lens focus, and formation of the real image by further propagation of the diffraction rays.



Two objects are defined to be resolved if the central (0th order) diffraction maxima of one object overlaps with the first diffraction minima of the other object in the image plane. For objects of sizes below this resolution limit ( $d \sim 260$  nm) such as single molecules or subcellular features, even though certain contrast mechanisms (e.g., dark field) may enable one to visualize these objects, it is nearly impossible to ascertain their correct dimensions.

Besides the lateral resolution defined previously, the microscopic image also has a finite z-resolution or depth of field,  $Z$ , given by:

$$Z = n\lambda / \text{NA}_{\text{obj}}^2$$

where  $n$  is the refractive index of the medium between the lens and the object.  $Z$  defines the distance along the axis of the lens where the image is in “focus,” or in other words it is the thickness of the image plane itself.

The magnification ( $M$ ) is a property of the lens and is dependent on the distance of the object from the lens ( $d_o$ ) and its corresponding image distance ( $d_i$ ).

$$M = d_i / d_o \text{ or}$$

$$M = f / (d_o - f)$$

In microscopy, since it is necessary for the objective lens to form a real, magnified image of the object at the RIIP,  $d_o$  needs to be such that  $2f > d_o > f$ . Magnification in microscopy results *only* from the lens(es) through which light diffracted by the object passing through, such as the objective and the eyepiece (Figure 1.2), and is given by

$$M = M_o \times M_e$$

where  $M_o$  and  $M_e$  are the magnifications of the objective and eyepiece lenses, respectively. In modern microscopes, the objective is often a combination of lenses (to remove aberrations and/or to achieve infinity corrected optics), and in such cases  $M_o$  will be the effective magnification resulting from that combination of lenses. It is the combination of the magnification and the NA of the lens that governs the brightness ( $B$ ) of the image:

$$B \propto (\text{NA}/M)^2 \text{ (for transmitted light)}$$

$$B \propto (\text{NA}^4 / M^2) \text{ (for epi-illumination)}$$

Therefore, the selection of lens for microscopy will depend on the magnification desired, resolution, brightness, and the microscopic technique employed. Often for routine examination of cells or tissue sections, a 20x objective is fine whereas for studies involving subcellular features or protein polymerization, a high NA lens like the oil immersion 63x or even 100x would be the objective of choice.

Contrast in transmitted light microscopy can only be achieved in two ways: (1) exploiting the capability of the human eye to distinguish between different wavelengths (or colors), and (2) generating sufficient modulation in intensities in the image formed so that it is detectable by the human eye. Contrast can thus arise

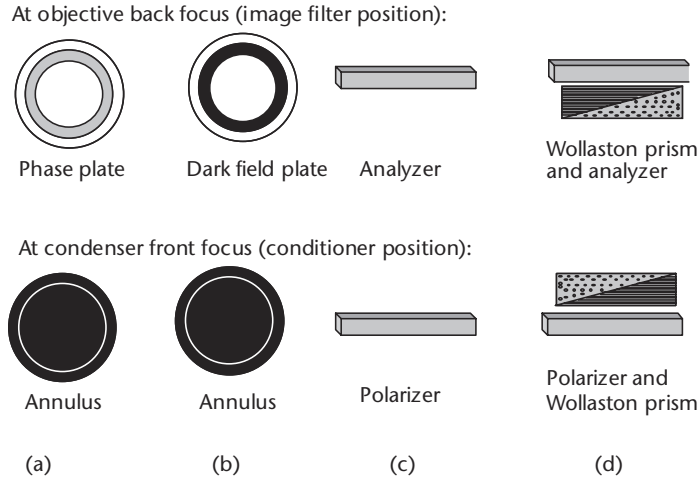
from light absorption, reflection, spatial variation in refractive index, scattering, diffraction, birefringence, fluorescence, and similar optical phenomena, which are exhibited by specific components of biological samples. Control of image contrast in the microscope can depend upon proper setting of aperture diaphragms, degree of optical aberration, contrast mechanism employed, the type of specimen, and the characteristics of the detector. Though one can see that a high NA is beneficial for a high resolution, a high NA may be detrimental to contrast in microscopy, as it may also enable stray or nonparaxial rays to enter the lenses. Since lens design is usually based on the assumption that only paraxial rays (rays nearly parallel to the lens axis) enter the lens, the nonparaxial rays in high NA lenses are sometimes the cause for *lens aberrations* [2] like astigmatism and so on.

For achieving contrast through color, biological samples are often stained for color using dyes or antibodies that could be either chromophores for normal bright field microscopy or fluorophores for fluorescence microscopy. For unstained samples, the generation of contrast involves enhancing the interference contrast between the diffracted and undiffracted rays by means of a conditioning element and its conjugate, resulting in techniques like phase contrast, dark field microscopy, polarization, or differential interference contrast microscopy as described in the following sections.

## 1.5 Phase Contrast Microscopy

The phase contrast microscopy is the most popular method for studying unstained biological samples that are transparent, like live or fixed cells. Phase contrast is based on the principal discovered by Zernike that light diffracted by a non-absorbing object has a phase shift of  $\lambda/4$  [4]. Thus, in phase contrast microscopy, by use of a special condenser annulus and its complementary phase ring, the amplitude of the central, undiffracted light that ordinarily passes through and around the specimen is reduced. These filters also introduce an additional phase shift of  $\lambda/4$  in the undiffracted light—see Figure 1.5(a). The diffracted or scattered light that falls mostly outside the phase ring does not suffer any phase change. Thus, due to presence of phase plate, the resultant phase difference between diffracted light (by the specimen) and undiffracted light is  $\sim \pm\lambda/2$ . These diffracted and undiffracted light rays then interfere at the image plane forming well-defined maxima or minima resulting in an increased contrast in the image formed.

Phase contrast images are often characterized by halos and shadows, which are low-intensity images of opposite contrast formed due to some amount of the diffracted rays passing through the phase ring. The phase annuli do limit the working NA of the optical system to a certain degree, thus reducing resolution. Phase contrast does not work well with thick specimens (such as several layers of cultured cells) because shifts in phase occur from areas slightly below or slightly above the plane that is in focus. Such phase shifts confuse the image and distort image detail. Phase contrast works best for monochromatic (green) light.



**Figure 1.5** Optical elements used to generate contrast in: (a) phase contrast, (b) dark field, (c) polarization, and (d) DIC microscopy. The bottom element in each set is used to modify the way the sample is illuminated and is placed at the condenser focus. For instance, the condenser annulus in (a and b) is used to illuminate the sample through a hollow cylinder of light, while the polarizer in (c and d) polarizes the light used for illuminating the sample. The top element is used to enhance contrast in the diffraction pattern formed by either reducing (as in a) or blocking (as in b) the undiffracted light or by detecting polarization and other changes introduced by the sample in the illumination light (as in c and d). This element is placed at the objective focus.

## 1.6 Dark Field Microscopy

Dark field microscopy is achieved by blocking off the central undiffracted rays of light (for  $m = 0$ ) from reaching the objective and/or the image plane. Only light scattered (reflected, refracted, diffracted) by the sample appears in the objective and in the image. This can be achieved by a setup similar to phase contrast wherein the phase plate has an opaque region that completely blocks off the undiffracted, direct light—see Figure 1.5(b). Alternatively, dark field can also be achieved by means of special condensers, such as the Abbe’s dark field condenser, which uses a hollow cone of light for illumination and where  $NA_{cond} \gg NA_{obj}$  [2]. The background in dark-field microscopy is therefore “dark,” and extremely high contrast is generated as scattered light from objects even below the limit of resolution can also be detected. The presence of single molecules and particles less than  $\sim 200$  nm in size can even be detected using this technique. However, for dark field microscopy, the specimen preparation and optical elements have to be very clean as any dirt/defect will also exhibit good contrast in the image. Second, darkfield illumination is less useful in revealing internal details in unstained samples.

## 1.7 Polarization Microscopy

This technique is based on use of polarized light, wherein the electric vector in the light wave is restricted to a specific plane. This is achieved by means of optical

components called *polarizer* made up of materials like calcite crystals. As shown in Figure 1.5(c), a polarizer kept at the condenser front focal plane will condition or polarize all incident light on the sample. The state of polarization can be detected by its conjugate element, the analyzer kept at the objective back focal plane. If the transmission axis of the polarizer and the analyzer are parallel, one can expect maximum intensity ( $I_0$ ) in the image plane, while if they are oriented at an angle  $\theta$ , the resultant intensity ( $I$ ) is given by the Malus law as

$$I = I_0 \cos^2 \theta$$

A good polarization microscope should have a nearly complete extinction of light when  $\theta = 90^\circ$  or the polarizer and analyzer are *crossed*. At this setting, any signals of increased light intensity would result from the properties of the sample to *rotate* the plane of polarization of the incident light, through properties called optical anisotropy or birefringence. It is often useful to have a rotatable sample stage for a polarization microscope to detect optical anisotropy in the sample. For quantitative analysis, specially designed compensator plates are used to determine the degree of optical anisotropy in the sample [2]. Polarization microscopy is useful for detecting the presence of optically anisotropic materials such as for visualization of microtubules in the mitotic spindle, chromatin within maturing spermatids, and the biocrystalline skeletal spicules in larval echinoderms [5].

## 1.8 Differential Interference Contrast Microscopy

Differential interference contrast (DIC) in some aspects is a combination of phase contrast and polarization microscopy. DIC relies on the presence of phase gradients in the sample, which can arise due to changes in optical thickness, the occurrence of edges or refractive index changes in biological samples. Specially designed DIC prisms (Wollaston or Normanski prisms), consisting of two geometrically identical quartz crystals with optic axis perpendicular to each other are utilized to shear the incident beam—see Figure 1.5(d). The resulting beam consists of sets of rays that are sheared spatially and have a different and definite phase differences between them before interacting with the specimen. This shear and phase shift is not constant for all the rays but differs for each pair of rays such that the incident beam on the sample consists of both a shear gradient and a phase gradient. The sample transmits and/or scatters the waves and introduces an additional phase difference between two sheared waves. Any change in refractive index, difference in optical path, chirality, or optical anisotropy can introduce a phase change between the sheared sets. The second DIC prism recombines the transmitted sheared beams, which can result in linear, circular, or elliptically polarized light emerging from the second DIC prism. The analyzer converts this emergent beam to linearly polarized light of various intensities that interfere at the image plane.

In DIC, optical path length gradients in the direction of wavefront shear are primarily responsible for contrast. Steep gradients in path length generate excellent contrast; regions having very shallow optical path slopes, such as those observed in extended, flat specimens, produce insignificant contrast and often appear in the

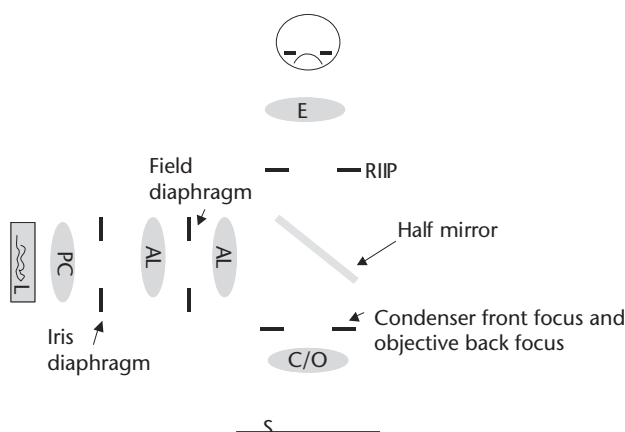
**Table 1.1** Comparison of Phase Contrast and DIC Microscopy

<i>Phase Contrast</i>	<i>DIC</i>
Interference between a reference (undiffracted) wave and diffracted waves	Interference between two sheared waves
Image intensity varies as a function of specimen optical path length magnitude	Optical path length <i>gradients</i> in the direction of wavefront <i>shear</i> are primarily responsible for contrast
Images can have “halos” and “shadows”	Images display the pseudo 3D relief shading
Cannot generally detect birefringence	Can detect birefringence also

image at the same intensity level as the background. DIC images often display the pseudo three-dimensional relief shading, which can be excellent to study the surface topography of cells. DIC can also detect birefringence often present in biological samples. Phase contrast and DIC are the two most popular techniques for studying unstained biological samples and are often used in conjugation with video enhancement [6]. Table 1.1 lists their comparative strengths and limitations.

## 1.9 Reflected Light Microscopy

As the name suggests, reflected light microscopy is the method of choice for imaging specimens that remain opaque even when ground to a thickness of 30 microns. It is also often called the incident light microscopy or epi-illumination microscopy, as the illumination of the sample is from above. As shown in Figure 1.6, the objective lens serves as both condenser and the objective. Therefore there is no need to adjust the NA (of the condenser) when changing objectives. The aperture



**Figure 1.6** Schematic representation of reflected light microscopy in an *epi-illumination* configuration. Besides the precondenser (PC), additional auxillary lenses (AL) are used to direct the illumination beam to the half-mirror. By means of a half-mirror, which partly reflects (the illumination light) and partly transmits (the reflected light), the objective here serves as both the condenser and the objective. Compare the positions of the field and the diffraction planes here with that for a transmitted light microscope in Figure 1.2.

diaphragm controls the angle of light reaching the specimen (which is generally kept 60% to 95% open and is sample dependent). The magnification is defined in the same manner as transmitted light microscopy (i.e., it is a product of  $M_o$  and  $M_e$ ). Since the objective also serves as the condenser, oil-immersion lenses are less frequently used, the working distance is generally larger, and all objectives in a turret may have different parfocal distances. Most contrast mechanisms for unstained samples are easily achieved even in reflected light as described here:

**Bright field:** Absorption, reflection, or diffraction by the specimen can lead to readily discernible variations in the image (from black through shades of gray, or color).

**Dark field:** Reflected dark field is very valuable if one is looking for small height differences on a specimen or if the specimen has a lot of height differences. In reflected light, dark field will show the true color of the specimen better than bright field.

**Polarized light:** This is mostly useful in materials science when one needs to study bireflectance or bireflexion (i.e., the change in intensity of the light reflected from a sample [mineral] as it is rotated on the microscope stage in polarized light). This property can be considered analogous to *birefringence* for transmitted light where for the refractive index is dependent on the plane of polarization of transmitted light.

**Phase:** Phase specimens show little difference in intensity and/or color; their feature details are extremely difficult to distinguish and require special treatment or contrast methods for reflected light microscopy.

**DIC:** Slopes, valleys, and other discontinuities on the surface of the specimen create optical path differences, which are transformed by reflected light DIC microscopy into amplitude or intensity variations that reveal a topographical profile. Unlike the situation with transmitted light and semi-transparent phase specimens, the image created in reflected light DIC can often be interpreted as a true three-dimensional representation of the surface geometry, provided a clear distinction can be realized between raised and lowered regions in the specimen.

**Stereomicroscope:** The human eyes and brain function together to produce what is referred to as *stereoscopic vision*, which provides spatial, three-dimensional images of the objects surrounding us. This is because of the brain's interpretation of the two slightly different images received from each of the retinas. The average human eyes are separated by a distance of approximately 64–65 mm, and each eye perceives an object from a somewhat different viewpoint that differs by a few degrees from the other. When transmitted to the brain, the images are fused together but still retain a high degree of depth perception. The stereomicroscope takes advantage of this ability to perceive depth by transmitting twin images that are inclined by a small angle (usually between 10 and 12 degrees) to yield a true stereoscopic effect. This is achieved by using an objective that forms the image at infinity. A telescopic eyepiece lens is used to focus the objective image to the eye; in fact, two eyepieces at slight inclination are used. Magnification is achieved by a zoom lens (hence stereomicroscopy

has limited magnification). Stereomicroscope thus results in a 3D topographical view and is most commonly used as a dissection microscope for biological samples.

## 1.10 Fluorescence Microscopy

Fluorescence microscopy is different from the conventional transmitted light microscopy techniques described in Sections 1.4 through 1.7 in the sense that, as with the reflected light microscopy, the objective does not collect light transmitted through the sample. Fluorescence is the absorption of photons by a molecule (also known as excitation) followed by the emission of photons of higher wavelength than those absorbed. The path of light in fluorescence microscopy is therefore different from all other techniques discussed previously, principally because there is no illumination of the sample—only *excitation* of the sample. By using a specially designed *filter cube* consisting of a set of three filters—an excitation filter, a dichroic and a suppression filter—the excitation light after being incident on the sample is prevented from reaching the objective. Only the fluorescence or the emitted light from the sample is allowed to reach the objective, after which the principals of image formation apply as described in Section 1.2. It is interesting to note that fluorescence microscopy images in some sense are similar to those of dark field microscopy as the background, which is usually nonfluorescent as “dark.” But unlike dark field microscopy, even objects inside the specimen can emit fluorescence, and hence one can also observe internal details of the sample. It is imperative that fluorescence microscopy involves use of fluorescent probes capable of emitting light in the detectable visible range (usually defined by the filters used). For biological applications, three principal types of probes are used for fluorescence microscopy dyes, quantum dots, and intrinsically fluorescent biomolecules [7], all of which need to be *conjugated* to specific biomolecules for analysis of their behavior, spatial or temporal distribution, and other processes. Table 1.2 summarizes the most popular contrast-generating microscopic technique based on the specimen type.

## 1.11 Light Microscopy in Biology

Biological samples fall into three main categories: single molecules, cells, and tissues. Because of the inherent resolution limit of light microscopy, the most extensively studied samples are cells (cytology) and tissues (histology). Isolated single molecules, though sometimes detectable by light microscopic techniques, are mostly beyond its resolution limits and are better suited for TEM or AFM examinations. Depending upon the type of samples to be examined, the light microscope can be used in one of the two settings: This first is the upright microscope, where the objective turret is fixed and the sample stage is adjustable along the microscope axis to enable focusing. This is especially desirable for high-magnification studies of samples contained on glass slides. The second setting is the inverted microscope, where the sample stage is fixed and the objective turret is moved along the microscope axis to focus the sample. This configuration is especially desirable for samples that may be affected by movement of the sample stage, such as cells kept



**Table 1.2** Selection of Imaging Technique for Biological Specimens

<i>Specimen Type</i>	<i>Imaging Technique</i>
Transparent specimens and phase objects:	Phase Contrast
Bacteria, spermatozoa, cells in glass containers, protozoa, mites, fibers	(DIC)
Light scattering objects:	Darkfield illumination
Diatoms, fibers, hairs, fresh water microorganisms, radiolarians, and so on	Phase contrast and DIC
Light refracting specimens:	Phase contrast
Colloidal suspensions, powders and minerals, liquids	DIC
Amplitude specimens:	Brightfield illumination
Stained tissue, naturally colored specimens, hair, and fibers	
Insects and marine algae	
Fluorescent specimens:	Fluorescence illumination
Cells in tissue culture, fluorochrome-stained sections	
Smears and spreads	
Birefringent specimens:	Polarized illumination
Mineral thin sections	
Liquid crystals	
Melted and recrystallized chemicals	
Hairs and fibers	
Bones and feathers	

in dishes containing fluid media, and also to better access the sample chamber for perfusion, microinjection, and so on. Another advantage is that one can use high NA objectives that have small working distances even with sample chambers that do not permit approach from above by bringing the objective from below the sample.

Depending upon the microscope configuration used (upright versus inverted), contrast mechanism employed, and specifications of the objective and condenser lenses used, the samples may be prepared on glass slides and cover slips of defined thickness or on plastic or glass cell-culture dishes. Besides identifying the correct substrate/chamber for mounting the specimen, biological samples require special considerations for microscopic examinations.

Although isolated biomolecules typically fall below the limit of resolution of light microscopy, the contrast mechanism techniques described in Sections 1.4 through 1.7 are often able to resolve polymerization of biomolecules. Microscopy has enabled the study of polymerization kinetics, rheological properties, and even-protein-protein interactions for protein polymers such as actin by total internal reflection microscopy [8], microtubules by fluorescence microscopy and other techniques [9], sickle-cell hemoglobin by video-enhanced DIC [10], collagen by dark-field microscopy [11], or fluorescence microscopy [12]. For these studies, usually the purified solution of proteins at concentrations ranging from tens of micrograms to a few milligrams is kept in a sealed glass slide and diffusion, fluctuations, growth, or depolymerization mechanism and kinetics of the fibers formed are studied often through video-enhanced microscopy.

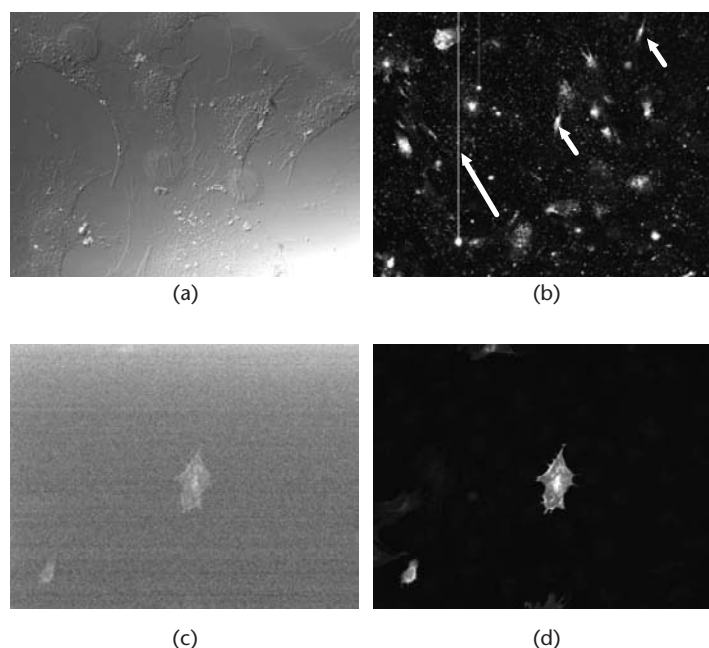


Cultured or isolated cells from plants or animal tissue can be readily examined using light microscopy. Since the cell samples need to be kept in their appropriate cell-culture media or buffer solutions, the inverted microscope is preferred for these studies. Microscopy of live cells involves specially designed chambers where the cells can be kept at desired temperatures (usually 37°C) and perfused with desired gases. It is often desirable to “fix” the samples in as lifelike a condition as possible. The fixation of cell samples usually involves use of a cross linking fixative such as formaldehyde, which binds the proteins and lipids together in their current position without disrupting their structure. An even stronger fixative, glutaraldehyde, is less commonly used for cell fixation in light microscopy, as it results in a strong autofluorescence signal that can interfere with the image, especially when using fluorescence microscopy. Formaldehyde has the added advantage that its reaction is reversible, and prolonged washing of the samples can remove much of the formaldehyde bound to the cells. Formaldehyde is especially beneficial for immuno-cyto or histochemistry because it has less extensive crosslinking and better penetration of antibodies. Almost all tissue samples undergo a specialized sample preparation procedure usually involving fixation, dehydration, paraffin embedding, and microtoming. The microtomed sections of tissue samples are usually 200 nm in thickness, which enables optimal penetration of the incident light and image formation. These histological sections are often stained with dyes (like hemotoxin and eosin) or labeled with antibodies to reveal localization of specific biomolecules at the subcellular level.

## 1.12 Noise and Artifacts in Microscopic Images

One often encounters artifacts or noise in microscopic images. A chief cause for this is improper alignment of the microscope, especially if the microscope is not Koehler aligned and used for DIC or phase contrast microscopy, or improper selection of lenses and optical elements used—see Figure 1.7(a). A second prime reason could be inadequate cleanliness of the optical elements, namely the condenser and objective lens (especially when moving from oil-immersion to air) and the eyepiece and any filters along the light path. And third, proper sample preparation is a key to high-quality microscopic images. Improper mounting of slides, uneven thickness of the sample section, dirt on the sample chamber or slide can all adversely affect the quality of microscopic images. Finally illumination sources should be periodically checked for the lifetime of the bulbs used, especially if the illumination intensity is unusually low and/or the lamp is fluctuating.

With the advance of electronic imaging technologies, electronic and video imaging is now a popular image acquisition technique for most modern light microscopes. Video imaging not only enhances image contrast and magnification, but also enables faster image acquisition (up to 30 frames/sec) and real-time imaging. Any light microscope with a camera port can be adapted for digital image acquisition or video microscopy by coupling a video camera with its control unit, a digital image processor, a TV monitor, and a VCR. However, accompanying these are also issues that can induce *electronic noise* in the microscopic images, especially for video cameras. In electronic image acquisition, one may have noticed that the



**Figure 1.7** Artifacts and noise in microscopic images. (a) Uneven illumination in a DIC image of mouse fibroblast cells due to improper Koehler alignment of the microscope. (b) Oversaturation of the detector by strong fluorescence intensities results in streaks or smears (arrows) in the image. (c) An image acquired using a net intensity below the detector threshold shows “snow” or granularity in the image. (d) Proper exposure time and intensity help overcome the electronic noise present in (c).

image brightness needs to be below the detector saturation limit to avoid streaks, smears, or *oversaturated* images—see Figure 1.7(b). On the other hand, the image intensity also needs to be above a specific threshold level or the image acquisition time and the camera aperture need to be properly adjusted to avoid snow or granularity in the image—see Figures 1.7(c, d). This is primarily because the signal voltage from camera or image tube needs to exceed the root mean square (rms) noise of the preamplifier in the camera. Additionally, electrical fixtures such as light sources, amplifiers, lasers, and motors can generate RF spikes or noise pulses that can appear as spikes across the image. Such noise can usually be overcome by proper grounding of the fixtures. In general, the higher the sensitivity of the camera, the more susceptible it will be to electronic noise.

A third category of noise that can arise in microscopy is acoustic noise arising due to mechanical vibrations. Such vibrations can be encountered through exhaust fans, refrigerators, vacuum pumps, or street noise. The most popular way to shield the microscope from acoustic noise arising from the floor or building is by mounting the microscope on a vibration isolation table, which has feedback-controlled pneumatic legs. Additional reduction in acoustic and other noises can be achieved by placing the microscope in a relatively isolated area, keeping the equipment covered, and maintaining a consistent temperature and humidity environment.

## 1.13 Trends in Light Microscopy

Microscopy of biological samples has undergone rapid advances since its inception in the seventeenth century through the coming together of researchers from interdisciplinary fields like biology, physics, chemistry, and engineering. Not only have there been advances in lens design and correction for aberrations but also in improved filters, DIC prisms, and cameras. The recent years have witnessed a strong contribution in design of new fluorescent probes, which have led to unprecedented breakthroughs in the resolution achievable through light microscopy. A number of fluorescence-based techniques have come in vogue, which not only enable nearly single-molecule imaging but provide new insights into functions of biomolecules both in *in vitro* and in live cells. Techniques like confocal microscopy (laser scanning, multiphoton, or spinning disk) [13, 14], combined with fluorescence resonance energy transfer (FRET), fluorescence lifetime imaging (FLIM) [15], total internal reflectance fluorescence (TIRF), and fluorescence recovery after photobleaching (FRAP) are rapidly becoming popular for several biological investigations.

Another facet of novel improvements in light-microscopy involves a combination of fluorescence capabilities with conventional contrast generation techniques in microscopy. For instance, an alternative approach to detect fluorescence polarization (FP) in FRET (FP-FRET) has been achieved by a combination of fluorescence and polarization microscopy [16]. FP-FRET is based on measuring fluorescence anisotropy of the emitted fluorescence and provides high contrast and unambiguous indication of FRET. Multicolor nonlinear microscopy of living tissue has been achieved by multiphoton excitation of intrinsically fluorescence biomolecules and analysis of second harmonic generation by supermolecular structures [17], also called the second-harmonic imaging microscopy (SHIM) [18]. This technique enables resolution and detail of standard histology without the use of exogenous stains. In another study, a combined system of DIC and TIRF with a transmitted all-side polished dove prism has been utilized to enable direct monitoring of fluorescent nanoparticle complexes as a gene delivery target in living cells [19]. In these experiments, while the DIC image provided precise information of the living cellular structures, the TIRF images of the nanoparticle complexes provided precise information on the distance between the cell membrane and the complexes ( $< 200$  nm) as well as the real-time localization of the individual complexes in the cells.

Cutting-edge research in microscopy continues to be aimed at improving the resolution in microscopic images. Recent work using stimulated emission depletion (STED) to quench excited fluorophores at the rim of the focal illumination spot has enabled a substantial increase in resolution to below the diffraction limit, giving a spot size of 100 nm [20]. The design of *switchable* fluorescent probes has enabled photoactivated localization microscopy (PALM) [21], wherein the researchers label the molecules they want to study with a photoactivatable probe and then expose those molecules to a small amount of violet light. The light activates fluorescence in a small percentage of molecules, and the microscope captures an image of those that are turned on until they bleach. The process is repeated thousands of times, with each repetition capturing the position of a different subset of molecules.

## Acknowledgments

The authors would like to acknowledge Dr. Cosmin Mihai for his contribution to Figures 1.3 and 1.7 and for feedback on this chapter.

## References

- [1] Abramowitz, M., *Microscope Basics and Beyond*, rev. ed., Olympus Microscopy Resource Center, 2003, <http://olympusmicro.com>.
- [2] Murphy, D. B., *Fundamentals of Light Microscopy and Electronic Imaging*, New York: John Wiley and Sons, 2001.
- [3] Inoué, S., and K. R. Spring, *Video Microscopy: The Fundamentals*, 2nd ed., New York: Plenum Press, 1997.
- [4] Zernike, F., "How I Discovered Phase Contrast," *Science*, Vol. 121, No. 3141, March 11, 1955, pp. 345–349.
- [5] Inoué, S., "Polarization Microscopy," *Curr. Protoc. Cell Biol.*, Chap. 4. Unit 4.9, February 2002.
- [6] Salmon, E. D., and P. Tran, "High-Resolution Video-Enhanced Differential Interference Contrast (VE-DIC) Light Microscopy," *Methods Cell Biol.*, No. 56, 1998, pp. 153–184.
- [7] Roessel, P. V., and A. H. Brand, "Imaging into the Future: Visualizing Gene Expression and Protein Interactions with Fluorescent Proteins," *Nature Cell Biol.*, Vol. 4, Jan 2002, pp. E15–E20.
- [8] Kuhn, J. R., and T. D. Pollard, "Real-Time Measurements of Actin Filament Polymerization by Total Internal Reflection Fluorescence Microscopy," *Biophysical Journal*, Vol. 88, February 2005, pp. 1387–1402.
- [9] Waterman-Storer, C. M., "Microtubules and Microscopes: How the Development of Light Microscopic Imaging Technologies Has Contributed to Discoveries About Microtubule Dynamics in Living Cells," *Mol. Biol. Cell.*, Vol. 9, No. 12, December 1998, pp. 3263–3271.
- [10] Agarwal, G., et al., "Sickle Hemoglobin Fibers: Mechanisms of Depolymerization," *J. Mol. Biol.*, Vol. 322, No. 2, September 13, 2002, pp. 395–412.
- [11] Liu, M. Y., M. L. Yeh, and Z. P. Luo, "In Vitro Regulation of Single Collagen Fibril Length by Buffer Compositions and Temperature," *Biomed. Mater. Eng.*, Vol. 15, No. 6, 2005, pp. 413–420.
- [12] Mihai, C., et al., "Discoidin Domain Receptor 2 Inhibits Fibrillogenesis of Collagen Type 1," *J. Mol. Biol.*, Vol. 361, No. 5, September 1, 2006, pp. 864–876.
- [13] Paddock, S., "Optical Sectioning: Slices of Life," *Science*, Vol. 295, February 15, 2002, pp. 1319–1321.
- [14] Piston, D. W., "Imaging Living Cells and Tissue by Two-Photon Excitation Microscopy," *Trends in Cell Biol.*, Vol. 9, February 1999, pp. 66–69.
- [15] Stephens, D. J., and V. J. Allan, "Light Microscopy Techniques for Live Cell Imaging," *Science*, Vol. 300, April 4, 2003.
- [16] Piston, D. W., and M. A. Rizzo, "FRET by Fluorescence Polarization Microscopy," *Methods Cell Biol.*, Vol. 85, 2008, pp. 415–430.
- [17] Zipfel, W. R., et al., "Live Tissue Intrinsic Emission Microscopy Using Multiphoton-Excited Native Fluorescence and Second Harmonic Generation," *Proc. Natl. Acad. Sci.*, Vol. 100, No. 12, June 10, 2003, pp. 7075–7080.
- [18] Campagnola, P. J., and L. M. Loew, "Second-Harmonic Imaging Microscopy for Visualizing Biomolecular Arrays in Cells, Tissues and Organisms," *Nat. Biotechnol.*, Vol. 21, No. 11, November 2003, pp. 1356–1360.
- [19] Lee, S., J. S. Choi, and S. H. Kang, "Combination of Differential Interference Contrast with Prism-Type Total Internal Fluorescence Microscope for Direct Observation of

- Polyamidoamine Dendrimer Nanoparticle as a Gene Delivery in Living Human Cells,” *J. Nanosci Nanotechnol.*, Vol. 7, No. 11, November 2007, pp. 3689–3694.
- [20] Klar, T. A., et al., “Fluorescence Microscopy with Diffraction Resolution Barrier Broken by Stimulated Emission,” *Proc. Natl. Acad. Sci.*, Vol. 97, No. 8206, 2000.
- [21] Betzig E., et al., “Imaging Intracellular Fluorescent Proteins at Nanometer Resolution,” *Science*, Vol. 313, No. 5793, September 15, 2006, pp. 1642–1645.
- [22] Manley, S., et al., “High-Density Mapping of Single-Molecule Trajectories with Photo-activated Localization Microscopy,” *Nat. Methods*, January 13, 2008.
- [23] Shribak, M., and S. Inoué, “Orientation-Independent Differential Interference Contrast Microscopy,” *Appl. Opt.*, Vol. 45, No. 3, January 20, 2006, pp. 460–469.

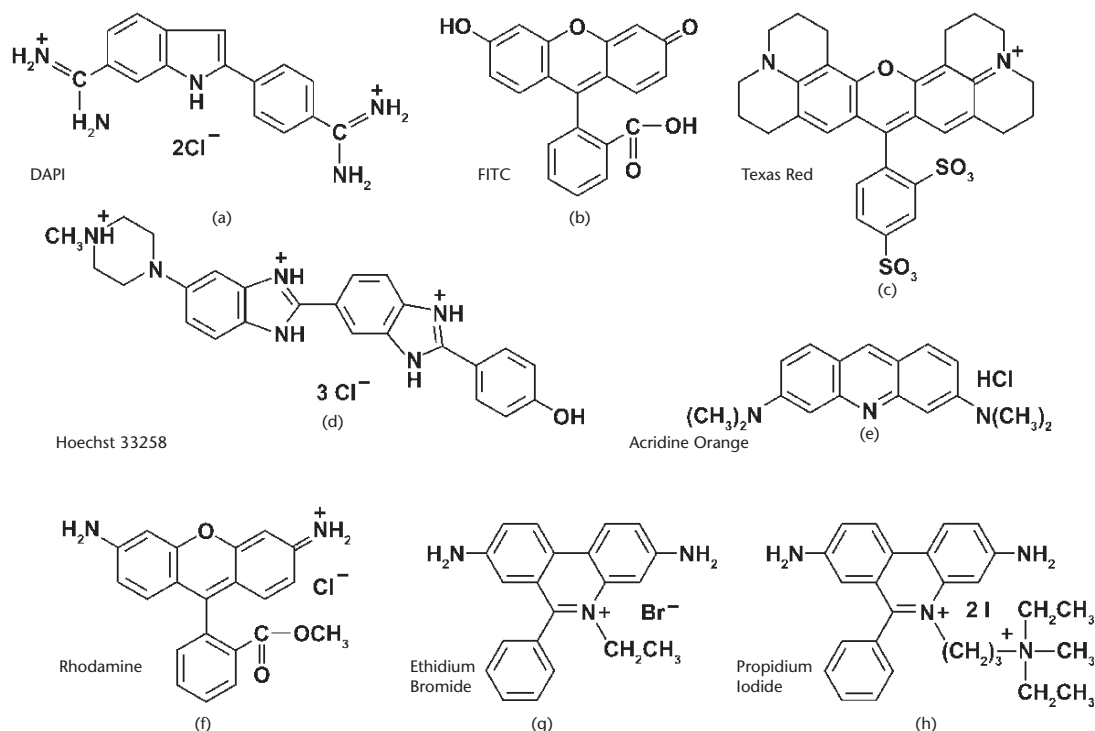
# Molecular Probes for Fluorescence Microscopy

Kristin L. Hazelwood, Scott G. Olenych, Christopher S. Murphy, and Michael W. Davidson

## 2.1 Introduction

Applications in biological microscopy now rely heavily on fluorescence as an imaging mode, primarily due to the high degree of sensitivity afforded by the technique coupled with the ability to specifically target structural components and dynamic processes in chemically fixed as well as living cells and tissues. Many fluorescent probes are constructed using a motif based on synthetic aromatic organic chemicals designed to bind with a biological macromolecule (for example, a protein or nucleic acid) or to localize within a specific structural region, such as the cytoskeleton, mitochondria, the Golgi apparatus, endoplasmic reticulum, and nucleus [1]. Other synthetic probes are employed to monitor dynamic processes and localized environmental variables, including concentrations of inorganic metallic ions, pH, reactive oxygen species, and membrane potential [2]. Fluorescent dyes are also useful in monitoring cellular integrity (live versus dead and apoptosis), endocytosis, exocytosis, membrane fluidity, protein trafficking, signal transduction, and enzymatic activity [3]. In addition, synthetic fluorescent probes have been widely applied to genetic mapping and chromosome analysis in the field of molecular genetics. Illustrated in Figure 2.1 are the chemical structures of several synthetic fluorescent dyes that have proven useful in all forms of optical microscopy. Throughout this chapter, the chemical structure of probes discussed in the text is displayed in accompanying figures. Although these structures may be intimidating for students who are not well versed in organic chemistry, they appear throughout the literature and in product information bulletins distributed by commercial vendors, and so are included as a reference for interested readers.

The history of synthetic fluorescent probes dates back more than a century to the late 1800s, when many of the cornerstone dyes for modern histology were developed. Among these were pararosaniline, methyl violet, malachite green, safranin O, methylene blue, and numerous azo (nitrogen) dyes, such as Bismarck brown [4]. Although these dyes were highly colored and capable of absorbing selected bands of visible light, most were only weakly fluorescent and would not be useful for the fluorescence microscopes that would be developed several decades later. However, several synthetic dye classes synthesized during this period, based on the xanthene and acridine heterocyclic ring systems, proved to be highly fluorescent and provided a foundation for the development of modern synthetic fluorescent probes. Most notable among these early fluorescent dyes were the substituted xanthenes, fluorescein and rhodamine B, and the biaminated acridine derivative, acridine orange.



**Figure 2.1** Traditional synthetic fluorescent probes used in widefield and laser scanning confocal microscopy: (a) 4',6-diamidino-2-phenylindole (DAPI); (b) fluorescein; (c) Texas Red; (d) Hoechst 33248; (e) acridine orange; (f) rhodamine; (g) ethidium bromide; and (h) propidium iodide.

Fluorochromes were introduced to fluorescence microscopy in the early twentieth century as vital stains for bacteria, protozoa, and trypanosomes, but did not see widespread use until the 1920s when fluorescence microscopy was first used to study dye binding in fixed tissues and living cells [4, 5]. However, it wasn't until the early 1940s that Albert Coons developed a technique for labeling antibodies with fluorescent dyes, thus giving birth to the field of immunofluorescence [6]. Over the past 60 years, advances in immunology and molecular biology have produced a wide spectrum of secondary antibodies and provided insight into the molecular design of fluorescent probes targeted at specific regions within macromolecular complexes.

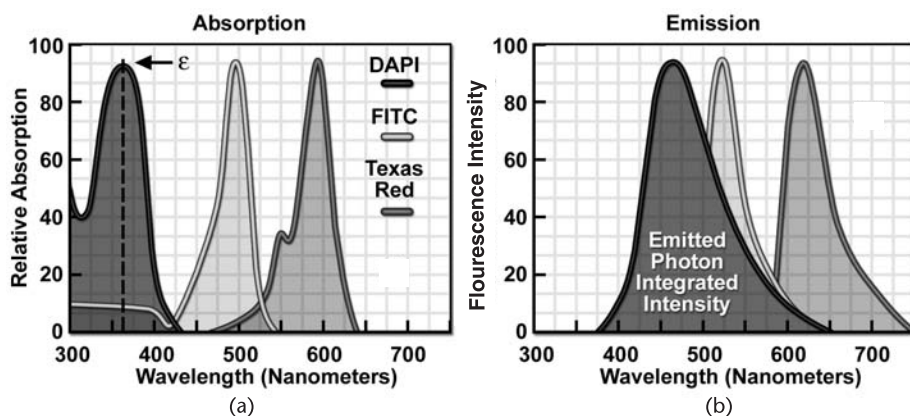
Fluorescent probe technology and cell biology were dramatically altered by the discovery of the green fluorescent protein (GFP) from jellyfish and the development of mutant spectral variants, which have opened the door to noninvasive fluorescence multicolor investigations of subcellular protein localization, intermolecular interactions, and trafficking using living cell cultures [7–10]. More recently, the development of nanometer-sized fluorescent semiconductor *quantum dots* has provided a new avenue for research in all imaging modalities using fluorescence microscopy [11, 12], and hybrid systems [13–15] that couple genetically encoded tags to synthetic fluorochromes are emerging as promising candidates for a variety of applications in live-cell imaging.



Despite the numerous advances made in fluorescent dye synthesis during the past few decades, there is very little solid evidence about molecular design rules for developing new synthetic and genetically encoded fluorochromes, particularly with regard to matching absorption spectra to available confocal laser excitation wavelengths. As a result, the number of fluorophores that have found widespread use in fluorescence microscopy is a limited subset of the many thousands that have been discovered.

## 2.2 Basic Characteristics of Fluorophores

Fluorophores are catalogued and described according to their absorption and fluorescence properties, including the spectral profiles, wavelengths of maximum absorbance and emission, and the fluorescence intensity of the emitted light [1, 3]. One of the most useful quantitative parameters for characterizing absorption spectra is the molar extinction coefficient [denoted with the Greek symbol  $\epsilon$ ; see Figure 2.2(a)], which is a direct measure of the ability of a molecule to absorb light. The extinction coefficient is useful for converting units of absorbance into units of molar concentration, and is determined by measuring the absorbance at a reference wavelength (usually the maximum characteristic of the absorbing species) for a molar concentration in a defined optical path length. The quantum yield of a fluorochrome or fluorophore represents a quantitative measure of fluorescence emission efficiency, and is expressed as the ratio of the number of photons emitted to the number of photons absorbed. In other words, the quantum yield represents the probability that a given excited fluorochrome will produce an emitted (fluorescence) photon. Quantum yields, by necessity, range between a value of zero and one, and fluorescent molecules commonly employed as probes in microscopy have



**Figure 2.2** Spectral profiles of popular traditional fluorophores. (a) Absorption spectra of DAPI, fluorescein (FITC), and Texas red. The point at which the extinction coefficient is measured is indicated ( $\epsilon$ ) with a dotted line. (b) Emission spectra of the dyes illustrating the area integrated (emitted photon integrated intensity) for determination of the quantum yield.



quantum yields ranging from very low (0.05 or less) to almost unity. In general, a high quantum yield is desirable in most imaging applications. The quantum yield of a given fluorophore varies, sometimes to large extremes, with environmental factors, such as metallic ion concentration, pH, and solvent polarity [3].

In most cases, the molar extinction coefficient for photon absorption is quantitatively measured and expressed at a specific wavelength, whereas the quantum efficiency is an assessment of the total integrated photon emission over the entire spectral band of the fluorophore (see Figure 2.2(b)). As opposed to traditional arc-discharge lamps used with the shortest range (10–20 nm) bandpass interference filters in widefield fluorescence microscopy, the laser systems used for fluorophore excitation in scanning confocal microscopy restrict excitation to specific laser spectral lines that encompass only a few nanometers [5,16]. The fluorescence emission spectrum for both techniques, however, is controlled by similar bandpass or long-pass filters that can cover tens to hundreds of nanometers [5]. Below saturation levels, fluorescence intensity is proportional to the product of the molar extinction coefficient and the quantum yield of the fluorophore, a relationship that can be utilized to judge the effectiveness of emission as a function of excitation wavelength(s). These parameters display approximately a 20-fold range in variation for the popular fluorophores commonly employed for investigations in confocal microscopy with quantum yields ranging from 0.05 to 1.0, and extinction coefficients ranging from ten thousand to a quarter million (liters per mole). In general, the absorption spectrum of a fluorophore is far less dependent upon environmental conditions than the fluorescence emission characteristics (spectral wavelength profile and quantum yield [3]).

Fluorophores chosen for fluorescence microscopy applications must exhibit a brightness level sufficient for the instrument to obtain image data that does not suffer from excessive photobleaching artifacts and low signal-to-noise ratios. In widefield fluorescence microscopy, excitation illumination levels are easily controlled with neutral density filters [17]. Excitation conditions in confocal microscopy are several orders of magnitude more severe, however, and restrictions imposed by characteristics of the fluorophores and efficiency of the microscope optical system become the dominating factor in determining excitation rate and emission collection strategies [3,5,18].

Because of the wavelength-restricted laser spectral lines employed to excite fluorophores in confocal microscopy (see Table 2.1), fluorescence emission intensity can be seriously restricted due to poor overlap of the excitation wavelengths with the fluorophore absorption band. In addition, the confocal pinhole aperture, which is critical in obtaining thin optical sections at high signal-to-noise ratios, is responsible for a 25–50% loss of emission intensity [5]. Photomultiplier tubes are the most common detectors in laser scanning confocal microscopy, but they suffer from a quantum efficiency that varies as a function of wavelength (especially in the red and infrared regions), further contributing to a wavelength-dependent loss of signal across the emission spectrum [19,20]. Collectively, the light losses in confocal microscopy can result in a reduction of intensity exceeding 50 times of the level typically observed in widefield fluorescence instruments. It should be clear from the preceding argument that fluorophore selection is one of the most

**Table 2.1** Laser and Arc-Discharge Lamp Spectral Lines (Listed in nm) Commonly Used in Laser Scanning and Widefield Fluorescence Microscopy

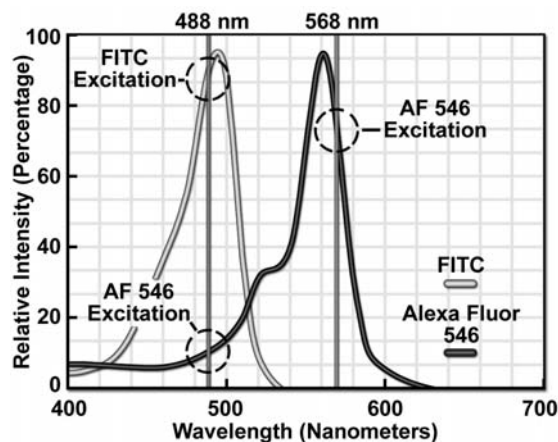
<i>Laser Type</i>	<i>Ultraviolet</i>	<i>Violet</i>	<i>Blue</i>	<i>Green</i>	<i>Yellow</i>	<i>Orange</i>	<i>Red</i>
Argon-Ion	351, 364	—	457, 477, 488	514	—	—	—
Diode	—	405, 440	—	—	—	—	—
DPSS	355	430, 442	457, 473	532	561	—	—
Helium-Cadmium	322, 354	442	—	—	—	—	—
Krypton-Argon	—	—	488	—	568	—	647
Green Helium-Neon	—	—	—	543	—	—	—
Yellow Helium-Neon	—	—	—	—	594	—	—
Orange Helium-Neon	—	—	—	—	—	612	—
Red Helium-Neon	—	—	—	—	—	—	633
Red Diode	—	—	—	—	—	—	635, 650
Mercury Arc	365	405, 436	546	—	579	—	—
Xenon Arc	—	467	—	—	—	—	—

critical aspects in all imaging modes for fluorescence microscopy, and instrumental efficiency must be carefully considered, as well, in order to produce high-quality images.

In confocal microscopy, irradiation of the fluorophores with a focused laser beam at high power densities increases the emission intensity up to the point of dye saturation, a condition whose parameters are dictated by the excited state lifetime [18]. In the excited state, fluorophores are unable to absorb another incident photon until they emit a lower-energy photon through the fluorescence process. As a result, a majority of the laser energy passes through the specimen undiminished and does not contribute to fluorophore excitation. Balancing fluorophore saturation with laser light intensity levels is, therefore, a critical condition for achieving the optimal signal-to-noise ratio in confocal experiments.

The number of molecular probes currently available for fluorescence microscopy runs in the hundreds [1, 4], with many dyes having absorption maxima closely associated with common laser spectral lines and widefield fluorescence filter combinations [1]. An exact match between a particular laser or mercury arc-discharge spectral line and the absorption maximum of a specific probe is not always possible, but the excitation efficiency of lines near the maximum is usually sufficient to produce a level of fluorescence emission that can be readily detected.

In Figure 2.3, the absorption spectra of two common probes are illustrated, along with the most efficient laser excitation lines. The green spectrum is the absorption profile of fluorescein isothiocyanate (FITC), which has an absorption maximum of 495 nm. Excitation of the FITC fluorophore at 488 nm using an argon-ion laser produces an emission efficiency of approximately 87%. In contrast, when the 477-nm or the 514-nm argon-ion laser lines are used to excite FITC, the



**Figure 2.3** Laser excitation efficiency of fluorescein and the rhodamine derivative, and Alexa Fluor 546 with the 488- and 568-nm spectral lines, respectively, of an argon-krypton laser.

emission efficiency drops to only 58% or 28%, respectively. Clearly, the 488-nm argon-ion (or krypton-argon) laser line is the most efficient source for excitation of this fluorophore. The right-hand spectrum in Figure 2.3 is the absorption profile of Alexa Fluor 546, a bi-sulfonated alicyclic xanthene (rhodamine) derivative with a maximum extinction coefficient at 556 nm. The most efficient laser excitation spectral line for Alexa Fluor 546 is the yellow 568-nm line from the krypton-argon mixed gas ion laser, which produces an emission efficiency of approximately 84%. The next closest laser spectral lines, the 543-nm line from the green helium-neon laser and the 594-nm lines from the yellow helium-neon laser, excite Alexa Fluor 546 with an efficiency of 43% and 4%, respectively. Note that the 488-nm argon-ion laser spectral line excites Alexa Fluor 546 with approximately 7% efficiency, a factor that can be of concern when conducting dual labeling experiments with FITC and Alexa Fluor 546 simultaneously.

Instrumentally, fluorescence emission collection can be optimized by careful selection of objectives, detector aperture dimensions, and dichromatic and barrier filters, as well as maintaining the optical train in precise alignment [21]. In most cases, low magnification objectives with a high numerical aperture should be chosen for the most demanding imaging conditions because light collection intensity increases as the fourth power of the numerical aperture, but only decreases as the square of the magnification. However, the most important limitations in light collection efficiency in fluorescence microscopy arise from restrictions imposed by the physical properties of the fluorophores themselves. As previously discussed, fluorescent probe development is limited by a lack of knowledge of the specific molecular properties responsible for producing optimum fluorescence characteristics, and the design rules are insufficiently understood to be helpful as a guide to the development of more efficient fluorophores. The current success in development of new fluorescent probes is a testament to the progress made through

the use of empirical data and assumptions about molecular structure extrapolated from the properties of existing dyes, many of which were first synthesized more than a hundred years ago.

## 2.3 Traditional Fluorescent Dyes

The choice of molecular probes for fluorescence microscopy must address the specific capabilities of the instrument to excite and detect fluorescence emission in the wavelength regions made available by the illumination system and detectors. Although the current lasers used in confocal microscopy (see Table 2.1) produce discrete lines in the ultraviolet, visible, and near-infrared portions of the spectrum, the location of these spectral lines does not always coincide with absorption maxima of popular fluorophores. The same is true for mercury and xenon arc-discharge lamps. In fact, it is not necessary for high intensity spectral lines to correspond exactly with the fluorophore wavelength of maximum absorption, but the intensity of fluorescence emission is regulated by the fluorophore extinction coefficient at the excitation wavelength (as discussed earlier). The most popular lasers for confocal microscopy are air-cooled argon and krypton-argon ion lasers, the relatively new diode lasers, and a variety of helium-neon systems [5, 16, 17]. Collectively, these lasers are capable of providing excitation at 20 or more specific wavelengths between 400 and 650 nm.

Several of the classical fluorescent probes that have been successfully utilized for many years in widefield fluorescence [3, 4], including fluorescein, Lissamine rhodamine, and Texas red, are also useful in confocal microscopy (Figure 2.1). Fluorescein has an absorption maximum at 495 nm, which coincides quite well with the 488-nm spectral line produced by argon-ion and krypton-argon lasers, as well as the 436 and 467 principal lines of the mercury and xenon arc-discharge lamps (respectively). In addition, the quantum yield is very high, and a significant amount of information has been gathered on the characteristics of this dye with respect to the physical and chemical properties [22]. On the negative side, the fluorescence emission intensity of fluorescein is heavily influenced by environmental factors (such as pH), and the relatively broad emission spectrum often overlaps with those of other fluorophores in dual and triple labeling experiments [3, 22, 23].

Tetramethyl rhodamine (TMR) and the isothiocyanate derivative (TRITC) are frequently employed in multiple labeling investigations in widefield microscopy due to their efficient excitation by the 546-nm spectral line from mercury arc-discharge lamps. These fluorochromes can be excited very effectively by the 543-nm line from helium-neon lasers, but not by the 514- or 568-nm lines from argon-ion and krypton-argon lasers [22]. When using krypton-based laser systems, Lissamine rhodamine is a far better choice in this fluorochrome class due to the absorption maximum at 575 nm and its spectral separation from fluorescein.

Several of the acridine dyes, first isolated in the nineteenth century, are useful as fluorescent probes in confocal microscopy [4]. The most widely utilized, acridine orange, consists of the basic acridine nucleus adorned with dimethylamino substituents located at the 3 and 6 positions of the aromatic tri-nuclear ring system.

This probe (Figure 2.1) binds strongly to DNA by intercalation of the acridine nucleus between successive base pairs, and it exhibits green fluorescence with a maximum wavelength of 530 nm [3, 4, 24]. In living cells, acridine orange diffuses across the cell membrane (by virtue of the dissociation constant for protonation) and accumulates in the lysosomes and other acidic vesicles. Similar to most acridines and related polynuclear aromatic nitrogen heterocycles, acridine orange has a relatively broad absorption spectrum, which enables the probe to be used with several wavelengths from the argon-ion laser.

Another popular synthetic dye that is useful in fluorescence microscopy is the phenanthridine derivative, propidium iodide (Figure 2.1). Propidium iodide binds to DNA in a manner similar to the acridines (via intercalation) to produce orange-red fluorescence centered at 617 nm [25, 26]. The positively charged fluorophore also has a high affinity for double-stranded RNA. Propidium has an absorption maximum at 536 nm and can be excited by the 488-nm or 514-nm spectral lines of an argon-ion (or krypton-argon) laser, or the 543-nm line from a green helium-neon laser. The dye is often employed as a counterstain to highlight cell nuclei during double or triple labeling of multiple intracellular structures. Environmental factors can affect the fluorescence spectrum of propidium, especially when the dye is used with mounting media containing glycerol. The structurally similar ethidium bromide, which also binds to DNA by intercalation [25], produces more background staining and is therefore not as effective as propidium.

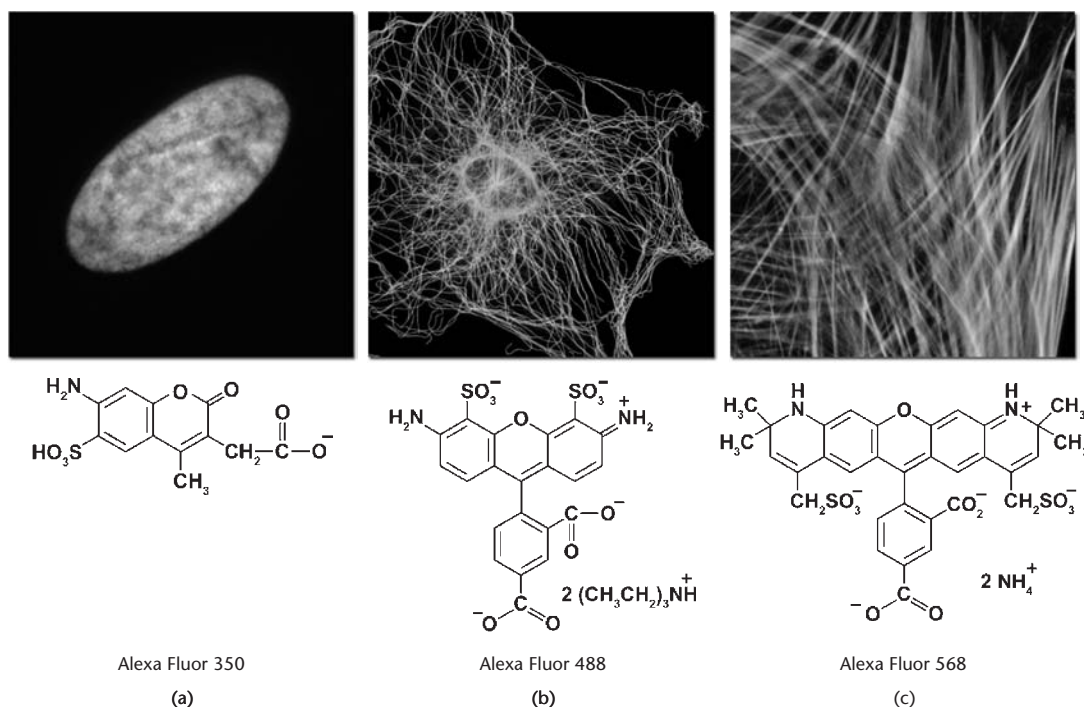
DNA and chromatin can also be stained with dyes that bind externally to the double helix. The most popular fluorochromes in this category are 4',6-diamidino-2-phenylindole (DAPI) and the bisbenzimidazole Hoechst dyes that are designated by the numbers 33258 (Figure 2.1), 33342, and 34580 [27–30]. These probes are quite water soluble and bind externally to AT-rich base pair clusters in the minor groove of double-stranded DNA with a dramatic increase in fluorescence intensity. Both dye classes can be stimulated by the 351-nm spectral line of high-power argon-ion lasers or the 354-nm line from a helium-cadmium laser. They are also efficiently excited by the 365-nm peak from the mercury arc-discharge lamp. Similar to the acridines and phenanthridines, these fluorescent probes are popular choices as a nuclear counterstain for use in multicolor fluorescent labeling protocols. The vivid blue fluorescence emission produces dramatic contrast when coupled to green, yellow, and red probes in adjacent cellular structures.

## 2.4 Alexa Fluor Dyes

The dramatic advances in modern fluorophore technology are exemplified by the Alexa Fluor dyes [1, 31, 32] introduced by Molecular Probes (Alexa Fluor is a registered trademark of Molecular Probes). These sulfonated rhodamine derivatives exhibit higher quantum yields for more intense fluorescence emission than spectrally similar probes, and have several additional improved features, including enhanced photostability, absorption spectra matched to common laser lines, pH insensitivity, and a high degree of water solubility. In fact, the resistance to photobleaching of Alexa Fluor dyes is so dramatic [32] that even when subjected

to irradiation by high-intensity laser sources, fluorescence intensity remains stable for relatively long periods of time in the absence of antifade reagents. This feature enables the water-soluble Alexa Fluor probes to be readily utilized for both live-cell and tissue section investigations, as well as in traditional fixed preparations.

Alexa Fluor dyes are available in a broad range of fluorescence excitation and emission wavelength maxima, ranging from the ultraviolet and deep blue to the near-infrared regions [1]. Alphanumeric names of the individual dyes are associated with the specific excitation laser or arc-discharge lamp spectral lines for which the probes are intended. For example, Alexa Fluor 488 is designed for excitation by the blue 488-nm line of the argon or krypton-argon ion lasers, while Alexa Fluor 568 is matched to the 568-nm spectral line of the krypton-argon laser. Several of the Alexa Fluor dyes are specifically designed for excitation by the blue diode laser (405 nm), the orange/yellow helium-neon laser (594 nm), or the red helium-neon laser (633 nm). Other Alexa Fluor dyes are intended for excitation with traditional mercury arc-discharge lamps in the visible (Alexa Fluor 546) or ultraviolet (Alexa Fluor 350, also useful with high-power argon-ion lasers), and solid-state red diode lasers (Alexa Fluor 680). Because of the large number of available excitation and



**Figure 2.4** Digital images (widefield fluorescence) of Alexa Fluor dyes used in immunofluorescence and conjugated to phallotoxins for subcellular localization investigations: (a) Alexa Fluor 350 conjugated to goat antimouse secondary antibodies targeting mouse antihistone (pan) primaries; (b) Alexa Fluor 488 conjugated to goat antirabbit secondary antibodies targeting rabbit anti- $\alpha$ -tubulin primaries; and (c) Alexa Fluor 568 conjugated to phalloidin (actin). Note the increasingly complex structure of Alexa Fluor dyes as emission wavelengths are increased.



emission wavelengths in the Alexa Fluor series, multiple labeling experiments can often be conducted exclusively with these dyes.

Alexa Fluor dyes are commercially available [1] as reactive intermediates in the form of maleimides, succinimidyl esters, and hydrazides, as well as prepared cytoskeletal probes (conjugated to phalloidin, G-actin, and rabbit skeletal muscle actin) and conjugates to lectin, dextrin, streptavidin, avidin, biocytin, and a wide variety of secondary antibodies. In the latter forms, the Alexa Fluor fluorophores provide a broad palette of tools for investigations in immunocytochemistry, neuroscience, and cellular biology (Figure 2.4). The family of probes has also been extended into a series of dyes having overlapping fluorescence emission maxima targeted at sophisticated confocal microscopy detection systems with spectral imaging and linear unmixing capabilities. For example, Alexa Fluor 488, Alexa Fluor 500, and Alexa Fluor 514 are visually similar in color with bright green fluorescence, but have spectrally distinct emission profiles. In addition, the three fluorochromes can be excited with the 488- or 514-nm spectral line from an argon-ion laser and are easily detected with traditional fluorescein filter combinations. In multispectral (x-y-l; referred to as a lambda stack) confocal imaging experiments, optical separation software can be employed to differentiate between the similar signals [33–36]. The overlapping emission spectra of Alexa Fluor 488, 500, and 514 are segregated into separate channels and differentiated using pseudocolor techniques when the three fluorophores are simultaneously combined in a triple label investigation.

## 2.5 Cyanine Dyes

The popular family of cyanine dyes, Cy2, Cy3, Cy5, Cy7, and their derivatives, are based on the partially saturated indole nitrogen heterocyclic nucleus with two aromatic units being connected via a polyalkene bridge of varying carbon number [3, 37]. These probes exhibit fluorescence excitation and emission profiles that are similar to many of the traditional dyes, such as fluorescein and tetramethylrhodamine, but with enhanced water solubility, photostability, and higher quantum yields. Most of the cyanine dyes are more environmentally stable than their traditional counterparts, rendering their fluorescence emission intensity less sensitive to pH and organic mounting media. In a manner similar to the Alexa Fluors, the excitation wavelengths of the Cy series of synthetic dyes are tuned specifically for use with common laser and arc-discharge sources, and the fluorescence emission can be detected with traditional filter combinations.

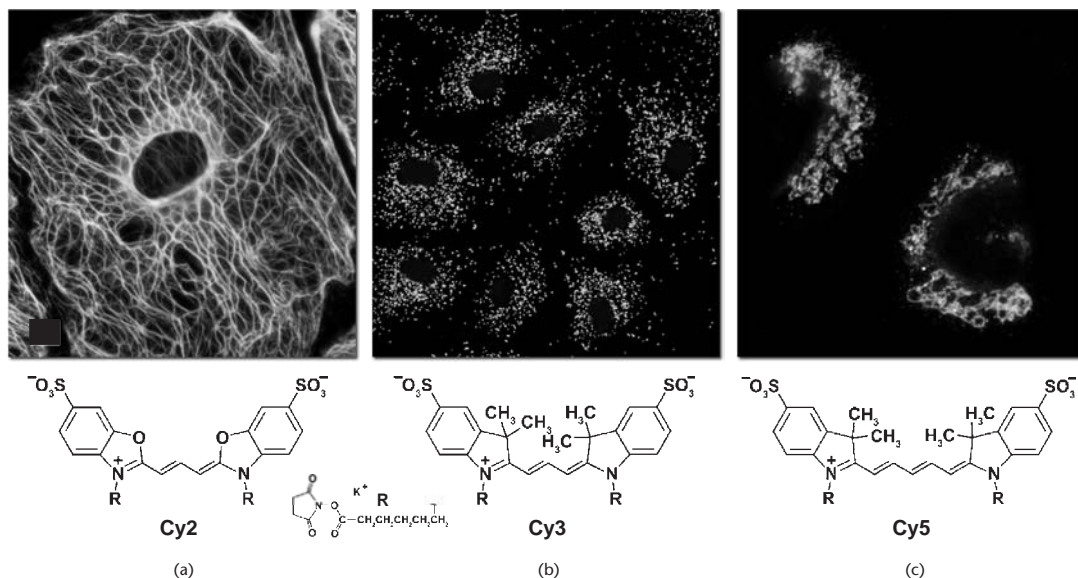
Marketed by a number of distributors, the cyanine dyes are readily available as reactive dyes or fluorophores coupled to a wide variety of secondary antibodies, dextrin, streptavidin, and egg-white avidin [38]. The cyanine dyes generally have broader absorption spectral regions than members of the Alexa Fluor family, making them somewhat more versatile in the choice of laser excitation sources for confocal microscopy [5]. For example, using the 547-nm spectral line from an argon-ion laser, Cy2 is about twice as efficient in fluorescence emission as Alexa Fluor 488. In an analogous manner, the 514-nm argon-ion laser line excites Cy3

with a much higher efficiency than Alexa Fluor 546, a spectrally similar probe. Emission profiles of the cyanine dyes are comparable in spectral width to the Alexa Fluor series.

Included in the cyanine dye series are the long-wavelength Cy5 derivatives, which are excited in the red region (650 nm) and emit in the far-red (680-nm) wavelengths. The Cy5 fluorophore is very efficiently excited by the 647-nm spectral line of the krypton-argon laser, the 633-nm line of the red helium-neon laser, or the 650-nm line of the red diode laser, providing versatility in laser choice. Because the emission spectral profile is significantly removed from traditional fluorophores excited by ultraviolet and blue illumination, Cy5 is often utilized as a third fluorophore in triple labeling experiments (Figure 2.5). However, similar to other probes with fluorescence emission in the far-red spectral region, Cy5 is not visible to the human eye and can only be detected electronically (using a specialized CCD camera system or photomultiplier). Therefore, the probe is seldom used in conventional widefield fluorescence experiments.

## 2.6 Fluorescent Environmental Probes

Fluorophores designed to probe the internal environment of living cells have been widely examined by a number of investigators, and many hundreds have been developed to monitor such effects as localized concentrations of alkali and alkaline



**Figure 2.5** Digital images (widefield fluorescence) of cyanine dyes used in immunofluorescence for subcellular localization investigations: (a) Cy2 conjugated to goat antimouse secondary antibodies targeting mouse antikeratin [18] primaries; (b) Cy3 conjugated to goat antirabbit secondary antibodies targeting rabbit antiperoxisomal membrane protein (PMP-70) primaries; and (c) Cy5 conjugated to goat antimouse secondary antibodies targeting mouse antigiantin primaries.

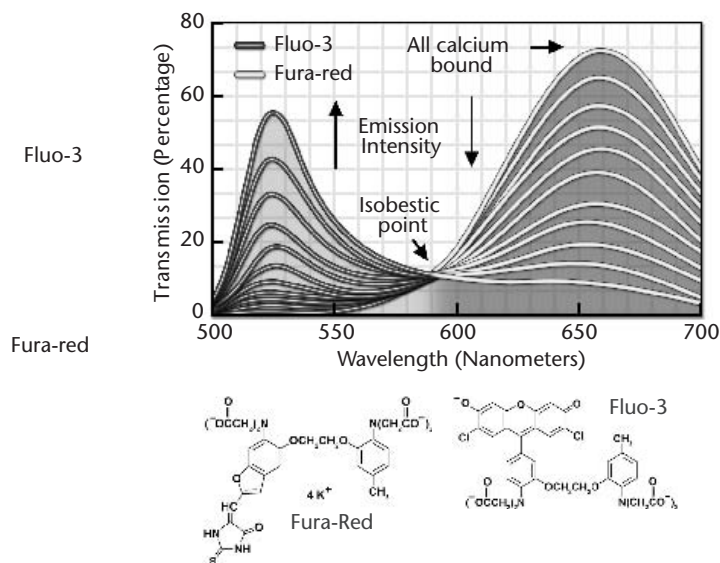


earth metals, heavy metals (employed biochemically as enzyme cofactors), inorganic ions, thiols and sulfides, and nitrite, as well as pH, solvent polarity, and membrane potential [1–5, 39, 40]. Originally, the experiments in this arena were focused on changes in the wavelength and/or intensity of absorption and emission spectra exhibited by fluorophores upon binding calcium ions in order to measure intracellular flux densities. These probes bind to the target ion with a high degree of specificity to produce the measured response and are often referred to as *spectrally sensitive indicators*. Ionic concentration changes are determined by the application of optical ratio signal analysis to monitor the association equilibrium between the ion and its host. The concentration values derived from this technique are largely independent of instrumental variations and probe concentration fluctuations due to photobleaching, loading parameters, and cell retention. In the past few years, a number of new agents have been developed that bind specific ions or respond with measurable features to other environmental conditions [1, 5].

Calcium is a metabolically important ion that plays a vital role in cellular response to many forms of external stimuli [41]. Because transient fluctuations in calcium ion concentration are typically involved when cells undergo a response, fluorophores must be designed to measure not only localized concentrations within segregated compartments, but should also produce quantitative changes when flux density waves progress throughout the cytoplasm. Many of the synthetic molecules designed to measure calcium levels are based on the nonfluorescent chelating agents EGTA and BAPTA, which have been used for years to sequester calcium ions in buffer solutions [5, 42, 43]. Two of the most common calcium probes are the ratiometric indicators Fura-2 and Indo-1, but these fluorophores are not particularly useful in confocal microscopy [5, 44]. The dyes are excited by ultraviolet light and exhibit a shift in the excitation or emission spectrum with the formation of isosbestic points when binding calcium. However, the optical aberrations associated with ultraviolet imaging, limited specimen penetration depths, and the expense of ultraviolet lasers have limited the utility of these probes in confocal microscopy.

Fluorophores that respond in the visible range to calcium ion fluxes are, unfortunately, not ratiometric indicators and do not exhibit a wavelength shift (typical of Fura-2 and Indo-1) upon binding, although they do undergo an increase or decrease in fluorescence intensity. The best example is Fluo-3, a complex xanthene derivative, which undergoes a dramatic increase in fluorescence emission at 525 nm (green) when excited by the 488-nm spectral line of an argon-ion or krypton-argon laser [5, 45]. Because isosbestic points are not present to assure the absence of concentration fluctuations, it is impossible to determine whether spectral changes are due to complex formation or a variation in concentration with Fluo-3 and similar fluorophores.

To overcome the problems associated with using visible light probes lacking wavelength shifts (and isosbestic points), several of these dyes are often utilized in combination for calcium measurements in confocal microscopy [46]. Fura-Red, a multinuclear imidazole and benzofuran heterocycle, exhibits a decrease in fluorescence at 650 nm when binding calcium. A ratiometric response to calcium ion fluxes can be obtained when a mixture of Fluo-3 and Fura-Red is excited at 488 nm and fluorescence is measured at the emission maxima (525 and 650 nm,



**Figure 2.6** Ratiometric measurement of calcium ion flux using a mixture of Fluo-3 and Fura-Red. The emission intensity of Fluo-3 increases monotonically while that of Fura-Red simultaneously decreases, producing an isobestic point when the dye concentrations are constant within the localized area being investigated.

respectively) of the two probes (see Figure 2.6). Because the emission intensity of Fluo-3 increases monotonically while that of Fura-Red simultaneously decreases, an isobestic point is obtained when the dye concentrations are constant within the localized area being investigated. Another benefit of using these probes together is the ability to measure fluorescence intensity fluctuations with a standard FITC/Texas red interference filter combination.

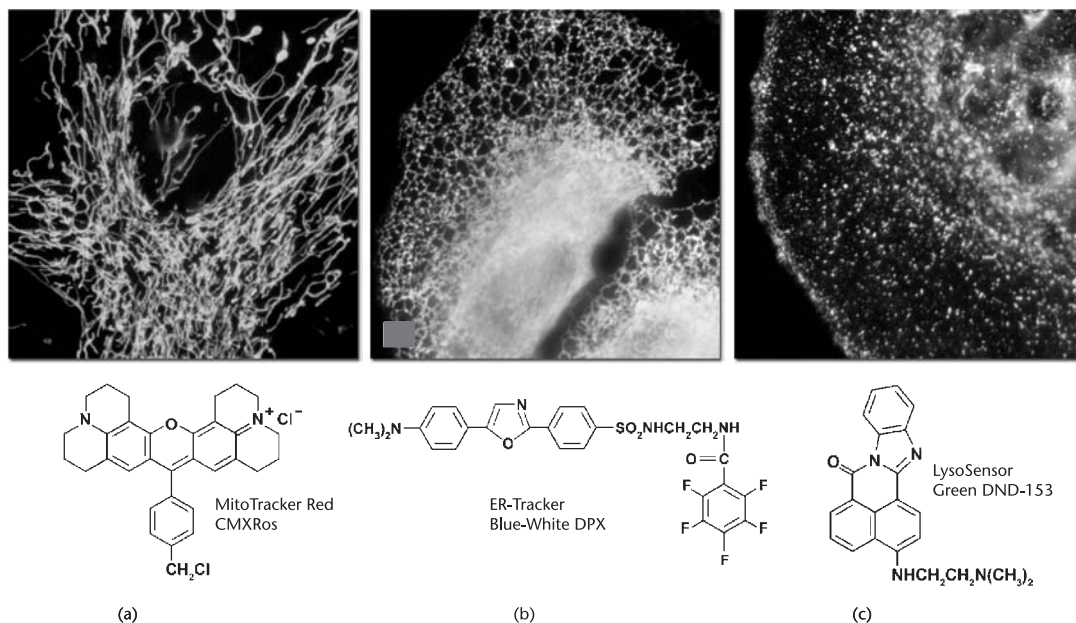
Quantitative measurements of ions other than calcium, such as magnesium, sodium, potassium, and zinc, are conducted in an analogous manner using similar fluorophores [1, 3, 5]. One of the most popular probes for magnesium, Mag-Fura-2 (structurally similar to Fura-Red), is also excited in the ultraviolet range and presents the same problems in fluorescence microscopy as Fura-2 and Indo-1. Fluorophores excited in the visible light region are becoming available for the analysis of many monovalent and divalent cations that exist at varying concentrations in the cellular matrix. Several synthetic organic probes have also been developed for monitoring the concentration of simple and complex anions.

Important fluorescence monitors for intracellular pH include a pyrene derivative known as HPTS or pyranine, the fluorescein derivative, BCECF, and another substituted xanthene termed carboxy SNARF-1 [1, 47–50]. Because many common fluorophores are sensitive to pH in the surrounding medium, changes in fluorescence intensity that are often attributed to biological interactions may actually occur as a result of protonation. In the physiological pH range (pH 6.8 to 7.4), the probes mentioned earlier are useful for dual-wavelength ratiometric measurements

and differ only in dye loading parameters. Simultaneous measurements of calcium ion concentration and pH can often be accomplished by combining a pH indicator, such as SNARF-1, with a calcium ion indicator (for example, Fura-2). Other probes have been developed for pH measurements in subcellular compartments, such as the lysosomes, as described next.

## 2.7 Organelle Probes

Fluorophores targeted at specific intracellular organelles, such as the mitochondria, lysosomes, Golgi apparatus, and endoplasmic reticulum, are useful for monitoring a variety of biological processes in living cells using confocal microscopy [1,3,5]. In general, organelle probes consist of a fluorochrome nucleus attached to a target-specific moiety that assists in localizing the fluorophore through covalent, electrostatic, hydrophobic, or similar types of bonds. Many of the fluorescent probes designed for selecting organelles are able to permeate or sequester within the cell membrane (and, therefore, are useful in living cells), while others must be installed using monoclonal antibodies with traditional immunocytochemistry techniques. In living cells, organelle probes are useful for investigating transport, respiration, mitosis, apoptosis, protein degradation, acidic compartments, and membrane phenomena. Cell impermeant immunofluorescence and direct labeling applications include targets for nuclear functions, cytoskeletal structure, organelle detection, and



probes for membrane integrity (Figure 2.7). In many cases, living cells that have been labeled with permeant probes can subsequently be fixed and counterstained with additional fluorophores in multicolor labeling experiments.

Mitochondrial probes are among the most useful fluorophores for investigating cellular respiration and are often employed along with other dyes in multiple labeling investigations. The traditional probes, rhodamine 123 and tetramethylrhodamine, are rapidly lost when cells are fixed and have largely been supplanted by newer, more specific, fluorophores developed by Molecular Probes [1,51,52]. These include the popular MitoTracker and MitoFluor series of structurally diverse xanthene, benzoxazole, indole, and benzimidazole heterocycles that are available in a variety of excitation and emission spectral profiles. The mechanism of action varies for each of the probes in this series, ranging from covalent attachment to oxidation within respiring mitochondrial membranes.

MitoTracker dyes (Figure 2.7) are retained quite well after cell fixation in formaldehyde and can often withstand lipophilic permeabilizing agents [51]. In contrast, the MitoFluor probes are designed specifically for actively respiring cells and are not suitable for fixation and counterstaining procedures [1]. Another popular mitochondrial probe, entitled JC-1, is useful as an indicator of membrane potential and in multiple staining experiments with fixed cells [53]. This carbocyanine dye exhibits green fluorescence at low concentrations, but can undergo intramolecular association within active mitochondria to produce a shift in emission to longer (red) wavelengths. The change in emission wavelength is useful in determining the ratio of active to nonactive mitochondria in living cells.

In general, weakly basic amines that are able to pass through membranes are the ideal candidates for investigating biosynthesis and pathogenesis in lysosomes [1–3,40]. Traditional lysosomal probes include the nonspecific phenazine and acridine derivatives neutral red and acridine orange, which are accumulated in the acidic vesicles upon being protonated [3,4]. Fluorescently labeled latex beads and macromolecules, such as dextran, can also be accumulated in lysosomes by endocytosis for a variety of experiments. However, the most useful tools for investigating lysosomal properties with fluorescence microscopy are the LysoTracker and LysoSensor (Figure 2.7) dyes developed by Molecular Probes [1,3,54]. These structurally diverse agents contain heterocyclic and aliphatic nitrogen moieties that modulate transport of the dyes into the lysosomes of living cells for both short-term and long-term studies. The LysoTracker probes, which are available in a variety of excitation and emission wavelengths [1], have high selectivity for acidic organelles and are capable of labeling cells at nanomolar concentrations. Several of the dyes are retained quite well after fixing and permeabilization of cells. In contrast, the LysoSensor fluorophores are designed for studying dynamic aspects of lysosome function in living cells. Fluorescence intensity dramatically increases in the LysoSensor series upon protonation, making these dyes useful as pH indicators [1]. A variety of Golgi apparatus-specific monoclonal antibodies have also been developed for use in immunocytochemistry assays [1,55–58].

Proteins and lipids are sorted and processed in the Golgi apparatus, which is typically stained with fluorescent derivatives of ceramides and sphingolipids [55]. These agents are highly lipophilic, and are therefore useful as markers for the

study of lipid transport and metabolism in live cells. Several of the most useful fluorophores for Golgi apparatus contain the complex heterocyclic *BODIPY* nucleus developed by Molecular Probes [1, 3, 59]. When coupled to sphingolipids, the *BODIPY* fluorophore is highly selective and exhibits a tolerance for photobleaching that is far superior to many other dyes. In addition, the emission spectrum is dependent upon concentration (shifting from green to red at higher concentrations), making the probes useful for locating and identifying intracellular structures that accumulate large quantities of lipids. During live-cell experiments, fluorescent lipid probes can undergo metabolism to derivatives that may bind to other subcellular features (Figure 2.7), a factor that can often complicate the analysis of experimental data.

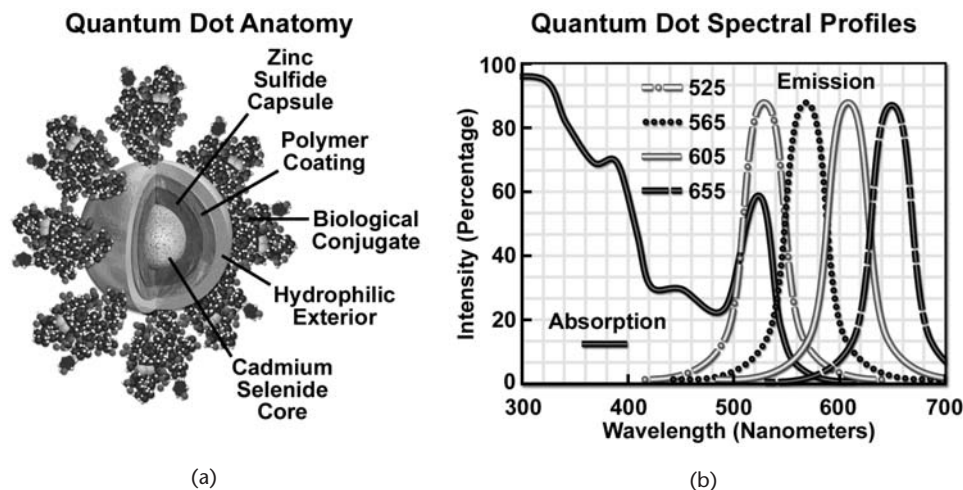
The most popular traditional probes for endoplasmic reticulum fluorescence analysis are the carbocyanine and xanthene dyes, DiOC(6) and several rhodamine derivatives, respectively [1, 3]. These dyes must be used with caution, however, because they can also accumulate in the mitochondria, Golgi apparatus, and other intracellular lipophilic regions. Newer, more photostable, probes have been developed for selective staining of the endoplasmic reticulum by several manufacturers. In particular, oxazole members of the Dapoxyl family produced by Molecular Probes are excellent agents for selective labeling of the endoplasmic reticulum in living cells (Figure 2.7), either alone or in combination with other dyes [1]. These probes are retained after fixation with formaldehyde, but can be lost with permeabilizing detergents. Another useful probe is Brefeldin A [59], a stereochemically complex fungal metabolite that serves as an inhibitor of protein trafficking out of the endoplasmic reticulum. Finally, similar to other organelles, monoclonal antibodies [56–58] have been developed that target the endoplasmic reticulum in fixed cells for immunocytochemistry investigations.

## 2.8 Quantum Dots

Nanometer-sized crystals of purified semiconductors known as quantum dots are emerging as a potentially useful fluorescent labeling agent for living and fixed cells in both traditional widefield and laser scanning confocal fluorescence microscopy [60–64]. Recently introduced techniques enable the purified tiny semiconductor crystals to be coated with a hydrophilic polymer shell and conjugated to antibodies or other biologically active peptides and carbohydrates for application in many of the classical immunocytochemistry protocols (see Figure 2.8). These probes have significant benefits over organic dyes and fluorescent proteins, including long-term photostability, high fluorescence intensity levels, and multiple colors with single-wavelength excitation for all emission profiles [60, 64].

Quantum dots produce illumination in a manner similar to the well-known semiconductor light emitting diodes, but are activated by absorption of a photon rather than an electrical stimulus. The absorbed photon creates an electron-hole pair that quickly recombines with the concurrent emission of a photon having lower energy. The most useful semiconductor discovered thus far for producing biological quantum dots is cadmium selenide (CdSe), a material in which the energy of the emitted photons is a function of the physical size of the nanocrystal particles.





**Figure 2.8** (a) Anatomy and (b) spectral profiles of quantum dots. (a) The CdSe core is encapsulated with a coating of ZnS, which in turn is coated with a polymer followed by a hydrophilic surface agent to which biological conjugates are attached. (b) The broad absorption spectrum of quantum dots exhibits an increasing extinction coefficient with decreasing wavelength. Quantum dot emission profiles, unlike those of other fluorophores, are symmetric and feature a narrow full-width at half maximum (FWHM).

Thus, quantum dots having sizes that differ only by tenths of a nanometer emit different wavelengths of light, with the smaller sizes emitting shorter wavelengths, and vice versa.

Unlike typical organic fluorophores or fluorescent proteins, which display highly defined spectral profiles, quantum dots have an absorption spectrum that increases steadily with decreasing wavelength (Figure 2.8). The extinction coefficients of quantum dots are typically 10 to 100 times higher than those of synthetic fluorophores or fluorescent proteins. Also in contrast with the latter probes, the fluorescence emission intensity is confined to a symmetrical peak with a maximum wavelength that is dependent on the dot size, but independent of the excitation wavelength [63]. As a result, the same emission profile is observed regardless of whether the quantum dot is excited at 300, 400, 500, or 600 nm, but the fluorescence intensity increases dramatically at shorter excitation wavelengths. For example, the extinction coefficient for a typical quantum dot conjugate that emits in the orange region (605 nm) is approximately five-fold higher when the semiconductor is excited at 400 versus 600 nm. The full width at half maximum value for a typical quantum dot conjugate is about 30 nm [63], and the spectral profile is not skewed toward the longer wavelengths (having higher intensity “tails”), such is the case with most organic fluorochromes. The narrow emission profile enables several quantum dot conjugates to be simultaneously observed with a minimal level of bleed-through.

For biological applications, a relatively uniform population of cadmium selenide crystals is covered with a surrounding semiconductor shell composed of zinc sulfide to improve the optical properties and prevent quenching by water. Next,

the core material is coated with a polymeric film and other ligands to decrease hydrophobicity and to improve the attachment efficiency of conjugated macromolecules. The final product is a biologically active particle that ranges in size from 10 to 30 nm, somewhere in the vicinity of a large protein [61]. Quantum dot conjugates are solubilized as a colloidal suspension in common biological buffers and may be incorporated into existing labeling protocols in place of classical staining reagents (such as organic fluorochrome-labeled secondary antibodies).

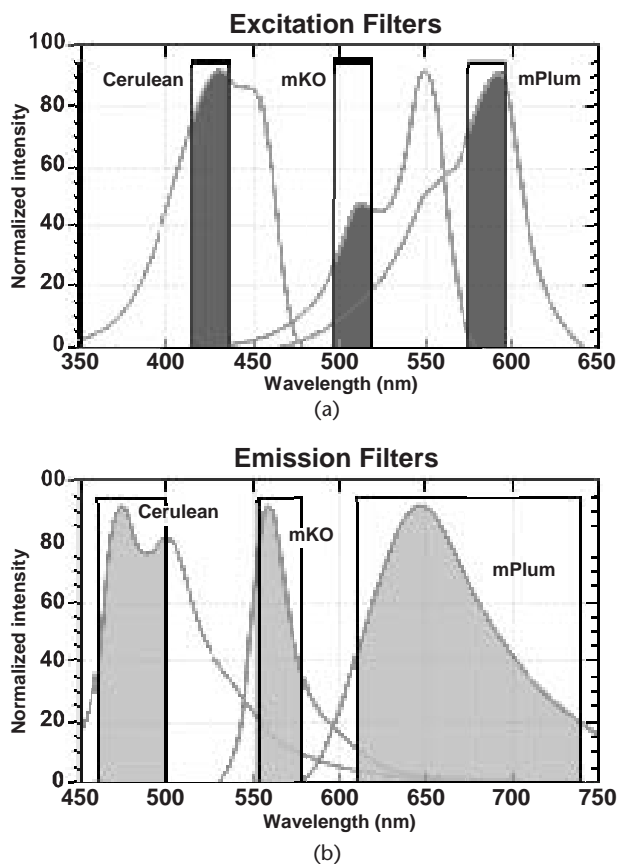
In confocal microscopy, quantum dots are excited with varying degrees of efficiency by most of the spectral lines produced by the common laser systems, including the argon-ion, helium-cadmium, krypton-argon, and the green helium-neon. Particularly effective at exciting quantum dots in the ultraviolet and violet regions are the new blue diode and diode-pumped solid-state lasers that have prominent spectral lines at 442 nm and below [63,64]. The 405-nm blue diode laser is an economical excitation source that is very effective for use with quantum dots due to their high extinction coefficient at this wavelength. Another advantage of using these fluorophores in confocal microscopy is the ability to stimulate multiple quantum dot sizes (and spectral colors) in the same specimen with a single excitation wavelength, making these probes excellent candidates for multiple labeling experiments [60, 64, 65].

The exceptional photostability of quantum dot conjugates is of great advantage in confocal microscopy when optical sections are being collected. Unlike the case of organic fluorophores, labeled structures situated away from the focal plane do not suffer from excessive photobleaching during repeated raster scanning of the specimen and yield more accurate three-dimensional volume models. Unfortunately, the large size of quantum dot conjugates prevents their efficient transfer through intact membranes, which necessarily restricts their use to permeabilized cells or as targets for extracellular or endocytosed proteins [13], thus severely limiting their applications in live-cell imaging. Recently reported gold and silver “nanodots” that are formed within hydrophilic dendramers are also very fluorescent and feature tunable wavelength profiles, similar to quantum dots, and should eventually provide another fluorophore alternative [66].

In widefield fluorescence microscopy, quantum dot conjugates are available for use with conventional dye-optimized filter combinations that are standard equipment on many microscopes. Excitation can be further enhanced by substituting a shortpass filter for the bandpass filter that accompanies most filter sets, thus optimizing the amount of lamp energy that can be utilized to excite the quantum dots. Several of the custom fluorescence filter manufacturers offer combinations specifically designed to be used with quantum dot conjugates.

## 2.9 Fluorescent Proteins

Over the past few years, the discovery and development of naturally occurring fluorescent proteins and mutated derivatives have rapidly advanced to center stage in the investigation of a wide spectrum of intracellular processes in living organisms [67–70]. These biological probes have provided scientists with the ability to



**Figure 2.9** (a) Spectral profiles and (b) recommended filter bandpass regions for multiple labeling with cyan (mCerulean), orange (mKusabira Orange), and far-red (mPlum) fluorescent proteins. The spectra of these proteins are sufficiently well separated for three-color imaging.

visualize, monitor, and track individual molecules with high spatial and temporal resolution in both steady-state and dynamic experimental scenarios. A wide variety of marine organisms have been the source of more than 100 fluorescent proteins and their analogs, which arm the investigator with a balanced palette of noninvasive biological probes for single, dual, and multispectral fluorescence analysis (see Figure 2.9) [69]. Among the advantages of fluorescent proteins over the traditional organic and the new semiconductor probes described earlier is their response to a wider variety of biological events and signals. Added to the ability to specifically target fluorescent probes in subcellular compartments, the extremely low or absent levels of phototoxicity, and the widespread compatibility with tissues and intact organisms, these biological macromolecules offer an exciting new frontier in live-cell imaging.

The first member of this series to be discovered, green fluorescent protein (GFP), was isolated from the North Atlantic jellyfish, *Aequorea victoria*, and found to exhibit a high degree of fluorescence without the aid of additional substrates



or coenzymes [67]. In native green fluorescent protein, the fluorescent moiety is a cyclized tripeptide derivative containing serine, tyrosine, and glycine that requires molecular oxygen for activation, but no additional cofactors or enzymes [71]. Subsequent investigations revealed that the GFP gene could be expressed in other organisms, including mammals, to yield fully functional analogs that display no adverse biological effects [72]. In fact, fluorescent proteins can be fused to virtually any protein in living cells using recombinant complementary DNA cloning technology, and the resulting fusion protein gene product expressed in cell lines adapted to standard tissue culture methodology. Lack of a need for cell-specific activation cofactors renders the fluorescent proteins much more useful as generalized probes than other biological macromolecules, such as the phycobiliproteins [73], which require insertion of accessory pigments in order to produce fluorescence.

Mutagenesis experiments with GFP and its derivatives have produced a large number of variants featuring improved folding and expression characteristics, which have eliminated wild-type dimerization artifacts and fine-tuned the absorption and fluorescence properties [70]. One of the earliest variants, known as enhanced green fluorescence protein (EGFP), contains codon substitutions that alleviate the temperature sensitivity and increases the efficiency of GFP expression in mammalian cells [74]. Proteins fused with EGFP can be observed at low light intensities for long time periods with minimal photobleaching. Enhanced green fluorescent protein fusion products are optimally excited by the 488-nm spectral line from argon and krypton-argon ion lasers in confocal microscopy or using a traditional FITC filter combination in widefield fluorescence. Either technique provides an excellent biological probe and instrument combination for examining intracellular protein pathways along with the structural dynamics of organelles and the cytoskeleton.

Additional mutation studies have uncovered GFP variants that exhibit a variety of absorption and emission characteristics across the entire visible spectral region [70], which have enabled researchers to develop probe combinations for simultaneous observation of two or more distinct fluorescent proteins in a single organism (Figure 2.9). Early investigations yielded improved blue fluorescent protein (BFP) and cyan fluorescent protein (CFP) mutants from simple amino acid substitutions that shifted the absorption and emission spectral profiles of wild-type GFP to lower wavelength regions [67]. Used in combination with GFP, these variants and their newly improved derivatives [70,75,76] are useful in resonance energy transfer (FRET) experiments and other investigations that rely on multi-color fluorescence imaging. Blue fluorescent protein derivatives can be efficiently excited with the 354-nm line from a high-power argon laser, while the more useful cyan derivative is excited by a number of violet and blue laser lines, including the 405-nm blue diode, the 442-nm helium-cadmium spectral line, and the 457-nm line from the standard argon-ion laser.

Another popular fluorescent protein derivative, the yellow fluorescent protein (YFP), was designed on the basis of the GFP crystalline structural analysis to red-shift the absorption and emission spectra [77]. Yellow fluorescent protein is optimally excited by the 514-nm spectral line of the argon-ion laser, and provides more intense emission than enhanced green fluorescent protein but is more sensitive

to low pH and high halogen ion concentrations. The enhanced yellow fluorescent protein derivative (EYFP) and other improved derivatives [70] are useful with the 514-argon-ion laser line, but can also be excited with relatively high efficiency by the 488-nm line from argon and krypton-argon lasers. Both of these fluorescent protein derivatives have been widely applied to protein-protein FRET investigations in combination with CFP, and, in addition, have proven useful in studies involving multiprotein trafficking.

Attempts to shift the absorption and emission spectra of *Aequorea victoria* fluorescent proteins to wavelengths in the orange and red regions of the spectrum have met with little success. However, fluorescent proteins from other marine species have enabled investigators to extend the available spectral regions to well within the red wavelength range. The DsRed fluorescent protein and its derivatives (most notably, mCherry [78] and mPlum [79]), originally isolated from the sea anemone *Discosoma striata*, are currently the most popular analogs for fluorescence analysis in the 575- to 650-nm region [70,79]. Another protein, HcRed from the *Heteractis crispa* purple anemone, is also a promising candidate for investigations in the longer wavelengths of the visible spectrum [80]. Newly developed “optical highlighter” fluorescent proteins [81], including photoactivatable green fluorescent protein (PA-GFP; [82]), Kaede [83] Eos [84], Dronpa [85], and kindling fluorescent protein 1 (KFP1; [86]), exhibit dramatic improvements over GFP (up to several thousand-fold) in fluorescence intensity when stimulated by violet laser illumination. These probes should prove useful in widefield and confocal fluorescence studies involving selective irradiation of specific target regions and the subsequent kinetic analysis of diffusional mobility and compartmental residency time of fusion proteins.

Among the key advantages of genetically encoded fluorescent proteins is the precise targeting that is accompanied by their ability to be directly fused to a protein of interest. Modern transfection and transgenic technology also renders exogenous DNA far easier to deliver into cells or whole organisms than synthetic dyes or quantum dots [13]. Among the drawbacks of fluorescent proteins is their large size relative to smaller synthetic fluorophores, the potential for dimerization and larger scale aggregation, a broader fluorescence emission spectrum compared to other fluorophores (approximately 60 nm versus 30–40 nm), and the possibility that fusion may interfere with the normal function of the target protein.

## 2.10 Hybrid Systems

Several research groups have recently developed “hybrid” systems that couple small, synthetic fluorescent molecules to genetically encoded targets as an alternative to fluorescent proteins, and these are emerging as promising candidates for applications in cell biology [13–15,87]. The basic strategy involves genetically fusing a target protein to the desired receptor (usually a protein domain or peptide sequence), which is then labeled with a small molecule fluorescent probe consisting of a receptor binding ligand coupled to a fluorophore. When added to cells in culture that have been previously transfected with the genetically encoded receptor,

the probe diffuses through the cell membrane and binds specifically and stably to the receptor fusion protein. The success of this approach relies on developing (or discovering) a receptor that is highly specific for the fluorescent probe (thus minimizing background fluorescence) and does not interfere with the function of the target protein.

The flagship hybrid system was first developed by Roger Tsien and associates [88] and involves a tetracysteine-biarsenical scheme that covalently binds a membrane-permeable biarsenical probe to a target protein modified by the addition of a 12-residue peptide sequence containing four strategically placed cysteines. The biarsenical probes, of which the two most prominent are named FAsH and ReAsH (Fluorescein or Resorufin Arsenical Helix Binder), attach to the receptor peptide sequence with picomolar affinity [89]. In order to reduce background fluorescence levels and toxicity to endogenous proteins, small dithiol antidotes are simultaneously administered to the live cells with the probe. Several rounds of improvement in the Tetracysteine motif have increased the affinity for biarsenical dyes, which has enabled lowering dye concentrations as well as the use of higher antidote levels [90].

After development of the tetracysteine-biarsenical system, several alternative ligand-receptor approaches have been reported for *in vivo* protein labeling. The most notable include the coupling of benzyl guanine derivatives with human O<sup>6</sup>-alkylguanine DNA alkyl transferase (hAGT) [91], and binding of a methotrexate-Texas Red conjugate to a dihydrofolate reductase fusion protein [92], although other systems are currently under development [93]. In general, the hybrid systems utilize traditional fluorochromes, such as fluorescein, rhodamine derivatives, and Texas Red, which enables these labels to be imaged with common laser lines and filter combinations in confocal and widefield fluorescence microscopy. The advantages of hybrid systems are greater versatility with respect to fluorescent proteins, but they remain hampered by higher background fluorescence levels and poorer contrast. Furthermore, these compounds have not yet been tested in transgenic animals and often require the receptors to be chemically reduced during labeling (i.e., cysteines). They also will not permit two different proteins in the same cell to be labeled simultaneously with different colors.

## 2.11 Quenching and Photobleaching

The consequences of quenching and photobleaching are suffered in practically all forms of fluorescence microscopy, and result in an effective reduction in the levels of emission [94, 95]. These artifacts should be of primary consideration when designing and executing fluorescence investigations. The two phenomena are distinct in that quenching is often reversible, whereas photobleaching is not [96]. Quenching arises from a variety of competing processes that induce nonradiative relaxation (without photon emission) of excited state electrons to the ground state, which may be either intramolecular or intermolecular in nature. Because non-radiative transition pathways compete with the fluorescence relaxation, they usually dramatically lower or, in some cases, completely eliminate emission. Most

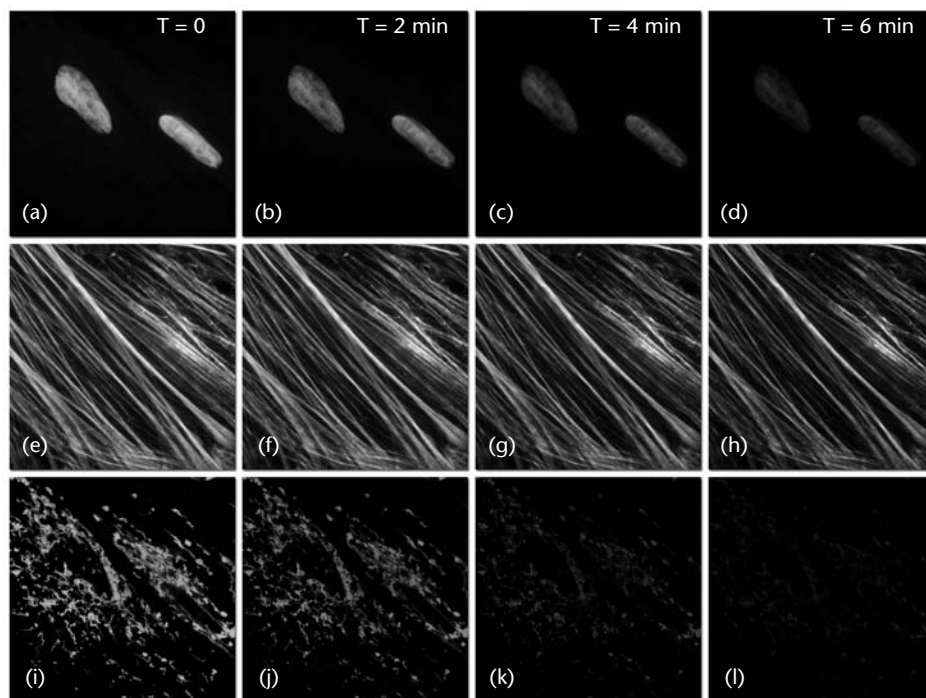
quenching processes act to reduce the excited state lifetime and the quantum yield of the affected fluorophore.

A common example of quenching is observed with the collision of an excited state fluorophore and another (nonfluorescent) molecule in solution, resulting in deactivation of the fluorophore and return to the ground state. In most cases, neither of the molecules is chemically altered in the collisional-quenching process. A wide variety of simple elements and compounds behave as collisional-quenching agents, including oxygen, halogens, amines, and many electron-deficient organic molecules [96]. Collisional quenching can reveal the presence of localized quencher molecules or moieties, which via diffusion or conformational change, may collide with the fluorophore during the excited state lifetime. The mechanisms for collisional quenching include electron transfer, spin-orbit coupling, and intersystem crossing to the excited triplet state [96, 97]. Other terms that are often utilized interchangeably with collisional quenching are internal conversion and dynamic quenching.

A second type of quenching mechanism, termed static or complex quenching, arises from nonfluorescent complexes formed between the quencher and fluorophore that serve to limit absorption by reducing the population of active, excitable molecules [96]. This effect occurs when the fluorescent species forms a reversible complex with the quencher molecule in the ground state and does not rely on diffusion or molecular collisions. In static quenching, fluorescence emission is reduced without altering the excited state lifetime. A fluorophore in the excited state can also be quenched by a dipolar resonance energy transfer mechanism when in close proximity with an acceptor molecule to which the excited state energy can be transferred nonradiatively [96]. In some cases, quenching can occur through nonmolecular mechanisms, such as attenuation of incident light by an absorbing species (including the chromophore itself).

In contrast to quenching, photobleaching (also termed fading) occurs when a fluorophore permanently loses the ability to fluoresce due to photon-induced chemical damage and covalent modification (see Figure 2.10, [94–97]). Upon transition from an excited singlet state to the excited triplet state, fluorophores may interact with another molecule to produce irreversible covalent modifications. The triplet state is relatively long-lived with respect to the singlet state, thus allowing excited molecules a much longer timeframe to undergo chemical reactions with components in the environment [96]. The average number of excitation and emission cycles that occur for a particular fluorophore before photobleaching is dependent upon the molecular structure and the local environment [95–97]. Some fluorophores bleach quickly after emitting only a few photons, while others that are more robust can undergo thousands or even millions of cycles before bleaching.

An important class of photobleaching events is represented by events that are photodynamic, meaning they involve the interaction of the fluorophore with a combination of light and oxygen [98–102]. Reactions between fluorophores and molecular oxygen permanently destroy fluorescence and yield a free radical singlet oxygen species that can chemically modify other molecules in living cells. The amount of photobleaching due to photodynamic events is a function of the molecular oxygen concentration and the proximal distance between the fluorophore,



**Figure 2.10** Differential photobleaching rates with synthetic fluorophores: Normal Tahr ovary (HJ1.Ov line) fibroblast cells were fixed and stained with DAPI (nuclei; (a)–(d)); Alexa Fluor 488 conjugated to phalloidin (actin cytoskeleton; (e)–(h)); and MitoTracker Red CMXRos (mitochondria; (i)–(l)). During illumination without a neutral density filter, time points were taken in 2-minute intervals using a fluorescence filter combination with bandwidths tuned to excite the three fluorophores simultaneously while also recording the combined emission signals. Note that all three fluorophores have a relatively high initial intensity, but the DAPI (b) and MitoTracker (j), intensities start to drop rapidly at 2 minutes and the MitoTracker is almost completely gone at 6 minutes (l). The Alexa Fluor 488 dye is more resistant to photobleaching and loses only about 50% intensity over the course of the timed sequence.

oxygen molecules, and other cellular components. Photobleaching can be reduced by limiting the exposure time of fluorophores to illumination or by lowering the excitation energy. However, these techniques also reduce the measurable fluorescence signal. In many cases, solutions of fluorophores or cell suspensions can be deoxygenated, but this is not feasible for living cells and tissues. Perhaps the best protection against photobleaching is to limit exposure of the fluorochrome to intense illumination (using neutral density filters) coupled with the judicious use of commercially available antifade reagents that can be added to the mounting solution or cell culture medium [95].

Under certain circumstances, the photobleaching effect can also be utilized to obtain specific information that would not otherwise be available. For example, in fluorescence recovery after photobleaching (FRAP) experiments, fluorophores within a target region are intentionally bleached with excessive levels of irradiation [103]. As new fluorophore molecules diffuse into the bleached region of the

specimen (recovery), the fluorescence emission intensity is monitored to determine the lateral diffusion rates of the target fluorophore. In this manner, the translational mobility of fluorescently labeled molecules can be ascertained within a very small (2 to 5  $\mu\text{m}$ ) region of a single cell or section of living tissue.

## 2.12 Conclusions

Although the subset of fluorophores that are advantageous in fluorescence microscopy is rapidly growing, many of the traditional probes that have been useful for years in widefield applications are still of little utility when constrained by fixed-wavelength laser spectral lines. Many of the limitations surrounding the use of fluorophores excited in the ultraviolet region will be eliminated with the introduction of advanced objectives designed to reduce aberration coupled with the gradual introduction of low-cost, high-power diode laser systems with spectral lines in these shorter wavelengths. The 405-nm blue diode laser is a rather cheap alternative to more expensive ion and Noble gas-based ultraviolet lasers, and is rapidly becoming available for most confocal microscope systems. Helium-neon lasers with spectral lines in the yellow and orange region have rendered some fluorophores useful that were previously limited to widefield applications. In addition, new diode-pumped solid-state lasers are being introduced with emission wavelengths in the ultraviolet, violet, and blue regions.

Continued advances in fluorophore design, dual-laser scanning, multispectral imaging, endoscopic instruments, and spinning disk applications will also be important in the coming years. The persistent problem of emission crossover due to spectral overlap, which occurs with many synthetic probes and fluorescent proteins in multicolor investigations, benefits significantly from spectral analysis and deconvolution of lambda stacks. Combined, these advances will dramatically improve the collection and analysis of data obtained from complex fluorescence experiments in live-cell imaging.

## References

- [1] Haugland, R. P., *The Handbook: A Guide to Fluorescent Probes and Labeling Technologies*, Chicago, IL: Invitrogen Molecular Probes, 2005.
- [2] Lemasters, J. J., et al., "Confocal Imaging of  $\text{Ca}^{2+}$ , pH, Electrical Potential and Membrane Permeability in Single Living Cells," *Methods in Enzymology*, Vol. 302, 1999, pp. 341–358.
- [3] Johnson, I., "Fluorescent Probes for Living Cells," *Histochemical Journal*, Vol. 30, 1998, pp. 123–140.
- [4] Kasten, F. H., "Introduction to Fluorescent Probes: Properties, History, and Applications," in *Fluorescent and Luminescent Probes for Biological Activity*, W. T. Mason, (ed.), New York: Academic Press, 1999, pp. 17–39.
- [5] Hibbs, A. R., *Confocal Microscopy for Biologists*, New York: Kluwer Academic, 2004, pp. 201–238.
- [6] Coons, A. H., et al., "Demonstration of Pneumococcal Antigen in Tissues by Use of Fluorescent Antibody," *Journal of Immunology*, Vol. 45, 1942, pp. 159–170.



- [7] Miyawaki, A., A. Sawano, and T. Kogure, "Lighting Up Cells: Labeling Proteins with Fluorophores," *Nature Cell Biology*, Vol. 5, 2003, pp. S1-S7.
- [8] Zhang, J., et al., "Creating New Fluorescent Probes for Cell Biology," *Nature Reviews Molecular Cell Biology*, Vol. 3, 2002, pp. 906-918.
- [9] Lippincott-Schwartz, J., and G. H. Patterson, "Development and Use of Fluorescent Protein Markers in Living Cells," *Science*, Vol. 300, 2003, pp. 87-91.
- [10] Tsien, R. Y., "Building and Breeding Molecules to Spy on Cells and Tumors," *Federation of European Biochemical Societies Letters*, Vol. 579, 2005, pp. 927-932.
- [11] Bruchez, J. R., et al., "Semiconductor Nanocrystals as Fluorescent Biological Labels," *Science*, Vol. 218, 1998, pp. 2013-2016.
- [12] Alivisatos, A. P., W. Gu, and C. Larabell, "Quantum Dots as Cellular Probes," *Annual Review of Biomedical Engineering*, Vol. 7, 2005, pp. 55-76.
- [13] Giepmans, B. N. G., et al., "The Fluorescent Toolbox for Assessing Protein Location and Function," *Science*, Vol. 312, 2006, pp. 217-223.
- [14] Gronemeyer, T., G. Godin, and K. Johnsson, "Adding Value to Fusion Proteins Through Covalent labeling," *Current Opinion in Biotechnology*, Vol. 16, 2005, pp. 453-458.
- [15] Johnsson, N., and K. Johnsson, "Chemical Tools for Biomolecular Imaging," *ACS Chemical Biology*, Vol. 2, 2007, pp. 31-38.
- [16] Gratton, E., and M. J. vandeVen, "Laser Sources for Confocal Microscopy," in *Handbook of Biological Confocal Microscopy*, J. B. Pawley, (ed.), New York: Plenum Press, 2006, pp. 80-125.
- [17] Murphy, D. B., *Fundamentals of Light Microscopy and Electronic Imaging*, New York: Wiley-Liss, 2001, pp. 29-42.
- [18] Tsien, R. Y., L. Ernst, and A. Waggoner, "Fluorophores for Confocal Microscopy," in *Handbook of Biological Confocal Microscopy*, J. B. Pawley, (ed.), New York: Plenum Press, 2006, pp. 338-352.
- [19] Spring, K. R., "Detectors for Fluorescence Microscopy," in *Methods in Cellular Imaging*, A. Periasamy, (ed.), New York: Oxford University Press, 2001, pp. 40-52.
- [20] Art, J., "Photon Detectors for Confocal Microscopy," in *Handbook of Biological Confocal Microscopy*, J. B. Pawley, (ed.), New York: Plenum Press, 2006, pp. 251-264.
- [21] Piston, D. W., G. H. Patterson, and S. M. Knobel, "Quantitative Imaging of the Green Fluorescent Protein (GFP)," in *Green Fluorescent Proteins, Methods in Cell Biology*, Vol. 58, K. F. Sullivan and S. A. Kay, (eds.), New York: Academic Press, 1999, pp. 31-47.
- [22] Wessendorf, M. W., and T. C. Brelje, "Which Fluorophore Is Brightest? A Comparison of the Staining Obtained Using Fluorescein, Tetramethylrhodamine, Lissamine Rhodamine, Texas Red and Cyanine 3.18," *Histochemistry*, Vol. 98, 1992, pp. 81-85.
- [23] Entwistle, A., and M. Noble, "The Use of Lucifer Yellow, BODIPY, FITC, TRITC, RITC and Texas Red for Dual Immunofluorescence Visualized with a Confocal Scanning Laser Microscope," *Journal of Microscopy*, Vol. 168, 1992, pp. 219-238.
- [24] Darzynkiewicz, Z., "Differential Staining of DNA and RNA in Intact Cells and Isolated Cell Nuclei with Acridine Orange," *Methods in Cell Biology*, Vol. 33, 1990, pp. 285-298.
- [25] Waring, M. J., "Complex Formation Between Ethidium Bromide and Nucleic Acids," *Journal of Molecular Biology*, Vol. 13, 1965, pp. 269-282.
- [26] Arndt-Jovin, D. J., and T. M. Jovin, "Fluorescence Labeling and Microscopy of DNA," in *Fluorescence Microscopy of Living Cells in Culture, Part B. Methods Cell Biol.*, D. L. Taylor and Y.-L. Wang, (eds.), Vol. 30, 1989, pp. 417-488.
- [27] Kubista, M., B. Akerman, and B. Norden, "Characterization of Interaction Between DNA and 4',6-diamidino-2-phenylindole by Optical Spectroscopy," *Biochemistry*, Vol. 26, 1987, pp. 4545-4553.



- [28] Loewe, H., and J. Urbanietz, "Basic Substituted 2,6-Bisbenzimidazole Derivatives: A Novel Series of Substances with Chemotherapeutic Activity," *Drug Research (Arzneim. Forsch.)*, Vol. 24, 1974, pp. 1927-1933.
- [29] Arndt-Jovin, D. J., and T. M. Jovin, "Analysis and Sorting of Living Cells According to Deoxyribonucleic Acid Content," *Journal Histochemistry Cytochemistry*, Vol. 25, 1977, pp. 585-589.
- [30] Durand, R. E., and P. L. Olive, "Cytotoxicity, Mutagenicity and DNA Damage by Hoechst 33342," *Journal Histochemistry Cytochemistry*, Vol. 30, 1982, pp. 111-116.
- [31] Panchuk-Voloshina, N., et al., "Alexa Dyes, A Series of New Fluorescent Dyes that Yield Exceptionally Bright, Photostable Conjugates," *Journal Histochemistry Cytochemistry*, Vol. 47, 1999, pp. 1179-1188.
- [32] Berlier, J. E., et al., "Quantitative Comparison of Long-Wavelength Alexa Fluor Dyes to Cy Dyes: Fluorescence of the Dyes and Their Conjugates," *Journal Histochemistry Cytochemistry*, Vol. 51, 2003, pp. 1699-1712.
- [33] Dickinson, M. E., et al., "Multi-Spectral Imaging and Linear Unmixing Add a Whole New Dimension to Laser Scanning Fluorescence Microscopy," *Biotechniques*, Vol. 31, 2001, pp. 1272-1278.
- [34] Zimmermann, T., J. Rietdorf, and R. Pepperkok, "Spectral Imaging and Its Applications in Live Cell Microscopy," *FEBS Letters*, Vol. 546, 2003, pp. 87-92.
- [35] Lansford, R., G. Bearman, and S. E. Fraser, "Resolution of Multiple Green Fluorescent Protein Variants and Dyes Using Two-Photon Microscopy and Imaging Spectroscopy," *Journal of Biomedical Optics*, Vol. 6, 2001, pp. 311-318.
- [36] Hiraoka, Y., T. Shimi, and T. Haraguchi, "Multispectral Imaging Fluorescence Microscopy for Living Cells," *Cell Structure and Function*, Vol. 27, 2002, pp. 367-374.
- [37] Mujumdar, R. B., et al., "Cyanine Dye Labeling Reagents: Sulfoindocyanine Succinimidyl Esters," *Bioconjugate Chemistry*, Vol. 4, 1993, pp. 105-111.
- [38] Ballou, B., et al., "Tumor Labeling *In Vivo* Using Cyanine-Conjugated Monoclonal Antibodies," *Cancer Immunology Immunotherapy*, Vol. 41, 1995, pp. 257-263.
- [39] Zorov, D. B., et al., "Examining Intracellular Organelle Function Using Fluorescent Probes," *Circulation Research*, Vol. 95, 2004, pp. 239-252.
- [40] Stephens, D. G., and R. Pepperkok, "The Many Ways to Cross the Plasma Membrane," *Proc. of the National Academy of Sciences USA*, Vol. 98, 2001, pp. 4295-4298.
- [41] Rudolf, R., et al., "Looking Forward to Seeing Calcium," *Nature Review Molecular Cell Biology*, Vol. 4, 2003, pp. 579-586.
- [42] Martin, H., et al., "Activation Kinetics of Skinned Cardiac Muscle by Laser Photolysis of Nitrophenyl-EGTA," *Biophysical Journal*, Vol. 86, 2004, pp. 978-990.
- [43] White C., and G. McGeown, "Imaging of Changes in Sarcoplasmic Reticulum  $[Ca^{2+}]$  Using Oregon Green BAPTA 5N and Confocal Laser Scanning Microscopy," *Cell Calcium*, Vol. 31, 2002, pp. 151-159.
- [44] Helm, P. J., A. Patwardhan, and E. M., Manders, "A Study of the Precision of Confocal, Ratiometric, Fura-2-Based  $[Ca^{2+}]$  Measurements," *Cell Calcium*, Vol. 22, 1997, pp. 287-298.
- [45] Rijkers, G. T., et al., "Improved Method for Measuring Intracellular  $Ca^{++}$  with Fluo-3," *Cytometry*, Vol. 11, 1990, pp. 923-927.
- [46] Schild, D., A. Jung, and H. A. Schultens, "Localization of Calcium Entry Through Calcium Channels in Olfactory Receptor Neurons Using a Laser Scanning Microscope and the Calcium Indicator Dyes Fluo-3 and Fura-Red," *Cell Calcium*, Vol. 15, 1994, pp. 341-348.
- [47] Willoughby, D., R. C. Thomas, and C. J. Schwiening, "Comparison of Simultaneous pH Measurements made with 8-Hydroxypyrene-1,3,6-Trisulphonic Acid (HPTS) and

- pH-Sensitive Microelectrodes in Snail Neurons,” *Pflügers Archives*, Vol. 436, 1998, pp. 615–622.
- [48] Ozkan, P., and R. Mutharasan, “A Rapid Method for Measuring Intracellular pH Using BCECF-AM,” *Biochemistry Biophysical Acta*, Vol. 1572, 2002, pp. 143–148.
- [49] Cody, S. H., et al., “Intracellular pH Mapping with SNARF-1 and Confocal Microscopy. I: A Quantitative Technique for Living Tissue and Isolated Cells,” *Micron*, Vol. 24, 1993, pp. 573–580.
- [50] Dubbin, P. N., S. H. Cody, and D. A. Williams, “Intracellular pH Mapping with SNARF-1 and Confocal Microscopy. II: pH Gradients Within Single Cultured Cells,” *Micron*, Vol. 24, 1993, pp. 581–586.
- [51] Poot, M., et al., “Analysis of Mitochondrial Morphology and Function with Novel Fixable Fluorescent Stains,” *Journal Histochemistry Cytochemistry*, Vol. 44, 1996, pp. 1363–1372.
- [52] Keij, J. F., C. Bell-Prince, and J. A. Steinkamp, “Staining of Mitochondrial Membranes with 10-Nonyl Acridine Orange, MitoFluor Green, and MitoTracker Green Is Affected by Mitochondrial Membrane Potential Altering Drugs,” *Cytometry*, Vol. 39, 2000, pp. 203–210.
- [53] Reers, M., et al., “Mitochondrial Membrane Potential Monitored by JC-1 Dye,” *Methods in Enzymology*, Vol. 260, 1995, pp. 406–417.
- [54] Price, O. T., C. Lau, and R. M. Zucker, “Quantitative Fluorescence of 5-FU-Treated Fetal Rat Limbs Using Confocal Laser Scanning Microscopy and LysoTracker Red,” *Cytometry*, Vol. 53A, 2003, pp. 9–21.
- [55] Pagano, R. E., and O. C. Martin, “Use of Fluorescent Analogs of Ceramide to Study the Golgi Apparatus of Animal Cells,” in *Cell Biology: A Laboratory Handbook*, Vol. 2, J. E. Celis, (ed.), Cold Spring Harbor, NY: Cold Spring Harbor Press, 1998, pp. 507–512.
- [56] Kumar, R. K., C. C. Chapple, and N. Hunter, “Improved Double Immunofluorescence for Confocal Laser Scanning Microscopy,” *Journal Histochemistry Cytochemistry*, Vol. 47, 1999, pp. 1213–1217.
- [57] Suzuki, T., et al., “DNA Staining for Fluorescence and Laser Confocal Microscopy,” *Journal Histochemistry Cytochemistry*, Vol. 45, 1997, pp. 49–53.
- [58] Haugland, R. P., “Coupling of Monoclonal Antibodies with Fluorophores,” in *Monoclonal Antibody Protocols: Methods in Molecular Biology*, Vol. 45, W. C. Davis, (ed.), Totowa, NJ: Humana Press, 1995, pp. 205–221.
- [59] Cole, L., et al., “ER-Tracker Dye and BODIPY-Brefeldin A Differentiate the Endoplasmic Reticulum and Golgi Bodies from the Tubular-Vacuole System in Living Hyphae of *Pisolithus tinctorius*,” *Journal of Microscopy*, Vol. 197, 2000, pp. 239–249.
- [60] Jaiswal, J. K., et al., “Long-Term Multiple Color Imaging of Live Cells Using Quantum Dot Bioconjugates,” *Nature Biotechnology*, Vol. 21, 2003, pp. 47–52.
- [61] Larson, D. R., et al., “Water Soluble Quantum Dots for Multiphoton Fluorescence Imaging *In Vivo*,” *Science*, Vol. 300, 2003, pp. 1434–1436.
- [62] Raymo, F. M., and I. Yildiz, “Luminescent Chemosensors Based on Semiconductor Quantum Dots,” *Physical Chemistry Chemical Physics*, Vol. 9, 2007, pp. 2036–2043.
- [63] Michalet, X., et al., “Quantum Dots for Live Cells, *In Vivo* Imaging, and Diagnostics,” *Science*, Vol. 307, 2005, pp. 538–544.
- [64] Gao, X., et al., “*In Vivo* Molecular and Cellular Imaging with Quantum Dots,” *Current Opinion in Biotechnology*, Vol. 16, 2005, pp. 63–72.
- [65] Lacoste, T. D., et al., “Ultrahigh-Resolution Multicolor Colocalization of Single Fluorescent Probes,” *Proc. of the National Academy of Sciences USA*, Vol. 97, 2000, pp. 9461–9466.

- [66] Lee, T. H., et al., "Single-Molecule Optoelectronics," *Accounts of Chemical Research*, Vol. 38, 2005, pp. 534-541.
- [67] Tsien, R. Y., "The Green Fluorescent Protein," *Annual Reviews in Biochemistry*, Vol. 67, 1998, pp. 509-544.
- [68] Remington, S. J., "Fluorescent Proteins: Maturation, Photochemistry, and Photophysics," *Current Opinion in Structural Biology*, Vol. 16, 2006, pp. 714-721.
- [69] Chudakov, D. M., S. Lukyanov, and K. A. Lukyanov, "Fluorescent Proteins as a Toolkit for *In Vivo* Imaging," *TRENDS in Biotechnology*, Vol. 23, 2005, pp. 605-613.
- [70] Shaner, N. C., Pl A. Steinbach, and R. Y. Tsien, "A Guide to Choosing Fluorescent Proteins," *Nature Methods*, Vol. 2, 2005, pp. 905-909.
- [71] Zimmer, M., "Green Fluorescent Protein: Applications, Structure, and Related Photo-physical Behavior," *Chemical Reviews*, Vol. 102, 2002, pp. 759-781.
- [72] Chalfie, M., et al., "Green Fluorescent Protein as a Marker for Gene Expression," *Science*, Vol. 263, 1994, pp. 802-805.
- [73] Glazer, A. N., "Light Guides: Directional Energy Transfer in a Photosynthetic Antenna," *Journal of Biological Chemistry*, Vol. 264, 1989, pp. 1-4.
- [74] Heim, R., A. B. Cubitt, and R. Y. Tsien, "Improved Green Fluorescence," *Nature*, Vol. 373, 1995, pp. 664-665.
- [75] Ai, H., et al., "Directed Evolution of a Monomeric, Bright and Photostable Version of *Clavularia* Cyan Fluorescent Protein: Structural Characterization and Applications in Fluorescent Imaging," *Biochemical Journal*, Vol. 400, 2006, pp. 531-540.
- [76] Ai, H., et al., "Exploration of New Chromophore Structures Leads to the Identification of Improved Blue Fluorescent Proteins," *Biochemistry*, Vol. 46, 2007, pp. 5904-5910.
- [77] Wachter, R. M., et al., "Structural Basis of Spectral Shifts in the Yellow-Emission Variants of Green Fluorescent Protein," *Structure*, Vol. 6, 1998, pp. 1267-1277.
- [78] Shaner, N. C., et al., "Improved Monomeric Red, Orange, and Yellow Fluorescent Proteins Derived from *Discosoma* sp. Red Fluorescent Protein," *Nature Biotechnology*, Vol. 22, 2004, pp. 1567-1572.
- [79] Matz, M. V., et al., "Fluorescent Proteins from Nonbioluminescent Anthozoa Species," *Nature Biotechnology*, Vol. 17, 1999, pp. 969-973.
- [80] Matz, M. V., K. A. Lukyanov, and S. A. Lukyanov, "Family of the Green Fluorescent Protein: Journey to the End of the Rainbow," *BioEssays*, Vol. 24, 2002, pp. 953-959.
- [81] Lukyanov, K. A., et al., "Photoactivatable Fluorescent Proteins," *Nature Reviews Molecular Cell Biology*, Vol. 6, 2005, pp. 885-891.
- [82] Patterson, G. H., and J. Lippincott-Schwartz, "A Photoactivatable GFP for Selective Photolabeling of Proteins and Cells," *Science*, Vol. 297, 2002, pp. 1873-1877.
- [83] Ando, R., et al., "An Optical Marker Based on the UV-Induced Green-to-Red Photoconversion of a Fluorescent Protein," *Proc. of the National Academy of Sciences USA*, Vol. 99, 2002, pp. 12651-12656.
- [84] Wiedenmann, J., et al., "EosFP, A Fluorescent Marker Protein with UV-Inducible Green-to-Red Fluorescence Conversion," *Proc. of the National Academy of Sciences USA*, Vol. 101, 2004, pp. 15905-15910.
- [85] Ando, R., H. Mizuno, and A. Miyawaki, "A Regulated Fast Nucleocytoplasmic Shuttling Observed by Reversible Protein Highlighting," *Science*, Vol. 306, 2004, pp. 1370-1373.
- [86] Chudakov, D. M., et al., "Kindling Fluorescent Proteins for Precise *In Vivo* Photolabeling," *Nature Biotechnology*, Vol. 21, 2003, pp. 191-194.
- [87] Miller, L. W., and V. W. Cornish, "Selective Chemical Labeling of Proteins in Living Cells," *Current Opinion in Chemical Biology*, Vol. 9, 2005, pp. 56-61.

- [88] Griffin, B. A., S. R. Adams, and R. Y. Tsien, "Specific Covalent Labeling of Recombinant Protein Molecules Inside Live Cells," *Science*, Vol. 281, 1998, pp. 269-272.
- [89] Adams, S. R., et al., "New Biarsenical Ligands and Tetracysteine Motifs for Protein Labeling in Vitro and in Vivo: Synthesis and Biological Applications," *Journal of the American Chemical Society*, Vol. 124, 2002, pp. 6063-6076.
- [90] Martin, B. R., et al., "Mammalian Cell-Based Optimization of the Biarsenical-Binding Tetracysteine Motif for Improved Fluorescence and Affinity," *Nature Biotechnology*, Vol. 23, 2005, pp. 1308-1314.
- [91] Keppler, A., et al., "Labeling of Fusion Proteins with Synthetic Fluorophores in Live Cells," *Proc. of the National Academy of Sciences USA*, Vol. 101, 2004, pp. 9955-9959.
- [92] Miller, L. W., et al., "Methotrexate Conjugates: A Molecular *In Vivo* Protein Tag," *Angewandte Chemie, International Edition*, Vol. 43, 2004, pp. 1672-1675.
- [93] Chen, I., and A. Y. Ting, "Site-Specific Labeling of Proteins with Small Molecules in Live Cells," *Current Opinion in Biotechnology*, Vol. 16, pp. 35-40.
- [94] Song, L., et al., "Photobleaching Kinetics of Fluorescein in Quantitative Fluorescence Microscopy," *Biophysical Journal*, Vol. 68, 1995, pp. 2588-2600.
- [95] Berrios, M., K. A. Conlon, and D. E. Colflesh, "Antifading Agents for Confocal Fluorescence Microscopy," *Methods in Enzymology*, Vol. 307, 1999, pp. 55-79.
- [96] Lakowicz, J. R., *Principles of Fluorescence Spectroscopy*, New York: Springer Science+Business Media, 2006, pp. 278-330.
- [97] Song, L., et al., "Influence of the Triplet Excited State on the Photobleaching Kinetics of Fluorescein in Microscopy," *Biophysical Journal*, Vol. 70, 1996, pp. 2959-2968.
- [98] Bunting, J. R., "A Test of the Singlet Oxygen Mechanism of Cationic Dye Photosensitization of Mitochondrial Damage," *Photochemistry and Photobiology*, Vol. 55, 1992, pp. 81-87.
- [99] Byers, G. W., S. Gross, and P. M. Henrichs, "Direct and Sensitized Photooxidation of Cyanine Dyes," *Photochemistry and Photobiology*, Vol. 23, 1976, pp. 37-43.
- [100] Dittrich, P. S., and P. Schuille, "Photobleaching and Stabilization of Fluorophores Used for Single Molecule Analysis with One- and Two-Photon Excitation," *Applied Physics B*, Vol. 73, 2001, pp. 829-837.
- [101] Gandin, E., Y. Lion and A. Van de Vorst, "Quantum Yield of Singlet Oxygen Production by Xanthene Derivatives," *Photochemistry and Photobiology*, Vol. 37, 1983, pp. 271-278.
- [102] Kanofsky, J. R., and P. D. Sima, "Structural and Environmental Requirements for Quenching of Singlet Oxygen by Cyanine Dyes," *Photochemistry and Photobiology*, Vol. 71, 2000, pp. 361-368.
- [103] Lippincott-Schwartz, J., N. Altan-Bonnet, and G. H. Patterson, "Photobleaching and Photoactivation: Following Protein Dynamics in Living Cells," *Nature Cell Biology*, Vol. 5, 2003, pp. S7-S14.

## Selected Bibliography

- Heim, R., D. C. Prasher, and R. Y. Tsien, "Wavelength Mutations and Posttranslational Autoxidation of Green Fluorescent Protein," *Proc. of the National Academy of Sciences, USA*, Vol. 91, 1994, pp. 12501-12504.
- Heim, R., and R. Y. Tsien, "Engineering Green Fluorescent Protein for Improved Brightness, Longer Wavelengths, and Fluorescence Resonance Energy Transfer," *Current Biology*, Vol. 6, 1996, pp. 178-182.

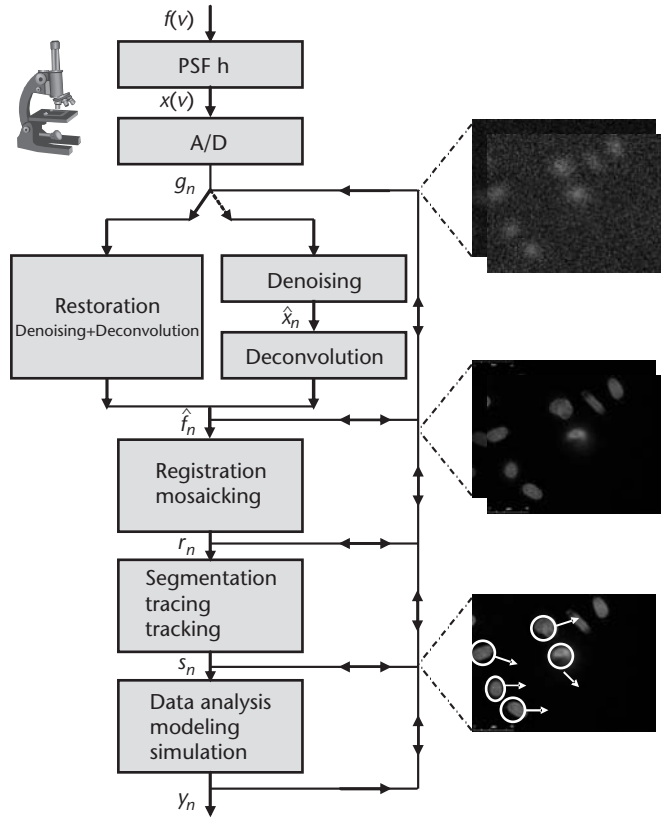
# Overview of Image Analysis Tools and Tasks for Microscopy

Jelena Kovačević and Gustavo K. Rohde

The advent of fluorescent proteins, together with the recent development of advanced high-resolution microscopes, have enabled scientists to probe the intricate structure and function of cells and subcellular structures with unprecedented accuracy and specificity. Imaging experiments have become the main source of data for biologists to test and validate hypotheses related to basic cellular and molecular phenomena. Computational methods for automated interpretation and information extraction from biological images have augmented the impact of imaging experiments and are quickly becoming a valuable extension of the microscope. Such studies have long been a major topic of biomedical research (see, for example, [1]), and the recent advances in microscopic image acquisition systems as well as sophisticated image processing algorithms indicate that this is a trend likely to continue [2, 3].

We present a brief overview of computer-aided image analysis tools and tasks for microscopy. While the tasks and applications we discuss are those currently needed in the field, the algorithms used to perform them are not often state of the art. Thus, our aim is to introduce the reader to the modern tools of signal processing and data mining for microscopy, highlighting opportunities for innovative research in the area. Some recent accomplishments can be found in the special issue of the *Signal Processing Magazine* on molecular and cellular bioimaging [4].

The overview of the system we discuss is given in Figure 3.1. We begin by reviewing a system-level approach that summarizes the physical aspects of acquisition described in Chapter 1 (the first two blocks in the figure, PSF and A/D conversion). Important features and artifacts of imaging acquisition systems such as sampling, blurring, and noise are briefly discussed in connection with traditional and modern techniques for automated artifact removal and information extraction (the blocks of denoising, deconvolution, and restoration in the figure). The chapter is structured around mathematical tools currently used, as well as some that are not, but have the potential for high impact in automated biological image analysis. We conclude the chapter by covering various image processing and analysis tasks needed in microscopy in the order they appear in a real system, starting with registration and mosaicing, followed by segmentation, tracing and tracking, and finally data modeling, analysis, and simulation (the last three blocks in the figure). The main aim of this chapter is to provide a concise overview of the state-of-the-art tools and algorithms for computer-aided extraction of quantitative information from images, in the hope that they become state-of-the-art tools in microscopy as well.



**Figure 3.1** A conceptual pipeline. The specimen is imaged using any of today’s microscopes, modeled by the input image  $f(v)$  passing through the blocks of PSF (properties of the microscope, described by convolution with  $h(v)$ ) and A/D conversion (analog-to-digital conversion, effects of sampling and digitization together with uncertainty introduced by various sources of noise), producing a digital image  $g_n$ . That digital image is then restored either via a denoising followed by deconvolution, or via joint denoising/deconvolution, producing a digital image  $\hat{f}_n$ . Various options are possible: the image could go through a registration/mosaicking processing producing  $r_n$ , segmentation/tracing/tracking producing  $s_n$  and finally a data analysis/modeling/simulations block with the output  $\gamma_n$ . At the input/output of each block, one can join the pathway to either skip a block or send feedback to previous block(s) in the system. (Images courtesy of K. N. Dahl.)

### 3.1 Image Analysis Framework

We first set up the framework in which we will examine digital images arising from typical microscopes (widefield, confocal, and others). As terms themselves can lead to confusion, we note the following: The term “digital image” typically refers to a continuous-domain image that has been both discretized (that is, sampled on a discrete grid), as well as digitized (that is, the intensity has been quantized for digital representation). Further, in the signal processing literature, “time” is often used to denote the image domain, although strictly speaking the domain of images



can be space, time, channels, and so on. Therefore, to avoid confusion, when speaking of the types of domains, we will refer to them as continuous domain and discrete domain (we will, however, keep the standard nomenclature, such as discrete-time Fourier transform, time frequency, and so on).

Without discretization, the result of imaging an object (specimen) would be a continuous-domain image. We introduce images (both continuous-domain as well as discrete-domain) as vectors in Hilbert spaces and acquisition/imaging systems as transformations from one Hilbert space into another. Most of these will be linear and can transform one continuous-domain image into another (continuous-domain filtering), a continuous-domain image into a discrete-domain one (analog-to-digital conversion (A/D)), or a discrete-domain image into a discrete-domain one (discrete-domain filtering). We will discuss all three of these in what follows. Again, a conceptual view of the whole system is given in Figure 3.1. An excellent reference text on foundations of image science is [5].

### 3.1.1 Continuous-Domain Image Processing

What we usually call a *microscope image* is an already acquired and thus discrete-domain data set, which we refer to from now on as a digital image. Since ultimately, what we really want to understand, analyze, and interpret are the biological characteristics of the underlying specimen, we must first understand the continuous-domain image at its root. While we should distinguish between the specimen and the image of the specimen, from now on we will assume that the continuous-domain image of the specimen is the ground truth.

#### 3.1.1.1 Framework

We will denote such an image as  $f(x, y, z, t, c)$ , where  $x, y$  are the two spatial dimensions in the focal plane of the objective,  $z$  is the third spatial dimension perpendicular to the focal plane,  $t$  is the time dimension in case of time-lapse imaging, and  $c$  denotes multiple channels. (Not all the dimensions are present in every case.) To make matters even simpler, we introduce a vector  $v = (x, y, z, t, c)$  that will allow us to add other dimensions to the vector if needed. The number of dimensions is denoted by  $d$  (five in this case). The image  $f(v)$  appears as the input to the system in Figure 3.1.

Very often, the value of  $f(v)$  is scalar—for example,  $f(v)$  could denote the intensity. It is also possible for  $f(v)$  to be vector valued, as in the case of color. For example, at any point in space and time,  $f(v)$  could be given in one of the standard, three-variable color models such as RGB, YUV, and HSV. We will keep the notation the same regardless of whether  $f(v)$  is scalar or vector valued; its meaning will be obvious from the context. For example,  $f(x, y)$  is typically called a 2-D slice,  $f(x, y, z)$  a z-stack, and  $f(x, y, t)$  a 2-D time series, while  $f(x, y, z, t)$  is a 3-D time series. In all these cases, the value can be either scalar or vector. For example,  $(r(x, y), g(x, y), b(x, y)) = f(x, y)$  is an RGB 2-D slice.

While in reality the domain of  $f$  is finite (that is, the domains of  $x, y, z, t, c$  are all of finite support), the domain of such images is often assumed to be infinite for ease of explanation. For example, while we might be imaging a specimen of finite



size  $100\ \mu\text{m} \times 100\ \mu\text{m}$  in the focal plane, we might use the tools that assume that the domain is infinite. This is also done to avoid more cumbersome tools operating on a finite domain (such as the circular convolution), although these tools have become standard as well.

### 3.1.1.2 Deterministic Versus Stochastic Description

For now, we limit ourselves to the deterministic treatment of images and transformations between them. The issues of randomness and uncertainty, such as those found when noise is present, will be discussed later.

### 3.1.1.3 Linear-Shift Invariant Systems and Point Spread Functions

Given an image  $f(v)$ , we may model the effect of the acquisition system on it as the operator  $H[\cdot]$ , resulting in  $x(v) = H[f(v)]$  (see Figure 3.1), where  $H$  is in general nonlinear. In image processing,  $H$  is termed a *filter*, and in practice, we most often assume that  $H$  is *linear*. In other words, an imaging, or acquisition, system is a linear transformation from one Hilbert space into another.

Another important property of filters is shift invariance. A system/filter is called *shift invariant* if, given the input/output pair  $(f(v), x(v))$ , the output of the system with the shifted input  $f(v - v_0)$  is a shifted output  $x(v - v_0)$ . Combining the properties of linearity and shift invariance gives rise to *linear shift-invariant (LSI)* systems; analysis is the simplest when the system is LSI. For an LSI system, the operation of the filter on the image is described by *convolution*, denoted by  $*$ ; given that each image  $f(v)$  can be written as

$$f(v) = \int f(r)\delta(v - r)dr \quad (3.1)$$

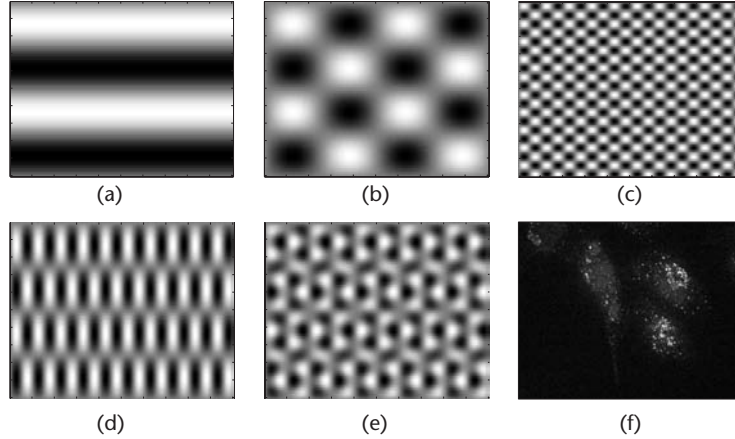
where  $\delta(v)$  is the Dirac pulse, the filtered image is given by

$$\begin{aligned} x(v) &= H\left[\int f(r)\delta(v - r)dr\right] = \int f(r)H[\delta(v - r)dr] \\ &= \int f(r)h(v - r)dr = (h * f)(v) \end{aligned} \quad (3.2)$$

Here, we have defined the *impulse response* or *point spread function (PSF)* of an LSI system  $h(v)$  as the output of the system to the input, which is a Dirac pulse  $\delta(v)$ . Note that the PSF is typically assumed to be positive, while this is not necessarily true for the impulse response.

### 3.1.1.4 The Fourier View

Because of the cumbersome form of the convolution, when analyzing images, one often resorts to using the *Fourier transform (FT)*, as the convolution becomes multiplication in the Fourier domain. For certain classes of images, the FT finds the harmonic content of the image, or, in other words, it tries to represent the image as a sum of sinusoids. Figure 3.2 shows a few examples of simple and more complex harmonic signals.



**Figure 3.2** Example images. (a) Simple 1-D sinusoidal image:  $f(x, y) = \sin(\pi/50)x$ . (b) 2-D sinusoidal image of low frequency:  $f(x, y) = \sin(\pi/50)x\sin(\pi/50)y$ . (c) 2-D sinusoidal image of high frequency:  $f(x, y) = \sin(\pi/10)x\sin(\pi/10)y$ . (d) 2-D sinusoidal image of different frequencies in the two directions:  $f(x, y) = \sin(\pi/50)x\sin(\pi/10)y$ . (e) 2-D image obtained as a sum of two frequencies in two directions:  $f(x, y) = \sin(\pi/50)x\sin(\pi/10)y + \sin(\pi/14)x\sin(\pi/20)y$ . (f) General image.

The FT of  $f(v)$  is given by (we follow the convention of using lowercase letters for the image data in the original domain, and uppercase ones for the same in the Fourier domain):

$$F(\omega) = \int_{\mathbb{R}^d} f(v) e^{-j\omega^T v} dv \quad (3.3)$$

where  $\omega, v$  are vectors in general. For a 2-D signal, (3.3) reads

$$F(\omega_1, \omega_2) = \int_{\mathbb{R}^2} f(v_1, v_2) e^{-j(\omega_1 v_1 + \omega_2 v_2)} dv_1 dv_2$$

Using (3.3) on the convolution expression (3.2), we obtain that the FT of  $x(v) = (h * f)(v)$  is  $X(\omega) = H(\omega)F(\omega)$ . The FT is valid assuming our signals belong to the space of square-integrable functions,  $\mathcal{L}^2(\mathbb{R})$ . If a signal is periodic (that is, if it lives on a circle) then the appropriate FT is called *Fourier series (FS)*.

#### 3.1.1.5 What This Means in Practice

In practice, the system we refer to in the impulse response of the system or PSF is the microscope itself; thus,  $h$  represents the optical properties of the microscope (with  $h$  positive). Knowing these properties allows us to determine the PSF and thus, if necessary, reverse the effects of the imaging system on the image itself (remember, our goal is to have access to as “pure” a version of our specimen image  $f(v)$  as possible). This is depicted in Figure 3.1, where the input is  $f(v)$ , and the output is the filtered version  $x(v)$ .

### 3.1.2 A/D Conversion

While it is clear that if it were possible, the underlying image would have most of its parameters continuous in nature (space and time at least), it is also intuitively clear that this is not the output of a microscope. The reason for this is that there is a minimum distance at which the responses from two separate points in the sample can be distinguished. This minimum distance leads to the notion of *resolution* in microscopy, somewhat different from the same term applied in signal processing (where it denotes the amount of information present in a signal).

Sampling, or discretization, can be performed without loss of information, if enough samples are taken to represent the continuous-domain image faithfully. Intuitively, this means that the continuous-domain image cannot “vary” too much as it would require too many samples to represent it well (that is, it must be somewhat “smooth”). This can be mathematically made precise by saying that if the continuous-domain image  $x(v)$  is bandlimited (that is, if its FT is zero above a certain frequency,  $|X(\omega)| = 0$ , for  $|\omega| > \omega_m$ , then it can be reconstructed from its samples taken at twice the maximum frequency  $\omega_s = 2\omega_m$ ). This is known under various names, such as Shannon sampling theorem [6]. The resulting samples are  $x_n = x(\mu n)$ , where  $n \in \Omega_s \subset \mathbb{Z}^d$  is a set of index coordinates (for example, pixels when  $d = 2$  or voxels when  $d = 3$ ), and  $\mu \in \mathbb{R}^d$  collects the sampling steps in each dimension. The original image  $x(v)$  can then be reconstructed from  $x_n$  via

$$x(v) = \sum_{n \in \Omega_s} x_n \prod_{i=1}^d \text{sinc}_{\mu_i}(v_i - n_i \mu_i) \quad (3.4)$$

where the sinc function is given as  $\text{sinc}_{\mu_i}(v_i) = \sin(\pi v_i / \mu_i) / (\pi v_i / \mu_i)$ .

Continuous-domain images are rarely truly bandlimited, and, thus, filtering is first performed to bandlimit the image before sampling, resulting in  $x(v) = (b * f)(v)$ . This, in turn means that the filtered image  $x(v)$  can be recovered perfectly from its samples  $x_n$ , though not the original one,  $f(v)$ . In practice, however, several issues (for example, noise, limited field of view) complicate the procedure, and algorithms to recover a good estimate of  $x(v)$  depend on many more assumptions to be detailed later in this chapter.

One way to account for various sources of uncertainty is to introduce the probability of observing the value  $\alpha_n$  at coordinate  $n$ ; this probability can be expressed as  $\mathcal{P}(\alpha_n; x_n)$ , where  $\mathcal{P}(\cdot)$  is a probability model that accounts for the uncertainty introduced due to noise in several steps during discretization. As is the case with most photon detection-based instruments, the primary source of uncertainty introduced is due to photon counting noise, where  $\mathcal{P}$  is given by a Poisson distribution:

$$\mathcal{P}(\alpha_n; x_n) = \frac{x_n^{\alpha_n} e^{-x_n}}{\alpha_n!} \quad (3.5)$$

Although photon-detection instruments are inherently limited by Poisson noise, photon counting effect is not the only source of uncertainty in the image. Other artifacts such as thermal noise and digitization noise (uncertainty introduced by storing only a certain number of bits to describe each pixel value) also play a role, and the overall probability model is more likely to be a mixture of several sources

of uncertainty. This is modeled in Figure 3.1 by the A/D block, where the input is the image  $x(v)$ , and the output, instead of being just a simple sampled version of the input  $x_n$ , is given as  $g_n = \beta(x(v), \text{noise})$ .

### 3.1.3 Discrete-Domain Image Processing

#### 3.1.3.1 Framework

As we have seen, after A/D (discretization/digitization), the resulting image is  $g_n$ , with  $n = (n_1, \dots, n_d)$ . For example, a gray-scale 2-D time series with  $N_3$  2-D slices of size  $N_1 \times N_2$ , will be denoted as  $g_{n_1, n_2, n_3}$ , where  $n_1$  and  $n_2$  are two spatial coordinates with domains  $n_1 = 0, \dots, N_1 - 1$ ,  $n_2 = 0, \dots, N_2 - 1$ , and  $n_3$  is the time coordinate with domain  $n_3 = 0, \dots, N_3 - 1$ .

We stress an important point: Assume, for simplicity, we deal with a digital image  $g_{n_1, n_2}$  (that is, just a single 2-D slice). One can look at this image in two ways:

1. The domain of  $n = (n_1, n_2)$  is infinite (that is,  $n \in \mathbb{Z}^2$ ). We then assume that the image is of finite energy, written as  $g_n \in \ell^2(\mathbb{Z}^2)$ , and is a set of  $N_1 \times N_2$  nonzero values in the plane. In this case, the discrete-time FT will be used (introduced in a moment) and the result of a convolution gives support larger than the one with which we started.
2. The domain of  $n = (n_1, n_2)$  is finite (that is,  $n_1 = 0, \dots, N_1 - 1$ , and  $n_2 = 0, \dots, N_2 - 1$ ). The image is of finite energy by construction. In other words, we assume that the digital image exists only on a discrete grid of size  $N_1 \times N_2$ . That also means that the convolution used is the circular convolution, which preserves the domain, and the appropriate Fourier transform is the discrete Fourier transform (also introduced in a moment).

While this distinction might seem unimportant, it has great consequences on the machinery we use.

#### 3.1.3.2 Linear Shift-Invariant System and Digital Filters

Similarly to what was shown in continuous domain, most of the time we deal with LSI systems—filters. For the discrete domain, these filters can model the effects after A/D (discretization/digitization) or can be additional digital filters applied to achieve a certain effect. Their operation on a discretized signal  $g_n$  can be described via convolution again as

$$(a * g)_n = \sum_m g_m a_{n-m} \quad (3.6)$$

Note that we use the same symbol  $*$  for both continuous-domain as well as the discrete-domain convolution; the meaning is clear from the context. In signal processing, when the the domain of the digital image is finite (as it is in practice, see our earlier comment), one often uses the *circular convolution*, which preserves the domain. In other words, while the convolution as defined in (3.6) produces a larger image as the result of filtering (how much larger depends on the filter), the circular

convolution produces the image of the same size. These various convolutions may seem confusing and cumbersome; in fact, mathematically, one is able to deal with this problem in a unified way by defining the spaces of signals and filters, and then deriving the appropriate forms of convolution as well as the FT [7]. While that treatment is beyond the scope of this introduction, the interested reader is encouraged to look up [7] for more details.

### 3.1.3.3 The Fourier View

Similarly to what was done in continuous domain, we often use the Fourier machinery to analyze digital images. As explained previously, one must distinguish between images for which we assume the domain is infinite (yet with only a finite number of nonzero values) from those whose domain is finite (which is the case in practice). As we have seen, the convolution in these two instances is different; so is the FT. Without going into mathematical details, we just give those two versions of the FT. Again, here we use the standard nomenclature for the FT using time as the domain, although the domain of images is space; this is done to avoid confusion when looking up relevant literature. To make matters simple, we give below 1-D versions:

*Discrete-Time Fourier Transform (DTFT)*

$$F(e^{j\omega}) = \sum_{n \in \mathbb{Z}} f_n e^{-j\mu\omega n} \quad \leftrightarrow \quad f_n = \frac{\mu}{2\pi} \int_{-\pi/\mu}^{\pi/\mu} F(e^{j\omega}) e^{j\mu\omega n} d\omega \quad (3.7)$$

*Discrete Fourier Transform (DFT)*

$$F_k = \sum_{n=0}^{N-1} f_n W_N^{-nk} \quad \leftrightarrow \quad f_n = \frac{1}{N} \sum_{k=0}^{N-1} F_k W_N^{nk} \quad (3.8)$$

with  $W_N = e^{j2\pi/N}$ . For example, for images, the 2-D DFT would have the form

$$f_{n_1, n_2} = \frac{1}{N_1 N_2} \sum_{k_1=0}^{N_1-1} \sum_{k_2=0}^{N_2-1} F_{k_1, k_2} W_{N_1}^{n_1 k_1} W_{N_2}^{n_2 k_2}$$

## 3.2 Image Analysis Tools for Microscopy

The aim in this section is to give an overview of tools, both those that are currently used as well as those we believe would be useful for solving imaging tasks in microscopy (see Section 3.3). As a plethora of such tools exist, we give a brief overview of only a subset of well-established methods for image analysis and synthesis using both predetermined vectors (functions) as well as vectors automatically learned from data. Other important image processing and data analysis tools applicable to microscopic image analysis include pattern recognition and machine learning methods for clustering and classification [8], as well as statistical signal processing methods for detection and estimation [9, 10].

### 3.2.1 Signal and Image Representations

Signal representations (signal being a microscope image in this case) aim to represent a signal in a different domain so that its salient characteristics might become obvious in that domain. For example, a simple image that is a sum of two different frequencies in horizontal and vertical directions might be difficult to interpret in the original/image domain (see Figure 3.2(e)), while its harmonic content is immediately obvious in the Fourier domain (having two single nonzero coefficients).

It is useful to consider signal/image representations in a more general framework; then, many of the tools we discuss are just specific instantiations of that framework (see [11, 12] for more details). Signals are usually assumed to “live” in a Hilbert space. Hilbert spaces are those spaces in which we are allowed to manipulate signals (add, multiply by a constant), measure them, compute inner products, and so on. We are also allowed to represent our signals in terms of *bases* (nonredundant representations) or *frames* (redundant representations). These representations are typically written as

$$g = \sum_{i \in I} G_i \varphi_i \quad (3.9)$$

where  $I$  is some index set,  $\varphi_i$  are basis/frame elements belonging to  $\Phi$ , and  $G_i$  are called transform coefficients (subband, Fourier or wavelet, in case of specific transforms). Mathematically,  $G_i \varphi_i$  is the projection of the signal onto the space spanned by  $\varphi_i$  and  $G_i$  is the value of that projection.<sup>1</sup> That projection is computed as

$$G_i = \langle \tilde{\varphi}_i, g \rangle \quad (3.10)$$

where  $\tilde{\varphi}_i$  form what is usually called a *dual basis/frame*  $\tilde{\Phi}$ .

The difference between bases and frames is that in the case of frames, there are more vectors than needed to represent a particular signal, making it a redundant representation. For example, any vector in a plane can be uniquely represented by two projections onto two noncolinear lines (subspaces). Projecting onto yet another line will not destroy the representation property; it will just make it redundant.

#### 3.2.1.1 Matrix View

It is possible to look at signal expansions using linear operators/matrices, offering a more compact, and very often a more easily understood, way of looking at representations. Equation (3.10) can be rewritten as

$$G = \tilde{\Phi}^* g \quad (3.11)$$

1. We are not being entirely rigorous here, as for infinite-dimensional spaces, bases have to be defined with some care; we gloss over those subtleties in this treatment.

where  $g$  is now a vector containing the input signal,  $G$  is the vector of transform coefficients and  $\tilde{\Phi}$  is the matrix containing the dual basis/frame vectors as its columns. Then, (3.9) can be written as:

$$g = \Phi G = \Phi \tilde{\Phi}^* g \quad (3.12)$$

from where it is obvious that for this to be a valid representation,  $\Phi \tilde{\Phi}^*$  must be an identity. For bases,  $\Phi$  and  $\tilde{\Phi}$  are square and  $\tilde{\Phi} = (\Phi^*)^{-1}$ , while for frames, the frame  $\Phi$  and the dual frame  $\tilde{\Phi}$  are both rectangular.

### 3.2.1.2 Spaces We Consider

For ease of notation, we will keep our discussion in 1-D; extensions to more than one dimension are most often obtained by separate application of 1-D concepts to each dimension in turn (Kronecker product).

Standard and most intuitive spaces with which we deal are real/complex Euclidean spaces  $\mathbb{R}^N$  and  $\mathbb{C}^N$ . In these spaces, signals are considered to be vectors of finite length  $N$ , and the inner product is the standard component-wise product. Then the index set  $I$  is just the set  $I = \{1, \dots, N\}$ .

In discrete-time signal processing we deal almost exclusively with sequences  $g$  having finite square sum or finite energy, where  $g = (\dots, g_{-1}, g_0, g_1, \dots)$  is, in general, complex-valued. Such a sequence  $g$  is a vector in the Hilbert space  $\ell^2(\mathbb{Z})$ .

### 3.2.1.3 Orthonormal Bases

In the case of nonredundant representations, when  $\tilde{\Phi} = \Phi$ , and thus  $\Phi \Phi^* = I$ , we deal with *orthonormal bases* (ONBs). Both projection and reconstruction are performed using the same set of basis vectors  $\Phi$ . Many properties hold for orthonormal bases.

#### *Orthonormality of Basis Vectors*

Since  $\Phi^* = \Phi$ ,  $\langle \varphi_i, \varphi_j \rangle = \delta_{i-j}$  (that is, basis vectors are orthonormal).

#### *Projections*

A characteristic of orthonormal bases allowing us to approximate signals is that an orthogonal projection onto a subspace spanned by a subset of basis vectors,  $\{\varphi_i\}_{i \in J}$ , where  $J$  is the index set of that subset is  $Pg = \sum_{i \in J} \langle \varphi_i, g \rangle \varphi_i$  (that is, it is a sum of projections onto individual one-dimensional subspaces spanned by each  $\varphi_i$ ). Beware that this is not true when  $\{\varphi_i\}_{i \in J}$  do not form an orthonormal system.

#### *Parseval's Equality*

The *Parseval's equality* is simply the *norm-preserving* property of ONBs. In other words,

$$\|g\|^2 = \sum_{i \in I} |\langle \varphi_i, g \rangle|^2 = \sum_{i \in I} |G_i|^2 \quad (3.13)$$



### Least-Squares Approximation

Suppose that we want to approximate a vector from a Hilbert space by a vector lying in the subspace  $S = \{\phi_i\}_{i \in J}$ . The orthogonal projection of  $g$  onto  $S$  is given earlier by  $Pg$ . The difference vector  $d = g - \hat{g}$  satisfies  $d \perp S$ . This approximation is best in the least-squares sense (that is,  $\min \|g - y\|$  for  $y$  in  $S$  is attained for  $y = \sum_i G_i \phi_i$  with  $G_i = \langle \phi_i, g \rangle$  being the expansion coefficients). In other words, the best approximation is our  $\hat{g} = Pg$ . An immediate consequence of this result is the successive approximation property of orthogonal expansions. Call  $\hat{g}^{(k)}$  the best approximation of  $g$  on the subspace spanned by  $\{\phi_1, \phi_2, \dots, \phi_k\}$ . Then the approximation  $\hat{g}^{(k+1)}$  is given by  $\hat{g}^{(k+1)} = \hat{g}^{(k)} + \langle \phi_{k+1}, g \rangle \phi_{k+1}$  (that is, the previous approximation plus the projection along the added vector  $\phi_{k+1}$ ).

Note that the successive approximation property does not hold for nonorthogonal bases. When calculating the approximation  $\hat{g}^{(k+1)}$ , one cannot simply add one term to the previous approximation, but has to recalculate the whole approximation.

#### 3.2.1.4 Tight Frames

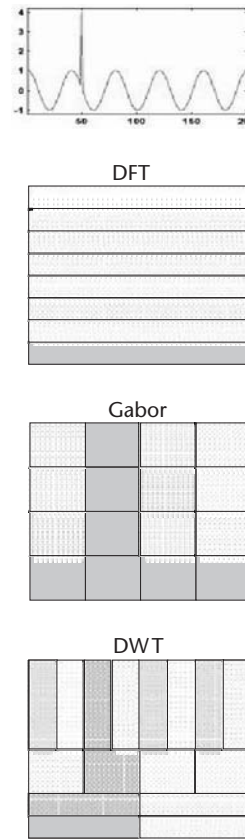
In case of redundant representations, when  $\tilde{\Phi} = \Phi$ , and thus  $\Phi\Phi^* = I$ , we deal with *Parseval tight frames (PTFs)* (when  $\Phi\Phi^* = cI$ , the frame is tight). Both projection and reconstruction are performed using the same set of frame vectors  $\Phi$  (albeit possibly scaled). Note, however, that while for bases,  $\Phi^*\Phi = I$  as well, this is not the case for frames. Orthonormality of frame vectors does not hold anymore as the vectors are not linearly independent, but a generalized sort of Parseval's equality still holds ( $\|g\|^2 = c \sum_{i \in I} |G_i|^2$ , with  $c = 1$  for PTFs). More details on frames can be found in [11, 12].

#### 3.2.1.5 How to Choose the Right Representation

From what we have described here, we have the option of choosing the nonredundant/redundant representation and then orthonormal/general for bases and tight/general for frames. Even once one of these four options is chosen, we are still left with the task of choosing the specific basis/frame elements. Fortunately, choices abound, and we now present some of those.

#### 3.2.1.6 Time-Frequency Considerations

One of the often-used criteria when choosing basis functions is how well they can represent certain local events in the original domain (space for images) as well as frequency. For example, a pure sinusoid is considered a perfectly local event in frequency, while a Dirac pulse is a perfectly local event in time (original domain). To see how a specific representation localizes in time (original domain) or frequency, one typically uses a conceptual tool called *time-frequency plane* (see Figure 3.3 for examples). Consider any of the three bottom diagrams. Each has time (original domain) on the horizontal axis and frequency on the vertical. The tiles represent the time-frequency distribution of the energy of the basis functions of the corresponding transform. For example, in the DFT, the tiles are all rectangles



**Figure 3.3** Energy distribution of a simple low-frequency signal with a Dirac pulse using different bases: DFT, Gabor, and DWT.

splitting the frequency into pieces, but going over all time. This is because the basis functions for the DFT cover all time but only pieces of frequency. Thus, one can see that the DFT will work well to isolate events local in frequency but will not isolate those local in time.

### 3.2.2 Fourier Analysis

When one is interested in the harmonic content of a signal, Fourier analysis is the tool of choice. The reason for this is that the representation functions are sinusoids (complex exponentials).

#### 3.2.2.1 Fourier Bases

Let us see how the Fourier view from the previous section fits into the representation framework we just introduced. We do this by looking at the DFT as a signal expansion (this is a short version of the same example in [11]), which, while ubiquitous, is rarely looked upon as a signal expansion or written in matrix form. The

easiest way to do that is to write the reconstruction expression (3.8) in matrix notation as

$$g = \frac{1}{N} \underbrace{\begin{pmatrix} 1 & 1 & \cdots & 1 \\ 1 & W_N & \cdots & W_N^{N-1} \\ \vdots & \vdots & \ddots & \vdots \\ 1 & W_N^{N-1} & \cdots & W_N \end{pmatrix}}_{\Phi = \text{DFT}_N} \underbrace{\begin{pmatrix} G_0 \\ G_1 \\ \vdots \\ G_{N-1} \end{pmatrix}}_G = \text{DFT}_N G \quad (3.14)$$

The DFT matrix defined here is not normalized—that is,  $(1/N)(\text{DFT}_N)(\text{DFT}_N^*) = I$ . If we normalized this matrix by  $1/\sqrt{N}$ , the DFT would exactly implement an orthonormal basis. The decomposition formula (3.8) in matrix notation becomes:

$$G = \text{DFT}_N^* g \quad (3.15)$$

The advantage of looking at the DFT in matrix form is that its operation now becomes “visual,” and projections onto the corresponding subspaces are easily seen. For example, for  $N = 2$ , the DFT would project onto a space with “smooth” signals (averaging) as well as the space of “detail” signals (differencing). One can also see that each of the coefficients will extract a specific range of “frequencies” from the signal (that is, it will measure how “wiggly” the signal is). An important point about the Fourier analysis is that while it extracts perfectly the frequency content of the signal, the local events in the original domain (for example, a spike in 1-D or edge in 2-D) are diluted over the whole frequency domain as each basis function will capture those local events. This is one of the reasons other techniques, such as wavelets, are used, where a trade-off between frequency and original domain localization can be achieved.

### 3.2.2.2 Fourier Frames

Similarly to Fourier bases, Fourier frames exist. They are known under the name *harmonic tight frames (HTFs)* and are obtained by projecting a Fourier basis from a larger space onto a smaller one. For example, given a DFT of size  $M \times M$ , we can obtain an HTF of size  $N \times M$ , with  $N < M$ , by deleting columns of the DFT. These representations possess similar properties to the DFT, except that they are redundant. As HTFs are possible for any combination of  $M, N$ , any redundancy can be achieved and the choice is governed by the application. More details on these frames can be found in [12].

### 3.2.3 Gabor Analysis

While the Fourier-type tools are best used on signals that are reasonably smooth, as that global behavior will be captured in the frequency domain, they are not appropriate for nonstationary signals. A classic example is that of a signal consisting of a sinusoid and a Dirac pulse. The sinusoid is captured by the Fourier tools, while the Dirac pulse is spread over all frequencies and its location is lost (see Figure 3.3, DFT). One way to deal with the problem is to window the Fourier basis functions so that just those with the support over the Dirac pulse will contain information

about it; all the other basis functions will not overlap and will thus contain no information about it. This leads to the *Gabor transform* (GT) (also called *short-time Fourier transform* (STFT)), which is pictorially shown in Figure 3.3, Gabor. Thus, upon observing that the coefficients corresponding to the basis functions with support coinciding with the support of the Dirac pulse contain more energy, one can conclude that the location of the Dirac pulse is somewhere within the range of that window (the window is shifted along the original axis to cover the entire original domain). This method still suffers from the problem that the “zoom” factor of the analysis, or how finely we can pinpoint the Dirac pulse, depends on the choice of the window. One can write the same equations as (3.14) and (3.15):

$$g = GTG, \quad GT = WDFT_N \quad (3.16)$$

$$G = GT^*g \quad (3.17)$$

where the GT is obtained by windowing the DFT by  $W$ . The window  $W$  is a diagonal matrix with window elements along the diagonal. Since the window multiplies the  $DFT_N$  on the left, it multiplies each DFT basis function in turn. The window  $W$  is typically chosen to be a symmetric lowpass filter.

### 3.2.4 Multiresolution Analysis

The *wavelet transform* (WT) and the *discrete wavelet transform* (DWT) arose in response to the problems the GT could not solve. The answer came as a tool with short basis functions at high frequencies together with long basis functions at low frequencies. As such, the WT is just the tool to tackle the earlier example (see Figure 3.3, DWT). Unlike the DFT and GT, which both have fixed basis functions, the WT (or DWT) allows for different families with the same time-frequency tiling as in the figure. These are obtained by choosing different template wavelets and then forming the whole basis from the template by shifts and dilations. While the DWT is an appropriate tool for this problem, it does not do so well if the frequency of the sinusoid is high, as then the position of the Dirac pulse cannot be distinguished in the high frequencies. *Multiresolution* (MR) techniques encompass a whole set of tools allowing for a rather arbitrary division of the time-frequency plane to match the signal at hand, including the one we just mentioned. As such, the DFT as well as the GT become subcases of it, with specific tilings.

#### 3.2.4.1 Implementing MR Transforms Using Filter Banks

These various MR transforms are implemented using filter banks (FBs), signal processing devices that split the frequency spectrum into parts. The basic frequency splitting is achieved through filtering and sampling, while reconstruction is done in the reverse direction, upsampling and filtering again. The analysis filter bank maps the signal into transform coefficients (also called subbands) as in (3.10) or (3.11), while the synthesis filter bank reconstructs the original signal from those, as in (3.9) or (3.12).

### 3.2.4.2 Discrete Wavelet Transform

The DWT achieves the tiling as in Figure 3.3, DWT, by iterating two-channel FBs on the lowpass (smoothing, coarse) channel. The number of iterations determines the number of leaves of the DWT (or any MR transform) as well as the level of coarseness at the last level (the more levels, the coarser). The actual filters used determine the basis functions are many: well-known families are Haar, Daubechies and Coiflets [6, 13, 14]. Depending on the basis functions used, we can have ONBs or general bases (Haar and Daubechies are ONBs, Coiflets are general bases with symmetries). For example, the three-level Haar DWT is given by the following matrix:

$$\text{DWT}_{3,\text{Haar}} = C \cdot \begin{pmatrix} 0 & 0 & 0 & 0 & 0 & 0 & 1 & -1 \\ 0 & 0 & 0 & 0 & 1 & -1 & 0 & 0 \\ 0 & 0 & 1 & -1 & 0 & 0 & 0 & 0 \\ 1 & -1 & 0 & 0 & 0 & 0 & 0 & 0 \\ 0 & 0 & 0 & 0 & 1 & 1 & -1 & -1 \\ 1 & 1 & -1 & -1 & 0 & 0 & 0 & 0 \\ 1 & 1 & 1 & 1 & -1 & -1 & -1 & -1 \\ 1 & 1 & 1 & 1 & 1 & 1 & 1 & 1 \end{pmatrix} \quad (3.18)$$

where  $C$  is a diagonal matrix of constants,  $C = \text{diag}(1/\sqrt{2}, 1/\sqrt{2}, 1/\sqrt{2}, 1/\sqrt{2}, 1/2, 1/2, 1/4, 1/4)$ , needed to make the DWT an ONB. Many others are possible leading to different values in the (3.18) matrix (assuming three levels).

### 3.2.4.3 Wavelet Packets and Variations

As one could have split the coarse channel again, one could have done it with the highpass as well. Thus, one can obtain arbitrary trees, anywhere from a full tree with  $J$  levels corresponding to a  $2^J$  GT, to a DWT with  $J$  levels, to an arbitrary tree with  $J$  levels (called *wavelet packet* (WP)).

One can also split the frequency range into  $N$  channels immediately, getting the DFT as a subcase. By splitting the  $N$ -channel filter bank further in any of these ways, one obtains an even more arbitrary tiling of the time-frequency plane.

### 3.2.4.4 Recommendations

The first goal in choosing one of these transforms is getting the one to represent the signal the best. In other words, the first concern should be matching the transform to the time-frequency distribution of the underlying signal (image). After that has been done successfully, the choice of particular filters and such may be attempted. However, choosing the appropriate transform is not easy; the idea behind WP is to grow a full tree and then prune back given a cost function, which might not be readily available. For example, in compression, people use the number of bits; thus, if pruning the tree at a particular branch leaves us with fewer bits, we do it; otherwise, we do not. Most often, we do not have an appropriate cost function, as was the case in [15], where the authors solved the problem by assigning weights to all the nodes in the tree. Then, the cost function is implemented implicitly; low

weights mean pruning of the branch, while high weight means the branch is kept. Many of these issues are discussed in [6].

### 3.2.5 Unsupervised, Data-Driven Representation and Analysis Methods

Except for the WP, the techniques described here use a predetermined set of vectors (functions) to represent signals and images. Alternatively, representation schemes can be built based on any available training data using automated learning approaches, an area of intense research. We now briefly review examples of data-driven representation and analysis methods, beginning with the *principal component analysis (PCA)* technique. Many more works for dimensionality reduction and data analysis exist (see, for example, [16, 17]), but for brevity these are not reviewed here.

#### 3.2.5.1 PCA

PCA is a method for reducing the dimensionality of a data set by finding a projection of the original set of vectors  $\{g_1, \dots, g_M\}$ , onto a lower-dimensional space, optimal in a mean-square (MS) sense. Assume that the dimensionality of the original space is  $N$  (that is, each  $g_i \in \mathbb{R}^N$ ) and that we want to reduce the dimensionality to  $L$ , with  $L \leq N$ . PCA accomplishes this task by finding an  $L$ -dimensional ONB  $\Phi = \{\varphi_1, \dots, \varphi_L\}$ , such that the error of the approximation between the original vectors and their approximations is minimized in the MS sense. In  $\Phi$ , the projections of the original vectors are expressed as:

$$\hat{g}_i = m + \sum_{k=1}^L \alpha_{k,i} \varphi_k, \quad i = 1, \dots, M \quad (3.19)$$

where  $m = (1/M) \sum_{i=1}^M g_i$  is the sample mean. We now find  $\varphi_k, k = 1, \dots, L$ , such that

$$\mathcal{E}(\varphi) = \sum_{i=1}^M \left\| m + \underbrace{\sum_{k=1}^L \alpha_{k,i} \varphi_k}_{\hat{g}_i} - g_i \right\|^2 \quad (3.20)$$

is minimized. It is fairly simple to prove [18], that the solution is found as the  $L$  eigenvectors  $\varphi_k, k = 1, \dots, L$ , corresponding to the  $L$  largest eigenvalues of the so-called scatter matrix (sample covariance):

$$S = \frac{1}{M} \sum_{i=1}^M (g_i - m)(g_i - m)^T \quad (3.21)$$

The coefficients  $\alpha_{k,i}$  are the values of the projections—that is, they are given by

$$\alpha_{k,i} = \langle g_i, \varphi_k \rangle \quad (3.22)$$

The eigenvectors  $\varphi_k$  can provide meaningful geometric insight into the distribution from which the samples  $g_i, i = 1, \dots, M$ , were drawn. The first eigenvector  $\varphi_1$  is the one for which the squared energy of the projection is maximum. The second

eigenvector  $\varphi_2$  is the one whose energy is also maximum, but it is constrained to be orthogonal to the first, and so on. Although PCA was originally developed as a statistical data analysis technique, modern uses of it include finding optimal linear subspaces for representing image data.

It is worth noting that while the terms Karhunen-Loève (KL) and PCA are often used interchangeably in the literature, a distinction can be made in that PCA refers to the diagonalization of the sample covariance matrix, while KL refers to the diagonalization of an ensemble covariance matrix.

### 3.2.5.2 ICA

The PCA framework is simple, efficient to compute, and extensively used in signal and image processing as well as general data analysis applications. While PCA finds orthogonal directions that best represent the data in the MS sense, *independent component analysis (ICA)* [19,20] finds directions that are most independent from each other. When the underlying distribution for the data is a multivariate Gaussian one, the coefficients  $\alpha_k$  are uncorrelated and therefore independent. If the underlying data does not originate from a multivariate Gaussian distribution, correlation does not imply statistical independence, and approximately independent coefficients may be obtained using ICA. Thus, the goal in ICA is to find vectors  $\varphi_k, k = 1, \dots, L$ , which produce coefficients  $\alpha_k$  that are not only uncorrelated but statistically independent as well. The process of computing independent components involves gradient-based nonlinear searches, normally initialized with results obtained from PCA. Implementation of this technique also depends on a proper definition of independence. The Kullback-Leibler distance [21] (not a true distance per se, but nonnegative nonetheless) is often used as a measure of statistical independence for ICA. However, because of issues related to computational complexity, practitioners are restricted to using surrogates such as kurtosis coefficients [19]. ICA is most used for deciphering the components, which, through addition, form a specific signal of interest—that is, they physically come from multiple sources (see [22] as well as Hyvarinen's web site for examples and demos [23]).

### 3.2.5.3 KPCA

Other extensions of the PCA framework include *kernel PCA (KPCA)* and *generalized PCA (GPCA)*. The idea in KPCA is to search for structure in the data by embedding it into a higher-dimensional (possibly infinite) space through a function  $\gamma(g_i)$ , taking values in the feature space  $\Gamma$ . The inner product in  $\Gamma$  is defined as  $\langle g_i, g_j \rangle_\Gamma = \langle \gamma(g_i), \gamma(g_j) \rangle$ , and defines a kernel  $\Lambda(g_i, g_j)$ , which can also be decomposed into a set of eigenvalues and eigenvectors to be used to estimate a low-dimensional representation of the original data (see [24] for more details about the computations involved). While KPCA can be used to extract interesting information from a set of data points, there is no general theory for choosing the kernel functions  $\Lambda$ . Polynomials and Gaussian kernels are often used, although their optimality for different applications is difficult to ascertain. Many of the modern methods for nonlinear dimensionality reduction can be interpreted as KPCA but with different kernel matrices [25].



### 3.2.5.4 GPCA

GPCA is a fairly recent contribution [26] with the same goal as the PCA, except that GPCA does not restrict the subspaces to be orthonormal with respect to each other, and each can be of a different dimension. In addition, GPCA identifies the membership of each data point. It starts by estimating a collection of polynomials from the data. Although the polynomials themselves are nonlinear, their coefficients can be estimated linearly from the data. Next, one point per subspace is segmented with clustering techniques, and a basis for the subspace passing through that point is obtained by evaluating appropriate derivatives.

### 3.2.5.5 ISOMAP

With the exception of KPCA, the previous approaches provide tools for finding linear subspaces, or a collection of linear subspaces, to analyze and represent image data. Given sufficient data, a larger class of nonlinear manifolds can be recovered using the *ISOMAP* algorithm [27], which can be described in two relatively simple steps. First, the “geodesic” distance between data points is estimated by constructing a neighborhood graph and then finding the shortest path through the graph that connects the two points. (This distance is not the usual Euclidean distance, but rather a distance that is adapted to the underlying geometry of the data.) The classical multidimensional scaling method [28] is used to compute low-dimensional coordinates for each point. The decay of the variance of the residual of the approximations as a function of the number of approximating dimensions can then be used to estimate the true dimensionality (free parameters) of the data.

### 3.2.5.6 LLE

Another class of nonlinear manifold learning algorithms involves searching for low-dimensional representations that best preserve local structures of the data. The *linear local embedding* (LLE) [29] algorithm is an example of such an approach. Like ISOMAP, the first step in the LLE algorithm is to compute the  $P$  nearest neighbors of each data point  $g_i$ . The second step is to assign weights  $\alpha_{k,i}$  to each nearest neighbor of each point such that

$$\mathcal{E}(\alpha) = \sum_{i=1}^M \left\| g_i - \sum_{k=1}^P \alpha_{k,i} g_k \right\|^2 \quad (3.23)$$

is minimized subject to the constraints that  $\alpha_{k,i} = 0$  if  $g_k$  is not among the  $P$  nearest neighbors of  $g_i$ , and that  $\sum_{k=1}^P \alpha_{k,i} = 1$  for all  $i$ . In the final step, LLE computes data points  $\hat{g}_i \in \mathbb{R}^L$ , with  $L < N$ , that best preserve the local properties of the data as represented by the sets of weights computed in the previous step, by minimizing

$$\mathcal{E}(\hat{g}) = \sum_{i=1}^M \left\| \hat{g}_i - \sum_{k=1}^P \alpha_{k,i} \hat{g}_k \right\|^2 \quad (3.24)$$

and computing the bottom  $M + 1$  eigenvectors of the matrix  $(I-A)^T(I-A)$ , where  $A_{k,i} = \alpha_{k,i}$ .

### 3.2.6 Statistical Estimation

The random variations introduced by system noise and artifacts, as well as uncertainty originating from the biological phenomena under observation, require stochastic image processing methods. In fact, several of the tasks and applications for microscopy we are about to review can be understood as statistical estimation problems [9], where the goal is to seek the solution to the problem at hand optimal in some probabilistic sense, requiring one to adopt some optimality criterion. We discuss two approaches based on the Bayesian approach, where both the data in the images as well as the quantities being estimated are viewed as random variables: minimum mean squared (MSE) estimators and maximum a posteriori (MAP) estimators.

#### 3.2.6.1 MSE Estimators

The minimum mean-squared error (MSE) between the estimate  $\hat{\theta}$  of some quantity  $\theta$ , denoted as  $\text{MSE}(\hat{\theta}) = E\{(\hat{\theta} - \theta)^2\}$ , where  $E$  is the expectation operator, is a desirable estimate since it minimizes the error of the estimate (on average). The Wiener filtering method given in (3.29) is an example of such an estimate.

#### 3.2.6.2 MAP Estimators

An interesting alternative is provided by the MAP estimation framework. Let  $g$  represent the observed image data and let  $b$  represent some pattern or hidden feature(s). In the Bayesian framework, an estimate of  $b$  is computed by maximizing the a posteriori probability (MAP)

$$p(b|g) = \frac{p(g|b)}{p(g)}p(b) \quad (3.25)$$

Since  $p(g)$  is constant with respect to  $b$ , maximizing (3.25) is equivalent to maximizing

$$p(g|b)p(b) \quad (3.26)$$

where  $p(g|b)$  is the so-called probabilistic data model, and  $p(b)$  is interpreted as a prior bias on  $b$ . Taking logarithms, the problem in (3.26) is equivalent to maximizing the following cost function

$$\Psi(b) = \log p(g|b) + \log p(b) \quad (3.27)$$

whose solution is the estimate  $\hat{b}$  we want to find:

$$\hat{b} = \arg \max_b \Psi(b) \quad (3.28)$$

The MAP problem is often recast as a minimization instead of maximization, by taking the negative of the previous quantities. When no prior knowledge on  $b$  is available, it is common for researchers so simply use equivalent to a maximum likelihood (ML) estimate of  $b$ .

Closed-form solutions for computing MAP estimates are rarely available due to the nonlinearity present in nearly all but the most trivial problems. Instead,

one is often required to solve (3.27) numerically. When  $b$  and  $g$  are interpreted to belong to a Hilbert space of continuous functions, the Bayesian framework reduces to solving a variational calculus problem. The forms of  $p(g|b)$  and  $p(b)$  specify the required function spaces to which  $g$  and  $b$  must belong (for example, square integrable, Sobolev, and bounded variation). A common approach is to derive maximization (minimization) approaches based on Euler-Lagrange equations from the maximization problem. Many algorithms in image restoration, segmentation, and registration discussed later in the chapter can be viewed within this framework.

### 3.2.6.3 Gradient-Based Estimators

When  $b$  is a finite-dimensional vector, standard gradient-based optimization approaches can be used, the most common of which is the steepest descent method. The cost function  $\Psi(b)$  is given by (3.27), where  $b$  is now a finite-dimensional vector. The steepest descent method computes  $\hat{b}$  by solving  $\nabla_b \Psi(b) = 0$  through the following three-step iterative approach: The estimate  $\hat{b}_k$  is iteratively updated by: (1) computing the gradient of the objective function  $\nabla_b \Psi(b) |_{b=\hat{b}_k}$ , (2) finding  $\tau$  such that  $\Psi(\hat{b}_k - \tau \nabla_b \Psi(b) |_{b=\hat{b}_k})$  is minimized, and (3) updating  $\hat{b}_{k+1} = \hat{b}_k - \tau \nabla_b \Psi(b) |_{b=\hat{b}_k}$ . Often, step (2) is bypassed and  $\tau$  is fixed to a small value.

## 3.3 Imaging Tasks in Microscopy

The goal in an imaging-based biological experiment is to extract structural, spatial, and functional quantitative information about some biological phenomenon accurately and, if possible, do so automatically. We now briefly review some of the canonical problems in microscopic image analysis for extracting such information, such as restoration, registration, and segmentation. A general view of the system, which this section follows, is given in Figure 3.1.

### 3.3.1 Intelligent Acquisition

Although the general process of acquisition was described in Section 3.1, a new set of techniques aiming at providing intelligence during the acquisition process has emerged.

The first motivation for these approaches is to enhance resolution. In laser scanning confocal microscopy, images are acquired line by line, pixel by pixel [30]. We can achieve significant time savings by only imaging those regions where we expect to find an object. These time savings could then be used to increase the frame rate, or to acquire the selected regions at a higher spatial resolution.

The second motivation is to reduce photobleaching and phototoxicity. In fluorescence microscopy, images are acquired by shining excitation light on the specimen to activate fluorescence. However, this can damage the fluorescent signal (photobleaching) [31], as well as the cell itself (phototoxicity) [32], thus limiting

the duration over which we can view a cellular process. By reducing the total area acquired in each frame, we reduce the overall exposure to excitation light, hence reducing both photobleaching and phototoxicity.

Intelligent acquisition of microscope images has not been studied until recently. In [33], the authors designed an algorithm to reduce the number of pixels sampled in a 2-D or 3-D image when using a laser scanning confocal microscope. They observed that a large portion of scanning time is spent on low fluorescence regions, which presumably contain little useful information. The approach is then to begin by scanning the field at a low resolution. Each scanned value is examined, and if found to be significant, the area around it is scanned at a higher resolution. The process is repeated iteratively.

In [34] instead, the authors provide intelligence while learning the data model. They study a large number of tiny moving objects over a sustained period of time. To assist with efficient acquisition, they develop and continually refine a model to describe the objects' motion. In [35], the authors provide algorithms for modeling objects' motions for the purposes of tracking, and although not used directly, their work helped inspire the approach in [34].

### 3.3.2 Deconvolution, Denoising, and Restoration

Microscope images typically contain artifacts that, if accentuated, may prevent reliable information extraction and interpretation of the image data. Two main sources of artifacts can be identified: blurring caused by the PSF  $h$  (see (3.2)), and noise arising from the electronics of A/D conversion (see Figure 3.1). The combined tasks of deconvolution (deblurring) and denoising are generally referred to as image enhancement or restoration, as shown in Figure 3.1. In the figure, two parallel paths are possible: (1) Joint denoising and deconvolution known as restoration, which as input has the output of the microscope  $g_n$ , and as the output, the estimate  $\hat{f}_n$  of the input image  $f(v)$ . Note that while the output of restoration is another digital image  $\hat{f}_n$ , the problem itself is posed in terms of its continuous-domain version—that is, finding the best estimate  $\hat{f}(v)$ . Our discussion in this section focuses mostly on this path. (2) Separate tasks of denoising, having as input the output of the microscope  $g_n$ , and as the output, the estimate  $\hat{x}_n$ , followed by deconvolution.

The problem of deconvolution in the presence of noise dates back many decades and has been applied to a variety of imaging problems related to astronomy, medicine, and many others, in addition to microscopy (for recent reviews, see [36–38]). Our purpose here is not to provide an extensive review of existing methodology, but rather an overview of important concepts often used, their relationship to Fourier analysis, as well as more modern ideas based on wavelets and sparse representations.

The plethora of restoration methods available can be classified according to different criteria. Some of the terminology associated with different methods available include linear versus nonlinear, least squares, maximum likelihood, expectation maximization, and blind versus model-based. Here we describe two different optimization criteria based on which several different methods have been designed,

beginning with the minimum MSE estimation. All of the methods being described assume an LSI degradation model (PSF) and can be applied in two or three dimensions.

### 3.3.2.1 MSE Estimation

The approach used here was described in Section 3.2.6. Let  $f(v)$  represent an image one wishes to reconstruct, ideally, by undoing the effects of the PSF by inverse filtering operation  $h_{\text{in}}$  on some measured data  $g(v)$ ,  $\hat{f}(v) = (h_{\text{in}} * g)(v)$ . The measured data  $g(v)$ , the original image  $f(v)$ , as well as its estimate  $\hat{f}(v)$ , can all be viewed as random variables due to the uncertainty introduced by noise sources. Thus, a reasonable criterion to minimize is the MSE between the linear estimate  $\hat{f}(v)$  and the real image  $f(v)$  (that is,  $E\{(f - \hat{f})^2\}$ ). Under assumptions explained next, it is possible to derive the well-known Wiener filter [39] solution to the problem, expressed in the Fourier domain as:

$$\hat{F}(\omega) = \underbrace{\frac{H(\omega)}{|H(\omega)|^2 + S_e(\omega)/S_g(\omega)}}_{H_{\text{in}}(\omega)} G(\omega) \quad (3.29)$$

where  $H(\omega)$  is the Fourier transform of the PSF,  $S_e(\omega)$  is the power spectral density of the noise source, and  $S_f(\omega)$  is the power spectral density of the image being measured. The previous derivation assumes that both the image and the noise source are well modeled by ergodic random variables, as well as that the noise is additive and white (uncorrelated). These assumptions are often violated in microscope imaging experiments. Moreover, the quantities  $S_e(\omega)$  and  $S_g(\omega)$  are seldom known, and practitioners often replace the ratio  $S_e(\omega)/S_g(\omega)$  by some constant  $c$ .

### 3.3.2.2 MAP Estimation

The approach used here was also described in Section 3.2.6. Here, we denote the ensemble of possible images by  $b$ , while the output estimate will be called  $\hat{f}$ . That is, we seek to maximize the posterior probability  $p(b|g) = (p(g|b)/p(g))p(b)$ , where  $p(g)$  does not depend on  $b$ , and  $p(b)$  represents the prior knowledge one may have about the image  $b$ . The cost function is the following functional (a version of (3.27)):

$$\Psi(b) = \phi(g, b) + cP(b) \quad (3.30)$$

where the logarithms have been subsumed into the previous terms,  $P(b)$  is a regularization function derived based on a priori knowledge, and  $c$  is an arbitrary constant. Its role is to prevent the solution to the algorithm from containing certain undesired characteristics such as excessive oscillations. Restoration algorithms are normally set up as minimization problems by defining the previous terms as the negative of the log of the probabilities.

### Modeling the Minimization Function

When the Poisson distribution is used to model  $p(g|b)$ , the minimization term  $\phi$  is defined as:

$$\phi_{\mathcal{P}}(g, b) = \int [(h * b)(v) - g(v) \log(h * b)(v)] dv \quad (3.31)$$

while the equivalent for a Gaussian distribution model for  $p(g|b)$  is:

$$\phi_{\mathcal{G}}(g, b) = \int |(h * b)(v) - g(v)|^2 dv = \|h * b - g\|_{L_2}^2 \quad (3.32)$$

Several algorithms can be derived to optimize these functionals. A classical example is the Richardson-Lucy (RL) algorithm: an iterative, unregularized algorithm that minimizes  $\phi_{\mathcal{P}}(g, b)$ , one out of a class of methods known to produce result images  $\hat{f}$  dominated by noise as the number of iterations increase. The addition of different priors on  $b$ , together with other constraints such as positiveness, can help overcome these difficulties.

### Modeling the Prior

Many different priors on  $b$ ,  $P(b)$ , have been used in the literature. One of the most often used is the  $L_p$ -type regularization:  $P_{\mathcal{Q}}(b) = \|Db\|_{L_p}^p$ , where  $D$  is a linear operator (often of a differential type) and  $p = 1$  or  $2$ . When  $p = 2$  this regularizer tends to minimize the energy of either the image itself ( $D = 1$ ) or properties of the image (for example, derivatives  $D = \nabla$ ). This leads to a Tikhonov-type regularizer [40], which tends to produce blurred estimates  $\hat{b}$ , countering the effect of the  $\phi(g, b)$  minimization term. In contrast,  $p = 1$  leads to so-called “sparsity” maximizing solutions, which tend to preserve edge structures better. Examples include total variation regularization terms ( $D = \nabla$ ) [41] and wavelet-based sparse representations (when  $Db$  refers to coefficients of the WT of the image) [42].

Other regularization methods include entropy-type priors, where one uses a model  $m(v)$  that represents the prior knowledge about the image. The entropy prior is defined as

$$P_{\mathcal{E}}(b) = \int \left[ b(v) - m(v) - b(v) \log \frac{b(v)}{m(v)} \right] dv \quad (3.33)$$

This entropy functional is an optimal distance measure for positive functions [43]. However, since a precise model for the image to be measured is often not available, researchers typically use a constant function leading to a preference for smooth functions [37].

Other regularization approaches exist, such as the Good’s roughness penalty [44], which often yields estimates of good quality in comparison with other methods [37]. In addition, for situations when a precise model for the PSF is unknown, there exist so called “blind” restoration algorithms that seek to estimate

both the image as well as the PSF. One notable example is based on the RL iterative algorithm described earlier [45].

Finally, in actual implementation, the overall functional  $\Psi(b)$  (consisting of any combination of the terms  $\phi_P, \phi_G, P_E, P_Q$ ) is discretized at the measured image grid of pixels, and the functional is minimized using standard approaches such as the steepest-gradient descent (see Section 3.2.6), conjugate gradient descent and Newton-type, as well as multiplicative methods [36,37,41]. Computational complexity is often a concern. Linear methods, such as the Wiener filter explained earlier, can be implemented in real time. More recent, nonlinear methods, such as the one described in [42], are more computationally demanding, although recent advances [46] may help overcome these difficulties.

### 3.3.3 Registration and Mosaicking

Image registration refers to the task of finding the spatial relationship and alignment between two or more images. Registration methods are useful for combining the information contained in multiple images of the same object, acquired by different instruments, and at perhaps different resolutions. Other applications include mosaicking as well as tracking objects in image time series. Here we provide an overview of image registration methods applicable to microscope images, beginning with semiautomatic landmark-based registration, followed by fully automated intensity-based methods.

#### 3.3.3.1 Registration

Let  $\Omega_{1,i} \in \mathbb{R}^d, i = 1, \dots, N_1$ , and  $\Omega_{2,k} \in \mathbb{R}^d, k = 1, \dots, N_2$ , be the pixel coordinates (in units of meters) of two images  $\hat{f}_1(\Omega_{1,i})$  and  $\hat{f}_2(\Omega_{2,k})$ , respectively. The goal in a registration (alignment) problem is to find a spatial transformation  $\beta$  that relates the coordinates of the source image to the coordinates of the target image:  $\tilde{\Omega}_{1,k} = \beta(\Omega_{2,k})$ . The value of the image  $\hat{f}_1$  at position  $\tilde{\Omega}_{1,k}$  does not exist in general, since the image  $\hat{f}_1$  is only defined at coordinates  $\Omega_{1,i} \in \mathbb{R}^d, i = 1, \dots, N_1$ . However, a reasonable guess may be computed by using standard, continuous, representations of the image  $\hat{f}_1(\Omega_1) = \sum_i \hat{f}_{1,i} \phi_i(\Omega_1)$ , as described in Section 3.1, to compute  $\hat{f}_1(\tilde{\Omega}_{1,k})$ .

With the knowledge of a set of  $N$  corresponding points  $p_{1,k} = p_{2,k}, k = 1, \dots, N$ , one is often able to compute a spatial transformation  $\beta$  by solving the following minimization problem:

$$\beta^{op} = \operatorname{argmin}_{\beta \in \mathcal{C}} \frac{1}{N} \sum_{k=1}^N \|\beta(p_{1,k}) - p_{2,k}\|^2 \quad (3.34)$$

where  $\mathcal{C}$  defines a certain class for the spatial transformation  $\beta$  and  $\|\cdot\|$  is the standard vector norm. This problem above is akin to the well-known Procrustes problem, and for the class of rigid-body transformations (rotations plus translations), the closed-form solution is known [47]. One first removes the mean from the coordinates  $p_{1,k} - \bar{p}_1$  and  $p_{2,k} - \bar{p}_2$ , with  $\bar{p}_1 = \frac{1}{N} \sum_{k=1}^N p_{1,k}$  and  $\bar{p}_2 = \frac{1}{N} \sum_{k=1}^N p_{2,k}$  (then these mean-zero values are assigned to  $p_{1,k}$  and  $p_{2,k}$ ). Define the matrix



$K = P_1^T P_2$ , where  $P_1$  and  $P_2$  are matrices with each row comprising of a vector  $p_{1,k}$  and  $p_{2,k}$ , respectively. The singular value decomposition  $K = UDV^T$  can be used to compute the rotation matrix  $R$  that aligns the two point clouds:

$$R = V\Delta U^T \quad (3.35)$$

with  $\Delta = \text{diag}(1, 1, \det(VU^T))$  as an example in three dimensions [48]. The translation component is given by  $a = \bar{p}_2 - R\bar{p}_1$  and the final transformation is given by  $\beta(p_1) = Rp_1 + a$ .

This framework can be extended to include other classes of spatial transformations, such as the set of transformations composed of linear combination of radial basis functions. If at least  $N$  basis functions are used, with minor assumptions, two point clouds can be matched exactly (that is, the error in (3.34) is 0). One often-used class of radial basis functions are thin-plate splines (see [49] for an example).

This methodology is not used universally, as the corresponding landmark points are often hard to obtain. Automated landmark extraction methods are difficult to implement, while manual landmark selection is cumbersome, time consuming, and often imprecise. Another important class of image registration methods are those that operate directly on the intensity values of the images  $\hat{f}_1$  and  $\hat{f}_2$  by solving a different optimization problem

$$\beta^{op} = \arg \min_{\beta \in \mathcal{C}} \Upsilon(\hat{f}_1, \hat{f}_2, \beta) \quad (3.36)$$

where  $\Upsilon(\cdot)$  refers to an objective function normally composed of: (1) a (dis)similarity measure between the intensity values of the target image  $\hat{f}_2(\Omega_1)$ , and warped source image  $\hat{f}_1(\beta(\Omega_1))$ , and (2) a constraint, or regularization term, so as to “bias”  $\beta$  toward any available prior information. Many different methods for intensity-based image registration exist and can be classified according to the type of spatial transformation  $\beta$ , the objective function  $\Upsilon$ , and optimization method chosen (for comprehensive reviews, see [50, 51]). Spatial transformations often used include rigid body, affine, polynomial, and linear combination of B-splines or radial basis functions, as well as elastic and fluid deformation models. Objective functions currently in use in the literature include the sum of squared differences between the intensity values of the target image  $\hat{f}_1(\Omega)$  and warped source image  $\hat{f}_2(\beta(\Omega))$ , their correlation coefficient, and their mutual information [52]. Optimization methods used include Powell’s direction set method [53], gradient descent, conjugate gradients, and Newton-type methods.

The landmark and intensity-based methods are not mutually exclusive and can be combined by adding the two terms into a single optimization problem:

$$\beta^{op} = \arg \min_{\beta \in \mathcal{C}} \frac{c_1}{N} \sum_{k=1}^N \|\beta(p_{1,k}) - p_{2,k}\|^2 + c_2 \Upsilon(\hat{f}_1, \hat{f}_2, \beta) \quad (3.37)$$

where  $c_1$  and  $c_2$  are arbitrary constants. For an example of such an approach, see [54].

### 3.3.3.2 Mosaicking

Automated and semiautomated image registration methods are essential for building image mosaics. Due to the limited field of view of magnification objectives, this operation is often necessary for obtaining a more global view of the object, but with sufficient resolution for intricate analysis. Automated stages for mosaicking exist, but are often not accurate enough [55]. Large mosaics may be built with the aid of image registration methods given slightly overlapping images (a recent example can be found in [56]). Other applications of image registration to microscopic image analysis include electrophoresis image alignment for protein analysis [57], as well as studies of tissue differentiation during the evolution of *Drosophila melanogaster* embryos [54].

### 3.3.4 Segmentation, Tracing, and Tracking

Broadly speaking, segmentation and tracing refer to the detection of relevant contiguous objects within an image as well as the determination of their positions. Segmentation and tracing methods allow for localized analysis within an image and are essential for extracting information pertaining to one or more specific objects (for example, cells and organelles) in an image, while tracking refers to the detection or estimation of objects as a function of time in time series data sets. Naturally, manual image segmentation, tracing, and tracking are all possible with the aid of modern computer display systems. However, given the enormous quantities of data produced by modern imaging systems, manual image interpretation and information extraction is not only costly, but also inaccurate and has poor reproducibility. We now briefly review some of the automatic and semiautomatic methods for cell and nuclear segmentation and neuronal tracing.

Segmentation, tracing, and tracking methods are typically the first step in many imaging applications and have been applied to the classification and clustering of cellular shape [58], cell biomass computation [59], leukocyte detection and tracking [60], neurite tracing [61], cell migration [62], subcellular analysis [63], and studies of the influence of Golgi-protein expression on the size of the Golgi apparatus [64], among others.

#### 3.3.4.1 Segmentation

The simplest and most widely used automated image segmentation method available is that of thresholding. This method consist of assigning the label of background to every pixel in the image whose value falls below a chosen threshold, while the label of foreground is assigned to each pixel that matches or exceeds the value of the threshold. More advanced thresholding methods choose the value of the threshold adaptively, through computation of global, or at times local, image histograms. However, thresholding methods alone are seldom effective, as microscope images contain noise and are not illuminated uniformly, as well as because they neglect to account for geometric information in the data. These methods are thus commonly used only as initialization to other, more elaborate ones.

### *Voronoi-Based Segmentation*

One such relatively simple technique is known as Voronoi diagram-based segmentation, often used when more than one relevant object (for example, cells, nuclei) are present. The idea is to use coordinates within each object (one coordinate per object to be segmented, obtained with the help of thresholding techniques) as representative coordinates for the entire object, and to “draw” edges and vertices so that each coordinate is enclosed by a single polygon. For example, this technique is often used to segment cell nuclei in images of DNA probes [65]. However, it does not perform well when the objects being segmented are asymmetric or are close in space. In these situations, a single point is too simplistic a description for the geometry of the object, and the edges computed may not respect the boundary of the objects being segmented.

### *Watershed Segmentation*

A more attractive technique is watershed segmentation, which can capture intricate object boundaries without overwhelming computational cost. The basic idea is to view a 2-D image, for example, as a topographical surface, and “flood” the surface from its local minima by considering its intensity level sets. When two regions are merging, a dam is built to represent an edge and boundary in the segmentation result. This technique can be applied directly to the raw image data as well as to processed images, such as edge-enhanced ones or distance-transformed ones. However, it is known to oversegment images and careful seeding (initialization) must be used [66,67].

### *Active-Contour Segmentation Methods*

The segmentation methods described here rely on a discrete interpretation of the image data in that any continuous properties of the objects being imaged are disregarded. In the past couple of decades, a different class of segmentation algorithms that explicitly include continuous information, such as curvature, has emerged, and is generally denoted as deformable models or active contours [68]. An active contour is a closed curve  $C(l)$ , with  $l$  some parameterization  $l \in [0, 1]$ , and  $C(0) = C(1)$  (in two dimensions, such a curve is represented by  $C(l) = (C_x(l), C_y(l))$ ). Active-contour segmentation methods seek to find the contours that best delineate different objects in an image. Kass et al. [69] formulate this as a variational optimization problem, with a cost function given by:

$$\Psi(C) = c_1 \int_0^1 \left| \frac{dC(l)}{dl} \right|^2 dl + c_2 \int_0^1 \left| \frac{d^2 C(l)}{dl^2} \right|^2 dl + c_3 \int_0^1 |\nabla r(C(l))|^2 dl \quad (3.38)$$

where  $c_1, c_2, c_3$  are arbitrary constants, and  $\nabla r(v)$  represents the gradient of the image  $r$ . This can be a sum of other applicable forces as well (see [70] for an example that includes a stochastic term). The cost function is minimized through variational methods [68] and leads to a partial differential equation-type solution to the problem,  $dC/dt = F(C, r)$ , with  $t$  being a time variable artificially included,

and  $F(C, r)$  representing a force (or sum of forces) term derived based on (3.38). This equation can be solved with Euler integration methods. Another interesting aspect of such methods is that the curve  $C(l)$  is normally parameterized using interpolating splines, for example. Parametric contours can be difficult to generalize to multiple object and changes in topology, as a reparameterization of the curve(s) is necessary. Again, as in the tasks described previously, the problem is posed in a continuous-domain setting and later discretized.

An alternative technology for propagating contours is based on the level-set methods [71], which avoid parameterization of the curve  $C$  by defining it implicitly as a level set (normally the zero level set) of a function  $\phi(v)$  ( $\{v|\phi(v) = 0\}$ ). For convenience,  $\phi(v)$  is normally defined over the same domain as the image data  $r(v)$ . The level-set function  $\phi$  is usually initialized as a signed distance function to an initial contour drawn over the image, and a typical implementation involves the following differential equation:

$$\frac{d\phi}{dt} = V(\kappa)|\nabla\phi| \quad (3.39)$$

where  $V(\kappa)$  is the so called speed function (normally involving image edges), while  $\kappa$  is the curvature of the contour, which can be computed directly from  $\phi$ . As mentioned previously for the active-contour equation (3.38), the corresponding level-set equation can be given as the sum of applicable forces (see [70], for example). The solution is obtained in steady state (the contours do not evolve anymore) using Euler-type integration methods. There are several advantages to the level-set formulation. As mentioned earlier, changes in topology are handled automatically without extra effort. In addition, it is an Eulerian formulation, meaning that all computations are done with respect to a fixed grid (as opposed to tracking a determined amount of propagating “particles” defining a contour). Therefore the technique can easily be extended to three or more dimensions (parameterized front propagation methods are complicated in three or more dimensions, especially if changes in topology are involved). The disadvantage of the level-set method is that the level-set function  $\phi$  needs to be computed throughout the domain of the image, even though only a contour (or sets of contours) is desired. Methods for computing  $\phi$  only in the neighborhood of its zero level set exist [71], although the speed-up is not substantial when the images consist of many contours close to each other. A novel approach to this computational problem is presented in [64]. The authors combine the power of active contours with the multiresolution (MR)/multiscale (MS) framework to compute forces using convolutions at different scales. This approach eliminates the need for the level-set framework and extensive computations, leading to a new class of active-contour methods dubbed multiscale active contours (MSAC) [64], with computational savings of one to two orders of magnitude. Modern image segmentation methods based on level sets can be generalized to include many different force terms and may not require image gradients, allowing for robust segmentation of objects without strong edges (see, for example, [72]). Other methods are based on the STACS algorithm we mentioned earlier [70], as well as follow-ups to that work, such as TPSTACS [73] as well as MSAC [64].

### 3.3.4.2 Tracing

The problem of tracing elongated pathways in image data is essentially a segmentation problem. The overall goal is the same as in segmentation: to detect and determine the location of a structure of interest. The significant geometric differences between neurons (normally elongated and not necessarily closed contours) and cells, for example, call for the development of a different methodology. Methods based on skeletonization [74] often fail because of the presence of noise, out-of-focus noise, and illumination artifacts. Those techniques that do not depend on skeletonization rely on a local path following approach. A starting point is given and a step is taken along a direction computed from the local intensity values of the image data. The approach can be summarized as an ordinary differential equation problem, where one seeks to find a path  $C(l)$  by solving

$$\frac{dC(l)}{dl} = t(l) \quad (3.40)$$

where  $t(l)$  is a vector that represents the tangential direction of the axon at location  $C(l)$  in the image. The tangential direction can be computed by matching, locally, a cylindrical model for the axon, as in [75]. Alternatively,  $t(l)$  can be computed from the eigenvectors of the Hessian (matrix of second derivatives) of the image data locally as in [61]. Such path following approaches often fail in the presence of noise and other artifacts (e.g., imperfect illumination), and thus typically require significant user interaction [61].

### 3.3.4.3 Tracking

Image-based tracking refers to the detection of relevant objects in image time series as well as the determination of their spatial positions in time. Tracking has been applied to modeling and understanding of biological molecular dynamics [76,77], as well as to understanding cell migration [60,62]. In a broad sense, tracking can be thought of as a time-dependent segmentation problem, and as in static image segmentation, a variety of methods exist. A comparison of methods for tracking single fluorescent particles is given in [78]. The simplest tracking algorithm consists of identifying potential molecules or cells by thresholding (possibly followed by morphological operations to remove holes and spurious artifacts) and then performing nearest neighbor matching. While this approach may be fruitful for tracking fluorescence particles in image data, it performs poorly when the objects being tracked change shape as time progresses [77]. For this reason, time-dependent active contours and deformable models are preferred for studies of cell migration, for example.

### 3.3.5 Classification and Clustering

The advent of modern, automated, digital microscopes, together with target-specific fluorescent probes, has enabled the collection of large amounts of image data whose impact can be vastly augmented through the use of high-throughput image screening and analysis methods. The image processing tasks described previously (restoration, registration, segmentation, tracking, and so on) can be combined

with traditional machine learning methodology to deliver powerful tools to aid discovery and validation for life sciences applications [79].

A prominent example is the application of image-based clustering and classification methods to the problem of subcellular localization of proteins within cellular compartments. The development of advanced protein tagging methods, with the aid of biological image database systems [80, 81] and advanced feature extraction, classification, and clustering methods, have enabled scientists to address the problem of analyzing subcellular location patterns on a proteome-wide basis, providing valuable information on the molecular mechanisms that dictate cell structure and function [15, 65]. Introduction of more advanced tools such as MR has been proposed in [15] for subcellular analysis, as well as in [82] for detection of developmental stages *Drosophila* embryos.

Yet another common use of classification methods in bioimaging is in cell cycle analysis and determination. Common applications include studying of the effects of gene suppression [83] as well as drug therapies [84]. The steps used to implement an image processing system capable of performing automated classification and analysis of cell cycle response are normally the same as for other applications and include, but are not limited to, image restoration, registration to remove translation and rotation dependency in numerical feature extraction, and training of the classifier.

### 3.3.6 Modeling

Computational imaging methods also have a place in modeling and simulation of biological phenomena at the cellular and subcellular scales. Quantitative information automatically extracted from images can be used for model selection, calculating model parameters, and for validating different models. We describe two applications of image-based modeling in cells and subcellular structures: computation of material parameters describing force distribution in cells as well as modeling the dynamical properties of microtubules.

The precise determination of the mechanical properties of cells, under different environments, can be used to gain a better understanding of a variety of biological phenomena. Finite-element models derived based on constitutive laws can be used to estimate stress-strain relationships, as well as other physical parameters, based on boundary conditions extracted from image data. Modeling and simulation of uniaxial cell stretching experiments were performed in [85], where cell boundaries were extracted (segmented) as a function of time from image of cells undergoing stretching.

Modeling has also been performed in an effort to understand the motion of subcellular structures with the aid of time-lapse microscopy [86]. One of the simplest and most used models for describing particle random motion is the autoregressive moving average (ARMA) model, where the goal is to describe the value of an observed variable as a linear combination of past values of that variable as well as past values of a white noise random variable [87]. In [86] localization information obtained from automated tracking algorithms [88] were used to estimate the parameters of an ARMA model for studying kinetochore microtubule dynamics in yeast. Another new area for modeling is that of intelligent acquisition,

discussed at the beginning of this section, where data set models, as opposed to the data itself, are learned and acquired [34].

### 3.4 Conclusions

Our aim in this chapter is to set a framework for analysis and interpretation of digital microscope images. To that end, we introduced a conceptual view of the system as in Figure 3.1 and gave a brief overview the modern tools of signal processing and data mining. While some of these tools are currently being used in the tasks given in Figure 3.1, many are not. By exposing the reader to a sampling of possible tools, we hope they will find way in more sophisticated algorithms than is presently available. The trend of automated microscope image analysis and interpretation is here to stay; bringing in the full power of mathematical and algorithmic advances is now our task.

### References

- [1] Prewitt, J., and M. Mendelsohn, "The Analysis of Cell Images," *Ann. N Y Acad. Sci.*, Vol. 128, No. 3, 1966, pp. 1035–1053.
- [2] Eils, R., and C. Athale, "Computational Imaging in Cell Biology," *Journ. Cell Biol.*, Vol. 161, No. 3, 2003, pp. 477–81.
- [3] Wang, Y., K. Hahn, R. Murphy, and A. Horwitz, "From Imaging to Understanding: Frontiers in Live Cell Imaging," *Journ. Cell Biol.*, Vol. 174, No. 4, 2006, pp. 481–484.
- [4] *IEEE Signal Proc. Mag.*, sp. iss. *Molec. Cellular Bioimaging*, May 2006.
- [5] Barrett, H., and K. Myers, *Foundations of Image Science*, New York: John Wiley & Sons, 2004.
- [6] Vetterli, M., and J. Kovačević, *Wavelets and Subband Coding: Signal Processing*, Englewood Cliffs, NJ: Prentice-Hall, 1995.
- [7] Püschel, M., and J. Moura, "Algebraic Signal Processing Theory: Foundation and 1-D Time," *IEEE Trans. on Signal Processing*, 2008.
- [8] Hastie, T., R. Tibshirani, and J. Friedman, *The Elements of Statistical Learning; Data Mining, Inference, and Prediction*, New York: Springer-Verlag, 2001.
- [9] Kay, S., *Fundamentals of Statistical Signal Processing: Estimation Theory*, Vol. I, Englewood Cliffs, NJ: Prentice-Hall, 1993.
- [10] Kay, S., *Fundamentals of Statistical Signal Processing: Detection Theory*, Vol. II, Englewood Cliffs, NJ: Prentice-Hall, 1993.
- [11] Kovačević, J., and A. Chebira, "Life Beyond Bases: The Advent of Frames (Part I)," *IEEE Signal Proc. Mag.*, Vol. 24, July 2007, pp. 86–104.
- [12] Kovačević, J., and A. Chebira, "Life Beyond Bases: The Advent of Frames (Part II)," *IEEE Signal Proc. Mag.*, Vol. 24, September 2007, pp. 115–125.
- [13] Mallat, S., *A Wavelet Tour of Signal Processing*, New York: Academic Press, 1999.
- [14] Daubechies, I., "Orthonormal Bases of Compactly Supported Wavelets," *Commun. Pure and Appl. Math.*, Vol. 41, November 1988, pp. 909–996.
- [15] Chebira, A., Y. Barbotin, C. Jackson, T. Merryman, G. Srinivasa, R. Murphy, and J. Kovačević, "A Multiresolution Approach to Automated Classification of Protein Sub-cellular Location Images," *BMC Bioinformatics*, Vol. 8, No. 210, 2007.



- [16] Belkin, M., and P. Niyogi, "Laplacian Eigenmaps for Dimensionality Reduction and Data Representation," *Neur. Comp.*, Vol. 13, 2003, pp. 1373-1396.
- [17] Donoho, D., and C. Grimes, "Hessian Eigenmaps: Locally Linear Embedding Techniques for High-Dimensional Data," *Natl. Acad. Sci.*, Vol. 100, 2003, pp. 5591-5596.
- [18] Duda, R., P. Hart, and D. Stork, *Pattern Classification*, New York: John Wiley & Sons, 2001.
- [19] Comon, P., "Independent Component Analysis: A New Concept?" *Signal Proc.*, Vol. 36, 1994, pp. 287-314.
- [20] Hyvärinen, A., "Survey on Independent Component Analysis," *Neural Computing Surveys*, Vol. 2, 1999, pp. 94-128.
- [21] Kullback, S., *Information Theory and Statistics*, New York: Dover Publications, 1968.
- [22] Bell, A., and T. Sejnowski, "The 'Independent Components' of Natural Scenes are Edge Filters," *Vis. Res.*, Vol. 37, No. 23, 1997, pp. 3327-3338.
- [23] A. Hyvärinen, ICA Web Site, <http://www.cs.helsinki.fi/u/ahyvarin/whatisica.shtml>.
- [24] Saul, L., K. Weinberger, J. Ham, F. Sha, and D. Lee, "Spectral Methods for Dimensionality Reduction," in *Semisupervised Learning*, Cambridge, MA: MIT Press, 2006.
- [25] Ham, J., D. Lee, S. Mika, and B. Schölkopf, *A Kernel View of the Dimensionality Reduction of Manifolds*, tech. rep., Max Planck Institute for Biological Cybernetics, 2003.
- [26] Vidal, R., Y. Ma, and S. Sastry, "Generalized Principal Component Analysis (GPCA)," *IEEE Trans. Patt. Anal. and Mach. Intelligence*, Vol. 27, No. 12, 2005, pp. 1-15.
- [27] Tenenbaum, J., V. de Silva, and J. Langford, "A Global Geometric Framework for Nonlinear Dimensionality Reduction," *Science*, Vol. 290, 2000, pp. 2319-2323.
- [28] Cox, T., and M. Cox, *Multidimensional Scaling*, London, U.K.: Chapman and Hall/CRC, 2001.
- [29] Roweis, S., and L. Saul, "Nonlinear Dimensionality Reduction by Locally Linear Embedding," *Science*, Vol. 290, 2000, pp. 2323-2326.
- [30] Inoué, S., "Foundations of Confocal Scanned Imaging in Light Microscopy," in *Handbook of Biological Confocal Microscopy*, 3rd ed., New York: Springer, 2006.
- [31] König, K., "Cell Damage During Multi-Photon Microscopy," in *Handbook of Biological Confocal Microscopy*, 3rd ed., New York: Springer, 2006.
- [32] Diaspro, A., G. Chirico, C. Usai, P. Ramoino, and J. Dobrucki, "Photobleaching," in *Handbook of Biological Confocal Microscopy*, 3rd ed., New York: Springer, 2006.
- [33] Merryman, T. E., and J. Kovačević, "Adaptive Multiresolution Acquisition of Fluorescence Microscopy Data Sets," *IEEE Trans. Image Proc.*, sp. iss. *Molecular and Cellular Bioimaging*, Vol. 14, September 2005, pp. 1246-1253.
- [34] Jackson, C., R. Murphy, and J. Kovačević, "Efficient Acquisition and Learning of Fluorescence Microscopy Data Models," *Proc. IEEE Int. Conf. Image Proc.*, Vol. 6, San Antonio, TX, Sep. 2007, pp. 245-248.
- [35] Genovesio, A., T. Liedl, V. Emiliani, W. Parak, M. Coppey-Moisán, and J. Olivo-Marin, "Multiple Particle Tracking in 3-D+t Microscopy: Method and Application to the Tracking of Endocytosed Quantum Dots," *IEEE Trans. Image Proc.*, Vol. 15, May 2006, pp. 1062-1070.
- [36] Sarder, P., and A. Nehorai, "Deconvolution Methods for 3-D Fluorescence Microscopy Images," *IEEE Signal Proc. Mag.*, sp. iss. *Molec. Cellular Bioimaging*, Vol. 23, May 2006, pp. 32-45.
- [37] Verveer, P., M. Gemkow, and T. Jovin, "A Comparison of Image Restoration Approaches Applied to Three-Dimensional Confocal and Wide-Field Fluorescence Microscopy," *Journ. Microscopy*, Vol. 193, No. 1, 1999, pp. 50-61.

- [38] Markham, J., and J. Conchello, "Fast Maximum-Likelihood Image-Restoration Algorithms for Three-Dimensional Fluorescence Microscopy," *Journ. Opt. Soc. Am. A*, Vol. 18, No. 5, 2001, pp. 1062–1071.
- [39] Castleman, K., "Image Restoration," in *Digital Image Processing*, Englewood Cliffs, NJ: Prentice-Hall, 1996.
- [40] Tikhonov, A., and V. Arsenin, *Solutions of Ill-Posed Problems*, New York: John Wiley & Sons, 1977.
- [41] Dey, N., L. Blanc-Feraud, C. Zimmer, Z. Kam, J. Olivo-Marin, and J. Zerubia, "A Deconvolution Method for Confocal Microscopy with Total Variation Regularization," *Proc. IEEE Int. Symp. Biomed. Imaging*, Arlington, VA, April 2004, pp. 1223–1226.
- [42] Figueiredo, M., and R. Nowak, "An EM Algorithm for Wavelet-Based Image Restoration," *IEEE Trans. Image Proc.*, Vol. 12, No. 8, 2003, pp. 906–916.
- [43] Skilling, J., "Maximum Entropy and Bayesian Methods," in *Classic Maximum Entropy*, Norwell, MA: Kluwer Academic Publishers, 1989.
- [44] Joshi, S., and M. Miller, "Maximum A Posteriori Estimation with Good's Roughness for Three-Dimensional Optical-Sectioning Microscopy," *Journ. Opt. Soc. Am. A*, Vol. 10, No. 5, 1993, pp. 1078–1085.
- [45] Fish, D., A. Brinicombe, E. Pike, and J. Walker, "Blind Deconvolution by Means of the Richardson-Lucy Algorithm," *Journ. Opt. Soc. Am. A*, Vol. 12, No. 1, 1995, pp. 58–65.
- [46] Vonesch, C., and M. Unser, "Fast Wavelet-Regularized Image Deconvolution," *Proc. IEEE Int. Symp. Biomed. Imaging*, Arlington, VA, April 2007, pp. 608–611.
- [47] Schönemann, P., "A Generalized Solution of the Orthogonal Procrustes Problem," *Psychometrika*, Vol. 31, 1966, pp. 1–10.
- [48] Hajnal, J., D. Hill, and D. Hawkes, *Medical Image Registration*, Boca Raton, FL: CRC Press, 2001.
- [49] Bookstein, F., "Principal Warps: Thin-Plate Splines and the Decomposition of Transformations," *IEEE Trans. Patt. Anal. and Mach. Intelligence*, Vol. 11, 1989, pp. 567–585.
- [50] Maintz, J., and M. Viergever, "A Survey of Medical Image Registration," *Med. Image Anal.*, Vol. 2, 1998, pp. 1–36.
- [51] Zitova, B., and J. Flusser, "Image Registration Methods: A Survey," *Image and Vis. Comp.*, Vol. 21, 2003, pp. 977–1000.
- [52] Pluim, J., J. Maintz, and M. Viergever, "Mutual-Information-Based Registration of Medical Images: A Survey," *IEEE Trans. Med. Imag.*, Vol. 22, 2003, pp. 986–1004.
- [53] Press, W., B. Flannery, S. Teukolsky, and W. Vetterling, *Numerical Recipes in C: The Art of Scientific Computing*, 2nd ed., Cambridge, U.K.: Cambridge Univ. Press, 1992.
- [54] Sorzano, C., P. Thévenaz, and M. Unser, "Elastic Registration of Biological Images Using Vector-Spline Regularization," *IEEE Trans. Biomed. Eng.*, Vol. 52, No. 4, 2005, pp. 652–663.
- [55] Vonesch, C., F. Aguet, J. Vonesch, and M. Unser, "The Colored Revolution of Bioimaging," *IEEE Signal Proc. Mag.*, sp. iss. *Molec. Cellular Bioimaging*, Vol. 23, May 2006, pp. 20–31.
- [56] Vercauteren, T., A. Perchant, G. Maladain, X. Pennec, and N. Ayache, "Robust Mosaicing with Correction of Motion Distortions and Tissue Deformations for In Vivo Fibered Microscopy," *Med. Image Anal.*, Vol. 10, 2006, pp. 673–692.
- [57] Rohr, K., P. Cathier, and S. Worz, "Elastic Registration of Electrophoresis Images Using Intensity Information and Point Landmarks," *Pattern Recogn.*, Vol. 37, No. 5, 2004, pp. 1035–1048.
- [58] Olson, A., N. Larson, and C. Heckman, "Classification of Cultured Mammalian Cells by Shape Analysis and Pattern Recognition," *Natl. Acad. Sci.*, Vol. 77, 1980, pp. 1516–1520.

- [59] Gray, A., D. Young, N. Martin, and C. Glasbey, "Cell Identification and Sizing Using Digital Image Analysis for Estimation of Cell Biomass in High Rate Algal Ponds," *Journ. Appl. Psychology*, Vol. 14, 2002, pp. 193-204.
- [60] Mukherjee, D., N. Ray, and S. Acton, "Level Set Analysis for Leukocyte Detection and Tracking," *IEEE Trans. Image Proc.*, Vol. 13, 2004, pp. 562-572.
- [61] Meijering, E., M. Jacob, J. Sarria, P. Steiner, H. Hirling, and M. Unser, "Design and Validation of a Tool for Neurite Tracing and Analysis in Fluorescence Microscopy Images," *Cytometry*, Vol. 58A, April 2004, pp. 167-176.
- [62] Zimmer, C., B. Zhang, A. Dufour, A. Thebaud, S. Berlemont, V. Meas-Yedid, and J. O. Marin, "On the Digital Trail of Mobile Cells," *IEEE Signal Proc. Mag.*, sp. iss. *Molec. Cellular Bioimaging*, Vol. 23, May 2006, pp. 54-62.
- [63] Chen, S., T. Zhao, G. Gordon, and R. Murphy, "A Novel Graphical Model Approach to Segmenting Cell Images," *Proc. IEEE Symp. Comp. Intelligence Bioinform. Comp. Biol.*, September 2006, pp. 1-8.
- [64] Srinivasa, G., M. Fickus, and J. Kovačević, "Multiscale Active Contour Transformations for the Segmentation of Fluorescence Microscope Images," *Proc. SPIE Conf. Wavelet Appl. in Signal and Image Proc.*, Vol. 6701:18, San Diego, CA, August 2007, pp. 1-15.
- [65] Glory, E., and R. Murphy, "Automated Subcellular Location Determination and High Throughput Microscopy," *Developmental Cell*, Vol. 12, 2007, pp. 7-16.
- [66] Velliste, M., and R. Murphy, "Automated Determination of Protein Subcellular Locations from 3D Fluorescence Microscope Images," *Proc. IEEE Int. Symp. Biomed. Imaging*, Washnigton, D.C., 2002, pp. 867-870.
- [67] Bengtsson, E., C. Wählby, and J. Lindblad, "Robust Cell Image Segmentation Methods," *Pattern Recogn. and Image Anal.*, Vol. 14, No. 2, 2004, pp. 157-167.
- [68] Xu, C., D. Pham, and J. Prince, "Medical Image Segmentation Using Deformable Models," in *Handbook of Medical Imaging*, J. Fitzpatric and M. Sonka, (eds.), New York: SPIE Press, 2000.
- [69] Kass, M., A. Witkin, and D. Terzopoulos, "Snakes: Active Contour Models," *Int. Journ. Comp. Vis.*, Vol. 1, No. 4, 1988, pp. 321-331.
- [70] Pluempitwiriwajew, C., J. Moura, Y. Wu, and C. Ho, "STACS: A New Active Contour Scheme for Cardiac MR Image Segmentation," *IEEE Trans. Med. Imag.*, Vol. 24, May 2005, pp. 593-603.
- [71] Osher, S., and R. Fedkiw, *Level Set Methods and Dynamic Implicit Surfaces*, New York: Springer-Verlag, 2003.
- [72] Chan, T., and L. Vese, "Active Contours Without Edges," *IEEE Trans. Image Proc.*, Vol. 10, February 2001, pp. 266-277.
- [73] Coulot, L., H. Kischner, A. Chebira, J. Moura, J. Kovačević, E. Osuna, and R. Murphy, "Topology Preserving STACS Segmentation of Protein Subcellular Location Images," *Proc. IEEE Int. Symp. Biomed. Imaging*, Arlington, VA, April 2006, pp. 566-569.
- [74] Cohen, A., B. Roysam, and J. Turner, "Automated Tracing and Volume Measurements of Neurons from 3-D Confocal Fluorescence Microscopy Data," *Journ. Microscopy*, Vol. 173, No. 2, 1994, pp. 103-114.
- [75] Al-Kofahi, K., S. Lasek, D. Szarowski, C. Page, G. Nagy, J. Turner, and B. Roysam, "Rapid Automated Three-Dimensional Tracing of Neurons from Confocal Image Stacks," *IEEE Trans. Inform. Tech. in Biomed.*, Vol. 6, June 2002, pp. 171-187.
- [76] Sage, D., F. Neumann, F. Hediger, S. Gasser, and M. Unser, "Automatic Tracking of Individual Fluorescence Particles: Application to the Study of Chromosome Dynamics," *IEEE Trans. Image Proc.*, Vol. 14, No. 3, 2005, pp. 1372-1383.
- [77] Meijering, E., I. Smal, and G. Danuser, "Tracking in Molecular Imaging," *IEEE Signal Proc. Mag.*, sp. iss., *Molec. Cellular Bioimaging*, Vol. 23, May 2006, pp. 46-53.

- [78] Cheezum, M., W. Walker, and W. Guilford, "Quantitative Comparison of Algorithms for Tracking Single Fluorescent Particles," *Biophys. Journ.*, Vol. 81, No. 4, 2001, pp. 2378-2388.
- [79] Zhou, X., and S. Wong, "Informatics Challenges of High-Throughput Microscopy," *IEEE Signal Proc. Mag.*, sp. iss., *Molec. Cellular Bioimaging*, Vol. 23, No. 3, 2006, pp. 64-71.
- [80] Huang, K., and R. Murphy, "From Quantitative Microscopy to Automated Image Understanding," *Journ. Biomed. Optics*, Vol. 9, 2004, pp. 893-912.
- [81] Goldberg, I., C. Alland, J. Burel, D. Creager, A. Falconi, H. Hochheiser, J. Johnston, J. Mellen, P. Sorger, and J. Swedlow, "The Open Microscopy Environment (OME) Data Model and XML File: Open Tools for Informatics and Quantitative Analysis in Biological Imaging," *Genome Biol.*, Vol. 6, No. 5, 2005, p. R47.
- [82] Kellogg, R., A. Chebira, A. Goyal, P. Cuadra, S. Zappe, J. Minden, and J. Kovačević, "Towards an Image Analysis Toolbox for High-Throughput Drosophila Embryo RNAi Screens," *Proc. IEEE Int. Symp. Biomed. Imaging*, Arlington, VA, April 2007, pp. 288-291.
- [83] Harder, N., B. Neumann, M. Held, U. Liebel, H. Erfle, J. Ellenberg, R. Eils, and K. Rohr, "Automated Recognition of Mitotic Patterns in Fluorescence Microscopy Images of Human Cells," *Proc. IEEE Int. Symp. Biomed. Imaging*, Arlington, VA, April 2006, pp. 1016-1019.
- [84] Chen, X., X. Zhou, and S. Wong, "Automated Segmentation, Classification, and Tracking of Cancer Cell Nuclei in Time-Lapse Microscopy," *IEEE Trans. Biomed. Eng.*, Vol. 53, No. 4, 2006, pp. 762-766.
- [85] Gladilin, E., A. Micoulet, B. Hosseini, K. Rohr, J. Spatz, and R. Eils, "3D Finite Element Analysis of Uniaxial Cell Stretching: From Image to Insight," *Phys. Biol.*, Vol. 4, June 2007, pp. 104-113.
- [86] Jaqaman, K., J. Dorn, G. Jelson, J. Tytell, P. K. Sorger, and G. Danuser, "Comparative Autoregressive Moving Average Analysis of Kinetochore Microtubule Dynamics in Yeast," *Biophys. Journ.*, Vol. 91, 2006, pp. 2312-2325.
- [87] Priestley, M., "Stationary Random Processes," in *Spectral Analysis and Time Series*, New York: Academic Press, 1981.
- [88] Dorn, J., K. Jaqaman, D. Rines, G. Jelson, P. Sorger, and G. Danuser, "Yeast Kinetochore Microtubule Dynamics Analyzed by High-Resolution Three-Dimensional Microscopy," *Biophys. Journ.*, Vol. 89, 2005, pp. 2835-2854.



# An Introduction to Fluorescence Microscopy: Basic Principles, Challenges, and Opportunities

François Aguet, Cédric Vonesch, Jean-Luc Vonesch, and Michael Unser

The discovery of fluorescent labels suitable for *in vivo* use and the development of high-resolution microscopes have transformed the fluorescence microscope into a mainstream tool, bringing about a revolution for biological imaging and having a profound impact on the way research is being conducted in the life sciences. Among a myriad of new imaging possibilities, subcellular components and processes can now be visualized *in vivo*, both structurally and functionally. Observations can be made in two or three dimensions, at different wavelengths (spectroscopy), and possibly with time-lapse imaging, to investigate dynamic processes.

The observation of many biological processes relies on the ability to identify and locate specific proteins within their cellular environment. Cells are mostly transparent in their natural state, and the immense number of molecules that constitute them are optically indistinguishable from one another. This makes the identification of a particular protein a very complex task—akin to finding a needle in a haystack. However, if a bright marker were attached to the protein of interest, it could very precisely indicate its position. Much effort has gone into finding suitable markers for this purpose, but it is only over the course of the past decade, with the advent of fluorescent proteins, that this concept has been revolutionized. These biological markers have the crucial properties necessary for dynamic observations of living cells: they are essentially harmless to the organism and can be attached to other proteins without impacting their function.

Fluorescence microscopy was invented almost a century ago, when microscopists were experimenting with ultraviolet light to achieve higher resolutions. In the very beginning, observations were limited to specimens that naturally fluoresce.<sup>1</sup> Rapidly, fluorescent dyes for staining tissues and cells were investigated. But it was not until the 1940s that fluorescence microscopy became popular, when A. Coons and M. Kaplan introduced a technique to label antibodies with a fluorescent dye to study antibody-antigen interactions, which profoundly changed the field of immunohistochemistry [1]. The discovery that really brought fluorescence microscopy to the forefront came in 1994, when M. Chalfie et al. succeeded in expressing a naturally fluorescent protein, the now famous green fluorescent protein (GFP), in living organisms [2]. This was a landmark evolution in the field, fostering a whole new class of tagging methods.

While genetic engineering is at the origin of this new methodology, a number of innovations from the fields of physics, optics, and mechanical and electrical

1. This property is called autofluorescence or primary fluorescence.

engineering have been combined to provide the necessary instrumentation. Impressive enhancements in classical microscopy have been achieved, and new imaging systems are actively being developed. A key element for the evolution of microscopy in general was the shift to digital imaging in the 1990s, with the availability of affordable high-sensitivity acquisition devices and powerful computer hardware.

The capabilities of today's systems often lead to enormous data sets that, in most cases, require postprocessing for their interpretation. Signal processing methods for biological research are only at their prelude; the needs are considerable and most probably not even clearly formulated yet. It is thus predictable that signal processing will be one of the main challenges of fluorescence microscopy in the forthcoming years.

The ambition of this chapter is to provide the reader with an introduction covering the key aspects of modern fluorescence microscopy. We begin by recalling the principles of fluorescence and review the history of discoveries that led to the instruments and techniques in use today. Next, we present the optics and examine various types of detectors used in fluorescence microscopy. A further section is devoted to a discussion of signal and image processing challenges in fluorescence microscopy, and, finally, we highlight some current developments and future perspectives in the field. This chapter is best read in conjunction with Chapters 1 and 3.

## 4.1 Fluorescence in Molecular and Cellular Biology

### 4.1.1 The Physical Principles of Fluorescence

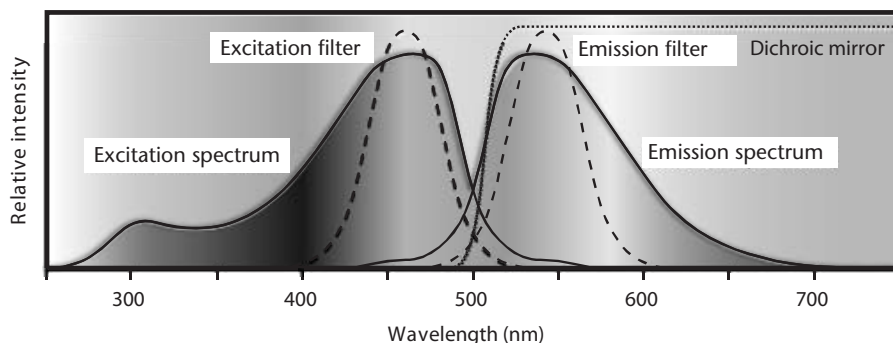
#### 4.1.1.1 Definition

*Fluorescence* is a phenomenon by which a molecule, upon illumination at a specific wavelength, reemits light at another (typically longer) wavelength. A molecule that has the ability to fluoresce is called a *fluorophore* or *fluorochrome*.<sup>2</sup> It has distinctive *excitation* and *emission* spectra (see Figure 4.1), although in practice, it is often characterized by the two wavelengths corresponding to the respective peak intensities of these spectra.

A molecule can exist in a variety of energetic states, which, for the most part, are determined by the configuration of its electrons and the vibrational agitation of its atomic nuclei. If a photon with sufficient energy is absorbed by a fluorophore, the latter moves from its ground state to an excited electronic state [see Figure 4.2(a)]. Fluorescence occurs when the excited molecule returns to the ground state by releasing energy through emission of a photon. Because some of the energy gained during excitation is converted to heat, the emitted photon has a lower energy than the absorbed one. This explains the difference in wavelength mentioned earlier (since  $E = h\nu = hc/\lambda$ ), which is also known as the Stokes shift. Fluorophores whose spectra present a large Stokes shift are usually preferred, since their emitted

- Specifically, the former describes an atomic compound responsible for fluorescence, while the latter is a more general term for a dye that renders a body fluorescent.



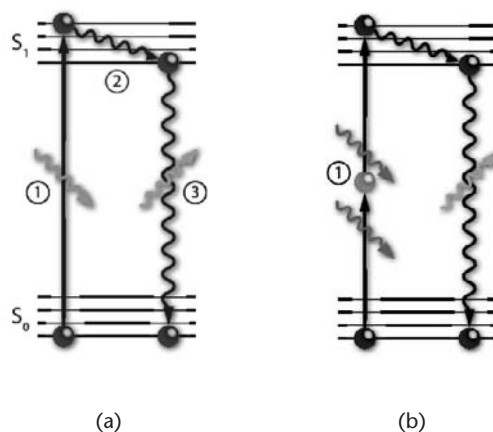


**Figure 4.1** Representation of typical excitation/emission spectra of a fluorophore (in relative intensities). The excitation spectrum shows the emission intensity as a function of excitation wavelength, and the emission spectrum shows the relative emission intensities as a function of emission wavelengths for an excitation at the peak absorption wavelength. Explanations on the filters are given in Section 4.2.

light can be separated from the excitation light more easily by the means of optical filters (see Figure 4.1).

#### 4.1.1.2 Related Phenomena

When in an excited state, a fluorophore can be forced to the ground state in a process called *stimulated emission*. Upon absorption of a second photon at the excitation wavelength, the molecule returns to the ground state by emitting two photons that are in phase and whose wavelengths are identical to the second photon's



**Figure 4.2** Jablonski diagrams representing the energy-level transitions involved in the fluorescence of GFP. Thick lines represent electronic energy levels; thin ones are associated vibrational energy levels. (a) Upon absorption of a photon at a specific wavelength, the molecule moves from the ground state  $S_0$  to the excited state  $S_1$  (1). Vibrational energies are immediately converted into heat in a process called vibrational relaxation (2). When the molecule returns to the ground state, the remaining energy is released via emission of a new photon at a longer wavelength. (b) In the case of two-photon excitation, the excitation wavelength is longer than the emission wavelength. The intermediate virtual state is indicated by (1).

wavelength. This phenomenon is relevant to some of the concepts discussed later, but is best known as the light-amplification principle behind lasers.

Another important concept is that of *multiphoton excitation*. A fluorophore can also be excited by the simultaneous absorption of two or more photons, given that the combined energy of the photons corresponds to the energy required for single-photon excitation [see Figure 4.2(b)]. In this particular situation the excitation wavelength is longer—in the case of two-photon excitation, twice as long as the single-photon excitation wavelength.

#### 4.1.2 The Green Revolution

The developments that had the biggest impact on biological research and made fluorescence microscopy ubiquitous took place during the past two decades. Consequently, we shall focus on this period for the remainder of this section. However, these recent developments could not have occurred without previous discoveries and inventions in a variety of fields, starting in the sixteenth century. An overview of events that played an essential role in contributing to the development of modern fluorescence microscopy is given in the form of a timeline in Figures 4.3 and 4.4.

In the early 1990s, fluorescent labeling techniques such as immunofluorescence<sup>3</sup> and covalent marking<sup>4</sup> were already widely in use for imaging. However, a straightforward means for selectively labeling a given protein with a non-perturbing fluorescent marker was not yet available. Only such a tag would make the *in vivo* observation of interactions between a specific protein with other proteins and the environment feasible.

The breakthrough came in 1994, when Chalfie et al. [2] succeeded in expressing a fluorescent protein that naturally occurs in a jellyfish species in other organisms by modifying their genome to code for this protein. At the origin of this innovation, accordingly dubbed “the green revolution” [3], was the discovery of GFP by Shimomura et al. in 1961 [4]. During their studies of the jellyfish *aequorea victoria*, whose fluorescing nature was described for the first time in 1955, they discovered that the source of the fluorescence was a naturally produced protein. Its chemical structure was reported by Shimomura in 1979, and in 1992, Prasher et al. cloned and determined its genetic sequence [5], paving the way for the work of Chalfie et al.

Since the first experiments with GFP, many variants have been engineered and discovered. From the naturally occurring GFP, called wtGFP for wild-type GFP, and from similar fluorescent proteins occurring in other marine organisms, new, more powerful mutants have been derived. Their properties range from different excitation and emission spectra<sup>5</sup> to stronger fluorescence and higher resistance to photobleaching [6]. Two widespread examples are cyan fluorescent protein (CFP)

3. A technique (also called immunostaining) for detecting an antigen (protein) with a fluorochrome-labeled antibody.
4. Proteins are purified, covalently labeled with a fluorescent molecule, and then introduced into cells.
5. The currently available fluorescent protein tags offer a wide choice of wavelengths within the visible spectrum.

- |              |  |
|--------------|--|
| 1565         | Nicolás Monardes observes luminescence in the extract of the wood <i>lignum nephriticum</i> , a substance used for treating kidney ailments.   |
| 1646         | Athanasius Kircher relates that an infusion of <i>lignum nephriticum</i> reflects blue and transmits yellow light.   |
| 1800         | Frederick William Herschel discovers infrared radiation.   |
| 1801         | Johann Wilhelm Ritter discovers the ultraviolet region of the spectrum.  |
| 1833         | David Brewster observes red radiation in a solution containing chlorophyll upon illuminating it with white light.  |
| 1845         | John F. W. Herschel (the son of F. W. Herschel) discovers the phenomenon of fluorescence in a quinine solution.  |
| 1852         | George Gabriel Stokes describes the luminescence observed in the fluorspar mineral as fluorescence, and formulates the Stokes law.   |
| 1871         | Adolf von Baeyer discovers and synthesizes <i>fluorescein</i> , still widely used as a dye.  |
| 1878         | Ernst Abbe formulates the theory that links resolution to the wavelength of light, and proposes the use of ultraviolet light to increase the resolution of microscopes.  |
| 1904         | August Köhler and Moritz von Rohr develop the ultraviolet microscope. Autofluorescence observed in the visible domain starts the era of fluorescence microscopy.   |
| 1905         | Albert Einstein describes the photoelectric effect.  |
| 1908         | August Köhler and Henry Friedrich Wilhelm Siedentopf build and demonstrate the first fluorescence microscope.  |
| 1911         | Max Haitinger coins the term <i>fluorochrome</i> to describe dyes that render non-fluorescent objects fluorescent. Numerous investigations into fluorescent dyes begin.  |
| 1911<br>1913 | The first commercialized fluorescence microscopes, using carbon arc lamps, are produced by Reichert (Otto Heimstädt and Carl F. W. Reichert, 1911) and Carl Zeiss (Heinrich Lehmann, 1913). Observations are limited to specimens that present autofluorescence. |
| 1929         | Philipp Ellinger and August Hirt propose a fluorescence microscope with epi-illumination for the observation of living organisms. They use the fluorochromes <i>fryptaflavine</i> , which stains cell nuclei, and <i>fluorescein</i> , to study kidney function. |

Figure 4.3 Early history of fluorescence microscopy.



Figure 4.4 Modern history of fluorescence microscopy.

and yellow fluorescent protein (YFP), named for their characteristic emission spectra.

Biologists can label virtually any desired protein with a fluorescent protein by means of straightforward procedures. The first step leading to the creation of a labeled protein is to append the marker protein's sequence to that of the target. The resulting sequence is then introduced into cells, where its transcription results in the synthesis of a *fusion protein*. A common means for doing this is by placing the gene onto a plasmid,<sup>6</sup> which can then be taken up by a cell. Such plasmids exist for a wide range of fluorescent proteins and are available from specialized companies.

The fusion protein (Color Plate 1) is expressed throughout the lifetime of the cell, as long as its sequence is present in the cell's nucleus. Note that this procedure typically results in the expression of both the fusion and natural versions of the protein, since the genetic sequence of the former does not replace that of the latter. Although the function and localization of the two variants are in most cases identical, it is necessary to verify that the label has no influence on cellular functions. For further details, we refer to [7, 8].

The availability of fluorescent protein tagging techniques led to a fundamental change in the way biological research is conducted and to an explosion of experimental possibilities (see also Section 4.5). For instance, within the past 10 years, the relative number of experiments dealing with live samples at the Institute of Genetics and Molecular and Cellular Biology (IGBMC) imaging center (Illkirch, France) increased by almost a hundred-fold.

## 4.2 Microscopes and Image Formation

We now turn our attention to the instrumentation for fluorescence imaging. This section provides a brief description of the two main types of image forming systems: widefield and confocal microscopes. While the former are usually less expensive than the latter (depending on the configuration), their optical resolution is intrinsically more limited, especially in the axial (i.e.,  $z$ ) direction. Both systems can yield volume images of the sample under inspection, possibly with the help of deconvolution. However, in widefield microscopes the volume is acquired plane by plane (as opposed to point by point in standard confocal systems), which allows for faster acquisitions.

### 4.2.1 The Widefield Microscope

#### 4.2.1.1 Principle

Widefield microscopy is based on the paradigm of Köhler illumination, according to which the sample is observed under a uniform light beam. Color Plate 2(a) shows

6. Plasmids are small, circular, double-stranded sequences of DNA that naturally occur in bacteria and are part of their genome. They can easily be introduced into cells, where they are expressed in the same fashion as chromosomal DNA. Plasmids are not replicated upon cellular division; however, in some cases they are integrated into the cell's chromosomal DNA.



how this is obtained in a simplified epi-illumination microscope: the light source (an arc or filament lamp) is magnified by the collector lens and projected onto the iris diaphragm. This aperture is located in a conjugate plane of the objective's back focal plane. Therefore the latter acts as a condenser lens and the intensity from the iris is uniformly dispatched on the sample.

Let us now consider a single point of the sample. It will reemit light by reflection and possibly by fluorescence. If located in the focal plane, this will generate a beam of parallel light rays through the microscope tube. The image is formed by integrating the effect of all secondary point sources within the specimen; it can be observed through the eyepiece or recorded by placing a CCD sensor in the image plane.

One of the critical parameters in this setting is the *numerical aperture* (NA); that is, the angular opening of the light cone emerging from the object and collected by the objective. The magnification effect results from the combination of the objective, tube, and ocular lenses.

#### 4.2.1.2 Components for Fluorescence Imaging

Fluorescence imaging requires specific additional components for controlling the spectrum of the light (see also Figure 4.1). While usual lamps produce “white light” (covering the whole visible spectra, with some peaks at characteristic wavelengths), the fluorescent sample has to be illuminated with a specific excitation wavelength. This is ensured by inserting an *excitation filter* on the illumination path. The *emission filter*, on the other hand, ensures that only the wavelength corresponding to fluorescence reemission gets transmitted to the sensor or to the eyepiece, whereas reflected light (at the excitation wavelength) is discarded. A *dichroic mirror* helps achieving this by reflecting light below a certain *transition wavelength* (which is chosen to be between the excitation and emission wavelengths of the fluorophore) and transmitting light above that wavelength.

#### 4.2.1.3 Incoherent Point Spread Function

Because of the random nature of photon reemission, fluorescence microscopy is an incoherent imaging process. This means that each point of the sample contributes independently (without interference) to the light intensity distribution in the image space. Moreover, in the paraxial approximation, moving the object does not influence its image, except for a shift. From a signal-processing standpoint, a widefield microscope can thus be modeled as a linear space-invariant system in intensity. In other words, the light intensity (which is the physical value measured by a photodetector) in the neighborhood of the primary imaging plane ( $z = 0$ ) is given by a convolution:

$$I(x, y, z) \propto \int_{\mathbb{R}^3} \left| h_{\lambda_{\text{em}}} \left( \frac{x}{M} - u, \frac{y}{M} - v, \frac{z}{M^2} - w \right) \right|^2 \chi(u, v, w) \, du \, dv \, dw \quad (4.1)$$

where  $M$  is the magnification of the objective (notice that the axial magnification is  $M^2$ ). Here,  $\chi$  is the characteristic function of the object; it describes its ability

to convert incident light into fluorescence intensity at the emission wavelength  $\lambda_{\text{em}}$  and is thus mostly related to the fluorophore concentration. The impulse response  $|h_{\lambda_{\text{em}}}|^2$  is called the incoherent (or intensity) *point spread function* (PSF), since it defines the image of an ideal point object ( $\chi(x, y, z) = \delta(x, y, z)$ ). For a given wavelength  $\lambda$  it is defined by a 2-D Fourier transform:

$$h_{\lambda}(x, y, z) = \int_{\mathbb{R}^2} P(u, v) \exp\left(i2\pi z \frac{u^2 + v^2}{2\lambda f^2}\right) \exp\left(-i2\pi \frac{xu + yv}{\lambda f}\right) du dv \quad (4.2)$$

In this expression  $f$  is the focal length of the objective.  $P$  represents the *pupil function*, which is an indicator function that corresponds to the circular aperture of the objective. Its radius  $r$  is related to the focal length by  $\text{NA} \simeq r/f$ . Notice the presence of the depth coordinate  $z$  in the phase factor—it accounts for the defocusing effect illustrated in Color Plate 2.

## 4.2.2 The Confocal Scanning Microscope

### 4.2.2.1 Principle

In a confocal microscope ([9], Color Plate 2(b)) the illuminating point source is usually obtained from a laser. The latter illuminates a pinhole located in a plane conjugate to the sample. In this way, the light is focused onto a very small volume of the sample, and the returning fluorescence radiation is collected by a photomultiplier tube (PMT [10]). The essential difference with a widefield microscope is the detection pinhole, which drastically reduces the proportion of light coming from out-of-focus points, especially in the axial direction.

Since only one point is observed at a time, the object has to be *scanned*. In the  $x$  and  $y$  dimensions, this is achieved by using a scan mirror, which deflects the illumination beam, hence moving the illumination spot in the same plane. In the  $z$  direction, the sample is usually moved mechanically by the means of a motorized stage. The ability to resolve different planes within the object is called *optical sectioning* and leads to a complete volumetric representation (a *stack* of 2-D images).

A critical parameter in this setting is the pinhole diameter, which is usually expressed in *Airy units* (AU).<sup>7</sup> One Airy unit corresponds to the size of the central disc of the PSF of the system (Color Plate 3, second image in the bottom row). The smaller the pinhole, the better the resolution; however, this also means that less light is collected, implying a higher noise level.

### 4.2.2.2 Incoherent Point Spread Function

The imaging process of fluorescent material can be modeled as follows: first, we have to take into account the effect of illumination, which consists of multiplying the fluorescence strength of the object by the PSF of the objective (taking into

7. After back-projection in the object space (i.e., dividing the effective diameter by the magnification factor).



account the scan coordinate  $(x_0, y_0, z_0)$ ). The reemitted light intensity is then given by

$$|h_{\lambda_{\text{ex}}}(x - x_0, y - y_0, z)|^2 \chi(x, y, z - z_0) \quad (4.3)$$

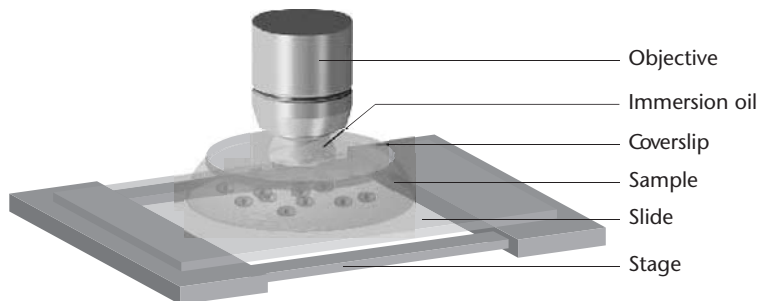
where  $\lambda_{\text{ex}}$  denotes the excitation wavelength. The intensity at the detector is the convolution of this expression with the objective PSF, evaluated at the origin (the position of the detection pinhole):

$$\int_{\mathbb{R}^3} |h_{\lambda_{\text{em}}}(x_0 - x, y_0 - y, -z)|^2 |h_{\lambda_{\text{ex}}}(x - x_0, y - y_0, z)|^2 \chi(x, y, z - z_0) dx dy dz \quad (4.4)$$

where  $\lambda_{\text{em}}$  denotes the reemission wavelength. Notice that we did not indicate the magnification factors here, which is equivalent to back-projecting the image into object space; also, the returning light beams are descanned when they hit back on the scanning mirror. Since  $h_{\lambda_{\text{ex}}}$  is symmetric in  $x$  and  $y$ , the final intensity PSF of the system is  $|h_{\lambda_{\text{ex}}} h_{\lambda_{\text{em}}}|^2$ , illustrated in the lower part of Color Plate 3. It shows that a confocal microscope has a PSF that is more concentrated in space than a widefield one (i.e., a better resolution, especially in the axial direction).

#### 4.2.3 Sample Setup and Aberrations

In an ideal optical system, wavefronts propagate without undergoing phase distortions, also called aberrations. Modern microscope optics are highly sophisticated and are corrected to high levels of precision to avoid such distortions. The optical properties of the sample play an important role in the formation and correction of aberrations. Samples are usually placed onto a glass slide and need to be covered with a glass coverslip for use with most objectives. As shown in Figure 4.5, there is an *immersion* layer between the objective and the sample (to increase resolution, an immersion medium with a high refractive index, such as oil, is used). To minimize aberrations, each objective is designed for a specific setup, corresponding to parameters such as the refractive index of the immersion medium, the coverslip thickness, and the imaging depth. Small deviations from these optimal values (e.g., due to temperature changes or incorrect sample preparation) can



**Figure 4.5** Schematic representation of a typical sample setup.

introduce aberrations. A common and often unavoidable source of aberrations is the imaging depth in situations where the refractive indices of the specimen and immersion layers are mismatched. In the case where this mismatch is significant, it may result in the PSF becoming nonstationary, especially along the axial direction  $z$  [11].

## 4.3 Detectors

Fluorescence imaging can sometimes be a real challenge due to very low light conditions. Especially for live samples undergoing fast biological changes, it may not be possible to integrate more than a few tens of photons at each sampling position. Such conditions call for very sensitive detection devices with very accurate synchronization and control.

### 4.3.1 Characteristic Parameters of Detection Systems

Most detectors are actually designed for specific applications and provide increased accuracy along the corresponding dimensions. In what follows, we briefly review the main characteristics of a detection device with respect to different parameters.

#### 4.3.1.1 Wavelength

One of the critical parameters of a detector is its *quantum efficiency* (i.e., the average rate of incoming photons that are converted into an electronic charge). This rate strongly depends on the wavelength and is therefore also called *spectral sensitivity*.

#### 4.3.1.2 Intensity

Some detectors operate by internal amplification of the light signal they receive, which leads to the notion of *gain*. Detectors with gain adjustment offer increased *interscene dynamic range* (that is, the range of intensity levels that they can adapt to) for different imaging situations. The *intrascene dynamic range* characterizes the range of intensities to which the sensor can respond linearly, for a given imaging situation. The maximum value, divided by the noise level, defines the peak *signal-to-noise ratio* (SNR). The *quantization precision* (number of bits per sample) must be chosen accordingly.

#### 4.3.1.3 Spatial Resolution

For array/line (respective point) detectors, the *pixel size* (respective detection aperture) represents a tradeoff between resolution and noise level. Another parameter is the effective *photosensitive area*, which may not cover the whole detector.

#### 4.3.1.4 Temporal Resolution

Long integration times will reduce noise but slow down the acquisition process. High *readout speeds* will allow faster frame rates/scan frequencies. For fluorescence

lifetime measurements, one needs to precisely know when a given event occurred, which requires high synchronization and timing accuracy.

#### 4.3.1.5 Operating Temperature

*Cooling* is often mandatory for noise reduction.

### 4.3.2 Detection Technologies

We can distinguish between two main types of detectors for fluorescence microscopy.

#### 4.3.2.1 Semiconductor Detectors

They are based on an internal photoelectric effect and are most often encountered as 2-D or 1-D array detectors. Typical examples are charge coupled device (CCD) [12] cameras for widefield microscopy.

Figure 4.6(a) presents the structure of a CCD sensor. Its elementary building block (pixel) is a metal-oxide-semiconductor (MOS) photocapacitor, whose role is to convert photons into electric charge. While the internal conversion process can achieve rates close to 100%, the transmission coefficients of the electrodes and the insulating layer limit the overall quantum efficiency of the detection to 40% at most. To improve upon this value, the photocapacitor can be illuminated from the silicon substrate side, or *back-illuminated*. However, this requires a complex (and expensive) etching process to reduce the substrate thickness.

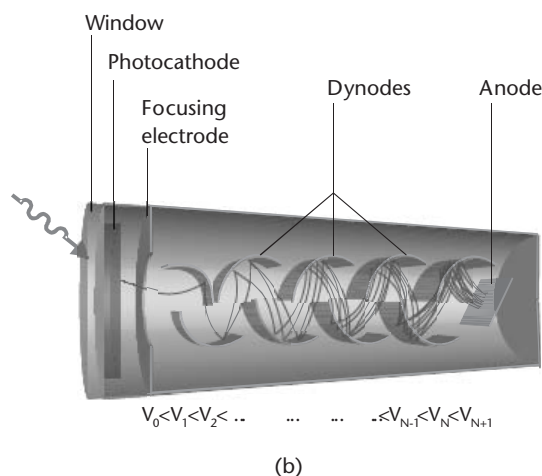
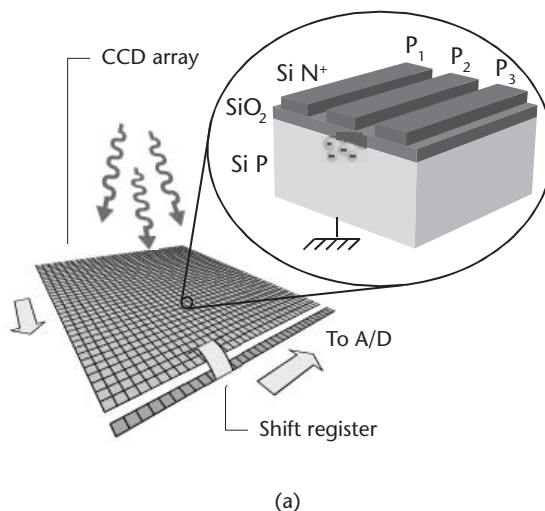
The accumulated charge is essentially a linear function of the number of incoming photons, until a saturation level is reached. Above that level, additional charges may diffuse to neighbouring pixels, an effect known as *blooming*. The maximum number of electrons, divided by the average number of electrons generated by noise (see the following), gives the peak SNR. High-sensitivity cameras can reach ratios of 30,000:1 or better.

In CCD detectors, the charges are read-out using an analog shift register.<sup>8</sup> In the full-frame transfer scheme illustrated in Figure 4.6(a), the charges of each pixel row are sequentially moved toward the shift register by adjusting the gate voltages  $P_1$ ,  $P_2$ , and  $P_3$  in a periodic pattern. At the register, each row is again sequentially “emptied,” and the charges are converted to voltages that are amplified and digitized.

#### 4.3.2.2 Photomultiplier Tubes (PMTs)

PMTs [10,13] are based on the photoemissive effect. They have no intrinsic spatial resolving power and are thus mostly used in combination with a scanning system

8. As opposed to digital shift-registers used in CMOS detectors, which allow each pixel to be accessed individually, at the expense of a reduced photosensitive area.



**Figure 4.6** Examples of detectors for fluorescence imaging. (a) MOS photocapacitor in a full-frame-transfer CCD array. Two layers of a semiconductor silicon crystal with (P-type or N-type) impurities are separated by insulating silicon dioxide ( $\text{SiO}_2$ ). When a photon penetrates into the substrate, it can excite electrons that are part of the crystalline structure. By applying suitable voltages at the electrodes (or gates)  $P_1$ ,  $P_2$ , and  $P_3$ , these are “trapped” under the  $\text{SiO}_2$  layer. (b) Transmission-mode PMT, composed of a vacuum tube and several electrodes that are applied a voltage gradient. The first one is protected from outside oxidation by a window that is transparent to light.

and a detection aperture, typically in confocal microscopes. Figure 4.6(b) shows the schematic diagram of a PMT.

When photons with sufficient energy hit the *photocathode*, they may excite electrons and induce their release inside the tube. These are directed toward the first dynode by means of a focusing electrode. There, some are reflected, while others are absorbed and can excite secondary electrons. The number of reflected and secondary electrons divided by the incoming electrons defines a single dynode gain  $g$ . In total, a series of  $n$  dynode stages (typically a dozen or more) is traversed before

the anode finally collects the electrons that have been produced. This principle can lead to very high gains,  $g^n$  being of the order of  $10^6$  to  $10^8$ .

The photocathode is a key element as it determines the quantum efficiency of the system for the most part. Typically, less than 30% of the incoming photons are effectively “converted” into electrons, depending on the wavelength.

## 4.4 Limiting Factors of Fluorescence Imaging

Two sources act as the principal limiting factors in fluorescence imaging: (1) the instrumentation, which, apart from its inherent resolution limitation, introduces measurement noise, and (2) the sample itself, whose optical properties and emission characteristics are often nonideal.

### 4.4.1 Noise Sources

#### 4.4.1.1 Photon Shot Noise

The fundamental limitation of any photodetector resides in the random nature of photon emission. The arrival of photons at the detector is well described by a Poisson process whose (statistical) intensity is proportional to the (physical) intensity of the fluorescence signal.

#### 4.4.1.2 Background Noise

The ambient radiation, especially in the infrared domain, can also be a significant source of noise; it often requires the use of additional filters at the detection stage.

#### 4.4.1.3 Dark Current

Among the numerous internal noise sources of the detector, thermal agitation is the most important. The higher the temperature, the higher the kinetic energy of the electrons. For semiconductor detectors, this results in so-called *dark currents* (that exist even in the absence of light), which tend to charge the photocapacitors when the integration time and/or the temperature are too high. For point detectors such as PMTs, thermal energy can trigger spontaneous electron emissions. Consequently, high-sensitivity detectors are very often cooled down to reduce thermal noise.

#### 4.4.1.4 Auxiliary Noise Sources

For semiconductor devices, additional noise is generated at read-out time. In particular, the charge transfer in CMOS sensors is less efficient than in CCD chips. Both technologies are subject to amplifier noise. For PMTs, there can be fluctuations in the internal gain of the unit, which also result in noise. Finally, any detector with digital output produces quantization noise.

### 4.4.2 Sample-Dependent Limitations

#### 4.4.2.1 Photobleaching

An important property of fluorophores is that they become more chemically reactive as they are being excited. Depending on the environment, they can undergo reactions that lead to permanent changes, by which the molecule loses its capability to fluoresce altogether, or becomes nonabsorbent for the specified excitation wavelength. This effect, called *photobleaching*, limits the total intensity of light, and, accordingly, the exposure time, until loss of fluorescence occurs. As a result, the observation time of a fluorescence-tagged specimen is limited. Photobleaching is a cumulative effect; this means that reducing the exposure time or excitation intensity will not prevent it, but merely reduce the rate at which it occurs.

#### 4.4.2.2 Autofluorescence

Many organic molecules are naturally fluorescent, and thus even unstained biological samples can emit fluorescence in the visible domain. This autofluorescence is an important source of noise when it overlaps with the emission of a selected fluorophore, especially when the latter is sparsely expressed or exhibits weak fluorescence. This interference can render the detection of a signal very difficult.

#### 4.4.2.3 Absorption and Scattering of the Medium

In a biological specimen, the intensity of the fluorescence signal decreases as the fluorophore's depth within the specimen increases. This attenuation is due to the absorption and scattering<sup>9</sup> of light; it strongly limits both the depth at which a fluorophore can be excited and the depth at which a fluorescence signal can be detected.<sup>10</sup> These effects are not always negligible. Therefore, to obtain truly quantitative measurements, it may be necessary to develop reconstruction algorithms that take into account the space-varying and complex nature of the refractive index.

## 4.5 Advanced Experimental Techniques

Besides standard imaging that involves the quantitative analysis of local fluorophore concentrations, there exist more sophisticated experimental techniques for studying protein-protein interactions and for investigating biological processes at the molecular scale. Among the techniques presented here, FLIM and FRET can be performed on both widefield and confocal microscopes. The photobleaching techniques, however, are usually performed with lasers and often require the ability to

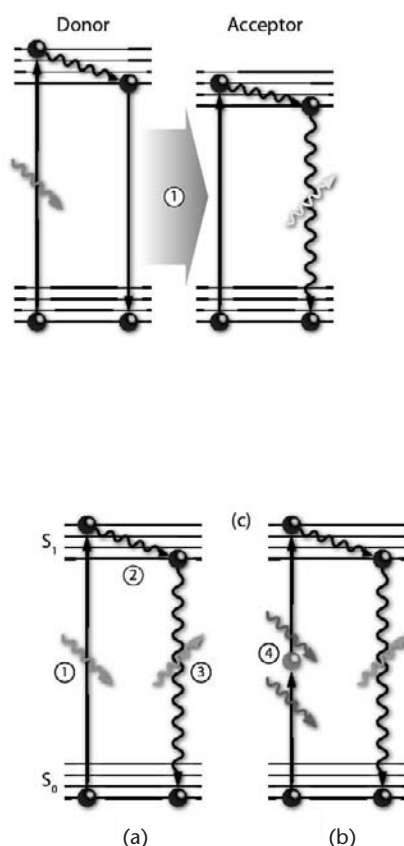
9. Scattering is the phenomenon by which particles with a refractive index different from the medium's index partially diffuse electromagnetic radiation in all directions. It commonly occurs when the particle sizes are comparable to the wavelength.
10. Typically in the 100- $\mu\text{m}$  range for one-photon confocal microscopy.

precisely define the region to be bleached; they are therefore mostly implemented on confocal microscopes.

#### 4.5.1 FRET

Protein-protein interactions take place at scales that are too small to be resolved by optical microscopy; however, they can be detected by exploiting a mechanism called fluorescence resonance energy transfer (FRET). This process is a direct transfer of energy (i.e., it does not involve the emission or absorption of a photon) between a suitable *donor* and an *acceptor*, as illustrated in Figure 4.7. FRET is only possible between two fluorophores if the emission spectrum of the donor overlaps with the excitation spectrum of the acceptor. An example of a suitable pair of fluorescent proteins is the aforementioned CFP/YFP couple.

The efficiency of FRET strongly depends on the distance that separates the two molecules (the rate is inversely proportional to the sixth power of the distance) and



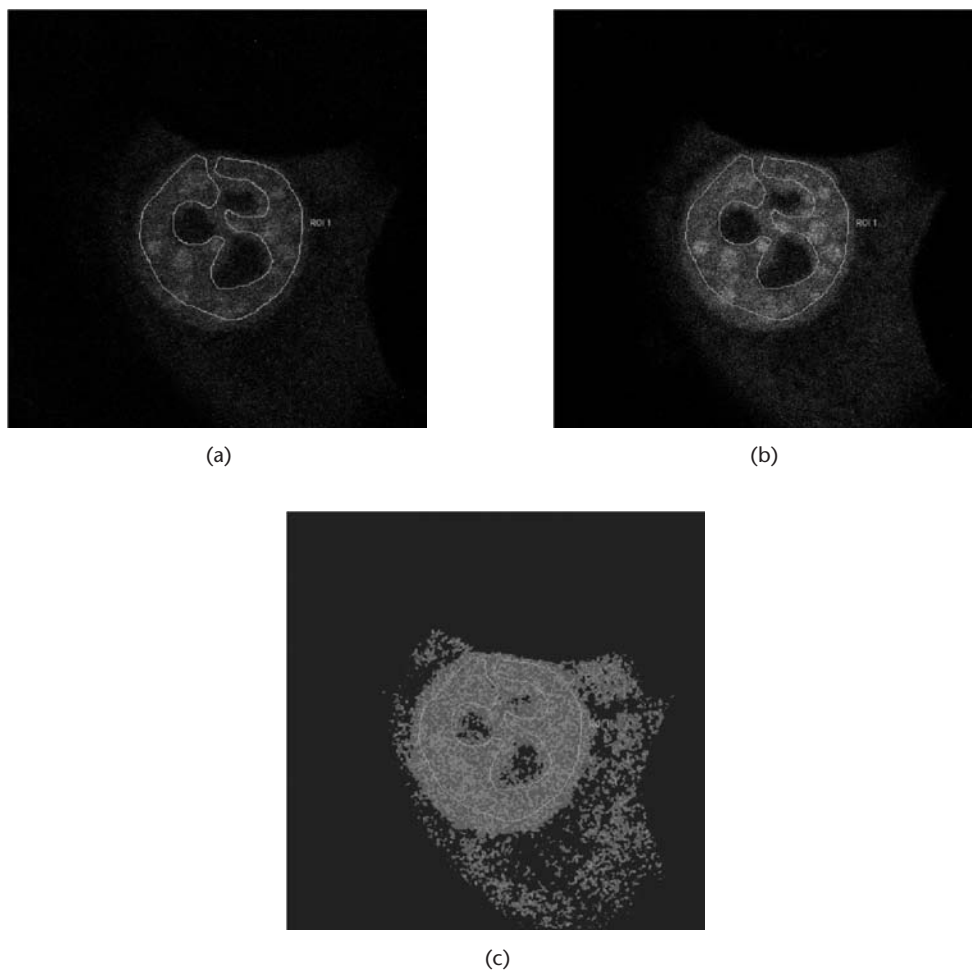
**Figure 4.7** (a–c) The principle of FRET between a suitable donor-acceptor pair: the energy of the excited donor molecule is transferred (without emission of a photon) to the acceptor after vibrational relaxation (1). For FRET to occur, the distance between the two molecules must typically be in the range of 1–10 nm [6].



on the relative orientation of their dipole moments. This means that FRET can be used to study the optical subresolution colocalization of a labeled protein pair of interest. FRET can also serve as an indicator of conformational changes in a protein: if complementary markers are placed at the extremities of the protein, then an energy transfer can occur when the protein folds [14]. Figure 4.8 illustrates a FRET experiment.

#### 4.5.2 FRAP

Although photobleaching has already been mentioned as a limitation, it can be exploited to study the intracellular dynamics of proteins. Fluorescence recovery



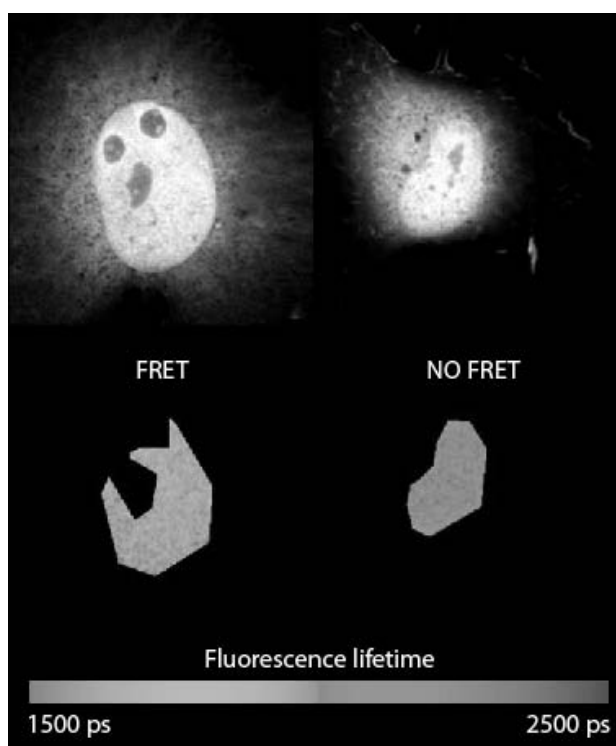
**Figure 4.8** Images from a FRET experiment, showing the (normalized) donor (a) and acceptor (b) channels. From these images, a computer-generated FRET-efficiency image is obtained (c). In this case, the scientists were interested in the average FRET efficiency inside a region of interest corresponding to the cell nucleus. (Courtesy of M. C. Rio, A. Baguet, and P. Kessler, IGBMC, Illkirch, France.)

after photobleaching (FRAP) consists of intentionally bleaching a small region of a cell using high-intensity light, thereby rendering it nonfluorescent. The region then regains its fluorescence as fluorophores from the surroundings enter and pass through it, which yields information about the diffusion and mobility of the labeled protein [15].

### 4.5.3 FLIM

All of the techniques discussed up to this point rely on intensity-based measurements. In the presence of autofluorescence, or when multiple fluorophores with similar emission spectra are used, it can be difficult to discriminate among the different signals. Intensity-based imaging is also highly dependent on fluorophore concentration.

In fluorescence lifetime imaging microscopy (FLIM), image contrast is generated based on the lifetime of fluorophores, which is the average time a fluorophore remains in the excited electronic state. The key point is that every fluorophore has a unique lifetime. A common method for measuring fluorescence lifetimes consists



**Figure 4.9** FLIM experiment for confirming the occurrence of FRET. The images show the fluorescence lifetime of the donor over two regions of interest corresponding to different cell nuclei. In the presence of FRET (left-hand side), the fluorescence lifetime is significantly reduced, due to the energy transfer to the acceptor. (Courtesy of C. Rochette-Egly, S. Lalevee and P. Kessler, IGBMC, Illkirch, France.)

of exciting fluorophores with a picosecond pulsed laser source and recording the arrival times of the emitted photons with a high-speed photodetector.

The lifetime of a fluorophore is sensitive to many environmental factors, such as oxygen concentration, pH, and calcium ion concentration. Thus, FLIM can be used to obtain information about the local environment of a particular fluorophore. FLIM can also serve as an experimental verification that FRET occurs (see Figure 4.9).

## 4.6 Signal and Image Processing Challenges

### 4.6.1 Data Size and Dimensionality

Modern research in biology requires quantitative experimental data. As a consequence, microscopes have developed into sophisticated digital image acquisition workstations that are capable of acquiring very large data sets of high dimensionality.

To get a better feeling of what is involved, consider an experiment monitored with a confocal microscope that requires the periodic (*time-lapse*) 3-D acquisition of a sample labeled with two fluorophores. This yields a 5-D data set indexed by the space coordinates  $x$ ,  $y$ , and  $z$ , the time  $t$ , and the wavelength parameter  $\lambda$ . Assuming that each image has a resolution of  $1,024 \times 1,024$  and that 32 slices are acquired per volume every 20 minutes over 24 hours with a 12-bit quantizer, the whole experiment results in nearly 7 GB of data. If a comparative analysis is performed, this figure must be multiplied by the total number of samples.

Studies involving comparable or even larger amounts of data are becoming commonplace. Even with today's performance level of computer hardware, the storage, extraction, manipulation, and representation of such data sets remain complex. One major challenge lies in the design of database systems and compression formats allowing for efficient retrieval and visualization (projections, 3-D rendering—see the example in Color Plate 4).

But most importantly, signal processing is becoming an indispensable expertise for the analysis and understanding of quantitative biological experiments; in fact, it is increasingly considered part of the experimental protocol itself, as a way to infer the validity of a biological model.

Without claiming exhaustiveness, we give examples of current image processing problems in biology among five main categories: image preparation, image restoration, image registration, image segmentation, and quantitative image analysis.

### 4.6.2 Image Preparation

#### 4.6.2.1 Image Calibration

Calibration is an important step both for image analysis and visualization. It can involve various preprocessing tasks such as histogram equalization, inhomogeneous illumination compensation, background correction, or image rescaling. While these tasks may appear relatively simple, some of them can rely on advanced signal processing.

#### 4.6.2.2 Image Simplification

In some cases, biological structures are too complex to be processed directly, and an image simplification step is required. To preserve the objects of interest, the operator can choose among the wide range of available tools (e.g., morphological operations, filtering, multiresolution structures, diffusion equations); application-specific solutions can also be envisaged.

#### 4.6.2.3 Feature Detection

Biological images often present characteristic elements such as particles and filaments. The detection of these features may require the development of optimized filters [16,17], as well as multiresolution methods [18]. Here, a challenging aspect is the shape variability observed in live-cell imaging.

Experimentalists should at least be aware of the aforementioned preparation operations; otherwise, they run the risk of a significant loss of information, thereby leading to questionable results at publication time. Algorithm designers, on the other hand, should put more efforts into education and the development of user-friendly imaging software.

### 4.6.3 Restoration

Restoration encompasses the classical problems of denoising and deconvolution.

#### 4.6.3.1 Denoising

Simple methods such as median filtering often need adaptation; for example, a 3-D stack may exhibit lower SNR levels as deeper portions of the object are imaged, due to absorption and/or autofluorescence. More generally, restoration methods should be based on physically realistic noise models (e.g., Poisson statistics) and take into account various noise sources (see Section 4.4). Advanced algorithms, relying on wavelet-domain thresholding strategies [19], PDE and variational formulations, or statistical frameworks, are just starting to be used in the field of bioimaging and deserve more exploration.

#### 4.6.3.2 Deconvolution

This operation requires an adequate characterization of the underlying imaging system, which can be either theoretical (involving a PSF model) or, frequently, experimental. In the latter case, the PSF is obtained by imaging subresolution fluorescent beads, under conditions as close as possible to the actual biological preparation. By averaging, possibly with simplifying assumptions (e.g., symmetry), a relatively noise-free PSF can be obtained. For further details concerning algorithmic deconvolution methods, we refer to [20,21].

One of the main challenges is the design of computationally tractable methods that take into account the nonstationarity of the PSF, especially in the axial direction (see Section 4.2.3). A recent attempt is the expectation maximization

(EM)-algorithm proposed by Preza and Conchello [22]. In their image-formation model, the object is divided into several layers that are associated with a series of (depth-dependent) PSFs. The image of each layer is then obtained from classical (stationary) convolutions.

#### 4.6.3.3 Other Inverse Problems

Restoration can also be considered in the wider framework of inverse problems.

One example concerns relatively thick objects with surface labeling, observed under a widefield microscope. Because of the 3-D conical extension of its PSF (Color Plate 2, top row on the left), such a system has a limited depth of field; that is, only a small slice of the object around the focal plane appears sharp. To compensate for this, images at different focal depths can be taken and fused together so as to obtain a single, entirely sharp image.<sup>11</sup> A state-of-the-art (so-called *extended-depth-of-field*) algorithm is described in [23]. Such a method can also be used to extract 3-D maps of the object's surface.

Another problem of interest is related to the detection and localization of subresolution particles [24]. New methods are under development that take into account the 3-D nonstationarity of the PSF to achieve precision in the nanometer range [25].

#### 4.6.4 Registration

Registration is a frequently needed postacquisition step. Here, researchers can take advantage of the availability of high-quality registration algorithms that were initially developed for medical imaging [26].

##### 4.6.4.1 Mosaicking

Because of the limited field of view of high-magnification objectives, it can be necessary to acquire multiple images of a sample (e.g., in a mosaic scheme). Despite the high accuracy that sample stages can achieve, perfect alignment is never possible. Rigid-body registration algorithms can correct this, provided the acquired images or volumes slightly overlap [27]. Within a given stack, it might also be necessary to compensate for pixel shifts between successive images. In addition, refraction indices—and thus focusing depths—are wavelength-dependent, which can necessitate the realignment of the different fluorescence channels.

##### 4.6.4.2 Imaging Live Samples

During time-lapse acquisitions, spatial drifts can occur due to thermal processes; the sample itself might also be subject to motion. Therefore, even if the parts of interest lie in a relatively thin slice, they may not be observable in a unique focal

11. This process should not be confused with deconvolution, which in particular yields a 3-D stack instead of a single image.

plane over the whole experiment. This implies that either a stack of neighboring planes must be acquired and the planes of interest must be extracted (or fused) or a real-time focusing algorithm must be used to control the stage.

More sophisticated elastic registration may be required for compensating the deformation of living tissues or for matching specimens of comparable shape [28].

If a periodic biological process is too fast to be imaged with sufficient time-resolution (such as the repetitive 3-D flow of blood cells in a heart), a registration approach may also be applied. In [29], images over several periods are recorded and reassembled so as to obtain a single period at a high frame rate.

#### 4.6.5 Segmentation

Segmentation is a mandatory step for image analysis. User interaction for the manual delineation of regions of interest is time-consuming and lacks reproducibility. The need for automated segmentation methods is therefore important (e.g., for local intensity measures, object and event counting, as well as tracking).

While simple approaches such as prefiltering and thresholding are available in commercial software packages, advanced techniques—for instance active contours [30]—have not yet been much exploited in the context of biological image analysis.

The most accurate segmentation methods are often application-dependent and typically require specific developments. For example, the tracing of neuronal dendrites can be improved using graph-optimization techniques [31].

In the context of live microscopy, it also makes good sense to adapt the segmentation methods so that they exploit temporal coherence (e.g., for the labeling of cells).

#### 4.6.6 Quantitative Analysis

##### 4.6.6.1 Data Preprocessing

In multispectral imaging, each pixel consists of (possibly a large number of) intensity measures at different wavelengths (obtained using different filter sets, an interferometer, or a diffractive system). If several fluorophores are used, their spectra are likely to overlap, and channel-crosstalk must be expected. This gives rise to *unmixing problems* [32] that can be solved by taking separate reference images of each fluorophore (to measure its contribution to each channel) and using, for example, a singular-value decomposition [33]. Blind separation methods may also be applicable. As a general observation, the correct normalization of spectral data is critical for the interpretation of fluorescence images. Quantitative assessments using FRET or ratio imaging (comparing the relative intensities of different wavelengths) require careful preprocessing based on physical parameters such as spectrum overlap or fluorophore concentration.

##### 4.6.6.2 Model Fitting

Other advanced fluorescence techniques are based on the fitting of parametric models: in FLIM, the fluorescence lifetimes are obtained by fitting (possibly mul-

tiple) exponential trends to the photon arrival densities; in FRAP, the diffusion coefficients characterize fluorescence recovery curves [34]. Generally speaking, quantitative research often relies on the mapping of physical or biochemical models in the image and/or time domains, especially for dynamic processes.

#### 4.6.6.3 Motion Assessment and Tracking

The diffusion of fluorescent proteins can be characterized by estimating motion fields. In many instances, it is interesting to track individual objects, which can also be a challenging task. We refer the reader to other sources that cover the broad field of movement analysis [35, 36].

#### 4.6.6.4 Pattern Recognition and Classification; Screening

Screening experiments consist of a systematic, automated study of a large number of samples—up to several hundreds of thousands (e.g., for the study of gene function or for drug discovery). This can involve terabytes of data and several weeks of computerized analysis. Pattern-recognition and classification algorithms play a major role in this analysis. In particular, one must identify how the biological characteristics of interest translate into measurable image features. Computational complexity is a strong limiting factor, while the reliability of the methods must be thoroughly validated [37].

## 4.7 Current and Future Trends

In addition to the signal processing tools that have been discussed in the previous section, both the probes [6] and the instrumentation are being refined constantly. We therefore close our discussion with a description of current trends and future directions in the field.

### 4.7.1 Fluorescent Labels

#### 4.7.1.1 Quantum Dots

Among the most recent developments are *quantum dots* [38], labels composed of a core nanometer-sized semiconductor crystal and an external protective shell. Their main advantages with respect to earlier fluorophores are their broader absorption and narrower emission spectra, resulting in brighter fluorescence. Also, they are more stable chemically and thus less subject to bleaching. These inorganic structures can be used for in vivo imaging, although they cannot be expressed by cells [39].

#### 4.7.1.2 Labeling of Recombinant Proteins

The principle of this technique is to create fusion proteins that are not fluorescent by themselves, but which express a receptor to which a specific label can be added



at a later time [40]. The label can be chosen from a wide range of fluorophores, with properties that GFP-type proteins may not be able to provide (such as higher resistance to photobleaching and stronger fluorescence). The receptor continues to be expressed in newly synthesized proteins, but only the stained proteins exhibit fluorescence, which allows for the selective labeling of a protein population at a given point in time.

#### 4.7.1.3 Enhanced Fluorescent Proteins

New fluorescent proteins are being developed that provide increased quantum efficiency (e.g., enhanced GFP, or eGFP, with a 35-fold increase in brightness with respect to the original GFP) or whose emission spectra are closer to infrared wavelengths (700 nm and above). These wavelengths are generally less absorbed by biological samples, hence allowing deeper observation. They are also less masked by cell autofluorescence occurring in the visible spectrum.

#### 4.7.1.4 Photocontrolable Proteins

Recent research has also been devoted to the design of *photoactivatable* [41] and *photoswitchable* [42, 43] proteins. The former exhibit little fluorescence in their initial, quiescent state. When exposed to a strong irradiation at a specific wavelength (usually lower than the fluorescence excitation wavelength), a hundred-fold or higher increase in fluorescence brightness can be observed. For switchable proteins, strong irradiation changes both the excitation and emission spectrum. For example PS-CFP [44] is sensitive to irradiation at 405 nm, which produces a 1,500-fold increase in its green-to-cyan ratio. Both types of labels can be used to activate and observe proteins in a specific region of a cell, without the interference of newly synthesized proteins or proteins outside of the selected region. This property is useful for protein lifetime and tracking as well as cell lineage studies.

### 4.7.2 Advanced Microscopy Systems

We conclude this section with some of the more advanced developments in the field of optics.

#### 4.7.2.1 Faster Scanning—Slit Detectors and Nipkow Disks

To cope with the high speed of some biological processes, the traditional confocal scanning microscope equipped with a point detector is often not sufficient. To accelerate the scanning process, a whole line can be imaged simultaneously by replacing the pinholes and the PMT by slit apertures and a linear camera. More generally, using, for example, a Nipkow-disk system [45], a 2-D illumination pattern can be shifted across the sample, allowing time lapse imaging at up to 120 frames per second. This comes with a significant tradeoff in terms of resolution, due to crosstalk between the different detection apertures.

#### 4.7.2.2 Deeper Imaging—Multiphoton Microscopy

In a multiphoton microscope [46], optical sectioning is achieved by properties of the illumination; as a consequence, there is no need for a detection pinhole in such a system. Very short laser pulses (in the pico- to femtosecond range) are sent to the sample in brief intervals (of the order of nanoseconds). The probability that two photons encounter the same molecule, hence bringing it to its excited state and making it fluoresce, is significant only in the very central region of the illumination spot. A key advantage is that the corresponding infrared wavelengths are less absorbed by biological tissues so that samples can be imaged much deeper than with traditional confocal systems (at a comparable resolution). Photobleaching and toxicity are also reduced because the excitation intensity is effectively concentrated at the focal spot.

#### 4.7.2.3 Increased Axial Resolution—Multiple Objective Imaging

Since the numerical aperture has such a fundamental influence on resolution, Hell et al. proposed to insert the sample between two objectives, so as to send and collect light from both sides; accordingly, they called the method  $4\pi$  microscopy [47]. Using computational methods, an improvement in axial resolution by a factor of six can be achieved. Such systems are commercially available, but they suffer from limitations on the sample thickness and sensitivity to differences in the length of the two optical paths. More recently, these ideas have been applied to widefield microscopy (I<sup>5</sup>M, [48]).

#### 4.7.2.4 Increased Resolution—STED Microscopy

One of the most advanced microscopy techniques to emerge from the quest for increased resolution is called STED, which stands for stimulated emission depletion [49] (see also Section 4.1.1.2). The principle is to prevent fluorescent molecules outside the very central region of the illumination spot from emitting light by forcing them back to their fundamental state. This is achieved by dividing the excitation into two brief successive laser pulses, where the second pulse is red-shifted and doughnut-shaped, having zero intensity at its center. Superimposed on the focal spot of the initial pulse, it induces stimulated emission, dramatically reducing the excitation volume, hence augmenting the resolution.

### 4.7.3 Super-Resolution: Photoactivated Localization-Based Techniques

Photoactivated localization microscopy (PALM) [50] and stochastic optical reconstruction microscopy (STORM) [51] are novel techniques based on imaging sparse subsets of photoactivable, respectively photoswitchable, fluorescent proteins (see Section 4.7.1.4). A sparse subset of activated molecules is obtained by illuminating the sample with a short laser pulse. The sample is then imaged until the molecules are either bleached or switched off, after which the process is repeated until the pool of activable proteins in the sample is depleted or until a sufficient amount of switchable proteins has been imaged. In a post-processing step, the individual

molecules from each subset image are localized to nanometer-scale accuracy. The resulting estimated positions and corresponding intensities are then used to render a composite super-resolved image. Limited only by the number of photons collected from each fluorophore, resolutions of 10–20 nm have been reached in practice, which rivals the performance of electron microscopes.

#### 4.7.3.1 Other Developments

Another promising technique to improve the resolution of widefield systems is structured illumination. Illuminating the object with sinusoidal patterns, combined with adequate processing, can result in a two-fold or higher [52] improvement of the microscope's spatial bandwidth. It also yields optical sectioning properties, and the processing can be done on specific hardware for real-time observation [53].

Another approach proposed by Stelzer et al., selective plane illumination microscope (SPIM), [54] consists of projecting the light onto the object perpendicularly to the optical axis, in a diffraction-limited plane; then only fluorescence from molecules within this excitation plane is collected using a traditional CCD sensor. This system provides true optical sectioning for widefield systems.

## 4.8 Conclusions

Although this panorama is necessarily incomplete, we hope to have convinced the reader of the invaluable role of fluorescence microscopy in modern biology. It owes its current popularity to the GFP-like fluorescent proteins that are the key ingredient for *in vivo* studies of molecular processes in cells. These are currently opening up a plethora of experimental possibilities that are only beginning to be explored.

This colored revolution could clearly not have happened without numerous technological advances. In particular, progress in optics and instrumentation has been considerable in recent years; there is now a consistent trend toward nonlinear techniques, such as multiphoton and saturated illumination imaging, which, with the help of computational methods, are contributing to overcoming Abbe's resolution barrier.

Signal processing is also at the heart of these developments and is expected to play an ever-increasing role in the field. It is already an integral part of optics and is becoming an essential tool for biologists, who rely more and more on imaging software to quantify their data.

Therefore, a crucial aspect of the research lies in the successful collaboration between signal processing engineers and biologists. In modern research institutes, imaging core facilities are expected to play an important mediating role in this interaction. Our advice to colleagues who want to be part of this effort is that they try to understand the physics and, to some extent, the biology in order to design better and more useful algorithms. We believe that it is truly worth the effort.

### Acknowledgments

This chapter is an extended version of “The Colored Revolution of Bioimaging,” by C. Vonesch, F. Aguet, J.-L. Vonesch, and M. Unser, which appeared in *IEEE Signal Processing Magazine* 23(3). © 2006 IEEE.

The authors thankfully acknowledge the helpful discussions they had with the following researchers in optics: C. J. R. Sheppard, E. Charbon, C. Depeursinge, and T. Lasser. They also thank M. Aguet, L. Baldi-Unser, and N. Garin for their advice on biological matters and their comments on the manuscript. The micrographs were kindly provided by the research groups of B. L. Kieffer, M. Labouesse, M.C. Rio, and C. Rochette-Egly, all at IGBMC, Unité Mixte de Recherches CNRS/INSERM/ Université Louis Pasteur, Illkirch, France.

### References

- [1] Coons, A. H., and M. H. Kaplan, “Localization of Antigen in Tissue Cells. II. Improvements in a method for the Detection of Antigen by Means of Fluorescent Antibody,” *Journal of Experimental Medicine*, Vol. 91, No. 1, 1950, pp. 1–13.
- [2] Chalfie, M., Y. Tu, G. Euskirchen, W. Ward, and D. C. Prasher, “Green Fluorescent Protein as a Marker for Gene Expression,” *Science*, Vol. 263, February 1994, pp. 802–805.
- [3] Stearns, T., “Green Fluorescent Protein: The Green Revolution,” *Current Biology*, Vol. 5, March 1995, pp. 262–264.
- [4] Shimomura, O., “The Discovery of Aequorin and Green Fluorescent Protein,” *Journal of Microscopy*, Vol. 217, January 2005, pp. 3–15.
- [5] Prasher, D. C., V. K. Eckenrode, W. W. Ward, F. G. Prendergast, and M. J. Cormier, “Primary Structure of the Aequorea Victoria Green-Fluorescent protein,” *Gene*, Vol. 111, February 1992, pp. 229–233.
- [6] Zhang, J., R. E. Campbell, A. Y. Ting, and R. Y. Tsien, “Creating New Fluorescent Probes for Cell Biology,” *Nature Reviews Molecular Cell Biology*, Vol. 3, December 2002, pp. 906–918.
- [7] Lippincott-Schwartz, J., and G. H. Patterson, “Development and Use of Fluorescent Protein Markers in Living Cells,” *Science*, Vol. 300, April 2003, pp. 87–91.
- [8] Miyawaki, A., A. Sawano, and T. Kogure, “Lighting Up Cells: Labelling Proteins with Fluorophores,” *Nature Cell Biology*, Vol. 5 (supplement), September 2003, pp. S1–S7.
- [9] Minsky, M., “Memoir on Inventing the Confocal Scanning Microscope,” *Scanning*, Vol. 10, August 1988, pp. 128–138.
- [10] Norton, P. R., *Handbook of Optics*, Vol. 1, New York: McGraw-Hill, 1995, pp. 15.3–15.100.
- [11] Gibson, S. F., and F. Lanni, “Experimental Test of an Analytical Model of Aberration in an Oil-Immersion Objective Lens Used in Three-Dimensional Light Microscopy,” *Journal of the Optical Society of America A*, Vol. 8, October 1991, pp. 1601–1613.
- [12] Boyle, W. S., and G. E. Smith, “Charge Coupled Semiconductor Devices,” *Bell System Technical Journal*, Vol. 49, April 1970, pp. 587–593.
- [13] Wampler, J. E., and K. Kutz, “Quantitative Fluorescence Microscopy Using Photomultiplier Tubes and Imaging Detectors,” *Methods Cell Biol.*, Vol. 29, 1989, pp. 239–267.
- [14] Lippincott-Schwartz, J., A.-B. Nihal, and G. H. Patterson, “Photobleaching and Photoactivation: Following Protein Dynamics in Living Cells,” *Nature Cell Biology*, Vol. 5, September 2003, pp. Suppl:S7–S14.

- [15] Selvin, P., "The Renaissance of Fluorescence Resonance Energy Transfer," *Nature Structural Biology*, Vol. 7, No. 9, 2000, pp. 730–734.
- [16] Jacob, M., and M. Unser, "Design of Steerable Filters for Feature Detection Using Canny-Like Criteria," *IEEE Transactions on Pattern Analysis and Machine Intelligence*, Vol. 26, August 2004, pp. 1007–1019.
- [17] Sage, D., F. R. Neumann, F. Hediger, S. M. Gasser, and M. Unser, "Automatic Tracking of Individual Fluorescence Particles: Application to the Study of Chromosome Dynamics," *IEEE Transactions on Image Processing*, 2005.
- [18] Olivo-Marin, J.-C., "Extraction of Spots in Biological Images Using Multiscale Products," *Pattern Recognition*, Vol. 35, September 2002, pp. 1989–1996.
- [19] de Monvel, J. B., S. L. Calvez, and M. Ulfendahl, "Image Restoration for Confocal Microscopy: Improving the Limits of Deconvolution, with Application to the Visualization of the Mammalian Hearing Organ," *Biophysical Journal*, Vol. 80, May 2001, pp. 2455–2470.
- [20] Sibarita, J.-B., "Deconvolution Microscopy," *Advances in Biochemical Engineering/Biotechnology*, Vol. 95, May 2005, pp. 201–243.
- [21] Wallace, W., L. H. Schaefer, and J. R. Swedlow, "A Workingperson's Guide to Deconvolution in Light Microscopy," *Biotechniques*, Vol. 31, November 2001, pp. 1076–1097.
- [22] Preza, C., and J. A. Conchello, "Depth-Variant Maximum-Likelihood Restoration for Three-Dimensional Fluorescence Microscopy," *Journal of the Optical Society of America A*, Vol. 21, September 2004, pp. 1593–1601.
- [23] Forster, B., D. V. D. Ville, J. Berent, D. Sage, and M. Unser, "Complex Wavelets for Extended Depth-of-Field: A New Method for the Fusion of Multichannel Microscopy Images," *Microscopy Research and Technique*, Vol. 65, September 2004, pp. 33–42.
- [24] Thomann, D., J. Dorn, P. K. Sorger, and G. Danuser, "Automatic Fluorescent Tag Localization II: Improvement in Super-Resolution by Relative Tracking," *Journal of Microscopy*, Vol. 211, September 2003, pp. 230–248.
- [25] Aguet, F., D. Van De Ville, and M. Unser, "A Maximum-Likelihood Formalism for Sub-Resolution Axial Localization of Fluorescent Nanoparticles," *Optics Express*, Vol. 13, 2005, pp. 10503–10522.
- [26] Brown, L. G., "A Survey of Image Registration Techniques," *ACM Comput. Surv.*, Vol. 24, 1992, pp. 325–376.
- [27] Thévenaz, P., and M. Unser, "User-Friendly Semiautomated Assembly of Accurate Image Mosaics in Microscopy," *Microscopy Research and Technique*, Vol. 70, No. 2, 2007, pp. 135–146.
- [28] Sorzano, C. Ó. S., P. Thévenaz, and M. Unser, "Elastic Registration of Biological Images Using Vector-Spline Regularization," *IEEE Transactions on Biomedical Engineering*, Vol. 52, April 2005, pp. 652–663.
- [29] Liebling, M., A. S. Forouhar, M. Gharib, S. E. Fraser, and M. E. Dickinson, "4-Dimensional Cardiac Imaging in Living Embryos Via Post-Acquisition Synchronization of Nongated Slice-Sequences," *Journal of Biomedical Optics*, 2005.
- [30] Zimmer, C., E. Labruyere, V. Meas-Yedid, N. Guillen, and J.-C. Olivo-Marin, "Segmentation and Tracking of Migrating Cells in Videomicroscopy with Parametric Active Contours: A Tool for Cell-Based Drug Testing," *IEEE Transactions on Medical Imaging*, Vol. 21, October 2002, pp. 1212–1221.
- [31] Meijering, E., M. Jacob, J.-C. Sarria, P. Steiner, H. Hirling, and M. Unser, "Design and Validation of a Tool for Neurite Tracing and Analysis in Fluorescence Microscopy Images," *Cytometry Part A*, Vol. 58A, April 2004, pp. 167–176.
- [32] Zimmermann, T., J. Rietdorf, and R. Pepperkok, "Spectral Imaging and Its Applications in Live Cell Microscopy," *FEBS Letters*, Vol. 546, July 2003, pp. 87–92.

- [33] Tsurui, H., H. Nishimura, S. Hattori, S. Hirose, K. Okumura, and T. Shirai, "Seven-Color Fluorescence Imaging of Tissue Samples Based on Fourier Spectroscopy and Singular Value Decomposition," *Journal of Histochemistry and Cytochemistry*, Vol. 48, May 2000, pp. 653–662.
- [34] Carrero, G., D. McDonald, E. Crawford, G. de Vries, and M. J. Hendzel, "Using FRAP and Mathematical Modeling to Determine the In Vivo Kinetics of Nuclear Proteins," *Methods*, Vol. 29, January 2003, pp. 14–28.
- [35] Meijering, E., I. Smal, and G. Danuser, "Tracking in Molecular Bioimaging," *IEEE Signal Processing Magazine*, Vol. 23, No. 3, 2006, pp. 46–53.
- [36] Zimmer, C., B. Zhang, A. Dufour, A. Thébaud, S. Berlemont, V. Meas-Yedid, and J.-C. Olivo Marin, "On the Digital Trail of Mobile Cells," *IEEE Signal Processing Magazine*, Vol. 23, No. 3, 2006, pp. 54–62.
- [37] Zhou, X., and S. T. C. Wong, "Informatics Challenges of High-Throughput Microscopy," *IEEE Signal Processing Magazine*, Vol. 23, No. 3, 2006, pp. 63–72.
- [38] Michalet, X., F. F. Pinaud, L. A. Bentolila, J. M. Tsay, S. Doose, J. J. Li, G. Sundaresan, A. M. Wu, S. S. Gambhir, and S. Weiss, "Quantum Dots for Live Cells, In Vivo Imaging, and Diagnostics," *Science*, Vol. 307, January 2005, pp. 538–544.
- [39] Dubertret, B., P. Skourides, D. J. Norris, V. Noireaux, A. H. Brivanlou, and A. Libchaber, "In Vivo Imaging of Quantum Dots Encapsulated in Phospholipid Micelles," *Science*, Vol. 298, 2002, pp. 1759–1762.
- [40] Griffin, B. A., S. R. Adams, and R. Y. Tsien, "Specific Covalent Labeling of Recombinant Protein Molecules Inside Live Cells," *Science*, Vol. 281, July 1998, pp. 269–272.
- [41] Patterson, G. H., and J. Lippincott-Schwartz, "A Photoactivatable GFP for Selective Photolabeling of Proteins and Cells," *Science*, Vol. 297, September 2002, pp. 1873–1877.
- [42] Marchant, J. S., G. E. Stutzmann, M. A. Leissring, F. M. LaFerla, and I. Parker, "Multiphoton-Evoked Color Change of DsRed as an Optical Highlighter for Cellular and Subcellular Labeling," *Nature Biotechnology*, Vol. 19, July 2001, pp. 645–649.
- [43] Ando, R., H. Hama, M. Yamamoto-Hino, H. Mizuno, and A. Miyawaki, "An Optical Marker Based on the UV-Induced Green-to-Red Photoconversion of a Fluorescent Protein," *Proceedings of the National Academy of Sciences*, Vol. 99, October 2002, pp. 12657–12662.
- [44] Chudakov, D. M., V. V. Verkhusha, D. B. Staroverov, E. A. Souslova, S. Lukyanov, and K. A. Lukyanov, "Photoswitchable Cyan Fluorescent Protein for Protein Tracking," *Nature Biotechnology*, Vol. 22, November 2004, pp. 1435–1439.
- [45] Petráň, M., M. Hadravský, M. Egger, and R. Galambos, "Tandem-Scanning Reflected-Light Microscope," *Journal of the Optical Society of America*, Vol. 58, No. 5, 1968, pp. 661–664.
- [46] Denk, W., J. H. Strickler, and W. W. Webb, "Two-Photon Laser Scanning Fluorescence Microscopy," *Science*, Vol. 248, April 1990, pp. 73–76.
- [47] Hell, S. W., and E. H. K. Stelzer, "Fundamental Improvement of Resolution with a 4pi-confocal Fluorescence Microscope Using Two-Photon Excitation," *Optics Communications*, Vol. 93, October 1992, pp. 277–282.
- [48] Gustafsson, M. G. L., D. A. Agard, and J. W. Sedat, "I<sup>5</sup>M: 3D Widefield Light Microscopy with Better Than 100 nm Axial Resolution," *Journal of Microscopy*, Vol. 195, July 1999, pp. 10–16.
- [49] Hell, S. W., and J. Wichmann, "Breaking the Diffraction Resolution Limit by Stimulated Emission: Stimulated-Emission-Depletion Fluorescence Microscopy," *Optics Letters*, Vol. 19, June 1994, pp. 780–782.
- [50] Betzig, E., G. H. Patterson, R. Sougrat, O. W. Lindwasser, S. Olenych, J. S. Bonifacio, M. W. Davidson, J. Lippincott-Schwartz, and H. F. Hess, "Imaging Intracellular

- Fluorescent Proteins at Nanometer Resolution,” *Science*, Vol. 313, No. 5793, 2006, pp. 1642–1645.
- [51] Bates, M., B. Huang, G. T. Dempsey, and X. Zhuang, “Multicolor Super-Resolution Imaging with Photo-Switchable Probes,” *Science*, Vol. 317, 2007, pp. 1749–1753.
- [52] Heintzmann, R., T. M. Jovin, and C. Cremer, “Saturated Patterned Excitation Microscopy (SPEM)—A Novel Concept for Optical Resolution Improvement,” *Journal of the Optical Society of America A*, Vol. 19, August 2002, pp. 1599–1609.
- [53] Mitić, J., T. Anhut, M. Meier, M. Ducros, A. Serov, and T. Lasser, “Optical Sectioning in Wide-Field Microscopy Obtained by Dynamic Structured Light Illumination and Detection Based on a Amart Pixel Detector Array,” *Optics Letters*, Vol. 28, May 2003, pp. 698–700.
- [54] Huiskens, J., J. Swoger, F. Del Bene, J. Wittbrodt, and E. H. Stelzer, “Optical Sectioning Deep Inside Live Embryos by Selective Plane Illumination Microscopy,” *Science*, Vol. 305, August 2004, pp. 1007–1009.
- [55] McMahon, L., R. Legouis, J.-L. Vonesch, and M. Labouesse, “Assembly of *C. Elegans* Apical Junctions Involves Positioning and Compaction by LET-413 and Protein Aggregation by the MAGUK Protein DLG-1,” *Journal of Cell Science*, Vol. 114, June 2001, pp. 2265–2277.



# FARSIGHT: A Divide and Conquer Methodology for Analyzing Complex and Dynamic Biological Microenvironments

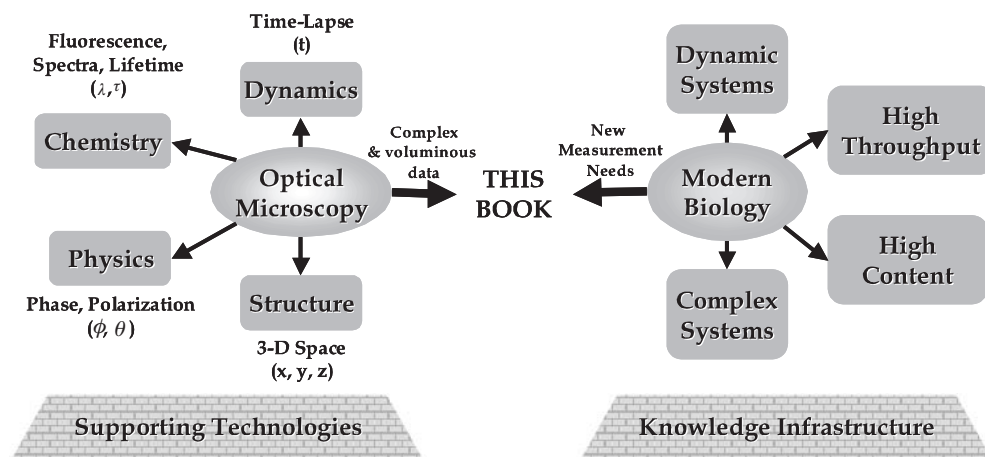
Badrinath Roysam, William Shain, Carol Barnes, William Mohler, Gang Lin, Christopher Bjornsson, Ying Chen, Yousef Al-Kofahi, and Arunachalam Narayanaswamy

## 5.1 Introduction

The modern optical microscope is a multidimensional imaging tool. It is capable of recording not only biological structures in their full three-dimensional (3-D) glory, but also a variety of biological processes occurring in cells and tissue. Importantly, it records these processes in their 3-D spatial context. For these reasons, it has become one of the great “work horses” of biological research that is widely used for diverse investigations at the subcellular, cellular, and tissue levels. The left half of Figure 5.1 illustrates some of the imaging dimensions that are accessible by modern optical microscopy.

*The spatial dimensions:* Imaging is indispensable when *spatial information* is important to a study. Several spatial factors influence cell behavior, including its 3-D morphology, location, orientation, structure of its microenvironment, and connectivity [1, 2]. Widespread availability of confocal and multiphoton microscopes [3–5] equipped with high-NA objectives have enabled routine high-resolution 3-D imaging of multiple structures and functional markers [6].

*The chemical dimensions:* Increasingly, the spatial dimension is imaged in combination with *chemical* information, largely derived from the use of fluorescent labels (dyes). A fluorescent label can be conjugated (attached) to a specific biochemical in tissue and observed optically. Currently a rather large library of fluorescent labels is available commercially, allowing most molecules of interest to be labeled with high specificity. In addition to labeling molecules of interest with a high degree of specificity, fluorescence technology allows us to label many biophysical activities of interest. For instance, voltage-sensitive fluorescent dyes indicate electrical activity in cells such as neurons [7]. Often, the properties of molecules of interest depend upon their chemical environment. Using the phenomenon of fluorescence lifetime microscopy (FLIM), modern microscopes can record environmental influences on properties of molecules [8]. Often, the proximity of two or more molecules is biologically



**Figure 5.1** Summarizing the background of this chapter. The left half illustrates some of the imaging dimensions that can be captured by optical microscopy. The right half illustrates some of the measurement needs arising in modern biological research.

informative. Using a technique known as fluorescent resonance energy transfer (FRET), modern microscopes can image molecular proximity [9].

One limitation of fluorescent dyes is that they are extrinsic substances that are not naturally present in cells and may affect the behavior of cells. They may even be toxic to cells. Interestingly, there is a method by which a cell can be tricked into manufacturing proteins that are naturally fluorescent. By carrying out a process known as gene transfection, it is possible to create a genetically modified cell that produces one or more fluorescent proteins whenever a chosen gene is transcribed [10]. These proteins are either structurally or functionally useful or mere reporters that indicate an event occurring inside a cell. A large number of such fluorescent proteins and transfected cells and animals are available for investigational use [10]. By using fluorescent protein technology, it is possible to observe specific structures and dynamic processes in living tissue.

By using multiple fluorescent labels simultaneously—a technique known as fluorescence multiplexing—contemporary microscopes can image multiple biochemicals simultaneously in their relative context. By choosing what biochemicals are labeled, fluorescence multiplexing can be made to reveal multiple structures and functional processes in their spatial context, revealing interrelationships among them. Indeed, measuring such relationships is a major focus of this chapter. We call it associative image analysis.

As a concrete example, the left panel in Color Plate 5 is a schematic diagram showing a subset of the tissue entities that come into play when a neuroprosthetic device (shown in gray) is inserted into cortical brain tissue [11, 12]. Brain tissue is a truly complex system composed of multiple interacting neuronal and glial cell types, immune system cells, and microvasculature [13]. A number of dynamic phenomena, including molecular gradients, reactions, transport, cell divisions,

migrations, and tissue reorganization are triggered by device insertion. These “reactive responses” culminate in functional isolation of the device and limit its useful lifetime to about 6–8 weeks [14].

Understanding brain tissue *as a system* is essential to developing the next generation of longer-lasting neural implants. To develop such an understanding, it is essential to measure each of the tissue constituents, as well as their spatio-temporal and functional interactions. Fluorescence light microscopy is uniquely suitable as a tool for enabling such measurements. The right panel of Color Plate 5 shows a 3-D confocal image ( $1,024 \times 1,024 \times 83 \times 5$ ) recorded using a Zeiss LSM-META microscope with spectral unmixing software [15]. This image has five fluorescent channels labeling cell nuclei, microglia, vasculature astrocytes, and Nissl-positive neurons (Nissl). Such simultaneous imaging has the key advantage of capturing the *relative spatial relationships* among the labeled entities.

*Although complex and voluminous, this image is but a partial snapshot of the complex brain tissue.* A more complete description can, in principle be obtained by using more fluorescent labels. Alternately, such a description can be assembled computationally from a series of such images that record different combinations of molecular species of interest in an overlapped manner. Another aspect of a more complete description is improved spatial resolution and greater spatial extent (with automated montaging [16]).

*The temporal dimension:* It is now possible to record a sequence of images of living cells and tissue periodically over extended durations without damaging them. This technique is known as time-lapse imaging. When 3-D spatial imaging is combined with time-lapse, the end result is a four-dimensional (4-D) movie. When multiple fluors are imaged three-dimensionally over time, the result is a five-dimensional (5-D) movie.

*Other physical properties:* Many of the structures and processes in tissue are revealed via certain physical properties that can be recorded by microscopes, often without the use of extrinsic labels [17–22]. For example, spatial and temporal fluctuations in refractive index and polarization properties of optically transparent tissues reveal structural and functional entities in tissues.

*Supporting infrastructure:* It would be naïve to think of the modern optical microscope as being composed mainly of optical components. They are supported and empowered by a variety of technologies ranging from optical and mechanical instrumentation through software algorithms. Software is arguably the most enabling aid. Deconvolution [23] software is widely used for improving the axial resolution of 3-D images, and has improved in speed and effectiveness. Unmixing software [15] enables multispectral microscopes such as the Zeiss META to allow imaging of multiple markers even when there is spectral overlap [24,25]. In addition to software tools, improved instrumentation for controlling the cell environment, sensitive cameras, faster scanners, and multiphoton imaging enable long-term live-tissue imaging [26,27]. High-throughput specimen preparation and imaging systems [28] are now available commercially (e.g., GE, Ventana, Inc., Cellomics, Inc.). Current trends point toward continued increase in resolution along spatial, spectral, and temporal

dimensions, adoption of new methods like FRET and spectral FLIM [8], and growth in throughput of tissue processed.

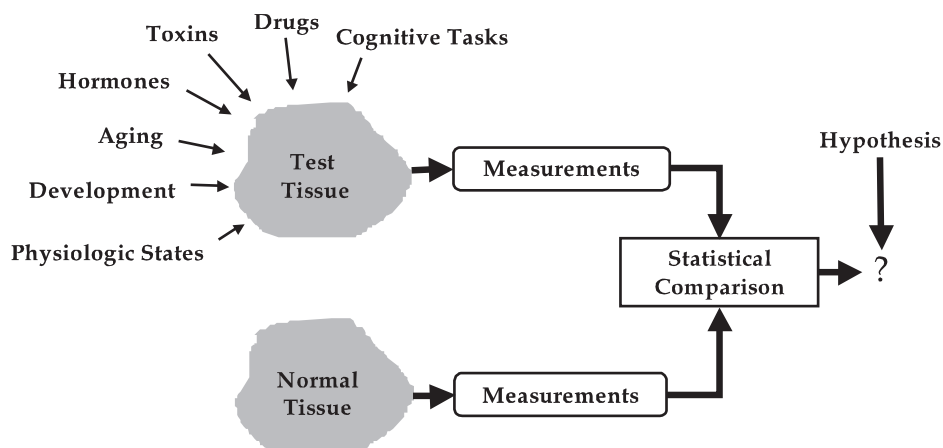
The impetus for multidimensional microscopy is modern biology. Even as optical microscopy and its associated technologies have advanced, the world of biology has undergone an equally dramatic transformation. Importantly, the entire human genome, and the genomes of important model organisms have been mapped. The science of genomics has ignited a second revolution—the science of proteomics.

The central dogma of molecular biology states that a gene is transcribed into messenger RNA (mRNA) that is translated into a protein. The contemporary view is that the static genome, comprising all the genes in an organism, is translated into the dynamic transcriptome comprising all the possible mRNAs that collectively give rise to the proteome comprising all the proteins in the organism. This view is more complex and more realistic, although harder to comprehend.

The public availability of large-scale databases containing the entire genome, and significant portions of the transcriptome and proteome, over the ordinary Internet is transforming the very manner in which biology is practiced. It is increasingly practical to bring into consideration the entire genome/proteome, or a major subset thereof, in order to solve a biological problem. This is an unprecedented level of leveraging. The successes of genomics and proteomics have in turn inspired numerous other mapping efforts—many of their names end in “omics.” For example, the mapping of signaling pathways in cells and tissue leads to the “signalome.” The mapping of cell types leads to the “cytome.” Finally, efforts are underway to link many of these databases to allow information to be related. In summary, modern biology is supported by a powerful knowledge/informatics infrastructure that has set the stage for a permanently rapid and further accelerating rate of advance in the life sciences.

The combination of knowledge infrastructure and modern instrumentation is enabling biologists to adopt bold new ways to do their work. It is also enabling them to do a lot of things faster and more effectively. From our standpoint, there is a shift from reporting of qualitative observations toward quantitative reporting. There is also a shift toward computational biology—a science that uses computation as an essential tool in the pursuit of biological knowledge. Traditionally, biology has been practiced in a *reductionist* style in which one strives to isolate a particular molecule, perhaps a gene or a protein, a signaling pathway, or a chemical reaction that is responsible for a particular structural or functional effect in a cell. In practice, one proposes a series of scientific hypotheses that are tested by experiment. Hypothesis testing requires one to compare unmodified normal (control) biological materials (cells, tissue, and so on) against treated (test) tissue.

The common types of treatments are indicated on the upper left portion of Figure 5.2 For example, scientists in the drug development industry are constantly subjecting test tissue to candidate drug compounds. As one attempts to compare the control and test samples in a careful manner, it is necessary to obtain quantitative measurements, so we can measure the statistical significance of the observed differences in tissue. Whenever there is a need for measurements with a spatial



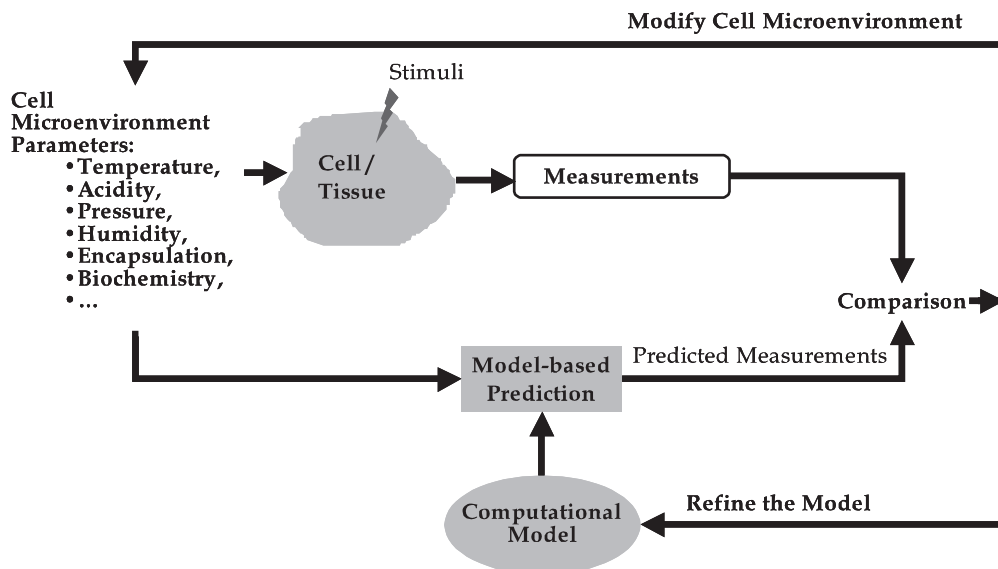
**Figure 5.2** Hypothesis testing—the traditional method of science. In a hypothesis test, measurements of normal and test tissue are compared statistically, resulting in either a validation or negation of the hypothesis. The results of a series of such hypothesis tests lead to an overall model of a system’s behavior. We are interested in image-based measurements in service of hypothesis testing.

aspect, imaging and image analysis become indispensable. We are specifically interested in such image-based measurements.

Increasingly, hypothesis-driven research is being replaced by *integrative systems biology* and discovery-driven research. Integrative systems biology treats a cell or a tissue as a complex *system*. A system is composed of multiple components that interact. Importantly, the interactions among components give rise to properties and behaviors, often referred to as *emergent behaviors* not observable in any individual component. Many of these systems are dynamic in nature, and can be observed by time-lapse imaging. One everyday example of a system is a watch—its behavior results from carefully orchestrated interactions among its many components. Merely putting all of the components of a watch in close proximity does not produce its behaviors.

From a systems perspective [29], modern microscopy is invaluable for its ability to record molecular species in the *spatial context* of intact tissue, unlike biochemical assays, gene arrays [30], and flow cytometry [31]. Combining the spatial, chemical, temporal, and physical dimensions, it is possible to image processes such as gene transcription, region-specific co-localization and transport, signaling, cell division, migration, development, tissue reorganization, and protein localization in their complete spatio-temporal context [32,33].

Systems biology can be thought of as the building of a simulator for the living system of interest. Naturally, we are interested in measuring the “realism” of this simulator. This can be done by observing the living system under a microscope and making measurements from the collected images. These measurements can be compared against the measurements generated by the simulator. The difference between the predicted and actual measurements is the *modeling error*. By analyzing this error, we return to the drawing board and refine the simulator, and the

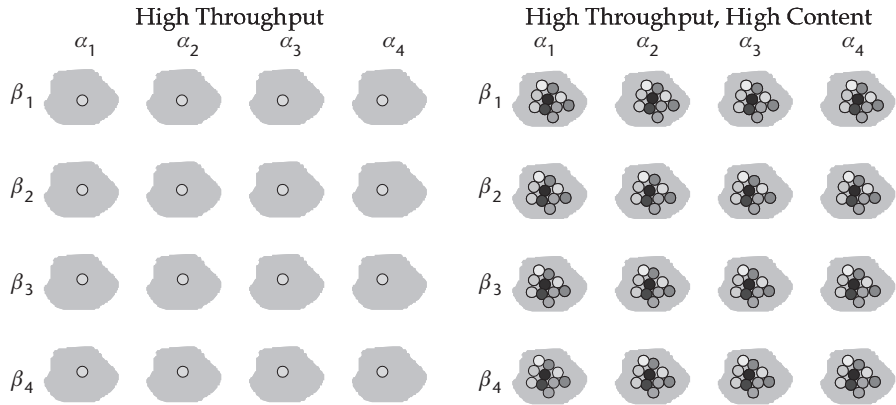


**Figure 5.3** Illustrating computational systems biology. The computational model is used by the “simulator” to predict cell/tissue properties as a function of cell microenvironment parameters and applied stimuli. These properties are measured and compared to the predictions. Differences lead to refinement of the model, the simulator, and new cell culturing parameters. We are interested in image-based measurements in service of systems biology.

underlying model of the system that it is based on. Figure 5.3 illustrates the manner in which systems biology is practiced.

In discovery-driven research, one collects extensive lists of measurements of system components without any hypotheses in mind. The measurements are analyzed to generate hints or “leads” about the system. Discovery-driven studies have been inspired by the availability and affordability of automated instruments and plentiful computing capacity. Many of these instruments operate in a *high throughput* manner in which multiple (often hundreds or thousands of) experiments are conducted in parallel rather than in sequence. The left half of Figure 5.4 illustrates a high-throughput experiment in which two parameters  $\alpha$  and  $\beta$  are varied systematically to generate an array of specimens that can be processed as a single unit. These parameters could, for example, represent a drug candidate and a modifier, applied at various concentrations. A single measurement is made for each specimen (indicated as a blue dot in Figure 5.4). The optimal combination of  $\alpha$  and  $\beta$  can be identified rather quickly compared to the situation in which the same set of experiments are carried out in a serial manner. High-throughput experimentation can also be inexpensive compared to serial experimentation, making it attractive for discovery-driven research.

The idea of high-throughput experimentation can be combined with another powerful idea—*high content* experimentation. In this paradigm, a large number of structural/functional measurements are collected for each specimen. This idea is illustrated in the right half of Figure 5.4. The multicolored dots indicate multiple measurements for each specimen.



**Figure 5.4** Illustrating the notions of high-throughput and high-content experimentation.

The end result of modern optical microscopy is an already large and still growing wealth of image data. *There is a compelling need for technologies to translate this wealth of imaging data into quantitative insight.* Two types of needs exist: (1) analysis of *complex data sets* involving interactions among multiple structures and functional markers, and multiple imaging dimensions; and (2) analysis of *large batches* of such images. Quantitative measurements are needed in contexts ranging from hypothesis testing, drug discovery, assay development, high-throughput assays, quantitative tissue engineering, cytomic mapping [34–36], and matters relating to bioinformatic efforts including ontologies [37] and systems biology [38].

In addition to the traditional need for measurements of cytologic and histologic structures, there is a pervasive need for measuring structures and functional markers in relation to each other, and measuring changes of these measurements over time (i.e., dynamics). It is desirable to do this rapidly, objectively, and accurately, with utmost automation, maximum fluorescence multiplexing, maximum sensitivity, and specificity, using fewest animals, and at minimum cost.

However, the principal barrier that remains to be overcome is the need for *automated image analysis technologies that can extract informative object-scale measurements from such images* in support of system-level investigations.

Importantly, these measurements should be meaningful and appropriate for systems analysis. Analyzing a complex system first requires identifying and *measuring each component of the system*. For the example in Color Plate 5, it is necessary to identify and delineate all of the cell types in the image, trace all the neuronal and glial processes, identify cell-cell connectivity, delineate the microvasculature and identify the branching points, and delineate the pial surface and the implant insertion site. For each of these structures, a large number of useful structural measurements can be computed. However, this is not sufficient—analyzing a complex system also requires measuring the *structural and functional relationships and interactions among the components*. For instance, the locations and orientations of each type of cell relative to neighboring cells of different types, the microvasculature, to the pial surface, and to the implant insertion site are instances of such measurements. At a higher level such measurements are needed as a function of



distance from the implant, over time, under various types of pathological conditions and drug treatments.

This example is not an isolated instance by any means. The adult neurovascular stem cell niche is an excellent example of an application with similar needs [1,2]. This is a multicellular three-dimensional structure with specific structural and functional interrelationships between the different cell types, the vasculature, and the lower ventricle. Multiple cell types in the niche are related by lineage, express different combinations of markers, and have specific asymmetries and orientations relative to the vasculature [39–41]. The niche is also characterized by dynamic cell migration behaviors. Tumors are another example of a complex microenvironment [42].

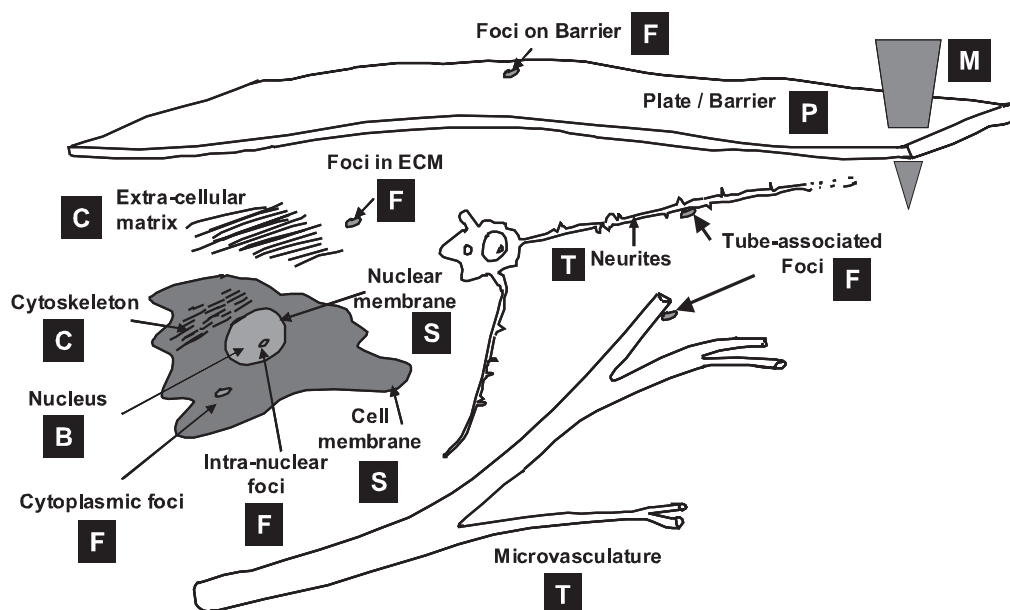
The past decade has resulted in large open-source segmentation and registration toolkits such as the NLM-sponsored Insight ([www.insight.org](http://www.insight.org)). However, they are not integrated within a logical framework specific to modern microscopy and contemporary tissue-level biology [38,43]. There is a compelling need for integrative tools that can accept a high-level task specified by a biologist and translate it into a series of subtasks, invoking appropriate image analysis algorithms with suitable settings. Finally, there is a need for tools that can rapidly scale up a small prototype study to a large batch of images. The methods described in this chapter are *specifically designed for the capabilities of modern optical microscopy and the image-based measurement needs of contemporary tissue-level biology*.

## 5.2 A Divide-and-Conquer Segmentation Strategy

Segmentation is the automatic delineation of objects in images. Its output is a set of objects. It is the most challenging image analysis step, and its accuracy has a direct bearing on the accuracy of the image-based measurements of ultimate interest. The best-available segmentation algorithms are model based (i.e., they rely on a mathematical model describing the expected range of morphologies and intensity patterns of the objects to be delineated).

Referring to Color Plate 5, brain tissue contains structures with extremely diverse morphologies. This observation has motivated us to consider a “divide-and-conquer” strategy. Specifically, it is very practical now to label each of the bio-molecules of interest using highly specific fluorescent labels and good specimen preparation protocols. Furthermore, spectrally resolved fluorescence microscopy combined with spectral unmixing can cleanly separate the emission spectra into a set of *pure channels* (i.e., channels containing only one type of object belonging to a known morphological class *most of the time*). Mixed channels containing more than one object type are still possible, but increasingly rare (we later describe methods to handle such cases).

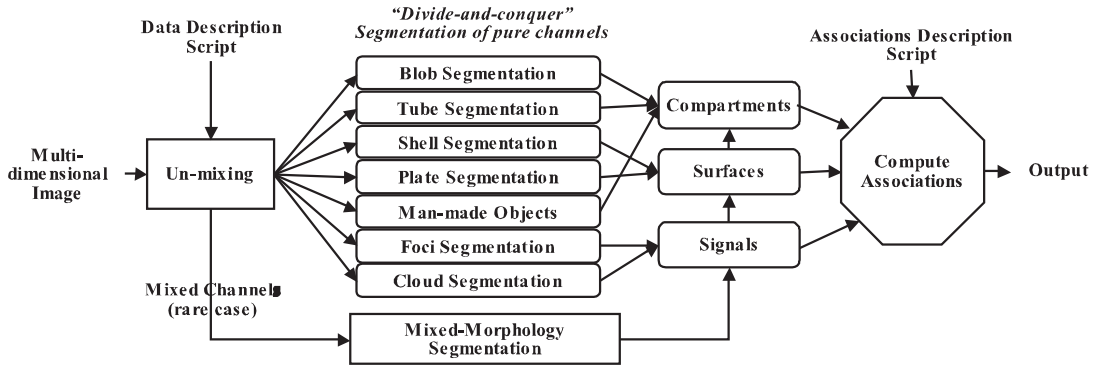
We are primarily interested in fluorescence microscopy at the cell and tissue level (20–100× objectives). Within this realm, we have found that, in spite of the variability in biological forms, it is possible to identify a “short list” of frequently occurring morphologies of biological entities—blobs (B), tubes (T), shells (S), foci (F), plates (P), clouds (C), and manmade objects (M). These morphologies are illus-



**Figure 5.5** Short list of object morphologies frequently observed in fluorescence cell/tissue imagery: B = blobs; T = tubes; S = shells; F = foci/punctae; P = plates; C = clouds; and M = manmade objects. A collection of mathematical models describing variations of these geometries guides the modular divide-and-conquer segmentation strategy.

trated in Figure 5.5. Commonly, *blobs* correspond to cell nuclei, *tubes* correspond to neurites/vasculature, *shells* correspond to nuclear/cell membranes, *foci* represent localized molecular concentrations such as mRNA at the site of transcription and adhesion sites, *plates* correspond to basal laminae, *clouds* correspond to cytoplasmic markers, and *manmade* objects correspond to implanted devices. This “short list” of morphologies is valid for the proposed biological studies—our working hypothesis is that it is applicable more broadly. These morphologies and their most common variations can be captured by a library of mathematical models. These models manifest as a library of segmentation algorithms, each specialized to handle one of these morphologies. In summary, a relatively small collection of segmentation algorithms (a few for each morphological class) can enable analysis of a surprisingly diverse application base. The morphological class of a fluorescently labeled entity is easily specified by the biologist, so we do not presume to determine that automatically. Such a divide-and-conquer segmentation strategy requires simpler segmentation programs that do not need to grapple with a mixture of objects types. Specialized algorithms can achieve higher levels of automation, accuracy, speed, and robustness.

Once the segmentations are validated, we can compute image-based measurements. The output of segmentation programs is a set of *objects* in each imaging channel. From a quantitation standpoint, these objects represent one of three types of biological entities: (1) a volumetric *compartment*; (2) a *surface* with negligible volume; or (3) a functional *signal* that could be distributed over compartments/surfaces/curves. In other words, each object in the image has one of three



**Figure 5.6** Summary of the divide-and-conquer strategy for segmentation and associative analysis. We refer to this as FARSIGHT (fluorescence association rules for quantitative image-based insight).

*operational interpretations.* This information is provided by the biological investigator while describing the image data. The diversity of biological investigational objectives implies that different measurements are important for different studies. Nevertheless, the types of measurements of interest can be classified into two broad categories: (1) intrinsic, and (2) associative. *Intrinsic measurements* quantify the features of objects in a single channel. *Associative measurements*, on the other hand, quantify relationships between objects from one or more channels.

These considerations motivate the processing architecture illustrated in Figure 5.6.

The following paragraphs summarize methods to segment some of the main morphological classes noted earlier.

*Blob segmentation algorithms* are discussed first. The seemingly straightforward task of segmenting blob-like objects such as fluorescently labeled nuclei continues to present challenges, especially when high levels of accuracy, automation, and reliability are required. The main sources of errors in blob segmentation include structural irregularity, intrimage and interimage variability (natural variability as well as variations due to drifts in staining protocols, and imaging instrumentation), ambiguities associated with tight clustering of blobs [44,45], clusters with multiple types of blobs, modeling inadequacies and ambiguities, weak cues for separating clusters, low axial resolution compared to the lateral resolution, low contrast, nonuniformity of fluorescent signal, and imaging noise. Other sources of error include depth-dependent attenuation, the anisotropic point spread function, and artifacts from tissue sectioning resulting in nuclei that are cut off or damaged.

*Model-based segmentation algorithms* have to date demonstrated the highest levels of segmentation accuracies [46–49]. Various methods have been proposed for object modeling in the literature (e.g., shape based modeling [50–54] and deformable modeling [55–58]). Deformable methods based on active contours and level-set based methods are widely used in medical image segmentation [59–62]. From the standpoint of high-throughput or large-scale nuclear segmentation, these methods are impractical at present. They are computationally too expensive, especially since the number of nuclei is large (typically thousands). Second, they lack the ability to split clusters of objects in a general manner. Finally, they depend on

effective initialization and are prone to drastic failure modes, such as “leakage” of a contour. Graph cuts [63] have been proposed for image segmentation problems where the cost of the cut corresponds to an energy function incorporating low-level information such as boundary and regional constraints. Although this method can compute globally optimal solutions, it has been difficult to include high-level information and split clusters of objects. For the core FARSIGHT blob segmentation algorithms, we use a multiple model-based extension [64] to our earlier algorithm [48], the main steps of which are illustrated in Figure 5.7.

The preprocessing step suppresses variations due to imaging noise, textural variations, and imaging artifacts. This enables adaptive thresholding to be used to extract connected groups of blobs. The watershed algorithm [65] is widely used for separating connected blobs. It is efficient, but prone to over-segmentation. In our prior work, we have made several enhancements to this algorithm. First, we have developed a method to filter markers extracted. The watershed uses markers based on the geometric distance map  $D$  [66]. We filter these markers to eliminate points that are too close to each other [67]. Next, we have [68] shown that the distance map  $D$  can be modified to include the intensity gradient field  $G$  as an additional cue using the following dimensionless modifier formula.

$$D' = D \times \exp \left( 1 - \frac{G - G_{\min}}{G_{\max} - G_{\min}} \right) \quad (5.1)$$

where  $G_{\min}$  and  $G_{\max}$  are the minimum and maximum values of the intensity gradient  $G$ . Reliably overcoming the remaining errors requires mathematical modeling of the blobs. We model blobs based on two types of features—*morphological features* such as volume, shape factors, convexity, and eccentricity, and *intensity features* such as median intensity, variance, and texture measures. The probability distribution of blob feature vectors denoted  $\mathbf{X}$  in the model. It is estimated from a set of *training examples*. These examples can be drawn automatically from the image data using an unsupervised algorithm as in [48], and/or from user-provided examples. In either case, the user can inspect and, if necessary, edit the examples. In our work, we use a nonparametric Parzen density estimate for modeling the distributions of feature vectors  $\mathbf{X}_j$  of these example blobs [69,70]:

$$p(\mathbf{X}) = \frac{1}{N} \sum_{j=1}^N \phi(\mathbf{X} - \mathbf{X}_j, w) \quad (5.2)$$

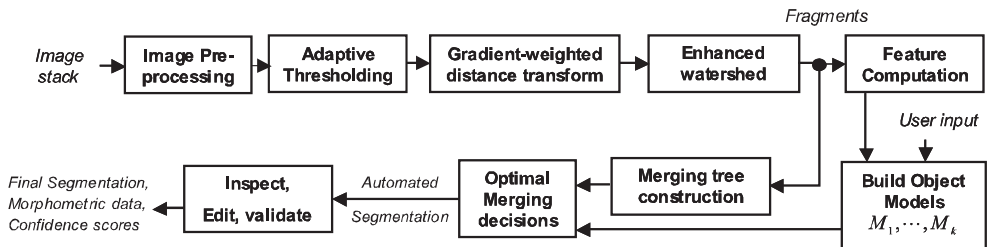


Figure 5.7 Flowchart illustrating the major steps in blob segmentation.

where  $\mathbf{X}_j$  is  $j$ th sample,  $\phi(\cdot)$  is the Parzen window function, and  $w$  is the window width [69]. For the window function, we use the Gaussian:

$$\phi(\mathbf{X}, w) = \frac{1}{\sqrt{(2\pi w^2)^m |\Sigma|}} \exp\left(-\frac{\mathbf{X}^T \Sigma^{-1} \mathbf{X}}{2w^2}\right) \quad (5.3)$$

where  $\Sigma$  denotes the covariance matrix of the  $m$ -dimensional feature vector  $\mathbf{X}$ . When the window size  $w$  is small, the influence of each training sample is limited to a small region. When it is larger, the distribution is smoother. We set  $w$  to the distance  $d$  from  $\mathbf{X}$  to the  $k$ th nearest neighbor among all the sample points [71]. To reduce computation, we ignore samples whose distance  $d > 3w$ . *One important aspect of brain tissue is the diversity of cell types with correspondingly diverse nuclear morphologies. To model this diversity, we use multiple models, one for each cell class  $c$ .* In summary, the overall posterior probability for modeling blobs of class  $c$  can be written as follows:

$$p(M_c | \mathbf{X}) = \sum_{j=1}^{N_c} \phi(\mathbf{X}_c^j, w) p(M_c) \quad (5.4)$$

where  $N_c$  is the sample size,  $\mathbf{X}_c^j$  is the  $j$ th feature vector, and  $p(M_c)$  is the a priori probability of class  $c$ . This model also provides us with a *confidence score* measuring how well each object fits the model  $M_c$  based on its feature vector  $\mathbf{X}$ . We will first use the confidence score to preextract all objects in the image for which the confidence value is high, representing well-segmented objects. Subsequent computations dwell on the ambiguous cases representing clusters that must be broken and/or fragments that must be merged. Finding the optimal combination of these operations is a combinatoric search problem. Our approach is to make this search efficient by building a *region adjacency graph* [72] to limit the search to neighboring fragments. We then construct a *hierarchical merging tree* to efficiently explore feasible merging decisions [48]. For each possible decision, we will compute the confidence score under each model  $M_c$ , and pick the highest-scoring model. Figure 5.8 illustrates multiple-model based fragment merging for hippocampal cell nuclei using two models  $M_1$  and  $M_2$  corresponding to neuronal and glial nuclei, respectively. The lower panels show two example merging trees, where the nodes with highest confidence scores are highlighted. The merging tree for object 72 indicates the need to merge it with object 180 under model  $M_1$ . Object 113, on the other hand, is not to be merged with any other object, since it has the maximum score by itself under model  $M_2$ . This method achieves a segmentation accuracy of 93.7 percent and a classification accuracy of 93.5 percent over five different brain regions (CA1, CA3, barrel cortex, gustatory cortex, and dentate gyrus). Much remains to be done to further improve the accuracy of nuclear segmentation. Recent papers have focused on improving the quality of markers provided to the watershed algorithm [73] and alternatives to watershed based on graph cuts [74].

Tube segmentation algorithms (T) are discussed next. Two families of algorithms have emerged for segmenting tube-like structures in biological images, one based on skeletonization [75, 76], and the other on recursive tracing [77–80]. Broadly, the latter greatly outperform the former in terms of speed, robustness to

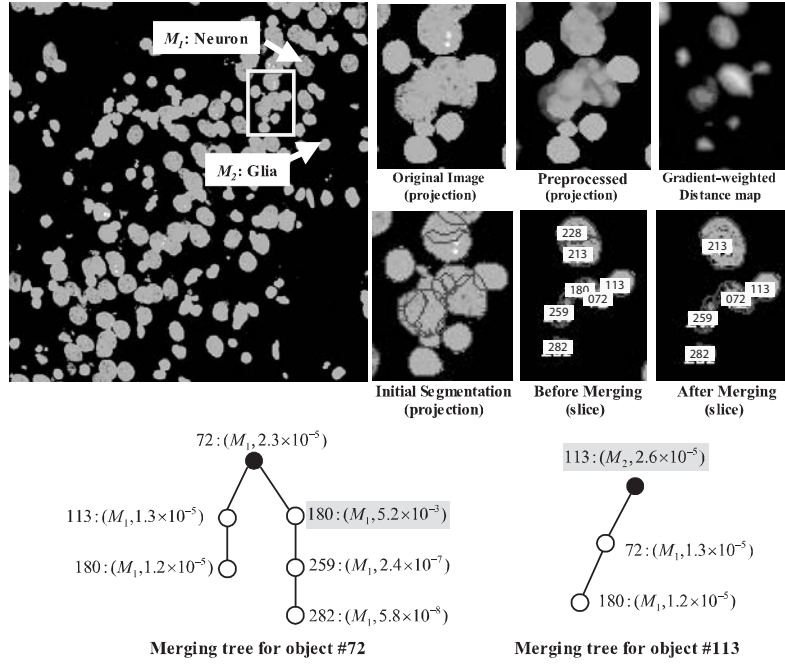


Figure 5.8 Illustrating multiple model-based object merging.

image complexities, and segmentation accuracy [81], and form the focus of our efforts. One recently developed algorithm [82] has been particularly successful. This algorithm is based on modeling the local geometry of tubes using a cylindroidal superellipsoid [83, 84]. The implicit form of the superellipsoid is given by [85]:

$$S(\mathbf{x} : \varepsilon) = \left( |x|^{\frac{2}{\varepsilon_2}} + |y|^{\frac{2}{\varepsilon_2}} \right)^{\frac{\varepsilon_2}{\varepsilon_1}} + |z|^{\frac{2}{\varepsilon_1}} \quad (5.5)$$

where  $\mathbf{x} = (x, y, z)$  are Cartesian coordinates, and  $\varepsilon = (\varepsilon_1, \varepsilon_2)$  are shape control parameters. For  $\varepsilon_1 \approx \varepsilon_2 \approx 1$  this generates ellipsoidal forms appropriate for modeling blobs. The 3-D geometry can be represented computationally using a triangular mesh following Bardinett et al. [86]. It can be geometrically transformed by a function  $T(\mathbf{x}; \sigma, \phi, \mu)$  consisting of scaling parameters  $\sigma = (\sigma_1, \sigma_2, \sigma_3)$ , a  $3 \times 3$  rotation matrix  $\mathbf{R}(\phi)$ , and a  $3 \times 1$  translation vector  $\mu$ . This transformation must be implemented using quaternions [87] to avoid a numerical instability known as *gimbal lock*. The function  $S(T^{-1}(\mathbf{x}; \sigma, \phi, \mu) : \varepsilon)$  is equal to 1 on the ellipsoid surface, is less than 1 in the interior, and greater than 1 on the exterior.

This model is flexible enough for modeling variations while providing strong constraints on vessel morphology, and yet offers much lower dimensionality compared to deformable models. It is more robust to neighboring structures compared to Hessian-based methods [88]. It extends to the more general class of star-shaped superquadrics [89] that allows us to capture boundary variations while preserving topology. With  $\varepsilon_1 \leq 1$  and  $\varepsilon_2 = 1$ , the superellipsoid in (5.5) is constrained to cylindroid forms. The first parameter sets the “squareness” of the model as



illustrated in Color Plate 6(a, b). This model can be rigidly transformed using the transformation  $T(\mathbf{x}; \sigma, \phi, \mu)$  as described earlier for blob segmentation. In addition, following the work of Solina et al. [89], the model can be linearly tapered by a slope parameter  $s$ , and bent by a turning parameter  $\gamma$  (Color Plate 6(c)). For convenience of notation, we denote the complete vector of geometric transformation parameters  $\Theta = [\sigma, \phi, \mu, \varepsilon, s, \gamma]$ . With this notation, the function  $S(T^{-1}(\mathbf{x}; \Theta) : \varepsilon)$  is equal to 1 on the model surface, less than 1 in the interior, and greater than 1 on the exterior.

For modeling the intensity (appearance), we rely on the median intensity level, and the expected variation due to staining or noise. For a given class of images, we directly estimate these model parameters from examples of small vessel segments provided by the user. For modeling image noise, we use a Gaussian in most cases and a Poisson model when the photon density falls below about 50 counts per pixel. To robustly fit the model  $V(\mathbf{x} : \Theta)$  to the local image data, we use the IRLS algorithm [90].

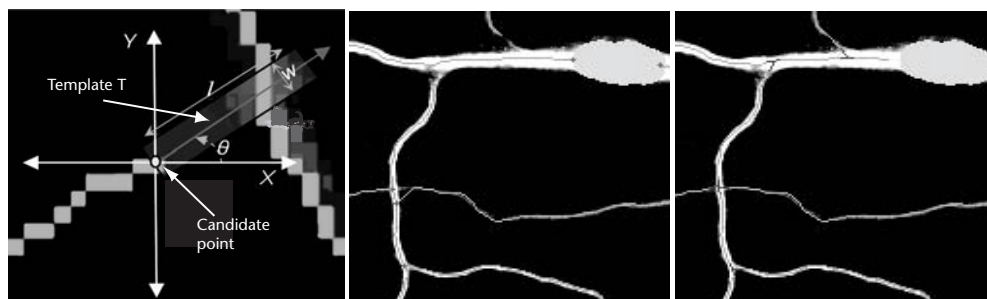
$$[\hat{\Theta}, \hat{I}_{\Omega}, \hat{I}_{\Delta}, \hat{I}_E] = \arg \min_{[\Theta, I_{\Omega}, I_{\Delta}, I_E]} \sum_{\mathbf{x}} \rho(I(\mathbf{x}) - V(\mathbf{x} : \Theta) / \sigma) \quad (5.6)$$

The overall tracing algorithm starts with a crude initial estimate, named “seed points” of vessel locations over a grid (table in Color Plate 6(d)). The earlier model is fit to the image data at each seed point, and a statistical confidence value is computed. Then the model is shifted by a small step size  $\Delta\mu$  along the major axis, and fitted again. This process is iterated repeatedly to trace the primary structure (“backbone”) of a tube [83]. The tracing is stopped when the confidence value falls below a set threshold, or a previous trace is encountered. For additional details, the reader is referred to [82].

This algorithm robustly traces the *primary* structure of neurites and vessels with negligible deviations at secondary structures. For regions that deviate in predictable ways, such as spiny neurons, we use a family of *secondary geometric models*. In this case, the overall local geometry of a tube is described by the primary model attached to a permissible secondary model. The geometry model must be coupled with an intensity model and fitted to image data. *Branch points* represent regions of the image that violate the tube model. Our method for optimal extraction of these important locations is to first perform an initial detection of branch points from trace intersections [91]. Then, we perform a generalized hypothesis test in which the orientation and width of the candidate segments are varied, and the settings with the highest likelihood are chosen [92]. This method is extremely effective (Figure 5.9). Compared with our earlier algorithm that has a detection rate of 84 percent [93], this method yielded a 91 percent detection rate with a comparable 11 percent false positive rate. It is able to localize the branch point to within 1.2 pixels on average, compared to a 2.4 pixel error in the prior method.

Cloud segmentation algorithms (C) are discussed next. Cytoplasmic stains commonly produce irregular cloud-like structures surrounding nuclei. Delineation of the foreground of a cloud from the background can be readily accomplished using adaptive gray-scale segmentation algorithms [94]. Challenges arise in two specific cases: (1) there is significant depth-dependent attenuation of the signal, so com-





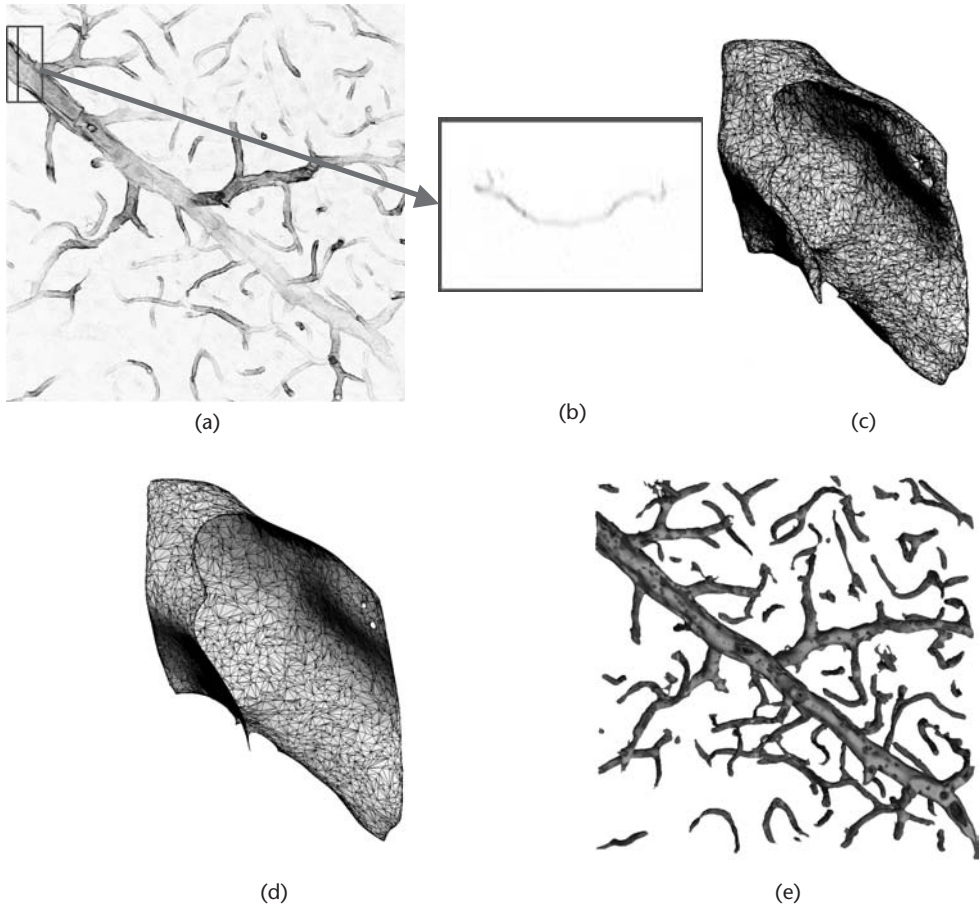
**Figure 5.9** The statistically optimal model-based method for refining branch point locations and angles.

pensation must be made, and (2) cloud signals from overlapping objects need to be separated. For the former, attenuation correction software [95] can be used. For the latter, Voronoi cells can be used to segment connected clouds into smaller components (usually one component per cell). From an intensity standpoint, the cloud could either be smoothly distributed in space, or have a texture (e.g., actin filaments). In this case, texture-based segmentation algorithms are appropriate.

- *Segmentation methods for foci/punctae (F)*: Best exemplified by FISH signals, adhesion foci, these objects can be treated as either small blobs, or small clouds consisting of high-intensity voxels extending axially to a few slices [96–105]. While blob/cloud segmentation algorithms could be used for them, it is advantageous to process them differently. While blobs and tubes are more likely spatial compartments, foci represent functional signals. Foci-containing channels can be preprocessed with noise removal, background subtraction, normalization, and autofluorescence correction algorithms. Then, they can be thresholded adaptively, and further processed based on size, shape, and intensity [96], or extracted by recursive reconstruction [103]. Clusters of foci can be separated by the watershed algorithm to enable correct counting, and foci below a set size are usually discarded as noise [94].

The main consequence of errors in segmenting foci is proportional errors in functional measurements since a large number of these are usually processed. The main sources of errors are imaging noise and uneven staining. The most common types of errors include missed foci, false detections, clustering or splitting of foci, and errors in intensity measurement. Due to the great variation of foci in size, shape, and intensity across different images or even within a single image, it is highly desirable that some parameters such as foreground threshold can be calculated adaptively.

- *Segmentation methods for plates (P) and hollow shells (S)*: Membranes/laminae play an important role in biological systems. The challenge to segmenting these structures is their small (often, subresolution) spatial footprint. One common case occurs when the basal lamina of a blood vessel is fluorescently labeled but is too thin to be segmented reliably using the



**Figure 5.10** The use of a surface segmentation algorithm for delineating vessels when a protein on the thin vessel membrane is fluorescently tagged. (a) Deconvolved projection image of brain vascular basal lamina ( $1,024 \times 1,024 \times 77$  voxels, lateral resolution  $0.35 \mu\text{m}$ , axial resolution  $0.85 \mu\text{m}$ ). (b) The small boxed region of the image is shown enlarged in Panel B. (c) Closeup rendering of subsampled surface segmentation and triangulation for the small boxed region on the upper left in panel A. (d) Result of medial surface extraction (thinning). (e) Color-coded display of full surface segmentation. Darker gray values indicate regions of high positive and negative curvature (inner walls of vessels and protrusions); lighter colors indicate regions of medium curvature.

tube segmentation algorithms. In these cases, robust surface detection and mesh extraction algorithms from computer graphics (e.g., marching tetrahedra [106]) are more effective compared to tube segmentation algorithms [107] (Figure 5.10). From a measurement standpoint, the fractal nature of surfaces [108–110] makes naïve measurements of surface area unstable and requires care. Specifically, any measurements should be restricted to a specific spatial scale. In analyzing tissue, one measurement of particular importance is the relationship of cells to the vasculature. Most of these measurements can be made using the Euclidean distance transform with respect to the outer vessel membrane [111]. Unlike surface area measurements, these distance measurements are unproblematic.

- *Segmentation methods for manmade objects (M)*: This is a category that represents objects such as neural implants and electrodes. It is straightforward, since the objects of interest are of precisely known rigid geometry that can be represented as a template. This template model can be fit to the image after subjecting it to rigid 3-D spatial transformation consisting of scale, rotation, and translation [112,113].

### 5.3 Computing and Representing Image-Based Measurements

As noted earlier, segmentation and object extraction sets the stage for making diverse object-scale measurements from the image data. Broadly speaking, the types of measurements of biological interest can be classified into two broad categories: (1) intrinsic, and (2) associative. *Intrinsic measurements* quantify the features of objects in a single channel. *Associative measurements* quantify relationships between objects from one or more channels.

The intrinsic measurements of each object are directly determined by its morphological class. They are commonly referred to as “object features” in the image analysis literature. Table 5.1 lists examples of common intrinsic measurements for the seven main classes. It is by no means comprehensive. Algorithms for computing object features are widely described in the literature [49,114].

Intrinsic measurements can be stored in a manner that is linked to objects. Specifically, most object extraction algorithms also yield a unique identifier (“object ID”) for each object. For example, an object identifier may point to a specific row in a table, database entry, or XML file in which the intrinsic features for that object are stored.

Associative measurements quantify spatial and/or temporal *associations/relationships* between objects extracted by segmentation. The complex brain tissues of interest to us contain a dense web of interesting spatial, temporal, and functional relationships. Spatial relationships among objects include proximity, adjacency, orientation, and connectivity. Temporal relationships include dynamic aspects such as cell migration, transport of biochemicals, and causal relationships among cellular events. Functional relationships are often intimately related to structural and/or temporal relationships, and the most important of these are indicated by the presence/absence, variations, and spatial transport of specific molecular constituents of tissue.

**Table 5.1** Common Intrinsic Measurements

<i>Object Morphology</i>	<i>Examples of Intrinsic Measurements</i>
Blobs	Location, diameter, volume, shape factor, surface area, eccentricity
Tubes	Centerline, surface locations, local diameter, branch points
Shells	Thickness, shape factors
Plate/Laminae	Thickness, surface area
Manmade objects	Location, pose
Foci	Location, brightness, diameter
Cloud	Brightness, texture measures

Given the large number of constituents in most types of tissue, a combinatorial number of associations can be imagined. However, a much smaller set of associations is biologically relevant and immediately useful. Regardless, it is important to choose a good representation that is capable of representing *any and all* associations among objects and their features (intrinsic measurements). Traditional two-dimensional representations such as tables and charts are often inadequate to capture the information in the network of associative measurements. To overcome this limitation, we have examined attributed graphs as an effective representation. In this representation, an association can be described in terms of graphs in which each object is a *node* with a set of attributes (intrinsic measurements of the object), and each association is a *link*. Nodes and their attributes are uniquely identifiable by their global object IDs. The attributes of each link are contained in a list of measurements arising from associating the respective objects. It is uniquely identifiable by the global IDs of the associated objects. In principle, one can propose a large number of associations between a set of objects. However, a much smaller set of associations are biologically meaningful, plausible, relevant, and interesting.

Graphs offer many advantages. First, they are supported by graph theory, a well-studied mathematical discipline that is specifically intended for abstract (application-independent) representation and analysis of any and all relationships [115]. Second, general-purpose software tools are available for visualizing and analyzing graphs (e.g., Graphviz, [www.graphviz.org](http://www.graphviz.org)). An attributed graph is composed of nodes representing objects and links representing associations among objects. Attached to each node is a list of intrinsic measurements (attributes) of the object, and attached to each link is a list of associative measurements quantifying the relationship. From a practical standpoint, the graph data structure can be represented conveniently as an extensible markup language (XML) file. This is a widely used data format that is both human and machine readable. Once an attributed graph is constructed, it can be queried to answer specific questions using common tools such as database query tools and spreadsheets. This is flexible, general, and extensible in the future.

The following paragraphs describe some of the basic classes of associative measurements.

### *Distance-Based Associative Measurements*

The geometric distance between a pair of objects is a simple yet powerful basis for association. Until recently, large-scale distance computations were computationally expensive. Fortunately, developments in computational geometry have produced efficient algorithms for computing dense 3-D Euclidean distance maps. These algorithms perform a rapid computation of distances to a chosen set of objects  $\{O_m(c_i), m = 1, 2, \dots, M\}$  from each voxel  $\mathbf{x}$  in the image [66]. A particularly relevant class of such maps is the signed distance map [111] that not only provides a distance readout  $D_{\{O_m(c_1)\}}(\mathbf{x})$ , but also the coordinates of the nearest object location. For example, consider a signed distance map computed for the segmentation of cell nuclei. This map can be looked up at any point  $\mathbf{x}$ . If the distance is zero (or close), the chosen image point is on/near the surface of the nuclei. A negative distance value indicates that the point is internal to the nuclear compartment, and

a positive distance indicates that the point is outside. The location of the closest point on the nucleus also provides a readout of the object ID of the nearest nucleus and thereby a link to all its properties.

Distance maps help define a set of standard/custom *zones* associated with each compartment/surface (inside/outside of a nucleus, small region outside a nucleus, and so on). A zone is the set of pixels that have distance values in a specified range  $\delta$ , and can be expressed as a spatial weight function. Zones are useful for efficiently computing *zone integrals*—the distance-weighted summation of a functional signal over a defined zone, for example:

$$\mathbf{Z}(c_i, c_j) = \int \omega_\delta(\mathbf{D}_{\{O(c_i)\}}(\mathbf{x})) c_j(\mathbf{x}) d\mathbf{x} \quad (5.7)$$

where  $\omega_\delta(\cdot)$  is a weighting function that is uniform in the range  $(0, \delta)$ , and  $\mathbf{D}_{\{O(c_i)\}}(\mathbf{x})$  is the Euclidean distance map relative to the objects observed in channel  $c_i$ , and  $c_j(\mathbf{x})$  is the signal in channel  $c_j$ . Zone integrals generalize many classical computations. For instance, FISH foci can be integrated over the interiors of cell nuclei, or their close cytoplasmic neighborhoods. In other words, the concept of zone integrals realizes all of the functionality of the 3DcatFISH system [73, 100, 116]. Zone integrals are particularly valuable as a tool for classifying cells based on molecular markers [117]. The result of a zone integral calculation is simply linked to the corresponding global object ID and stored in the database.

As a concrete example, Color Plate 7 shows a five-channel 3-D image of brain tissue surrounding a neural implant insertion site. A Zeiss META system with spectral unmixing software was used to record DAPI, Iba-1, laminin, and GFAP, indicating cell nuclei, microglia, vasculature, and astrocytes, respectively. Channels  $\{c_1(\mathbf{r}) \dots c_5(\mathbf{r})\}$  correspond, respectively, to cell nuclei, vessels, Nissl neurotrace signal, astrocytes' processes, and a microglial marker Iba-1. Segmentation of each type of object in the 3-D confocal images is a nontrivial task that is greatly simplified by the spectral unmixing, since each channel contains one type of image object. Separate model-based segmentation algorithms were applied to each channel individually (see Color Plate 8). First, the diverse population of cell nuclei in the DAPI channel ( $c_1$ ) were segmented using a 3-D blob segmentation algorithm [64]. This produces a set of blobs  $\{N(c_1)\}_{n=1}^N$  and a corresponding vector of morphometric and intensity-based features denoted  $\theta_{n=1}^N$ . Cytoplasmic processes of astrocytes  $\{A\}_{k=1}^K$  in the GFAP channel were traced using a 3-D neurite tracing algorithm [118]. The blood vessels in the Laminin channel  $\{V\}_{m=1}^M$  were segmented using a robust tracing algorithm based on 3-D modeling of vasculature using superellipsoids [82]. In recent work, we have adopted the surface segmentation approach instead [119]. Panel D is a composite of all the segmentations illustrating the amount of object data that can be extracted.

Once the automated segmentations are complete, it is usually prudent to inspect them and edit any segmentation errors using a graphical visualization and editing software tool. This sets the stage for further analysis. Color Plate 9 illustrates some basic distance-based associative features. Panels A and B illustrate the use of a distance measure to identify vascular endothelial cell that are easily distinguished based on their intimate contact with the vessel marker signal

and their distinctive elongated morphology. Signed distance maps are a versatile common tool for making such measurements. For instance, the vascular endothelial cells are identifiable based on their distinctive morphologies and close proximity to vessels  $\Delta(c_1, c_2) = D_{V(c_2)}(\bar{\mathbf{x}}_{N(c_1)})$ , where  $\bar{\mathbf{x}}_{N(c_1)}$  are the centroids of nuclei in channel  $c_1$ . Panels C, D, and F illustrate computation of zone integrals  $Z(c_1, c_3)$ ,  $Z(c_1, c_5)$ , &  $Z(c_1, c_4)$ , respectively, for identifying neurons, microglia, and astrocytes. Panel E shows another feature that is valuable in identifying astrocytes—the close proximity of the convergence point of astrocytes processes (shown as a green cross) to the cell nucleus.

The union of the set of intrinsic and associative measurements can be used to classify nuclei into four different classes. In our work, we have used support vector machine classifiers, although any appropriate classifier may be used [70]. Intuitively, neurons, microglia, and astrocytes were classified based on the overall set of features and association with a *cloud* of NeuroTrace, Iba1 signal, or GFAP signal, respectively, that completely surround the nucleus. Endothelial cells were classified by their flattened shape and close proximity to the extra striate body area (EBA) and blood vessels.

Once cells are classified, it is possible to “query” the segmentations in diverse ways depending upon the distance map that is chosen. As a simple yet general query mechanism, we describe the use of conditional distributions. Many biologically relevant questions revolve around the distance of cells to the vasculature or to the implant site. For this, we compute multiple distance maps for each reference structure of interest. The background in panel G shows the map relative to the implant site. Panel H shows the map relative to the vasculature. This feature is expressed simply as follows:

$$\Delta(c_1, c_2) = D_{V(c_2)}(\bar{\mathbf{x}}_{N(c_1)})$$

where  $\bar{\mathbf{x}}_{N(c_1)}$  are the centroids of nuclei in channel  $c_1$ . The first map can be used to answer the following biological question: what is the distribution of various cell types as a function of their distance from the implant insertion site? The histogram in panel I shows an increase in the number of microglia/macrophages and a reduction in the number of neurons near the insertion site. Similar histograms can be generated relative to the vasculature to answer analogous questions about cell distributions [117]. This histogram is merely one instance of a large family of queries that can be posed in terms of empirical probability distributions of the form  $P(\mathbf{X}|\mathbf{Y})$ . In general, the user specifies a subject of objects  $\mathbf{Y}$ . Specifying all objects results in an unconditional distribution. For this subset, the user next specifies the list of measurements  $\mathbf{X}$  whose joint distribution is desired. Specifying just one measurement in the list produces a univariate histogram. Specifying multiple measurements results in a joint histogram. Normalizing the histograms produces empirical probability distributions. These distributions can be analyzed further using multivariate statistics packages. To analyze cell-cell distance patterns, we compute a  $k$  nearest-neighbor graph, either for all cells, or just a selected subset. These are illustrated in Color Plate 9(e, f), respectively. These patterns have been used to identify cell layers in the hippocampus [119].



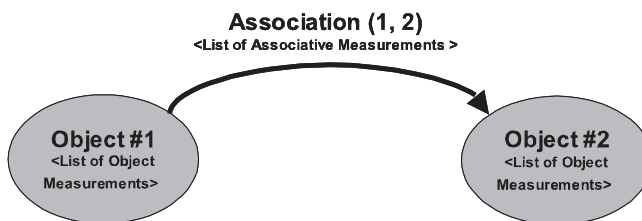
## 5.4 Analysis of Spatio-Temporal Associations

The previous section focused on spatial associations. When we are interested in analyzing dynamic biological systems, the temporal dimension naturally enters the analysis. The traditional approach to studying dynamic systems is based on the use of fixed specimens. The specimens are sampled from different animals at different points of time. Each specimen represents a static snapshot of the dynamic processes of interest. In this case, temporal analysis simply reduces to computing intrinsic measurements for the fixed images at each time point and plotting them as a function of time for observing trends and conducting further statistical analysis. The traditional method is quite inefficient in terms of time and cost. Each static snapshot provides a rather incomplete view. The investigator is, in effect, synthesizing an understanding of the dynamic phenomenon from a series of incomplete snapshots.

Increasingly, the traditional method for analyzing dynamic systems is giving way to much more efficient methods that rely on direct imaging of a living specimen using time-lapse microscopy. This advance is enabled by a convergence of several advances. First, the development of light detectors with high quantum efficiency permits more of the fluorescence to be captured. This allows a weaker illumination of the biological specimen that in turn allows the specimen to stay alive much longer under the microscope. Second, the advent of fluorescent protein labeling allows the investigator to avoid the use of fluorescent stains that are toxic to the specimen. Third, the advent of multiphoton microscopy has allowed the microscope to excite the fluors only at a chosen point in the specimen while avoiding excitation above and below that chosen point, greatly reducing photobleaching and scatter. This permits specimens to be imaged much more deeply (up to 1,000  $\mu\text{m}$ ). This is especially important for accessing deeply embedded structures in living animals such as mice (i.e., *in vivo* microscopy). Finally, these advances are supported by a variety of low-level advances in instrumentation—for example, methods to maintain specimens at the correct temperature (37°C for mammalian specimens), humidity, and gaseous mixture; surgical techniques to create optical access to structures for chronic imaging with correct alignment from one temporal sample to the next (aligned chronic observation windows); and such other technologies.

Prima facie, the technology of direct time-lapse imaging, may appear complex and expensive, but it has several powerful advantages. First, a single time-lapse series is far more informative than hundreds of temporal snapshots from different specimens, since it allows us to track the behaviors of individual cells/organelles accurately. Indeed, the traditional method can easily miss/hide subtle dynamic phenomena. From the representation standpoint, temporal associations do not pose any unforeseen difficulties, since the graph-theoretic approach illustrated in Figure 5.11 remains valid. Specifically, the links now imply associations over time. So the overall graph of associations can contain spatial as well as temporal associations. There are two basic approaches for defining associations over time. In the first case, a living specimen is imaged over time using time-lapse microscopy. If the sampling frequency is high enough, the changes from one temporal sampling



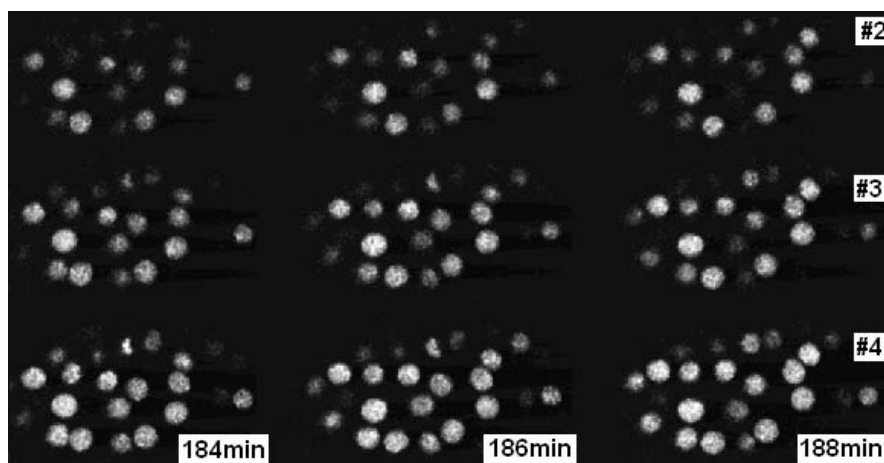


**Figure 5.11** Illustrating the natural graph-theoretic interpretation of associative measurements.

point (a frame) are modest, and it becomes possible to detect changes and track objects.

Figure 5.12 shows three sample snapshots from a much longer movie of 3-D time-lapse imaging of a developing *C. elegans* nematode embryo at 184 minutes, 186 minutes, and 188 minutes. The histone (H1) in the nuclei of this embryo was tagged with green fluorescent protein (GFP) and imaged by a spinning disk confocal microscope at 2-minute intervals. Each 3-D image frame is an image stack with 63 focal planes (at 6 pixels/ $\mu\text{m}$ ). The cells divide and migrate in a complex pattern as the embryo develops. There is a compelling need to segment and count these cells, track and map their spatio-temporal migration patterns, and compute the exact lineage of each cell [120]. The problem of segmenting nuclei in confocal images has been discussed in the previous section, and by many other authors [121].

The problem of tracking a large and growing population of cells in a developing embryo is, in principle, a multiple-hypothesis tracking problem in 3-D space [122]. Methods of multiple-cell tracking in literature can be generally classified into two categories. The first category consists of methods such as active contours [123] and Kalman filtering, in which one identifies individual cells in the first time-point stack and then follows each segmented cell independently throughout the rest of

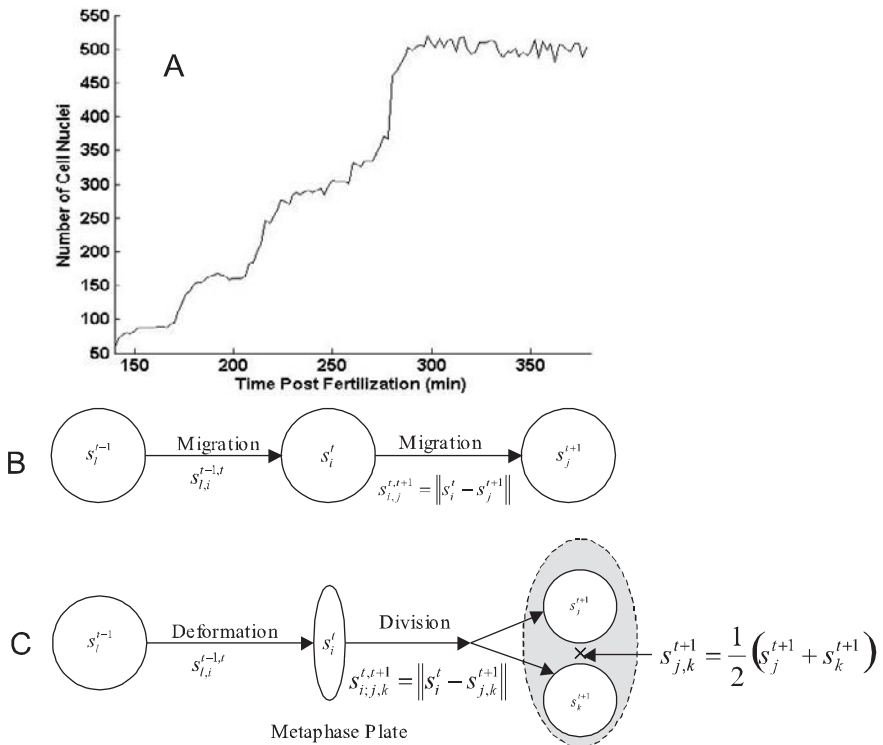


**Figure 5.12** Three sample frames from a much longer 4-D movie recording of a histone H1::GFP tagged *C. elegans* embryo at three time-points (184~188 minutes) and 3 focal planes (#2~#4). (Courtesy of William Mohler, University of Connecticut.)

the image sequence. This conceptually straightforward method can accurately link corresponding cells that migrate smoothly in spatial and temporal domains. However, it is prone to errors when handling abrupt events cell division, in which case the smoothness assumption fails to hold. The second category involves detecting cells in each stack independently (or otherwise), followed by an object-association computation to find corresponding cells in temporally contiguous image stacks. This strategy can naturally deal with topology changes stack by stack, and enables automated lineage analysis. We next describe a simplified multiple-cell-tracking algorithm from the second category.

Figure 5.13(a) shows a plot of cell counts obtained from segmenting the nuclei in the 4-D data shown in Figure 5.12. The segmentation also results in a vector of features for each nucleus, including its  $(x, y, z)$  coordinates, volume, average intensity, texture (standard deviation of intensity gradient), surface area, convexity, shape factor, and eccentricity, that can be used for correspondence estimation. These features can be broadly divided into two subsets—the spatial subset and the morphological subset.

Consider the following simplified model—a cell can either migrate (Figure 5.13(b)) or divide into two daughter cells (Figure 5.13(c)). This defines two possible hypotheses: (1)  $H_M$ : the cell has migrated, which calls for a 1-to-1 matching; (2)  $H_D$ : the cell has divided, which calls for a 1-to-2 matching. Events such as



**Figure 5.13** Steps in the analysis of the *C. elegans* dataset. (a) Plot of cell counts as a function of time, as determined by automated nuclear segmentation. (b) The model for cell migration. (c) The model for cell division.

apoptosis and other imaging-related events such as entry/exit of cells relative to the field of the microscope will be discussed later.

We proceed to describe a Bayesian approach to describing the patterns of cell migration and division. Let  $s_l^{t-1}$ ,  $s_i^t$  &  $s_j^{t+1}$  denote the spatial locations of corresponding nuclei detected in frames  $(t-1)$ ,  $t$ , &  $(t+1)$ , respectively. Let  $s_{l,i}^{t-1,t}$  and  $s_{i,j}^{t,t+1}$  denote the displacements between the corresponding points of time (i.e.,  $s_{i,j}^{t,t+1} = \|s_i^t - s_j^{t+1}\|$ ). Then, a simple approach to modeling displacements associated with cell migrations is based on assuming normality and can be written as follows:

$$d_M(i^t, j^{t+1}) = (s_{i,j}^{t,t+1} - \mu_s)^T \Sigma_s^{-1} (s_{i,j}^{t,t+1} - \mu_s)$$

where  $\Sigma_s$  is a covariance matrix, and  $\mu_s$  is the mean of 3-D displacement learned from a training set. In the case of a cell division, the dividing (mother) cell first forms a distinctive elongated metaphase plate [Figure 5.13(c)], and then splits to form two daughter cells, denoted  $j$  and  $k$ , respectively. A simple approach to modeling this event (again, assuming normality) is to describe it in terms of the deformation associated with formation of the metaphase plate, as follows:

$$d_{deform}(l^{t-1}, i^t) = (m_{l,i}^{t-1,t} - \mu_m)^T \Sigma_m^{-1} (m_{l,i}^{t-1,t} - \mu_m)$$

where  $m_{l,i}^{t-1,t} = \|m_l^{t-1} - m_i^t\|$  is the change in one or more morphological feature(s) between time  $(t-1)$  &  $t$ , and  $(\mu_m, \Sigma_m)$  are learned from training examples. To describe the cell splitting between times  $(t-1)$  &  $t$ , one simple approach is to assume that the point midway between the centroids of the daughter cells  $s_{j,k}^{t+1} = \frac{1}{2}(s_j^{t+1} + s_k^{t+1})$  moves in a manner not unlike a migrating cell, but with a different set of parameters  $(\mu_{div}, \Sigma_{div})$ . This can be described by the following model:

$$d_{split}(i^t, j^{t+1}, k^{t+1}) = (s_{i,j,k}^{t,t+1} - \mu_{div})^T \Sigma_{div}^{-1} (s_{i,j,k}^{t,t+1} - \mu_{div})$$

There are additional constraints available. For example, nuclear texture is an indicator of the state of the cell in the cell cycle. Nuclei with texture value larger than a preset threshold are probably undergoing cleavage. For each possible splitting nucleus in  $I_t$ , we exhaustively search two cells as the candidates for daughter cells within a small neighborhood  $R$  in  $I_{t+1}$ . Another constraint is the length of the cell cycle (28–30 minutes). A cell is unlikely to divide much faster than the known cell cycle rate. A cell has at most two successors and only one ancestor. Forbidden cell behaviors include disappearance without cell death and appearance without cell division.

The dissimilarity measures and constraints described here can form the basis for correspondence estimation. A migrating cell has one and only one correspondence with a cell in the next stack. For this case, a conventional assignment method (e.g., the Hungarian Algorithm [124]) often leads to satisfactory results. In case of cell division, we must extend this idea to 1-to-2 mapping, in order to match a splitting cell with its daughter cells. In a forward-tracking framework, we aim to match  $N$  nuclei detected in the image stack  $I_t$  with  $M$  nuclei segmented in next stack  $I_{t+1}$ , based on an appropriate resemblance measure, where  $i = 1, \dots, N$ ;  $j = 1, \dots,$

M. This  $N$ -to- $M$  ( $N \neq M$ ) matching task turns out to be a rectangular assignment problem that can be solved optimally by linear programming.

To determine the optimal set of matches between two successive time point stacks, we use an algorithm designed by Al-Kofahi et al. [125], integrating all feasible cell movement and division hypotheses, and formulating the rectangular assignment problem as follows. Given  $M$  cells in  $I^t$  and  $N$  cells in  $I^{t+1}$  with  $L$  hypotheses and their dissimilarity scores, we construct a matrix  $A$  of size  $L \times (M + N)$ . Each row corresponds to a feasible cell migration or division hypothesis. The first  $M$  columns correspond to cells in  $I^t$ , while the remaining  $N$  columns correspond to cells in  $I^{t+1}$ . For a row that represents a match between cells  $i^t$  and  $j^{t+1}$  under a movement hypothesis (e.g.,  $1 \rightarrow 1$  in Table 2.1), its dissimilarity score is evenly split between columns  $i$  and  $M + j$  of this row, and the remaining columns are set to zero. For a row that represents the division hypothesis of cell  $i^t$  into cells  $m^{t+1}$  and  $n^{t+1}$ , the score is evenly distributed among columns  $i$ ,  $M + m$ , and  $M + n$  of this row, while the remaining columns are set to zero. Therefore, the matching problem turns out to be a search for a subset of rows in matrix  $A$ , such that the summation of entries in these rows is minimized. The optimal subset is found by solving the following integer programming problem [125]:

$$\min_x (Av)^T x \text{ subject to } B^T x \leq v \quad (5.8)$$

The solution  $x$  is a binary vector of size  $L \times 1$ , where

$$x_k = \begin{cases} 1 & \text{if the row } k \text{ is in the optimal subset} \\ 0 & \text{otherwise} \end{cases} \quad k = 1, \dots, L$$

$v$  is a vector of ones of size  $(M + N) \times 1$ :

$$v = (1 \ 1 \ \dots \ 1)^T$$

$B$  is a binary matrix of the same size as  $A$ , whose entry is defined by:

$$B_{i,j} = \begin{cases} 1 & \text{if } A_{i,j} > 0 \\ 0 & \text{otherwise} \end{cases}$$

The probable outputs of the algorithm are generally divided into following cases:

1. 1-to-1 matches corresponding to cell migration;
2. 1-to-2 matches representing cell division;

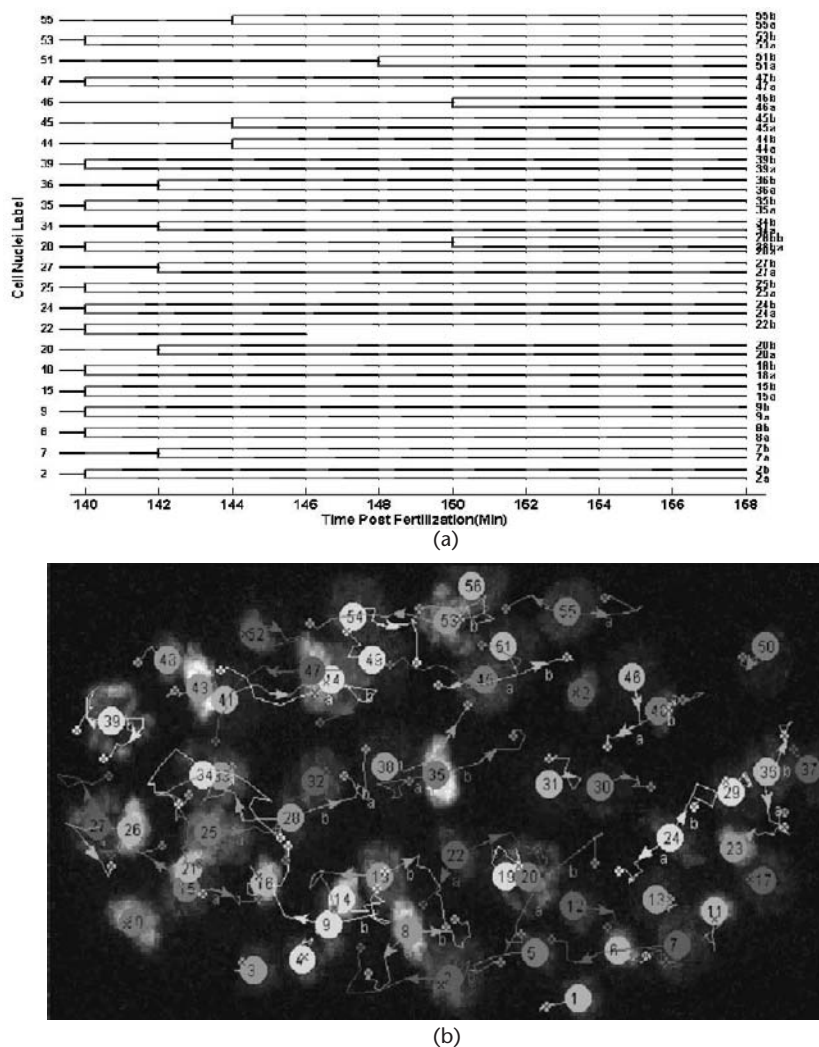
3. 1-to-0 when a cell in  $I_t$  cannot find any descendent in  $I_{t+1}$ ;
4. 0-to-1 when a cell in  $I_{t+1}$  does not have any correspondence in  $I_t$ .

When case 3 occurs under the assumption that no cell moves off the image scene of microscopy, there are two possibilities: either the cell is dead after the time point  $t$  and shrinks to disappear since then, or the cell is present in  $I_{t+1}$  but undetected during segmentation. Sulston et al. [126, 127] presented a figure of marker events versus number of cells during embryogenesis of *C. elegans*, from which the first cell death generally happens no earlier than 300-cells stage. Based on this ground truth, in our tracking experiment from 56-cell to 90-cell stage, case 3 always implies a momentary missing detection error in  $I_{t+1}$  rather than a real cell death event. To eliminate this error, for the cell  $i_t$  undetected in  $I_{t+1}$ , we buffer its lineage path from the origin to time point  $t$ , copy the feature vector  $f_i^t = (x_i^t, y_i^t, z_i^t, T_i^t)$  in  $I_t$ , virtually insert it into  $I_{t+1}$ , and continue the matching procedure afterward. If the missed cell is matched in subsequent frames of  $I_{t+1}$ , we simply integrate the correspondence into the buffered lineage path to build a complete track for the cell.

We also assume that no cell enters the field of view, so that the number of cells in a stack increases only if a cell division event happens (i.e., no cell emerges spontaneously). So, case 4 in our experiment is considered a false positive arising from segmentation error, which calls for refinement before we construct cell lineage tree. Cells in  $I_{t+1}$  that are not assigned to any cells in  $I_t$  are simply eliminated from our tracking procedure thereafter.

Cell lineage describes the embryonic history of *C. elegans*, beginning with a single fertilized zygote, splitting into two daughter cells, and then dividing into more descendents to a multicellular adult finally [128]. The result of multiple-cell tracking enables us to link a cell's predecessor and its successors in a time series, and track them forward and backward over time. The ancestor-descendent relationship is intuitively depicted by means of a family tree. Figure 5.5 shows an example of cell lineage tree: The cell  $i^t$  represented by the root node splits into two child nodes  $m^{t+1}$  and  $n^{t+1}$ . At the successive time point,  $m^{t+1}$  moves to  $h^{t+2}$  with no cleavage, while  $n^{t+1}$  divides into two subnodes  $j^{t+2}$  and  $k^{t+2}$ . Figure 5.14(a) shows a partial lineage map obtained from the 4-D image series. Figure 5.14(b) shows the pattern of cell migrations for embryogenesis stage: 56-cells  $\sim$  90-cells (time span: 140  $\sim$  170 minutes postfertilization). Of the 34 cell division events, the automated method missed one division.

The worm example described earlier contained a single fluorescent protein. By leveraging recent advances in multiphoton time-lapse microscopy, and multiplex fluorescent protein labeling, Bousso et al. [129] have developed the technology to perform direct imaging of multiple structural and functional molecules in living specimens over extended durations. Their system can record five-dimensional movies (3-D space, time, spectra) revealing the activities of multiple cell types and vasculature in their full 3-D and changing multicellular habitat. Figure 5.15 shows one sample frame (2-D projection of a 3-D image at a single point in time) from a 5-D movie of the active thymic microenvironment. The full 5-D movie shows the complex migration and interaction patterns occurring in a crowded field of

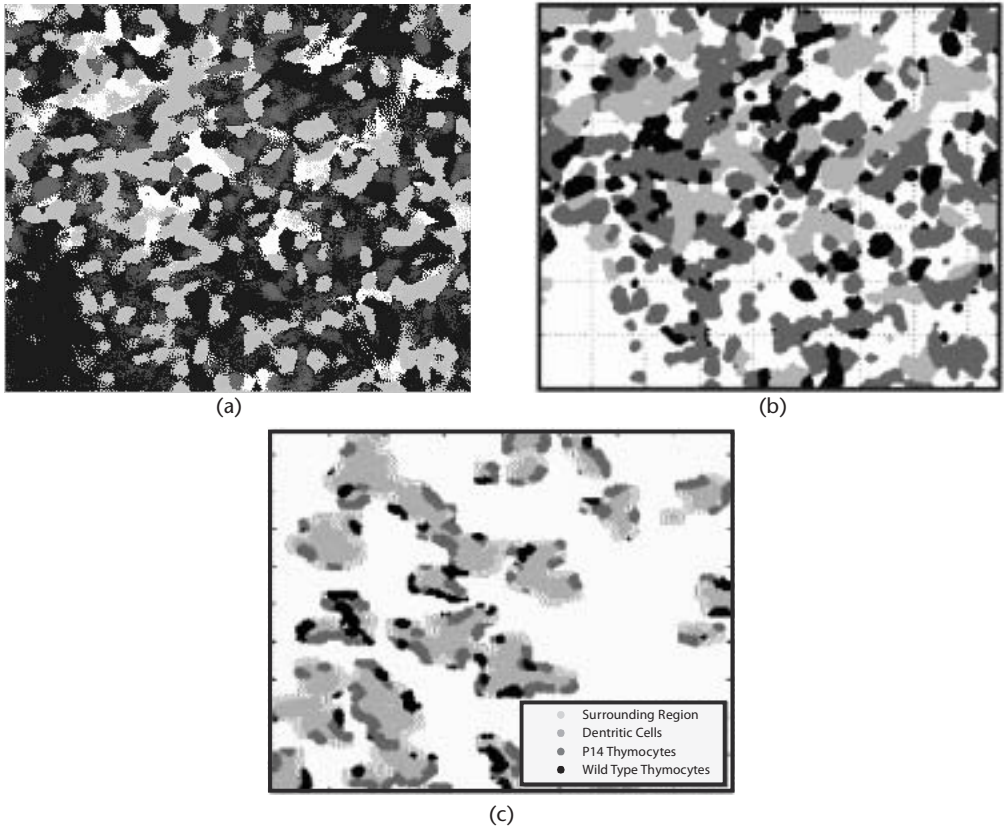


**Figure 5.14** Two methods to visualize segmentation and tracking results: (a) Partial color-coded lineage map for 18 minutes (140–158 minutes post fertilization). (b) Combined map for 30 minutes showing initial cell locations as numbered circles, arrows indicating migration paths, and crosses indicating final locations of cells, overlaid on a maximum-value projection of the initial image. The complete results can be visualized with 3-D interactive graphics and over time as a movie on a computer screen.

wild-type and genetically modified (P14) thymocytes, as well as dendritic cells in the developing thymic lobe of a mouse, allowing the cell interaction processes to be studied in relationship to the vasculature for the first time.

A single 5-D movie is vastly more informative than several hundred or more lower-dimensional images, since it records the activities of multiple cell types in a manner that preserves their full spatial and temporal context. Multiple movies can reveal aspects of the normal immune system and the effects of genetic/pharmacological manipulations. Figure 5.15 is a static 2-D projection of just one





**Figure 5.15** (a) 2-D projection of one frame from a 5-D movie showing YFP expressing dendritic cells (DCs, shown in yellow), P14 thymocytes (green), and wild-type thymocytes (blue); (b) segmentation results; and (c) analysis of cell-cell interactions, an instance of spatial association at each time sample. In the presented grayscale version the various colors are mapped as follows: green to light gray, blue to dark gray, and yellow to white. (Data courtesy of Ellen Robey, UC Berkeley.)

frame from a 5-D movie recording the complex migration and interaction patterns occurring in a crowded field of wild-type (blue) and genetically modified (P14) thymocytes (green), and dendritic cells (YFP) in the developing thymic lobe of a mouse. In this case, cell segmentation and tracking must be performed for each channel after spectral unmixing. After this, it becomes possible to quantify associations in space between cell types. In this case, the cell-cell interaction frequencies and durations are of interest.

## 5.5 Validation of Automated Image Analysis Results

Validating the results of automated segmentation and tracking is of obvious importance [130,131]. The classical approach to validation is to compare automated results to “ground truth data” that is known to be an accurate result. The notion of ground truth is appealing in principle but elusive in practice. One approach to



ground truth generation is to create a phantom image (or image sequence) with known parameters. This is helpful for evaluating several aspects of image analysis algorithms (e.g., performance as a function of signal-to-noise ratios) and specific morphological characteristics of objects.

Once an algorithm is validated in this manner and applied to real-world datasets, there still remains the problem of assessing the performance of the algorithm, and, importantly, performing some form of quality control so that the results from automated image analysis are sufficiently accurate for the biological investigator to use in his/her studies. A practical strategy for validating automated image analysis results for real data is to use the currently best-available “gold standard.” In this regard, the human observer continues to be the most widely accepted and versatile gold standard, since the human visual system remains unbeatable for visual tasks. This is not to imply that the human observer is perfect—this is far from true, as we discuss further later. Given an image and a stated task (e.g., an image containing fluorescently labeled cell nuclei that must be counted), it is possible to run the automated image analysis algorithms to produce a set of results—we denote them **A**. Then, the same images can be handed over to a human observer who produces a set of results—we denote them **H**. *Prima facie*, the difference between **A** and **B** can provide us with an assessment of the accuracy of **A**. However, this assumes that **H** is possible and perfect. In practice, many image analysis tasks are extremely difficult to conduct manually. This is particularly true of time-lapse 3-D and multichannel data (e.g., the data shown in Figure 5.15). When manual analysis is possible, **H** is subject to errors from at least two sources—*intersubject variations* and *intrasubject variations*. The former are understandable—individuals vary greatly in their manual image analysis abilities. The latter are surprising to many—the same individual may produce different results on two different days for the same image. Many human factors, including the level of attentiveness, fatigue, habituation, and focus, cause variations in results.

To minimize intersubject errors, it is desirable to employ “expert observers” who are known to be particularly adept, given their deep knowledge and familiarity with the nature of the image data. On the other hand, even an expert observer can be undesirable at times—this is the issue of disinterest. In this regard, it is particularly undesirable for the algorithm developer to validate his/her own results. In statistical terms, a disinterested expert observer’s analysis has the lowest possible bias and variance. The bias of the disinterested observer is low, whereas an observer with a personal agenda may have an unacceptable bias. Recognizing and obtaining the services of expert observers who are also demonstrably disinterested is notoriously difficult.

One approach to overcome intersubject errors is to hand the image to multiple independent observers, say,  $N$  of them, who analyze the image without consulting each other and produce a set of results—we denote them  $\{\mathbf{H}_1, \mathbf{H}_2, \dots, \mathbf{H}_N\}$ . Any protocol that uses multiple observers is termed *multiobserver validation*, and is de rigueur for good quality work. One can imagine many ways to compare **A** against  $\{\mathbf{H}_1, \mathbf{H}_2, \dots, \mathbf{H}_N\}$ , and several approaches have been described in the literature. The main difficulty is the handling of conflicting assessments. For example,

one observer may count a cell, whereas another may not, and have a well-reasoned justification for doing so.

One practical protocol for multiobserver validation that we have used with great success is to convene a meeting the  $N$  observers and request that they discuss their differing assessments and arrive at a multiobserver consensus, denoted  $H^*$ . Now,  $A$  can be compared against  $H^*$ . Given the very nonlinear nature of consensus building, it is nearly impossible to quantitatively establish the bias and variance of  $H^*$  compared to  $H$  or  $\{H_1, H_2, \dots, H_N\}$ . However, our experience (aided by common sense) indicates that the multiobserver consensus represents one of the best-available gold standards today. This is most useful when newly developed algorithms are being evaluated for the first time.

The main limitations of multiobserver consensus is cost (primarily since manpower is generally expensive) and slowness. It cannot be scaled easily to large-scale and/or high-throughput studies. Actually, the greatest limitation of multiobserver validation as outlined here is that it only provides an assessment of how an algorithm performs in general over a chosen ensemble of images but does not tell us anything about how accurate  $A$  is for a specific image that is not in the chosen ensemble. Arguably, this “quality control” type of question is the most germane and important in a real-world application, since the answer to this question determines whether or not the biological investigator chooses to use the automated analysis results for his/her biological investigations. Practically speaking, the professional goal of image analysts is to develop algorithms and software that are actually adopted by biological researchers in their scientific investigations. This has remained a challenge even after many years of progress. It is fair to state that overcoming the “adoption barrier” remains one of the greatest challenges for computational image analysts and computer vision researchers. This is an issue with surprising complexity that includes not only objective factors such as measurable performance of algorithms, but also subjective and cultural factors that are difficult to document precisely. In the following paragraphs, we describe fresh approaches to validation and performance assessment in the context of cell and tissue image analysis.

The *edit-based validation* protocol is designed for practical operational use (i.e., for evaluating the quality of an automated image analysis result  $A$  for a specific image on which the algorithm(s) in question has been run for the first time). This methodology is most appropriate for mature algorithms that are generally expected to produce results with a high accuracy (typically in the 90–100 percent range). If such performance levels are indicated by a quick visual survey, it makes intuitive sense to simply edit the automated results to correct the few errors that remain. If the list of user edits is denoted  $E$ , then the application of these edits to the automated result  $A$  produces results, denoted  $E(A)$ , that are acceptable to the biological investigator. A reasonable expectation in this regard is that the effort required to edit will scale with the error rate of the automated algorithm, rather than the size/complexity of the image. For instance, if the algorithm’s performance improves from 90 percent to 95 percent, the user’s effort is halved. This implies that edit-based validation can be very scalable.

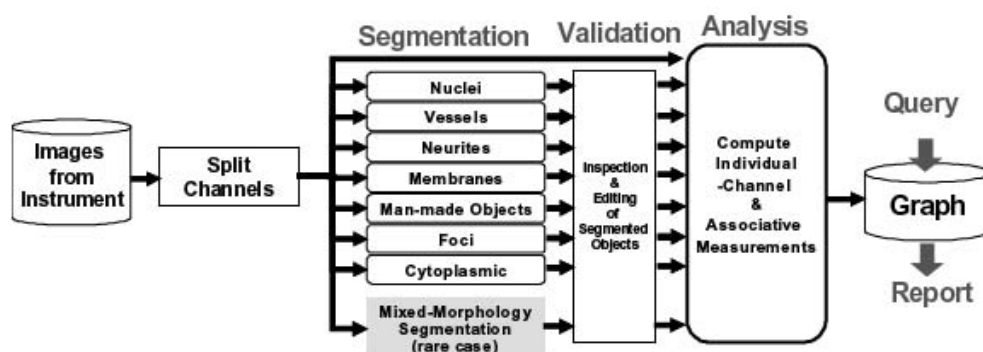
Aside from the effort factor, the edit-based validation can overcome the adoption barrier, since the user has had a chance to inspect the automated results and

edit out any errors that were detected by visual inspection to his/her satisfaction. Even as the user edits the errors, it is straightforward to record them. This record provides a very detailed performance assessment that can be analyzed to uncover algorithm flaws and opportunities for improvement. We have found these facts to be generally true in our experience. There is plenty of opportunity to optimize edit-based validation. In general, better visualization of the automated results in the context of the original image data leads to better detection/assessments of errors. In a similar vein, there is plenty of opportunity to make the editing operations efficient by automating repetitious/group operations. Better computer graphics tools can improve visualization and reduce the effort involved in editing. Finally, there is the opportunity to learn from patterns of user edits and improve segmentation results based on the learning.

Notwithstanding its many advantages, the idea of edit-based validation is nevertheless fraught with a few caveats, none of which, fortunately, are overwhelming. First, the subjectivity of the user remains—and it is reasonable to expect intra- and interobserver variations. In this regard, multiobserver edit-based protocols can be considered. For example, a consensus of editors may make sense in some applications. A more streamlined form of validation would be to use just two editors. After the first round of editing, presumably done by a junior investigator/technician, a second “supervisory” inspection and editing can be performed by a senior investigator. Another error that is peculiar to edit-based protocols is the detection threshold—errors that are either subvisual or subtle may be ignored by the user even if he/she is aware of them. In general, the user will choose to edit only the errors that are perceived to influence the biological conclusions of the investigation.

## 5.6 Summary, Discussion, and Future Directions

The idea of associative image analysis is now feasible and appropriate for meeting the quantification needs of a new generation of biological studies that are attempt-



**Figure 5.16** Summarizing the FARSIGHT “divide-and-conquer” framework for processing multi-dimensional microscope images to extract meaningful insights driven by queries posed on a graph data structure that brings together intrinsic and associative spatio-temporal measurements.

ing to understand complex and dynamic biological systems. Although diverse and arcane forms of associative measurements can be imagined, we are finding that even the simplest forms are immediately useful. Happily, all forms of associations can be represented in a common and versatile form offered by graph theory. Graphs can be queried in simple and sophisticated ways to yield actionable insights. In summary, we envision future image analysis systems as providing an end-to-end solution by allowing a biological investigator to go all the way from images to actionable insights. Figure 5.16 brings together many of the ideas discussed in this chapter, and provides a roadmap for building future image analysis systems. In our work, we use the acronym FARSIGHT to describe our integrative modular framework. Translating this conceptual framework to a software framework is the focus of our current work.

## References

- [1] Quinones-Hinojosa, A., "Cellular Composition and Cytoarchitecture of the Adult Human Subventricular Zone: A Niche of Neural Stem Cells," *J. Comp. Neurol.*, Vol. 494, No. 3, 2006, pp. 415-434.
- [2] Fuchs, E., and G. Guasch, "Socializing with the Neighbors: Stem Cells and Their Niche," *Cell*, Vol. 116, 2004, pp. 769-778.
- [3] Brown, E. B., et al., "In Vivo Measurement of Gene Expression, Angiogenesis and Physiological Function in Tumors Using Multiphoton Laser Scanning Microscopy," *Nature Medicine*, Vol. 7, No. 7, 2001, pp. 864-868.
- [4] So, P. T., et al., "Two-Photon Excitation Fluorescence Microscopy," *Annual Review of Biomedical Engineering*, Vol. 2, 2000, pp. 399-429.
- [5] Zipfel, W.R., R.M. Williams, and W. W. Webb, "Nonlinear Magic: Multiphoton Microscopy in the Biosciences," *Nat. Biotechnol.*, Vol. 21, No. 11, 2003, pp. 1369-177.
- [6] Hell, S. W., "Toward Fluorescence Nanoscopy," *Nat. Biotechnol.*, Vol. 21, No. 11, 2003, pp. 1347-1355.
- [7] Dumas D., and J. F. Stoltz, "New Tool to Monitor Membrane Potential by FRET Voltage Sensitive Dye (FRET-VSD) Using Spectral and Fluorescence Lifetime Imaging Microscopy (FLIM): Interest in Cell Engineering," *Clin. Hemorheol. Microcirc.*, Vol. 33, No. 3, 2005, pp. 293-302.
- [8] Wallrabe, H, and A. Periasamy, "FRET-FLIM Microscopy and Spectroscopy in the Biomedical Sciences," *Current Opinion in Biotechnology*, Vol. 16, 2005, pp. 19-27.
- [9] Chen, Y., M. Elangovan, and A. Periasamy, "FRET Data Analysis: The Algorithm," in *Molecular Imaging: FRET Microscopy and Spectroscopy*, A. Periasamy and R. N. Day, (eds.), Oxford, U.K.: Oxford University Press, 2005.
- [10] Shaner, N. C., P. A. Steinbach, and R. Y. Tsien, "A Guide to Choosing Fluorescent Proteins," *Nat. Methods*, Vol. 2, No. 12, 2005, pp. 905-909.
- [11] Bjornsson C. S., et al., "Effects of Insertion Conditions on Tissue Strain and Vascular Damage During Neuroprosthetic Device Insertion," *J. Neural Eng.*, Vol. 3, No. 3, 2006, pp. 196-207.
- [12] Shain W., et al., "Controlling Cellular Reactive Responses Around Neural Prosthetic Devices Using Peripheral and Local Intervention Strategies," *IEEE Trans. Neural Syst. Rehabil. Eng.*, Vol. 11, No. 2, 2003, pp. 186-188.
- [13] Bear, M. F., *Neuroscience: Exploring the Brain*, Baltimore, MD: Lippincott Williams & Wilkins, 2006.

- [14] Spataro L., et al., "Dexamethasone Treatment Reduces Astroglia Responses to Inserted Neuroprosthetic Devices in Rat Neocortex," *Exp. Neurol.*, Vol. 194, No. 2, 2005, pp. 289-300.
- [15] Dickinson, M., et al., "Multi-Spectral Imaging and Linear Unmixing Add a Whole New Dimension to Laser Scanning Fluorescence Microscopy," *BioTechniques*, Vol. 31, No. 6, 2001, pp. 1272-1278.
- [16] Becker, D. E., et al., "Automated 3-D Montage Synthesis from Laser-Scanning Confocal Images: Application to Quantitative Tissue-Level Cytological Analysis," *Cytometry*, Vol. 25, No. 3, 1996, pp. 235-245.
- [17] Ziv, N. E., and S. J. Smith, "Evidence for a Role of Dendritic Filopodia in Synaptogenesis and Spine Formation," *Neuron*, Vol. 17, No. 1, 1996, pp. 91-102.
- [18] Diaspro, A., *Confocal and Two-Photon Microscopy: Foundations, Applications, and Advances*, New York: Wiley-Liss, 2002.
- [19] Matsumoto, B., American Society for Cell B., *Cell Biological Applications of Confocal Microscopy*, New York: Academic Press, 2002.
- [20] Sheppard C., D. Shotton, and Royal Microscopical Society (Great Britain), *Confocal Laser Scanning Microscopy*, Oxford, U.K.: BIOS Scientific Publishers, New York: Springer, 1997.
- [21] Dickinson, M., "Multiphoton, Multispectral Laser Scanning Microscopy," in *Live Cell Imaging: A Laboratory Manual*, R. D. Goldman and D. S. Spector, (eds.), New York: Cold Spring Harbor Laboratory Press, 2005.
- [22] Hogenboom, D. O., et al., "Three-Dimensional Images Generated by Quadrature Interferometry," *Optics Letters*, Vol. 23, No. 10, 1998, pp. 783-785.
- [23] Holmes, T. J., et al., "Light Microscopic Images Reconstructed by Maximum Likelihood Deconvolution," in *Handbook of Confocal Microscopy*, Vol. 2, J. Pawley (ed.), New York: Plenum Press, 1995.
- [24] Zimmermann, T., et al., "Spectral Imaging and Linear Un-Mixing Enables Improved FRET Efficiency with a Novel GFP2-YFP FRET Pair," *FEBS Lett.*, Vol. 531, No. 2, 2002, pp. 245-249.
- [25] Zimmermann, T., J. Rietdorf, and R. Pepperkok, "Spectral Imaging and Its Applications in Live Cell Microscopy," *FEBS Lett.*, Vol. 546, No. 1, 2003, pp. 87-92.
- [26] Brown, E., "Dynamic Imaging of Collagen and Its Modulation in Tumors In Vivo Using Second-Harmonic Generation," *Nat. Med.*, Vol. 9, No. 6, 2003, pp. 796-800.
- [27] Campagnola, P. J., and L. M. Loew, "Second-Harmonic Imaging Microscopy for Visualizing Biomolecular Arrays in Cells, Tissues and Organisms," *Nat. Biotechnol.*, Vol. 21, No. 11, 2003, pp. 1356-1360.
- [28] Wu, C. C., "High-Throughput Morphometric Analysis of Individual Neurons," *Cereb. Cortex*, Vol. 14, No. 5, 2004, pp. 543-554.
- [29] Boris, M., et al., "Quantitative Cell Biology with the Virtual Cell," *TRENDS in Cell Biology*, Vol. 13, No. 11, 2003, pp. 570-576.
- [30] Kohane, I. S., A. T. Kho, and A. J. Butte, *Microarrays for an Integrative Genomics*, Cambridge, MA: MIT Press, 2003.
- [31] Shapiro, H. M., *Practical Flow Cytometry*, New York: Wiley-Liss, 2003.
- [32] Fraser, S. T., et al., "Using a Histone Yellow Fluorescent Protein Fusion for Tagging and Tracking Endothelial Cells in ES Cells and Mice," *Genesis*, Vol. 42, No. 3, 2005, pp. 162-171.
- [33] Sekar, R. B., and A. Periasamy, "Fluorescence Resonance Energy Transfer (FRET) Microscopy Imaging of Live Cell Protein Localization," *Journal of Cell Biology*, Vol. 160, 2003, pp. 629-633.

- [34] Ecker, R. C., and G. E. Steiner, "Microscopy-Based Multicolor Tissue Cytometry at the Single-Cell Level," *Cytometry*, Vol. 59A, No. 2, 2004, pp. 182-190.
- [35] Ecker, R. C., et al., "Application of Spectral Imaging Microscopy in Cytomics and Fluorescence Resonance Energy Transfer (FRET) Analysis," *Cytometry*, Vol. 59A, No. 2, 2004, pp. 172-181.
- [36] Valet, G. J., F. Leary, and A. Tarnok, "Cytomics—New Technologies: Towards a Human Cytochrome Project," *Cytometry*, Vol. 59A, No. 2, 2004, pp. 167-171.
- [37] Bard, J., "SYRaMA: An Ontology for Cell Types," *Genome Biology*, Vol. 6, No. 2, 2005.
- [38] Hucka, M., et al., "The Systems Biology Markup Language (SBML): A Medium for Representation and Exchange of Biochemical Network Models," *Bioinformatics*, Vol. 19, No. 4, 2003, pp. 524-531.
- [39] Pumiglia, K., and S. Temple, "PEDF: Bridging Neurovascular Interactions in the Stem Cell Niche," *Nat. Neurosci.*, Vol. 9, No. 3, 2006, pp. 299-300.
- [40] Shen, Q., et al., "Endothelial Cells Stimulate Self-Renewal and Expand Neurogenesis of Neural Stem Cells," *Science*, Vol. 304, No. 5675, 2004, pp. 1338-1340.
- [41] Temple, S., and X. Qian, "Vertebrate Neural Progenitor Cells: Subtypes and Regulation," *Curr. Opin. Neurobiol.*, Vol. 6, No. 1, 1996, pp. 11-17.
- [42] Fukumura, D., and R. K. Jain, "Tumor Microenvironment Abnormalities: Causes, Consequences, and Strategies to Normalize," *J. Cell Biochem.*, 2006.
- [43] Shapiro, B. E., et al., "MathSBML: A Package for Manipulating SBML-Based Biological Models," *Bioinformatics*, 2004.
- [44] Björn Nilsson, A. H., "Segmentation of Complex Cell Clusters in Microscopic Images: Application to Bone Marrow Samples, Part A," *Cytometry*, Vol. 66A, No. 1, 2005, pp. 24-31.
- [45] Baggett, D., et al., "Whole Cell Segmentation in Solid Tissue Sections, Part A," *Cytometry*, Vol. 67A, No. 2, 2005, pp. 137-143.
- [46] Cong, G., and B. Parvin, "Model-Based Segmentation of Nuclei," *Pattern Recognition*, Vol. 33, No. 8, 2000, pp. 1383-1393.
- [47] Lee, K.-M., and W. N. Street, "Model-Based Detection, Segmentation, and Classification for Image Analysis Using On-Line Shape Learning," *Machine Vision and Applications*, Vol. 13, No. 4, 2003, pp. 222-233.
- [48] Lin, G., et al., "Hierarchical, Model-Based Merging of Multiple Fragments for Improved Three-Dimensional Segmentation of Nuclei," *Cytometry*, Vol. 63, No. 1, 2005, pp. 20-33.
- [49] Pizer, S. M., et al., "Segmentation, Registration, and Measurement of Shape Variation Via Image Object Shape," *IEEE Trans. on Med. Imaging*, Vol. 18, No. 10, 1999, pp. 851-865.
- [50] Ezquerro, N., and R. Mullick, "Knowledge-Guided Segmentation of 3D Imagery," *Graphical Models and Image Processing*, Vol. 58, No. 6, 1996, pp. 510-523.
- [51] Bernard, R., M. Kanduser, and F. Pernus, "Model-Based Automated Detection of Mammalian Cell Colonies," *Physics in Medicine and Biology*, Vol. 46, 2001, pp. 3061-3072.
- [52] Chassery, J., and C. Garbay, "An Iterative Segmentation Method Based on a Contextual Color and Shape Criterion," *IEEE Trans. on Pattern Analysis and Machine Intelligence*, Vol. 6, No. 6, 1984, pp. 794-800.
- [53] Liu, L. S. S., *Region Segmentation Via Deformable Model-Guided Split and Merge*, Boston University Computer Science Technical Report 2000, No. 2000-24.
- [54] Mitchell, S. C., "3-D Active Appearance Models: Segmentation of Cardiac MR and Ultrasound Images," *IEEE Trans. on Medical Imaging*, Vol. 21, No. 9, 2002, pp. 1167-1178.



- [55] McInerney, T., and D. Terzopoulos, "Deformable Models in Medical Image Analysis: A Survey," *Medical Image Analysis*, Vol. 1, No. 2, 1996, pp. 91-108.
- [56] Staib, L. H., and J. S. Duncan, "Model-Based Deformable Surface Finding for Medical Images," *IEEE Trans. on Medical Imaging*, Vol. 15, No. 5, 1996, pp. 720-731.
- [57] Ghanei, A., and H. Soltanian-Zadeh, "A Discrete Curvature-Based Deformable Surface Model with Application to Segmentation of Volumetric Images," *IEEE Trans. on Information Technology in Biomedicine*, Vol. 6, No. 4, 2002, pp. 285-295.
- [58] Niessen, W. J., B. M. ter Haar Romeny, and M. A. Viergever, "Geodesic Deformable Models for Medical Image Analysis," *IEEE Trans. on Med. Imaging*, Vol. 17, No. 4, 1998, pp. 634-641.
- [59] Osher, S. J. F. R., *Level Set Methods and Dynamic Implicit Surfaces*, New York: Springer, 2002.
- [60] Suri, J. S., et al., "Shape Recovery Algorithms Using Level Sets in 2-D/3-D Medical Imagery: A State-of-the-Art Review," *IEEE Trans. on Inf. Technol. Biomed.*, Vol. 6, No. 1, 2002, pp. 8-28.
- [61] Jeong, J. W., et al., "Segmentation Methodology for Automated Classification and Differentiation of Soft Tissues in Multiband Images of High-Resolution Ultrasonic Transmission Tomography," *IEEE Trans. on Med. Imaging*, Vol. 25, No. 8, 2006, pp. 1068-1078.
- [62] Bertalmio, M., G. Sapiro, and G. Randall, "Region Tracking on Level-Sets Methods," *IEEE Trans. on Med. Imaging*, Vol. 18, No. 5, 1999, pp. 448-451.
- [63] Shi, J., and J. Malik, "Normalized Cuts and Image Segmentation," *IEEE Trans. on Pattern Analysis and Machine Intelligence*, Vol. 22, No. 8, 2000, pp. 888-905.
- [64] Lin, G., et al., "A Multi-Model Approach to Simultaneous Segmentation and Classification of Heterogeneous Populations of Cell Nuclei in 3D Confocal Microscope Images," *Cytometry*, Vol. 71, No. 9, 2007, pp. 724-736.
- [65] Malpica, N., et al., "Applying Watershed Algorithms to the Segmentation of Clustered Nuclei," *Cytometry*, Vol. 28, No. 4, 1997, pp. 289-297.
- [66] Breu, H. G. J., D. Kirkpatrick, and M. Werman, "Linear Time Euclidean Distance Transform Algorithms," *IEEE Trans. on Pattern Analysis and Machine Intelligence*, Vol. 17, No. 5, 1995, pp. 529-533.
- [67] Ancin, H., et al., "Advances in Automated 3-D Image Analyses of Cell Populations Imaged by Confocal Microscopy," *Cytometry*, Vol. 25, No. 3, 1996, pp. 221-234.
- [68] Lin, G., et al., "A Hybrid 3D Watershed Algorithm Incorporating Gradient Cues and Object Models for Automatic Segmentation of Nuclei in Confocal Image Stacks," *Cytometry*, Vol. 56, No. 1, 2003, pp. 23-36.
- [69] Parzen, E., "On the Estimation of a Probability Density Function and Mode," *Annals of Mathematical Statistics*, Vol. 33, 1962, pp. 1065-1076.
- [70] Duda, R. O., P. E. Hart, and D. G. Stork, *Pattern Classification*, New York: Wiley, 2001.
- [71] Alpaydin, E., *Introduction to Machine Learning*, Cambridge, MA: MIT Press, 2004.
- [72] Tutte, W. T., *Graph Theory*, New York: Cambridge University Press, 1984.
- [73] Lin, G., et al., "A Hybrid 3D Watershed Algorithm Incorporating Gradient Cues and Object Models for Automatic Segmentation of Nuclei in Confocal Image Stacks," *Cytometry*, Vol. 56A, No. 1, 2003, pp. 23-36.
- [74] Massoptier, L., and S. Casciaro, "Fully Automatic Liver Segmentation Through Graph-Cut Technique," *Conf. Proc. IEEE Eng. Med. Biol. Soc.*, Vol. 1, 2007, pp. 5243-5246.
- [75] Cohen, A. R., B. Roysam, and J. N. Turner, "Automated Tracing and Volume Measurements of Neurons from 3-D Confocal Fluorescence Microscopy Data (Pt. 2)," *J. Microsc.*, Vol. 173, 1994, pp. 103-114.



- [76] He, W., et al., "Automated Three-Dimensional Tracing of Neurons in Confocal and Brightfield Images," *Microsc. Microanal.*, Vol. 9, No. 4, 2003, pp. 296–310.
- [77] Al-Kofahi, K. A., et al., "Rapid Automated Three-Dimensional Tracing of Neurons from Confocal Image Stacks," *IEEE Trans. on Information Technology in Biomedicine*, Vol. 6, No. 2, 2002, pp. 171–187.
- [78] Al-Kofahi, K. A., et al., "Median-Based Robust Algorithms for Tracing Neurons from Noisy Confocal Microscope Images," *IEEE Trans. on Information Technology in Biomedicine*, Vol. 7, No. 4, 2003, pp. 302–317.
- [79] Can, A., et al., "Rapid Automated Tracing and Feature Extraction from Retinal Fundus Images Using Direct Exploratory Algorithms," *IEEE Trans. on Information Technology in Biomedicine*, Vol. 3, No. 2, 1999, pp. 125–138.
- [80] Wink, O., W. J. Niessen, and M. A. Viergever, "Multiscale Vessel Tracking," *IEEE Trans. on Med. Imaging*, Vol. 23, No. 1, 2004, pp. 130–133.
- [81] Suri, J. S., et al., "A Review on MR Vascular Image Processing: Skeleton Versus Nonskeleton Approaches: Part II," *IEEE Trans. on Inf. Technol. Biomed.*, Vol. 6, No. 4, 2002, pp. 338–350.
- [82] Tyrrell, J. A., et al., "Robust 3-D Modeling of Vasculature Imagery Using Superellipsoids," *IEEE Trans. on Medical Imaging*, Vol. 26, No. 2, 2007, pp. 223–237.
- [83] Tyrrell, J. A., et al., "A 2-D/3-D Model-Based Method to Quantify the Complexity of Microvasculature Imaged by In Vivo Multiphoton Microscopy," *Microvasc. Res.*, Vol. 70, No. 3, 2005, pp. 165–178.
- [84] Suri, J. S., et al., "White and Black Blood Volumetric Angiographic Filtering: Ellipsoidal Scale-Space Approach," *IEEE Trans. on Inf. Technol. Biomed.*, Vol. 6, No. 2, 2002, pp. 142–158.
- [85] Barr, A., "Superquadrics and Angle-Preserving Transformations," *IEEE Computer Graphics and Applications*, Vol. 1, No. 1, 1981, pp. 11–23.
- [86] Bardinet, E. A. N., and L. D. Cohen, "Fitting of Isosurfaces Using Superquadrics and Free-Form Deformations," *IEEE Workshop on Biomedical Image Analysis*, 1994, pp. 184–193.
- [87] Shoemake, K., "Animating Rotation with Quaternion Curves," *Computer Graphics*, Vol. 19, 1985, pp. 245–254.
- [88] Frangi, A. F., et al., "Quantitative Analysis of Vascular Morphology from 3D MR Angiograms: In Vitro and In Vivo Results," *Magn. Reson. Med.*, Vol. 45, No. 2, 2001, pp. 311–322.
- [89] Solina, F. B. R., "Recovery of Parametric Models from Range Images: The Case for Superquadrics with Global Deformations," *IEEE Trans. on Pattern Analysis and Machine Intelligence*, Vol. 12, No. 2, 1990, pp. 131–147.
- [90] Mahadevan, V., et al., "Robust Model-Based Vasculature Detection in Noisy Biomedical Images," *IEEE Trans. on Inf. Technol. Biomed.*, Vol. 8, No. 3, 2004, pp. 360–376.
- [91] Al-Kofahi, K. A., et al., "Median-Based Robust Algorithms for Tracing Neurons from Noisy Confocal Microscope Images," *IEEE Trans. on Inf. Technol. Biomed.*, Vol. 7, No. 4, 2003, pp. 302–317.
- [92] Al-Kofahi, Y., et al., "Improved Detection of Branching Points in Algorithms for Automated Neuron Tracing from 3D Confocal Images," *Cytometry*, Vol. 73, No. 1, 2008, pp. 36–43.
- [93] Al-Kofahi, K. A., et al., "Rapid Automated Three-Dimensional Tracing of Neurons from Confocal Image Stacks," *IEEE Trans. on Inf. Technol. Biomed.*, Vol. 6, No. 2, 2002, pp. 171–187.
- [94] Saha, P. K. U. J., "Optimum Image Thresholding Via Class Uncertainty and Region Homogeneity," *IEEE Trans. on Pattern Analysis and Machine Intelligence*, Vol. 23, No. 7, 2001, pp. 689–706.

- [95] Can, A., et al., "Attenuation Correction in Confocal Laser Microscopes: A Novel Two-View Approach (Pt. 1)," *J. Microsc.*, Vol. 211, 2003, pp. 67-79.
- [96] Adiga, P. S. U., and B. B. Chaudhuri, "Efficient Cell Segmentation Tool for Confocal Microscopy Tissue Images and Quantitative Evaluation of FISH Signals," *Microscopy Research and Technique*, Vol. 44, No. 1, 1999, pp. 49-68.
- [97] Aubele, M., et al., "Comparative FISH Analysis of Numerical Chromosome 7 Abnormalities in 5-Micron and 15-Micron Paraffin-Embedded Tissue Sections from Prostatic Carcinoma," *Histochem. Cell Biology*, Vol. 107, No. 2, 1997, pp. 121-126.
- [98] Carothers, A., "Counting, Measuring, and Mapping in FISH-Labelled Cells: Sample Size Considerations and Implications for Automation," *Cytometry*, Vol. 16, 1994, pp. 298-304.
- [99] Castleman, K. R., and B. S. White, "Dot Count Proportion Estimation in FISH Specimens," *Bioimaging*, Vol. 3, No. 2, 2001, pp. 88-93.
- [100] Chawla, M. K., et al., "3D-catFISH: A System for Automated Quantitative Three-Dimensional Compartmental Analysis of Temporal Gene Transcription Activity Imaged by Fluorescence In Situ Hybridization," *J. Neurosci Methods*, Vol. 139, No. 1, 2004, pp. 13-24.
- [101] Heintzmann, R., G. Kreth, and C. Cremer, "Reconstruction of Axial Tomographic High Resolution Data from Confocal Fluorescence Microscopy: A Method for Improving 3D FISH Images," *Analytical Cellular Pathology: the journal of the European Society for Analytical Cellular Pathology*, Vol. 20, No. 1, 2000, pp. 7-15.
- [102] Netten, H., et al., "FISH and Chips: Automation of Fluorescent Dot Counting in Interphase Cell Nuclei," *Cytometry*, Vol. 28, No. 1, 1997, pp. 1-10.
- [103] Solórzano, C. O. D., et al., "Automated FISH Spot Counting in Interphase Nuclei: Statistical Validation and Data Correction," *Cytometry*, Vol. 31, No. 2, 1998, pp. 93-99.
- [104] Dhingra, K., et al., "Quantitative Analysis of Chromosome In Situ Hybridization Signal in Paraffin-Embedded Tissue Sections," *Cytometry*, Vol. 16, 1994, pp. 100-112.
- [105] Krijtenburg, P. J., et al., "Comparison of Automated and Manual Analysis of Interphase in Situ Hybridization Signals in Tissue Sections and Nuclear Suspensions," *Cytometry*, Vol. 25, No. 1, 1996, pp. 99-103.
- [106] Schroeder, W., and K. W. L. Martin, *The Visualization Toolkit: An Object-Oriented Approach to 3D Graphics*, Clifton Park, NY: Kitware, 2004.
- [107] Yim, P. J., et al., "Vessel Surface Reconstruction with a Tubular Deformable Model," *IEEE Trans. Med. Imaging*, Vol. 20, No. 12, 2001, pp. 1411-1421.
- [108] Guidolin, D., et al., "A New Image Analysis Method Based on Topological and Fractal Parameters to Evaluate The Angiostatic Activity of Docetaxel by Using the Matrigel Assay in Vitro," *Microvascular Research*, Vol. 67, No. 2, 2004, pp. 117-124.
- [109] Kimler, V. A., et al., "Characterization of Melanophore Morphology by Fractal Dimension Analysis," *Pigment Cell Res.*, Vol. 17, No. 2, 2004, pp. 165-172.
- [110] Krasowska, M., et al., "Patterning of Endocytic Vesicles and Its Control by Voltage-Gated Na(+) Channel Activity in Rat Prostate Cancer Cells: Fractal Analyses," *European Biophysics Journal*, 2004.
- [111] Cuisenaire, O., "Fast Euclidean Distance Transformations by Propagation Using Multiple Neighbourhoods," *Computer Vision and Image Understanding*, Vol. 76, No. 2, 1999, pp. 163-172.
- [112] Roysam, B., et al., "Algorithms for Automated Characterization of Cell Populations in Thick Specimens from 3-D Confocal Fluorescence Microscopy Data (Pt. 2)," *J. Microsc.*, Vol. 173, 1994, pp. 115-126.
- [113] Bhattacharjya, A., and B. Roysam, "Joint Solution of Low, Intermediate and High-Level Vision Tasks by Evolutionary Optimization: Application to Computer Vision at Low SNR," *IEEE Trans. on Neural Networks*, Vol. 5, No. 1, 1994, pp. 83-95.

- [114] Russ, J. C., *Computer-Assisted Microscopy: The Measurement and Analysis of Images*, New York: Plenum Press, 1990.
- [115] Balakrishnan, R., and K. Ranganathan, *A Textbook of Graph Theory*, New York: Springer, 2000.
- [116] Guzowski, J. F., et al., "Mapping Behaviorally Relevant Neural Circuits with Immediate-Early Gene Expression," *Curr. Opin. Neurobiol.*, Vol. 15, No. 5, 2005, pp. 599-606.
- [117] Lin, G., et al., "Automated Image Analysis Methods for 3-D Quantification of the Neurovascular Unit from Multichannel Confocal Microscope Images," *Cytometry*, Vol. 66, No. 1, 2005, pp. 9-23.
- [118] Abdul-Karim, M. A., et al., "Automated Tracing and Change Analysis of Angiogenic Vasculature from in Vivo Multiphoton Confocal Image Time Series," *Microvasc. Res.*, Vol. 66, No. 2, 2003, pp. 113-125.
- [119] Bjornsson, C., et al., "Associative Image Analysis: A Method for Automated Quantification of 3D Multi-Parameter Images of Brain Tissue," *Journal of Neuroscience Methods*, 2008.
- [120] Bao, Z., et al., "Automated Cell Lineage Tracing in *Caenorhabditis Elegans*," *Proc. Natl. Acad. Sci. USA*, Vol. 103, No. 8, 2006, pp. 2707-2012.
- [121] Parvin, B., et al., "Iterative Voting for Inference of Structural Saliency and Characterization of Subcellular Events," *IEEE Trans. on Image Process*, Vol. 16, No. 3, 2007, pp. 615-623.
- [122] Meijering, E., I. Smal, and G. Danuser, "Tracking in Molecular Bioimaging," *IEEE Signal Processing Magazine*, May 2006, pp. 46-53.
- [123] Sun, Z., and D. Yu, "Motion Tracking of Coronary Vessel Segment Based on Active Contour Model," *Sheng Wu Yi Xue Gong Cheng Xue Za Zhi*, Vol. 24, No. 1, 2007, pp. 9-14.
- [124] Kuhn, H. W., "The Hungarian Method for the Assignment Problem," *Naval Research Logistics Quarterly*, 1995, pp. 83-87.
- [125] Al-Kofahi, O., et al., "Automated Cell Lineage Tracing: A High-Throughput Method to Analyze Clonal Development Established with Murine Neural Progenitor Cells Developmental Cell," *Cell Cycle*, February 1, 2006, Vol. 5, No. 3.
- [126] Sulston, J., "Cell Lineage," in *The Nematode Caenorhabditis Elegans*, W. B. Wood, (ed.), Cold Spring Harbor, NY: Cold Spring Harbor Laboratory, 1988, pp. 123-155.
- [127] Sulston, J. E., et al., "The Embryonic Cell Lineage of the Nematode *Caenorhabditis Elegans*," *Developmental Biology*, Vol. 100, No. 1, 1983, pp. 64-119.
- [128] Moore, A. J., "Science as a Way of Knowing-Developmental Biology," *The American Society of Zoologists*, Vol. 27, 1987, pp. 415-573.
- [129] Bousso, P., and E. A. Robey, "Dynamic Behavior of T Cells and Thymocytes in Lymphoid Organs as Revealed by Two-Photon Microscopy," *Immunity*, Vol. 21, No. 3, 2004, pp. 349-355.
- [130] Christensen, H. I., and P. Jonathon, *Empirical Evaluation Methods in Computer Vision*, New York: World Scientific Publishing Company, 2002.
- [131] Bowyer, K. W., and J. P. Philips, *Empirical Evaluation Techniques in Computer Vision*, New York: Wiley-IEEE Computer Society Press, 1998.

# MST-Cut: A Minimum Spanning Tree-Based Image Mining Tool and Its Applications in Automatic Clustering of Fruit Fly Embryonic Gene Expression Patterns and Predicting Regulatory Motifs

Hanchuan Peng

## 6.1 Introduction

RNA in situ hybridization [1] provides a powerful way to visualize gene-expression patterns directly. This technique localizes specific mRNA sequences in tissues/cells by hybridizing a labeled complementary nucleotide probe to the sequence of interest in fixed tissues. Visualizing the probe by colorimetric or fluorescent microscopy allows for the production of high-quality images recording the spatial location and intensity of gene expression. Projects are underway to systematically collect RNA in situ expression patterns for a large number of genes during development in several organisms, including nematodes [2] and fruit flies [3].

Traditionally such in situ data have been analyzed via direct visual inspection of microscope images to determine the appropriate ontological annotations of expression patterns using a controlled vocabulary. For large in situ image databases with significant complexity, this manual process becomes very expensive; thus, it is desirable to complement this manual process with methods to automatically analyze in situ images. Automatic analyses would make the annotation process more rapid and consistent, and may identify biologically significant features missed during manual curation.

Recently we developed a series of new techniques for the analysis of fly gene expression pattern images during embryogenesis. These techniques include the following:

- *Image retrieval* [4]: detecting genes with similar expression patterns from image databases like Berkeley Drosophila Genome Project (BDGP);
- *Image clustering* [5]: identifying groups of potentially co-regulated fly genes;
- *Image classification and recognition* [6, 7]: automatically recognizing and annotating gene expression patterns using ontology terms;
- *Manifold learning* [4]: reconstructing the 3-D developmental dynamics of fly gene expression in embryogenesis;
- *Image registration* [4]: aligning images of gene expression patterns in fly embryos.

These methods have been used in the analysis of more than 1,700 fly genes with 20,000 images extracted from the BDGP database. In addition, the joint analyses of the image data and other types of data, such as gene sequences and CHIP-chip protein-DNA binding data, have also been considered. For example, in Section 6.3, we show how the predicted image phenotypic clusters can be combined with several available fly genomes (*D. melanogaster*, *D. simulans*, and so on) to predict regulatory sequence motifs.

In this chapter, we focus on a case study how to make use of a minimum spanning tree (MST)-based tool, MST-Cut, to cluster the gene expression pattern images, based on which the genetic regulatory sequence motifs can be detected.

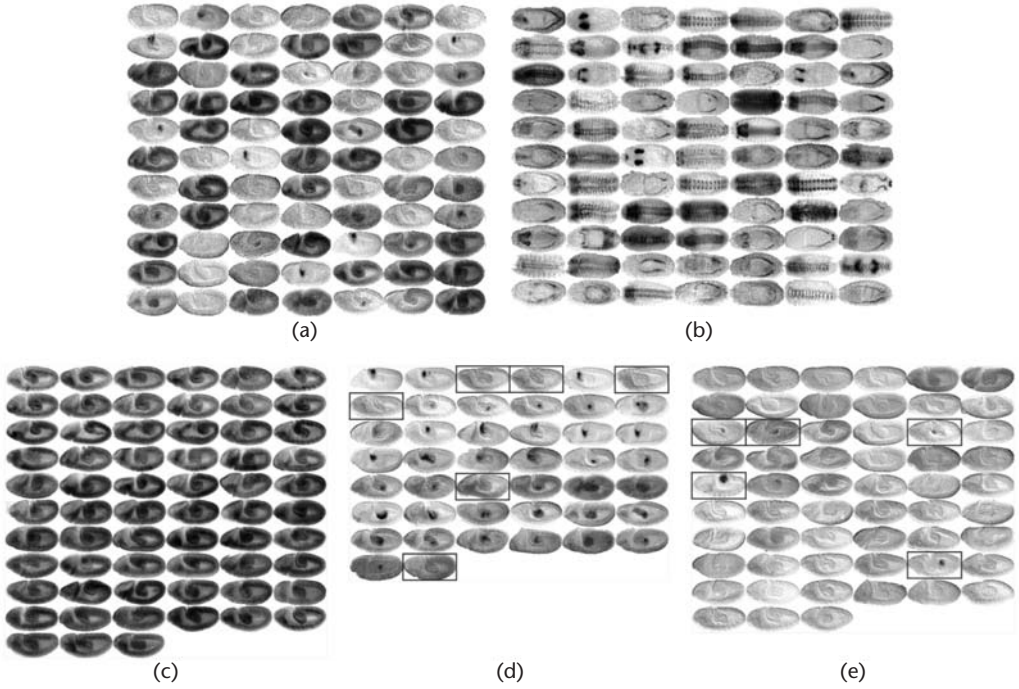
## 6.2 MST

Let's consider a weighted, undirected graph  $G = (V, E)$ , where  $V$  denotes a set of nodes and  $E$  denotes the set of edges between any pair of nodes. In the following discussion of image analysis, each node  $g \in V$  ( $|V| = N$ ) represents an image (i.e., either the original image or a feature vector of this image), and the edge weight  $s$  between a pair of nodes is the distance of the respective image/feature vectors. This graph  $G$  can be equivalently described as an  $N \times N$  similarity matrix,  $S$ , of all the  $N$  nodes.

A minimum spanning tree of the graph  $G$  is the subgraph that spans every node in  $G$ , but the overall sum of edges is minimum. Indeed, an MST has exactly  $N-1$  edges and is unique to a given  $G$  if every edge has a distinct weight. An MST can be efficiently constructed in different ways. One of the most used algorithms is Prim's algorithm [8], which delivers a tree in  $O(|E| + N \ln N)$  time when one uses a Fibonacci heap [8]. In our applications the graph  $G$  is not particularly sparse (i.e.  $|E|$  is  $O(N^2)$ ). Our MST-Cut algorithm uses the tree structure as the indicator of how the data should be partitioned efficiently.

## 6.3 MST-Cut for Clustering of Coexpressed/Coregulated Genes

In the first case study, we consider how to cluster genes based on their embryogenesis expression patterns. At the basic level, suppose each gene has one representative image of its in situ mRNA expression pattern; the goal can be simply illustrated in Figure 6.1(a, c–e), where examples of mixed images in Figure 6.1(a) would be optimally separated as three clusters in Figure 6.1(b, c, d), respectively. More sophisticatedly, gene expression patterns at different developmental stages can be clustered separately; these results will then be assembled to predict the coexpressed genes that share similar expression patterns over certain developmental period. The coexpressed genes have a higher chance to be coregulated by the same group of genetic factors; thus, the combination of these phenotype-clustering results and gene sequence analysis can help detect regulatory elements such as sequence motifs.



**Figure 6.1** Image clustering of in situ hybridization mRNA gene expression patterns of fly embryos: (a) and (b) are examples of the input patterns in the datasets P4\_lateral and P6\_dorsal\_ventral, respectively; (c), (d), and (e) are the three image clusters generated using MST-Cut for the P4\_lateral data. The erroneously clustered images, which were determined via visual inspection, are marked using boxes.

### 6.3.1 MST-Cut Clustering Algorithm

MST-Cut [5] is a data-clustering method based on partitioning the graph  $G$ . In this case, each node represents a data point (i.e., an image or the respective feature vector of an image). A data cluster is a connected component, consisting of a group of nodes, in the graph. Intuitively, we want to partition  $G$  into  $K$  pieces or clusters ( $K < N$  and generally  $K$  is unknown) so that (1) each piece/cluster is a single connected component, (2) within each cluster the total distance of data samples is minimized (or equivalently, the total similarity is maximized), and (3) across clusters the total distance is maximized (or equivalently, total similarity of data samples is minimized). Denote the distance between the  $i$ th and  $j$ th samples as  $d_{ij}$ , where  $1 \leq i, j \leq N$ . Let  $D = [d_{ij}]$ , which is symmetric,  $A_1, A_2, \dots, A_K$  denote the  $K$  clusters, and  $d_{mn}$  ( $1 \leq m, n \leq K$ ) denote the sum of the distance matrix values of nodes in  $A_m$  and  $A_n$ . Thus,  $K$ -way clustering simultaneously optimizes all conditions in (6.1), where  $K$  is unknown.

$$\begin{cases} \min D_{ii}, & i = 1, \dots, K \\ \max D_{ij}, & 1 \leq i, j \leq K, i \neq j \end{cases} \quad (6.1)$$



The criterion (6.1) is called MinMaxPartition criterion. One way to combine the optimization conditions in (6.1) is to optimize (6.2),

$$\min \sum_{i=1}^K \sum_{\substack{j=1 \\ j \neq i}}^K \left( \frac{D_{ii} + D_{jj}}{D_{ij}} \right) \quad (6.2)$$

Generally, it is difficult to solve the  $K$ -way partition exactly, mainly because it is highly combinatorial and the complexity of an exhaustive search is  $O(K^N)$ . An alternative method is to iteratively perform  $K-1$  two-way cuts. At each step we face the much simpler problem of optimizing (6.3), which minimizes the intracluster distance and maximizes the intercluster distance simultaneously. In this case, a brute force search for the best partition has the complexity  $O(2^N)$ .

$$\min \frac{D_{11} + D_{22}}{D_{12}} \quad (6.3)$$

Note that there are other ways to define clusters in  $G$ , besides the MinMax-Partition criterion. For example, one intuition is that the pair of nodes that have the strongest tie or largest similarity should belong to the same cluster, if each of them were enclosed by a cluster with more than one node (i.e., they were not outliers). However, different ways to generate clusters are not always consistent with each other. This inconsistency happens mainly when the distance/similarity score is nontransitive (i.e., the conditions that a node  $g_1$  is similar to  $g_2$  and  $g_2$  is similar to  $g_3$  do not imply  $g_1$  is similar to  $g_3$ ). Therefore, we need to avoid using nontransitive distance/similarity scores in clustering. We consider two commonly Euclidean distance scores, the  $L_1$  and  $L_2$  distances. Because of the triangular inequality for the Euclidean distance metrics (i.e.,  $d_{13} < d_{12} + d_{23}$ ), it is impossible that  $d_{13}$  would turn out to be large if both  $d_{12}$  and  $d_{23}$  are small. Thus, the  $L_1$  and  $L_2$  scores have a transitive nature and are suitable for clustering.

For the graph  $G$  represented by the whole distance matrix of all pairs of image samples, we can safely eliminate edges with the biggest distance while keeping the graph as a completely connected component. Removing edges in decreasing order of distance, subject to the condition that the graph does not break into pieces eventually leads to an MST. An MST connects all nodes (image samples) in the graph but has the minimum overall edge distance-scores. MST captures the basic cluster structures in the data, because the nodes that are more similar to each other are always connected in a shorter path in the tree.

We propose a simple algorithm, called MST-Cut, to optimize the condition in (6.3). Because there are only  $N-1$  edges in the tree graph and removal of one edge will bipartition the graph, finding two clusters of nodes can be done by eliminating one edge in the tree. Since there are only  $N-1$  different partition results, we can compare all of them to choose the best partition that minimizes (6.3) in  $O(N^2)$  time.

There are two ways to generate  $K$  clusters. One way is to extend the MST-Cut to find  $K$  clusters simultaneously, by minimizing (6.2). This can be done in a brute force way to search all combinations of the  $K-1$  edges dropped in the MST. The complexity is  $O(\binom{N-1}{K-1} \cdot N)$ . Another more efficient way is to repeat the bipartition



process on the subtrees until  $K$  clusters are found. At each graph bipartition step, we choose the cluster that has the biggest intracluster distance for further partition. This cannot generate  $K$  clusters that are globally optimal, but the complexity is significantly reduced to  $O(KN^2)$  time.

#### 6.3.1.1 Related Algorithms

Clustering analysis is a fundamental problem in pattern recognition applications. Many methods (e.g., K-means, Gaussian-mixture-model, and agglomerative-clustering) have been proposed in the past decades. (For good reviews, see books such as [9].) However, many of these methods are less appropriate for clustering embryonic images. For example, K-means is often prone to local minima, and a method based on Gaussian mixture models is often very slow.

There are several MST-based clustering methods. The simplest MST partition method is to iteratively remove the tree-edges with the smallest similarities. For real data where clusters are not far away from each other, usually many leaves are cut, resulting in bad clusters. Another method is the simple agglomerative-clustering, which can be viewed as an application of the Kruskal's algorithm [8] in generating an MST. A third method is to use the node-addition order of Prim's algorithm in constructing an MST [10]. Following this order, all nodes in a target cluster must be traversed before any nodes in a different cluster may be encountered. Clusters are formed via searching "valleys" of adjacent edges that have small distance scores. This algorithm works well when there are very dense clusters so that these valleys are apparent. As far as we have tested, this is not the case here. Compared to all these earlier MST-based methods, our new method considers more global constraints and can produce better results.

Another very interesting method is called spectral clustering, which was developed in recent years to convert the combinatorial search problem in (6.3) as a linear search problem [11, 12]. Spectral clustering uses top eigenvectors of the transformed similarity matrix  $S$  as indicators of clusters. However, in practice, small similarity entries less than a threshold in  $S$  are often set to 0 to improve the results. At the same time,  $S$  becomes sparse; thus, it is possible to speed up the searching of top-eigenvectors significantly. This makes it possible to deal with large problem like image segmentation where there are hundreds of thousands nodes in the graph  $G$ . The best threshold is often determined empirically. We note that in the limiting case, we can apply the spectral clustering on the MST, which is the sparsest connected graph. In this case, the partition result will be exactly the same as that generated by our MST-Cut method, because both spectral clustering and MST-Cut optimize the same function. However, MST-Cut is faster, because it does not involve extra computation of eigenvectors. We also show quantitative comparison of MST-Cut and spectral clustering in Section 6.3.2.

#### 6.3.2 Embryonic Image Clustering

Two-dimensional embryonic images of gene expression patterns are usually acquired using a light microscope equipped with a digital camera. In the following

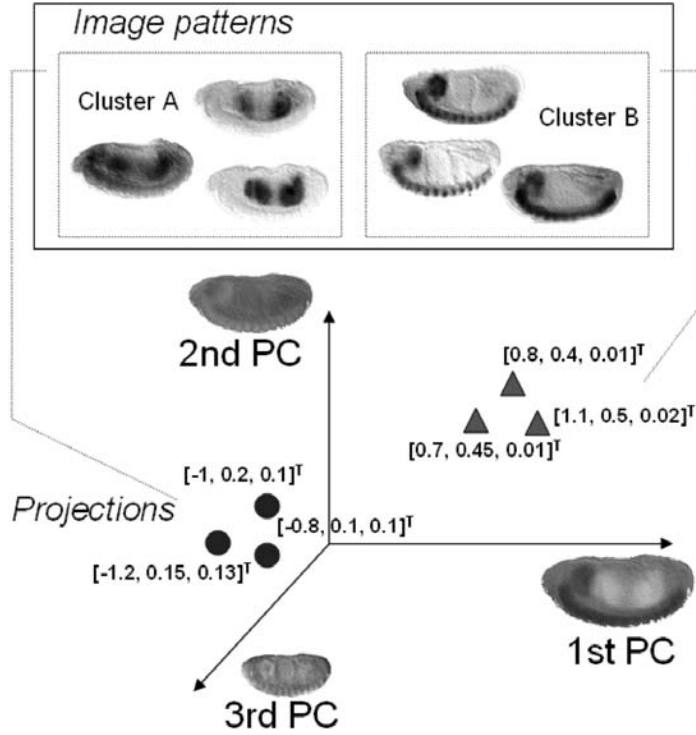
analysis of Berkeley Drosophila Genome Project (BDGP) data, a single embryo often resides in the central part of the image. This embryo can have arbitrary orientation. Because the embryonic region typically has much richer texture information than the image background, it can be simply segmented from the image background based on thresholding the local variance. For the segmented embryo, we compute the principal direction along which the variation of all embryonic pixel-coordinates is greatest. This direction is called the longest axis, which usually corresponds to the anterior-posterior (AP) axis of an embryo. We then rotate the embryo region so that its longest axis is horizontal. These image-preprocessing steps have been developed in our earlier work and applied to all images before any subsequent manipulations. For experiments in this chapter, we select several subsets from the full BDGP database to study the performance of our method. Some image examples can be seen in Figure 6.1(a, b).

### 6.3.2.1 Eigen-Embryo Feature Vectors

The first step in our method is to generate feature vectors that characterize each image. Assume we have  $N$  images of in situ expression patterns  $I_1, I_2, \dots, I_N$ , each having  $M$  pixels. One way to generate features is to consider local feature decomposition such as Gaussian mixture models. However, because different images can have different traits, the local-decomposition approach does not provide a canonical feature space where the distribution of all image-patterns can be measured simultaneously. Thus, clustering performance is limited.

The alternate approach in this study is to decompose an image as a linear combination of a series of mutually orthogonal basis functions using the principal component analysis (PCA). PCA computes the principal directions (i.e., the basis functions) of the distribution of a dataset and projects data points from its original space to a lower dimensional space whose axes are these principal directions. These principal directions are the eigenvectors associated with the largest eigenvalues of the data covariance matrix. When applied to images, each eigenvector is an eigen-image. They form an orthogonal set of basis functions in which the original data points or images are described. This eigen-image analysis method, which was first applied to human-face recognition [13], uses the coordinates of an image in the eigen-image space as a feature vector that represents the original image.

Figure 6.2 illustrates the basic scheme of eigen-embryo analysis. In the pool of input images, two clusters are mixed together. Each cluster has a dark image, a bright image, and an image that is neither very dark nor very bright. Although visually we can see these two clusters of images have different expression patterns, it is not easy for a computer clustering program to separate them in the space of the raw image because the pixel intensity is the most pronounced feature in these six images, which obscures the cluster boundary. By projecting these images to the subspace of the first three principal eigenvectors, or eigen-embryos, we represent each image using a feature vector  $w$ , which form the coordinate of image patterns in the 3-D subspace. The cluster structure becomes apparent in the subspace, as indicated by small triangles and circles among which the cluster boundary can be easily drawn. Note that in the first principal component (PC), the dark curved



**Figure 6.2** Schematic illustration of the feature-vector generation and clustering using eigen-image analysis. For better visualization, various eigen-embryo sizes indicate the ordering of PCs (e.g., the first eigen-embryo has the biggest size).

structure (ventral nerve cord and brain) and light two-blob structure (guts) indicate the most prominent features to distinguish these six image patterns.

Mathematically, eigen-image analysis derives a short feature vector  $w$  to represent each image  $I$ , which is an  $M \times 1$  vector. We first compute the centroid pattern of these  $N$  images,  $\Theta$ . Each input image then differs from this centroid pattern by  $X_k = I_k - \Theta$ . Let  $X = [X_1, \dots, X_N]$ . Then the covariance matrix is  $C = XX^T/M$ . The eigenvectors of the  $L$  largest eigenvalues of  $C$  form a subspace into which each image is projected by describing it as a weighted sum of these  $L$  eigen-images. This set of weights  $[w_1, w_2, \dots, w_L]^T$  is a point in the  $L$ -dimensional eigen-image space and is called its feature vector. Denoting the  $i$ th eigenvector as  $v_i$ , the  $i$ th coordinate of the feature vector for image  $I$  is,  $w_i = v_i^T(I - \Theta)$ . By describing each image in terms of the  $L$  most significant eigen-images, the major variation of the data distribution is preserved, noise and redundancy are largely eliminated, and the distances between the feature vectors can be viewed as the distances between points in an  $L$ -dimensional space.

Note that the eigen-embryo model does not only help reduce noise and keep the major information, but also conveniently preserves the relative Euclidian distance of patterns in a low-dimensional space. As pointed out in Section 6.3.1, it is important to use Euclidian distances for MST-Cut clustering; thus, the eigen-embryo model is suitable for MST-Cut.

### 6.3.2.2 Measures of Clustering Performance

We use the  $F$ -measure score between the predicted clusters and the ground truth clusters to evaluate the performance of clustering algorithm.  $F$ -measure can be written in the form of precision  $P$  and recall  $R$ , which are widely used in information retrieval [14]. Precision  $P$  defines the proportion of retrieved results that are relevant. Recall  $R$  defines the proportion of relevant results that are retrieved. Suppose we have a predicted cluster  $H$  and a ground truth cluster  $\Omega$ . The precision and recall are defined as:

$$P = |H \cap \Omega| / |\Omega| \quad (6.4)$$

$$R = |H \cap \Omega| / |H| \quad (6.5)$$

Precision and recall can be combined as the  $F$ -measure using (6.6). It is easy to see  $F$ -measure value falls into the range  $[0, 1]$ . The larger the  $F$ -measure, the better the clustering results.

$$f = 2 \cdot \frac{P \cdot R}{P + R} \quad (6.6)$$

In our clustering case, assume there are  $K$  ground truth clusters  $\Omega_1, \dots, \Omega_K$ , and the clustering program returns  $M$  predicted clusters  $H_1, \dots, H_M$ . For each pair of ground truth cluster and the predicted cluster, we can compute the  $F$ -measure score  $f_{ij}$ ,  $1 \leq i \leq K$  and  $1 \leq j \leq M$ , using (6.6). We define the following  $F$ -score to summarize the whole array of results.

$$F = \frac{\sum_{i=1}^K |\Omega_i| \max_{j=1, \dots, M} f_{ij}}{\sum_{i=1}^K |\Omega_i|} \quad (6.7)$$

$F$ -score has the range of 0–1; the larger the number, the better the clustering results.

## 6.4 Experiments

### 6.4.1 Performance of MST-Cut on Synthetic Datasets

Before we show the real examples how MST-Cut can be used to detect co-expressed genes, we quantitatively compare our method against a few others.

For comparison, we select several subsets of *mRNA* expression pattern images and determined the *ground truth* clusters of these images. Here we show results of two datasets. The first one is called P4.Lateral, which corresponds to the lateral view of 167 embryos at the developmental stage 9–10 (i.e., phase 4 in [4], or about 4.8–6 hours after fruit fly egg hatching). In P4.Lateral, there are three clusters manually determined by two human subjects. The consensus is used as the ground

truth clusters. As shown in a few sample images in Figure 6.1(a), these three clusters include the following:

1. Gene expression patterns in the primordium of embryonic ectoderm regions (including procephalic, anterior, posterior, ventral, and dorsal ectoderms), nervous system (like ventral nerve cord), and guts (like external foregut and inclusive hindgut). The gene expression in these regions forms a curved structure in many images. There are 64 image samples in this cluster.
2. Gene expression patterns only in the foregut and hindgut regions. These patterns can be seen as one small dark dot in the middle of the embryo. There are 44 samples in this cluster.
3. No apparent gene expression patterns. There could be some artifacts (light gray shadows) that look like patterns in the ectoderm regions. There are 59 image samples in this cluster.

The second synthetic dataset, called P6\_dorsal\_ventral, corresponds to 230 dorsal and ventral views of embryos around the developmental stage 13–16 (phase 6 in [3], or about 10–12 hours after hatching). In this dataset, there are three manually determined clusters too. Some examples are shown in Figure 6.1(b).

Next, we compare MST-Cut against several existing methods to investigate if the combination of eigen-embryo analysis and MST-Cut improves the cluster-prediction. Here we show (1) the comparison of results of the eigen-embryo feature-vector matching to the global image matching to see if the low-dimensional features are effective, and (2) the comparison of results of MST-Cut against the spectral clustering method in [12] and another MST-based clustering method in [10] to see if MST-Cut improves the prediction.

The results are summarized in Table 6.1. We see that for both  $L_1$  and  $L_2$  distance scores, the improvements of the eigen-embryo matching over the global matching, and those of MST-Cut over the two previous clustering methods, are significant. For example, the  $F$ -scores of our method are always higher than or around 0.9, whereas the  $F$ -scores of the comparing methods are around 0.7. Also note that for all the three clustering methods, the overall results for the eigen-image matching are better than those for global image matching. In Table 6.1, we also show the average result of random clustering. The average  $F$ -score of our method (above 0.9) is much higher than that of the random clustering method, indicating our method succeeds in finding the meaningful clusters in this dataset.

Figure 6.1(c–e) shows three clusters generated using our eigen-embryo MST-Cut. We marked the erroneously clustered images using blue boxes. It is seen that the first cluster is predicted 100 percent correctly. There are a few errors for the second and third clusters. For the second cluster, errors come mostly from images with artifact expressions in the foregut and hindgut regions. For the third cluster, the errors are mainly due to the very subtle middle dark-blob feature. In (e), there is one error where there is a strong dark blob in the center region of the embryo (see the second blue-boxed image in the left-most column). We find this error occurs because the dark blob has a different position from most other images in the cluster 2 in Figure 6.1(d). There are ways to correct all these erroneous

**Table 6.1** F-Measure Scores for MST-Cut Clustering the P6\_dorsalventral Dataset (the Value Shown in the Table Is the Maximal F-Measure Scores of the Results Obtained Using L1 and L2 Distances— $\max(F(L1), F(L2))$ ) of Eigen-Images on Quantized Images and Those of Grayscale Images)

[illegible]

predictions. For example, we can first consider enhancing the local features using context information and then use the eigen-image-based MST-Cut clustering.

In some cases, a biologist may be interested in first “extracting” the gene expression pattern from an embryonic image by thresholding it. Various thresholds could be used to generate a binarized image [15, 16], where the pixel intensity values 1 and 0 indicate whether or not there is gene expression pattern at a pixel location. Thus, we also test if the MST-Cut-based eigen-embryo clustering method consistently produces better clustering than the global pattern matching. The results for the dataset P6\_dorsal\_ventral are shown in Table 6.1. It can be seen that for differently binarization thresholds, the eigen-embryo model always produces a significantly higher F-measure score than global matching. The average is 0.783, much higher than that of the global matching, 0.691. This is also consistent with the results obtained for the grayscale images without any thresholding (i.e., 0.739 versus 0.689). Hence Tables 6.1 and 6.2 together indicate the combination of MST-Cut and the eigen-embryo model is very effective for clustering embryonic gene expression patterns.

#### 6.4.2 Detection of Coregulated Genes and Regulatory Motifs

It is known that coexpressed genes have similar spatial-temporal expression patterns over a range of embryo developmental stages. They might also be coregulated in some modules in a genetic regulatory network. One way to detect coexpressed genes is to examine if several genes always have patterns that belong to the same cluster for multiple developmental stages. This condition-specific co-expression information is useful to infer whether the respective genes share common regulators and how some genes are turned on/off under different conditions.

We design the following method to detect groups of genes that have similar expression patterns. The 16 developmental stages of *Drosophila* embryogenesis can be categorized as six phases: stages 1–3, stages 4–6, stages 7–8, stages 9–10, stages 11–12, and stages 13–16, which coincide with major developmental transitions (e.g., gastrulation). Thus, we check the image clustering results phase by phase for every gene. The genes that have patterns in the same cluster of any specified phases are taken as a gene group.

One problem with gene grouping is the unbalanced image numbers for different genes. For example, if at phase 4 a gene has five image patterns while another gene has only one image pattern, the number of image samples will bias the image

**Table 6.2** F-Measure Scores of Different Clustering Methods for P4\_lateral (for MST-Cut, the Feature Vector Length  $L$  is 30)

Clustering Methods	Spectral Clustering in [12]		MST Clustering in [10]		MST-Cut	
	$L_1$	$L_2$	$L_1$	$L_2$	$L_1$	$L_2$
Similarity scores						
Global matching	0.69	0.69	0.67	0.67	0.69	0.70
Eigen-embryo matching	0.74	0.69	0.63	0.66	0.92	0.93
Random clustering	0.346±0.002 (based on 20 trials)					



$S_Q$ query genes		Stage 4-6		Stage 7-8		Stage 9-10		Stage 11-12	
<i>snail</i> (CG3956)			AEAISN, EAISN, MAISN, S,TMAISN		AEA, TMA		PCEP, VECP, VNCP		MLP,PCP, NOVNS, OSA,PCN, SNSSA, VSCSA
<i>tinman</i> (CG7895)			CB, S, FAISN, MAISN, TMAISN		FA, TMA		EFP, TMA		CLP, CMP, VMP
<i>twist</i> (CG2956)			AEAISN, CB, S, MAISN, TMAISN		AEA, HMA, TMA		HMPP, TMA		DPMP, LVMP, SMP
<i>tkv</i> (CG14026)			CB, S		VEA		MEP, PCEP, VNCP		AMP, PMP, TP
Predicted motifs	Some genes in $S_R$	Stage 4-6		Stage 7-8		Stage 9-10		Stage 11-12	
	<i>Ngp</i> (CG6501)		CB		HA, HMA, PTEA, TMA		IHP, PP, SGBSA, SGDSA, TMP		AMP,HPP, PMP,SDP, SGBP, VMP
	<i>NetA</i> (CG18657)		MAISN, S		HMA, TMA, VNA		HMPP, MEP,TMP, PCEP, VNCP		MLP, PCP, VMP
	<i>Sema-5c</i> (CG5661)		AAISN, AISN, DEAISN		DEA, VEA		AEP,AM, DECP, IHP,PTEP, VECP		AMP, FP, HPP,PMP, SGBP, VEPP
	<i>msk</i> (CG7935)		CB, S		HA, PC, TMA		HMPP, IHP, TMA		FP, GC, HPP
	<i>Dcp-1</i> (CG5370)		CB		AEA, PTEA, VEA		AEP, DECP, PTEP		DEDP, HPP, TP, VEPP
	<i>Set</i> (CG4299)		CB		VEA		VNCP		ECBG, ECBN, LCN
	CG2083		—		HA, PCEA, VEA		IHP, PCEP, VNCP, VP		ECBN, EOLP, HPP,PCN, NOVNS
	CG30023		S		HMA, TMA		TMA		FP, TP

**Figure 6.3** A detected group of four genes with known gene regulation relationships for mesoderm patterning in fly embryogenesis and examples of sequence motif detection, along with the retrieved genes using the respective motifs. In this example, the gene group  $S_Q$  was obtained by finding a tight image cluster for stage 7-8 (highlighted). For each gene in  $S_Q$ , one representative embryo image is shown for each stage-range, followed by the respective eigen-features (as we do not have appropriate lateral-view images for *snail* and *tkv* at stage 9-10, we only show the original BDGP images, without the eigen-feature). Three motifs detected using the entire upstream regions of the homologous genes in five fly species are shown, along with two or three randomly selected example genes in the subsequent genome-wide motif scanning results. BDGP ISH images and annotations are also shown, without image cropping or orientation correction. Short terms of annotations: AM, amnioserosa; AAISN, amnioserosa anlage in statu nascendi; AISN, anlage in statu nascendi; AEA, anterior endoderm anlage; AEAISN, anterior endoderm anlage in statu nascendi;

clustering algorithm and consequently produce a poor score for gene grouping. Hence, for a specific phase, when there are multiple images for a single gene, we compute the mean pattern of this gene and use this synthetic pattern in image clustering. The clustering results are more reliable when each gene has exactly one most representative image pattern at every phase.

We apply our method to detect coexpressed genes that share common spatial expression patterns during the course of embryogenesis. We note that in the BDGP database, several genes do not have dorsal/ventral images for late developmental stages, and in many dorsal/ventral images the expression stains of both dorsal and ventral tissues overlap together. At the same time, as far as we have observed, it is rare that two genes with similar lateral patterns over the course of embryogenesis have very distinct dorsal/ventral patterns. Therefore, at this stage, we consider only lateral-view images. With the additional requirement that a gene has at least one expression image at every developmental phase, we use a set of 456 genes. If at a particular phase a target gene has more than one image, our computer program merges these images as one single “representative” image by taking their simple

average. In this way, the clustering algorithm would not be biased by the image numbers of genes. We have found many interesting clusters. In the following, we focus on one typical group of predicted co-expressed genes.

One example [6] is shown in Figure 6.3. For stage 7–8, we detect a cluster of four genes, *snail*, *tinman*, *twist*, and *tkv* (*thickveins*) share very similar patterns and eigen-features. It is seen that they also have comparable patterns for several other stages. Interestingly, these genes are known determinants of mesoderm in *Drosophila*. Both *snail* and *twist* are activated by highest levels of the *Dorsal* nuclear gradient in the ventral-most region of the early embryo (blastoderm stage

---

**Figure 6.3** (*continued*) AEP, anterior endoderm primordium; AMP, anterior midgut primordium; CMP, cardiac mesoderm primordium; CB, cellular blastoderm; CLP, clypeo-labral primordium; DEA, dorsal ectoderm anlage; DEAIN, dorsal ectoderm anlage in statu nascendi; DECP, dorsal ectoderm primordium; DEDP, dorsal epidermis primordium; DPMP, dorsal pharyngeal muscle primordium; ECBG, embryonic central brain glia; ECBN, embryonic central brain neuron; EOLP, embryonic optic lobe primordium; EAIN, endoderm anlage in statu nascendi; EFP, external foregut primordium; FA, foregut anlage; FAISN, foregut anlage in statu nascendi; FP, foregut primordium; GC, germ cell; HMPP, head mesoderm P2 primordium; HMA, head mesoderm anlage; HA, hindgut anlage; HPP, hindgut proper primordium; IHP, inclusive hindgut primordium; LCN, lateral cord neuron; LVMP, longitudinal visceral mesoderm primordium; MEP, mesectoderm primordium; MAISN, mesoderm anlage in statu nascendi; MLP, midline primordium; NOVNS, neuroblasts of ventral nervous system; OSA, oenocyte specific anlage; PC, pole cell; PTEA, posterior endoderm anlage; PTEP, posterior endoderm primordium; PMP, posterior midgut primordium; PCEA, procephalic ectoderm anlage; PCEP, procephalic ectoderm primordium; PCN, procephalic neuroblasts; PCP, protocerebrum primordium; PP, proventriculus primordium; SDP, salivary duct primordium; SGBSA, salivary gland body specific anlage; SGDSA, salivary gland duct specific anlage; SGBP, salivary gland body primordium; SNSSA, sensory nervous system specific anlage; SMP, somatic muscle primordium; S, subset; TP, tracheal primordium; TMA, trunk mesoderm anlage; TMAISN, trunk mesoderm anlage in statu nascendi; TMP, trunk mesoderm primordium; VEA, ventral ectoderm anlage; VECp, ventral ectoderm primordium; VEPP, ventral epidermis primordium; VNCP, ventral nerve cord primordium; VNA, ventral neuroderm anlage; VSCSA, ventral sensory complex specific anlage; VMP, visceral muscle primordium; and VP, visual primordium.

4–6). The gene *tinman* is activated in turn by *twist*, reaching peak early expression in the invaginating mesoderm (gastrulation stage 7–8) and is a conserved key regulator of cardiac identity during mesodermal differentiation. Activity of *tkv* in the entire mesoderm induces ectopic *tinman* expression in the ventral mesoderm, and this results in the ectopic formation of heart precursors in a defined area of the ventrolateral mesoderm. This cluster indicates that our method can detect transcriptional regulators and targets in a functional network of the early fly embryo.

Detecting sequence motifs based on coexpressed genes is a very useful way to study gene functions. Thus, we next detected the sequence motifs of the genes in these coexpression clusters using eight related fly species *D. melanogaster*, *D. simulans*, *D. yakuba*, *D. erecta*, and *D. ananassae*, *D. pseudoobscura*, *D. virilis*, and *D. mojavensis*. To prove the principle, we used the several sequence motif search tools PhyloCon [17], PhyME [18], MEME [19], and MAST [20] to compare the entire upstream regions of a cluster of coexpressed query genes, called  $S_Q$ , and predict potential motifs. Each motif was then used to scan the entire *D. melanogaster* genome to retrieve a set of genes, denoted as  $S_R$ , for which an abundance of this motif is detected in their upstream regions. The expression patterns of genes in  $S_R$  were then compared against those of genes in  $S_Q$ . As an example, for the  $S_Q$  cluster in Figure 6.2, three predicted motifs are shown. For each of them, we exemplify the gene expression patterns and BDGP gene ontology annotations of two or three retrieved genes in the genome-wide motif scanning. Visibly for every developmental stage range, the gene expression patterns of the retrieved genes are similar to those of the query genes. This visual inspection is also consistent with the fact that all these genes share a lot of common BDGP annotations, such as trunk mesoderm anlage (TMA), ventral ectoderm anlage (VEA) for stage 7–8, and ventral nerve cord primordium (VNCP) for stage 9–10, indicating that the detected motifs are likely meaningful. This example of motif prediction verification demonstrates the strength of the coexpressed/coregulated gene detection based on our image-clustering approach.

## 6.5 Conclusions

This chapter presents a case study demonstrating how an efficient image-clustering method, MST-Cut, can be used to find meaningful image and gene clusters of gene expression patterns and further used for predicting regulatory sequence motifs. This method can also be used for gene expression pattern image data of different species, such as mice or *C. elegans* [21].

### Acknowledgments

We thank members of BDGP for discussions and providing the fly embryonic data to test the computing methods in this chapter. We thank Gene Myers, Fuhui Long, Michael Eisen, Garmay Leung, Eisen lab, and Sean Eddy for great contributions to this work.

## References

- [1] Lehmann, R., and D. Tautz, "In Situ Hybridization to RNA," in *Drosophila Melanogaster: Practical Uses in Cell and Molecular Biology, Methods in Cell Biology* Vol. 44, L. S. B. Goldstein and E. A. Fyrberg, (eds.), New York: Academic Press, 1994, pp. 575-598.
- [2] Hope, I. A., et al., "The C. Elegans Expression Pattern Database: A Beginning," *Trends in Genetics*, Vol. 12, No. 9, 1996, pp. 370-371.
- [3] BDGP: Berkeley Drosophila Genome Project (fruitfly.org).
- [4] Peng, H. C., and E. W. Myers, "Comparing In Situ mRNA Expression Patterns of Drosophila Embryos," *Proc. 8th Annual Int. Conf. on Research in Computational Molecular Biology*, San Diego, CA, 2004, pp. 157-166.
- [5] Peng, H. C., et al., "Clustering Gene Expression Patterns of Fly Embryos," *Proc. IEEE ISBI 2006*, Washington, DC, 2006, pp. 1144-1147.
- [6] Peng, H. C., et al., "Automatic Image Analysis for Gene Expression Patterns of Fly Embryos," *BMC Cell Biology*, Supp. 1, Vol. 8, 2007, pp. S7.
- [7] Zhou, J., and H. C. Peng, "Automatic Recognition and Annotation of Gene Expression Patterns of Fly Embryos," *Bioinformatics*, Vol. 23, No. 5, 2007, pp. 589-596.
- [8] Corman, T. H., C. E. Leiserson, and R. L. Rivest, *Introduction to Algorithms*, Cambridge: MIT Press, 2001.
- [9] Duda, R. O., P. E. Hart, and D. G. Stork, *Pattern Classification*, 2nd ed., New York: John Wiley & Sons, 2000.
- [10] Olman, V., D., Xu, and Y. Xu, "CUBIC: Identification of Regulatory Binding Sites Through Data Clustering," *JBCB*, Vol. 1, No. 1, 2003, pp. 21-40.
- [11] Shi, J., and J. Malik, "Normalized Cuts and Image Segmentation," *IEEE TPAMI*, Vol. 22, No. 8, 2000, pp. 888-905.
- [12] Ding, C., et al., "A Min-Max Cut Algorithm for Graph Partitioning and Data Clustering," *ICDM 2001*, 2001, pp. 107-114.
- [13] Turk, M., and A. Pentland, "Eigenfaces for Recognition," *J. of Cognitive Neuroscience*, Vol. 3, No. 1, 1991, pp. 71-86.
- [14] van Rijsbergen, K., *Information Retrieval*, 2nd ed., London: Butterworth, 1979.
- [15] Otsu, N., "A Threshold Selection Method from Gray-Level Histograms," *IEEE Trans. on Systems, Man, and Cybernetics*, Vol. 9, No. 1, 1979, pp. 62-66.
- [16] Peng, H. C., et al., "Hierarchical Genetic Image Segmentation Algorithm Based on Histogram Dichotomy," *Electronics Letters*, Vol. 36, No. 10, 2000, pp. 872-874.
- [17] Wang, T., and G. Stormo, "Combining Phylogenetic Data with Co-Regulated Genes to Identify Regulatory Motifs," *Bioinformatics*, Vol. 19, No. 18, 2003, pp. 2369-2380.
- [18] Sinha, S., M. Blanchette, and M. Tompa, "PhyME: A Probabilistic Algorithm for Finding Motifs in Sets of Orthologous Sequences," *BMC Bioinformatics*, Vol. 5, 2004, p. 170.
- [19] Timothy, L. B., and C. Elkan, "Fitting a Mixture Model by Expectation Maximization to Discover Motifs in Biopolymers," *Proc. of 2nd Int. Conf. on Intelligent Systems for Molecular Biology*, Menlo Park, CA, 1994, pp. 28-36.
- [20] Timothy, L. B., and M. Gribskov, "Combining Evidence Using P-Values: Application to Sequence Homology Searches," *Bioinformatics*, Vol. 14, 1998, pp. 48-54.
- [21] Long, F., et al., "A 3D Digital Cell Atlas for the First Larval Stage of C. Elegans Hermaphrodite," *HHMI JFRC Technical Report*, 2006.

## Selected Bibliography

Peng, H. C., et al., "Reconstructing a Developmental Time Series of 3D Gene Expression Patterns in *Drosophila* Embryos," *Proc. 46th Annual Drosophila Research Conference*, San Diego, CA, 2005.

# Simulation and Estimation of Intracellular Dynamics and Trafficking

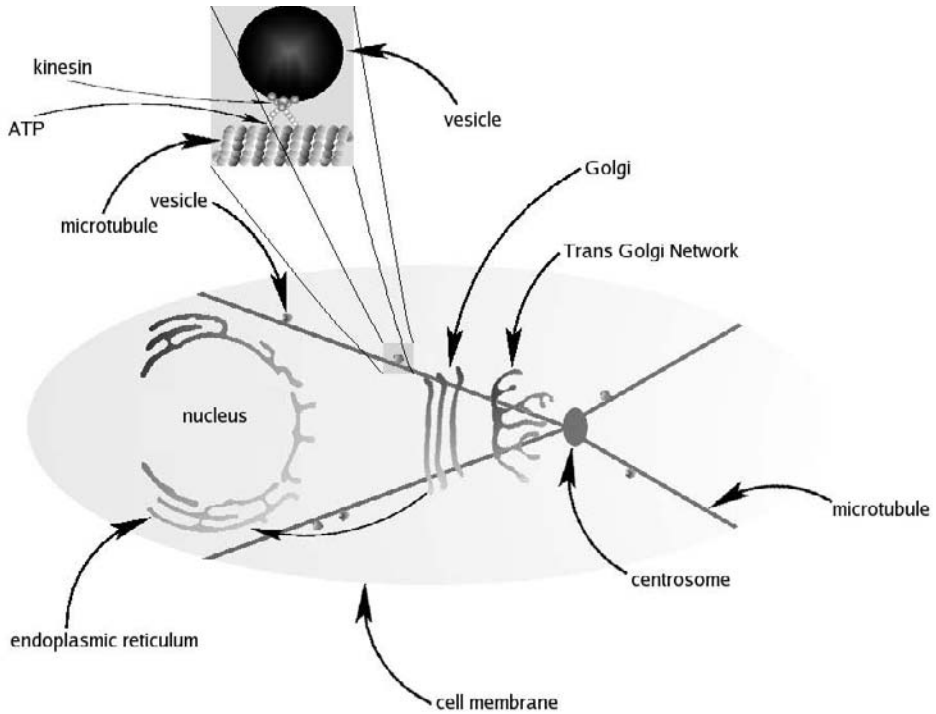
Jérôme Boulanger, Thierry Pécot, Patrick Bouthemy, Jean Salamero, Jean-Baptiste Sibarita, and Charles Kervrann

In this chapter, we present an original modeling framework for membrane trafficking modeling and video-microscopy. Understanding the complexity of cellular processes requires a better knowledge of their dynamic properties and geometric structures. Over the last decade, progresses in cellular and molecular biology as well as in microscopy allow cell visualization while acquiring multidimensional data of their fastly occurring activities.

The proposed method is devoted to the analysis of the dynamical content of microscopy image sequences corresponding to dynamical events related to membrane transport. This chapter is organized as follows. In Section 7.1, the major biological issues are introduced, as well as the optical instruments used for investigation. In this chapter, video-microscopy reveals the dynamical behavior of tagged proteins within the living cell. To capture the movements of these proteins, we propose new models to mimic trafficking of proteins within the cell by making the analogy with computer networks or road networks (Section 7.2). In addition, we provide a framework for *simulating* the foreground and background components observed in real image sequences. Section 7.3 is dedicated to the estimation of the background model. In Section 7.4, we consider the problem of estimating the origin-destination probabilities of the tagged proteins for the trafficking network.

## 7.1 Context

To guarantee the structure, cohesion, and functions of the organism, the eukariotic cell exchanges information between its compartments and organelles: endosomes, Golgi apparatus, and endoplasmic reticulum (ER), and so on. These intracellular exchanges require physical supports or networks for communication. Transportation of molecules from a donor compartment to an acceptor compartment is actually guided by the cell cytoskeleton made of actin filaments, intermediate filaments, and microtubules. The interactions of membranes with microtubules are mediated by several classes of proteins, notably motor proteins of the dynein and kinesin families. The involvement of these motors in the dynamics of various organelles including transport intermediates and cellular structures along microtubules is now well established. In our study, the transport intermediates corresponding to small spherical vesicles move along these “rails”—that is, the microtubules organized by the centrosome (see Figure 7.1). The molecular motors transform the ATP energy



**Figure 7.1** Cell compartments and organelles involved in our study.

produced into a driving energy either in the polymerization direction (e.g., kinesin) or in the depolymerization direction (e.g., dynein) of microtubules, also in action. In what follows, we will assume that the velocities of microtubules is relatively low when compared to the velocities of vesicles.

### 7.1.1 Introduction to Intracellular Traffic

In eukaryotic cells, the constant dynamic process ensuring the steady state distribution of membrane resident proteins and maintaining a balance in the lipid composition of the internal membranes is tightly regulated by a number of proteins. Among these proteins, some are members of the family of Rab-GTPases that bind reversibly to specific membranes within the cells. It is established that the GTPases of the Rab family (about 60 members for human cells) are responsible for the recruitment of proteins that form the vesicles. In this chapter, we will focus on the traffic between the Golgi apparatus and ER, presumably regulated by two isoforms of the Rab6-GTPase, Rab6A and Rab6A', which differ in only a few amino acids. Rab6 is suspected to select among the set of molecular motors those that are the more appropriate for moving molecules to their final destinations in an intracellular compartment. It is now established that Rab6A defines a novel retrograde pathway that is the flux of proteins and lipids from the Golgi apparatus to the ER. More precisely, Rabkinesin-6, a Golgi-associated kinesin-like protein



that only interacts with Rab6A, could be involved in the movement of retrograde transport intermediates between Golgi and ER, but this function is still a matter of controversy. This pathway is also used by certain toxins to reach ER.

We visualized a fluorescent-protein (FP) fusion to Rab6, a Golgi-associated GTPase. Observation of protein dynamics in live cells using fusions to the green fluorescent protein (GFP) and video-microscopy (Fast 4D deconvolution microscopy) enables us to clarify the respective role of Rab6A and Rab6A' in retrograde transport. Thanks to the technological developments performed by the imaging facilities team of the UMR 144 and the Institut Curie, fast dynamics of FP-Rab6 in living cells can be captured in 3-D. We observe that Rab6A mainly associates with the cytosolic face of the Golgi apparatus. Cellular dynamics of Rab6A should be influenced by at least three distinct phenomena: (1) lateral diffusion dictated by lipid movement within a continuum of membranes, (2) continuous exchange between cytosolic and membrane bound pools, and (3) directional motion on membrane transport intermediates. While Rab6A-GFP is concentrated on the cytosolic face of the Golgi membranes, it also associates with rapidly moving transport intermediates that are believed to reach particular stable structures or vesicular clusters located at the cell periphery and referred as end points or ER entry points.

### 7.1.2 Introduction to Living Cell Microscopy

Light microscopy provides cell biologists with the unique possibility of monitoring living samples in their native state. Thanks to recent progress in cellular biology, molecular biology, and microscopy, it is now feasible to observe the cellular activities of various organelles within the cell, in three dimensions, at high spatial and temporal resolutions. These observations are achieved by means of optical sectioning microscopy, in which images are recorded while the focal plane is rapidly and precisely raised through the sample. The three-dimensional (3-D) acquisition process is repeated at several time points during a given period, leading to the collection of image stacks in four dimensions (4-D). The introduction of natural fluorescent probes such as green fluorescent protein (GFP), combined with the increase in the sensitivity of high-resolution detectors, have made it possible to observe living cells for a long period of time at low light excitation levels. It is now routinely possible to collect images of living cells at up to 30 frames per second at optical resolution without disturbing the cell activity. In most intracellular trafficking studies, the optical resolution of wide-field microscopy, which is in the range of the wavelength of light used, is not sufficiently high to optically resolve the organelles of interest. Together with the need for acquisition speed and low light excitation level, they result in blurring and noise, making the data difficult to analyze. Confocal microscopes provide higher spatial resolution in the axial direction, but it is at the expense of loss of precious photons in the detection side. Considering speeds and spatial distribution of organelles taking part in the membrane trafficking, and more especially in the case of Rab6A proteins, we have chosen to perform data acquisition using rapid 4-D wide-field microscopy combined with deconvolution. Actually, part of this protein is carried through a large number of vesicles moving at speeds reaching up to few microns per second in three dimensions. Nevertheless, even

with this rapid technique and the use of image restoration process, the collected images remain difficult to analyze by traditional image analysis methodologies.

Image processing methods have already been developed to reliably track the vesicles over time, with promising results. The computed trajectories can then be used to evaluate trafficking (orientation, velocities, and so on). In this chapter, we propose an alternative and global approach, motivated by actors and components “in motion.” This investigation is of major importance since supervising and/or controlling traffic means that appropriate drugs could be used to either better regulate or limit communication between compartments. The proliferation of cancerous cells could be potentially controlled by stopping molecule transportation.

## 7.2 Modeling and Simulation Framework

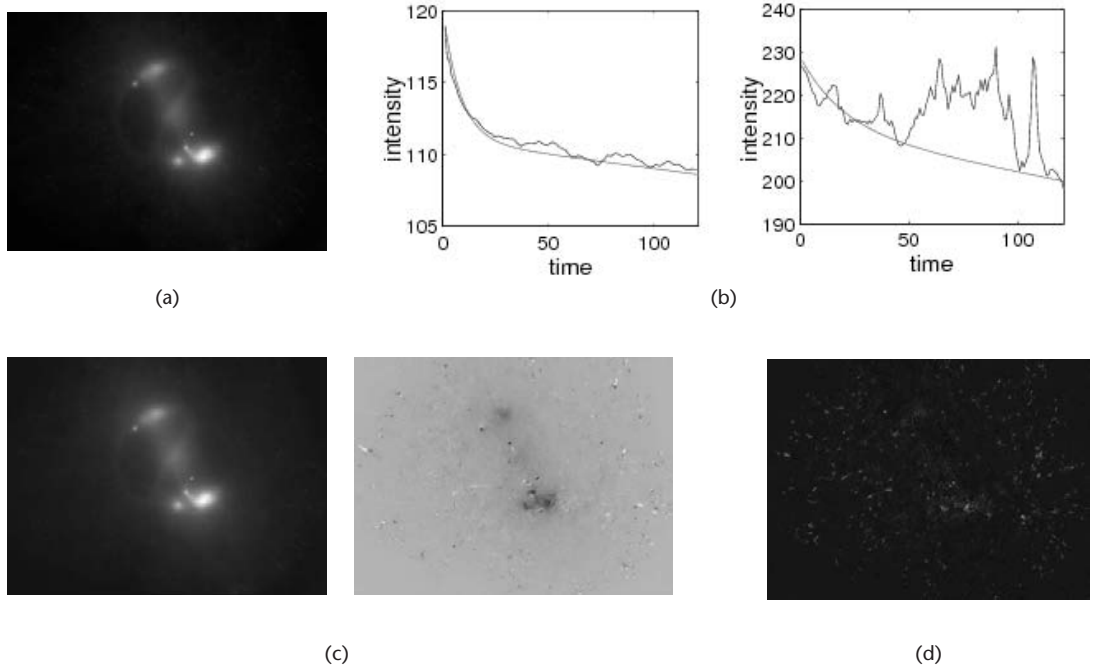
In this section, we present the modeling and a simulation approach for intracellular membrane trafficking. We first introduce the computational model and then provide a method to simulate microscopy image sequences and applications.

### 7.2.1 Intracellular Trafficking Models in Video-Microscopy

Two kinds of approaches have been mainly investigated for modeling image sequences: *data-driven modeling* and *physics-based modeling*. Physics-based approaches exploit physical properties of the scene and optical characteristics of imaging systems to set up an image model. The main advantage relies on the fact that model parameters are given by physics. Hence, they directly correspond to the real world as explained in [1,2] and can be thus easily interpreted. It is worth noting that the complexity of scenes and models is usually an obstacle to this approach, and the *inverse problems* related to the estimation parameters are severely “ill-posed.” *Data-driven modeling* aims at describing image sequences through statistical models learned from real images [3]. This approach is used to mimic a set of dynamical processes occurring frequently in real image sequences, but is not able to describe the physical properties of real processes. *Data-driven* and *physics-based* approaches can be also combined to describe the main components of the image sequences. In video-microscopy and GFP-tagging, these components are essentially the moving objects (foreground), the slowly varying cytosol (background), and some noise due to the acquisition system. Figure 7.2 illustrates this decomposition into background and foreground components. In this section, we propose models for these two components.

#### 7.2.1.1 Background Modeling in Video-Microscopy

In images sequences, large structures and compartments within the cell like the Golgi apparatus and the cytosol appear as nearly static during the observation time interval. In the case of images showing fluorescently tagged particles, the global image intensity is proved to vary slowly along time. This can be due to several physical phenomena, such as photobleaching or diffusion of fluorescent proteins within the cell. Therefore, it is appropriate to propose a model able to describe



**Figure 7.2** (a) GFP-tagging microscopy image. (b) Temporal intensity signals for two different pixels of the image (a). (c) The two components of the background of the image (a). (d) Foreground of the image (a).

the slowly spatially and temporally varying background, since a stationary model would be too restrictive. The modeling of moving small objects corresponding to transport intermediates with variable velocities will be addressed in Section 7.3.

First, we have conducted experiments showing that the intensity variation with respect to time can be captured by a linear model for each pixel of the image sequence, mainly because we are dealing with sequences of limited length. This crude modeling provides a compact representation of the background, described by two 2-D maps corresponding to the two spatially varying parameters. Nevertheless, these parameters are spatially correlated, which must be taken into account later in the estimation process. Note that the proposed approach is general and valid for polynomial models and/or exponential forms if required. Formally, we propose the following image sequence model for the background:

$$f_i(t) = a_i + b_i t + u_i(t) + \varepsilon_i(t) \quad (7.1)$$

where  $f_i(t)$  denotes the intensity observed at pixel  $p_i = (x_i, y_i)^T$  and time  $t$ , and the two coefficients  $a_i$  and  $b_i$  vary with the spatial image position  $p_i$ . The function  $u_i(t)$  is a positive function that describes the intensity of moving intermediate transports (or vesicles) if any, and  $\varepsilon_i(t)$  is the error term assumed to be described by an additive white Gaussian noise. This model is able to describe the background intensity of the whole image sequence with only two 2-D maps  $\{a_i\}$  and  $\{b_i\}$ , whose size is

equal to the size of each image extracted from the temporal sequence. Section 7.3 proposes a statistical method to estimate both the maps  $\{a_i\}$  and  $\{b_i\}$ .

#### 7.2.1.2 Intracellular Membrane Trafficking Modeling

Acquired image sequences contain small bright and fast moving blobs superimposed against slowly varying background. These objects indicate the location of tagged proteins bounded to vesicle membranes. By using these transport intermediates, molecules are passed from a donor compartment to an acceptor compartment.

A simple and commonly adopted model to represent these blobs is a 2-D Gaussian function whose standard deviation is related to the size of the blob. Theoretically, the object diameters range from 60 nm to 150 nm, and the resolution of the microscope is about  $200 \times 200 \times 500$  nm. Accordingly, the diameter of blobs is expected to be below this spatial resolution. However, the point spread function of the video-microscope makes them appear as larger structures even if a deconvolution process is applied [4]. Furthermore, when the density of objects increases, vesicles gather together and constitute small aggregates or rods [5].

These objects are also known to move along microtubules (i.e., along elongated protein polymers that have an exceptional bending stiffness). Microtubules are conveyor belts inside the cells. They drive vesicles, granules, organelles like mitochondria, and chromosomes via special attachment proteins using molecular motors. It is established that molecular motors form a class of proteins responsible for the intracellular transport within the cells. The dynein and kinesin proteins are two different motors associated with microtubules. We consider in our study that in stable conditions, the speed of these motors is constant. This mainly explains why the observed velocity of vesicles is approximately constant if they move along the same microtubule [6].

Vesicles use a microtubule network to carry molecules from a donor compartment to an acceptor compartment (i.e., from the Golgi apparatus to the endoplasmic reticulum). Accordingly, instead of brownian motion or random walks for the vesicles, we consider directed walk models and associated statistical graphs. Hence, each origin vertex and destination vertex of the graph are specific sites on the microtubule network. In addition, once origin-destination pairs have been defined, paths between two vertices are computed according to a routing mechanism. Each object follows a preferential path to reach its target destination. The so-called “origin-destination modeling” is a key point of the proposed framework and is related to the concept of network tomography, as the proposed framework and is related to the concept of network tomography, as we shall see in Section 7.4.

### 7.2.2 Intracellular Traffic Simulation

#### 7.2.2.1 Motivations

In many application fields such as medical imaging or astronomy, simulations are required for validating physical models and understanding recorded data. We give the rationale behind the idea of simulation methods for video-microscopy.

First, realistic simulations of dynamical processes usually give a qualitative representation of the observed spatio-temporal biological events. Simulation can then be considered as a computational tool useful for understanding some mechanisms of internal components within the cell. Then, by interacting with the control parameters, an expert can artificially generate processes of the real world provided the underlying dynamical models are known; this philosophy has been successfully exploited to understand dynamics of microtubule networks [7,8]. By modeling two sets of descriptors respectively computed from a real image sequence and a simulated sequence using an optimization procedure, artificial data can be computed. The set of estimated control parameters can be then considered as a parsimonious representation of the underlying process.

Moreover, simulated image sequences constitute a set of ground truths that can be exploited to measure the performance of object detection, object tracking, and optical flow algorithms [9,10]. Benchmarking data sets are necessary to get reference data and are now widely used in computer vision to evaluate image analysis algorithms [11,12]. Most of image processing tasks cannot be done manually, and they must be fast, reliable, and reproducible. In biomedical imaging, simulation of ground truths is also a crucial and challenging problem. Thus realistic benchmarks have to be generated for each target application.

Simulation methods must be *controllable* [13] with a limited number of parameters. In most cases, the parameters are related not only to the physical properties of the system, but also to the properties of the objects of interest observed in the image, such as scale and velocity. By using a representation with a few degrees of freedom, the simulation method becomes more interactive and intuitive, and allows the expert to bring some a priori knowledge or to plan a set of experiments by editing the simulation. In our case, the expert specifies the locations of origin and destination for the moving objects and then modifies traffic statistics. At last, the expert feedback can be used to set up a realistic simulation.

#### 7.2.2.2 Background Simulation

In our study, the background model associated with the cytosol and other static organelles is described by two 2-D maps  $\{a_i\}$  and  $\{b_i\}$ . These maps can be estimated from acquired data using the procedure described in Section 7.3 or given a priori. Typically, a completely synthetic example can also be obtained by setting the first and the last frame of the sequence corresponding to the background.

#### 7.2.2.3 Membrane Trafficking Simulation

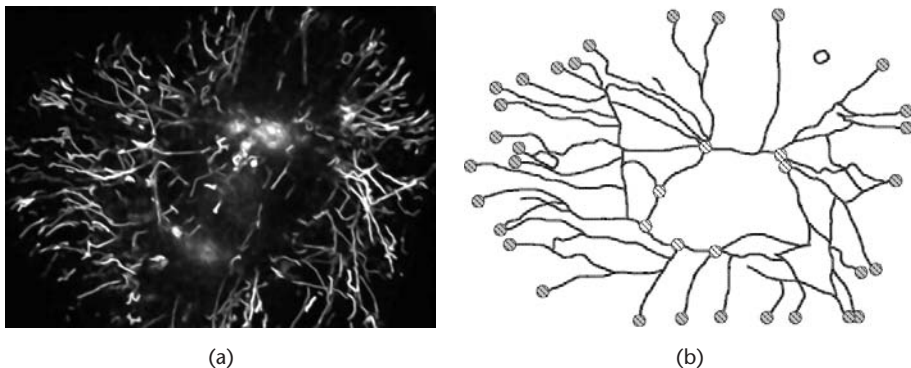
Foreground components are generated using a four-step approach. First, the network is extracted from a real image sequence or provided by a user. Then, the origin-destination pairs are selected, and the paths between the corresponding nodes are computed in a third step. Finally, we simulate moving vesicles and trains/aggregates from computed locations and paths. In the following, this procedure is described in detail.

### Network Extraction

For a trafficking simulation, a microtubule network must be first computed. At first glance, we could exploit the self-organization properties of the microtubule network and try to simulate data as already proposed in [8,14]. Based on the interaction between the motors (e.g., kinesine) and microtubules, the author describes some characteristic conformations such as mitotic spindle. However, even if the approach is attractive, this computer simulation describes only the behavior of the microtubule network *in vitro*; it is not adapted for the more complex *in vivo* case in which the microtubules interact with other organelles of the cell. To produce a synthetic but realistic microtubule network, we decide to use real image sequences as input data for modeling. In what follows, the microtubule network is crudely computed from a maximum intensity projection (MIP) map with respect to time (i.e., from the paths used by the tagged objects). Typically, Figure 7.3(a) shows the MIP map of a sequence made of 300 images corresponding to 10 minutes. This simple method allows us to select a subset of paths mainly used for the intracellular trafficking, leading to a network with low complexity; this approach has been successfully used for the construction of kymograms [6]. However, as shown in Figure 7.3(a), all the paths are not complete, especially if the sequence duration is too short. The gaps are then filled in by using a painting software and ad hoc image processing tools. Furthermore, the positions of the roads are extracted from the network image using the *unbiased line detection* algorithm described in [15]. Finally, each road is described by its length, its width, and its origin and destination nodes. Note that the network could also be fluorescently tagged, but the resulting network is too complex and individual microtubules cannot be easily extracted at the desired spatial resolution.

### Selection of Origin-Destination Pairs

Once the network has been computed, the expert needs to specify the origin and destination nodes on the network. Since the role and function of end regions are



**Figure 7.3** (a) Maximum intensity projection map computed from an image sequence. The paths used by the vesicles appear as bright filaments. The maximum intensity projection map has been simplified using the method described in [26]. (b) Representation of a realistic synthetic network. This network is based on a maximum intensity projection map shown in (a) and has been manually simplified.



partially unknown, a node can be labeled as an origin and a destination node, while the other nodes represent the intersection points of the network and are only used for routing. In Figure 7.3(b), the origin and destination nodes have been manually selected by the expert. The destination nodes are represented by full disks and correspond to end points while the origin nodes corresponding to the membrane of the Golgi apparatus appear as striped disks. In this simulation, vesicles are going only from the Golgi to the end points located at the periphery of the cell. Thus, the retrograde transport from end point to the Golgi is prohibited and assumed to be inhibited by biochemical alterations. Note that origin-destination pair maps are important cues in image sequence analysis, also called birth/death maps in [13].

### *Path Computation*

In our approach, a path is defined as the minimal path between the origin and the destination nodes and is computed using the Dijkstra algorithm [16]. In that case, the weight associated with each edge can be defined as a function of the length of the corresponding road (other parameters can also be considered: speed associated with edges, number of vesicles on each edge, and so on). Finally, the vesicles are moved along the estimated roads with velocities given by the speed limit of the roads. At each time step, the vesicle is then displaced along the microtubule with a distance proportional to the adaptive velocity.

### *Photometric Rendering*

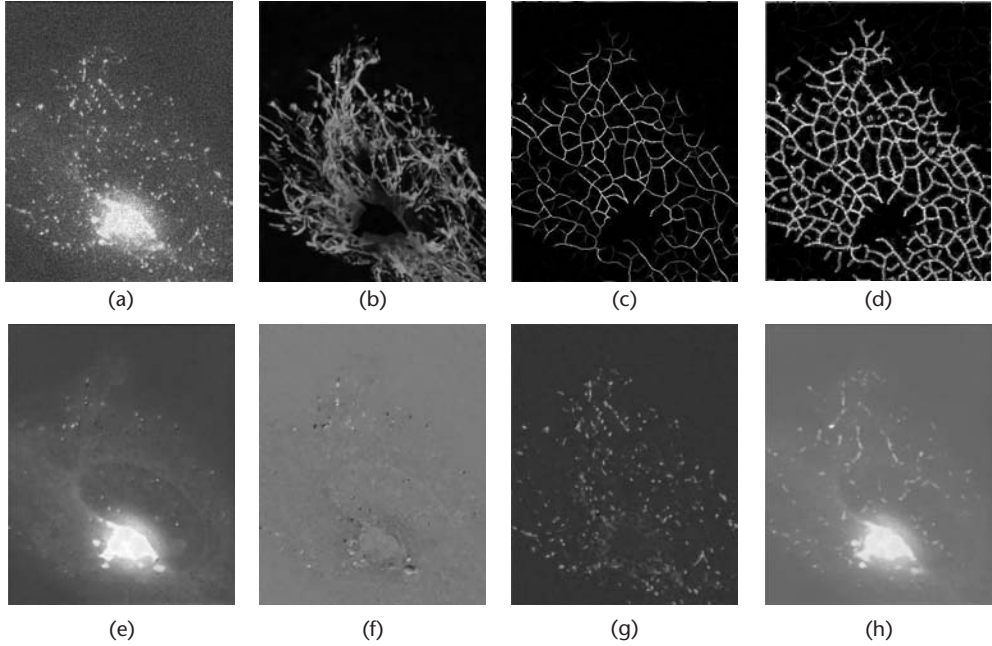
Vesicles are superimposed against the background and are represented by anisotropic Gaussian blobs with variances related to the spot size ranging from 60 nm to 150 nm. The size of the vesicles in the image is then close to the pixel size. In addition, the covariance matrix of the anisotropic Gaussian blob is a function of the displacement direction (aligned with the microtubule direction), and the ellipticity is a function of the velocity. Finally, split-and-merge processes of several vesicles occur in real image sequences. These processes form rods, also further considered as a unique object since the merged blobs move along the same microtubule.

### **7.2.3 Example**

In this experiment, we propose to use a real image sequence to simulate a sequence with similar photometric and dynamical contents. This requires the estimation of the model parameters from the acquired image sequence (see Sections 7.3 and 7.4).

We propose to use the sequence shown in Figure 7.4(a) that represents vesicles moving from the Golgi apparatus to the endoplasmic reticulum. Parameters of the dynamical background are first estimated as it will be described in Section 7.3. The two corresponding 2-D maps  $\{a_i\}$  and  $\{b_i\}$  are, respectively, shown in Figure 7.4(e, f). Given these maps, the background is subtracted from the original image to obtain the sequence of residuals shown in Figure 7.4(g), which is a noisy representation of moving blobs. The main paths used by vesicles during the 150 frames of the real sequence can be observed on the maximum intensity projection





**Figure 7.4** Simulation of a microscopy image sequence from a real image sequence. (a) One frame of the maximum intensity projection sequence *wrt*  $z$  axis (depth) computed from an original 3-D+time image sequence; (b) maximum intensity projection 2-D map *wrt* time  $t$ ; (c) results of steerable filtering; (d) results of the unbiased line detector; (e) map  $\{a_i\}$ ; (f) map  $\{b_i\}$ ; (g) residual map; and (h) noise-free image reconstruction from estimated parameters.

map in the time direction, for which the residuals are shown in Figure 7.4(b). We can enhance the maximum intensity projection map using optimal steerable filters [17] (Figure 7.4(c)). The *unbiased line detection* algorithm [15] is also applied to the enhanced image for estimating the positions of the roads shown in Figure 7.4(d). Finally 150 vesicles are moved given the estimated network. The velocities of the vesicles are tuned so that the simulated sequence is visually similar to the original input sequence.

## 7.3 Background Estimation in Video-Microscopy

In this section, we describe a method for estimating the parameters of the background model defined by (7.1). We start by considering the pixel-wise estimation of the parameters  $(a_i, b_i)$  for each spatial position  $p_i$ . We propose then a method for taking into account spatial correlations to derive two *regularized* maps  $\{a_i\}$  and  $\{b_i\}$ .

### 7.3.1 Pixel-Wise Estimation

First, let us consider the estimation of parameters  $a_i$  and  $b_i$  for a single temporal 1-D signal. Note that the proposed estimation procedure must be very fast to

process each temporal signal, since it is applied to a  $3D+time$  image sequence (several millions of voxels). Besides, as shown in Figure 7.2, vesicles may have a stochastic behavior and stop for a long time. Consequently, temporal signals cannot be easily classified, and prior motion detection cannot be used to extract the moving objects from the background. In the proposed approach, the estimation of the dynamical background will be then based on image intensity. Also, since the background is masked by moving vesicles viewed as outliers, we will also resort to a robust estimation framework, as explained in the next section.

Parameters  $a_i$  and  $b_i$  in (7.1) are estimated by minimizing a robust error function defined by  $E(a_i, b_i) = \sum_{t=1}^n \rho(f_i(t) - (a_i + b_i t))$ , where  $n$  is the number of samples in the 1-D signal, and  $\rho(\cdot)$  is a robust function. A local minimum of  $E(a_i, b_i)$  is commonly obtained by using the iteratively reweighted least squares (IRLS) procedure.

The choice of the robust function  $\rho$  is usually guided by the noise probability density function [18]. In our case, the overall noise is the sum of two components  $u_i(t)$  and  $\varepsilon_i(t)$ . Since  $u_i(t)$  usually takes high positive values (vesicles appear as bright blobs in the image), we decide to choose an asymmetric robust function (Leclerc estimator [19,20]) plotted in Figure 7.5(a) and defined as

$$\rho(z) = \begin{cases} 1 - \exp\left(-\frac{z^2}{\lambda^2 \sigma_1^2}\right) & \text{if } z \leq 0, \\ 1 - \exp\left(-\frac{z^2}{\lambda^2 \sigma_2^2}\right) & \text{otherwise,} \end{cases} \quad (7.2)$$

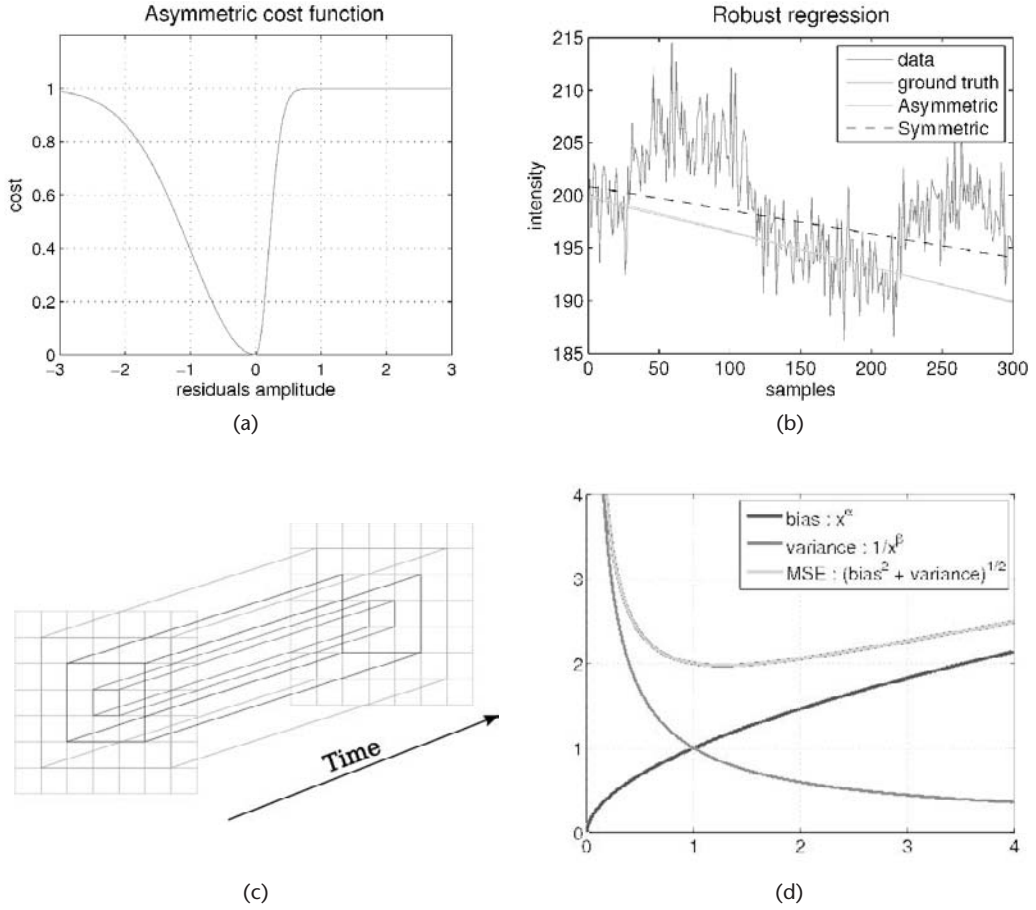
where  $\sigma_1$  and  $\sigma_2$  are two scale parameters and  $\lambda$  acts as a threshold chosen in the range [1,3]. This threshold is relative to the point where the derivative of the  $\rho'(\cdot)$ -function is zero (see [21]). The scale factor  $\sigma_2$  can be estimated by applying a robust least-trimmed squares (LTS) estimator to the *pseudo-residuals* (see [22]) defined as  $s_i(t) = (f_i(t+1) - f_i(t))/\sqrt{2}$ , where the coefficient  $1/\sqrt{2}$  ensures that  $\mathbb{E}[(s_i(t))^2] = \mathbb{E}[(f_i(t))^2]$ . The scale factor  $\sigma_1$  is estimated by using the variance of the residuals given by the least-mean-squares estimator and obtained at the initialization of the estimated procedure. Let us point out that in regions where there are no moving vesicles,  $\sigma_1$  and  $\sigma_2$  are found to be almost equal.

As a matter of fact, even though the proposed estimator is slightly biased [20], simulations proved that the  $L_2$  risk of the estimator is smaller with an asymmetric cost function when data are corrupted by an additive positive signal. Finally, as shown in Figure 7.5(b), the proposed estimator is able to deal with heavily contaminated data and outperforms the symmetric Leclerc M-estimator.

However, this point-wise procedure is not sufficient to accurately estimate the background parameters for all the pixels/voxels. For improving estimations quality, we propose exploiting the spatial correlation between the parameters  $a_i$  and  $b_i$ .

### 7.3.2 Spatial Coherence for Background Estimation

Spatial regularization can be accomplished by adopting the *bias-variance tradeoff* framework already described in [23–26]. Instead of using a single temporal signal



**Figure 7.5** (a) Asymmetric Leclerc robust function. (b) Regression using an asymmetric and symmetric robust Leclerc function. The asymmetric estimator fits perfectly the ground truth while the symmetric function provides biased results (dotted line). (c) Set of nested tubes  $\{\mathcal{T}_{i,k}\}_{k=1,\dots,3}$ . (d) Bias-variance trade-off principle. When the tube diameter increases, the bias increases and the variance decreases. The optimum is achieved when the bias and the variance are of the same order.

for each pixel  $p_i$  to estimate  $a_i$  and  $b_i$ , a set of temporal 1-D signals is first collected in a spatial neighborhood of pixel  $p_i$ . A set of nested space-time tubes is considered by taking the pixels in a growing spatial square neighborhood of  $p_i$  (see Figure 7.5(c)). Each tube  $\mathcal{T}_{i,k}$  at  $p_i$  is parameterized by its diameter  $\phi_{i,k}$ , where  $k \in [1, \dots, K]$  denotes the iteration of the procedure.

To select the optimal diameter of the space-time tube at pixel  $p_i$ , the point-wise  $L_2$  risk  $\mathbb{E}[(\hat{\theta}_i - \theta_i)^2]$  (decomposed into two parts: squared bias and variance) of the estimator is minimized, where  $\theta_i = (a_i, b_i)$  denotes the true value, and  $\hat{\theta}_i$  is the corresponding estimator at pixel  $p_i$ . As shown in Figure 7.5(d), while the diameter  $\phi_{i,k}$  increases with  $k$ , the bias increases too. This can be explained by the fact that the data cannot be described any longer by a unique parametric model. In contrast, by taking more data points, the variance decreases. This behavior, also

called *bias-variance tradeoff*, is exploited to detect the minimum of the point-wise  $L_2$  risk, which is nearly equal to twice the variance [23] (see Figure 7.5(d)).

For each diameter  $\phi_{i,k}$ , new estimates of the background model parameters  $\hat{\theta}_{i,k}$  and the associated covariance matrix  $\hat{C}_{i,k}$  (as proposed in [18]) are computed with the procedure described in Section 7.3.1, but by using all the data taken in the considered spatial neighborhood. Furthermore, it can be shown that the *bias-variance tradeoff* can be expressed with the following statistical test [26]:

$$\frac{n-2+1}{2n} \left( \hat{\theta}_{i,k} - \hat{\theta}_{i,k'} \right)^T \hat{C}_{i,k'}^{-1} \left( \hat{\theta}_{i,k} - \hat{\theta}_{i,k'} \right) < \eta \quad (7.3)$$

for all  $1 \leq k' < k$ , where the threshold  $\eta$  is defined as a quantile of a Fisher distribution of parameters 2 and  $n-2-1$ , since we use an estimator of the covariance matrix. While this inequality is satisfied, the diameter of the tube is increased and the estimation process is continued.

### 7.3.3 Example

We now describe an experiment that demonstrates the performance of the estimation method. For this purpose, we use the real image sequence shown in Figure 7.4(a). The estimated maps  $\{\hat{a}_i\}$  and  $\{\hat{b}_i\}$  are, respectively, shown in Figure 7.4(e, f). The map  $\{\hat{a}_i\}$  related to the static component of the background model reveals several interesting locations in the cell. The very bright region is associated to the Golgi apparatus, while the bean-shaped darker region indicates the location of the nucleus. Finally, Figure 7.4(g) shows the residual map containing only the vesicles, appearing as small blobs in the foreground of the image sequence. Next section deals with the estimation of the model parameters describing the foreground.

## 7.4 Foreground Analysis: Network Tomography

We propose here a method to estimate flows between origin-destination (OD) pairs. If these flows are known, simulation can be performed as described in Section 7.2. This approach was applied to the analysis of road trafficking [27], and more recently to communication networks [28].

Usual approaches for traffic analysis in video-microscopy aim at tracking each object. The most commonly used tracking concept is the connexionist approach [29, 30] consisting of detecting particles independently in each frame and then linking the detected objects over time. In the case of Rab6 analysis, temporal sampling is quite low compared to the speed of the numerous vesicles. Then, the correspondence between the detected objects and their entire trajectories (data association) is very hard to compute. Recent data association combined with sophisticated particle filtering techniques [31], fast marching methods [32], or graph theory-based methods [10, 33] have been successfully applied and solve the tracking problem in these difficult conditions. In this chapter, we propose an alternative framework also consistent with traffic modeling. Note that the OD flow problem is also related to the extraction of kymograms in video-microscopy image

sequence [6] in the sense that it also uses the microtubule network as a priori information.

In this section, we first introduce the concept of network tomography (NT). Then, we propose an original approach to measure activities on the network edges, which amounts to counting vesicles in regions, avoiding tracking, and motion estimation. Finally, we present an optimization framework to estimate the origin-destination flows from these measurements.

#### 7.4.1 Network Tomography Principle

We now introduce the principle of NT and its application to video-microscopy trafficking. In Section 7.2, a network model has been introduced to describe the foreground in the image sequences. In this model, the graph associated with the microtubule network is composed of vertices associated with crossings or origin and destination nodes, and edges associated to “roads” used by the vesicles. To estimate flows of objects, a straightforward approach would be to measure the activity on the roads. However, this requires an accurate localization of the roads and reliable detection of the vesicles which are both known to be hard problems in computer vision. In what follows, we consider a network with a limited number of nodes (to indicate cell regions obtained by image partitioning).

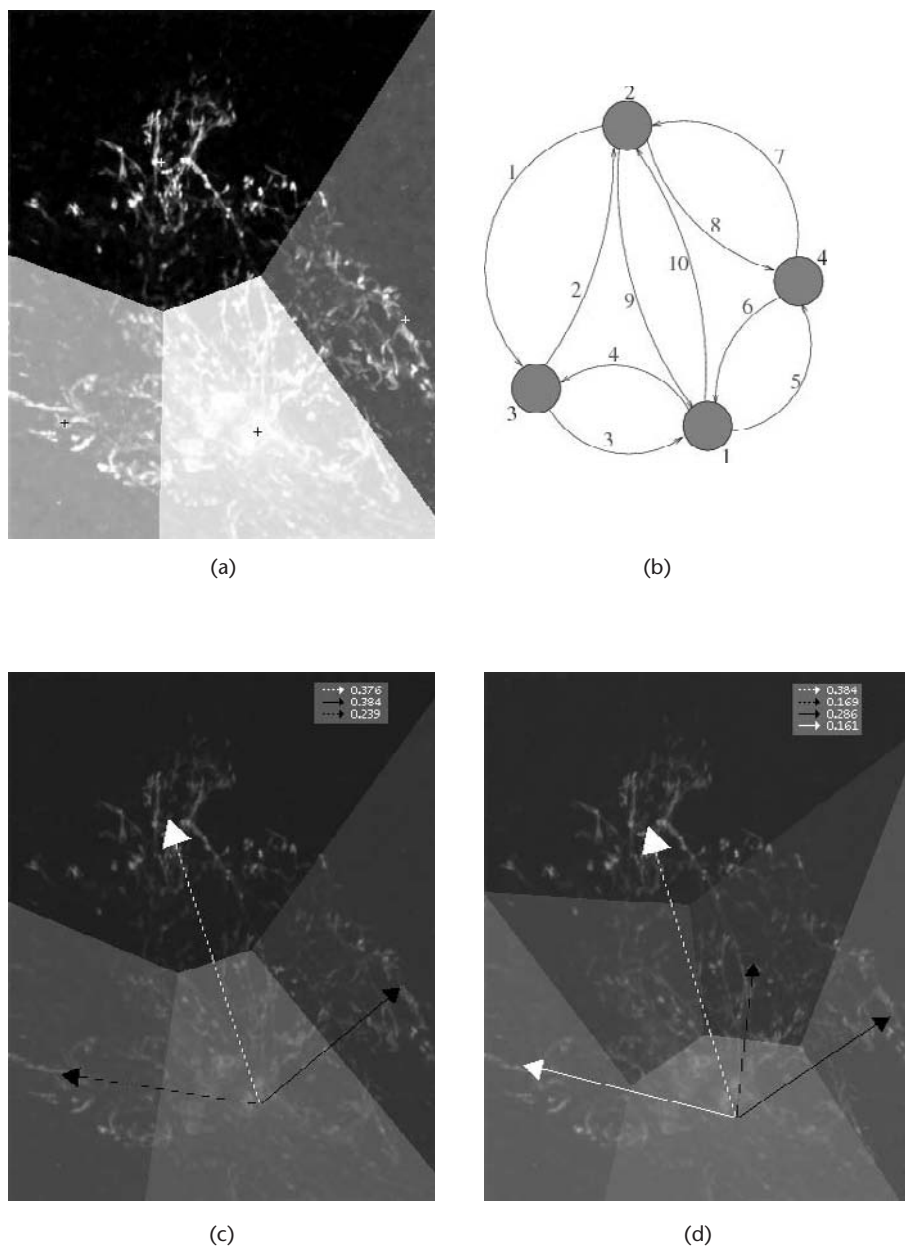
##### 7.4.1.1 Partitioning the Cell Region

The maximum intensity projection (MIP) map in the direction of time axis is a precious key for partitioning the imaged region. We assume that the likely regions of origin or destination correspond to brighter spots in the MIP map because vesicles are temporally stocked in these areas. For illustration, the MIP map extracted from the image sequence shown in Figure 7.4(a) is given in Figure 7.4(g). A possible image partitioning consists of arbitrarily dividing the MIP image into Voronoi cells given a set of labeled regions obtained automatically or supplied by the expert biologist if required, as proposed in [34]. A partition for the cell observed in the image sequence of Figure 7.4(a) is typically illustrated in Figure 7.6(a), where the centers are represented as crosses and the different regions appear in gray levels, while the MIP map is depicted in the background. In practical imaging, the Voronoi diagram is computed using the *qhull* library [35].

Note that the Voronoi diagram can be described by an adjacency graph (Figure 7.6(b)), which is consistent with the NT concept used for tracking. The different Voronoi cells represent the set of vertices  $V$ , while the boundaries between the cells represent the set of edges  $E$ , so the graph  $G(E, V)$  is wholly defined. Finally, we introduce two edges in the graph between two neighboring cells for bidirectional trafficking.

##### 7.4.1.2 Network Tomography Concept

We present more formally the estimation of the OD flows on the designed network. The graph  $G$  is composed of  $n$  vertices and  $r$  edges. An *origin/destination pair* is a *couple* of vertices in the graph linking an *origin* vertex to a *destination* vertex. So,



**Figure 7.6** (a) Partition of the image sequence shown in Figure 7.4(a) by using a Voronoi decomposition. The different regions appear in gray levels, their centers appear as crosses, and the MIP map is depicted in the background; (b) the corresponding graph; and (c) and (d) results obtained by applying the NT-based approach on the sequence of the Figure 7.4(a). The arrows represent the estimated OD pairs, and the corresponding numbers at the top right represent traffic proportions. For these two experiments, the region at the bottom is imposed to be an origin region.

**Table 7.1** Part of Matrix **A** Corresponding to the Graph Shown in Figure 7.6(b)

OD Pairs	<i>Edges</i>									
	1	2	3	4	5	6	7	8	9	10
$1 \rightarrow 2$	0	0	0	0	0	0	0	0	0	1
$1 \rightarrow 3$	0	0	0	1	0	0	0	0	0	0
$1 \rightarrow 4$	0	0	0	0	1	0	0	0	0	0
$2 \rightarrow 1$	0	0	0	0	0	0	0	0	1	0
$2 \rightarrow 3$	1	0	0	0	0	0	0	0	0	0
$2 \rightarrow 4$	0	0	0	0	0	0	0	1	0	0
$3 \rightarrow 1$	0	0	1	0	0	0	0	0	0	0
$3 \rightarrow 2$	0	1	0	0	0	0	0	0	0	0
$3 \rightarrow 4$	0	0	1	0	1	0	0	0	0	0
...						...				

the set of all possible OD pairs is composed of  $c = n(n - 1)$  elements. Given the number of objects detected as going from one vertex to a neighbor vertex in the graph, the goal consists of estimating how many vesicles use each OD pair, by linking OD pairs with edges, thanks to a routing procedure. This problem is then similar to determining the source-destination trafficking based on link measurements in computer networks [28].

Let  $X_{j,t}$ ,  $j = 1, \dots, c$  be the number of “transmitted” vesicles on the OD pair  $j$  at time  $t$ . The measurements  $\mathbf{Y}_t = (Y_{1,t}, \dots, Y_{r,t})^T$  are the number of vesicles that pass from one vertex to another vertex at time  $t$ . In this traffic flow problem, we then assume the following model:

$$\mathbf{Y}_t = \mathbf{A}\mathbf{X}_t \quad (7.4)$$

where  $\mathbf{X}_t = (x_{1,t}, \dots, x_{c,t})^T$ , and  $\mathbf{A}$  denotes an  $r \times c$  routing matrix, which has binary elements  $A_{ij} = 1$  if edge  $i$  is in the path for the OD pair  $j$ , and 0 otherwise. The path between two vertices in the graph is defined as the shortest path between these two vertices. For illustration, if we consider the simple example shown in Figure 7.6(b), some rows of the matrix  $\mathbf{A}$  are presented in Table 7.1. The aim is to estimate  $\mathbf{X}_t$  given  $\mathbf{A}$ , but in image sequences, the counting analysis data  $\mathbf{Y}_t$  are not available and must be carefully computed. We address this problem in the next section.

#### 7.4.2 Measurements

The application of NT requires knowing exactly how many vesicles are moving from one Voronoi cell to another one at each time step. Our idea is to compute the difference of the number of vesicles observed at two consecutive time steps in each neighboring region and then to infer the exact number of vesicles that crosses each common boundary. Moreover, we assume that the level of fluorescence is proportional to the number of objects at each pixel. So the difference of image intensity between two time steps represents the difference of the number of objects in each region. Preliminary, the background corresponding to the Golgi Apparatus



**Table 7.2** Definition of Matrix **M** Corresponding to the Graph Shown in Figure 7.6(b)

Vertices	Edges									
	1	2	3	4	5	6	7	8	9	10
1	0	0	1	-1	-1	1	0	0	1	1
2	-1	1	0	0	0	0	1	-1	-1	-1
3	1	-1	-1	1	0	0	0	0	0	0
4	0	0	0	0	1	-1	-1	1	0	0

and the cytosol is removed using the preprocessing algorithm, as explained in Section 7.3. We illustrate this idea using a simple example.

We consider the fluorescence exchanges at vertex 1 in the graph shown in Figure 7.6(b). Let  $Z_{v,t}$  be the total amount of fluorescence at vertex  $v$  and time  $t$ , and let  $Y_{e,t}$  be the level of fluorescence to be determined on edge  $e$  at time  $t$ :

$$Z_{1,t+1} - Z_{1,t} = Y_{3,t+1} - Y_{4,t+1} + Y_{6,t+1} - Y_{5,t+1} + Y_{9,t+1} - Y_{10,t+1}$$

This equation can be extended to all vertices: let  $\Delta\mathbf{Z}$  be the  $n \times t$  matrix corresponding to the difference of fluorescence in each region between two consecutive time steps, with  $n$  the number of regions and  $t$  the number of images in the sequence. Let  $\mathbf{Y}$  be the  $r \times t$  matrix representing the level of fluorescence that fluctuates from one region to another at each time, with  $r$  denoting the number of edges. We define  $\mathbf{M}$  as the so-called “neighborhood  $n \times r$  matrix” composed of ternary elements  $m = \{-1, 0, 1\}$  that links the regions according to the neighborhood relationships. For example, in the graph of Figure 7.6(b),  $\mathbf{M}$  is defined as shown in Table 7.2. Then, we have the linear equation:

$$\Delta\mathbf{Z} = \mathbf{M}\mathbf{Y} \quad (7.5)$$

Our aim is to estimate  $\mathbf{Y}$  with  $r > n$  given  $\Delta\mathbf{Z}$ , to solve an *under-constrained* problem. Additional constraints are necessary for solving (7.5). First, we assume that all the components of  $\mathbf{Y}$  are positive since the edges are unidirectional. In addition, the  $\Delta\mathbf{Z}$  rows are assumed to be independent and identically distributed (i.i.d.), and Gaussian distributed. This leads to the following optimization problem:

$$\hat{\mathbf{Y}} = \min_{\mathbf{Y}} \|\Delta\mathbf{Z} - \mathbf{M}\mathbf{Y}\|^2 \text{ subject to } \mathbf{Y} \geq 0$$

solved by a nonnegative least square algorithm. The estimated measurements are further used for NT.

### 7.4.3 Problem Optimization

Once the data are estimated, we have to estimate  $\mathbf{X}_t$  from (7.4). The inherent randomness of the measurements motivates the adoption of a statistical approach.

#### 7.4.3.1 General Case

We reasonably assume that the whole traffic is temporally distributed as a Poisson process—(i.e.,  $\mathbf{X}_{j,t} \sim \text{Poisson}(\lambda_j)$ ). Then, the number  $c$  is greater than  $r$ , and the problem is under constrained. Additional constraints are necessary for solving this *inverse problem*. First, in [28], the author proposed introducing constraints related to the assumption that the traffic is temporally Poisson distributed. The NT method amounts then to estimating the values  $\lambda_j$  given the additional set of equations corresponding to temporal averages:

$$\begin{cases} \bar{Y}_i = \sum_{k=1}^c A_{i,k} \lambda_k, & i = 1, \dots, r \\ \text{cov}(Y_i, Y_{i'}) = \sum_{k=1}^c A_{i,k} A_{i',k} \lambda_k, & 1 \leq i \leq i' \leq r \end{cases}$$

This set of equations gives a system of  $r(r+3)/2$  linear equations that forms an overconstrained problem that can be better solved with the conditions  $\lambda_i \geq 0$ . Moreover, in this study, the aim is not to obtain the number of vesicles that utilize each path, but to estimate the proportions of vesicles on each path. Hence, unlike previous methods [28,34,36], we impose the condition  $\sum_{i=1}^c \lambda_i = 1$  as an additional constraint. The previous system can be written more compactly as:

$$\begin{pmatrix} \bar{\mathbf{Y}} \\ \mathbf{S} \end{pmatrix} = \begin{pmatrix} \mathbf{A} \\ \mathbf{B} \end{pmatrix} \Lambda \quad (7.6)$$

where  $\Lambda = (\lambda_1, \dots, \lambda_c)^T$  contains the temporal mean of the traffic flow,  $\mathbf{S} = \{\text{cov}(Y_i, Y_{i'})\}$  is the sample covariance matrix rewritten as a vector of length  $r(r+1)/2$ , and  $\mathbf{B}$  is an  $(r(r+1)/2) \times c$  matrix with the  $(i, i')$ th row of  $\mathbf{B}$  being the element-wise product of row  $i$  and row  $i'$  of the matrix  $\mathbf{A}$ .

The system can be solved using the estimation-maximization (EM) method [28, 36] or the convex-projection algorithms [34]. In our case, we adapt a nonnegative mean square estimation that also provides a simple and reliable way to estimate the OD traffic  $\hat{\Lambda}$ . Note that a review of existing methods is proposed in [37].

#### 7.4.3.2 More Constraints and A Priori Knowledge

When the expert specifies the origin or destination regions, the problem is better constrained and the solution is expected to be more relevant. If we assume that the origins or destinations are known, this can be casted into additional hard constraints. Typically, if the Voronoi cell  $r$  is the single origin region to be considered, then all the OD pairs involving other origin cells except  $r$  should be discarded. Hence, let  $\mathcal{R}$  be the set of OD pairs for which  $r$  is the origin vertex. Then, if  $\mathcal{O}$  denotes the set of all OD pairs,  $\mathbf{A}$  can be modified as follows:

$$\mathbf{A}(:, \mathcal{O} \setminus \mathcal{A}) = 0$$

with  $\mathbf{A}(:, \mathcal{O} \setminus \mathcal{A}) = \{\mathbf{A}(1, \mathcal{O} \setminus \mathcal{A}); \mathbf{A}(2, \mathcal{O} \setminus \mathcal{A}); \dots; \mathbf{A}(r, \mathcal{O} \setminus \mathcal{A})\}$ . The same modeling can be applied for imposing additional origin or destination regions. This

demonstrates the flexibility of the approach, adapted to situations when prior knowledge is required.

#### 7.4.4 Experiments

In this section, we propose two experiments to demonstrate the ability of the NT-based approach for a real image sequence. All these experiments are tested by considering the sequence shown in Figure 7.4(a). This sequence is composed of 150 images extracted from a fast 4-D deconvolution microscopy (wide-field) process [6]. First, the background has been removed during a preprocessing step. The estimated results are reported in Figure 7.6(c, d). In these figures, the Voronoi cells are in gray levels, while the MIP map is shown in the background by transparency. The different estimated OD pairs appear as arrows, and the corresponding numbers at the right top of the figures are the estimated proportions of moving vesicles for each OD pair.

A first experience was carried out with a crude segmentation (Figure 7.6(c)). According to the expert biologists, the vesicles are moving from the Golgi Apparatus (the region at the bottom) to end points located at the periphery of the cell (corresponding to the three other regions)—that is why we impose the region at the bottom to be the origin Voronoi cell. The results obtained with this additional hard constraint correspond to trafficking from the Golgi Apparatus to the end points. In that case, the traffic tends to be a little denser in the regions at the top and on the right than in the region on the left.

In another experiment corresponding to another partition of the image shown in Figure 7.6(d), two Voronoi cells are added between the origin cell and the destination cells. The Voronoi cell located at the bottom is still constrained to be the origin cell. With this partitioning, another destination cell appears at the top right of the compartment. This is not in contradiction with the expert biologists since this region is located on the periphery of the cell. We observe that the amount of traffic that had the right Voronoi cell for destination in the previous experiment is divided into the two destination cells on the right of the compartment for this experiment.

## 7.5 Conclusions

We have described an original framework for the analysis of the dynamical content of fluorescence video-microscopy dedicated to the intracellular membrane trafficking. We have briefly introduced the biological context and fluorescence video-microscopy, and presented a data-based modeling for the intracellular trafficking. The proposed model is parametric with few degrees of freedom and relies on the separation between background/foreground. It provides a statistical description of the events observed in the cell. This modeling can be used for image simulation; the input parameters are either specified by the user or estimated beforehand from real image sequences. In the latter case, a point-wise adaptive estimation is presented for estimating the parameters related to the background of the sequence. Then,

network tomography is used to recover from the sequence the origin-destination probabilities associated to the particles. Measurements are a critical point in this framework, and an original method is described to avoid motion estimation and tracking in noisy video-microscopy.

Even though these preliminary results are encouraging, this new estimation/simulation approach still needs further development. We hope that it will help to better understand the mechanisms involved in the intracellular traffic.

## References

- [1] Chowdhury, D., L. Santen, and A. Schadschneider, "Statistical Physics of Vehicular Traffic and Some Related Systems," *Physics Reports*, Vol. 329, 2000, p. 199.
- [2] Helbing, D., "Traffic and Related Self-Driven Many-Particle Systems," *Review of Modern Physics*, Vol. 73, October 2001, pp. 1067-1141.
- [3] Soatto, S., G. Doretto, and Y. N. Wu, "Dynamic Textures," *Proc. of ICCV'2001*, Vol. 2, Vancouver, Canada, July 2001, pp. 439-446.
- [4] Sibarita, J.-B., H. Magnin, and J. R. De Mey, "Ultra-Fast 4D Microscopy and High Throughput Distributed Deconvolution," *Proc. of IEEE ISBI'2002*, Washington, D.C., June 2002, pp. 769-772.
- [5] Zhang, B., J. Enninga, J.-C. Olivo-Marin, and C. Zimmer, "Automated Super-Resolution Detection of Fluorescent Rods in 2D," *Proc. of IEEE ISBI'2006*, Washington, D.C., April 2006, pp. 1296-1299.
- [6] Sibarita, J.-B., V. Racine, and J. Salamero, "Quantification of Membrane Trafficking on a 3D Cytoskeleton Network in Living Cells," *Proc. of IEEE ISBI'2006*, Washington, D.C., April 2006.
- [7] Gibbons, F., J. Chauwin, M. Desposito, and J. José, "A Dynamical Model of Kinesin-Microtubule Motility Assays," *Biophysical Journal*, Vol. 80, June 2001, pp. 2515-2526.
- [8] Nédélec, F., "Computer Simulations Reveal Motor Properties Generating Stable Antiparallel Microtubule Interactions," *Journal of Cell Biology*, Vol. 158, September 2001, pp. 1005-1015.
- [9] Genovesio, A., T. Liedl, V. Emiliani, W. J. Parak, M. Coppey-Moisán, and J.-C. Olivo-Marin, "Multiple Particle Tracking in 3D+t Microscopy: Method and Application to the Tracking of Endocytosed Quantum Dots," *IEEE Trans. on IP*, Vol. 15, May 2006, pp. 1062-1070.
- [10] Racine, V., A. Hertzog, J. Jouaneau, J. Salamero, C. Kervrann, and J.-B. Sibarita, "Multiple Target Tracking of 3D Fluorescent Objects Based on Simulated Annealing," *Proc. of IEEE ISBI'2006*, Washington, D.C., April 2006.
- [11] Portilla, J., V. Strela, M. Wainwright, and E. Simoncelli, "Image Denoising Using Scale Mixtures of Gaussians in the Wavelet Domain," *IEEE Trans. on IP*, Vol. 12, November 2003, pp. 1338-1351.
- [12] Barron, J. L., D. J. Fleet, and S. S. Beauchemin, "Performance of Optical Flow Techniques," *IJCV*, Vol. 12, January 1994, pp. 43-77.
- [13] Wang, Y., and S. C. Zhu, "Modeling Textured Motion: Particle, Wave and Sketch," *Proc. of ICCV 2003*, October 2003.
- [14] Surrey, T., F. Nédélec, S. Leibler, and E. Karenti, "Physical Properties Determining Self-Organization of Motors and Microtubules," *Science*, Vol. 292, May 2001, pp. 1167-1171.
- [15] Steger, C., "An Unbiased Detector of Curvilinear Structures," *IEEE Trans. on PAMI*, Vol. 20, February 1998, pp. 113-125.

- [16] Dijkstra, E. W., "A Note on Two Problems in Connexion with Graphs," *Numerische Mathematik*, Vol. 1, December 1959, pp. 269–271.
- [17] Jacob, M., and M. Unser, "Design of Steerable Filters for Feature Detection Using Canny-Like Criterion," *IEEE Trans. on PAMI*, Vol. 26, August 2004, pp. 1007–1019.
- [18] Ieng, S.-S., J.-P. Tarel, and P. Charbonnier, "Evaluation of Robust Fitting Based Detection," *Proc. of ECCV'2004*, Vol. 2, Prague, Czech Republic, May 2004, pp. 341–352.
- [19] Allende, H., A. Frery, J. Galbiati, and L. Pizarro, "M-Estimator with Asymmetric Influence Function: The  $\mathcal{G}_a^0$  Distribution Case," *Journal of Statistical Computation and Simulation*, Vol. 76, November 2006, pp. 941–946.
- [20] Ruckstuhl, A., M. Jacobson, R. Field, and J. Dodd, "Baseline Subtraction Using Robust Local Regression Estimation," *Journal of Quantitative Spectroscopy and Radiative Transfer*, Vol. 68, January 2001, pp. 179–193.
- [21] Black, M., G. Sapiro, D. Marimont, and D. Heeger, "Robust Anisotropic Diffusion," *IEEE Trans. on IP*, Vol. 7, March 1998, pp. 421–432.
- [22] Gasser, T., L. Sroka, and C. Jennen-Steinmetz, "Residual Variance and Residual Pattern in Nonlinear Regression," *Biometrika*, Vol. 73, 1986, pp. 625–633.
- [23] Lepski, O., "Asymptotically Minimax Adaptive Estimation 1: Upper Bounds," *SIAM Journal Theory of Probability and Application*, Vol. 36, No. 4, 1991, pp. 654–659.
- [24] Maurizot, M., P. Bouthemy, B. Delyon, A. Iouditski, and J.-M. Odobez, "Determination of Singular Points in 2D Deformable Flow Fields," *Proc. of ICIP'1995*, Vol. 3, Washington, D.C., October 1995, pp. 488–491.
- [25] Ercole, C., A. Foi, V. Katkovnik, and K. Egiazarian, "Spatio-Temporal Pointwise Adaptive Denoising in Video: 3D Non Parametric Approach," *Proc. of 1st International Workshop on Video Processing and Quality Metrics for Consumer Electronics, VPQM 2005*, Scottsdale, AZ, January 2005.
- [26] Kervrann, C., and J. Boulanger, "Optimal Spatial Adaptation for Patch-Based Image Denoising," *IEEE Trans. on IP*, Vol. 15, No. 10, 2006, pp. 2866–2878.
- [27] Cascetta, E., and S. Nguyen, "A Unified Framework for Estimating or Updating Origin/Destination Matrices from Traffic Counts," *Transportation Research*, Vol. 22, No. 6, 1988, pp. 437–455.
- [28] Vardi, Y., "Network Tomography: Estimation Source-Destination Traffic Intensities from Link Data," *Journal of the American Statistical Association*, Vol. 91, March 1996, pp. 365–377.
- [29] Anderson, C., G. Georgiou, I. Morrison, G. Stevenson, and R. Cherry, "Tracking of Cell Surface Receptors by Fluorescence Digital Imaging Microscopy Using a Charged-Coupled Device Camera. Low-Density Lipoprotein and Influenza Virus Receptor Mobility at 4 Degrees C," *Journal of Cell Science*, Vol. 101, 1992, pp. 415–425.
- [30] Sbalzarini, I., and P. Koumoutsakos, "Feature Point Tracking and Trajectory Analysis for Video Imaging in Cell Biology," *Journal of Structural Biology*, Vol. 151, 2005, pp. 182–195.
- [31] Smal, I., W. Niessen, and E. Meijering, "Advanced Particle Filtering for Multiple Object Tracking in Dynamic Fluorescence Microscopy Images," *Proc. of IEEE ISBI 2007*, Arlington, VA, April 2007, pp. 1048–1051.
- [32] Bonneau, S., M. Dahan, and L. D. Cohen, "Tracking Single Quantum Dots in Live Cells with Minimal Paths," *Proc. of IEEE CVPR'2005*, Vol. 3, San Diego, CA, June 2005, pp. 141–149.
- [33] Thomann, D., J. Dorn, P. Sorger, and G. Danuser, "Automatic Fluorescent Tag Localization II: Improvement in Super-Resolution by Relative Tracking," *Journal of Microscopy*, Vol. 211, September 2003, pp. 230–248.
- [34] Boyd, J. E., J. Meloche, and Y. Vardi, "Statistical Tracking in Video Traffic Surveillance," *Proc. of ICCV'99*, Vol. 1, Kerkira, Greece, September 1999, pp. 163–168.

- [35] Barber, C., D. Dobkin, and H. T. Huhdanpaa, "The Quickhull Algorithm for Convex Hulls," *ACM Transactions on Mathematical Software*, Vol. 22, December 1996, pp. 469–483.
- [36] Santini, S., "Analysis of Traffic Flow in Urban Areas Using Web Cameras," *Fifth IEEE Workshop on Applications of Computer Vision*, Vol. 596, 2000, pp. 140–145.
- [37] Medina, A., N. Taft, K. Salamatian, S. Bhattacharyya, and C. Diot, "Traffic Matrix Estimation: Existing Techniques and New Directions," *Proc. of Conference on Applications, Technologies, Architectures, and Protocols for Computer Communications, SIGCOMM '02*, New York, 2002, pp. 161–174.

# Techniques for Cellular and Tissue-Based Image Quantitation of Protein Biomarkers

Ali Can, Musodiq Bello, Xiaodong Tao, Michael Gerdes, Anup Sood, Michael C. Montalto, and Fiona Ginty

## 8.1 Current Methods for Histological and Tissue-Based Biomarker

Hematoxylin-Eosin (H&E) staining of thin (5–7 micron) tissue sections has been used by pathologists for well over 100 years and is widely accepted as the foundation of disease classification. Hematoxylin stains cell nuclei blue, while eosin, as a counter-stain, stains cytoplasm and connective tissue pink. Due to its long history, as well as low cost, fast preparation, and easy image acquisition, there is a strong belief that H&E will continue to be the common practice for the foreseeable future [1, 2].

Pathologists typically make diagnostic decisions from H&E stained tissue sections based on the attributes of cell size, shape, texture, and color contrast of various fine features as viewed under a microscope [3]. Although a pathologist is well trained to decipher fine differences in tissue features, the analysis is inherently subjective, and use of objective quantitative analysis is limited in current clinical practice. With the advancement of digital microscopy, high-quality microscopic images of specimens are becoming digitally available in large quantities [4]. Digital technology will likely lend itself to quantitative objective analysis of H&E stained tissue sections [5, 6]. However, the complex interpretations that are learned through years of training and that rely on the complexities of the human mind will be difficult to fully recapitulate, even with current and future computational power.

One area in clinical pathology practice that lends itself more readily to quantitative image analysis is immunohistochemistry (IHC) and fluorescence in situ hybridization (FISH), collectively known as *molecular pathology*. The advent of IHC in the 1970s enabled the visualization of specific protein biomarkers using antibodies tagged with chromogenic substrates. This technique coexists with and augments H&E and is becoming increasingly favored for prognostic purposes. Routine clinical tests include detection of estrogen and progesterone receptors (ER, PR) by IHC and determination of the ERBB2 (HER-2) receptor level based on IHC or gene copy number by fluorescent in situ hybridization (FISH). These tests are critically important for determination of appropriate therapy. ER positive [ER(+)] patients are offered antiestrogen therapy and patients with HER-2 over expression or amplification are offered Herceptin [7]. The only systemic alternative currently available for ER-negative [ER(-)] patients is chemotherapy.

Like H&E, IHC succumbs to the limitation of subjective quantitation and is typically analyzed in a semi-quantitative manner by visual inspection. This limitation



is inherent to chromagenic staining methods [3]. For this reason, image analysis methods that can objectively assess the intensity of chromagenic substrates are gaining traction in clinical practice, and several standard IHC tests have recently become FDA approved [8]. More recently, immunofluorescent methods that lend themselves to more sensitive and linearly quantitative techniques are beginning to emerge [9]. The clinical value of automated fluorescence-based image analysis of protein biomarkers has been demonstrated in breast cancer [9] and lung cancer [10]. Although such methods are not yet approved for routine clinical use, it is likely that they will lead to new diagnostic approaches in clinical pathology.

## 8.2 Multiplexing

Gene and protein arrays are commonly used for measuring multiple targets (multiplexing) at the molecular level. However, gene expression may not represent actual protein expression, nor does it provide information on the cellular localization within the context of the tissue specimen. Multiplexing directly on tissue or cells, without the need for extraction and dispersion on chips, preserves the spatial integrity of proteins while still allowing the assessment of multiple interactions between those proteins. This provides an entirely new way of examining biomarkers and could shed light on previously unexamined relationships between spatial location and protein-protein interactions.

For example, prediction of disease outcome or therapeutic response will likely require the analysis of multiple components from several biological pathways. In oncology, many cancer types are very heterogeneous in phenotype and require complex screening. Breast cancer is a typical example whereby a single patient may be screened for expression of different hormone receptors (estrogen and progesterone), keratin profile to determine tumor subtype (luminal or basal), and over-expression of the oncogene Her2 for which an antibody therapy exists as an adjuvant therapy [11]. Through multiplexing analysis, it will become increasingly possible to provide customized medicine.

### 8.2.1 Fluorescence Microscopy

An important advantage of immunofluorescent techniques for tissue-based biomarker interrogation is the ability to multiplex proteins in a single tissue section. Fluorescence lends itself to multiplexing for two main reasons: (1) there is a wide range of fluorophore dyes and/or nanocrystals with nonoverlapping emission spectra, and (2) sequential staining and imaging is possible with methods such as photobleaching. Detection agents can take the form of small organic molecules (such as Cy5 and Alexa dyes, FITC, and Rhodamine), nanocrystals (“quantum dots”) [12], proteins with inherent fluorescent properties [13], and genetic tags that have been coupled with fluorochromes [14]. These molecules are frequently functionalized to couple efficiently with other biological agents such as antibodies or nucleic acids. The main forms of multiplexing include 3–4 “channels” through standard fluorescence microscopy, 5–6 channel analysis with quantum dots, “spectral barcoding” in which a finite number of dyes are mixed in combination and precise

spectral characteristics are determined on a per-pixel basis, and repeated use of a few fluorescent channels through regulating the dyes' fluorescent properties such as photobleaching or antibody denaturation/stripping. A common requirement of all these methods is the ability to digitally reconstruct the patterns seen for the different biomarkers. This is accomplished through either digital "layering" in which multiple images are overlapped on top of one another [15, 16], or spectral unmixing in which numerous agents, each with unique spectral properties, are detected simultaneously [17].

### 8.2.2 Fluorescent Dyes

There are numerous fluorescent dyes available for use as labeling agents to tag detection agents in biological samples [14]. These dyes each have unique spectral properties, in particular differing wavelengths of light for excitation and the resulting fluorescent emission. Detection is accomplished by the use of band pass and dichroic filters, allowing specific wavelengths of light to pass such that for a given filter combination a single fluorochrome is seen [18]. It is typical to examine blue, green, orange, and red fluorochromes in this manner whereby the spectrum of each dye is distinct so that there is no cross-talk between the different fluorochromes. Using combinations of dyes together allows a higher level of multiplexing to be obtained through the generation of unique spectral signatures. These methods have been utilized in human genetic analysis in a process known as spectral karyotyping to detect each individual human chromosome and to determine rearrangements or fragmentation in cytogenetic analysis [19].

One potential drawback to fluorescent dyes is the impermanence of signal and loss of activity with time. A second potential limitation, which has been overcome to a large degree with advances in CCD camera technology, is the limits of detection of low signal abundance. A third challenge is the auto-fluorescence generated by the tissues. The longer the exposure required to detect the signal, the more auto-fluorescence is also accumulated in the resultant image. Thus, the amount of light generated specifically by the fluorochromes must be a certain degree above the noise in the system, which largely stems from tissue auto-fluorescence. Several hardware applications such as laser scanning confocal microscopy and the use of structured light with multiple image acquisition (such as the Zeiss Apotome) allow a mechanical mechanism for removing the auto-fluorescence [20]. Through the use of spectral acquisition and deconvolution, the analysis of individual pixels based on wavelengths of light passing through the detector (such as liquid crystal tunable filters) can be used in numerous multiplexing platforms for signal detection [17].

### 8.2.3 Quantum Dots

Quantum dots have been used for multispectral analysis of biological specimens [21, 22]. These are nanostructures containing a photo-activatable metal core (such as CdSe/ZnS) surrounded by a shell. Fluorescence can be generated from these molecules by excitation in the near UV range, which produces a fluorescence with very distinct peak spectral output spanning as low as 10 nm, allowing

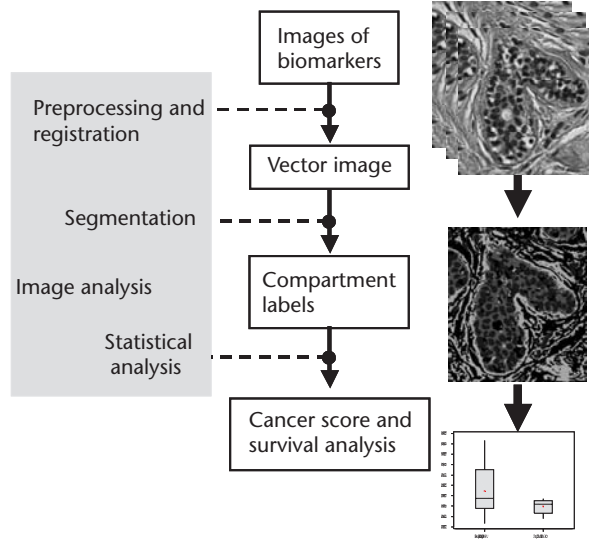
for spectral separation between the different nanostructures. Through coupling of the nanospheres to avidin and binding to biotinylated antibodies, five distinct molecules were visualized along with nuclear staining with 4'6-DiAmidino-2-PhenylIndole (DAPI) [23]. Quantum dots have also been used for FISH analysis for multiplexed analysis of cellular mRNAs and cytogenetic analysis of human chromosomes [24–27]. The main limitation to the level of multiplexing achievable with quantum dots are the size of the nanoparticles, and full application of the use of these particles for molecular analysis will be accomplished through ongoing development.

#### 8.2.4 Photobleaching

Fluorescent dyes are inherently unstable to photo bleaching and can be inactivated by exposure to proper wavelengths to photo-excite the fluorescent dyes, rendering them incapable of further fluorescence. However, for some dyes, their susceptibility to photobleaching has enabled multiplexing. Using this approach, a dye-labeled antibody can be localized to the sample of interest, imaged to record the localization pattern, photobleached to clear the localization pattern, then reincubated with a second dye-labeled antibody, and the process is sequentially repeated. Methods for measuring multiple protein networks in tissue (the *toponome*) have relied on the use of photo bleaching to localize more than 100 antigens in a single sample [28]. This method has a limitation in that the fluorescent dyes must be directly coupled to the antibodies to achieve high-level multiplexing. For complex tissue samples and low abundance proteins, signal amplification may be needed to generate sufficient signal.

### 8.3 Image Analysis

Tissue microarrays (TMAs) provide the means for simultaneous analysis of tissue from large numbers of patients. Tissue microarrays contain hundreds of tissue spots (approximately 0.6 mm or greater in diameter) originating from cores of tissue from regions of interest in paraffin-embedded tumor samples. The tissue cores are transferred to a recipient paraffin block, in a precisely spaced array pattern. Each block can generate 100–500 sections analyzed using independent IHC tests and can serve as a valuable discovery tool for tissue-based biomarkers [29, 30]. However, the large amount of information in TMAs and the high dimensional nature of the data makes automated image analysis algorithms essential for high throughput segmentation of TMA images into subcellular compartments (i.e., cytoplasm, nucleus, membrane) and quantitation of biomarkers in these compartments [9]. In the following sections we describe algorithms for registering and segmenting multichannel microscopic images of breast TMAs into subcellular compartments for automated quantitation of multiple target proteins. The multichannel images of different biomarkers are obtained by a multistep image acquisition procedure. These images are corrected for nonuniform illumination. A robust, multiresolution image registration algorithm is applied to transform images into the same coordinate system. A multichannel segmentation method is then applied to segment



**Figure 8.1** Schematic representation of image processing procedures. In this chapter, we focus on the steps in the shaded box.

the registered images into subcellular compartments. The algorithms are general and able to handle multiple images with arbitrary number of channels that are acquired in multiple steps. Finally, multiple target proteins are superimposed on individual compartments to calculate metrics associated with subcellular protein expressions and translocation. The overall workflow is shown in Figure 8.1. In the following sections, we describe the details of each of the preprocessing, registration, segmentation, and quantitation steps.

### 8.3.1 Image Preprocessing

In the preprocessing step, raw images are smoothed by a Gaussian filter to remove noise. Nonuniform illumination is also corrected. The illumination pattern can be estimated from the images or directly computed by using calibration targets. Most filter-cube and microscope manufacturers carry fluorescent plastic that can be used for calibration. If the calibration images are not taken during the acquisition, the illumination pattern can be estimated from a series of images. The observed image,  $I(x, y)$ , can be modeled as a product of the excitation pattern,  $E(x, y)$ , and the emission pattern,  $M(x, y)$ . While the emission pattern captures the tissue-dependent staining, the excitation pattern captures the illumination.

$$I(x, y) = E(x, y)M(x, y) \quad (8.1)$$

In the logarithm domain, the previous equation can be transformed to a linear form:

$$\log(I(x, y)) = \log(E(x, y)) + \log(M(x, y)) \quad (8.2)$$

From a set of  $N$  images, let  $I_n(x, y)$  denote ordered set of pixels. In other words, the pixels are sorted for any given  $(x, y)$  location such that

$$I_1(x, y) \leq I_2(x, y) \leq \cdots I_n(x, y) \cdots \leq I_N(x, y) \quad (8.3)$$

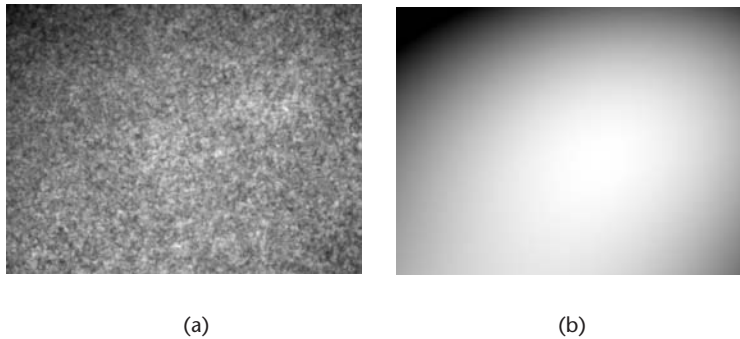
Assuming that a certain percentage ( $p$ ) of the image is formed from stained tissue (nonzero background), then a trimmed average of the brightest pixels can be used to estimate the excitation pattern:

$$E'_{\text{AVE}}(x, y) = \frac{1}{N - K + 1} \sum_{n=K}^N \log(I_n(x, y)) \quad (8.4)$$

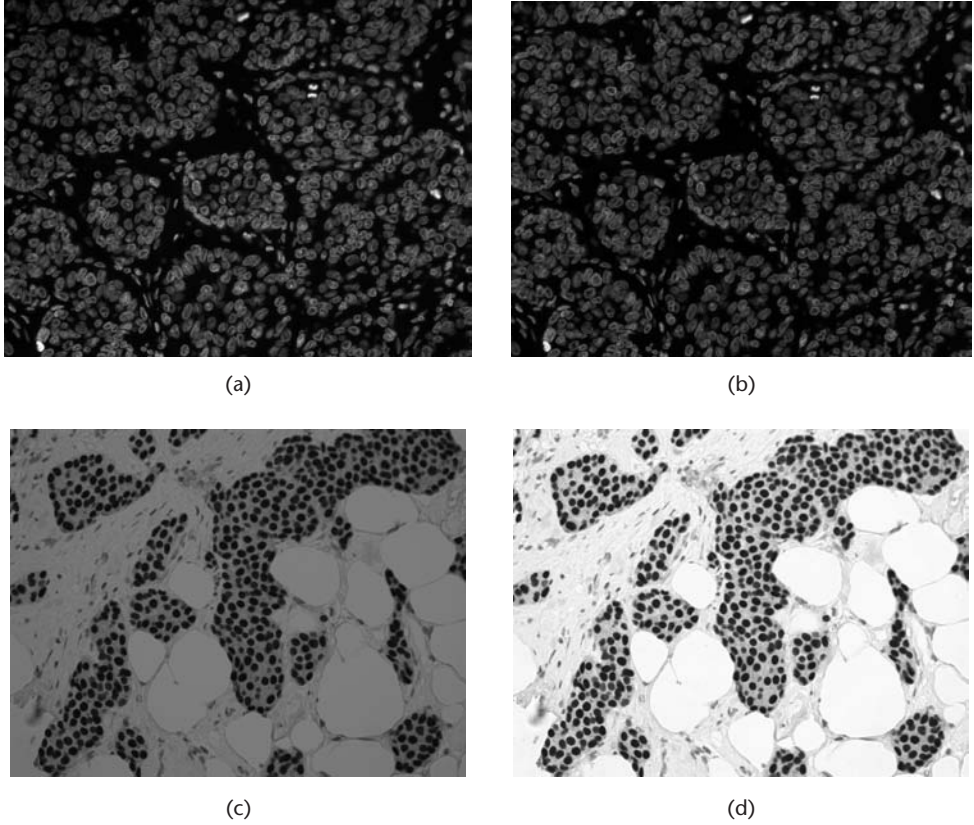
where  $K$  is set to an integer closest to  $N(1-p) + 1$ . In our experiments, we set  $p$  to 0.1 (10 percent). In (8.4), the average emission pattern of the tissue is assumed to be uniform. Since the images are recovered up to a scale factor, we can drop the constant term introduced by the uniform emission pattern. This approximation holds if a large number of images are used in the averaging process. However a large percentage of pixels (90 percent) are already excluded to eliminate the non-tissue pixels in the images. To overcome the limited sampling size, we approximate the log of the excitation pattern with polynomials;

$$E'_{\text{AVE}}(x, y) = \sum_{0 \leq i, j \leq p; i+j \leq p} a_{ij} x^i y^j \quad (8.5)$$

The parameters  $a_{ij}$  are solved by minimizing the mean squared error [31]. The surface generated by the polynomial coefficients are then used to correct individual images. A sample average excitation pattern and the estimated polynomial illumination surface are shown in Figure 8.2(a, b), respectively. Figure 8.3(a, b) shows a fluorescent image before correction and after correction, respectively. Use of polynomial surface to estimate the illumination pattern is not limited to fluorescent microscopy; brightfield image can be corrected similarly. If each color channel is corrected separately, this corrects for the color temperature of the light source as well—see Figure 8.3(c, d).



**Figure 8.2** Trimmed average image of one channel; and (b) a third-order polynomial approximation of the illumination pattern.



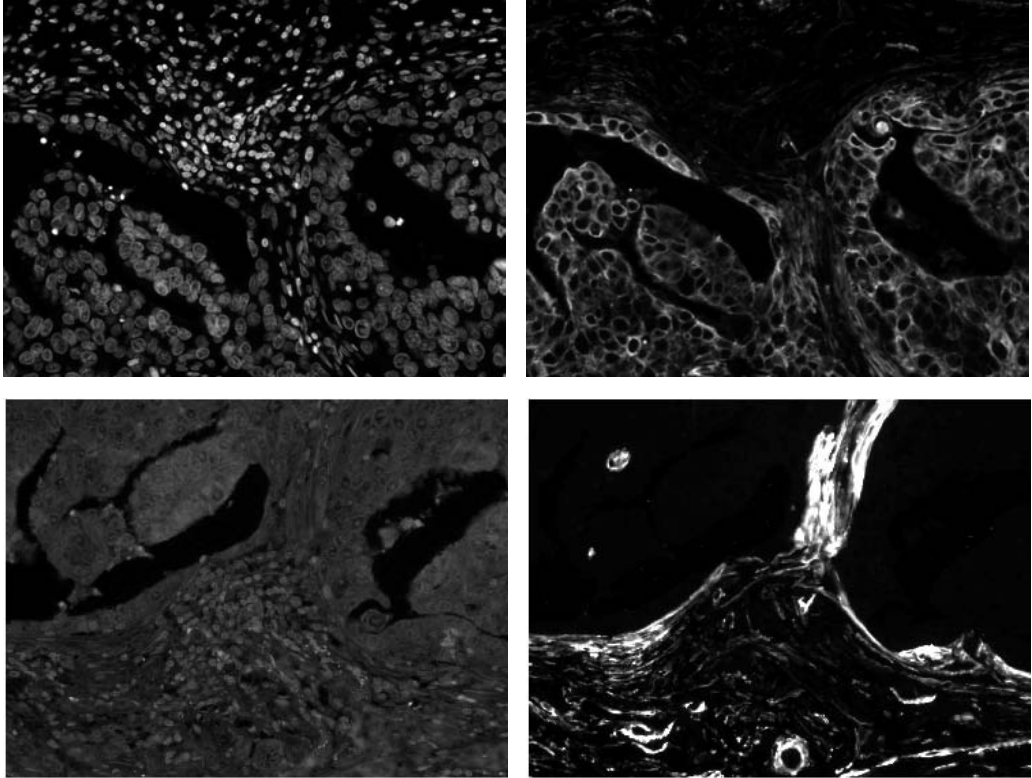
**Figure 8.3** Fluorescent image showing DAPI staining: (a) before correction, and (b) after illumination correction. A bright field DAB staining image before illumination correction: (c) before correction, and (d) after illumination correction.

### 8.3.2 Image Registration

Image registration techniques, such as mutual information or correlation-based techniques, can be used to register images from each step of a sequentially multiplexed study and align them accurately. The experiments are designed such that at each step of the sequential staining, images of the nuclei are acquired. Figure 8.4 shows an example sequence of images where the first image is the image of the nuclei. Similarly, the nuclei can be stained by Hematoxylin in the H&E stain. The first nuclei image is set as the reference image, and each of the subsequent nuclei images are registered to the reference. Once the transformation parameters are estimated, then all the channels can be mapped onto the reference coordinate system.

Given two set of nuclei images, one being the reference image from the first step,  $I_N^1(x, y)$ , and the second being either from the subsequent fluorescent acquisitions or the nuclei channel from the final H&E step,  $I_N^k(x, y)$ , we find a transformation  $T^{k,1}$ , such that the image similarity measure between  $I_N^1(x, y)$  and  $I_N^k(T^{k,1}(x, y))$  is maximized. Different combinations of transformations and image





**Figure 8.4** Four channels of one tissue sample. The top row shows images from the first imaging round with a nucleus-stain (left) and a membrane-stain (right). The bottom row shows images from the second imaging round with cyan fluorescent protein (CFP) stain (left) and smooth muscle actin stain (right).

similarity measures have different performance computation requirements and are suitable for different applications. In this work, we use a rigid transformation and a mutual information-based image similarity measure [32,42]:

$$S(\mathbf{t}) = - \sum_l \sum_{\kappa} p(\iota, \kappa | \mathbf{t}) \log \frac{p(\iota, \kappa | \mathbf{t})}{p_M(\iota | \mathbf{t}) p_F(\kappa)} \quad (8.6)$$

where  $p$ ,  $p_M$ , and  $p_F$  are the joint, marginal moving, and marginal fixed probability distribution of the image intensities;  $\mathbf{t}$  is the parameter vector of the transform; and  $\iota$  and  $\kappa$  are the intensity values in the respective images. In order to improve the robustness of the algorithm, we use a multiresolution strategy to find the transform that aligns the two images. Color Plate col10 illustrates the registration of a breast cancer tissue image using the DAPI channel and subsequent transformation of the CFP channel image using the registration results of the DAPI channel.

While for fluorescent acquisitions, the nuclei images are part of the experiment (DAPI acquisition in our case), computing the nuclei image from color images of



the H&E needs an additional step. The red, green, and blue components of the H&E image are used to generate nuclei image using the following equation:

$$I_N^{\text{HE}}(x, y) = c \cdot \left( I_{\text{BLUE}}^{\text{HE}}(x, y) / \sqrt{I_{\text{RED}}^{\text{HE}}(x, y) \cdot I_{\text{GREEN}}^{\text{HE}}(x, y)} \right)^\gamma \quad (8.7)$$

where  $c$  and  $\gamma$  are tuning parameters for contrast and gamma correction, respectively. Since the hematoxylin stains the nuclei to blue, the highest contrast is achieved when the blue channel is normalized by the geometric mean of the red and green channels. Color Plate 11(a, b) shows an H&E image and its estimated nuclei component computed by (8.7), respectively. A two-channel fluorescent imaging of the same tissue stained with molecular biomarkers with green representing a membrane related marker (beta-catenin) and blue representing a nuclei related stain (DAPI) are shown in Color Plate 11(c) and Color Plate 11(d), respectively. The registered DAPI image in the H&E coordinate system is shown in Color Plate 11(e). The registration parameters estimated from the DAPI and H&E images are then used to map the beta-catenin channel into the H&E coordinate system (shown in green color in Color Plate 11(f)).

### 8.3.3 Image Segmentation

Subcellular quantification of target proteins requires segmentation of the subcellular compartments, such as nuclei, membrane, and cytoplasm. The segmentation can be achieved by either segmenting each channel separately or segmenting all channels at once. Segmentation of ridge-like and blob-like structures is one of the most common segmentation tasks in medical and life sciences imaging applications. Commonly, such applications require detecting vessels [43], bronchial tree [44], bones [45,46], and nodules [47–49] in medical applications, and detecting neurons [42, 50], nuclei [51], and membrane [52] structures in microscopy applications. Partitioning of a multiple channel digital image into multiple segments (regions/compartments) is one of the most critical steps for quantifying one or more biomarkers in molecular cell biology, molecular pathology, and pharmaceutical research.

Subcellular segmentation can be achieved in most cases using a single channel. For many of the approaches in the literature, preprocessing of the images is required to reduce noise or to extract features from the images. Common preprocessing steps include thresholding, edge detection, and smoothing. A number of cellular-level segmentation tasks have been accomplished by combining only these preprocessing steps. In [53], median filtering and morphological operations of erosion and dilation were adapted to segment melanomas and lymphocytes. Binary thresholding was similarly combined with morphological operations and image thinning to segment cells in histology images in [54]. However, more intelligent preprocessing is needed for nontrivial applications. In [55,56], cellular images of breast tissue were denoised using a nonlinear diffusion filter followed by a directional coherence filter to enhance the boundaries of the nucleus. A nonlinear illumination correction method was described earlier.

Region-based segmentation, in which the image is divided into regions based on some homogeneity criteria, is commonly used. Typically, segmentation starts from a seed pixel or region (e.g., center of the nucleus) determined automatically or specified by some user interaction, and then grows to include neighboring pixels that meet a specified intensity, texture, or shape criteria. In the connected-threshold region-growing algorithm [57], for example, all neighboring pixels between an upper and lower threshold values are included recursively. This is after smoothing with an edge-preserving smoothing filter such as anisotropic diffusion [52], curvature flow [53], and bilateral [53] filters. In a fluorescence cellular microscopy image, the seed points may be obtained by initial thresholding, using a top-hat filter [58] or by computing distance transforms to obtain pixels in the cells, which are then grown to the cellular boundaries. In the confidence-connected region-growing approach [34, 59–62], the mean and standard deviation of the seed region, and all pixels around the region that fall within a range of the mean, are recursively accepted as part of the region. When there are no more pixels to include, the mean and standard deviation of the newly obtained region is computed and the process iterated a few times. The isolated-connected algorithm [34, 35] in which two seed points are given from two different regions (e.g., nucleus and cytoplasm) can be used to segment the whole cell. The goal of the algorithm is to grow a region that is connected to the first region but not connected to the second. A binary search is used to find the optimal separating intensity value. In [63] region growing was employed after binary thresholding to segment the nuclei in FISH images. In Color Plate 12(b), the result of membrane segmentation is overlaid on the tissue image. A membrane-stained channel image was smoothed with curvature flow filter to remove the noise while preserving the membrane markings. A nonmaximal suppression algorithm was then employed to remove spurious signals and retain only those that form a continuous boundary.

### 8.3.4 A Unified Segmentation Algorithm

While different segmentation algorithms can be used for each of the nuclei and membrane compartments, an alternative is to use the same algorithm in different modes. For example, the curvature metric derived from nuclei and membrane images can be used as metrics to classify segments using supervised or unsupervised (parametric or nonparametric) algorithms [64]. A commonly used approach to computing curvature-based metrics is to extract them from the eigenvalues of the Hessian matrix. Due to their invariance to rigid transformations, these metrics can be used for a broad class of ridge-like and blob-like structures [65]. The Hessian of an image  $I(x, y)$  is defined as

$$H(I(x, y)) = \begin{bmatrix} \frac{\partial^2 I(x, y)}{\partial x^2} & \frac{\partial^2 I(x, y)}{\partial x \partial y} \\ \frac{\partial^2 I(x, y)}{\partial y \partial x} & \frac{\partial^2 I(x, y)}{\partial y^2} \end{bmatrix} \quad (8.8)$$

The eigenvalues ( $\lambda_1(x, y) \leq \lambda_2(x, y)$ ) of the Hessian matrix can be either numerically calculated or analytically written in terms of the elements of the Hessian Matrix:

$$\lambda_{12}(x, y) = \frac{1}{2} \left\{ \frac{\partial^2 I(x, y)}{\partial x^2} + \frac{\partial^2 I(x, y)}{\partial y^2} \mp \sqrt{\left( \frac{\partial^2 I(x, y)}{\partial x^2} - \frac{\partial^2 I(x, y)}{\partial y^2} \right)^2 + 4 \left( \frac{\partial^2 I(x, y)}{\partial x \partial y} \right)^2} \right\} \quad (8.9)$$

The eigenvalues encode the curvature information of the image and provide useful cues for detecting ridge-like membrane structures or blob-like nuclei structures. However, the eigenvalues are dependent on image brightness. We define the following two curvature-based features that are independent of image brightness:

$$\theta(x, y) = \tan^{-1} \left( \frac{\lambda_1(x, y)}{\lambda_2(x, y)} \right) \quad (8.10)$$

$$\phi(x, y) = \tan^{-1} \frac{(\lambda_1(x, y)^2 + \lambda_2(x, y)^2)^{1/2}}{I(x, y)} \quad (8.11)$$

and refer to them as shape index and normalized-curvature index, respectively. This is essentially the same as defining the eigenvalues in a polar coordinate system. This transformation also results in bounded features  $-\frac{3\pi}{4} \leq \theta(x, y) \leq \frac{\pi}{4}$ , and  $0 \leq \phi(x, y) \leq \pi/2$ .

A general likelihood function estimator that calculates the probability maps of vessel-, membrane-, and nuclei-like structures in images can be formulated by exploring the expected values of the features. For example, for bright membrane- and vessel-like structures, the shape index is close to  $-\pi/2$ , whereas for blob-like nuclei structures, the shape index is close to  $-3\pi/4$ . These constraints are used to compute the initial foreground set for membrane and nuclei structures. Also, for bright structures, it is less likely for objects to have nonnegative shape index values compared to noise, where nonnegative values can easily occur. An initial segmentation based on the shape index and the normalized-curvature index separates the image pixels into three subsets: background, foreground, and indeterminate. Indeterminate subsets comprise all the pixels that are not included in the background or foreground subsets. From these subsets, the background and foreground intensity distributions, as well as the intensity log-likelihood functions, are estimated. The algorithm keeps iterating by using two out of the three features at a time to estimate the distribution of the feature that is left out. Usually three iterations are sufficient for a convergence. In the final step, these log-likelihood functions are combined to determine the overall likelihood function. A probability map that represents the probability of a pixel being a foreground is calculated.

This nonparametric method is different from existing parametric approaches, because it can handle arbitrary mixtures of blob- and ridge-like structures. This is essential in applications such as in tissue imaging where a nuclei image in an epithelial tissue comprises both ridge- and blob-like structures. The network of

membrane structures in tissue images is another example where the intersection of ridges can form structures that are partially blobs. Accurate segmentation of membrane and nuclei structures forms the base for higher level scoring and statistical analysis applications. For example, distribution of a target protein on each of the segmented compartments can be quantified and related to clinical outcomes. Scores measuring translocation of a protein between segmented compartments can reveal protein-specific pathways and response to drug therapy. Using the spatial and intensity interrelation of nuclei and membrane biomarkers, it is possible to separate the epithelial nuclei from the stromal nuclei. Color Plate 13 shows sample images of membrane and nuclei and their segmentation results.

### 8.3.5 Segmentation of Cytoplasm and Epithelial Regions

Cytoplasm can be detected either by using a specific marker or detecting it computationally. Based on binary image morphological operations, Ding [63] describes a method that identifies the cytoplasm as the region around the nuclei. While this works well for sparse cell images, defining these regions in tissue is more complicated. Whenever we have membrane compartment in addition to nuclei we can determine the cytoplasm as the region between membrane and nuclei.

Let us denote the thresholded nuclei, and membrane sets with  $M(x, y)$ , and  $N(x, y)$ , respectively. Cytoplasm, denoted by  $C(x, y)$ , is defined as the union of sets of small regions circumscribed by membrane alone or membrane and nuclei pixels—see green regions in Color Plate 13(b, d). Only pixels that are not defined as  $M(x, y)$  or  $N(x, y)$  can be defined as  $C(x, y)$ .

Epithelial and stromal regions are morphologically different. Let  $U(x, y)$  defined as

$$U(x, y) = C(x, y) \cup M(x, y) \cup N(x, y) \quad (8.12)$$

denote the superset union of the nuclei, cytoplasm, and membrane sets. Since the stromal nuclei are not connected through membrane structures and are sparsely distributed, they can be detected by a connected component analysis of  $U(x, y)$ . An epithelial mask,  $E(x, y)$ , is generated as a union of large connected components of  $U(x, y)$ . For the sample images, any connected component larger than 800 pixels is accepted as a part of the epithelial mask. The nuclei set is then separated into epithelial nuclei ( $N_e(x, y)$ ) and stromal nuclei ( $N_s(x, y)$ ) by masking,

$$N_e(x, y) = N(x, y) \cdot E(x, y) \quad (8.13)$$

$$N_s(x, y) = N(x, y) \cdot (1 - E(x, y)) \quad (8.14)$$

Color Plate 13(b) and Color Plate 13(d) show the separated epithelial nuclei (blue) from the stromal nuclei (gray).

## 8.4 Multichannel Segmentation Techniques

After images are registered, points with the same coordinates in different channels correspond to the same structural location. Each pixel in the image has a vector

of features (i.e., intensity values of images from different channels). These features are then used to segment the vector valued image into different subcellular compartments.

Many segmentation algorithms have been developed for digital microscopic images. In this work, we use one of the most widely used segmentation algorithms,  $k$ -means clustering, for its simplicity and robustness. The  $k$ -means clustering algorithm divides feature space into clusters and maximizes the distances between the cluster centers. An iterative procedure is used to find these cluster centers. Each pixel is given the same label as the cluster center that is closest to it in the feature space.

Suppose  $I(x, y) = [I_1(x, y), \dots, I_c(x, y)]$ ,  $(x, y) \in \Omega$  is a  $c$ -channel image of one tissue sample. The  $k$ -means segmentation algorithm proceeds as follows:

*Step 0.* Initialize cluster centers “ $\mu_1, \dots, \mu_k$ .”

*Step 1.* Assign a label  $l(x, y)$  to each pixel based on its distance in the feature space to the cluster centers:

$$l(x, y) = \operatorname{argmin}_j \|I(x, y) - \mu_j\| \quad (8.15)$$

*Step 2.* Update cluster centers as follows:

$$\mu_j = \frac{1}{N_j} \sum_{l(x, y)=j} I(x, y) \quad (8.16)$$

where the summation is over all image pixels with label  $j$ , and  $N_j$  is the total number of pixels with label  $j$ .

*Step 3.* Go to step 1 if not convergent.

Convergence is achieved when the changes in clusters centers are smaller than a preset threshold. The  $k$ -means segmentation result of the multiplexed images shown in Figure 8.4 is shown in Color Plate 12(a).

Two rounds of images were acquired for a TMA with 60 samples, including both normal breast tissues and breast cancer tissues. Each round consisted of multiple biomarkers. Figure 8.4 shows four images of these markers for one tissue sample. The  $k$ -means segmentation algorithm is applied to segment multichannel images into five compartments. Color Plate 12(a) shows one typical segmentation result: nucleus (blue), membrane (red), smooth muscle (violet), cytoplasm (green), and background (black). Color Plate 12(b) shows the overlay of the boundaries of the membrane class on one membrane-stained channel.

## 8.5 Quantitation of Subcellular Biomarkers

A number of steps are required for quantitation of subcellular biomarkers. The membrane compartment of tumor cells can be identified by pan-cadherin staining,

and 4',6-Diamidino-2-phenylindole (DAPI) is used to identify nuclei. A nonlinear nonparametric mapping function with multiple inputs, including the local geometry of the pixel +distributions as well as the intensity values, maps each of these two channels to probability values indicating the likelihood of pan-cadherin pixels being membrane and the likelihood of DAPI pixels being nuclei. To define cytoplasm, a definite decision for each pixel can be determined by thresholding the probability maps at a 50 percent rate. For example, a 50 percent probability of a pixel on a DAPI image implies that the pixel is equally likely to be background and nucleus.

The distribution of biomarkers in each of these regions can be represented by a probability distribution function (PDF). For example the PDF of the biomarker on the membrane corresponds to its weighted empirical distribution, where the membrane probability map determines the weights. We denote the mean and the standard deviation of the biomarker distribution on each of the regions as  $\mu_R$ , and  $\sigma_R$ , respectively, where  $R$  can be any of the nuclei, membrane, cytoplasm, or extra cellular matrix (ECM) regions. ECM is defined as all the nonbackground pixels not classified as nuclei, membrane, or cytoplasm. Compartmental biomarker distribution can then be related to disease outcome or response to therapy.

## 8.6 Summary

Quantitation of multiple tissue-based biomarkers requires several sequential steps, including tissue staining with target specific antibodies labeled with fluorescent reagents, image capture, preprocessing, registration, segmentation, and subcellular quantitation. This provides the flexibility to quantify biomarkers in more than one cellular compartment, thus maximizing the amount of data present in a tissue image and enabling more extensive analysis of the role of biomarkers in predicting response to therapy and patient survival.

### Acknowledgments

The authors would like to thank the significant contributions of Maximilian Seel, Harvey Cline, and Melinda Larsen to this chapter.

## References

- [1] Fox, H., "Is H&E Morphology Coming to an End?" *Journal of Clinical Pathology*, Vol. 53, 2000, pp. 38–40.
- [2] Kirkham, N., "The Pathologist in the 21st Century Generalist or Specialist?" *Journal of Clinical Pathology*, Vol. 53 (Millennial reviews), 2000, pp. 7–9.
- [3] Dolled-Filhart, M., et al., "Quantitative In Situ Analysis of Beta-Catenin Expression in

- Breast Cancer Shows Decreased Expression Is Associated with Poor Outcome,” *Cancer Res.*, Vol. 66, No. 10, 2006, pp. 5487–5494.
- [4] Schubert, W., et al., “Analyzing Proteome Topology and Function by Automated Multidimensional Fluorescence Microscopy,” *Nature Biotechnology*, Vol. 24, No. 10, 2006, pp. 1270–1278.
- [5] Kayser, K., et al., “Digitized Pathology, Theory and Experiences in Automated Tissue-Based Virtual Diagnosis,” *Rom. J. Morphol. Embryol.*, Vol. 47, No. 1, 2006, pp. 21–28.
- [6] Schrader, T., et al., “The Diagnostic Path: A Useful Visualisation Tool in Virtual Microscopy,” *Diagn. Pathol.*, Vol. 1, 2006, p. 40.
- [7] Pauletti, G., et al., “Assessment of Methods for Tissue-Based Detection of the HER-2/neu Alteration in Human Breast Cancer: A Direct Comparison of Fluorescence In Situ Hybridization and Immunohistochemistry,” *Journal of Clinical Oncology*, Vol. 18, No. 21, 2000, p. 3651.
- [8] Cregger, M., A. J. Berger, and D. L. Rimm, “Immunohistochemistry and Quantitative Analysis of Protein Expression,” *Arch. Pathol. Lab. Med.*, 2006, Vol. 130, No. 7, pp. 1026–1030.
- [9] Camp, R. L., G. D. Chung, and D. L. Rimm, “Automated Subcellular Localization and Quantification of Protein Expression in Tissue Microarrays,” *Nature Medicine*, Vol. 11, 2002, pp. 1323–1327.
- [10] Zheng, Z., et al., “DNA Synthesis and Repair Genes RRM1 and ERCC1 in Lung Cancer,” *N. Engl. J. Med.*, Vol. 356, No. 8, 2007, pp. 800–808.
- [11] Pusztai, L., et al., Molecular Classification of Breast Cancer: Limitations and Potential,” *Oncologist*, Vol. 11, No. 8, 2006, pp. 868–877.
- [12] Smith, A. M., and S. Nie, “Chemical Analysis and Cellular Imaging with Quantum Dots,” *Analyst*, Vol. 129, No. 8, 2004, pp. 672–677.
- [13] Hoffman, R. M., “Advantages of Multi-Color Fluorescent Proteins for Whole-Body and In Vivo Cellular Imaging,” *J. Biomed. Opt.*, Vol. 10, No. 4, 2005, p. 41202.
- [14] Giepmans, B. N., et al., “The Fluorescent Toolbox for Assessing Protein Location and Function,” *Science*, Vol. 312, No. 5771, 2006, pp. 217–224.
- [15] McCabe, A., et al., “Automated Quantitative Analysis (AQUA) of In Situ Protein Expression, Antibody Concentration, and Prognosis,” *J. Natl. Cancer Inst.*, Vol. 97, No. 24, 2005, pp. 1808–1815.
- [16] Schubert, W., “Topological Proteomics, Toponomics, MELK-Technology,” *Adv. Biochem. Eng. Biotechnol.*, Vol. 83, 2003, pp. 189–209.
- [17] Levenson, R. M., and J. R. Mansfield, “Multispectral Imaging in Biology and Medicine: Slices of Life,” *Cytometry*, Vol. 69, No. 8, 2006, pp. 748–758.
- [18] Petty, H. R., “Fluorescence Microscopy: Established and Emerging Methods, Experimental Strategies, and Applications in Immunology,” *Microsc. Res. Tech.*, Vol. 70, No. 8, 2007, pp. 687–709.
- [19] Liehr, T., et al., “Multicolor FISH Probe Sets and Their Applications,” *Histol. Histopathol.*, Vol. 19, No. 1, 2004, pp. 229–237.
- [20] Conchello, J. A., and J. W. Lichtman, “Optical Sectioning Microscopy,” *Nat. Methods*, Vol. 2, No. 12, 2005, pp. 920–931.
- [21] Xing, Y., et al., “Molecular Profiling of Single Cancer Cells and Clinical Tissue Specimens with Semiconductor Quantum Dots,” *Int. J. Nanomedicine*, Vol. 1, No. 4, 2006, pp. 473–481.
- [22] Zhang, Y., et al., “Nanobiotechnology: Quantum Dots in Bioimaging,” *Expert Rev. Proteomics*, Vol. 4, No. 4, 2007, pp. 565–572.



- [23] Fountaine, T. J., et al., "Multispectral Imaging of Clinically Relevant Cellular Targets in Tonsil and Lymphoid Tissue Using Semiconductor Quantum Dots," *Mod. Pathol.*, Vol. 19, No. 9, 2006, pp. 1181-1191.
- [24] Bentolila, L. A., and S. Weiss, "Single-Step Multicolor Fluorescence in Situ Hybridization Using Semiconductor Quantum Dot-DNA Conjugates," *Cell Biochem. Biophys.*, Vol. 45, No. 1, 2006, pp. 59-70.
- [25] Chan, P., et al., "Method for Multiplex Cellular Detection of mRNAs Using Quantum Dot Fluorescent In Situ Hybridization," *Nucleic Acids Res.*, Vol. 33, No. 18, 2005, p. e161.
- [26] Knoll, J. H., "Human Metaphase Chromosome FISH Using Quantum Dot Conjugates," *Methods Mol. Biol.*, Vol. 374, 2007, pp. 55-66.
- [27] Uen, Y. H., et al., "Clinical Significance of MUC1 and c-Met RT-PCR Detection of Circulating Tumor Cells in Patients with Gastric Carcinoma," *Clin. Chim. Acta.*, Vol. 367, Nos. 1-2, 2006, pp. 55-61.
- [28] Schubert, W., "Exploring Molecular Networks Directly in the Cell," *Cytometry*, Vol. 69, No. 3, 2006, pp. 109-112.
- [29] Rimm, D.L., et al., "Tissue Microarray: A New Technology for Amplification of Tissue Resources," *Cancer J.*, Vol. 7, No. 1, 2001, pp. 24-31.
- [30] Seligson, D. B., "The Tissue Micro-Array as a Translational Research Tool for Biomarker Profiling and Validation," *Biomarkers*, 2005, Vol. 10, pp. S77-S82.
- [31] Mattes, D., et al., "PET-CT Image Registration in the Chest Using Free-Form Deformations," *IEEE Trans. on Med. Imag.*, Vol. 22, No. 1, 2003, pp. 120-128.
- [32] Abdul-Karim, M. A., et al., "Automated Tracing and Change Analysis of Angiogenic Vasculature from In Vivo Multiphoton Confocal Image Time Series," *Microvasc. Res.*, Vol. 66, No. 2, 2003, pp. 113-125.
- [33] Can, A., et al., "Rapid Automated Tracing and Feature Extraction from Retinal Fundusimages Using Direct Exploratory Algorithms," *IEEE Trans. on Information Technology in Biomedicine*, Vol. 3, No. 2, 1999, pp. 125-138.
- [34] Frangi, A. F., et al., "Multiscale Vessel Enhancement Filtering," *Medical Imaging Computing and Computer-Assisted Intervention*, Vol. 1496, 1998, pp. 130-137.
- [35] Kirbas, C., and F. Quek, "A Review of Vessel Extraction Techniques and Algorithms," *ACM Computing Surveys*, Vol. 36, No. 2, 2004, pp. 81-121.
- [36] Krissian, K., et al., "Model-Based Detection of Tubular Structures in 3 D Images," *Computer Vision and Image Understanding*, Vol. 80, No. 2, 2000, pp. 130-171.
- [37] Nain, D., A. Yezzi, and G. Turk, "Vessel Segmentation Using a Shape Driven Flow," *Medical Imaging Computing and Computer-Assisted Intervention*, Vol. 3216, 2004, pp. 51-59.
- [38] Niemeijer, M., et al., "Comparative Study of Retinal Vessel Segmentation Methods on a New Publicly Available Database," *Proc. of SPIE*, Vol. 5370, 2004, p. 648.
- [39] Pham, D., "Blind Separation of Instantaneous Mixture of Sources Via an Independent Component Analysis," *IEEE Trans. on Signal Processing*, Vol. 44, No. 11, 1996, pp. 2768-2779.
- [40] Staal, J., et al., "Ridge-Based Vessel Segmentation in Color Images of the Retina," *IEEE Trans. on Medical Imaging*, Vol. 23, No. 4, 2004, pp. 501-509.
- [41] Zana, F., and J. C. Klein, "A Multimodal Registration Algorithm of Eye Fundus Images Using Vessels Detection and Hough Transform," *IEEE Trans. on Medical Engineering*, Vol. 18, No. 5, 1999, pp. 419-428.
- [42] Lin, G., et al., "Automated Image Analysis Methods for 3-D Quantification of the Neurovascular Unit from Multichannel Confocal Microscope Images, Part A," *Cytometry*, Vol. 66, 2005, pp. 9-23.

- [43] Shi, L., E. A. Hoffman, and J. M. Reinhardt, "Segmentation of the Ovine Lung in 3D CT Images," *Proc. of SPIE Medical Imaging*, Vol. 5369, 2004.
- [44] Descoteaux, M., et al., "Bone Enhancement Filtering: Application to Sinus Bone Segmentation and Simulation of Pituitary Surgery," *Medical Image Computing and Computer-Assisted Intervention*, 2005, pp. 9–16.
- [45] Mendonca, P. R., et al., "Model-Based Analysis of Local Shape for Lesion Detection in CT Scans," *Proc. of the Intl. Conf. on Medical Image Computing and Computer-Assisted Intervention*, Palm Springs, CA, 2005.
- [46] Rahul, B., et al., "Part-Based Local Shape Models for Colon Polyp Detection," *Proc. of the Intl. Conf. on Medical Image Computing and Computer-Assisted Intervention*, Copenhagen, Denmark, 2006.
- [47] Al-Kofahi, K. A., et al., "Median-Based Robust Algorithms for Tracing Neurons from Noisy Confocal Microscope Images," *IEEE Trans. on Information Technology in Biomedicine*, Vol. 7, No. 4, 2003, pp. 302–317.
- [48] Al-Kofahi, K. A., et al., "Rapid Automated Three-Dimensional Tracing of Neurons from Confocalimage Stacks," *IEEE Trans. on Information Technology in Biomedicine*, Vol. 6, No. 2, 2002, pp. 171–187.
- [49] Meijering, E., et al., "Neurite Tracing in Fluorescence Microscopy Images Using Ridge Filtering and Graph Searching: Principles and Validation," *IEEE International Symposium on Biomedical Imaging: Macro to Nano*, 2004, pp. 1219–1222.
- [50] Anoraganingrum, D., "Cell Segmentation with Median Filter and Mathematical Morphology Operation," *Proc. of the 10th Intl. Conf. on Image Analysis and Processing*, 1999, p. 1043.
- [51] Nedzved, A., S. Ablameyko, and I. Pitasi. "Morphological Segmentation of Histology Cell Images," *Proc. 15th International Conference on Pattern Recognition*, 2000.
- [52] Adiga, U., et al., "High-Throughput Analysis of Multispectral Images of Breast Cancer Tissue," *IEEE Trans. on Imag. Proc.*, Vol. 15, No. 8, 2006, pp. 2259–2268.
- [53] Ibanez, L., et al., *The ITK Software Guide: The Insight Segmentation and Registration Toolkit*, Clifton Park, NY: Kitware Inc., 2005.
- [54] Perona, P., and J. Malik, "Scale-Space and Edge Detection Using Anisotropic Diffusion," *IEEE Trans. on Pattern Analysis and Machine Intelligence*, Vol. 12, No. 7, 1990, pp. 629–639.
- [55] Malladi, R., and J. A. Sethian, "Image Processing Via Level Set Curvature Flow," *Proc. of the National Academy of Sciences*, Vol. 92, No. 15, 1995, pp. 7046–7050.
- [56] Malladi, R., and J. A. Sethian, "Image Processing: Flows Under Min/Max Curvature and Mean Curvature," *Graphical Models and Image Processing*, Vol. 58, No. 2, 1996, pp. 127–141.
- [57] Shi, J., and C. Tomasi, "Good Features to Track," *1994 IEEE Computer Society Conference on Computer Vision and Pattern Recognition*, 1994.
- [58] Clocksin, W. F., and B. Lerner, "Automatic Analysis of Fluorescence In-Situ Hybridisation Images," *Proc. of the 11th British Machine Vision Conf.*, 2000, pp. 666–674.
- [59] McCulloch, C. C., et al., "Model-Based Detection of Lung Nodules in Computed Tomography Exams: Thoracic Computer-Aided Diagnosis," *Academic Radiology*, Vol. 11, No. 3, 2004, pp. 258–266.
- [60] Melonakos, J., et al., "A Probabilistic Model for Haustral Curvatures with Applications to Colon CAD," *Medical Image Computing and Computer-Assisted Intervention*, Vol. 4792, 2007, pp. 420–427.
- [61] Mendonça, P. R. S., et al., "Lung Nodule Detection Via Bayesian Voxel Labeling," *Information Processing in Medical Imaging*, pp. 134–145.

- [62] Sofka, M., and C. V. Stewart, "Retinal Vessel Centerline Extraction Using Multiscale Matched Filters, Confidence and Edge Measures," *IEEE Trans. on Med. Imag.*, Vol. 25, 2006, pp. 1531-1546.
- [63] Ding, G., et al., "Characterization and Quantitation of NFkB Nuclear Translocation Induced by Interleukin-1 and Tumor Necrosis Factor- $\alpha$ ," *J. Biol. Chem.*, Vol. 273, 1998, pp. 28897-28905.
- [64] Nattkemper, T. W., "Automatic Segmentation of Digital Micrographs: A Survey," *Proc. 11th World Congr. Medical Informatics (MEDINFO)*, Pt. 2, 2004, pp. 847-851.
- [65] Hoos, A., et al., "Validation of Tissue Microarrays for Immunohistochemical Profiling of Cancer Specimens Using the Example of Human Fibroblastic Tumors," *Am. J. Pathol.*, Vol. 158, No. 4, 2001, pp. 1245-1251.

# Methods for High-Content, High-Throughput, Image-Based Cell Screening

Thouis R. Jones, Anne E. Carpenter, Polina Golland, and David M. Sabatini

## 9.1 Introduction

One of the most basic tools of modern biology is visual inspection of cells using a microscope. Modern techniques, such as immunofluorescent staining and robotic microscopes, have only magnified its importance for the exploration of biological mechanisms. However, visual analysis can also become a major bottleneck in large, image-based screens, where tens to hundreds of thousands of individual cell populations are perturbed (genetically or chemically) and examined to find those populations yielding an interesting phenotype. Several genome-scale screens have relied on visual scoring by experts [1, 2]. There are benefits to manual scoring, such as the ability of a trained biologist to quickly intuit meaning from appearance, the robustness of the human visual system to irrelevant variations in illumination and contrast, as well as humans' ability to deal with the wide variety of phenotypes that cells can present.

However, automatic image cytometry has several advantages over manual scoring: simultaneous capture of a wide variety of measurements for each cell in each image (versus scoring a few features per image), quantitative rather than qualitative scoring, ease of reproducibility, detection of more subtle changes than is possible by eye, and the main benefits, elimination of tedious manual labor and much faster analysis of images.

Several groups have made use of automated cell image analysis [3–9], demonstrating the efficacy of such an approach. These groups have either made use of expensive and inflexible commercial systems, often bundled with a particular imaging platform, or they have developed their own software, seldom used outside of the original lab because of its specificity to a particular screen. In order to reduce the duplication of effort in this area, and to make tools for automated cell-image analysis more widely available, we have created CellProfiler, an open-source, modular system for cell-image analysis [10].

This chapter describes the key algorithms in CellProfiler and our overall strategies for accomplishing high-throughput image analysis. These include illumination correction to normalize for biases in the illumination and optical path of the microscope, identification of cells versus background, segmentation of individual cells, and capture of a wide variety of per-cell measurements (the “high-content” aspect of our work). We discuss methods and techniques for exploration and analysis of the resulting data and illustrate their application to real-world biological experiments.

## 9.2 Challenges in Image-Based High-Content Screening

We have analyzed several large screens with our system. This chapter presents some of the challenges inherent to image-based screens and the methods we use to address those difficulties. We will use two screens in particular as examples. The first is a set of cell microarrays, single glass slides with cells growing on an array of “spots” printed with gene-knockdown reagents [11]. The second is from an experiment screening ~5,000 RNA-interference lentiviral vectors targeted to silence ~1,000 human genes, run in a set of 384-well plates [12]. Both experiments produced thousands of high-resolution ( $512 \times 512$  pixels or larger) images, each containing hundreds or thousands of cells. Each image contains cells with a single gene’s expression knocked down (decreased).

These experiments suffered from a variety of biases and sources of noise. Both showed illumination variation of around a factor of 1.5 within the field of view, swamping many measurements with noise if not corrected. The cell microarray experiment was performed with *Drosophila melanogaster* Kc167 cells, which are notoriously difficult to segment accurately [13]. Also in this experiment, significant post-measurement biases were detected based on spot position on the slide, due to variations in cell seeding density, concentrations of nutrients or stain, or other factors.

For both screens, discovery of unknown “interesting” phenotypes was and is an open-ended goal. We take a wide variety of per-cell measurements, because we do not know which measurements will be most useful or interesting a priori, both in the particular screen and for future explorations. Capturing a wide variety of measurements provides the most freedom in postcytometry analysis but also leads to difficulties in finding which subset of hundreds of measurements can most effectively discriminate a particular phenotype.

Moreover, even in the more goal-directed screens, we are often focused on identifying cells that are different from the “usual” cell in ways that may not be completely specified. Algorithms and methods that work well on normal cells can fail completely when faced with cells that vary significantly in appearance. Robustness to wide variation in cell appearance is therefore an overarching concern in all of our work.

In the following section, we discuss how each of these issues arose during screens and the methods we used to overcome these challenges.

## 9.3 Methods

### 9.3.1 Illumination and Staining Correction

Any image- and cell-based screen involves several devices whose physical limitations lead to biased measurements. One of the most pervasive of these is non-uniformity in the optical path of the microscope and the imager. It is typical for the overall illumination to vary by 50% across the field of view, making segmentation of individual cells more difficult and seriously compromising intensity-based measurements. Since many such measurements vary less than two-fold in a group

of cells, they will be useless unless the illumination is corrected in some way. Fortunately, such variation is consistent from image to image within a single screen, provided few systematic elements change within the screen (i.e., the microscope and optical components are kept the same, the same type of slide or plate is used consistently throughout the experiment, and the images are taken in as short a span as is feasible). We include uneven incoming illumination, sensor biases, and illumination variation due to lens and slide imperfections under the single term “illumination variation.” Another source of bias, particularly in slide-based experiments, is variation in stain concentration, which can also vary by as much as a factor of two, as discussed next.

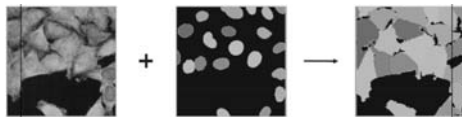
We correct illumination and staining variation simultaneously. To do so, we need to estimate their effect on images. We model the image-forming process at pixel  $(x, y)$  in a particular image  $I$ , located at  $(i, j)$  in the physical layout, as

$$\log I_{x,y,i,j,c} = L_{x,y} + S_{i,j} + \mathcal{N}(\mu_c, \Sigma_c) \quad (9.1)$$

where  $I$  is the image,  $L_{x,y}$  is the illumination function,  $S_{i,j}$  the concentration of stain within that image, and  $c$  is a class label (e.g., background, cell body, or nucleus) for the pixel at  $(x, y)$ . We model these classes as multidimensional normal distributions, with means  $\mu_c$  and covariances  $\Sigma_c$ , with one dimension for each staining channel. Note that we use log-intensities to convert the multiplicative physical process of image formation to an additive model, and that we assume that staining concentration  $S$  varies little within an image, and illumination  $L$  is identical image to image. Also, this model conflates the magnitude of  $\mu_c$ ,  $L$ , and  $S$ , but since we lack any data that give physical units, we only need to estimate these quantities up to a scale factor. Given a few million randomly sampled pixels from a collection of images, fitting this model using smooth functions for  $L$  and  $S$  using expectation-maximization (EM), in which estimation of the per-pixel labels  $c$  are estimated in alternation with the parameters of the model, is fairly straightforward, with a few adjustments to handle nonlinear dependencies between  $L$ ,  $S$ , and  $\Sigma_c$  in the EM update equations [14, 15].

In the cell microarray experiments, we found that the cell distribution was uniform in the field of view (Figure 9.1). The average intensities for the three channels (i.e., stains) and the (uniform) cell distribution are shown in Figure 9.1.

In the well-based experiments, each well was imaged in four different locations. Each location had a significantly different cell distribution due to well-edge effects, but the illumination functions  $L$  were the same across locations (as judged by solving for them separately). In well-based experiments, the physical



**Figure 9.1** Our cell segmentation algorithm takes as input the stained image of the cell and a labeling of individual nuclei. The cell-stain channel is thresholded and a single cell per nucleus is identified as the Voronoi diagram of that nucleus, computed under a metric guided by features in the cell-stain image and constrained to the thresholded foreground.

connection between adjacent wells is not as strong as in slide-based experiments, so  $S$  is assumed to be constant well-to-well. Methods for normalizing well-based experiments may be applicable in this setting [16].

Illumination correction is vital for accurate segmentation and measurement of cells. This process is similar in many ways to methods for combined bias-correction and segmentation used in MRI analysis [17,18]. Although we have considered combining pixel-class decisions (i.e., choosing  $c$  in (9.1)) and illumination correction into a single process, we are somewhat limited in this direction by the large amount of variation in cell appearance within screens. Our focus in screens is often the outliers and extreme cases, so any segmentation algorithm must be robust to dramatic changes in appearance, including shifts in overall intensities. For this reason, we separate illumination correction and segmentation.

### 9.3.2 Segmentation

The primary benefit of image-based assays is the capture of a large number of per-cell measurements. This prevents the conflation of multimodal populations, as in expression profiling with gene expression microarrays, and provides a much richer data source than other methods, such as flow cytometry. To exploit the full potential of this data, however, it is necessary to accurately segment individual cells within each image.

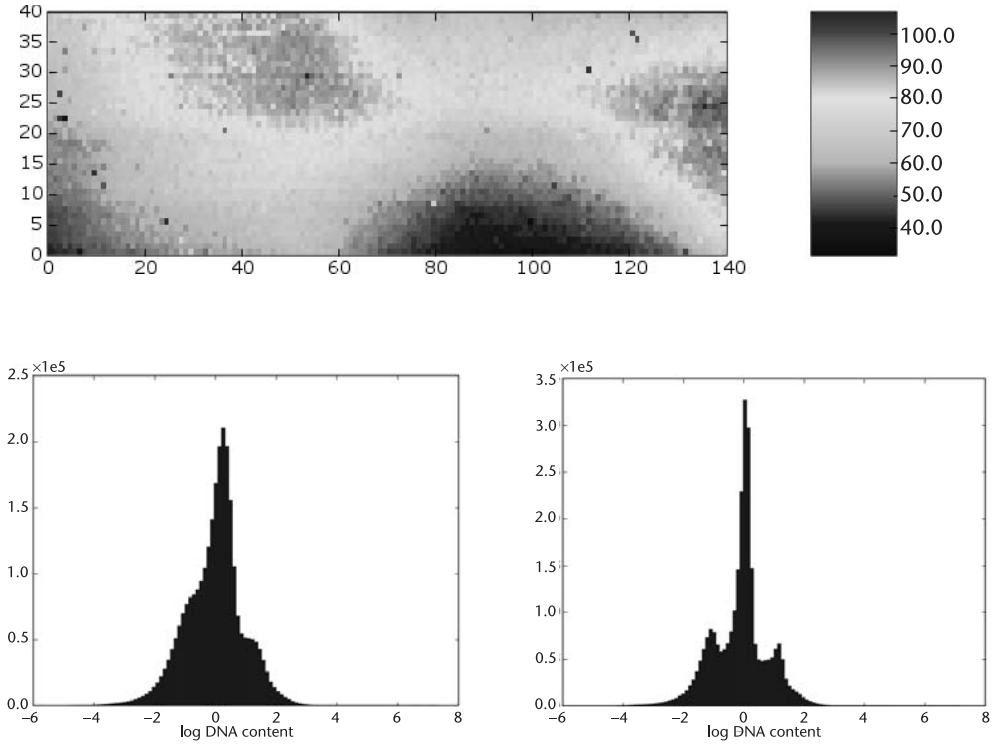
Unfortunately, the appearance of cells is highly variable from assay to assay. Experiments use different types of cells, different staining protocols, different growth substrates, and, of course, different conditions within each assay. All of these prevent a single approach from being optimal for all cases. We have implemented several methods in our system in a modular fashion, so we can easily adapt to new screens.

We have developed a successful, general approach for cell segmentation. Nuclei are more uniform in shape and more easily separated from one another than cells, so we first segment nuclei via automatic thresholding, then use segmented nuclei to guide the segmentation of individual cells, as diagrammed in Figure 9.2. We threshold the nuclear image using a regularized version of Otsu's method [19] or our own implementation that fits a Gaussian mixture to pixel intensities. After thresholding the nuclear channel, we separate nuclei that appear to abut or overlap by locating well-separated peaks in the intensity image, and use either a watershed transformation [20] or Voronoi regions of the peaks to place nuclear boundaries, as in related work [21–23]. Our thresholding and segmentation system are modular, so the user can experiment with different approaches on a small set of images to determine the best option or modify existing modules for a particular experiment.

Given segmented nuclei, segmentation of individual cells is a matter of locating the borders between adjacent cells. The wide variety of cellular phenotypes (even within a single screen) prevents us from knowing the particular appearance of cell borders, and, in fact, in many screens' cellular borders may change significantly in response to a particular condition, such as a gene's knockdown. For this reason, we use a very general method for placing cell borders.

A priori, we assume that a pixel we have classified as being “within some cell” is more likely to be associated with the closest nucleus in the image. This naturally





**Figure 9.2** Top: Median cell DNA content plotted on the physical layout of the slide in the cell microarray experiment, with staining variation correction disabled. Bottom left: DNA content histogram for all cells on the slide, prior to bias correction. Bottom right: DNA content histogram after bias correction. DNA content is measured by total intensity of the DNA stain within the nucleus, with unknown units. For this cell line, the dominant peak is made up of  $4N$  cells, in which the DNA has duplicated, but the cells have not yet divided. The horizontal axis labels show relative values only.

suggests using the Voronoi regions of the nuclei to place borders between cells. Another common approach is to assume the borders of the cells are brighter or darker and use a watershed transformation to place boundaries. Both of these approaches are commonly used in image cytometry [24, 25]. However, the first approach makes no reference to the cytoskeletal stain (i.e., information on where the border of the cell is actually located), and the second relies on the borders of the cells being of a significantly different intensity from the cell interiors and is overly sensitive to noise in pixels at cell boundaries. In our experience, both of these methods provide unsatisfactory results in practice. We combine and extend these approaches by defining a distance between pixels that makes dissimilar pixels farther apart, and use this metric to compute distorted nearest-neighbor regions.

We define similarity in terms of pixel neighborhoods. The distance between adjacent pixels at positions  $i$  and  $j$  is computed as

$$\frac{((i - j)^T \nabla g(I))^2 + \lambda \|i - j\|^2}{1 + \lambda} \quad (9.2)$$

where  $g(I)$  is a smoothed version of the image,  $\nabla$  is the gradient operator,  $\|i - j\|$  is the Euclidean distance between pixels  $i$  and  $j$ , and  $\lambda$  is a regularization term that balances between image-based and Euclidean distances, ranging from zero (distances from image features only) to infinity (Euclidean distance between pixels only). Distances between nonadjacent pixels are computed as the shortest path stepping between adjacent pixels, and cells are segmented via Voronoi regions of nuclei under this metric. More details of this approach are given in our earlier work [26].

### 9.3.3 Measurements

After segmentation, it is possible to make per-cell measurements for each image. Even if the screen is very targeted and the staining protocol has been tuned to give a simple binary answer, we capture a wide variety of measurements in order to maximize our ability to make inferences from the data.

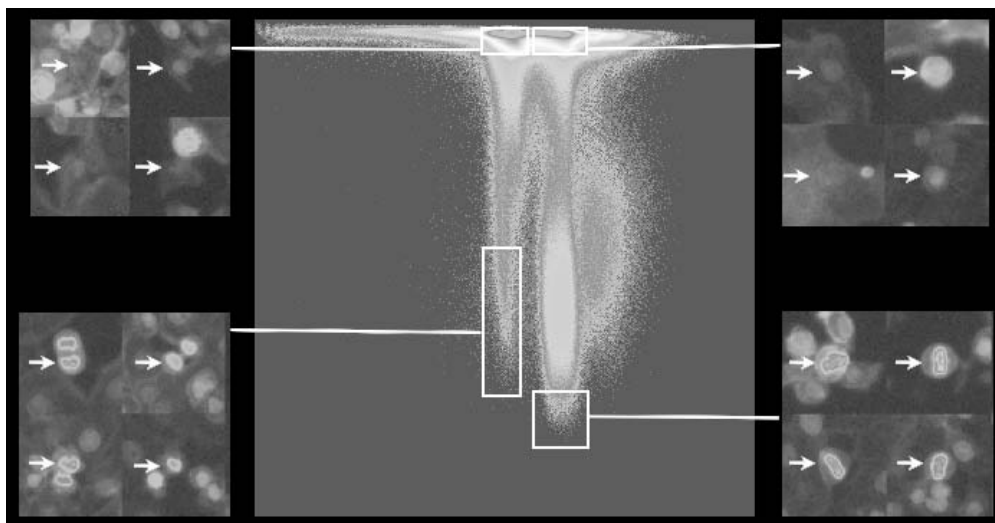
For each cell, we make measurements of its morphology (e.g., area, perimeter, extent, convexity, and several Zernike moments), and intensity and texture of the various stains (e.g., mean and standard deviation of intensity, correlation of stains, and Gabor filter response at various scales). Measurements are also broken down by cellular compartment (nucleus, cytoplasm, and entire cell). A full discussion of which measurements to use in a given screen is not germane to this chapter, but our guiding principle has been that, although it can make inference more difficult, taking too many measurements is better than taking too few. Adding new measurements to our system is simple because of its modular design.

Many of the measurements we capture have a clear biological meaning, such as cell size, or total DNA staining intensity in the nucleus (proportional to the amount of DNA present). Others have a less obvious connection to the biology of the cell, such as the eccentricity of the nucleus, or amount of variation in the cytoskeletal stain. Although we may not be able to assign meaning to every measurement, we can still make use of them when performing analyses or when classifying cells, as discussed in Section 9.3.5.

### 9.3.4 Spatial Bias Correction

Before measurements can be used to make biologically useful statements, we must control for systematic biases as much as possible. Biases in the data often come from variation across the physical layout of the slide or multiwell plate in which the experiments were performed (i.e., “plate effects” and “edge effects” [16]).

Some measurements can be corrected by fitting a smooth function to the data on the physical layout and dividing the corresponding per-cell measurements at each position by the smooth function. For example, if we skip correcting for staining variation and plot median per-cell DNA intensity on the slide layout for a 5,600-spot ( $140 \times 40$ ) slide (Figure 9.3, top), we observe a spatially varying bias, due to the uncorrected inhomogeneity in the stain for DNA. We can adjust for this bias by applying a 2-D median filter to the  $140 \times 40$  values and correcting each cell’s measurement via subtraction or division of the smoothed value, depending



**Figure 9.3** Simplified examples of per-cell classifiers. The central scatterplot shows total DNA content (horizontal axis) versus mean phospho-histone H3 staining intensity for each cell in the screen of human genes. Phospho-histone H3 is present in cells undergoing cell division (mitosis). Selecting different regions in the scatterplot selects different subpopulations of cells, as shown in the insets. Each inset shows four subimages; each subimage shows a random cell from the corresponding subpopulation (marked) and its surrounding image neighborhood. Counterclockwise from lower left:  $2N$  cells (normal complement of chromosomes),  $4N$  cells (DNA duplicated), Metaphase (condensed DNA, preparing to separate), and Anaphase/Telophase (daughter cells separating). This is also the progression of the cell cycle. A gene knockdown causing enrichment in any of these subpopulations relative to controls is likely a regulator of that phase of the cell cycle. Most classifiers involve many more measurements. (From: [10]. © 2006 BioMed Central Ltd. Reprinted with permission.)

on the most likely physical cause. The improvement in the per-cell DNA content histogram is obvious (Figure 9.3, bottom left versus right).

In some cases, it is difficult to determine how to correct a particular measurement or combination of measurements. Nonlinear interactions of cells with their environment makes it nearly impossible to remove all biases before making inferences from the data. Therefore, we make maximum use of nearby control spots or wells and check each measurement we use against the physical layout (as in Figure 9.3). Bias correction is an active area of research [16, 27].

### 9.3.5 Exploration and Inference

We take several approaches to exploring data from high-throughput, high-content screens. For example, (1) per-cell measurements can be combined to give per-gene values by taking means, medians, and so on, or by using other data-reduction techniques; (2) pairs of populations produced by different gene knockdowns can be compared directly using distribution-based metrics; or (3) individual cells can be classified by their measurements, and gene knockdowns compared by how they change the balance of different classes of cells. We discuss each of these approaches next.

### 9.3.5.1 Per-Gene Measurements

Each per-cell measurement can be converted to a per-gene measurement by taking the mean, median, or otherwise reducing each measurement to a small set of parameters. This approach works particularly well when the screen focuses on a simple single parameter readout (e.g., presence of a given protein), or if the goal is to find gene knockdowns that have an easily measured effect (e.g., cause cells to grow larger). For example, Color Plate 14 shows a scatterplot of per-gene mean cell size versus mean nuclear size. Three replicates knocking down the *D. melanogaster* gene *ial* are highlighted, in which cells and nuclei have grown larger than controls.

This approach is also effective for early, open-ended exploration, where identification of outliers is the primary task, especially since it can be applied to any measurement without prior knowledge about that measurement's biological implications.

Reducing the data in this way makes it weakly analogous to the data from gene-chips, in which mean expression level is measured for a large number of proteins. Like gene-chips, this approach can suffer from an over-reduction of measurements [28]. For example, knocking down a gene may cause some cells to double in size, and an equivalent fraction to halve in size, but this would not affect the mean cell size [28]. In contrast, if we work with measurements' distributions directly, such differences are easily detected.

### 9.3.5.2 Population Comparisons

To compare two populations' measurements directly without first reducing to a single per-gene value, we can apply distribution comparisons, such as the Kolmogorov-Smirnov [5] or Kuiper [29] tests, or compute sample-based information-theoretic estimates, such as the Kullback-Leibler divergence between the two distributions [30]. These can be used to compare each sample against a set of positive or negative controls, or against the full slide-wide cell population, yielding a more experiment-specific per-gene measurement as discussed earlier.

Comparing gene knockdowns' populations via a single or small set of per-cell measurements, as in Color Plate 14(b) is similar to exploring data from flow cytometry, in which a few measurements are taken for a large number of cells, though flow cytometry allows fewer samples to be analyzed than image cytometry. The number of measurements is also much more limited compared to automatic image-based cytometry.

### 9.3.5.3 Per-Cell Classification

To take full advantage of the large number of per-cell measurements, our primary method of exploration is via per-cell classifiers. We build or train classifiers that identify a phenotype of interest and apply them to the full screen in order to determine which conditions or gene knockdowns cause enrichment or depletion in those phenotypes. Our goal is to understand the function of genes, with the underlying assumption that gene knockdowns that cause similar changes in phenotype have similar functions in the cell.

In particular, we advocate the per-cell classifier approach because it detects very small changes in the percentage of cells falling into a particular class. Some phenotypes, such as mitotic (replicating) cells, are less than 1% of cells at the background level and increase only three-fold above this level in outliers and positive controls [10]. These changes are so small relative to the full population that they are swamped if measurements are blindly combined into per-gene values, or when comparing two otherwise similar distributions.

Given a classifier for cells showing a known phenotype, the list of gene knockdowns that enrich or deplete that phenotype can be used to impute function for those genes. For example, if we build a classifier for cells in metaphase, knockdowns that cause enrichment of that phenotype probably have a regulatory function in the metaphase to anaphase transition. Simplified examples of per-cell classifiers are shown in Figure 9.4, in which classifiers were constructed to identify different phases of the cell cycle based on a pair of measurements, total nuclear DNA content (as measured by the DNA stain), and mean nuclear phospho-H3 content (a marker for mitosis). If a gene knockdown significantly changes the fraction of cells landing in one (or more) of these classifiers, it is likely to be a regulator for those phases of the cell cycle. Most classifiers are more complicated than this, involving a larger number of per-cell measurements [10].

To compute enrichments and p-values, we treat the output of classifiers as Bernoulli random variables. If negative controls are available in the screen, then enrichments are computed relative to those controls. Otherwise, we use the full screen-wide cell population as the control, the operative assumption being that for each phenotype, knockdown of most genes will not affect that phenotype. There are two justifications for this assumption: many genes are not expressed under experimental conditions, so they cannot be depleted by knockdown, and even if most genes were to have an effect on the phenotype of interest, our interest would be in those with the strongest effect.

The phenotypes targeted by the classifier can be biologically well characterized, such as cells in a particular phase of the cell cycle (as previously), or simply cells that have a novel appearance, without a well-defined biological interpretation attached. For an uncharacterized phenotype, the group of gene knockdowns causing enrichment or depletion in that phenotype can be informative, depending on the group of gene knockdowns causing similar effects. For example, the genes in the group might share a physical or biochemical property, suggesting the underlying mechanism for the phenotypic change. However, if the group contains genes with a similar, known function, the uncharacterized genes in the group can be hypothesized to also share that function. This also allows for the identification of new, hypothetical cellular processes, rather than simply identifying genes involved in known processes.

The per-cell classifier approach can also be applied to a particular gene's knockdown that might not show a human-discernable phenotype, but for which we can still build a classifier. If the classifier is effective at separating the cells with the target gene knocked down from the cell population at large, the implication is that there is a measurable phenotype caused by the target gene's knockdown, and other knockdowns that cause the same phenotype have a similar function. However,

due to natural variation from well to well or spot to spot, it is often possible for a classifier to differentiate two images with otherwise identical conditions, such as two control wells. It is therefore necessary to characterize how much classifiers are affected by such variation, an area of active research [4].

One of the benefits of the classifier-based approach is that it is less susceptible to spatial biases when the classifier is trained by a human, compared to data-reduction or full-population comparison methods, because of the robustness of the human visual system to these biases. Note, however, that the nonlinear effect of environment on cells can cause biases in the fraction of cells of a particular phenotype, so the results of applying the classifier should be checked for spatial bias, similar to Figure 9.3.

The classifier approach is reminiscent of example-based image retrieval [31, 32]. However, rather than searching for images as the primary goal, we are using similar techniques to quickly categorize subimages of cells, with the intent of determining the number and distribution of cells matching our query specification.

After finding hits in a particular screen, follow-up work may be necessary to validate the results. If there are a sufficient number of replicates, or data from other screens are available, it may be possible to make a categorical statement about a gene knockdown's effect without further experimental work. However, in almost all cases, biologists will investigate the mechanism of the effect in traditional follow-up experiments. In many cases, therefore, analysis of automated screens acts as an attention-focusing device.

## 9.4 Discussion

This chapter has presented several methods applicable to high-content, high-throughput image-based screens of cells. Such screens are particularly valuable in biological and pharmaceutical research. We have developed CellProfiler [10], a modular, open-source system incorporating these methods, and will soon release a companion data visualization and analysis tool, CellVisualizer ([cellvisualizer.org](http://cellvisualizer.org)).

High-throughput, high-content screening is a powerful technique for making discoveries about cellular processes, genetic pathways, and drug candidates. It also poses new challenges and requires novel techniques to realize its full potential as a discovery tool. Algorithms for identifying, segmenting, and measuring individual cells must deal with noise and biases, be robust to a wide variety of cell appearances, and must be accurate enough to allow very small ( $<1\%$ ) subpopulations to be identified accurately. However, the payoff for the increased effort is a dramatically more powerful method for detecting changes in cells under different experimental conditions, through the use of per-cell data and classifiers, compared to more traditional techniques. These methods have been proven in one of the first large-scale automatic screens to appear in the biological literature [12].

For reasons of scope, this chapter does not include a discussion of the architecture and design of our system implementing the techniques presented here. We

aimed to make the system as modular and extensible as possible, while maintaining a user-friendly interface. We believe it has been successful in these respects, particularly given its use in a variety of noncell screening tasks (e.g., counting and classifying yeast colonies on Petri dishes, counting nuclear subcompartments/speckles, and tumor measurement [33]).

### Acknowledgments

This work was supported by an academic grant from the Society for Biomolecular Sciences (AEC), a fellowship from the Merck/MIT computational and systems biology initiative (AEC), the MIT EECS/Whitehead/Broad Training Program in Computational Biology (NIH grant DK070069-01; TRJ), NIH grant R01 GM072555-01 (DMS), and a grant awarded by the U.S. Army Medical Research Acquisition Activity: W81XWH-05-1-0318-DS (DMS), although no official endorsement by the government should be inferred. AEC is a Novartis fellow of the Life Sciences Research Foundation.

### References

- [1] Kiger, A. A., B. Baum, S. Jones, M. R. Jones, A. Coulson, C. Echeverri, and N. Perrimon, "A functional genomic analysis of cell morphology using RNA interference," *J. Biol.*, Vol. 2, No. 1475-4924 (Electronic), 2003, p. 27.
- [2] Kim, J. K., H. W. Gabel, R. S. Kamath, M. Tewari, A. Pasquinelli, J.-F. Rual, S. Kennedy, M. Dybbs, N. Bertin, J. M. Kaplan, M. Vidal, and G. Ruvkun, "Functional genomic analysis of RNA interference in *C. elegans*," *Science*, Vol. 308, No. 1095-9203 (Electronic), 2005, pp. 1164-1167.
- [3] Bakal, C., J. Aach, G. Church, and N. Perrimon, "Quantitative morphological signatures define local signaling networks regulating cell morphology," *Science*, Vol. 316, No. 5832, 2007, pp. 1753-1756.
- [4] Loo, L.-H., L. F. Wu, and S. J. Altschuler, "Image-based multivariate profiling of drug responses from single cells," *Nat Methods*, Vol. 4, No. 5, pp. 445-453, 2007.
- [5] Perlman, Z. E., M. D. Slack, Y. Feng, T. J. Mitchison, L. F. Wu, and S. J. Altschuler, "Multidimensional drug profiling by automated microscopy," *Science*, Vol. 306, No. 1095-9203 (Electronic), 2004, pp. 1194-1198.
- [6] Philips, J. A., E. J. Rubin, and N. Perrimon, "Drosophila RNAi screen reveals cd36 family member required for mycobacterial infection," *Science*, Vol. 309, No. 1095-9203 (Electronic), 2005, pp. 1251-1253.
- [7] Harada, J. N., K. E. Bower, A. P. Orth, S. Callaway, C. G. Nelson, C. Laris, J. B. Hogenesch, P. K. Vogt, and S. K. Chanda, "Identification of novel mammalian growth regulatory factors by genome-scale quantitative image analysis," *Genome Res.*, Vol. 15, No. 1088-9051, 2005, pp. 1136-44.
- [8] Pelkmans, L., E. Fava, H. Grabner, M. Hannus, B. Habermann, E. Krausz, and M. Zerial, "Genome-wide analysis of human kinases in clathrin- and caveolae/raft-mediated endocytosis," *Nature*, Vol. 436, No. 1476-4687 (Electronic), 2005, pp. 78-86.
- [9] Pipalia, N. H., A. Huang, H. Ralph, M. Rujoi, and F. R. Maxfield, "Automated microscopy screening for compounds that partially revert cholesterol accumulation in niemann-pick c cells," *J. Lipid. Res.*, Vol. 47, No. 0022-2275, 2006, pp. 284-301.



- [10] Carpenter, A. E., T. R. Jones, M. Lamprecht, D. B. Wheeler, C. Clarke, I. H. Kang, O. Friman, D. A. Guertin, J. H. Chang, R. Lindquist, J. Moffat, P. Golland, and D. M. Sabatini, "CellProfiler: image analysis software for identifying and quantifying cell phenotypes," *Genome Biology*, Vol. 7, No. 10, 2006, p. R100.
- [11] Wheeler, D. B., S. N. Bailey, D. A. Guertin, A. E. Carpenter, C. O. Higgins, and D. M. Sabatini, "RNAi living-cell microarrays for loss-of-function screens in *Drosophila melanogaster* cells," 2004.
- [12] Moffat, J., D. A. Grueneberg, X. Yang, S. Y. Kim, A. M. Kloepper, G. Hinkle, B. Piqani, T. M. Eisenhaure, B. Luo, J. K. Grenier, A. E. Carpenter, S. Y. Foo, S. A. Stewart, B. R. Stockwell, N. Hacohen, W. C. Hahn, E. S. Lander, D. M. Sabatini, and D. E. Root, "A lentiviral RNAi library for human and mouse genes applied to an arrayed viral high-content screen," *Cell*, Vol. 124, No. 0092-8674, 2006, pp. 1283-98.
- [13] Armknecht, S., M. Boutros, A. Kiger, K. Nybakken, B. Mathey-Prevot, and N. Perrimon, "High-throughput RNA interference screens in *Drosophila* tissue culture cells," *Methods Enzymol.*, Vol. 392, No. 0076-6879, 2005, pp. 55-73.
- [14] Jones, T. R., "Predicting Gene Function from Images of Cells," Ph.D. thesis, MIT, 2007.
- [15] Jones, T. R., A. E. Carpenter, P. Golland, and D. M. Sabatini, "Cell Profiler: Free Cell Image Analysis Software for High Throughput Screening," *Society for Biomolecular Screening Annual Meeting*, September 2005.
- [16] Root, D. E., B. P. Kelley, and B. R. Stockwell, "Detecting spatial patterns in biological array experiments," *J. Biomol. Screen.*, Vol. 8, No. 1087-0571, 2003, pp. 393-398.
- [17] Wells, W., W. Grimson, R. Kikinis, and F. Jolesz, "Adaptive segmentation of MRI data," *IEEE TMI*, Vol. 15, 1996, pp. 429-442.
- [18] Leemput, K. V., F. Maes, D. Vanermeulen, and P. Suetens, "Automated model-based bias field correction of MR images of the brain," *IEEE TMI*, Vol. 18, 1999, pp. 885-895.
- [19] Otsu, N., "A threshold selection method from gray level histograms," *IEEE Trans. Systems, Man and Cybernetics*, Vol. 9, March 1979, pp. 62-66.
- [20] Beucher, S., "The watershed transformation applied to image segmentation," *Scanning Microscopy International*, Vol. 6, 1992, pp. 299-314.
- [21] Malpica, N., C. O. de Solorzano, J. J. Vaquero, A. Santos, I. Vallcorba, J. M. Garcia-Sagredo, and F. del Pozo, "Applying watershed algorithms to the segmentation of clustered nuclei," *Cytometry*, Vol. 28, No. 0196-4763, 1997, pp. 289-297.
- [22] Meyer, F., and S. Beucher, "Morphological segmentation," *Journal of Visual Communication on Image Representation*, Vol. 1, 1990, pp. 21-46.
- [23] Wahlby, C., I.-M. Sintorn, F. Erlandsson, G. Borgefors, and E. Bengtsson, "Combining intensity, edge and shape information for 2d and 3d segmentation of cell nuclei in tissue sections," *J. Microsc.*, Vol. 215, No. 0022-2720, 2004, pp. 67-76.
- [24] Wahlby, C., "Algorithms for Applied Digital Image Cytometry," Ph.D. thesis, 2003.
- [25] Beucher, S., "The watershed transformation applied to image segmentation," *Scanning Microscopy International*, Vol. 6, 1992, pp. 299-314.
- [26] Jones, T. R., A. E. Carpenter, and P. Golland, "Voronoi-based segmentation of cells on image manifolds," in *CVBIA*, Y. Liu, T. Jiang, and C. Zhang, (eds.), vol. 3765 of *Lecture Notes in Computer Science*, New York: Springer, 2005, pp. 535-543.
- [27] Kevorkov, D., and V. Makarenkov, "Statistical analysis of systematic errors in high-throughput screening," *J. Biomol. Screen.*, Vol. 10, No. 1087-0571, 2005, pp. 557-567.
- [28] Levsky, J. M., and R. H. Singer, "Gene expression and the myth of the average cell," *Trends Cell Biol.*, Vol. 13, No. 0962-8924, 2003, pp. 4-6.
- [29] Kuiper, N. H., "Tests concerning random points on a circle," *Proc. K. Ned. Akad. Wet., Ser. A*, Vol. 63, 1962, pp. 38-47.

- [30] Kullback, S., and R. A. Leibler, "On information and sufficiency," *Annals of Mathematical Statistics*, Vol. 22, 1951, pp. 79-86.
- [31] Muller, H., N. Michoux, D. Bandon, and A. Geissbuhler, "A review of content-based image retrieval systems in medical applications-clinical benefits and future directions," *Int. J. Med. Inform.*, Vol. 73, No. 1386-5056, 2004, pp. 1-23.
- [32] Tieu, K., and P. Viola, "Boosting image retrieval," *Int. J. Comput. Vision*, Vol. 56, No. 1-2, 2004, pp. 17-36.
- [33] Lamprecht, M. R., D. M. Sabatini, and A. E. Carpenter, "Cellprofiler: free, versatile software for automated biological image analysis," *Biotechniques*, Vol. 42, No. 1, 2007, pp. 71-75.



# Particle Tracking in 3D+t Biological Imaging

Auguste Genovesio and Jean-Christophe Olivo-Marin

## 10.1 Introduction

The advent of multidimensional microscopy has enabled biologists to visualize cells, tissues, and organs in their intrinsic 3-D and 3D+t geometry, in contrast to the limited 2-D representations that were available until recently. These new technologies are already impacting biological research in such different areas as high-throughput image-based drug screening, cellular therapies, cell and developmental biology, and gene expression studies, as they are putting at hand the imaging of the inner working of living cells in their natural context. Expectations are high for breakthroughs in areas such as cell response and motility modification by drugs, control of targeted sequence incorporation into the chromatin for cell therapy, spatial-temporal organization of the cell and its changes with time or under infection, assessment of pathogens routing into the cell, interaction between proteins, and sanitary control of pathogen evolution, to name but a few.

Deciphering the complex machinery of cell functions and dysfunction necessitates a detailed understanding of the dynamics of proteins, organelles, and cell populations. This in turn calls for large-scale multidimensional image-based assays to cover the wide range of highly variable and intricate properties of biological material.

This chapter is concerned with the tracking of microscopic particles on four-dimensional (3D+t) image data coming from biological imaging. The automatic tracking of biological particles in 3D+t microscopy sequences is presently one of the major challenges in biological image processing, and it constitutes one of the major bottlenecks for the full exploitation of multidimensional microscopy sequences documenting studies on biological object dynamics.

In this presentation we will mainly consider methods that decouple the detection and the tracking processes and, moreover, we will just address the tracking step. This is because although detection of biological objects is a topic of considerable importance and has sparked a huge field of research still very active [1,2], it can be considered a mature field whose full coverage is beyond the scope of this chapter. Conversely, we feel that fewer efforts have been devoted to research or reports on data filtering and association in the context of biological imaging and that this chapter is a good opportunity to give a comprehensive assessment on these two topics. In consequence, we will consider throughout this chapter that a set of measurements performed by a detector, be it a simple thresholding [3] or a more sophisticated one [4], and consisting at least of the spatial coordinates of the objects, is given as an input to a tracker and that this tracker, through a

combination of filtering and data associations steps, outputs the trajectories and dynamics of the moving objects.

Despite the lack of a standardized framework for tracking methods mostly due to a very large set of diverse applications and highly different biological contexts, several problems are recurrent in tracking applications and have often led to similar solutions. We will first present a number of such methods published in the literature, and thereafter we will concentrate on the work we have been developing over the past years. Although we acknowledge that other approaches may be equally worthwhile, we also believe that the specific set of methods we have proposed is particularly adapted to the problem of tracking multiple particles in biological sequences, as it allows us to detect with high accuracy multiple biological objects moving in three-dimensional space and to follow moving objects switching between different dynamics characteristics. The main ingredients of our method are a detection step based on wavelets that is robust to the local variation of contrast and to the imaging noise and a Bayesian tracker that allows us to predict the next position of a spot knowing its past positions and increases the reliability of the data association step.

In the last section of this chapter, we will illustrate the tracking of microscopic particles by a number of biological applications in cell biology of infectious diseases.

At present, a considerable part of biological imaging is based on the use of *in vivo* multidimensional fluorescence microscopy, allowing for the visualization of specific biological processes in real time and three dimensions. The introduction of novel microscopy techniques like optical sectioning or confocal microscopy has opened the road to a whole series of research perspectives dedicated to the study of cellular dynamics, and to the links between cellular functions and spatial-temporal localization. For example, it is nowadays routine in cell biology to film cells, organelles, and pathogens to document infectious disease processes in living systems [5–8]. In many such applications, the fluorescently labeled biological objects are visualized as small bright spots superimposed on an uneven background, where a spot is defined as an object that is relatively small and compact and has no clear border, and whose intensity is both diffuse and higher than that of its immediate neighborhood. The reliable quantitative study of motility and dynamic properties requires the computation of parameters like number of spots, position, spatial distribution, movement phases, speed, and diffusion coefficients, and therefore requires that all the spots in the image sequences are detected and tracked [9, 10]. In the context of living cellular systems, spot tracking can be made particularly difficult by the facts that the dynamics of each spot can change over time or that spots may aggregate temporarily, making their appearance change and their proper detection more difficult [10]. Not surprisingly, many biological object motility studies are based on the study of a few handpicked particles that represent only a small subset of the total [6]. On top of being tedious and time consuming, this type of manual tracking is prone to many errors, is highly dependent on the operator's skills and perception [5], and can introduce a strong bias in the analysis. It is therefore of utmost importance to develop methods to perform the tracking in

an automatic, reproducible, and unprejudiced manner, such as the ones presented in the sequel.

## 10.2 Main Tracking Methods

In this section, we describe the main tracking methods and put them in perspective relative to our problem set by examining the advantages and drawbacks of each of them. As stated earlier, Bayesian tracking has proved to be the method of choice for our applications, and therefore we will be studying it in more detail in this section.

### 10.2.1 Autocorrelation Methods

The method that is used the most to track an object in a sequence of images is probably the autocorrelation tracking method [11–14] and its derivations [15–19]. This is due to the relative simplicity of its concept and use.

The idea is to find in each image  $I_t$ , a region  $\mathcal{P}$  that “most resembles” the reference area  $T$  that we are looking for and that corresponds to the object that we are tracking. In most applications, this reference area is regularly updated to take into account object deformation or change in angle of view. It is therefore a question of finding the area in image  $T$  that minimizes the sum of the squares of standard deviation [20,21], which amounts to maximizing the least expensive function of *cross correlation*:

$$R(i, j) = \sum_{x, y \in \mathcal{P}} T(x, y) \cdot I(x - i, y - j) \quad (10.1)$$

We can ultimately make this criterion more robust with respect to local variations in energy by considering its normalized version

$$N(i, j) = \frac{\sum_{x, y \in \mathcal{P}} T(x, y) \cdot I(x - i, y - j)}{\sqrt{\sum_{x, y \in \mathcal{P}} T(x, y)^2 \cdot \sum_{x, y \in \mathcal{P}} I(x - i, y - j)^2}} \quad (10.2)$$

A mini reference image is selected from the first image in the sequence. The maximum of the correlation function is searched for in the rest of the images. A stage updating the base mini-image is carried out regularly to allow for slight deformation of the object. This consists of replacing the mini-image with the part of the current image that maximizes the correlation. The technique of tracking by correlation has two advantages: it offers relative simplicity of implementation, and it is effective on objects that do not change shape and for which we always have the same viewpoint (supervision of a production line, for example). However, the basic version also has some deficiencies: (1) the definition of the basic mini-image is ad hoc; (2) changes in topology (entry, exit, separation, and fusion of objects) are

not managed; (3) intersections with objects and other occlusions are not handled; (4) it is sensitive to object deformation (even with updating of the mini-image), although [14] presents a version that allows a geometric transformation of the object; and (5) it is highly sensitive to noise. All these disadvantages make these methods highly inefficient for tracking multiple fluorescent spots.

### 10.2.2 Deterministic Methods

Whereas the previous methods propose an implicit solution to the problem of tracking because the tracking is integrated within the object segmentation, deterministic methods propose separating segmentation from the problem of tracking itself. This is because a detection method is used to obtain a set of points that are identified in time, thanks to a point correspondence method. We refer to [22–29] for various types of approaches and to [30] for a comparison of some of these methods with each other.

If  $\mathbf{x}_t$  is the position  $(x, y)$  of an object in image  $t$ , we perform a point correspondence on three successive images by minimizing the cost function proposed by Sethi [22]:

$$c = \gamma_1 \left[ 1 - \frac{(\mathbf{x}_t - \mathbf{x}_{t-1}) \cdot (\mathbf{x}_{t+1} - \mathbf{x}_t)}{\|\mathbf{x}_t - \mathbf{x}_{t-1}\| \times \|\mathbf{x}_{t+1} - \mathbf{x}_t\|} \right] + \gamma_2 \left[ 1 - 2 \frac{\sqrt{\|\mathbf{x}_t - \mathbf{x}_{t-1}\| \times \|\mathbf{x}_{t+1} - \mathbf{x}_t\|}}{\|\mathbf{x}_t - \mathbf{x}_{t-1}\| + \|\mathbf{x}_{t+1} - \mathbf{x}_t\|} \right] \quad (10.3)$$

This cost function formulates the hypothesis of object trajectory regularity because the first term favors sequences of points that do not change direction, whereas the second favors sequences of points whose speed is constant. Each of the previously cited authors adapts this cost function to the conditions of their application.

A detection method is used to locate the points that represent the objects to be tracked in all the images in the sequence. The set of trajectories that minimizes  $c$  for every  $t$  may be obtained thanks to several techniques, the most used one being dynamic programming. These methods have advantages that have already allowed their implementation in commercial software: they are efficient on sequences of points that have been clearly detected, and they offer relative simplicity of implementation. They also have major disadvantages for our applications: they rely on the hypothesis of regularity that is poorly adapted to multiple objects whose movement varies between them and in time, they do not take into account fusions or separations of objects in over- or underdetection, and they are sensitive to false detections.

### 10.2.3 Multiple Particle Tracking Methods

A large body of work has addressed the tracking of single particles in optical microscopy (see [31] for a review) and of multiple spots in military or video imaging [32, 33], including the ones presented in the previous sections. Conversely, relatively little effort has been devoted to multiple particle tracking (MPT) in the cellular and molecular imaging domain [29, 34–40]. Conventional MPT methods



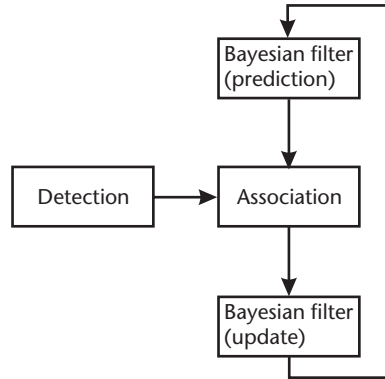
in 2-D are based on simple intensity thresholding [34], template matching [38] or local maxima extraction [35] for detecting the spots and on nearest neighbor association (NNA) [34], or constrained NNA [35] to perform the tracking. These methods work well on image sequences showing a limited number of very bright spots on a uniform background, but they fail as soon as the intensity of the spots is not modal, the spots are embedded in noisy images, the density of spots is high, or the displacement of spots is higher than the interspot spacing. In [36], a solution to improve on the previous methods is proposed. It uses the combination of four techniques—highly sensitive object detection, fuzzy logic-based dynamic object tracking, computer graphical visualization, and measurement in time-space. Although this method is effective when working with well-separated objects, it shows some limitations in keeping up with aggregating ones. A more robust algorithm is presented in [29,37], based on ideas from operational research and graph theory. It proceeds in four steps: particle detection, generation of candidate matches (i.e., a set of possible displacement vectors between successive frames), scoring of candidate matches, and selection of the candidate subset with maximum global score and no topological ambiguity. The method, however, relies on a number of heuristic rules and on a priori information on the movements of objects to be effective. The method in [41] does not use the traditional frame-by-frame approach but rather considers the whole sequence as a spatiotemporal volume where the tracks are defined as minimal paths in an image-dependent metric. Finally, it is worth noting that most of these algorithms are difficult to extend to four-dimensional data and that such extensions have not been reported.

Tracking in 3D+t has been addressed only more recently, either in the case of single particles [42] or multiple particles [43]. The method in [42] uses a matched filter as a prefiltering step to a dynamic programming procedure that extracts the trajectory. The method in [43] uses a 3-D PSF model for spot detection and associates spots on the basis of the weighted minimal distance between them.

#### 10.2.4 Bayesian Methods

The modeling of a tracking problem can be represented by a “state-space” approach [32,44–47]. A state vector represents an object in the form of a set of characteristics. When an object changes, its state vector changes as well. From a set of measurements obtained thanks to a detection stage and a set of a priori knowledge, an association method is combined with a prediction-estimate method to obtain a sequence of densities of the state of each object that are conditional on the measurements. These densities are then used in an estimate of the trajectory of each object.

Bayesian tracking is made up of three components and is carried out in four stages for each image in the sequence. The three components, as shown in Figure 10.1, are: (1) a detection method, adapted to the objects that we are trying to track, is used to form measurements for each of these objects in each image in the sequence; (2) a Bayesian filter, accompanied by a priori dynamics and observations in the form of densities, that is used to predict and estimate the density of a state that is conditional on successive measurements; and (3) an association method that



**Figure 10.1** General diagram of Bayesian tracking.

is used to reattribute each measurement to the source that produced it to obtain a correct estimate of the filters. Each of these three components will be detailed next.

The actual tracking is carried out in four stages:

1. The prediction stage of the Bayesian filter produces a density conditional for each state on past measurements.
2. The detection stage provides a set of measurements.
3. The association stage is used to determine whether a measurement comes from an object and, if so, from which object, in order to contribute to updating the density related to the object that generated it.
4. The updating stage combines each filter and the measurement (or the measurements, depending on the methods) that has (or have) been attributed to it to produce the density of the state conditional on past and present measurements.

This method has proved to be the one that is best adapted to our problem set for the following reasons: (1) it offers the possibility of generating a prediction from a general representation of each object; (2) it allows progressive correction of this prediction as measurements are obtained; (3) if the objects change greatly in time, it is used to avoid trying to track each of their points precisely, but instead tracks a general description represented by a state vector; and (4) a state vector may comprise not only the spatial position, but also the volume and the mean intensity of a spot.

We shall see that Bayesian tracking nonetheless has drawbacks: (1) the detection stage, which cannot be considered to be a perfect stage in tracking fluorescent spots, systematically violates some hypotheses stated by the current association methods, which as we shall see leads to many errors; and (2) the use of Bayesian filters requires a certain amount of a priori knowledge such as the densities of transition and observation probabilities, which may be unavailable or difficult to obtain.

## 10.3 Analysis of Bayesian Filters

This section offers an analysis of the second component in Bayesian tracking: filtering. As we have seen, modeling the tracking problem may be represented by a “state-space” approach. We are trying to obtain the changes in the state of an object in the form of a probability density of a vector known as a state vector. The subsequent densities are obtained from the measurements of the sensor and from two densities assumed to be known and that represent the changes and the measurement of the state.

Using a Bayesian filter is of primary importance for two reasons. The first is that it is used to create one or more predictions of the state density at the  $t + 1$  stage, where only measurements from 1 to  $t$  are available. In order to minimize errors of association, the precision of this prediction is of primary importance in the context of tracking multiple objects. The second reason is that the detection procedure produces measurements that are imprecise in nature due to the detection noise. A Bayesian filter is used to obtain a more accurate estimate of the state of each object by bringing into play a priori knowledge and a correction that takes prediction errors into account.

The way to resolve the problem of Bayesian filtering involves a conceptual solution that can be obtained analytically on the basis of firm hypotheses or can only be approximated when some conditions are not fulfilled. We present various Bayesian filters and propose some examples to illustrate their capacity to estimate the evolution of a state vector. We shall see in particular that one of them, the interacting multiple models (IMM) filter, is quite well adapted to our problem set because it is used to take into account a transition that suddenly changes models over the course of time.

### 10.3.1 The Conceptual Filter

The changes in an object is represented by a sequence of hidden states  $\{\mathbf{x}_t, t \in \mathbb{N}\}$  whose Markovian character is modeled in its most general form by:

$$\mathbf{x}_t | \mathbf{x}_{t-1} \sim p(\mathbf{x}_t | \mathbf{x}_{t-1}) \quad (10.4)$$

This process generates in turn a sequence of measurements  $\{\mathbf{z}_t, t \in \mathbb{N}\}$ , modeled by:

$$\mathbf{z}_t | \mathbf{x}_t \sim p(\mathbf{z}_t | \mathbf{x}_t) \quad (10.5)$$

In the rest of this document, (10.4) corresponds to the *temporal a priori* referred to as “transition” (from state  $t - 1$  to state  $t$ ) and (10.5) corresponds to the *likelihood* referred to as “observation.” We suppose that  $p(\mathbf{x}_t | \mathbf{x}_{t-1})$  and  $p(\mathbf{z}_t | \mathbf{x}_t)$  are known. In the presence of additive noise, the system takes the following form:

$$\begin{cases} \mathbf{x}_t = f_t(\mathbf{x}_{t-1}) + \mathbf{v}_t \\ \mathbf{z}_t = h_t(\mathbf{x}_t) + \mu_t \end{cases} \quad (10.6)$$

where  $\{v_t, t \in \mathbb{N}\}$  and  $\{\mu_t, t \in \mathbb{N}\}$ , respectively called the process noise and measurement noise of the state space representation, are sequences of random vectors and there is no a priori hypothesis concerning  $f_t$  and  $h_t$ . When  $f_t$  and  $h_t$  are linear, this can be written

$$\begin{cases} \mathbf{x}_t = \mathbf{F}_t \mathbf{x}_{t-1} + \mathbf{v}_t \\ \mathbf{z}_t = \mathbf{H}_t \mathbf{x}_t + \mu_t \end{cases} \quad (10.7)$$

Finally, when we suppose as well that  $v_t$  and  $\mu_t$  are Gaussian with  $v_t \sim \mathcal{N}(\mathbf{v}_t; 0, \mathbf{Q}_t)$  and  $\mu_t \sim \mathcal{N}(\mu_t; 0, \mathbf{R}_t)$ , the system can also be written:

$$\begin{cases} \mathbf{x}_t | \mathbf{x}_{t-1} \sim \mathcal{N}(\mathbf{x}_t; \mathbf{F}_t \mathbf{x}_{t-1}, \mathbf{Q}_t) \\ \mathbf{z}_t | \mathbf{x}_t \sim \mathcal{N}(\mathbf{z}_t; \mathbf{H}_t \mathbf{x}_t, \mathbf{R}_t) \end{cases} \quad (10.8)$$

We define  $Z_t = \{\mathbf{z}_t^1, \dots, \mathbf{z}_t^i\}$  as all measurements recorded in stage  $t$  and  $Z_{1:t} = \{Z_1, \dots, Z_t\}$  the set of all the measurements recorded since stage 1. For the moment, we suppose that there are no association problems and that we obtain one measurement per stage *i.e.*  $\forall t, Z_t = \{\mathbf{z}_t\}$  and therefore also  $Z_{1:t} = \{\mathbf{z}_1, \dots, \mathbf{z}_t\}$ .

Let us return to our most general system described by (10.4) and (10.5). The Bayesian framework corresponds to these problem sets quite nicely because we are trying to estimate the density  $p(\mathbf{x}_t | Z_{1:t})$  recursively (*i.e.*, as we obtain  $\mathbf{z}_t$ ). This construction is carried out in two stages: a prediction stage in which we obtain an a priori density  $p(\mathbf{x}_t | Z_{1:t-1})$  from  $p(\mathbf{x}_{t-1} | Z_{1:t-1})$  and an update stage where  $p(\mathbf{x}_t | Z_{1:t-1})$  is corrected to obtain the a posteriori density  $p(\mathbf{x}_t | Z_{1:t})$ . As (10.4) describes a first-order Markov process, the Chapman-Kolmogorov equation:

$$p(\mathbf{x}_t | Z_{1:t-1}) = \int p(\mathbf{x}_t | \mathbf{x}_{t-1}) p(\mathbf{x}_{t-1} | Z_{t-1}) d\mathbf{x}_{t-1} \quad (10.9)$$

allows us to obtain the prediction  $p(\mathbf{x}_t | Z_{1:t-1})$  without prior knowledge of  $\mathbf{z}_t$ . When an extra measurement  $\mathbf{z}_t$  is available,  $p(\mathbf{x}_t | Z_{1:t-1})$  is corrected by applying the Bayes rule:

$$p(\mathbf{x}_t | Z_{1:t}) = \frac{p(\mathbf{z}_t | \mathbf{x}_t) p(\mathbf{x}_t | Z_{1:t-1})}{p(\mathbf{z}_t | Z_{1:t-1})} \quad (10.10)$$

where

$$p(\mathbf{z}_t | Z_{1:t-1}) = \int p(\mathbf{z}_t | \mathbf{x}_t) p(\mathbf{x}_t | Z_{1:t-1}) d\mathbf{x}_t \quad (10.11)$$

In practice however, this scheme cannot be applied because the multidimensional integral in (10.9) and (10.10) cannot be computed in the general case. Several solutions have been proposed to make the problem tractable by imposing some constraints on the density distributions. Depending on the constraints and on the a priori information available on the system, the solution to the posterior density can be optimal, as in the case of the well-known Kalman filter (KF) (optimal in the MMSE sense for a linear Gaussian density) [48], suboptimal, yet more efficient to approximate the posterior density in nonlinear/non-Gaussian cases (in the case of the extended Kalman filter (EKF) [32], the Kalman unscented filter [49], or the particle filter (PF) [44, 50, 51]), or exact in the case of the grid-based filter

(GBF) [44]. All the previous filters are bound to use just one dynamic model in their scheme, however, which is problematic when the objects' dynamics vary with time as is the case with biological objects. The interacting multiple models (IMM) filter [52, 53] instead has been designed in the context of radar imaging, with the capability to have different models in parallel and to select and switch to the model that is more accurate to represent the movement during a given period. The IMM has the additional ability to rapidly self-adapt to transitions. This altogether ranks the IMM among the best choices for biologicals applications. The first application of IMM to biological imaging was proposed in [54] with several models adapted to biological object dynamics.

### 10.3.2 The Kalman Filter

#### 10.3.2.1 Description (See Algorithm 10.1 in Appendix 10A)

Under some conditions, the Kalman filter [48, 55] allows us to obtain an optimal estimate of  $p(\mathbf{x}_t|Z_t)$ . This method is used in many fields: in ballistics [32, 33], in video microscopy [38, 39, 56], and for tracking humans [57] and cars [58]. Some methods consider object contour points [59], whereas others use colors [60]. The Kalman filter is also used in conjuncture with other techniques, such as autocorrelation [61], active contours [62, 63], or level sets [62]. Reference [64] also presents a method for depth estimates in a sequence of images. See also [65, 66] for the problems linked to estimating their parameters.

In the context of what we have just described, let's formulate the following hypotheses:

1.  $p(\mathbf{x}_{t-1}|Z_{t-1})$  Gaussian;
2.  $p(\mathbf{v}_t)$  and  $p(\mu_t)$  are on zero mean Gaussians with a known autocovariance matrix;
3.  $f_t$  and  $h_t$  linear and known;

then  $p(\mathbf{x}_t|Z_t)$  is also Gaussian, and in [48] R. E. Kalman shows that we can obtain his parameters recursively.

On the basis of hypotheses 2 and 3, the system formed by (10.4) and (10.5) can be rewritten

$$\begin{cases} \mathbf{x}_t = \mathbf{F}_t \mathbf{x}_{t-1} + \mathbf{v}_t \\ \mathbf{z}_t = \mathbf{H}_t \mathbf{x}_t + \mu_t \end{cases} \quad (10.12)$$

with

$$p(\mathbf{v}_t) = \mathcal{N}(\mathbf{v}_t; 0, \mathbf{Q}_{t-1}) \quad (10.13)$$

$$p(\mu_t) = \mathcal{N}(\mu_t; 0, \mathbf{R}_t) \quad (10.14)$$

$$\mathbb{E}[\mathbf{v}(i)\mu^T(j)] = 0 \quad \forall i, j \quad (10.15)$$

$$\mathbb{E}[\mathbf{v}(i)\mathbf{v}^T(j)] = 0 \quad \forall i \neq j \quad (10.16)$$

$$\mathbb{E}[\boldsymbol{\mu}(i)\boldsymbol{\mu}^T(j)] = 0 \quad \forall i \neq j \quad (10.17)$$

On the basis of hypothesis 1, we have:

$$p(\mathbf{x}_{t-1}|Z_{1:t-1}) = \mathcal{N}(\mathbf{x}_{t-1}; \mathbf{x}_{t-1|t-1}, \mathbf{P}_{t-1|t-1}) \quad (10.18)$$

and (10.9) and (10.10) give us

$$p(\mathbf{x}_t|Z_{1:t-1}) = \mathcal{N}(\mathbf{x}_t; \mathbf{x}_{t|t-1}, \mathbf{P}_{t|t-1}) \quad (10.19)$$

$$p(\mathbf{x}_t|Z_{1:t}) = \mathcal{N}(\mathbf{x}_t; \mathbf{x}_{t|t}, \mathbf{P}_{t|t}) \quad (10.20)$$

with

$$\mathbf{x}_{t|t-1} = \mathbf{F}_t \mathbf{x}_{t-1|t-1} \quad (10.21)$$

$$\mathbf{P}_{t|t-1} = \mathbf{F}_t \mathbf{P}_{t-1|t-1} \mathbf{F}_t^T + \mathbf{Q}_t \quad (10.22)$$

$$\mathbf{x}_{t|t} = \mathbf{x}_{t|t-1} + \mathbf{K}_t(\mathbf{z}_t - \mathbf{H}_t \mathbf{x}_{t|t-1}) \quad (10.23)$$

$$\mathbf{P}_{t|t} = \mathbf{P}_{t|t-1} - \mathbf{K}_t \mathbf{H}_t \mathbf{P}_{t|t-1} \quad (10.24)$$

where  $\mathcal{N}(\mathbf{x}; \mathbf{m}, \mathbf{P})$  is a Gaussian density of argument  $\mathbf{x}$ , with mean  $\mathbf{m}$  and covariance matrix  $\mathbf{P}$ , and

$$\mathbf{S}_t = \mathbf{H}_t \mathbf{P}_{t|t-1} \mathbf{H}_t^T + \mathbf{R}_t \quad (10.25)$$

$$\mathbf{K}_t = \mathbf{P}_{t|t-1} \mathbf{H}_t^T \mathbf{S}_t^{-1} \quad (10.26)$$

### 10.3.2.2 Example

A Markovian process  $\mathbf{x}_t$  is generated according to the system described by (10.12). The state vector  $\mathbf{x}_t$  is composed as follows:

$$\mathbf{x}_t = \begin{bmatrix} x_t \\ \dot{x}_t \end{bmatrix} = \begin{bmatrix} \text{position} \\ \text{speed} \end{bmatrix} \quad (10.27)$$

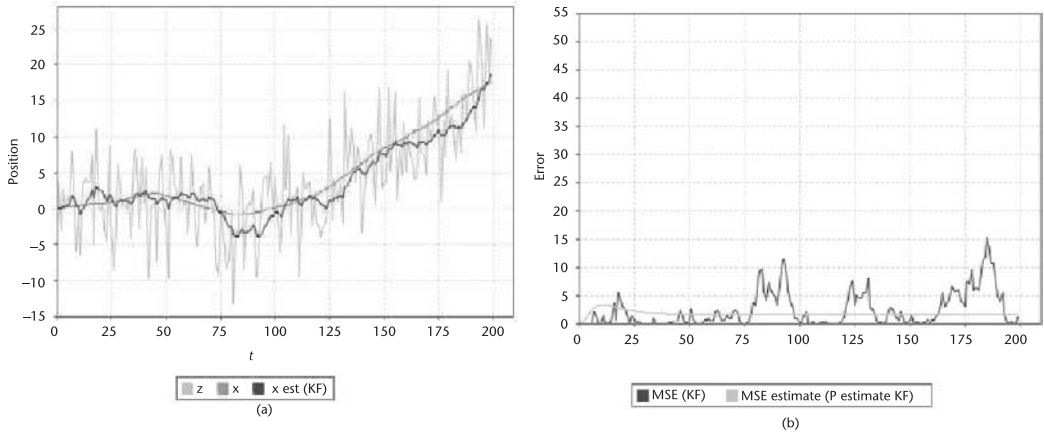
The system parameters are as follows:

$$\mathbf{F} = \begin{bmatrix} 1 & 1 \\ 0 & 1 \end{bmatrix} \mathbf{H} = [1 \quad 0] \mathbf{Q} = \begin{bmatrix} 0.0002 & 0 \\ 0 & 0.0004 \end{bmatrix} \mathbf{R} = [20] \quad (10.28)$$

The process is initialized by:

$$\mathbf{x}_{0|0} = \begin{bmatrix} 0 \\ 0.5 \end{bmatrix} \text{ and } \mathbf{P}_{0|0} = \begin{bmatrix} 0.1 & 0 \\ 0 & 0.1 \end{bmatrix} \quad (10.29)$$

therefore, as we can see, a relatively stable movement whose measurement is highly disturbed. A Kalman filter assigned with parameters used to generate data is applied to measured signal  $z$ . Figure 10.2 shows that the estimate obtained is close

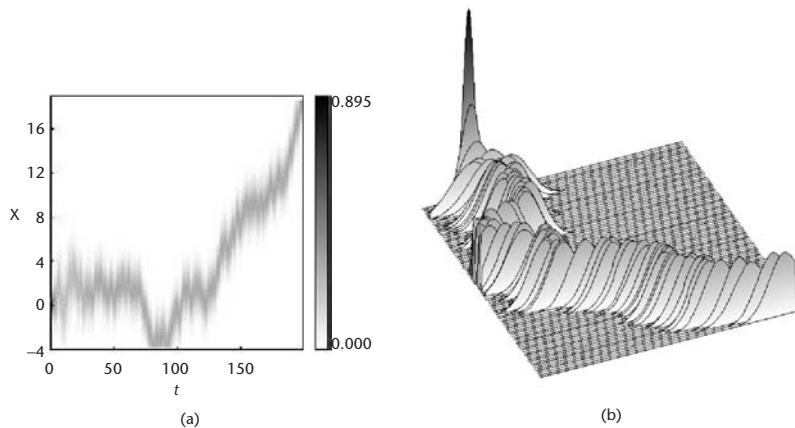


**Figure 10.2** (a, b) Estimate of signal  $x$  by Kalman filtering from measurements  $z$ . The estimate of the signal is correct and the estimate of error is also correct on average.

to actual values. Figure 10.3 shows the propagation of  $p(\mathbf{z}_t|\mathbf{x})$ . We observe that the error estimated by the filter converges with this. This is due to the fact that  $\mathbf{F}$ ,  $\mathbf{H}$ ,  $\mathbf{Q}$ , and  $\mathbf{R}$  do not vary over the course of time. Figures 10.4 and 10.5 show the filtering of the same signal with a Kalman filter whose transition matrix does not correspond to the one used to generate the signal. This is because it is replaced by the following matrix, which does not at all correspond to the broadcast signal:

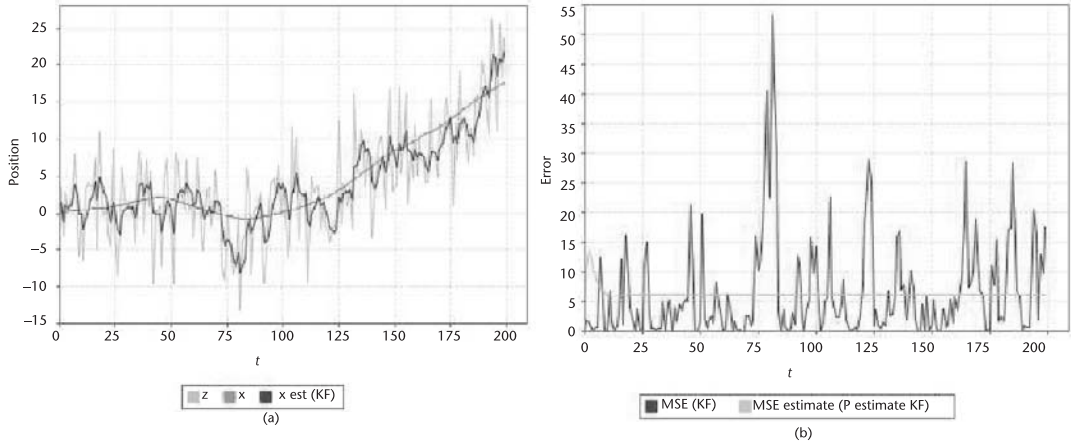
$$\mathbf{F} = \begin{bmatrix} 1 & -15 \\ 0 & 1 \end{bmatrix} \quad (10.30)$$

It is interesting to observe that the estimate no longer trusts the model quickly and relies more strongly on the data (i.e.,  $x$  estimate follows  $z$ ). Generally speaking, the mean-square error shows that the filter is much more powerful than under the optimal conditions of the first trial. This tends to show that the elaboration



**Figure 10.3** Reconstituted propagation of  $p(\mathbf{z}_t|\mathbf{x}_t)$  for the example in Figure 10.2 from the Kalman filter parameters.





**Figure 10.4** Estimate of signal  $x$  by Kalman filtering from measurements  $z$ . The transition matrix of the filter differs from the transition matrix used to generate the signal. The error shows that the estimate is not as good as for the example in Figure 10.2.

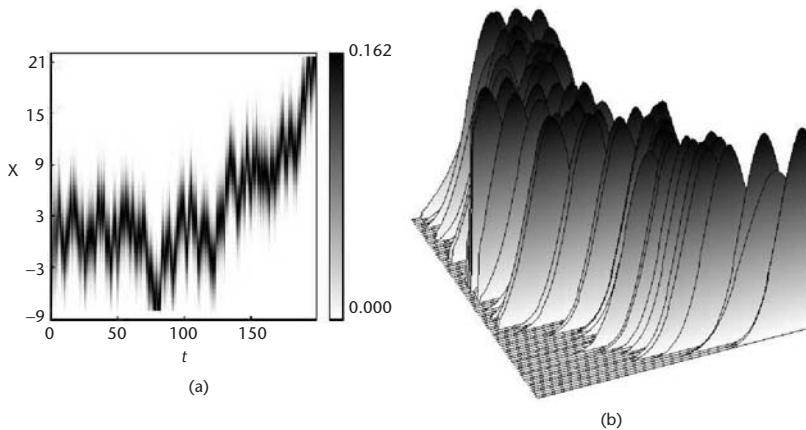
of the model's parameters holds an important role in evaluating a state sequence correctly.

### 10.3.3 The Filter Based on a Grid

#### 10.3.3.1 Description (See Algorithm 10.2 in Appendix 10A)

If the state space is constituted from a finite number of discrete states  $\mathbf{x}_t^i, i = 1, \dots, N$ , then an optimal filter can be obtained as follows. We observe for each state  $\mathbf{x}_{t-1}^i$ :

$$Pr(\mathbf{x}_{t-1} = \mathbf{x}_{t-1}^i | Z_{1:t-1}) = w_{t-1|t-1}^i \quad (10.31)$$



**Figure 10.5** Reconstituted propagation of  $p(z_t | \mathbf{x}_t)$  for the example in Figure 10.4 from Kalman filtering parameters.

the density of probability at  $t - 1$  may be written

$$p(\mathbf{x}_{t-1}|Z_{1:t-1}) = \sum_{i=1}^N w_{t-1|t-1}^i \delta(\mathbf{x}_{t-1} - \mathbf{x}_{t-1}^i) \quad (10.32)$$

where  $\delta(\cdot)$  is the Dirac measure. We therefore obtain with (10.9)

$$p(\mathbf{x}_t|Z_{1:t-1}) = \sum_{i=1}^N w_{t|t-1}^i \delta(\mathbf{x}_t - \mathbf{x}_t^i) \quad (10.33)$$

and with (10.10)

$$p(\mathbf{x}_t|Z_{1:t}) = \sum_{i=1}^N w_{t|t}^i \delta(\mathbf{x}_t - \mathbf{x}_t^i) \quad (10.34)$$

with

$$w_{t|t-1}^i \triangleq \sum_{j=1}^N w_{t-1|t-1}^j p(\mathbf{x}_t^i | \mathbf{x}_{t-1}^j) \quad (10.35)$$

and

$$w_{t|t}^i \triangleq \frac{w_{t|t-1}^i p(\mathbf{z}_t | \mathbf{x}_t^i)}{\sum_{j=1}^N w_{t|t-1}^j p(\mathbf{z}_t | \mathbf{x}_t^j)} \quad (10.36)$$

### 10.3.3.2 Example

In the context of this work, the density of a posteriori probability that we are looking for is not discrete but continuous. The grid-based filter that is presented here is only discrete for the approximation made from it (see Section 10.3.6), when it is applied to the evaluation of a continuous density. An example is then developed in this context.

## 10.3.4 The Extended Kalman Filter

### 10.3.4.1 Description (See Algorithm 10.3 in Appendix 10A)

If, in the context of the Kalman filter, we abandon the hypothesis of the linearity of  $f_t$  and  $h_t$ , the system can be rewritten

$$\mathbf{x}_t = f_t(\mathbf{x}_{t-1}) + \mathbf{v}_{t-1} \quad (10.37)$$

$$\mathbf{z}_t = h_t(\mathbf{x}_t) + \mu_t \quad (10.38)$$

and the Gaussianness of  $p(\mathbf{x}_t|Z_{1:t})$  is not a priori propagated. The idea of the extended Kalman filter [44, 55, 67] or *extended Kalman filter* (EKF) is to linearize  $f_t$  and  $h_t$  locally and then apply the Kalman filter. This is because if we consider the first-order derivatives of  $f_t$  and  $h_t$ :

$$\hat{\mathbf{F}}_t = \left. \frac{df_t(\mathbf{x})}{d\mathbf{x}} \right|_{\mathbf{x}=\mathbf{x}_{t-1|t-1}} \quad (10.39)$$

and

$$\hat{\mathbf{H}}_t = \left. \frac{dh_t(\mathbf{x})}{d\mathbf{x}} \right|_{\mathbf{x}=\mathbf{x}_{t|t-1}} \quad (10.40)$$

then  $p(\mathbf{x}_t|Z_t)$  can be approximated by a Gaussian and from

$$p(\mathbf{x}_{t-1}|Z_{1:t-1}) \approx \mathcal{N}(\mathbf{x}_{t-1}; \mathbf{x}_{t-1|t-1}, \mathbf{P}_{t-1|t-1}) \quad (10.41)$$

(10.9) and (10.10) give us

$$p(\mathbf{x}_t|Z_{1:t-1}) \approx \mathcal{N}(\mathbf{x}_t; \mathbf{x}_{t|t-1}, \mathbf{P}_{t|t-1}) \quad (10.42)$$

$$p(\mathbf{x}_t|Z_{1:t}) \approx \mathcal{N}(\mathbf{x}_t; \mathbf{x}_{t|t}, \mathbf{P}_{t|t}) \quad (10.43)$$

with

$$\mathbf{x}_{t|t-1} = f_t(\mathbf{x}_{t-1|t-1}) \quad (10.44)$$

$$\mathbf{P}_{t|t-1} = \hat{\mathbf{F}}_t \mathbf{P}_{t-1|t-1} \hat{\mathbf{F}}_t^T + \mathbf{Q}_t \quad (10.45)$$

$$\mathbf{x}_{t|t} = \mathbf{x}_{t|t-1} + \mathbf{K}_t(\mathbf{z}_t - h_t(\mathbf{x}_{t|t-1})) \quad (10.46)$$

$$\mathbf{P}_{t|t} = \mathbf{P}_{t|t-1} - \mathbf{K}_t \hat{\mathbf{H}}_t \mathbf{P}_{t|t-1} \quad (10.47)$$

where

$$\mathbf{S}_t = \hat{\mathbf{H}}_t \mathbf{P}_{t|t-1} \hat{\mathbf{H}}_t^T + \mathbf{R}_t \quad (10.48)$$

$$\mathbf{K}_t = \mathbf{P}_{t|t-1} \hat{\mathbf{H}}_t^T \mathbf{S}_t^{-1} \quad (10.49)$$

#### 10.3.4.2 Example

A Markov process  $\mathbf{x}_t$  is generated according to the system described by:

$$\mathbf{x}_t = f(\mathbf{x}_{t-1}) + \mathbf{v}_{t-1} \quad (10.50)$$

$$\mathbf{z}_t = \mathbf{H}\mathbf{x}_t + \mu_t \quad (10.51)$$

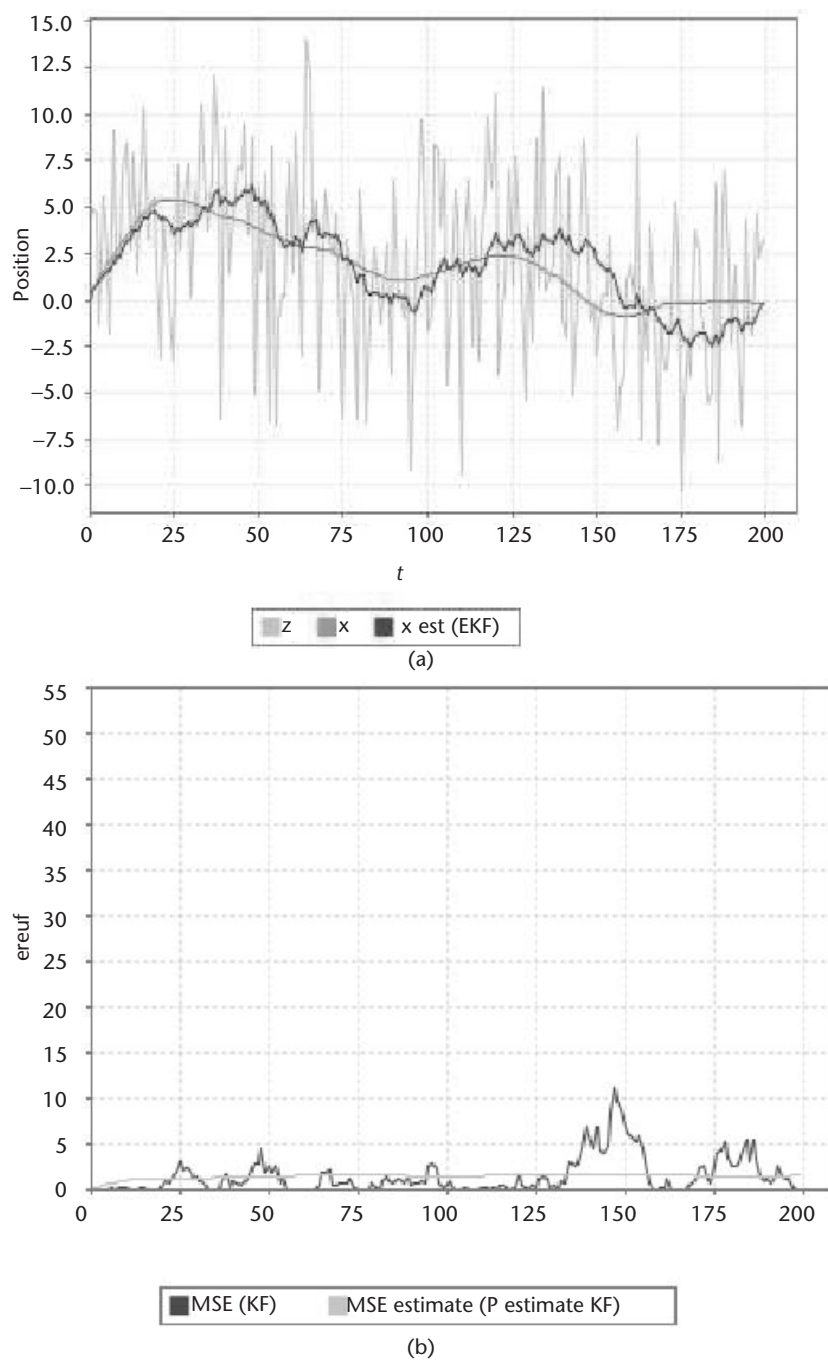
where the state vector  $\mathbf{x}_t$  is always composed of:

$$\mathbf{x}_t = \begin{bmatrix} x_t \\ \dot{x}_t \end{bmatrix} = \begin{bmatrix} \text{position} \\ \text{speed} \end{bmatrix} \quad (10.52)$$

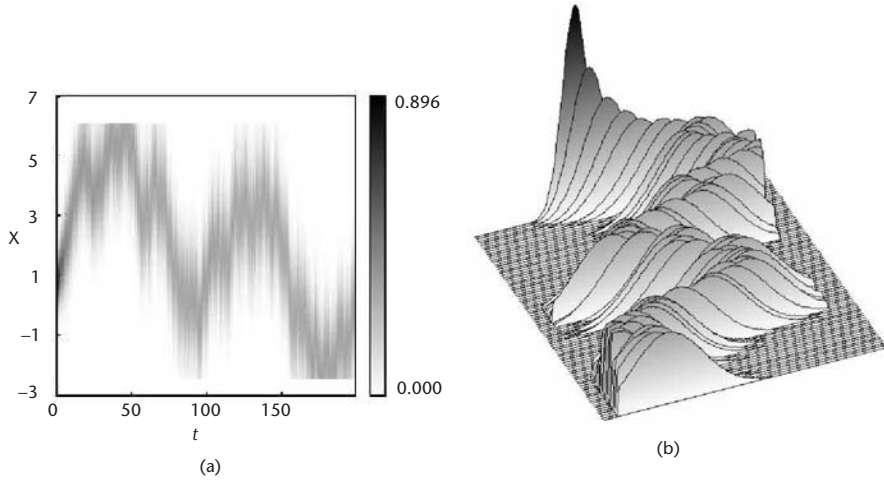
and the system parameters are as follows:

$$f(\mathbf{x}_{t-1}) = \begin{bmatrix} x_{t-1} + \dot{x}_{t-1} \\ \frac{\dot{x}_{t-1}}{1 + \dot{x}_{t-1}^2} \end{bmatrix} \quad (10.53)$$

$$\mathbf{H} = [1 \ 0] \mathbf{Q} = \begin{bmatrix} 0.0002 & 0 \\ 0 & 0.0004 \end{bmatrix} \mathbf{R} = [20] \quad (10.54)$$



**Figure 10.6** Estimate of a nonlinear signal  $x$  by extended Kalman filtering from measurements  $z$ . The signal, despite being quite noisy, is correctly estimated.



**Figure 10.7** Reconstituted propagation of  $p(\mathbf{z}_t|\mathbf{x}_t)$  for the example in Figure 10.6 from the EKF parameters. Because the estimate is a high quality one, we may suppose that the propagation proposed in this way by the EKF is realistic, in particular its unified modal character.

initialized by

$$\mathbf{x}_{0|0} = \begin{bmatrix} 0 \\ 0.5 \end{bmatrix} \text{ and } \mathbf{P}_{0|0} = \begin{bmatrix} 0.1 & 0 \\ 0 & 0.1 \end{bmatrix} \quad (10.55)$$

in this case also the measurement of nonlinear change is highly disturbed. An extended Kalman filter assigned the parameters used for the generation of data is applied to the measured signal  $\mathbf{z}$ . The Jacobian of  $f$  is equal to:

$$J_f(\mathbf{x}) = \begin{bmatrix} 1 & 1 \\ 0 & \frac{1-\dot{x}}{(1+\dot{x}^2)^2} \end{bmatrix} \quad (10.56)$$

Figure 10.6 shows that the estimate obtained is close to the true values. The propagation of  $p(\mathbf{z}_t|\mathbf{x}_t)$  is shown in Figure 10.7.

### 10.3.5 The Interacting Multiple Model Filter

#### 10.3.5.1 Description (see Algorithm 10.4 in Appendix 10A)

The *interacting multiple model* (IMM) filter is a vector-estimating algorithm whose evolution is governed by a system of model permutations represented by Markov coefficients. The IMM, originally developed by Blom [53], has been made popular thanks to [52]. It is modified in [68, 69]. For recent uses of the IMM and derivatives of it, refer to [33, 70–73].

The system now has the following form:

$$\mathbf{x}_t = \mathbf{F}_t^j \mathbf{x}_{t-1} + \mathbf{v}_t^j \quad (10.57)$$

$$\mathbf{z}_t = \mathbf{H}_t^j \mathbf{x}_t + \mathbf{w}_t^j \quad (10.58)$$

$\mathbf{F}_t^j$  is the transition matrix of the system during the observed event:

$$M_t^j = \{\text{model } j \text{ is active at time } t\} \quad (10.59)$$

$\mathbf{H}_t^j$  is the observation matrix for  $M_t^j$ . Vectors  $\mathbf{v}_t^j$  and  $\mathbf{w}_t^j$  represent system and observation noise. We suppose them to be Gaussians, blank, mutually independent, zero mean, and with a covariance matrix  $\mathbf{Q}_t^j$  and  $\mathbf{R}_t^j$ , respectively.  $i, j \in \{1, \dots, r\}$  are the indices of the  $r$  models.

The permutations between models are governed by a finite state Markov chain following the probabilities

$$p_{ij} = \Pr\{M_t^j | M_{t-1}^i\} \quad (10.60)$$

to pass from  $M_{t-1}^i$  to  $M_t^j$ . The  $r^2$  probabilities  $p_{ij}$  are assumed to be known. If we have no a priori knowledge of these, they can be set with the same  $\frac{1}{r}$  value at the start. The optimal approach to filter the state of the system would be to consider all possible sequences of events; however, this would imply an exponential increase in the number of filters. For feasibility reasons, the IMM estimator [33, 52] uses an approximation that considers the two most recent periods only.

The IMM estimator is a recursive process that breaks down into several stages at each iteration, the objective being to obtain an estimate of state

$$\mathbf{x}_{t|t} = \mathbb{E}(\mathbf{x}_t | Z_{1:t}) \quad (10.61)$$

and covariance

$$\mathbf{P}_{t|t} = \mathbb{E}(\tilde{\mathbf{x}}_t \tilde{\mathbf{x}}_t^T | Z_{1:t}) \quad (10.62)$$

where  $\tilde{\mathbf{x}}_t = \mathbf{x}_t - \mathbf{x}_{t|t}$ . The stages that make up an iteration are described next.

First of all, for every entry into the filter, the estimates of state and covariance are calculated with

$$\mathbf{x}_{t-1|t-1}^{0j} = \sum_{i=1}^r \mu_{t-1|t-1}^{ij} \mathbf{x}_{t-1|t-1}^i \quad (10.63)$$

$$\begin{aligned} \mathbf{P}_{t-1|t-1}^{0j} = \sum_{i=1}^r \mu_{t-1|t-1}^{ij} \left\{ \mathbf{P}_{t-1|t-1}^i + \left[ \mathbf{x}_{t-1|t-1}^i - \mathbf{x}_{t-1|t-1}^{0j} \right] \right. \\ \left. \left[ \mathbf{x}_{t-1|t-1}^i - \mathbf{x}_{t-1|t-1}^{0j} \right]^T \right\} \end{aligned} \quad (10.64)$$

where the conditional probability of each model is given by

$$\begin{aligned} \mu_{t-1|t-1}^{ij} &= \Pr\{M_t^j | M_{t-1}^i, Z_{t-1}\} \\ &= \frac{p_{ij} \mu_{t-1|t-1}^i}{\mu_{t|t-1}^j} \end{aligned} \quad (10.65)$$

and the prediction of the probability of each model is given by

$$\mu_{t|t-1}^j = Pr\{M^j(t)|Z_{t-1}\} \quad (10.66)$$

$$= \sum_{i=1}^r p_{ij} \mu_{t-1|t-1}^i \quad (10.67)$$

Then, for each filter, the updating of the estimates of state  $\mathbf{x}_{t|t}^j$  and covariance  $\mathbf{P}_{t|t}^j$  is given by the equations of the Kalman filter that produce an optimal estimate and can be calculated in parallel for each model because they are totally independent. We have therefore:

$$\mathbf{x}_{t|t-1}^j = \mathbf{F}_t^j \mathbf{x}_{t-1|t-1}^{0j} \quad (10.68)$$

$$\mathbf{P}_{t|t-1}^j = \mathbf{F}_t^j \mathbf{P}_{t-1|t-1}^{0j} [\mathbf{F}_t^j]^T + \mathbf{Q}_t^j \quad (10.69)$$

$$\mathbf{x}_{t|t}^j = \mathbf{x}_{t|t-1}^j + \mathbf{K}_t^j (\mathbf{z}_t - \mathbf{H}_t^j \mathbf{x}_{t|t-1}^j) \quad (10.70)$$

$$\mathbf{P}_{t|t}^j = \mathbf{P}_{t|t-1}^j - \mathbf{K}_t^j \mathbf{H}_t^j \mathbf{P}_{t|t-1}^j \quad (10.71)$$

where

$$\mathbf{S}_t^j = \mathbf{H}_t^j \mathbf{P}_{t|t-1}^j [\mathbf{H}_t^j]^T + \mathbf{R}_t^j \quad (10.72)$$

$$\mathbf{K}_t^j = \mathbf{P}_{t|t-1}^j [\mathbf{H}_t^j]^T [\mathbf{S}_t^j]^{-1} \quad (10.73)$$

Finally, because  $\{\mathbf{z}_t|M_t^j, Z_{t-1}\}$  is considered to be Gaussian with dimension  $\dim(\mathbf{z}_t)$ , the likelihood of each filter corresponding to  $M_t^j$  is given by:

$$\Lambda_t^j = \frac{1}{\sqrt{\det[2\pi\mathbf{S}_t^j]}} \exp\left\{\frac{-1}{2} [\tilde{\mathbf{z}}_t]^T [\mathbf{S}_t^j]^{-1} \tilde{\mathbf{z}}_t\right\} \quad (10.74)$$

The probability of  $M_t^j$  is therefore

$$\mu_{t|t}^j = Pr\{M_t^j|Z_t\} \quad (10.75)$$

$$= \frac{\mu_{t|t-1}^j \Lambda_t^j}{\sum_{i=1}^r \mu_{t|t-1}^i \Lambda_t^i} \quad (10.76)$$

and the combined estimates of state and covariance are:

$$\mathbf{x}_{t|t} = \sum_{j=1}^r \mu_{t|t}^j \mathbf{x}_{t|t}^j \quad (10.77)$$

$$(10.78)$$



and

$$\mathbf{P}_{t|t} = \sum_{j=1}^r \mu_{t|t}^j \left\{ \mathbf{P}_{t|t}^j + \left[ \mathbf{x}_{t|t}^j - \mathbf{x}_{t|t} \right] \left[ \mathbf{x}_{t|t}^j - \mathbf{x}_{t|t} \right]^T \right\}. \quad (10.79)$$

### 10.3.5.2 Example

A Markov process  $\mathbf{x}_t$  is generated by alternating between the systems described by (10.12) with the following parameter:

For system 1:

$$\mathbf{F}^1 = \begin{bmatrix} 1 & 1 \\ 0 & 1 \end{bmatrix} \mathbf{H}^1 = [1 \quad 0] \mathbf{Q}^1 = \begin{bmatrix} 0.0002 & 0 \\ 0 & 0.0004 \end{bmatrix} \mathbf{R}^1 = [5] \quad (10.80)$$

For system 2:

$$\mathbf{F}^2 = \begin{bmatrix} 1 & -1 \\ 0 & 1 \end{bmatrix} \mathbf{H}^2 = [1 \quad 0] \mathbf{Q}^2 = \begin{bmatrix} 0.0002 & 0 \\ 0 & 0.0004 \end{bmatrix} \mathbf{R}^2 = [5] \quad (10.81)$$

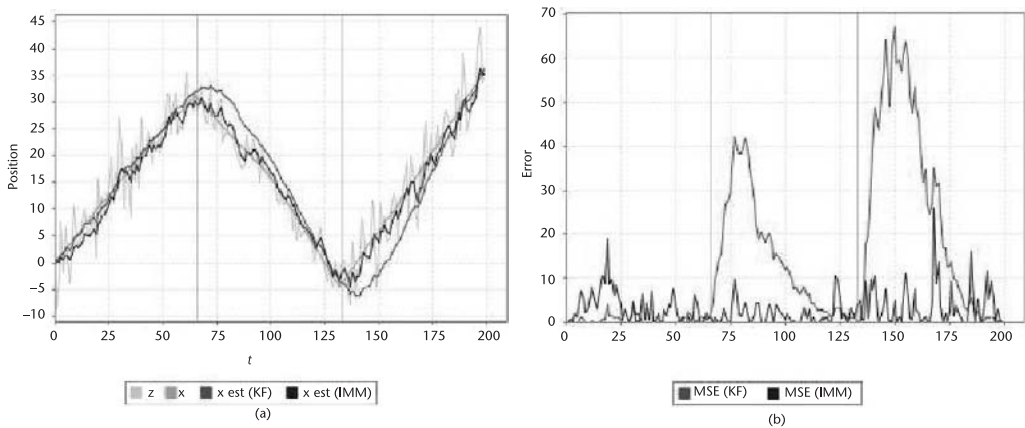
The sequence is initialized by:

$$\mathbf{x}_{0|0} = \begin{bmatrix} 0 \\ 0.5 \end{bmatrix} \text{ and } \mathbf{P}_{0|0} = \begin{bmatrix} 0.1 & 0 \\ 0 & 0.1 \end{bmatrix} \quad (10.82)$$

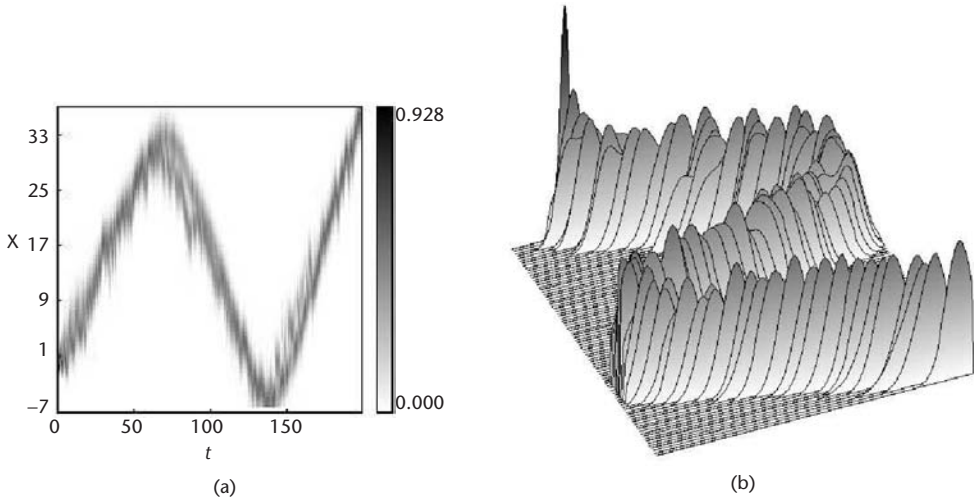
Here also (see the Kalman Filter) the state vector is described by

$$\mathbf{x}_t = \begin{bmatrix} x_t \\ \dot{x}_t \end{bmatrix} = \begin{bmatrix} \text{position} \\ \text{speed} \end{bmatrix} \quad (10.83)$$

These two systems form a relatively stable signal whose measurement is reasonably disturbed. This is because measurement is only disturbed by additive Gaussian noise with variance 5 (i.e., not as high as in the test of the Kalman filter). This is



**Figure 10.8** (a, b) Estimate of signal  $x$  moving from one system to another by Kalman filtering and IMM filtering from measurements  $z$ . In these figures, we see that the Kalman filter that is fixed on one of the two models does not adapt quickly to the sudden change in transition. The IMM passes very quickly from one model to another without problem.



**Figure 10.9** Reconstituted propagation of  $p(\mathbf{z}_t|\mathbf{x}_t)$  for the example in Figure 10.8 from the parameters of the IMM. Here we observe the bimodality in the critical moments of changes in transition.

to explain the capacity of the IMM to switch from one of its models to the other. The 200 iterations therefore include an initial third of a signal realized using model 1, a second third using model 2, and a final third using model 1 again. The results can be seen in Figure 10.8. We observe that the Kalman filter is more efficient in the first third, which corresponds to the model that it uses. On the other hand, it adapts very poorly to sudden changes in dynamics, modeled by the change to model 2. We see that the Kalman filter estimate takes some time to recover the true value every time a model is changed. At the same time, the IMM correctly estimates the signal in these sudden changes. We also observe this effect on the error curves. Finally, we observe that the density obtained by the IMM (Figure 10.9) is an  $r$ -modal density with  $r$  being the number of models.

The capacity of the IMM to adapt quickly to changes in transition will be used to model the successive attitudes of biological objects over the course of time. The IMM turns out to be the filter that is most adapted to our problem set.

### 10.3.6 The Approximated Filter Based on a Grid

#### 10.3.6.1 Description

If space is continuous but cannot be decomposed into  $N_s$  cells  $\{\mathbf{x}_t^i, i = 1, \dots, N_s\}$  we can then approximate  $p(\mathbf{x}_t|Z_{1:t})$  by:

$$p(\mathbf{x}_t|Z_{1:t}) \approx \sum_{i=1}^N w_t^i \delta(\mathbf{x}_t - \mathbf{x}_t^i) \quad (10.84)$$

And therefore apply the filter based on a grid described in Section 10.3.3.

### 10.3.6.2 Example

If we know that the signal that we are trying to estimate is limited, we can establish a grid on the area under consideration and suppose that  $\mathbf{x}_t$  only takes the discrete states defined in this way for values.

A Markov process  $\mathbf{x}_t = [x_t]$  is generated according to the following system:

$$\mathbf{x}_t = f_t(\mathbf{x}_{t-1}) + \mathbf{v}_t \quad (10.85)$$

$$\mathbf{z}_t = h_t(\mathbf{x}_t) + \mu_t \quad (10.86)$$

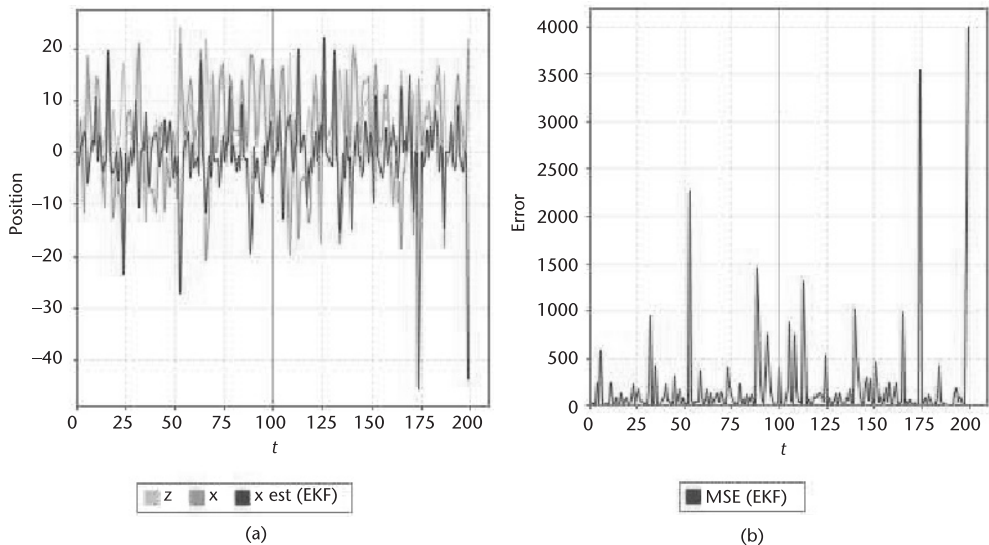
with for transition

$$f_t(\mathbf{x}_{t-1}) = \frac{\mathbf{x}_{t-1}}{2} + \frac{25\mathbf{x}_{t-1}}{1 + \mathbf{x}_{t-1}^2} + 8 \cos 1.2t \quad (10.87)$$

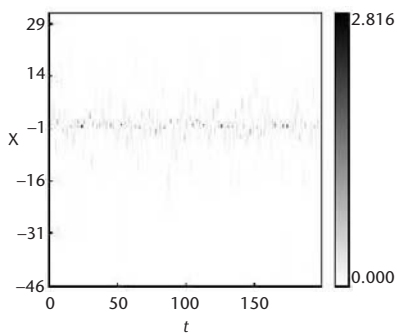
highly nonlinear (used to describe physical phenomena and in previous simulations [44,74–76]) and for observation:

$$h_t(\mathbf{x}_t) = \frac{\mathbf{x}_t^2}{20} \quad (10.88)$$

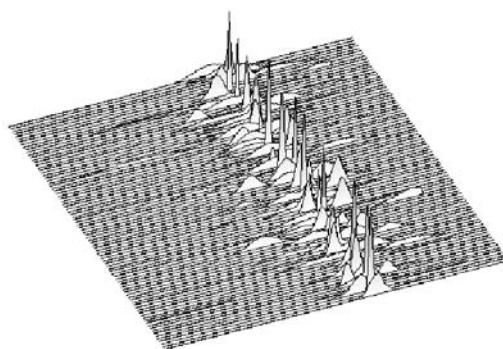
Noise is set to  $\mathbf{Q} = [10]$  and  $\mathbf{R} = [1]$  and the measurement equals simply  $\mathbf{z}_t = [z_t]$ . Figures 10.10 and 10.11 show that an extended Kalman filter is not adapted to this type of transition. On the other hand, with a grid of 20 cells from  $-30$  to  $30$  we obtain the result shown in Figures 10.12 and 10.13. If we move to a grid definition of 200 cells, we obtain the result shown in Figures 10.14 and 10.15. We observe that while this result is no doubt the best one that we will obtain from among the Bayesian filters described in this section for this type of transition, there



**Figure 10.10** (a, b) Estimate of a nonlinear, non-Gaussian signal  $x$  by extended Kalman filtering from measurement  $z$ . Estimate by an extended Kalman filter proves to be very inefficient, as the evolution of MSE shows.

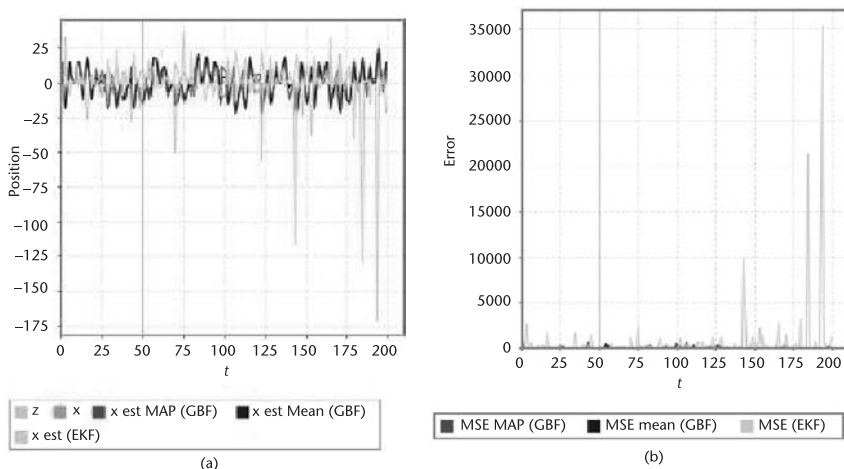


(a)

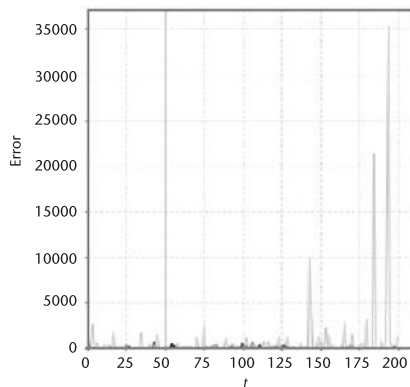


(b)

**Figure 10.11** (a, b) Propagation of  $p(z_t | x_t)$  for the example in Figure 10.10. The multimodality of a posteriori density makes its estimate by an extended Kalman filter that tries to approximate it by a Gaussian inefficient.

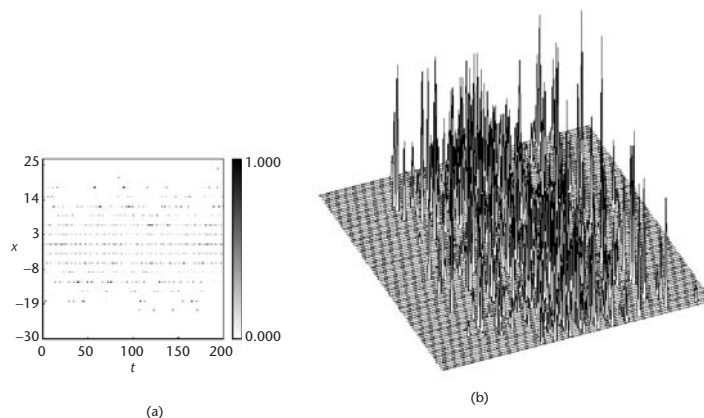


(a)



(b)

**Figure 10.12** (a, b) Estimate of a nonlinear signal  $x$  by approximated filtering based on a grid of 20 cells from measurements  $z$ . The error shows that the approximated filter based on a grid is more efficient than the extended Kalman filter, which is not adapted to this type of transition.



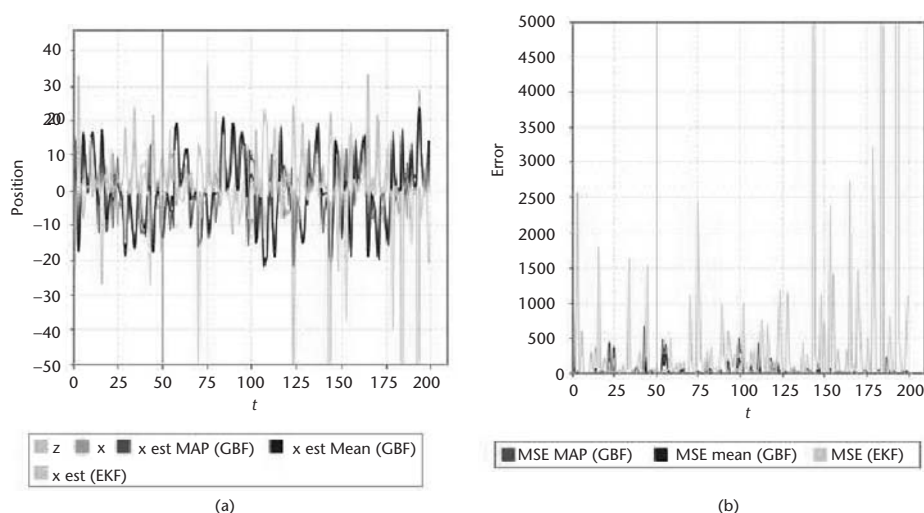
**Figure 10.13** (a, b) Propagation of  $p(z_t|x_t)$  for the example in Figure 10.12. Weak definition does not allow us to obtain a very precise density.

are two major drawbacks: calculation is too costly and consequently prohibitive for the use that we intend to make of it (especially in higher dimensions) and the area should be limited (here the signal oscillates around 0 and is always contained between  $-30$  and  $+30$ ).

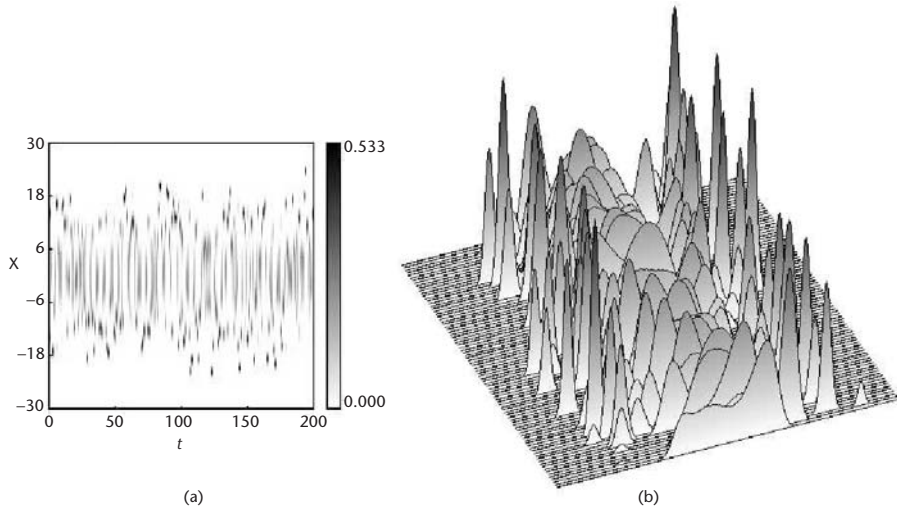
### 10.3.7 The Particle Filter

#### 10.3.7.1 Description (See Algorithms 10.5, 10.6, and 10.7 in Appendix 10A)

The particle filter, also referred to as a condensation algorithm or even a bootstrap filter, produces a suboptimal solution by a stochastic draw. It appeared in



**Figure 10.14** (a, b) Estimate of a nonlinear signal  $x$  by approximated filtering based on a grid of 200 cells from measurements  $z$ .



**Figure 10.15** (a, b) Propagation of  $p(\mathbf{z}_t|\mathbf{x}_t)$  for the example in Figure 10.14. Here we see that the a posteriori density comes out very clearly. It is non-Gaussian and multimodal. Moreover, the strong nonlinearity of the transition produces a density that is alternately mono-modal and multimodal.

1996 in [50] and then in [77]. For a quick introduction we may refer to the highly didactic [44]. For a more in-depth development, see [51]. For multiobject applications, see [78, 79]; see also [80–83]. Reference [84] is interested in the problem of the unknown number of objects and [85] in the uncertainty in the modelling parameters, while [86] proposes an important function in the form of a combination of Gaussians. Finally, [87] proposes a Gaussian particle filter that is used to estimate the nonlinear evolution of a Gaussian density. In a second article in the same issue [88], they extend this filter to a sum of Gaussians. An application of the particle filter to the tracking of microtubules in wide-field fluorescence microscopy is presented in [89].

The general idea is to approximate the density being sought by a set of particles  $\mathbf{x}_t^i, i = 1, \dots, N$  and their associated weights  $w_t^i$ . These weights are obtained every time  $t$  according to the principle “of weighted sampling” or *importance sampling* (IS) [86]. If at stage  $t$  we have a cloud of points  $\{\mathbf{x}_t^i, w_t^i\}_{i=0}^N$ , the density of a posteriori probability can be approximated by

$$p(\mathbf{x}_t|Z_{1:t}) \approx \sum_{i=1}^N w_t^i \delta(\mathbf{x}_t - \mathbf{x}_t^i) \quad (10.89)$$

where the normalized weight of the  $i$ th particle  $w_t^i$  can be obtained recursively with (Algorithm 10.5):

$$w_t^i \propto w_{t-1}^i \frac{p(\mathbf{z}_t|\mathbf{x}_t^i)p(\mathbf{x}_t^i|\mathbf{x}_{t-1}^i)}{q(\mathbf{x}_t^i|\mathbf{x}_{t-1}^i, \mathbf{z}_t)} \quad (10.90)$$

$q(\cdot)$  is the importance function according to which we can generate samples  $x^i$ . This cloud of points  $\{x_t^i, w_t^i\}_{i=0}^N$  can therefore be used to calculate any estimator because

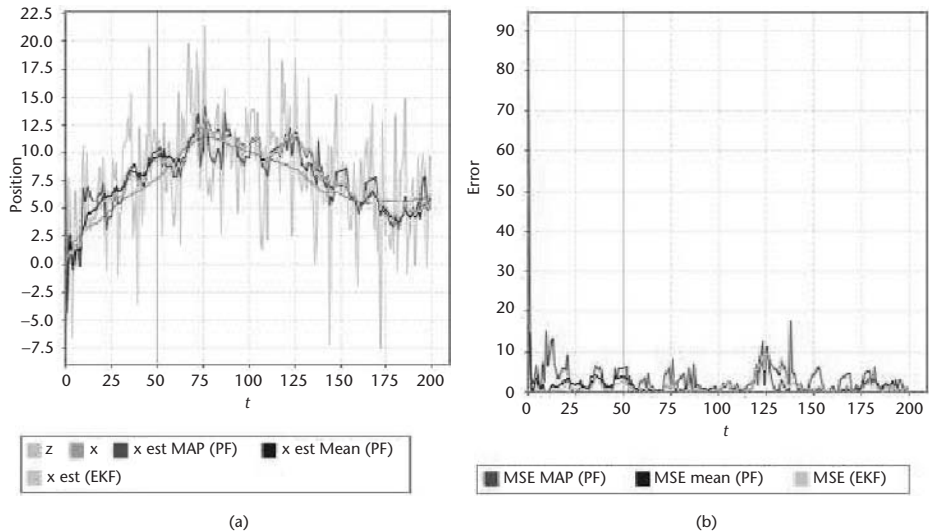
$$\hat{\mathbb{E}}_p[f(\mathbf{x}_t)] = \sum_{i=1}^N w_t^i f(\mathbf{x}_t^i) \quad (10.91)$$

The sequential importance sampling (SIS) algorithm (Algorithm 10.5) is not used in practice because it leads to degeneracy of particles that have no reason to be concentrated in regions of high densities. A high quantity of particles may temporarily solve this problem but in the mid-term, a resampling stage is necessary. The sequential importance resampling (SIR): Algorithm 10.7 proposes such a resampling. When a significant part of the particles is judged to be inefficient (i.e., at a very low weight), a resampling stage is carried out. This resampling deletes every inefficient particle and replaces it by the doubling of an efficient particle.

At every iteration, after the calculation of standardized weights, an estimate of the number of efficient particles is obtained with

$$n_{\text{eff}} \approx \frac{1}{\sum_{i=1}^N (w_t^i)^2} \quad (10.92)$$

We can therefore decide to carry out a resampling stage when  $n_{\text{eff}}$  is significantly lower in the total number of particles. For example, when  $n_{\text{eff}} < \frac{N}{4}$ . The resampling stage is described in (Algorithm 10.6).



**Figure 10.16** (a, b) Estimate of a signal  $x$  by particle filtering from measurement  $z$ . The mean estimator is revealed to be better than the MAP estimator for this example. Moreover, the extended Kalman filter also obtains a good result.



### 10.3.7.2 Example

The example of the extended Kalman filter is used again here:

$$\mathbf{x}_t = \begin{bmatrix} x_t \\ \dot{x}_t \end{bmatrix}, f(\mathbf{x}_{t-1}) = \begin{bmatrix} x_{t-1} + \dot{x}_{t-1} \\ \frac{\dot{x}_{t-1}}{1 + \dot{x}_{t-1}^2} \end{bmatrix}, \mathbf{z}_t = [z_t] \text{ and } \mathbf{H} = [1 \ 0] \quad (10.93)$$

In Figures 10.16 and 10.17 we observe that the result of the *mean* estimator of the particle filter is comparable to the estimator of the extended Kalman filter. The particle filter is therefore no more efficient on a Gaussian density than an extended Kalman filter if the transition is not strongly nonlinear.

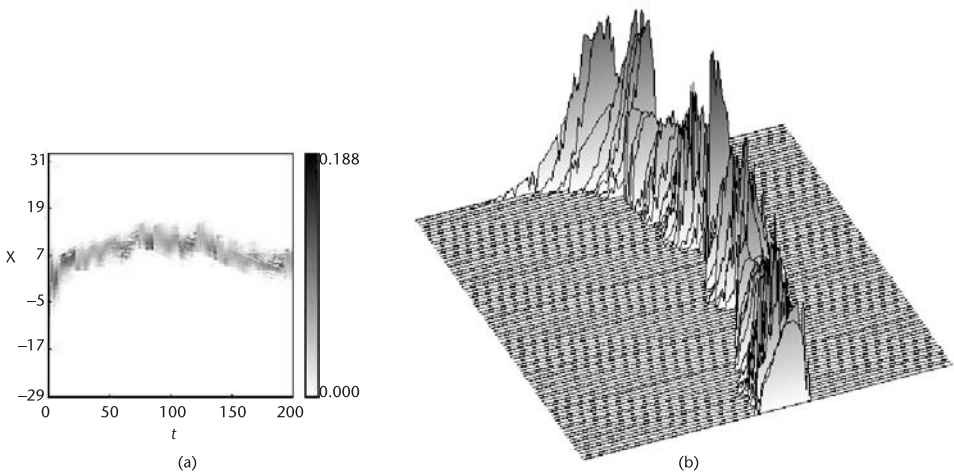
The nonlinear, non-Gaussian example of the approximated filter based on a grid is also used again here:

$$f_t(\mathbf{x}_{t-1}) = \frac{\mathbf{x}_{t-1}}{2} + \frac{25\mathbf{x}_{t-1}}{1 + \mathbf{x}_{t-1}^2} + 8 \cos 1.2t \quad (10.94)$$

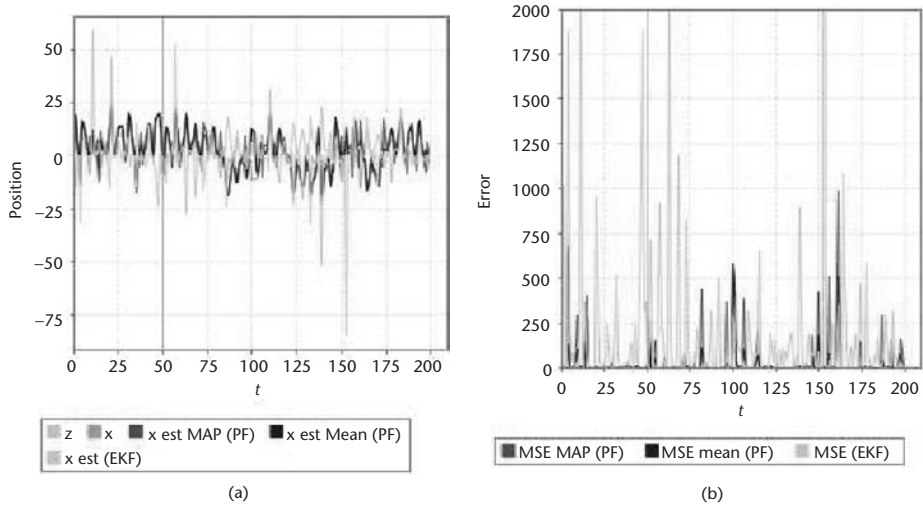
$$h_t(\mathbf{x}_t) = \frac{\mathbf{x}_t^2}{20} \quad (10.95)$$

The particle filter with resampling is again compared to the extended Kalman filter. Figure 10.18 gives the *maximum a posteriori* and *mean* result of the estimators with 30 particles; the propagation of  $p(\mathbf{z}_t/\mathbf{x}_t)$  is shown in Figure 10.19. In both cases, the particle filter gives a better estimate. Figures 10.20 and 10.21 show the result of the same filter with 4,000 particles; density is refined.

Unlike the projectiles studied in ballistics, most biological objects are likely to change transition type frequently. Moreover, for a very short period of time (i.e., between two changes), we propose efficient modeling of this transition by a linear application on the last positions accompanied by Gaussian uncertainty. An IMM



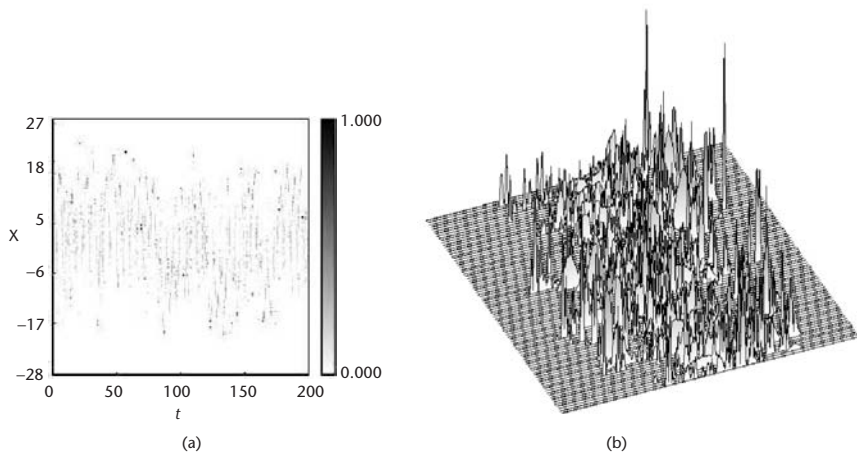
**Figure 10.17** Propagation of  $p(\mathbf{z}_t/\mathbf{x}_t)$  for the example in Figure 10.16.



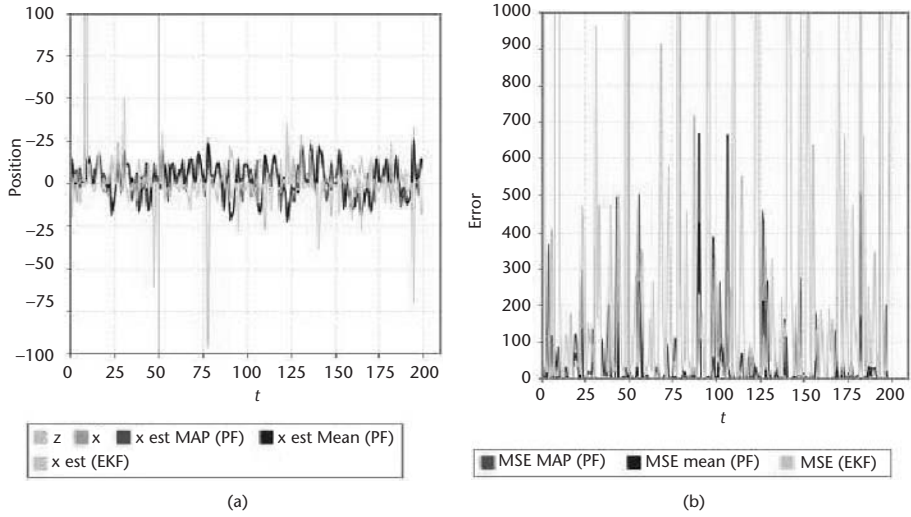
**Figure 10.18** (a, b) Estimate of a signal  $x$  by SIR particle filtering with 50 particles from measurement  $z$ .

is therefore well adapted to this problem. Moreover, unlike the filters based on a grid or with particles, it is reasonably algorithmically complex because it is as close as possible equivalent to as many Kalman filters as there are models. This point is important because we will sometimes be manipulating several hundreds of objects.

Subsequently, we propose in Section 10.6.2 several transition models that will be used conjointly by an IMM to predict and estimate the state of each of our objects. First of all, we will analyze the third component of Bayesian tracking,



**Figure 10.19** (a, b) Propagation  $p(z_t|x_t)$  for the example in Figure 10.18. We observe that density  $p(z_t|x_t)$  is poorly modelizable by a Gaussian density because it is not single-modal. This explains the failure of the extended Kalman filter.

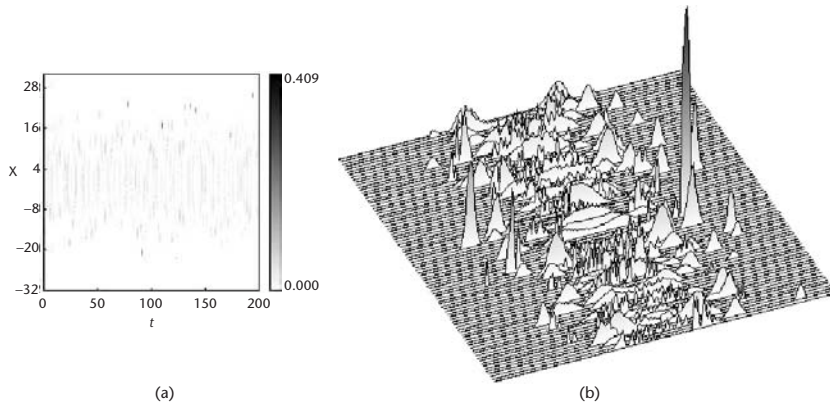


**Figure 10.20** (a, b) Estimate of a signal  $x$  by SIR particle filtering with 4,000 particles from measurement  $z$ .

which from our point of view is the component that is least adapted to tracking fluorescent spots.

## 10.4 Description of the Main Association Methods

Data association is a crucial step when tracking several particles in the presence of clutter. Indeed, as the detection may miss or wrongly detect objects, naive association methods will create inconsistent associations leading to disconnected trajectories in subsequent images. Among the numerous methods that have been developed to tackle this problem, the most popular algorithms are the nearest neighbor (NN) [32], the Joint Probabilistic Data Association (JPDA) [33, 90], and



**Figure 10.21** (a, b) Propagation of  $p(z_t|x_t)$  for the example in Figure 10.20. The same SIR particle filter is used this time with 4,000 particles to refine the density.

the multihypothesis tracking (MHT) [91, 92], but none of them is really adapted to the specific needs of MPT. The NN is very sensitive to noise and performs quite badly even with moderate noise levels. The JPDA, which computes the joint probability of all the different associations, requires the number of objects to be known in advance and remain constant during the sequence, a condition not met in our applications where the number of particles varies in time. The MHT algorithm is very compelling conceptually, as it is based on the dynamic computation of the probability tree describing all possible associations of particles over time. Notwithstanding its theoretical advantages, it rapidly becomes intractable because the complexity increases exponentially with the number of tracked objects. There are no established and reliable implementations for applications where the number of considered objects exceeds a few units; thus, the MHT does not fully satisfy the demand of being able to handle several tens or hundreds of particles. The aforementioned methods are presented in this section.

All tracking methods a Bayesian filter that apply obtain a predicted measurement and a search window thanks to the propagation of  $p(\mathbf{x}_t|Z_t)$ . This is because the state previously estimated is extrapolated with (10.9), and the predicted measurement is obtained from this extrapolation and from the observation model. The predicted measurement is an estimate at stage  $t - 1$  of what measurement  $\mathbf{z}_t$  will be at stage  $t$ . It is always written  $\mathbf{z}_{t|t-1}$  and depends on the filter used. Because our model includes an aleatory component, the predicted measurement does not correspond to the actual measurement but from the Bayesian filter, and it is possible to obtain an area around the predicted measurement in which we will find the actual measurement with a certain probability.

In the Kalman filter, for example, the predicted state and its covariance are estimates obtained as follows:

$$\mathbf{x}_{t|t-1} = \mathbb{E}(\mathbf{x}_t|Z_{1:t-1}) \quad (10.96)$$

$$= \mathbf{F}_t \mathbf{x}_{t-1|t-1} \quad (10.97)$$

$$\mathbf{P}_{t|t-1} = \mathbb{E}(\tilde{\mathbf{x}}_{t|t-1} \tilde{\mathbf{x}}_{t|t-1}^T | Z_{1:t-1}) \quad (10.98)$$

$$= \mathbf{F}_t \mathbf{P}_{t-1|t-1} \mathbf{F}_t^T + \mathbf{Q}_t \quad (10.99)$$

with  $\tilde{\mathbf{x}}_{t|t-1} = \mathbf{x}_t - \mathbf{x}_{t|t-1}$ . Then, the predicted measurement is obtained from the predicted state and, in parallel, the covariance of error on the predicted measurement is obtained from the covariance of the predicted state:

$$\mathbf{z}_{t|t-1} = \mathbb{E}(\mathbf{z}_t|Z_{1:t-1}) \quad (10.100)$$

$$= \mathbf{H}_t \mathbf{x}_{t|t-1} \quad (10.101)$$

$$\mathbf{S}_t = \mathbb{E}(\tilde{\mathbf{z}}_{t|t-1} \tilde{\mathbf{z}}_{t|t-1}^T | Z_{1:t-1}) \quad (10.102)$$

$$= \mathbf{H}_t \mathbf{P}_{t|t-1} \mathbf{H}_t^T + \mathbf{R}_t \quad (10.103)$$

with  $\tilde{\mathbf{z}}_{t|t-1} = \mathbf{z}_t - \mathbf{z}_{t|t-1}$ . The density of  $\{\mathbf{z}_t | Z_{1:t-1}\}$  in stage  $t - 1$  is therefore

$$\Lambda_t = \frac{1}{\sqrt{\det[2\pi\mathbf{S}_t]}} \exp \left\{ -\frac{1}{2} \tilde{\mathbf{z}}_{t|t-1}^T \mathbf{S}_t^{-1} \tilde{\mathbf{z}}_{t|t-1} \right\} \quad (10.104)$$

We are trying to determine a volume around the predicted measurement such that the measurement of the object is within this volume with, for example, a probability  $P_G > 0.95$ . A measurement  $\mathbf{z}_t^i$  will therefore be within the volume if

$$d^2(\mathbf{z}_{t|t-1}, \mathbf{z}_t^i) < g^2 \quad (10.105)$$

with  $g$  selected from a table of the  $\chi_{dim(z)}^2$  and

$$d^2(\mathbf{z}_{t|t-1}, \mathbf{z}_t^i) = [\mathbf{z}_t^i - \mathbf{z}_{t|t-1}]^T \mathbf{S}_t^{-1} [\mathbf{z}_t^i - \mathbf{z}_{t|t-1}] \quad (10.106)$$

The association stage will therefore consist of using the measurement candidate or candidates to update the filter of each article being tracked. This stage is not without difficulty because it is a question of carrying out the measurement that best corresponds to it at every prediction, and doing so for all predictions simultaneously. The literature offers several methods, the main ones of which are referred to here.

Subsequently,  $\theta_{ij}$  designates the association of measurement  $j$  with prediction  $i$ , and  $\theta$  designates a feasible joint association event  $\theta = \{\theta_{i_0j_0}, \dots, \theta_{i_Nj_N}\}$ .

#### 10.4.1 The Nearest Neighbor (ML)

When tracking is carried out on a single object in the presence of noise, the nearest neighbor method selects the candidate that minimizes the distance between prediction and measurements (see Algorithm Appendix 10A Appendix 10A). Because the Euclidean distance does not correctly reflect the similarity of one measurement to a predicted measurement, a distance linked to the likelihood of the filter of each prediction is preferred to it. Moreover, we may, for example, directly maximize likelihood (*ML*)—see (10.104). In a Gaussian density, this amounts to minimizing the Mahalanobis distance—see (10.105)—(also known as standardized distance) between prediction and measurement.

When tracking is carried out on several objects, there are two approaches. The first is an optimal approach that consists of solving the following problem:

$$\min \sum_{i=0}^n \sum_{j=0}^m c_{ij} \mathbb{1}_{\{\theta_{ij}\}} \quad (10.107)$$

$$\forall j \neq 0 \sum_i \mathbb{1}_{\{\theta_{ij}\}} = 1 \quad (10.108)$$

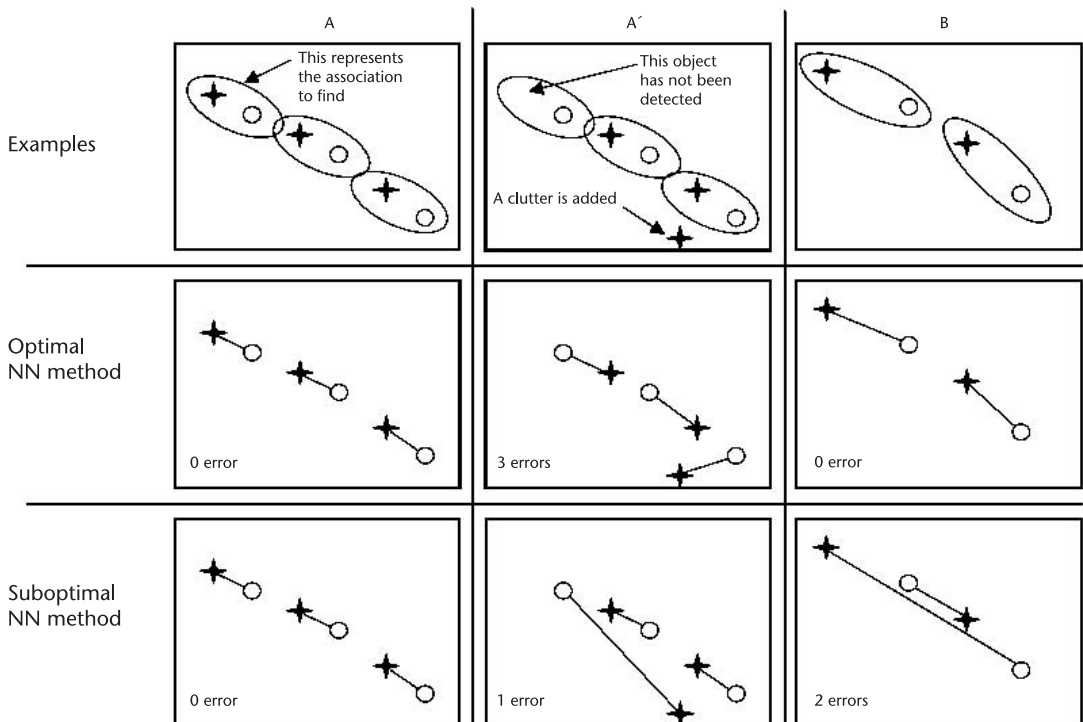
$$\forall i \neq 0 \sum_j \mathbb{1}_{\{\theta_{ij}\}} = 1 \quad (10.109)$$

$$\text{where } c_{ij} = \begin{cases} -\log\left(\frac{P_D \Lambda_t(\theta_{ij})}{\Lambda_t(\theta_{0j})}\right) & \text{if } -\log(\cdot) < 0 \\ 0 & \text{if } i = 0 \text{ or } j = 0 \\ \infty & \text{otherwise} \end{cases} \quad (10.110)$$

where  $\Lambda_t(\theta_{ij})$  is the likelihood of the event  $\theta_{ij} = \{\text{the trajectory } i \text{ is associated with measurement } j\}$ , trajectory 0 has the specificity of being associated with all the nonassociated measurements, and measurement 0 has the specificity of being associated with all the trajectories without a measurement in the search window. Finally,  $P_D$  is the probability of detecting an object.

Jonker and Volgenant's algorithm, for example, [93] or the Hungarian algorithm [94] are used to obtain the solution for this problem. This optimal approach is very sensitive to noise. This is because, if an object is over- or underdetected, all associations may be staggered to satisfy the global criterion. Figure 10.22 illustrates this.

A way of getting around this problem is to use a suboptimal approach (Algorithm 10.8 in Appendix 10A). This works as follows: after determination of all the search windows, the  $c_{ij}$  are calculated for the validated measurements. Then



**Figure 10.22** The nearest neighbors: comparison between optimal and suboptimal solution.

the smallest value  $c_{ij}$  is determined, and the trajectory  $i_0$  is associated with measurement  $j_0$ . Then, these two elements are eliminated for the rest of the approach. The process is reiterated until there are no more associations possible.

#### 10.4.2 Multihypothesis Tracking (MHT)

The MHT algorithm [71, 91, 92, 95] relies on an elegant theoretical model because it proposes maximizing the probability of each concatenation of associations from time 1 to time  $t$  (see Algorithm 10.9 in Appendix 10A). This algorithm supposes that a measurement is either a detected object, a false alarm, or a new object. At time  $t$ , a feasible joint association event that links all  $\mathbf{Z}_t$  to all  $\mathbf{Z}_{t|t-1}$  of predictions is observed  $\theta_t^l$ . Each feasible joint association event therefore contains a set of measurements composed as follows:

- $\tau$  measurements come from detected tracked objects.
- $\nu$  measurements come from detected new objects.
- $\phi$  measurements are false alarms.

Three indicators are defined in this way:

$$\tau_j = \tau_j[\theta_t^k] = \begin{cases} 1 & \text{if } \mathbf{z}_t^j \text{ comes from a detected tracked object} \\ 0 & \text{otherwise} \end{cases} \quad (10.111)$$

$$\nu_j = \nu_j[\theta_t^k] = \begin{cases} 1 & \text{if } \mathbf{z}_t^j \text{ is a new detected object} \\ 0 & \text{otherwise} \end{cases} \quad (10.112)$$

$$\delta_i = \delta_i[\theta_t^k] = \begin{cases} 1 & \text{If object } i \text{ is detected at time } t \\ 0 & \text{otherwise} \end{cases} \quad (10.113)$$

with  $\tau = \sum_{j=1}^m \tau_j$ ,  $\nu = \sum_{j=1}^m \nu_j$  and  $\phi = m - \tau - \nu$  (where  $m$  is the total number of measurements). A cumulative feasible joint association event hypothesis  $l$  of time 1 at time  $t$  is entered  $\Theta_{1:t}^l$ . This is the concatenation of a cumulative feasible joint association event hypothesis  $s$  of time 1 at time  $t-1$  and of a feasible joint association event  $k$  at time  $t$ :

$$\Theta_{1:t}^l = \{\Theta_{1:t-1}^s, \theta_t^k\} \quad (10.114)$$

The probability of such a hypothesis can be calculated by applying Bayes' rule:

$$P\{\Theta_{1:t}^l | \mathbf{Z}_{1:t}\} = P\{\theta_t^k, \Theta_{1:t-1}^s | \mathbf{Z}_t, \mathbf{Z}_{1:t-1}\} \quad (10.115)$$

$$= \frac{1}{c} p[\mathbf{Z}_t | \theta_t^k, \Theta_{1:t-1}^s, \mathbf{Z}_{1:t-1}] \quad (10.116)$$

$$P\{\theta_t^k | \Theta_{1:t-1}^s, \mathbf{Z}_{1:t-1}\} \quad (10.117)$$

$$P\{\Theta_{1:t-1}^s | \mathbf{Z}_{1:t-1}\} \quad (10.118)$$



where (10.118) is obtained during the previous iteration, (10.116) equals:

$$p\{\mathbf{Z}_t|\boldsymbol{\theta}_t^k, \Theta_{1:t-1}^s, \mathbf{Z}_{1:t-1}\} = \prod_j [\Lambda_j^i]^{\tau_j} V^{-(1-\tau_j)} \quad (10.119)$$

$$= V^{-\phi-v} \prod_i [\Lambda_i^j]^{\tau_j} \quad (10.120)$$

and (10.117) equals:

$$P\{\boldsymbol{\theta}_t^k|\Theta_{1:t-1}^s, \mathbf{Z}_{1:t-1}\} = \frac{\phi!v!}{m} \mu_F(\phi) \mu_N(v) \prod_i (P_D^i)^{\delta_i} (1 - P_D^i)^{1-\delta_i} \quad (10.121)$$

We have therefore:

$$\begin{aligned} P\{\boldsymbol{\theta}_{1:t}^l|\mathbf{Z}_{1:t}\} &= \frac{1}{c} \frac{\phi!v!}{m} \mu_F(\phi) \mu_N(v) V^{-\phi-v} \prod_j [\Lambda_j^i]^{\tau_j} \\ &\times \prod_i (P_D^i)^{\delta_i} (1 - P_D^i)^{1-\delta_i} P\{\Theta_{1:t-1}^s|\mathbf{Z}_{1:t-1}\} \end{aligned}$$

Because this algorithm amounts to creating a tree of hypotheses that increases exponentially with time, its complexity makes it inapplicable as is. It can however be used suboptimally by applying a strategy that deletes large sets of hypotheses over the course of time. Cox et al. [92] proposed an implementation of MHT using Murty's algorithm [96] to find the  $k$ -best solutions to the association problem stated in this way. In this article, some methods to reduce the calculation load considerably are also proposed. However, this algorithm only remains applicable for tracking some objects in the presence of some false detections.

We observe that there is a probabilistic version of the MHT: the PMHT. Also theoretically elegant for an object, the associations are considered to be independent for several objects, which is debatable. In practice, according to [97], it reveals itself to be at best equivalent to the PDAF described in the next section. It is no doubt because the PDAF is moreover much less numerically complex than the PMHT has never had true success.

### 10.4.3 The Probabilistic Data Association Filter (PDAF)

The PDAF [27, 32, 98, 99] produces the probability that each measurement contained in the search window is the correct measurement or, on the contrary, that none of them corresponds to the tracked object (see Algorithm 10.10 in Appendix 10A). The various measurements that are read in this way are taken into account along with their respective probabilities to update the filter. The filter is therefore updated not with one measurement, with which it would have been associated, but with all the measurements contained in its validation filter weighted by their respective probability. The hypotheses formulated are as follows: a single object is present in the scene; one of the measurements is the measurement of this object and the others are false detections or noise. Discrimination between measurements from the object and measurements from errors or noise is based on a difference in distribution.

If  $m$  measurements are contained in the search window, as shown in Figure 10.23, the probability that  $\mathbf{z}_t^i$  comes from the object equals

$$\beta_i = \frac{e_i}{b + \sum_{l=1}^m e_l} \quad (i = 1, \dots, m) \quad (10.122)$$

and the probability that none of the measurements corresponds to the tracked object equals

$$\beta_0 = \frac{b}{b + \sum_{l=1}^m e_l} \quad (10.123)$$

with

$$e_i = \exp \left\{ -\frac{1}{2} d^2(\mathbf{z}_t^i) \right\} \quad (10.124)$$

$$b = \frac{m}{V} \sqrt{\det[2\pi\mathbf{S}_t]} \frac{1 - P_D P_G}{P_D} \quad (10.125)$$

where  $V$  is the volume of the search window,  $P_D$  is the probability of detection, and  $P_G$  is the probability that the measurement of the object is effectively contained in the validation area. The state of the filter is then updated as follows:

$$\mathbf{x}_{t|t} = \mathbf{x}_{t|t-1} + \mathbf{K}_t \mathbf{v}_t \quad (10.126)$$

with  $\mathbf{v}_t$  the combined residue:

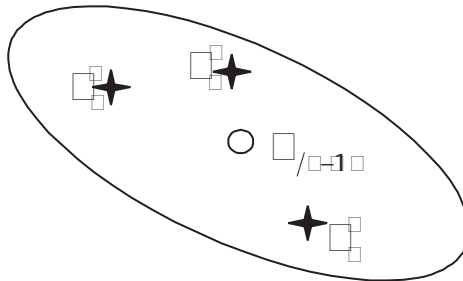
$$\mathbf{v}_t = \sum_{i=1}^m \beta_i \mathbf{v}_t^i \quad (10.127)$$

where

$$\mathbf{v}_t^i = \mathbf{z}_t^i - \mathbf{H}_t \mathbf{x}_{t|t-1} \quad (10.128)$$

and the covariance is updated as follows:

$$\mathbf{P}_{t|t} = \beta_0 \mathbf{P}_{t|t-1} + [1 - \beta_0] \mathbf{P}_t^c + \tilde{\mathbf{P}}_t \quad (10.129)$$



**Figure 10.23** Search window around the predicted measurement.

where

$$\mathbf{P}_t^c = \mathbf{P}_{t|t-1} - \mathbf{K}_t \mathbf{S}_t \mathbf{K}_t^T \quad (10.130)$$

and

$$\tilde{\mathbf{P}}_t = \mathbf{K}_t \left[ \sum_{i=1}^m \beta_0 v_t^i [v_t^i]^T - v_t v_t^T \right] \quad (10.131)$$

#### 10.4.4 Joint PDAF (JPDAF)

The JPDAF is the joint version of the PDAF (see Algorithm 10.11 in Appendix 10A). This association method considers that a measurement is exclusively on the basis of preference:

- A detected object with a Gaussian distribution;
- A false alarm with a uniform or a Poisson distribution.

Moreover, the number of objects is set and known (no object leaves or enters the scene). A  *$\theta$  joint association event* is a set of association events  $\theta_{ij}$  between a prediction  $i$  and a measurement  $j$ . A *feasible joint association event* is a set of  $\theta_{ij}$  such that each prediction  $i$  is associated with a single measurement  $j$  that it does not share, and each measurement  $j$  is associated with a single prediction  $i$  that it does not share. The probability of each  $\theta$  is obtained with:

$$P\{\theta | \mathbf{Z}_{1:t}\} = \frac{1}{c} \frac{\phi!}{V^\phi} \prod_j (\Lambda_{ij})^{\tau_j} \prod_i \{(P_D^i)^{\delta_i} (1 - P_D^i)^{1-\delta_i}\} \quad (10.132)$$

with

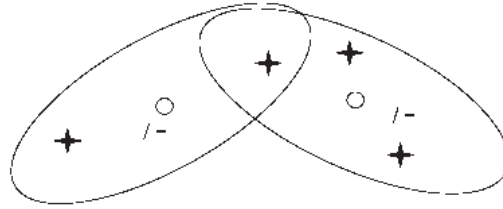
$$\tau_j = \tau_j[\theta_t^j] = \begin{cases} 1 & \text{if } \mathbf{z}_t^j \text{ comes from a detected object} \\ 0 & \text{otherwise} \end{cases} \quad (10.133)$$

$$\delta_i = \delta_i[\theta_t^j] = \begin{cases} 1 & \text{if object } i \text{ is detected at time } t \\ 0 & \text{otherwise} \end{cases} \quad (10.134)$$

$P_D^i$  is the probability of detection of object  $i$  (considered to be known),  $\phi$  is the number of measurements coming from false alarms,  $V$  is the hyper-volume of the search window (see Figure 10.24), and  $\Lambda_{ij}$  is the Gaussian likelihood of measurement  $j$  for trajectory  $i_j$ . The configured version of the JPDAF considers that the number of false detections is modeled by a Poisson law with the parameter  $\lambda$  (considered to be known) and is obtained by replacing  $\frac{\phi!}{V^\phi}$  with  $\lambda^\phi$  in (10.132).

The marginal probabilities of each association event are obtained from the joint law as follows:

$$\beta_{ij} = P\{\theta_{ij} | \mathbf{Z}_{1:t}\} = \sum_{\theta: \theta_{ij} \in \theta} P\{\theta | \mathbf{Z}_{1:t}\} \quad (10.135)$$



**Figure 10.24** JPDAF: Volumes of the search window around the predicted measurements.

These marginal probabilities are used to weight each corresponding measurement for the update of each PDAF in (10.126) and (10.129).

The use of several independent PDAFs to track several objects often leads to the blocking of several filters on the same object. This is because if several filters are updated with the same measurements over several successive iterations, it will no longer be possible to differentiate them again. The JPDAF is used to work around this problem by not allowing a configuration where several objects can simultaneously make the same hypothesis on the same measurement. The associations are therefore interdependent. This is the meaning of the *feasible joint association event*.

In particular, all these association methods have their source in air traffic problems [32]. Applied to fluorescent spots, they define new problems because the hypotheses that they define do not predict the various cases that detection produces on a permanent basis. This is what we will show in the next section.

## 10.5 Particle Tracking: Methods for Biological Imaging

In the previous sections, we reviewed the filtering and association methods. Some of them are more adapted to particle tracking in the context of biological image than others. A specific aspect of biological object is that their dynamics can vary abruptly and frequently over time leading to association problems. To handle this, we believe the use of an IMM filter with several dynamic models allows us to achieve a good prediction during the transition between movements. Also, to avoid creating inconsistent associations leading to disconnected trajectories in subsequent images, two important facts have to be taken into consideration: (1) a detection does not necessarily correspond to a real object but could have been generated by clutter; and (2) an object might have been missed (not detected). Finally, we can rarely assume the number of object will remain constant during the sequence. To properly handle these situations, the tracking algorithm has to be able either to terminate a track if a wrong measurement has been generated or to provide a predicted measurement that will be used to temporarily retain a track in case a real measurement can be assigned in the subsequent images. Also, as the number of object do not remain constant, a robust association can be achieve thanks to the suboptimal maximization of the likelihood of each filter.

This method is flexible since the detection method (which is not discussed here) can be adapted to the application as long as it produces measurement of objects at each time frame. In the following, for each detected spot, we form a measurement vector  $\mathbf{z}$  (see [100]) consisting of the location  $(x, y, z)$ , volume  $v$ , and mean intensity  $i$  of the spot at time  $t$ :

$$\mathbf{z}_t = [x_t, y_t, z_t, v_t, i_t]^T \quad (10.136)$$

which will be used to estimate a spot state in the tracking steps.

### 10.5.1 Proposed Dynamic Models for the IMM

To adapt the IMM to biological imaging, we propose using three different models of dynamics: random walk (RW), first-order linear extrapolation (FLE), and second-order linear extrapolation (SLE). They model Brownian motion and directed movement with constant speed or acceleration, which are representative modes of motion encountered in biology [7, 101]. We make the additional realistic hypothesis that during movement, the biological objects can switch abruptly between the three models. This description is complemented by the hypothesis that the volume  $v_t$  and the mean intensity  $i_t$  of each spot remain approximately constant with an additive Gaussian noise. By writing the state vector as a concatenation of three successive locations,

$$\mathbf{x}_t = [x_t, y_t, z_t, v_t, i_t, x_{t-1}, y_{t-1}, z_{t-1}, x_{t-2}, y_{t-2}, z_{t-2}]^T \quad (10.137)$$

each of three models can be represented by a linear application, thus enabling us to take into account in the IMM up to three consecutive vector states while still lying within a Markov process of order 1.

The three models are as follows:

1. RW model, which makes the assumption that the next state is defined by the previous state and an additive Gaussian noise:

$$\mathbf{F}^1 = \begin{bmatrix} \begin{array}{ccccc|ccccc} 1 & 0 & 0 & 0 & 0 & 0 & 0 & 0 & 0 & 0 & 0 \\ 0 & 1 & 0 & 0 & 0 & 0 & 0 & 0 & 0 & 0 & 0 \\ 0 & 0 & 1 & 0 & 0 & 0 & 0 & 0 & 0 & 0 & 0 \\ 0 & 0 & 0 & 1 & 0 & 0 & 0 & 0 & 0 & 0 & 0 \\ 0 & 0 & 0 & 0 & 1 & 0 & 0 & 0 & 0 & 0 & 0 \\ \hline 1 & 0 & 0 & 0 & 0 & 0 & 0 & 0 & 0 & 0 & 0 \\ 0 & 1 & 0 & 0 & 0 & 0 & 0 & 0 & 0 & 0 & 0 \\ 0 & 0 & 1 & 0 & 0 & 0 & 0 & 0 & 0 & 0 & 0 \\ 0 & 0 & 0 & 0 & 0 & 1 & 0 & 0 & 0 & 0 & 0 \\ 0 & 0 & 0 & 0 & 0 & 0 & 1 & 0 & 0 & 0 & 0 \\ 0 & 0 & 0 & 0 & 0 & 0 & 0 & 1 & 0 & 0 & 0 \end{array} \end{bmatrix}$$

2. FLE model, which makes the assumption that the next state is defined by the linear extrapolation of the last two 3-D locations while keeping the same intensity and volume:

$$\mathbf{F}^2 = \left[ \begin{array}{cccccc|cccc} 2 & 0 & 0 & 0 & 0 & -1 & 0 & 0 & 0 & 0 & 0 \\ 0 & 2 & 0 & 0 & 0 & 0 & -1 & 0 & 0 & 0 & 0 \\ 0 & 0 & 2 & 0 & 0 & 0 & 0 & -1 & 0 & 0 & 0 \\ 0 & 0 & 0 & 1 & 0 & 0 & 0 & 0 & 0 & 0 & 0 \\ 0 & 0 & 0 & 0 & 1 & 0 & 0 & 0 & 0 & 0 & 0 \\ 1 & 0 & 0 & 0 & 0 & 0 & 0 & 0 & 0 & 0 & 0 \\ 0 & 1 & 0 & 0 & 0 & 0 & 0 & 0 & 0 & 0 & 0 \\ 0 & 0 & 1 & 0 & 0 & 0 & 0 & 0 & 0 & 0 & 0 \\ \hline 0 & 0 & 0 & 0 & 0 & 1 & 0 & 0 & 0 & 0 & 0 \\ 0 & 0 & 0 & 0 & 0 & 0 & 1 & 0 & 0 & 0 & 0 \\ 0 & 0 & 0 & 0 & 0 & 0 & 0 & 1 & 0 & 0 & 0 \end{array} \right]$$

3. SLE model, which makes the assumption that the next state is defined by the linear extrapolation of the three last 3-D locations while keeping the same intensity and volume:

$$\mathbf{F}^3 = \left[ \begin{array}{cccccc|cccc} 3 & 0 & 0 & 0 & 0 & -3 & 0 & 0 & 1 & 0 & 0 \\ 0 & 3 & 0 & 0 & 0 & 0 & -3 & 0 & 0 & 1 & 0 \\ 0 & 0 & 3 & 0 & 0 & 0 & 0 & -3 & 0 & 0 & 1 \\ 0 & 0 & 0 & 1 & 0 & 0 & 0 & 0 & 0 & 0 & 0 \\ 0 & 0 & 0 & 0 & 1 & 0 & 0 & 0 & 0 & 0 & 0 \\ 1 & 0 & 0 & 0 & 0 & 0 & 0 & 0 & 0 & 0 & 0 \\ 0 & 1 & 0 & 0 & 0 & 0 & 0 & 0 & 0 & 0 & 0 \\ 0 & 0 & 1 & 0 & 0 & 0 & 0 & 0 & 0 & 0 & 0 \\ 0 & 0 & 0 & 0 & 0 & 1 & 0 & 0 & 0 & 0 & 0 \\ 0 & 0 & 0 & 0 & 0 & 0 & 1 & 0 & 0 & 0 & 0 \\ 0 & 0 & 0 & 0 & 0 & 0 & 0 & 1 & 0 & 0 & 0 \end{array} \right]$$

The observation model  $\mathbf{H}$  related to the measurement vector (10.136) is common to all three models:

$$\mathbf{H} = \left[ \begin{array}{cccccccccccc} 1 & 0 & 0 & 0 & 0 & 0 & 0 & 0 & 0 & 0 & 0 & 0 \\ 0 & 1 & 0 & 0 & 0 & 0 & 0 & 0 & 0 & 0 & 0 & 0 \\ 0 & 0 & 1 & 0 & 0 & 0 & 0 & 0 & 0 & 0 & 0 & 0 \\ 0 & 0 & 0 & 1 & 0 & 0 & 0 & 0 & 0 & 0 & 0 & 0 \\ 0 & 0 & 0 & 0 & 1 & 0 & 0 & 0 & 0 & 0 & 0 & 0 \end{array} \right] \quad (10.138)$$

To finish, the initialization of the covariances of transition  $\mathbf{Q}_0$  and observation  $\mathbf{R}_0$  can be estimated from isolated objects. We will see in the following section that  $\mathbf{Q}_t$  can be updated over time to adapt the search window (or validation gate) to the dynamic of the objects.

### 10.5.2 Adaptive Validation Gate

After the prediction stage, the predicted measurement for a Kalman filter is given by  $\hat{\mathbf{z}}_{t|t-1} = \mathbf{H}_t \hat{\mathbf{x}}_{t|t-1}$ . So for each filter, a validation gate around the predicted measurement can be defined as follows:

$$G_t = \{\mathbf{z}_t, [\mathbf{z}_t - \hat{\mathbf{z}}_{t|t-1}^i]^T [\mathbf{S}_t]^{-1} [\mathbf{z}_t - \hat{\mathbf{z}}_{t|t-1}^i] \leq g^2\}$$

where  $\mathbf{S}_t$  is the innovation covariance and  $g$  is determined from a  $\chi_{dim(\mathbf{z})}^2$  table as corresponding to a gating probability chosen to be  $> 0.95$ . In the following, we show how to reduce this search area as much as possible, under the constraint that the valid candidate must be contained therein. This is done by estimating the covariance of the transition noise at each time step in order to update it. Let  $\mathbf{v}_t$  be a random process vector with zero mean and covariance matrix  $\mathbf{Q}_t$ . Then, an estimate of  $\mathbf{Q}_t$  at each time step  $t$  when a realization  $\tilde{\mathbf{v}}_t$  of  $\mathbf{v}_t$  becomes available, can be computed by the following methods, for which we give the expression and the potential pitfalls:

1. If the model is well designed and the noise induced by the transition process is constant, we can choose:

$$\hat{\mathbf{Q}}_t = \mathbf{Q}_0 \quad (10.139)$$

that is, the estimate is a constant. Not updating the covariance of the transition noise can, however, lead to problems if the input value is not correctly chosen. If it is too small, the target will probably get out of the validation gate. Conversely, if it is too large, the gate will probably contain lots of clutter and other targets, leading to possible association errors.

2. If we observe that the covariance of the transition noise evolves with time, we can compute the sample variance as being an estimate for  $\mathbf{Q}_t$  at each time step  $t$ :

$$\hat{\mathbf{Q}}_t = \frac{1}{t} \sum_{i=0}^t \tilde{\mathbf{v}}_i \tilde{\mathbf{v}}_i^T \quad (10.140)$$

3. Since this expression may lead to computational bottlenecks, we prefer its recursive equivalent, which consists of computing recursively the sample variance at each  $t$ :

$$\hat{\mathbf{Q}}_t = \frac{t-1}{t} \hat{\mathbf{Q}}_{t-1} + \frac{1}{t} \tilde{\mathbf{v}}_t \tilde{\mathbf{v}}_t^T \quad (10.141)$$

In this case, it is clear that  $\hat{\mathbf{Q}}_t$  converges to a constant value because the newcomers are given less and less weight when  $t$  grows. This has the negative effect that sudden variations of the target behavior cannot be taken into account properly and therefore lead to losing the track.

4. To try to tackle the previous problem, the weight  $\frac{t-1}{t}$  can be replaced by a constant “memory” factor  $\alpha$ ,  $0 < \alpha < 1$ . Then, at each time  $t$ , the covariance estimate is obtained with

$$\hat{\mathbf{Q}}_t = \alpha \hat{\mathbf{Q}}_{t-1} + (1 - \alpha) \tilde{\mathbf{v}}_t \tilde{\mathbf{v}}_t^T \quad (10.142)$$



This method has the advantage of controlling the confidence in a new evaluation of the error. However, as it reinforces the weight of last similar values, it has the negative effect of shrinking the validation gate to small values and will produce the same effect as method 3 when  $\tilde{v}_t$  is small during a significant amount of time.

5. To limit the shrinking of the validation gate, it is also possible to set a minimal value on the recursive estimate of the covariance  $\hat{Q}_t$ . This therefore leads to the following expression:

$$\hat{Q}_t = \alpha \hat{Q}_{t-1} + \beta \tilde{v}_t \tilde{v}_t^T + \gamma Q_0, \quad (10.143)$$

with  $\alpha + \beta + \gamma = 1$ , where  $\alpha$  is the “memory” factor,  $\gamma$  determines the weight of the minimal gate and  $Q_0$  determines the shape of the gate.

In the context of Gaussian Bayesian target tracking, we get successive values of  $\tilde{v}_t$  by computing the error that is made between the state estimate  $\hat{\mathbf{x}}_{t|t}$  and the predicted one,  $\hat{\mathbf{x}}_{t|t-1}$ :

$$\tilde{v}_t = \hat{\mathbf{x}}_{t|t} - \hat{\mathbf{x}}_{t|t-1} \quad (10.144)$$

This value can be obtained with a Kalman filter, an extended Kalman filter, and also in our case with each filter of an interacting multiple model filter.

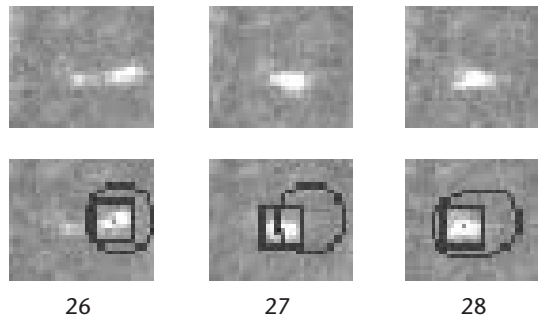
To illustrate the methods 1, 3, 4, and 5 [40] and compare their effectiveness in updating the transition noise covariance, we run the tracking algorithm with a Kalman filter on sequences such as those shown in Figure 10.25.

For each track, at each step, the following measures are computed:

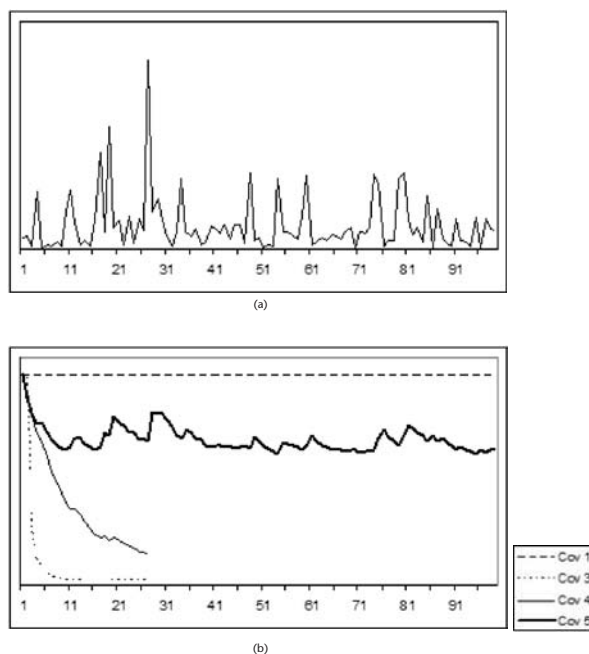
- The Mahalanobis distance between predicted measurement and real associated measurement:

$$d_t = [\mathbf{z}_t - \hat{\mathbf{z}}_{t|t-1}^i]^T [\mathbf{S}_t]^{-1} [\mathbf{z}_t - \hat{\mathbf{z}}_{t|t-1}^i] \quad (10.145)$$

- The volume of the validation gate (i.e., except for a constant, the product of the eigenvalues of the residual covariance  $S_t$ ). In our case, the validation



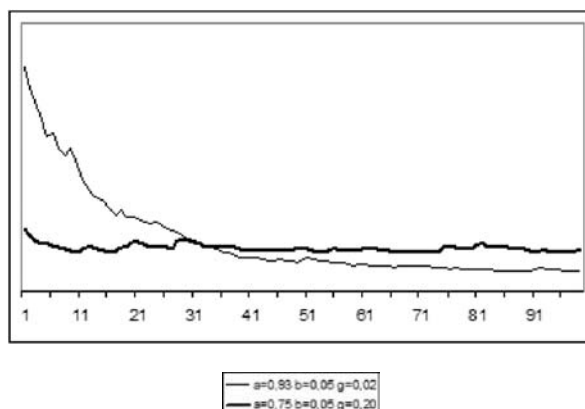
**Figure 10.25** First row: cropped frames 26, 27, and 28 of a video-microscopy sequence. Second row: the tracked spot moves suddenly to the opposite direction at frame 27 and keeps being in the validation gate on next frame thanks to method 5.



**Figure 10.26** (a) Error of measurement prediction. (b) Volume of validation gate. When the object suddenly changes its direction at frame 27, the error is high and only the methods 1 and 5 are able to keep the object within the validation gate.

gate is an hyper ellipsoid in four dimensions, as each measure is constructed with the location  $x, y$ , the area  $a$ , and the intensity  $i$  of each detected spot with method [4].

Figure 10.26 presents the evolution of these measures for the fluorescent spot of Figure 10.25 computed with methods 1, 3, 4, and 5. This object is typical and represents well the behavior of all tested spots in that it changes dynamics very



**Figure 10.27** Effect of the variation of parameters in method 5.

suddenly between two frames. It can be seen that only methods 1 and 5 succeed in keeping the object inside of the validation gate, while methods 3 and 4 lose the object because the volume decreases too much to handle the unexpected event of the sudden change in direction of the object in frame 27, as shown by the error graph. Also, method 5 is able to adapt the validation volume to a shape related to the error and to a size that is smaller than the one given by method 1.

Figure 10.27 shows the influence of changing the parameters of method 5. In the example, the thick curve is a smoother version of the one in Figure 10.26, where  $\beta$  has a smaller value. The thin curve presents a configuration where the “memory” factor  $\alpha$  is increased and the minimal gate is decreased, leading the validation volume to take more time to adapt itself to a smaller minimum.

### 10.5.3 Association

At each time frame, a set of predicted estimations is provided by the IMM and, parallelly, a set of measurements is provided by the detector. To form the correct tracks, it is necessary thereafter to go through an association stage. This consists of finding the best assignment between detections and the predicted estimations.

The assignment is made as follows: first, we compute the maximum likelihood of the innovation among the models in each IMM that we denote  $\Lambda_t^{\max}(i, l)$ . That is to say, for each measurement  $\mathbf{m}_i(t), i \in \{1, \dots, m\}$  and track  $T_l, l \in \{1, \dots, n\}$ , we find the value which maximizes (10.74).

Each of them is used to form the following matrix:

$$\mathbf{L} = \begin{bmatrix} \vdots \\ \dots \Lambda_t^{\max}(i, l) \dots \\ \vdots \end{bmatrix} \quad (10.146)$$

This is done only for the measurements that are within the validation gates (i.e., the Mahalanobis distance between predicted and estimated measurements is inferior to the square of a given  $g$  which is determined from a  $\chi_{\dim(m)}^2$  table as corresponding to a gating probability chosen to be at least 0.95).

The assignments  $(a_0, \dots, a_{\min(n, m)})$  are then found according to the following:

$$a_k = (i_k, l_k) = \arg \max_{(i, l) \in \mathbf{J}_k} \mathbf{L}(i, l) \quad (10.147)$$

with

$$\begin{cases} \mathbf{J}_0 &= \{(i, l) / i \in \{1, \dots, m\}, l \in \{1, \dots, n\}\} \\ \mathbf{J}_{k+1} &= \mathbf{J}_k \setminus \{(i, l) / \{i = i_k\} \cup \{l = l_k\}\} \end{cases} \quad (10.148)$$

The search for assignments stops when  $\mathbf{J}_k = \{\emptyset\}$ . Even though this assignment technique is suboptimal in a global sense—that is, it may occur that

$$\exists B^* = \{b_0, \dots, b_{\min(n, m)}\}, \quad \sum_k \mathbf{L}(a_k) < \sum_k \mathbf{L}(b_k) \quad (10.149)$$

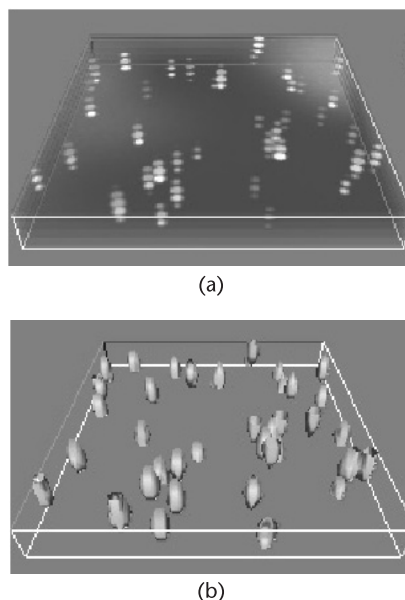
it produces, in context of biological applications, much better results than an algorithm for optimal assignment between two sets such as for example, the Jonker and Volgenant algorithm [93]. When dealing with biological data, the JVC algorithm is not able to output correct associations on more than the first five time points in a sequence. This can be explained by the fact that the JVC algorithm requires the cardinality of the two sets is equal, an assumption that is not met in our case as we are trying to resolve an ill-posed problem where the number of predicted measurements never equals the number of measurements.

## 10.6 Applications

### 10.6.1 Validation on Synthetic Data

In order to assess the quality of the method and its adaptability to biological data, sequences were generated with artificial spots whose characteristics are as close as possible to fluorescent spots. The spots are represented by 3-D Gaussian shapes with different random covariance matrices in order to get different shapes of different sizes. An example of generated spots and their detection is presented in Figure 10.28.

To test the robustness of the tracking algorithm to the density of spots, 10, 20, 30, or 40 spots were included in  $100 \times 100 \times 10$  image stacks (the resulting spot density then being  $d = 0.1, 0.2, 0.3, 0.4$ , for 10, 20, 30, and 40 spots), five sequences of 30 time points for each condition (20 sequences in total) were generated.



**Figure 10.28** Example of detection of synthetic spots. (a) Synthetic  $100 \times 100 \times 5$  image stack with 40 synthetic spots and added Gaussian noise ( $\sigma = 10$ ). Note the similarity with real microscopy data in Figure 10.1. (b) Detected spots.

Here, the size of the test volumes was kept small in order to achieve relatively high densities of spots within tractable volumes. In each sequence, the spots were made to move randomly and their direction changed randomly at a random time of between 1 and 5 frames, with an additional random modification of the covariance matrix of the 3-D Gaussian shapes with time to make their aspect change. To simulate real-world conditions, spots were allowed to temporarily aggregate and cross. Also, a simulated background was generated by using a mixture of Gaussians with high variance, and white Gaussian noise was added to the sequence in order to represent the noise present in typical microscopy images. Finally, the image stacks have a lower resolution in the  $z$  direction to simulate the anisotropic resolution of 3-D microscopy images.

Table 10.1 gives a summary of the influence of the density of spots within the same volume on the performances of the algorithm. The results show that even with a high density of spots, the performances of the algorithm are satisfactory, and that the IMM clearly outperforms the results achieved by using a KF with any of the three models (RW, FLE, or SLE) taken alone.

Color Plate 15 shows a synthetic sequence that was generated with 160 synthetic spots in a volume similar to typical real microscopic 3-D confocal images, resulting in a spot density of  $d = 0.25$ . By applying the IMM filter to the data on this sequence, we could achieve a tracking with 85 percent of true positive and 6.1 percent of false positives, which is in good agreement with the results in Table 10.1.


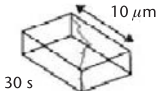
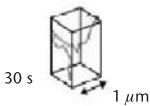
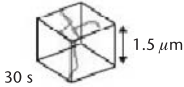
The 3D+t (4-D) tracking methods developed and set out in this chapter have been applied to a number of problems in microbiology and cellular biology. They have been used to discover and quantify certain phenomena with precision. A complete software application has been developed with the double purpose of allowing evolution in the algorithms and an ergonomic use by biologists.

It is worth noting that microscopy platforms and some specialized publishers also propose software packages that carry out (semi)automatic tracking of objects. The main ones are in particular Imaris, DiaTrack, and TIKAL. These software use deterministic methods that have proven not to be able to manage properly fusions or split of objects. They can, however, be used in images very noisy particle flow but do not extract satisfactory data from objects that evolve in all directions. The field is in full evolution, and it is highly probable that the availability of this type of application will increase notably in the near future.

**Table 10.1** Influence of the Number of Spots on the Quality of Tracking

<i>Spot density</i>	<i>Single Model</i>			
	<i>RW</i>	<i>FLE</i>	<i>SLE</i>	<i>IMM</i>
0.1	80 / 0	86.7 / 0	86.7 / 0	90 / 3.7
0.2	78.3 / 2.1	75 / 2.2	76.7 / 2.2	80 / 2.1
0.3	73.3 / 7.6	71.1 / 3.1	71.1 / 1.6	80 / 6.9
0.4	61.7 / 1.4	64.2 / 1.3	63.3 / 2.6	66.6 / 2.5

The mean results for the analysis of five sequences of 30  $100 \times 100 \times 5$  image stacks for each spot density. Results are expressed as the percentage of true positives and false positives given by the tracking procedure.

	Type	Velocity	3D tracks	Movement characteristics
Movement I	Microtubule-directed	Peaks at 0.1–1 $\mu\text{m/s}$		Directed
Movement II	Actin-directed	Under 0.03 $\mu\text{m/s}$		Directed
Movement III	Docking at the nuclear membrane	Under 0.03 $\mu\text{m/s}$		Confined
Movement IV	Intranuclear movement	Under 0.005 $\mu\text{m/s}$		Diffusive

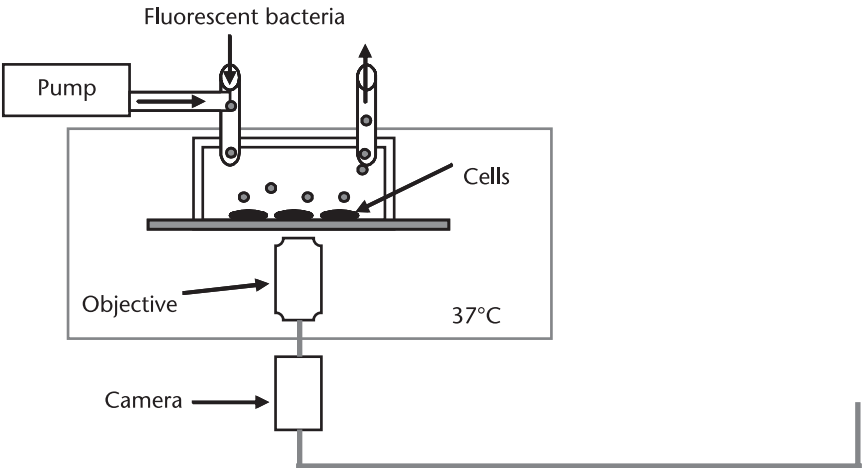
**Figure 10.29** Summary of the various phases of HIV-1 movements. (From: [101]. © 2006 NPG. Reprinted with permission.)

10.6.2 Applications to Cell Biology

10.6.2.1 Motility of HIV-1 Complexes

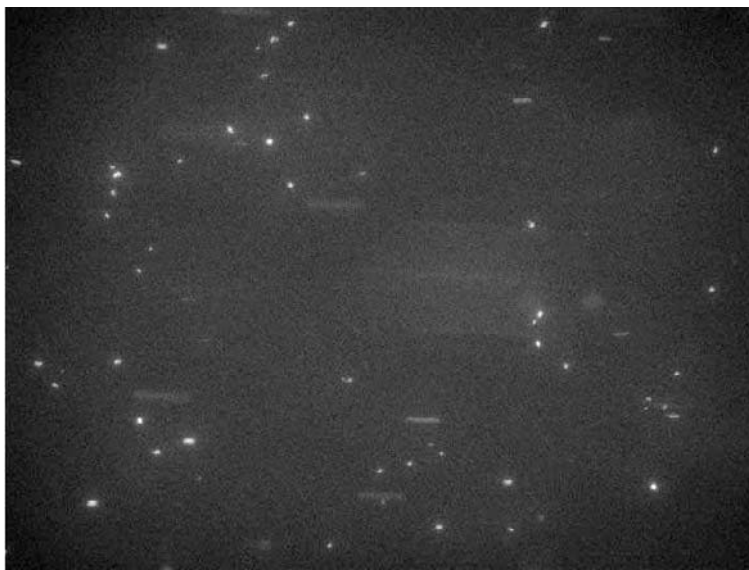
Thanks to the labeling of HIV-1 integrase with a small tetracycline tag, which entirely preserves virus infectivity, both intracytoplasmic and intranuclear HIV-1 complexes were imaged in 3-D over time [101]. We used our computer vision program for automated 3D+t particle tracking and analysis of intracellular HIV-1 kinetic parameters (see Figure 10.29).

In the cytoplasm, HIV-1 complexes underwent directed movements toward the nuclear compartment, which are kinetically characteristic of both microtubule- and actin-dependent transport (see Color Plate 16(a)). Docking of HIV-1 at the nuclear membrane was consistently preceded by actin-directed movements in the

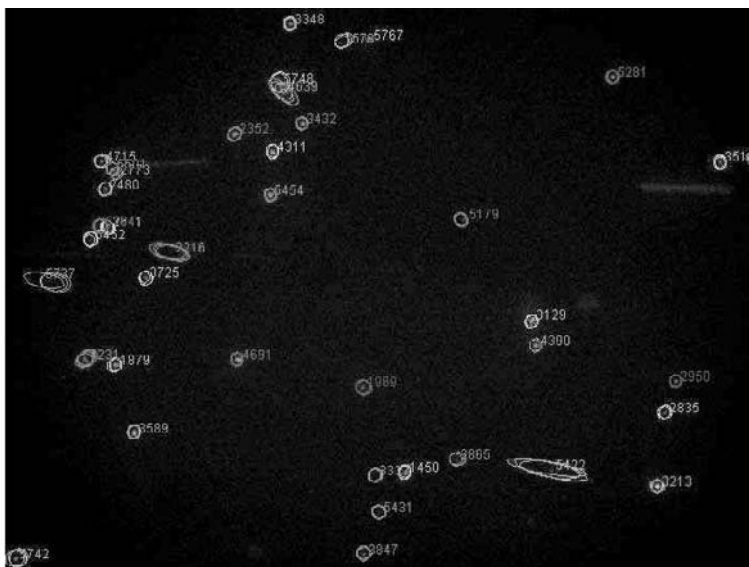


**Figure 10.30** System set up for the observation of a flow of bacteria labeled by fluorescence above a cell layer.

perinuclear area (see Color Plate 16(b)), and concordantly, microtubule-directed movements from the cell periphery to the perinuclear area were followed by slower shorter-ranging actin-mediated displacements.



(a)



(b)

**Figure 10.31** (a) Image of a flow of bacteria. The bacteria marked by fluorescence cross the screen from left to right. Some of them, in the low flow layers, manage to attach themselves to cells that are not visible here. (b) Automatic tracking of a flow of bacteria. Each bacterium that adheres to the cell wall is automatically taken into account and tracked when it moves and/or when it detaches when it cannot resist the stream.



Once docked, HIV-1 complexes exhibited vibratory movements in a very confined volume. Intranuclear complexes then adopted diffusive movements suggestive of interaction with host cell chromatin. This work has introduced new insight into the kinetic characteristics of the different movements exhibited by HIV-1 complexes within infected cells, and provides an invaluable tool for the study of virus/host cell interactions during infection.

#### 10.6.2.2 Adhesion of *Neisseria meningitidis*

*N. meningitidis* is a strictly human pathogen agent responsible for septicaemias and meningitis [102]. This bacterium asymptotically colonizes the nasopharynx in a significant percentage of the population. The pathogenic process is initiated by the crossing of this epithelium by the bacterium, thus allowing the bacterium to access the blood circulation. *N. meningitidis* is able to survive and to proliferate in the blood stream. It can then colonize and cross the haemato-encephalic barrier. The adhesive properties of *N. meningitidis* are crucial for these two stages in crossing cellular barriers because they are initiated by adhesion of bacteria to cells. The adhesion capacities of meningococci have generally been studied under static conditions, whereas it adheres under conditions of blood flow (i.e., in the presence of hydrodynamic forces). The importance of hydrodynamic forces in adhesive phenomena has been highlighted in particular in studies of the interaction of leucocytes with endothelial cells. The role of these forces during adhesion of the meningococcus to the endothelial cells is still poorly known. The objective of this application was to reevaluate the adhesion factors of the meningococcus under conditions of flow. To do this, an experimental approach was developed using a laminar flow chamber (Figure 10.30). We first characterized pili-dependent adhesion in flow and brought out the irreversible character of this adhesion. Another type of adhesion, which is pili-independent, was also discovered. This second adhesion, which is effective in weak flows, does not resist high shearing constraints very much (Figure 10.31). However, it presents an interesting characteristic: rolling of bacteria over cells before they are detached that could facilitate colonization of new sites of infection.

## 10.7 Conclusions

This chapter has presented a general overview of state-of-the-art methods for tracking multiple fluorescent spots in 3D+t video-microscopy sequences. After a survey of the main tracking techniques, we have given an in-depth presentation of Bayesian multiobject tracking, which is made up of three components: (1) a detector that produces measurements of the spots from every image in the sequence, (2) a Bayesian filter that is used to create a prediction of the measurement of each of the objects using predefined models and past measurements, and (3) an association method that is used to determine the measurement(s) used in updating the filters. We have described the main Bayesian filters and association methods. We have then presented the results of a quantitative evaluation of the method on syn-

thetic data, which shows that Bayesian multiple object tracking makes it possible to track a high number of moving particles. Finally, we have described some of its applications to cell biology.

Tracking performances for multiple objects in the previously described environment is directly linked to the density of objects, the quality and precision of their detection, and track initialization. Here we have discussed the robustness to density but not the detection and initialization parts that are highly related to the considered application and images. It is worth noting that the methodological field remains largely open and that several studies still need to be undertaken to solve standing problems in biological particle tracking. A number of studies have already integrated the concepts of superresolution for improving the detection efficiency in cases of highly interacting particles and facilitating downstream processing of tracks [103]. Other studies define an initialization clutter envelope curve that establishes a link assessing the minimal quality of the initialization needed when a given density of object is considered. Also, several offline methods propose splitting the multiple particle tracking problem into several subtasks, with a first step where states are associated and then a second step where micro tracks are formed that are associated in a third step to eventually form tracks. A method that also takes into account the photobleaching of fluorescent particles is given in [89]. Finally, recent methods have been proposed to handle difficult cases such as when objects temporarily split, fuse, or do both simultaneously with their neighbours and developed the concept of virtual measurements [104].

## References

- [1] Ober, R. J., S. Ram, and E. S. Ward, "Localization Accuracy in Single-Molecule Microscopy," *Biophysical Journal*, Vol. 86, No. 2, February 2004, pp. 1185–1200.
- [2] Aguet, F., D. Van de Ville, and M. Unser, "A Maximum-Likelihood Formalism for Sub-Resolution Axial Localization of Fluorescent Nanoparticles," *Optics Express*, Vol. 13, December 2005, pp. 10503–10522.
- [3] Otsu, N., "A Threshold Selection Method From Gray-Level Histograms," *IEEE Transactions on Systems, Man and Cybernetics*, Vol. 9, No. 1, 1979, pp. 62–66.
- [4] Olivo-Marin, J.-C., "Extraction of Spots in Biological Images Using Multiscale Products," *Pattern Recognition*, Vol. 35, No. 9, 2002, pp. 1989–1996.
- [5] Zimmer, C., E. Labruiere, V. Meas-Yedid, N. Guillen, and J.-C. Olivo-Marin, "Segmentation and Tracking of Migrating Cells in Videomicroscopy with Parametric Active Contours: A Tool for Cell-Based Drug Testing," *IEEE Transactions on Medical Imaging*, Vol. 21, No. 10, October 2002, pp. 1212–1221.
- [6] McDonald, D., M. A. Vodicka, G. Lucero, T. M. Svitkina, G. G. Borisy, M. Emerman, and T. J. Hope, "Visualization of the Intracellular Behavior of HIV in Living Cells," *Cell Biology*, Vol. 159, 2002, pp. 441–452.
- [7] Lakadamyali, M., M. J. Rust, H. P. Babcock, and X. Zhuang, "Visualizing Infection of Individual Influenza Viruses," *PNAS*, Vol. 100, 2003, pp. 9280–9285.
- [8] Frishneck, F., P. Baldacci, B. Martin, C. Zimmer, S. Thiberge, J.-C. Olivo-Marin, S. L. Shorte, and R. Menard, "Imaging Movement of Malaria Parasites During Transmission by Anopheles Mosquitoes," *Cellular Microbiology*, Vol. 6, 2004, pp. 687–694.

- [9] Murphy, C., R. Saffrich, J.-C. Olivo-Marin, A. Giner, W. Ansorge, T. Fotsis, and M. Zerial, "Dual Function of rhoD in Vesicular Movement and Cell Motility," *European Journal of Cell Biology*, Vol. 80, No. 6, 2001, pp. 391–398.
- [10] Toomre, D., P. Keller, J. White, J.-C. Olivo, and K. Simons, "Dual-Color Visualisation of Trans-Golgi Network to Plasma Membrane Traffic Along Microtubules in Living Cells," *Journal of Cell Science*, Vol. 112, No. 1, 1999, pp. 21–33.
- [11] November, L. J., and G. W. Simon, "Precise Proper-Motion Measurement of Solar Granulation," *The Astrophysical Journal*, Vol. 333, October 1988, pp. 427–442.
- [12] Aschwanden, P., and W. Guggenbuhl, "Experimental Results From a Comparative Study on Correlation Type Registration Algorithms," *Robust Computer Vision*, Vol. 1, Wichmann, 1992, pp. 268–282.
- [13] Crowley, J. L., F. Berard, and J. Coutaz, "Finger Tracking as an Input Device for Augmented Reality," *International Workshop on Face and Gesture Recognition*, Zurich, Switzerland, June 1995, pp. 195–200.
- [14] Von Seelen, U., and R. Bajcsy, *Adaptive Correlation Tracking of Targets with Changing Scale*, Tech. Rep., GRASP Laboratory, June 1996.
- [15] Lewis, J. P., "Fast Template Matching," *Vision Interface*, 1995, pp. 120–123.
- [16] Badenas, J., J. Miguel, and F. Pla, "Motion-Based Segmentation and Region Tracking in Image Sequences," *Pattern Recognition*, Vol. 34, 2001, pp. 661–670.
- [17] Ohyama, W., T. Wakabayashi, K. Sekioka, F. Kimura, and S. Tsuruoka, "Automatic Tracking of Local Myocardial Motion by Correlation Weighted Velocity Method," *Proceedings of the International Conference on Pattern Recognition*, 2002, Vol. I, pp. 711–714.
- [18] Choi, M.-S., and W.-Y. Kim, "A Novel Two Stage Template Matching Method for Rotation and Illumination Invariance," *Pattern Recognition*, Vol. 35, 2002, pp. 119–129.
- [19] Dell'Acqua, F., and P. Gamba, "Rain Pattern Tracking by Means of COTREC and Modal Matching," *Optical Engineering*, Vol. 41, No. 2, February 2002, pp. 278–286.
- [20] Duda, R. O., and P. E. Hart, *Pattern Classification and Scene Analysis*, New York: John Wiley and Sons, 1973.
- [21] Duda, R. O., P. E. Hart, and D. G. Stork, *Pattern Classification*, 2nd ed., New York: Wiley-Interscience, 2000.
- [22] Sethi, J. K., and R. Jain, "Finding Trajectories of Feature Points in a Monocular Image Sequence," *IEEE Transactions on Pattern Analysis and Machine Intelligence*, Vol. 9, 1987, pp. 56–73.
- [23] Salari, V., and I. K. Sethii, "Feature Point Correspondence in the Presence of Occlusion," *IEEE Transactions on Pattern Analysis and Machine Intelligence*, Vol. 12, No. 1, 1990, pp. 87–91.
- [24] Rangarajan, K., and M. Shah, "Establishing Motion Correspondence," *CVGIP: Image Underst.*, Vol. 54, No. 1, 1991, pp. 56–73.
- [25] Hwang, V. S., "Tracking Feature Points in Time-Varying Images Using An Opportunistic Selection Approach," *Pattern Recognition*, Vol. 22, No. 3, 1999, pp. 247–256.
- [26] Chetverikov, D., and J. Verestoy, "Feature Point Tracking for Incomplete Trajectories," *Computing*, Vol. 62, No. 4, 1999, pp. 321–338.
- [27] Veenman, C. J., M. J. T. Reinders, and E. Backer, "A Composite Model and Algorithm for Motion Correspondence," *Proceedings of the Sixth Annual Conference of the Advanced School for Computing and Imaging*, Belgium, June 2000.
- [28] Veenman, C. J., M. J. T. Reinders, and E. Backer, "Resolving Motion Correspondence for Densely Moving Points," *IEEE Transactions on Pattern Analysis and Machine Intelligence*, Vol. 23, No. 1, 2001, pp. 54–72.

- [29] Vallotton, P., A. Ponti, C. M. Waterman-Storer, E. D. Salmon, and G. Danuser, "Recovery, Visualization, and Analysis of Actin and Tubulin Polymer Flow in Live Cells: A Fluorescent Speckle Microscopy Study," *Biophysical Journal*, Vol. 85, October 2003, pp. 1289–1306.
- [30] Verestoy, J., and D. Chetverikov, "Experimental Comparative Evaluation of Feature Point Tracking Algorithms," *Proceedings of the Theoretical Foundations of Computer Vision, TFCV on Performance Evaluation in Computer Vision*, 1998, pp. 167–168.
- [31] Cheezum, M. K., W. F. Walker, and W. H. Guilford, "Quantitative Comparison of Algorithms for Tracking Single Fluorescent Particles," *Biophysical Journal*, Vol. 81, October 2001, pp. 2378–2388.
- [32] Bar-Shalom, Y., and T. E. Fortmann, *Tracking and Data Association*, New York: Academic Press, 1988.
- [33] Bar-Shalom, Y., and W. Dale Blair, *Multitarget-Multisensor Tracking Applications and Advances*, Vol. III, Norwood, MA: Artech House, 2000.
- [34] Apgar, J., Y. Tseng, E. Federov, M. Herwig, S. Almo, and D. Wirtz, "Multiple-Particle Tracking Measurements of Heterogeneities in Solutions of Actin Filaments and Actin Bundles," *Biophysical Journal*, Vol. 79, 2000, pp. 1095–1106.
- [35] Crocker, J. C., and D. G. Grier, "Methods of Digital Video Microscopy for Colloidal Studies," *Journal of Colloid and Interface Science*, Vol. 179, 1996, pp. 298–310.
- [36] Tvarusko, W., M. Bentele, T. Misteli, R. Rudolf, C. Kaether, D. L. Spector, H. H. Gerdes, and R. Eils, "Time-Resolved Analysis and Visualization of Dynamic Processes in Living Cells," *Cell Biology*, Vol. 96, July 1999, pp. 7950–7955.
- [37] Ponti, A., P. Vallotton, W. C. Salmon, C. M. Waterman-Storer, and G. Danuser, "Computational Analysis of F-Actin Turnover in Cortical Actin Meshworks Using Fluorescent Speckle Microscopy," *Biophysical Journal*, Vol. 84, May 2003, pp. 3336–3352.
- [38] Briquet-Laugier, F., C. Boulin, and J.-C. Olivo-Marin, "Analysis of Moving Biological Objects in Video Microscopy Sequences," *Proceedings of SPIE*, 1998, Vol. 3642, pp. 1–11.
- [39] Genovesio, A., and J. -C. Olivo-Marin, "Tracking Fluorescent Spots in Biological Video Microscopy," *Proceedings of SPIE—Three-Dimensional and Multidimensional Microscopy: Image Acquisition and Processing X*, J.-A. Conchello, C.J. Cogswell, and T. Wilson, Eds., January 2003, Vol. 4964, San Jose, California, pp. 98–105.
- [40] Genovesio, A., Z. Belhassine, and J.-C. Olivo-Marin, "Adaptive Gating in Gaussian bayesian Multi-Target Tracking," *Proceedings of the IEEE International Conference on Image Processing*, Vol. 1, October 2004, pp. 147–150.
- [41] Bonneau, S., M. Dahan, and L. D. Cohen, "Single Quantum Dot Tracking Based on Perceptual Grouping Using Minimal Paths in a Spatiotemporal Volume," *IEEE Transactions on Image Processing*, Vol. 14, No. 9, September 2005, pp. 1384–1395.
- [42] Sage, D., F. R. Neumann, F. Hediger, S. M. Gasser, and M. Unser, "Automatic Tracking of Individual Fluorescence Particles: Application to the Study of Chromosome Dynamics," *IEEE Transactions on Image Processing*, Vol. 14, No. 9, September 2005, pp. 1372–1384.
- [43] Thomann, D., D. R. Rines, P. K. Sorger, and G. Danuser, "Automatic Fluorescent Tag Detection in 3D with Super-Resolution: Application to the Analysis of Chromosome Movement," *Journal of Microscopy*, Vol. 208, No. 1, October 2002, pp. 49–64.
- [44] Arulampalam, M. S., S. Maskell, N. Gordon, and T. Clapp, "A Tutorial on Particle Filters for Online Nonlinear/Non-Gaussian Bayesian Tracking," *IEEE Transactions on Signal Processing*, Vol. 50, No. 2, 2002, pp. 174–188.
- [45] Cassidy, M. J., and W. D. Penny, "Bayesian Nonstationary Autoregressive Models for Biomedical Signal Analysis," *IEEE Transactions on Biomedical Engineering*, Vol. 49, No. 10, 2002, pp. 1142–1152.

- [46] Farina, A., "Cramér-Rao Bound for Nonlinear Filtering with  $P_d < 1$  and Its Application to Target Tracking," *IEEE Transactions on Signal Processing*, Vol. 50, No. 8, 2002, pp. 1916-1924.
- [47] Tao, H., H. S. Sawhney, and R. Kumar, "Object Tracking with Bayesian Estimation of Dynamic Layer Representations," *IEEE Transactions on Pattern Analysis and Machine Intelligence*, Vol. 24, No. 1, 2002, pp. 75-89.
- [48] Kalman, R. E., "A New Approach to Linear Filtering and Prediction Problems," *Transactions of the ASME-Journal of Basic Engineering*, Vol. 82, No. D, 1960, pp. 35-45.
- [49] Julier, S. J., J. K. Uhlmann, and H. F. Durrant-Whyte, "A New Approach for Filtering Nonlinear Systems," *Proceedings of the 1995 American Control Conference*, Washington, D.C., June 1995, pp. 1628-1632.
- [50] Isard, M., and A. Blake, "Contour Tracking by Stochastic Propagation of Conditional Density," *Proceedings of the European Conference on Computer Vision*, Vol. 1, 1996, pp. 343-356.
- [51] Doucet, A., "On Sequential Simulation-Based Methods for Bayesian Filtering," Technical report cued/f-infeng/tr.310, Signal Processing Group, Departement of Engineering, University of Cambridge CB2 1PZ Cambridge, 1998.
- [52] Blom, H. A. P., and Y. Bar-Shalom, "The Interacting Multiple Model Algorithm for Systems with Markovian Switching Coefficients," *IEEE Transactions on Automatic Control*, Vol. 33, No. 8, August 1988, pp. 780-783.
- [53] Blom, H. A. P., "An Efficient Filter for Abruptly Changing Systems," *Proceedings of the 23rd IEEE Conference on Decision and Control*, Las Vegas, NV, December 1984, pp. 656-658.
- [54] Genovesio, A., T. Liedl, V. Emiliani, W. J. Parak, M. Coppey-Moisán, and J.-C. Olivo-Marin, "Multiple Particle Tracking in 3D+T Microscopy: Methods and Application to the Tracking of Endocytosed Quantum Dots," *IEEE Transactions on Image Processing*, Vol. 15, No. 5, 2006, pp. 1062-1070.
- [55] Schutter, J. D., J. D. Geeter, T. Lefebvre, and H. Bruyninckx, *Kalman Filter: A Tutorial*, Division of Production Engineering, Machine Design and Automation (PMA) Celestijnenlaan 300 B, B-3001 Heverlee, Belgium and SCK CEN Belgian Nuclear Energy Research Center Boeretang 200, B-2400 Mol, Belgium Katholieke Universiteit Leuven, October 1999.
- [56] Genovesio, A., and J.-C. Olivo-Marin, "Tracking de Cibles Mouvantes Multiples en Vidéomicroscopie," *Proceedings of the International Conference on Image and Signal Processing*, Agadir, Morocco, June 2003, pp. 725-728.
- [57] Jang, D.-S., S.-W. Jang, and H.-I. Choi, "2D Human Body Tracking with Structural Kalman Filter," *Pattern Recognition*, Vol. 35, 2002, pp. 2041-2049.
- [58] Gil, S., and R. Milanes, "Comparing Features for Target Tracking in Traffic Scenes," *Pattern Recognition*, Vol. 29, No. 8, 1996, pp. 1285-1296.
- [59] Chen, Y., T. Huang, and Y. Rui, "Parametric Countour Tracking Using Unscented Kalman Filter," *Proc. IEEE Int. Conf. Image Processing ICIP 2002, III*, 2002, pp. 613-616.
- [60] Nguyen, H. T., and W. M. Smeulders, "Template Tracking Using Color Invariant Pixel Features," *Proceedings of the IEEE International Conference on Image Processing*, Vol. 1, 2002.
- [61] Nguyen Ngoc, S., F. Briquet-Laugier, C. Boulín, and J.-C. Olivo-Marin, "Adaptive Detection for Moving Biological Objects in Video Microscopy Sequences," *Proceedings of the International Conference on Image Processing*, Vol. 3, 1997, pp. 484-487.
- [62] Jang, D.-S., and H.-I. Choi, "Active Models for Tracking Moving Objects," *Pattern Recognition*, 2000, Vol. 33, pp. 1135-1146.

- [63] Peterfreund, N., "Robust Tracking of Position and Velocity with Kalman Snakes," *IEEE Transactions on Pattern Analysis and Machine Intelligence*, Vol. 21, No. 6, June 1999, pp. 564-569.
- [64] Hung, Y. S., "A Kalman Filter Approach to Direct Depth Estimation Incorporating Surface Structure," *IEEE Transactions on Pattern Analysis and Machine Intelligence*, Vol. 21, No. 6, June 1999, pp. 570-575.
- [65] Mehra, R. K., "On the Identification of Variances and Adaptive Kalman Filtering," *IEEE Transactions on Automatic Control*, Vol. 15, No. 2, April 1970, pp. 175-184.
- [66] Lee, H. G., and M. J. Tahk, "A New Input Estimation Algorithm for Target Tracking Problem," *Proceedings of the Korean Automatic Control Conference*, October 1998.
- [67] Reece, S., "Nonlinear Kalman Filtering with Semi-Parametric Biscay Distributions," *IEEE Transactions on Signal Processing*, Vol. 49, No. 11, 2001, pp. 2445-2453.
- [68] Johnston, L. A., and V. Krishnamurthy, "An Improvement to the Interacting Multiple Model (IMM) Algorithm," *IEEE Transactions on Image Processing*, Vol. 49, No. 12, 2001, pp. 2909-2923.
- [69] Jilkov, V. P., and X. R. Li, "Online Bayesian Estimation of Transition Probabilities for Markovian Jump Systems," *IEEE Transactions on Signal Processing*, Vol. 52, No. 6, June 2004, pp. 1620-1630.
- [70] Marques, J. S., and J. M. Lemos, "Optimal and Suboptimal Shape Tracking Based on Multiple Switched Dynamic Models," *Image and Vision Computing*, Vol. 19, 2001, pp. 539-550.
- [71] Tissainayagam, P., and D. Suter, "Performance Prediction Analysis of a Point Feature Tracker Based on Different Motion Models," *Computer Vision and Image Understanding*, Vol. 84, 2001, pp. 104-125.
- [72] Simeonova, I., and T. Semerdjiev, "Specific Features of IMM Tracking Filter Design," *Information and Security, an International Journal*, Vol. 9, 2002, pp. 154-165.
- [73] Nascimento, J. C., and J. S. Marques, "Improving the Robustness of Parametric Shape Tracking with Switched Multiple Models," *Pattern Recognition*, Vol. 35, 2002, pp. 2711-2718.
- [74] Carlin, B. P., N. G. Polson, and D. S. Stoffer, "A Monte Carlo Approach to Nonnormal and Non-Linear State-Space Modeling," *Journal of the American Statistical Association*, Vol. 87, No. 418, 1992, pp. 493-500.
- [75] Gordon, N., D. Salomon, and A. Smith, "Novel Approach to Nonlinear/Non-Gaussian Bayesian State Estimation," *IEE Proceedings F: Radar and Signal Processing*, Vol. 140, No. 2, 1993, pp. 107-113.
- [76] Kitagawa, G., "Monte Carlo Filter and Smoother for Non-Gaussian Non-Linear State Space Models," *Journal of Computational and Graphical Statistics*, Vol. 5, No. 1, 1996, pp. 1-25.
- [77] Isard, M., and A. Blake, "Condensation—Conditional Density Propagation for Visual Tracking," *International Journal of Computer Vision*, Vol. 29, No. 1, 1998, pp. 5-28.
- [78] Tao, H., and R. Kumar, "A Sampling Algorithm for Tracking Multiple Objects," *Proceedings of the International Conference on Computer Vision Workshop on Vision Algorithms*, Vol. 1883, September 2000, pp. 53-68.
- [79] Hue, C., and J. P. Le Cadre, "Sequential Monte Carlo Method for Multiple Target Tracking and Data Fusion," *IEEE Transactions on Signal Processing*, Vol. 50, No. 2, February 2002, pp. 309-325.
- [80] Orton, M., and W. Fitzgerald, "A Bayesian Approach to Tracking Multiple Targets Using Sensor Arrays and Particle Filters," *IEEE Transactions on Signal Processing*, Vol. 50, No. 2, February 2002, pp. 216-223.
- [81] Li, P., T. Zhang, and A. E. C Pece, "Visual Contour Tracking Based on Particle Filters," *IVC*, Vol. 21, No. 1, January 2003, pp. 111-123.



- [82] Bruno, M. G. S., "Bayesian Methods for Multiaspect Target Tracking in Image Sequences," *IEEE Transactions on Signal Processing*, Vol. 52, No. 7, July 2004, pp. 1848-1861.
- [83] Jacquet, P., and W. Szpankowski, "A Universal Predictor Based on Pattern Matching," *IEEE Transactions on Information Theory*, Vol. 48, No. 6, June 2002, pp. 1462-1472.
- [84] Larocque, J.-R., J. P. Reilly, and W. Ng, "Particle Filter for Tracking an Unknown Number of Sources," *IEEE Transactions on Signal Processing*, Vol. 50, No. 12, December 2002, pp. 2926-2937.
- [85] Wang, F., "Robust Kalman Filters for Linear Time-Varying Systems with Stochastic Parametric Uncertainties," *IEEE Transactions on Signal Processing*, Vol. 50, No. 4, 2002, pp. 803-813.
- [86] Arnaud, E., and E. Mémín, "Optimal Importance Sampling for Tracking in Image Sequences: Application for Tracking in Image Sequences," *Proceedings of the European Conference on Computer Vision*, Prague, Czech Republic, May 2004.
- [87] Kotecha, J. H., and P. M. Djurić, "Gaussian Sum Particle Filtering," *IEEE Transactions on Signal Processing*, Vol. 51, No. 10, 2003, pp. 2602-2612.
- [88] Kotecha, J. H., and P. M. Djurić, "Gaussian Particle Filtering," *IEEE Transactions on Signal Processing*, Vol. 51, No. 10, 2003, pp. 2592-2601.
- [89] Smal, I., W. Niessen, and E. Meijering, "Advanced Particle Filtering for Multiple Object Tracking in Dynamic Fluorescence Microscopy Images," *4th IEEE International Symposium on Biomedical Imaging*, Washington D.C., April 2007.
- [90] Fortmann, T., Y. Bar-Shalom, and M. Scheffe, "Multi-Target Tracking Using Joint Probabilistic Data Association," *Proceedings of the 19th IEEE Conference on Decision Control*, December 1980.
- [91] Reid, D. B., "An Algorithm for Tracking Multiple Targets," *IEEE Transactions on Automatic Control*, Vol. AC-24, December 1979, pp. 843-854.
- [92] Cox, I. J., and S. L. Hingorani, "An Efficient Implementation of Reid's Multiple Hypothesis Tracking Algorithm and Its Evaluation for the Purpose of Visual Tracking," *IEEE Transactions on Pattern Analysis and Machine Intelligence*, Vol. 18, No. 2, February 1996, pp. 138-150.
- [93] Jonker, R., and A. Volgenant, "A Shortest Augmenting Path Algorithm for Dense and Sparse Linear Assignment Problems," *Computing*, Vol. 38, 1987, pp. 325-340.
- [94] Kuhn, H. K., "The Hungarian Method for Solving the Assignment Problem," *Naval Research Logistics Quarterly*, Vol. 2, 1995, pp. 83-97.
- [95] Buckley, K., A. Vaddiraju, and R. Perry, "A New Pruning/Merging Algorithm for MHT Multitarget Tracking," *Proc. Radar*, May 2000.
- [96] Murty, K. G., "An Algorithm for Ranking All the Assignments in Order of Increasing Cost," *Operations Research*, Vol. 16, 1968, pp. 682-687.
- [97] Willet, P., Y. Ruan, and R. Streit, "Pmht: Problems and Some Solutions," *IEEE Transactions on Aerospace and Electronic Systems*, Vol. 38, No. 3, 2002, pp. 738-754.
- [98] Rasmussen, C., and G. Hager, "Probabilistic Data Association Methods for Tracking Visual Objects," *IEEE Transactions on Pattern Analysis and Machine Intelligence*, Vol. 23, No. 6, June 2001, pp. 560-576.
- [99] Willet, P., R. Niu, and Y. Bar-Shalom, "Integration of Bayes Detection with Target Tracking," *IEEE Transactions on Signal Processing*, Vol. 49, No. 1, January 2001, pp. 17-29.
- [100] Genovesio, A., B. Zhang, and J.-C. Olivo-Marin, "Tracking of Multiple Fluorescent Biological Objects in Three Dimensional Video Microscopy," *Proceedings of the IEEE International Conference on Image Processing*, Barcelona, Spain, Vol. 1, September 2003, pp. 1105-1108.



- [101] Arhel, N., A. Genovesio, K. A. Kim, S. Miko, E. Perret, J.-C. Olivo-Marin, S. Shorte, and P. Charneau, "Quantitative Four-Dimensional Tracking of Cytoplasmic and Nuclear HIV-1 Complexes," *Nature Methods*, Vol. 3, 2006, pp. 817-24.
- [102] Mairey, E., E. Donnadieu, A. Genovesio, J.-C. Olivo-Marin, X. Nassif, and G. Dumenil, "Cerebral Microcirculation Shear Stress Levels Determine Neisseria Meningitidis Attachment Sites Along the Blood-Brain Barrier," *Journal of Experimental Medicine*, Vol. 8, 2006, pp. 1939-1950.
- [103] Danuser, G., "Super-Resolution Tracking of Weak Fluorescent Markers in 3D: Application in Dissecting the Mechanics of Chromosome Segregation Using Fluorescence Imaging and Molecular Genetics in Yeast," *Proceedings of the Second 2004 IEEE International Symposium on Biomedical Imaging: From Nano to Macro (ISBI'04)*, 2004.
- [104] Genovesio, A., and J.-C. Olivo-Marin, "Split and Merge Data Association Filter for Dense Multi-Target Tracking," *Proceedings of the International Conference on Pattern Recognition*, Cambridge, United Kingdom, August 2004.

## Appendix 10A Pseudocodes for the Algorithms

---

### Algorithm 10.1 Kalman Filter

---

**Require:**  $F_t, H_t, Q_t, R_t, z_t, x_{t-1|t-1}$  and  $P_{t-1|t-1}$

**Ensure:**  $x_{t|t}$  et  $P_{t|t}$

{Prediction:}

$$x_{t|t-1} = F_t x_{t-1|t-1}$$

$$P_{t|t-1} = F_t P_{t-1|t-1} F_t^T + Q_t$$

{Update:}

$$z_t = \text{measurement}()$$

$$S_t = H_t P_{t|t-1} H_t^T + R_t$$

$$K_t = P_{t|t-1} H_t^T S_t^{-1}$$

$$x_{t|t} = x_{t|t-1} + K_t (z_t - H_t x_{t|t-1})$$

$$P_{t|t} = P_{t|t-1} - K_t H_t P_{t|t-1}$$


---

---

### Algorithm 10.2 Grid-Based Filter

---

**Require:**  $\{x_{t-1}^i, w_{t-1|t-1}^i\}, i = 1, \dots, N, p(z_t|x_t), p(x_t|x_{t-1})$  and  $z_t$

**Ensure:**  $\{x_t^i, w_{t|t}^i\}, i = 1, \dots, N$

{Prediction:}

for  $i=1 \rightarrow N$  do

  for  $j=1 \rightarrow N$  do

$$w_{t|t-1}^j += w_{t-1|t-1}^j p(x_t^i | x_{t-1}^j)$$

  end for

end for

{Update:}

$$z_t = \text{measurement}()$$

for  $i=1 \rightarrow N$  do

$$w_{t|t}^i += w_{t|t-1}^i p(z_t | x_t^i)$$

end for

---

```

for i=1→N do
     $w_{t|t}^i = \frac{w_{t|t-1}^i p(z_t | \mathbf{x}_t^i)}{w_{t|t}^i}$ 
end for

```

---



---

**Algorithm 10.3** Extended Kalman Filter

---

**Require:**  $f_t$  differentiable,  $h_t$  differentiable,  $Q_t$ ,  $R_t$ ,  $z_t$ ,  $\mathbf{x}_{t-1|t-1}$  and  $P_{t-1|t-1}$

**Ensure:**  $\mathbf{x}_{t|t}$  et  $P_{t|t}$

```

{Prediction:}
 $\hat{\mathbf{F}}_t = \left. \frac{df_t(\mathbf{x})}{d\mathbf{x}} \right|_{\mathbf{x}=\mathbf{x}_{t-1|t-1}}$ 
 $\hat{\mathbf{H}}_t = \left. \frac{dh_t(\mathbf{x})}{d\mathbf{x}} \right|_{\mathbf{x}=\mathbf{x}_{t|t-1}}$ 
 $\mathbf{x}_{t|t-1} = f_t(\mathbf{x}_{t-1|t-1})$ 
 $P_{t|t-1} = \hat{\mathbf{F}}_t P_{t-1|t-1} \hat{\mathbf{F}}_t^T + Q_t$ 

{Update:}
 $z_t = \text{measurement}()$ 
 $S_t = \hat{\mathbf{H}}_t P_{t|t-1} \hat{\mathbf{H}}_t^T + R_t$ 
 $K_t = P_{t|t-1} \hat{\mathbf{H}}_t^T S_t^{-1}$ 
 $\mathbf{x}_{t|t} = \mathbf{x}_{t|t-1} + K_t (z_t - h_t(\mathbf{x}_{t|t-1}))$ 
 $P_{t|t} = P_{t|t-1} - K_t \hat{\mathbf{H}}_t P_{t|t-1}$ 

```

---



---

**Algorithm 10.4** Interacting Multiple Model Filter

---

**Require:**  $r$  Kalman filters ( $F_t^j$ ,  $H_t^j$ ,  $Q_t^j$ ,  $R_t^j$ ,  $\mathbf{x}_{t-1|t-1}^j$ ,  $P_{t-1|t-1}^j$ ),  $p_{ij}$ ,  $\mu_{t-1|t-1}^i$  and  $z_t$

**Ensure:**  $\mathbf{x}_{t|t}$  et  $P_{t|t}$

```

{1 - Interaction :}
for j=1→r do
    for i=1→rdo
         $\mu_{t|t-1}^i += p_{ij} \mu_{t-1|t-1}^i$ 
    end for
end for

for j=1→r do
    for i=1→r do
         $\mu_{t-1|t-1}^{ij} = \frac{p_{ij} \mu_{t-1|t-1}^i}{\mu_{t|t-1}^i}$ 
    end for
end for

for j=1→r do
    for i=1→r do
         $\mathbf{x}_{t-1|t-1}^{0j} += \mu_{t-1|t-1}^{ij} \mathbf{x}_{t-1|t-1}^i$ 
         $P_{t-1|t-1}^{0j} += \mu_{t-1|t-1}^{ij} \left\{ P_{t-1|t-1}^i + \left[ \mathbf{x}_{t-1|t-1}^i - \mathbf{x}_{t-1|t-1}^{0j} \right] \left[ \mathbf{x}_{t-1|t-1}^i - \mathbf{x}_{t-1|t-1}^{0j} \right]^T \right\}$ 
    end for
end for

```

---

---

```

{2 - Update of each filter (distributable computing) :}
for j=1→r do
   $\mathbf{x}_{t|t-1}^j, \mathbf{P}_{t|t-1}^j \leftarrow$  Kalman prediction for model  $j$ 
end for
{3 - Update of each filter (distributable computing) :}
 $\mathbf{z}_t = \text{measurement}()$ 
for j=1→r do
   $\mathbf{S}_t^j, \mathbf{K}_t^j, \mathbf{x}_{t|t}^j, \mathbf{P}_{t|t}^j \leftarrow$  Kalman update for model  $j$ 
end for
{4 - Update of switching probabilities:}
for j=1→r do
   $\Lambda_t^j = \frac{1}{\sqrt{\det[2\pi\mathbf{S}_t^j]}} \exp\left\{\frac{-1}{2} [\tilde{\mathbf{z}}_t^j]^T [\mathbf{S}_t^j]^{-1} \tilde{\mathbf{z}}_t^j\right\}$ 
 $\mu_{t|t}^j = \frac{\mu_{t|t-1}^j \Lambda_t^j}{\sum_{i=1}^r \mu_{t|t-1}^i \Lambda_t^i}$ 
end for
{5 - Estimation:}
for j=1→r do
   $\mathbf{x}_{t|t} \mathrel{+}= \mu_{t|t}^j \mathbf{x}_{t|t}^j$ 
 $\mathbf{P}_{t|t} \mathrel{+}= \mu_{t|t}^j \left\{ \mathbf{P}_{t|t}^j + [\mathbf{x}_{t|t}^j - \mathbf{x}_{t|t}] [\mathbf{x}_{t|t}^j - \mathbf{x}_{t|t}]^T \right\}$ 
end for

```

---



---

**Algorithm 10.5** Particle Filter SIS

---

**Require:**  $\{\mathbf{x}_{t-1}^i, w_{t-1}^i\}_{i=1}^N$ ,  $p(\mathbf{z}_t|\mathbf{x}_t)$ ,  $p(\mathbf{x}_t|\mathbf{x}_{t-1})$ ,  $x^i \sim q(\mathbf{x}_t|\mathbf{x}_{t-1}^i, \mathbf{z}_t)$  and  $\mathbf{z}_t$

**Ensure:**  $\{\mathbf{x}_t^i, w_t^i\}_{i=1}^N$

```

{1 - Initialization:}
 $\mathbf{z}_0 = \text{measurement}()$ 
for i=1→N do
   $\mathbf{x}_0^i \sim q(\mathbf{x}_0|\mathbf{z}_0)$ 
   $w_0^i = \frac{1}{N}$ 
end for

{2 - Sample particles, compute the non normalized weights and the total weight
(distributable computing)}
 $\mathbf{z}_t = \text{measurement}()$ 
for i=1→N do
   $\mathbf{x}_t^i \sim q(\mathbf{x}_t|\mathbf{x}_{t-1}^i, \mathbf{z}_t)$ 
 $w_t^i = w_{t-1}^i \frac{p(\mathbf{z}_t|\mathbf{x}_t^i)p(\mathbf{x}_t^i|\mathbf{x}_{t-1}^i)}{q(\mathbf{x}_t^i|\mathbf{x}_{t-1}^i, \mathbf{z}_t)}$ 
 $w_t \mathrel{+}= w_t^i$ 
end for

```

```

{3 - Compute the normalized weights:}
for i=1→N do
     $w_t^i = \frac{w_t^i}{w_t}$ 
end for

{Go to 2}

```

---



---

**Algorithm 10.6** Resampling

---

**Require:**  $\{\mathbf{x}_t^i, w_t^i\}_{i=1}^N$

**Ensure:**  $\{\mathbf{x}_t'^i, w_t'^i\}_{i=1}^N$

```

{Particles to resample are randomly selected with a probability associated with their weight.}
for i=1→N do

    {Sample  $u$  from a uniform law on  $[0,1]$ : }
     $u \sim U(0,1)$ 

    {Find the smallest  $j$  such that the cumulated weight is inferior to  $u$ :}
     $w = 0$ 
     $j = 1$ 
    while  $w < u$  do
         $w += w_t^j$ 
         $j += 1$ 
    end while

    {Create a new particle:}
     $\mathbf{x}_t'^i = \mathbf{x}_t^j$ 
     $w_t'^i = \frac{1}{N}$ 
end for

```

---



---

**Algorithm 10.7** Particle Filter with Resampling

---

**Require:**  $\{\mathbf{x}_{t-1}^i, w_{t-1}^i\}_{i=1}^N$ ,  $p(\mathbf{z}_t|\mathbf{x}_t)$ ,  $p(\mathbf{x}_t|\mathbf{x}_{t-1})$ ,  $x^i \sim q(\mathbf{x}_t|\mathbf{x}_{t-1}^i, \mathbf{z}_t)$  and  $\mathbf{z}_t$

**Ensure:**  $\{\mathbf{x}_t^i, w_t^i\}_{i=1}^N$

```

{1 - Initialization:}
 $\mathbf{z}_0 = \text{measurement}()$ 
for i=1→N do
     $\mathbf{x}_0^i \sim q(\mathbf{x}_0|\mathbf{z}_0)$ 
     $w_0^i = \frac{1}{N}$ 
end for

```

```

{2 - Sample particles, compute the nonnormalized weights and the total weight
(distributable computing):}
 $\mathbf{z}_t = \text{measurement}()$ 

```

---

```

for i=1→N do
   $x_t^i \sim q(x_t | x_{t-1}^i, z_t)$ 
   $w_t^i = w_{t-1}^i \frac{p(z_t | x_t^i) p(x_t^i | x_{t-1}^i)}{q(x_t^i | x_{t-1}^i, z_t)}$ 
   $w_t += w_t^i$ 
end for

{3 - Compute the normalized weights:}
for i=1→N do
   $w_t^i = \frac{w_t^i}{w_t}$ 
end for

{4 - Resample if necessary:}
for i=1→N do
   $w_{2t} += (w_t^i)^2$ 
end for
 $n_{\text{eff}} = \frac{1}{w_{2t}}$ 
if  $n_{\text{eff}} < \frac{N}{4}$  then
   $\{x_t^i, w_t^i\}_{i=1}^N = \text{Resample}(\{x_t^i, w_t^i\}_{i=1}^N)$ 
end if

{Go to 2}

```

---



---

**Algorithm 10.8** Suboptimal Nearest Neighbor Association

---

**Require:**  $Z_t = \{z_t^1, \dots, z_t^M\}$  and  $Z_{t|t-1} = \{z_{t|t-1}^1, \dots, z_{t|t-1}^N\}$

**Ensure:**  $\theta$  sub optimal

```

{Compute the likelihoods:}
for i=1 →N do
  for j=1 →M do
    Compute  $c_{ij}$  with (10.110)
  end for
end for

{Initialization:}
 $I = \{1, \dots, N\}$ 
 $J = \{1, \dots, M\}$ 

{Associations:}
while  $I \neq \{\emptyset\}$  AND  $J \neq \{\emptyset\}$  do
   $\theta_{ij} = \{(i,j), \min_{i,j} c_{ij}\}$ 
   $I = I \setminus \{i\}$ 
   $J = J \setminus \{j\}$ 
end while

```

---

**Algorithm 10.9** MHT Association**Require:**  $Z_{1:t}$ **Ensure:**  $\Theta_{1:t}$  suboptimal

{1 - Initialization to  $t=0$ : generate first hypotheses—that is, all probabilities such that:  
 - a measurement is a clutter  
 - a measurement is an object}

{2 - Set the probability of an hypothesis to  $\lambda_F^\phi$  with  $\phi$  the number of clutter in this hypothesis}

{3 - Normalize those probabilities}

**for**  $t=1 \rightarrow T$  **do**

  {4 - Add a level to the hypothesis tree, that is, generate all hypothesis of feasible joint association event  $\theta^t$  such that:  
   - a measurement is associated to a track if it is validated by this track  
   - a track is associated with at most one measurement  
   - a measurement that is not associated with an existing track is either a clutter or a new object}

  {5 - Compute the probability of each hypothesis of cumulated feasible joint association event  $\Theta_{1:t}^t$  with (10.115)}

  {6 - Normalize those probabilities}

  {7 - Pruning 1 (N-scan-back):  
   - climb back to  $d$  levels in the hypothesis tree  
   - compute the sum of probabilities of all subtrees for each node at this level  
   - keep only the subtree which has the highest probability}

  {8 - Pruning 2: keep only the  $k$  hypotheses of highest probabilities}

**end for**

{9 - Association: climb back the tree from the hypothesis  $\Theta_{1:t}$  of highest probability to reconstruct the association sequence}

**Algorithm 10.10** Probabilistic Data Association**Require:**  $\forall t, F_t, H_t, Q_t, R_t, Z_t, x_{0|0}$  and  $P_{0|0}$ **Ensure:**  $\forall t > 1, x_{t|t}$  et  $P_{t|t}$ 

**for**  $t=1 \rightarrow T$  **do**

  {1 - Prediction:}  
 $x_{t|t-1} = F_t x_{t-1|t-1}$   
 $P_{t|t-1} = F_t P_{t-1|t-1} F_t^T + Q_t$

  {2 - Update:}  
 $Z_t = \text{measurements}()$   
 $S_t = H_t P_{t|t-1} H_t^T + R_t$   
 $K_t = P_{t|t-1} H_t^T S_t^{-1}$   
   Initialize  $\beta_0$  with (10.123)  
   Compute all the  $\beta_i$  with (10.122)  
 $x_{t|t} = x_{t|t-1} + K_t \sum_{i=1}^m \beta_i [z_t^i - H_t x_{t|t-1}]$   
 $P_{t|t} = \beta_0 P_{t|t-1} + [1 - \beta_0] P_t^c + \tilde{P}_t$

**end for**

---

**Algorithm 10.11** Joint Probabilistic Data Association
 

---

**Require:**  $\forall t, \forall i, \mathbf{F}_t^i, \mathbf{H}_t^i, \mathbf{Q}_t^i, \mathbf{R}_t^i, \mathbf{Z}_t^i, \mathbf{x}_{0|0}^i$  and  $\mathbf{P}_{0|0}^i$

**Ensure:**  $\forall t > 1, \forall i, \mathbf{x}_{t|t}^i$  et  $\mathbf{P}_{t|t}^i$

```

for  $t=1 \rightarrow T$ 
  for  $i=0 \rightarrow N$  do
    {1 - Prediction:}
     $\mathbf{x}_{t|t-1}^i = \mathbf{F}_t^i \mathbf{x}_{t-1|t-1}^i$ 
     $\mathbf{P}_{t|t-1}^i = \mathbf{F}_t^i \mathbf{P}_{t-1|t-1}^i [\mathbf{F}_t^i]^T + \mathbf{Q}_t^i$ 
  end for
   $\mathbf{Z}_t = \text{measurements}()$ 

  {2 - Find all feasible joint association events:
  - a measurement can be generated by an object
  - a measurement can be a clutter
  - an object can generate at most one measurement}

  {3 - Compute the joint probabilities  $P\{\theta | \mathbf{Z}_{1:t}\}$  with (10.132), the marginal
  probabilities  $\beta_{ij}$  of each association with (10.135), and  $\beta_{i0}$  with (10.123).}

  {4 - Update:}
  for  $i=0 \rightarrow N$ 
     $\mathbf{S}_t^i = \mathbf{H}_t^i \mathbf{P}_{t|t-1}^i [\mathbf{H}_t^i]^T + \mathbf{R}_t^i$ 
     $\mathbf{K}_t^i = \mathbf{P}_{t|t-1}^i \mathbf{H}_t^{iT} [\mathbf{S}_t^i]^{-1}$ 
     $\mathbf{x}_{t|t}^i = \mathbf{x}_{t|t-1}^i + \mathbf{K}_t^i \sum_{j=1}^m \beta_{ij} [z_t^j - \mathbf{H}_t^i \mathbf{x}_{t|t-1}^i]$ 
     $\mathbf{P}_{t|t}^i = \beta_{i0} \mathbf{P}_{t|t-1}^i + [1 - \beta_{i0}] [\mathbf{P}^i]_t^c + \tilde{\mathbf{P}}_t^i$ 
  end for
end for

```

---



# Automated Analysis of the Mitotic Phases of Human Cells in 3-D Fluorescence Microscopy Image Sequences

Nathalie Harder, Felipe Mora-Bermúdez, William J. Godinez, Jan Ellenberg, Roland Eils, and Karl Rohr

## 11.1 Introduction

In recent years the technology of *RNA interference* (RNAi) has become the method of choice for identifying the biological function of genes in the field of functional genomics. With this screening method all known genes of an organism are systematically silenced, one after the other, and the resulting morphological changes are analyzed. However, such large-scale knockdown screens provide enormous amounts of data, which require tools for automated image analysis.

Our work is carried out within the European Union project MitoCheck, which aims to explore the coordination of mitotic processes in human cells at a molecular level and to contribute to revealing the mechanisms of cancer development. To identify the genes that are involved in cell division (mitosis), genome-wide high-throughput RNAi primary screens are performed. In addition, RNAi secondary screens are performed, and they have a higher spatial and temporal resolution and involve several hundred genes. Fluorescence microscopy time-lapse images of the treated cell cultures are acquired to study the effect of the silenced genes on mitosis. This contribution is concerned with the automated evaluation of an assay to analyze the duration of the different phases in mitotic progression. The goal is to identify significant elongations of mitotic phases caused by gene knockdown. To automatically detect whether mitotic phases of treated cells are longer than normal cells, cells have to be observed throughout their life cycle, and for each time point the respective phase has to be determined.

Previous work on automated analysis of cell images has been done in different application fields. Based on fluorescence microscopy imaging, complete cells as well as single subcellular structures have been studied. The automated recognition of subcellular structures is a major task in location proteomics, and work has been done in this field given 2-D (e.g., [1,2]) and 3-D (e.g., [3]) single-cell images. Classification of complete cells has been performed, for example, to investigate the influence of drugs on cellular proteins [4]. In [5] tracking of cells in 2-D microscopy images has been used to improve segmentation and cell quantification. Automated analysis of cell images plays an increasingly important role, particularly for the evaluation of high-throughput cell phenotype screens. Approaches for *single-frame* multicell 2-D images have been described in [6–8]. Recently, work

has been done on automatically processing multicell 2-D time-lapse images. In [9] level set methods and a Kalman filter have been used to track complete cells in 2-D phase-contrast microscopy images. In [10] and in chapter 12, a level set segmentation scheme has been applied to track mitotic nuclei in 2-D fluorescence microscopy images, where the cells have been marked with a dynamic cell cycle marker. The latter two approaches enable a classification of the cells into no more than four different cell cycle phases.

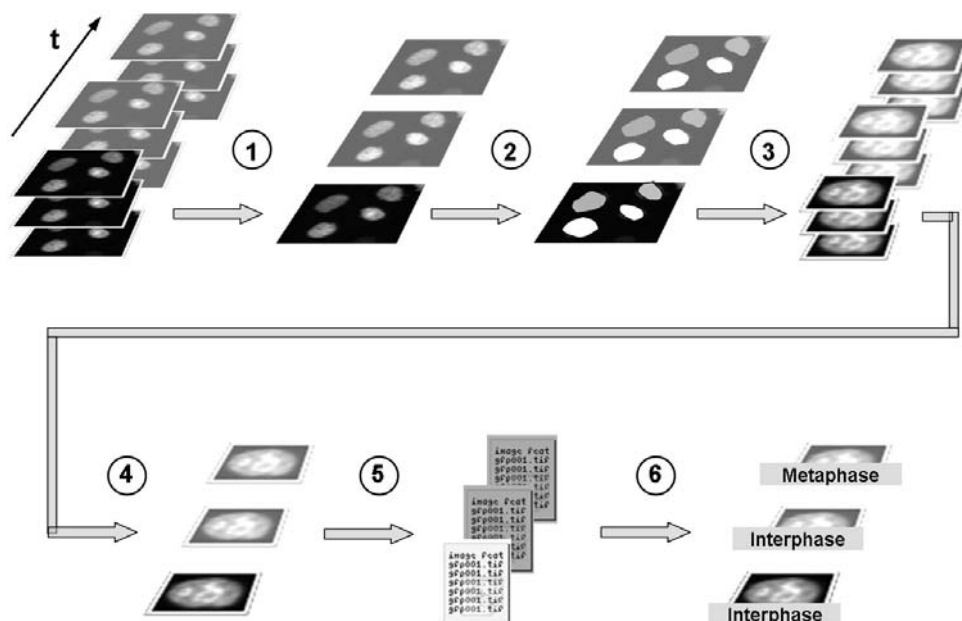
We have developed an approach to analyze multicell *image sequences* from large-scale RNAi secondary screens. In comparison to previous work, we analyze 3-D cell array time-lapse images that include multiple cell nuclei in *different mitotic phases*. Each image of an image sequence contains three slices that have been acquired with a confocal fluorescence microscope. Our computational scheme for analyzing the duration of mitotic phases consists of four main steps: segmentation of multicell images, tracking of cells, image feature extraction, and classification into seven mitotic phases. For fast and accurate segmentation, we use a region adaptive thresholding technique. Our tracking scheme is able to cope with the splitting of cells during mitosis, which is important in our application. With this scheme tree-structured tracks, which represent cell pedigrees, are computed. Based on the tracking result we automatically select the most informative slice out of the 3-D image, which is then used for feature extraction. Compared to previous work, we incorporate temporal changes of the cell morphology between ancestrally related cells by directly including dynamic image features. A support vector machine classifier is used to classify the cells into the following seven mitotic phases: *Interphase*, *Prophase*, *Prometaphase*, *Metaphase*, *Anaphase1*, *Anaphase2*, and *Telophase*. Based on the classification result in subsequent images, the duration of the different phases can be determined.

Our approach has been successfully applied to four image sequences from large-scale RNAi screens. We have compared the performance with ground truth provided by manual evaluation, and it turned out that we obtain an average accuracy of around 89% and an overall accuracy of 94.6% for the classification.

## 11.2 Methods

### 11.2.1 Image Analysis Workflow

For a detailed analysis of the different phases of dividing cells, high-resolution confocal fluorescence microscopy images of the cell nuclei have been acquired. Compared to previous work we here use 3-D images consisting of three confocal planes (slices). The reason to use several confocal planes is that cells change their morphology during mitosis (i.e., in the interphase they are flat, but with the beginning of cell division they arch upward and take the shape of a hemisphere). Therefore, if we would use the same focal plane throughout the cell cycle, the chromatin structure could not be observed in all phases. Since we are using multicell images that contain cells in different mitotic phases, it is impossible to define one focal plane per time step that represents all cells well. Therefore, three slices from three different focal planes that cover the range of possible cell shape changes



**Figure 11.1** Image analysis workflow. (1) Maximum intensity projection of multicell 3-D images, (2) segmentation and tracking in multicell 2-D images, (3) extraction of 3-D regions of interest including single cells based on the segmentation and tracking results, (4) selection of most informative slice, (5) image feature extraction, and (6) classification.

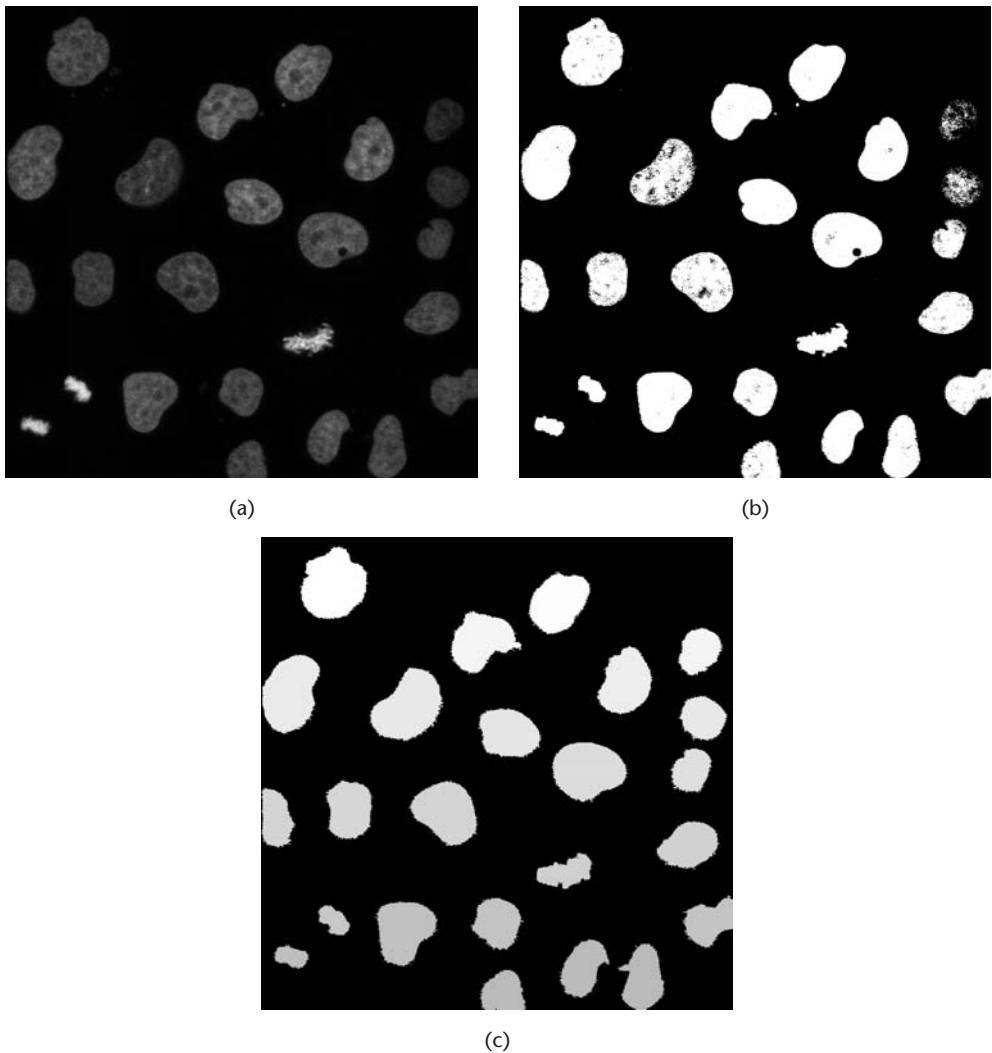
are acquired. Because of technical reasons in the image acquisition process, the number of slices is restricted to three. This relatively small number of slices does not allow a complete 3-D analysis. Thus, we apply the workflow shown in Figure 11.1 for automated analysis. In the first step, we apply a maximum intensity projection (MIP) for each time step, resulting in 2-D multicell images. In the second step, we perform segmentation and tracking based on these MIP images to determine the correspondences of cell nuclei in subsequent frames. Based on the segmentation and tracking result, we now go back to the original 3-D images and define 3-D regions of interest (ROIs) for each cell. For each 3-D ROI we choose the slice that contains the most information for feature selection. The reason for using the single slice images instead of the projected images is that these images contain more detailed information about the inner intensity structure (e.g., the texture) of a nucleus than the MIP images. Finally, static and dynamic image features are extracted, and classification is performed resulting in a sequence of cell cycle phases for each cell trajectory.

### 11.2.2 Segmentation of Multicell Images

Since we have to cope with a large number of multicell images, fast and reliable segmentation of single objects is crucial. Various advanced segmentation algorithms have been described in the literature, but as computation time plays an important role in our application, the speed of the algorithm is a decisive criterion. We have investigated different thresholding techniques that we have previously used

for analyzing static 2-D multicell images [8]. It turned out that computing one threshold for the whole image (*global thresholding*) does not produce satisfying results, especially for low-contrast cells (see Figure 11.2(b)). Instead, computing local thresholds for subregions of the image (*local adaptive thresholding*) results in an accurate segmentation of the cell nuclei (see Figure 11.2(c)). Consequently, we apply the following technique for region adaptive thresholding.

The algorithm uses a quadratic sliding window to calculate local thresholds for different image regions. A local threshold is only calculated if the variance within the window reaches a user-defined threshold, else a global threshold is used [11]. This ensures that the local threshold is calculated only for regions that contain some information, which significantly reduces the computation time. The computed local



**Figure 11.2** Segmentation example. (a) Original image. (b) Segmentation result using global Otsu threshold. (c) Segmentation result using local adaptive thresholding.

threshold can be applied to the image in three different ways: (1) only to the central pixel of the sliding window, (2) to a quadratic subregion at the center of the window, or (3) to the whole region enclosed by the window. Version (1) produces results of the highest accuracy but on the other hand requires the highest computation time since the threshold computation has to be performed for each single pixel. Version (3) is quickest but is prone to produce segmentation errors at the transitions of adjacent windows that have highly differing thresholds. A good tradeoff between computation time and segmentation accuracy can be achieved with version (2). Since adjacent windows partly overlap, changes of the computed thresholds are less abrupt, which significantly reduces segmentation errors. Still, the computation time is much lower than for version (1) since not single pixels but whole regions are thresholded at once. Hence, we used version (2) to segment the projected images. For our data, a window width of about the radius of an average cell nucleus and a subregion width of 4 pixels produced best results.

To calculate the global and the local intensity thresholds, we applied two histogram-based threshold, selection schemes: *Otsu* thresholding [12] and *minimum error* thresholding [13]. We found that the combination of [12] to determine the global threshold and [13] to determine the local thresholds yielded the best results (see Figure 11.2(c)). After threshold-based segmentation, a hole-filling and a labeling algorithm are applied.

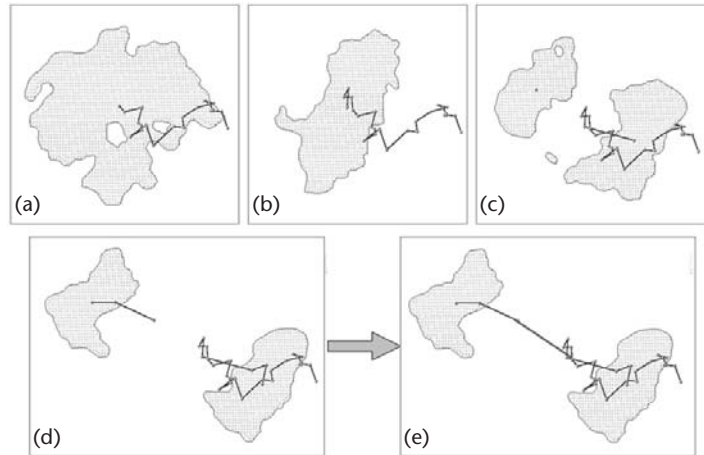
### 11.2.3 Tracking of Mitotic Cell Nuclei

To analyze the mitotic behavior of single cells in multicell images, a tracking scheme that determines the temporal connections and can handle splitting objects is required. We have developed the following two-step tracking scheme. First, initial, nonsplitting trajectories are established, and second, mitotic events are detected and the related trajectories are merged.

In the first step, the initial trajectories are determined using a feature point tracking algorithm based on [14]. As feature points we use the centers of gravity of segmented cell nuclei. For each frame of an image sequence, the algorithm considers the predecessor and the successor frame. In these frames, object correspondences are determined by searching for trajectories with maximum smoothness. For one feature point the smoothness of trajectories is determined with all potential predecessor and successor feature points within a certain Euclidean distance. To this end, the following cost function described in [14] is applied

$$\delta(\vec{u}, \vec{v}) = w_1 \left( 1 - \frac{\vec{u} \cdot \vec{v}}{|\vec{u}| \cdot |\vec{v}|} \right) + w_2 \left( 1 - \frac{2 \cdot (|\vec{u}| \cdot |\vec{v}|)^{1/2}}{|\vec{u}| + |\vec{v}|} \right) \quad (11.1)$$

Here,  $\vec{u}$  and  $\vec{v}$  represent the displacement vectors from the predecessor frame to the current frame and from the current frame to the successor frame, and  $w_1, w_2$  are two positive weights. The first term represents the angle between adjacent displacement vectors. Large angles (i.e., sudden changes of the direction) are punished with higher costs, compared to trajectories with smaller angles and thus smoother changes of direction. The second term takes into account the change in the distance



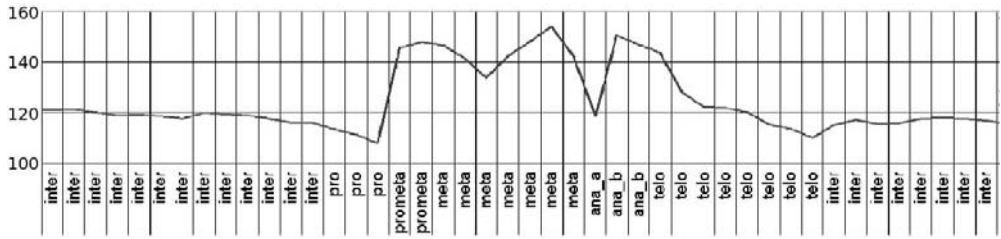
**Figure 11.3** Tracking example. (a–c) Tracking of a segmented mitotic nucleus, (d) result without mitosis detection, and (e) result after mitosis detection and track merging.

of corresponding feature points by exploiting the ratio of the geometric mean and the arithmetic mean of the distances. Here, trajectories with strongly changing distances cause higher costs than those with relatively smoothly changing distances. The influence of the changes of the direction and the distance on the result can be controlled by using the weights  $w_1$  and  $w_2$  for the two terms.

In the second step, all trajectories that do not start in the first frame are taken into account as possible mitosis events. The decision whether a trajectory should be treated as mitosis event is made depending on the overlap-distance ratio of potential parent and child objects [15]. Large overlaps and short distances indicate a high likelihood for an ancestral relationship. If the computed overlap-distance ratio exceeds an experimentally determined threshold of 0.2, we assume a mitosis event, and the corresponding tracks are finally merged resulting in tree-structured trajectories. As an example, Figure 11.3 shows the trajectories of a splitting cell nucleus before and after mitosis detection.

#### 11.2.4 Extraction of Static and Dynamic Features

As described in Section 11.2.1, we compute for each cell nucleus 3-D regions of interest in the original 3-D images. Within these ROIs we select the cell's individual *most informative slice* in order to compute image features. Two selection criteria for determining the slice that contains the most information have been tested: the maximum total intensity and the maximum entropy. We found that the *maximum-intensity* criterion performs very well compared to manual selection, whereas the *maximum-entropy* criterion often fails and shows a high sensitivity to noise. Consequently, we here apply the *maximum-intensity* criterion. The reason for using the original image slices for feature extraction is because using the projected images would implicate a loss of information concerning the original intensity structure. In particular, fine textures, which are important for the classification of certain



**Figure 11.4** Dynamic features. Mean intensity for a dividing cell and manually assigned phases of mitosis.

phases (e.g., early Prophase when the chromatin starts to condense), are blurred in the projected images.

Within the most informative slice, we compute a set of static and dynamic features for each cell nucleus. The static features comprise granularity features, object- and edge-related features, tree-structured wavelet features [16], Haralick texture features [17], grayscale invariants [18], and Zernike moments [19]. The dynamic features represent the morphological changes of cells in adjacent frames. To this end, we compute the difference of three basic features (*object size*, *mean intensity*, and *standard deviation of the intensity*) for each cell to its predecessor and to its successor. We chose these three features because they exhibit characteristic changes during mitosis. As an example, Figure 11.4 shows a plot of the mean intensity, over time for a dividing cell. It can be seen that, for example, between *Prophase* and *Prometaphase* there is a steep rise of the mean intensity, and for *Anaphase1* there is a characteristic spike. In total, we compute 332 features for each cell nucleus. For the training set, we standardize each feature with regard to a mean value of zero and a standard deviation of one. In the test set, the feature values are linearly transformed based on the transformation parameters from the training set.

### 11.2.5 Classification

We apply a support vector machine (SVM) classifier [20] with a Gaussian radial basis function (RBF) as kernel function to classify the nuclei into the seven classes *Interphase*, *Prophase*, *Prometaphase*, *Metaphase*, *Anaphase1*, *Anaphase2*, and *Telophase* (see Figure 11.5). SVMs are mathematically well-founded, and they have the advantage of overcoming the *curse of dimensionality*, which is a problem for many machine learning techniques in high-dimensional feature space: SVMs are not prone to over-fitting (i.e., they show a good generalization performance), and they do not exhibit intractable complexity for high-dimensional training data [21]. This allows us to work with the complete feature set, and we skip the feature selection step.

We use the software package LIBSVM [22] for SVM classification. Here, the multiclass classification problem is solved with a “one-against-one” approach. For  $k$  classes this method constructs  $k(k - 1)/2$  binary classifiers and trains each classifier for two classes. To optimize the penalty parameter  $C$  and the kernel parameter  $\gamma$  for the radial basis function, we perform a three-fold cross-validation with



varying values of  $C$  and  $\gamma$  on the training set (model selection) prior to the actual training of the classifier.

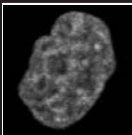
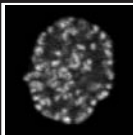

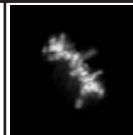
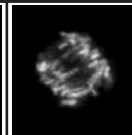


## 11.3 Experimental Results

### 11.3.1 Image Data

Here, we use 3-D image sequences that have been acquired with a confocal fluorescence microscope in the framework of the EU project MitoCheck at the European Molecular Biology Laboratory. Chromosome morphology is visualized using a HeLa (Kyoto) cell line stably expressing the chromosomal marker histone 2B-EGFP. One image contains about 20 nuclei with an average diameter of approximately 100–150 pixels (in the Interphase). All images have a gray value depth of 8 bits and a spatial resolution of  $1,024 \times 1,024$  pixels. Each image sequence comprises 124 to 128 time steps with a temporal resolution of 7 minutes and three image slices per time step.

### 11.3.2 Classification Results

We have applied our approach given four 3-D multicell image sequences. Using maximum intensity projection for all stacks of all sequences resulted in 500 projected multicell images. These images have been segmented and tracked. The tracking scheme was able to detect 80.0% of all occurring mitosis events (determined by visual inspection). Since the subsequent processing steps rely on correctly detected mitosis events, we corrected the remaining ones manually. Static and dynamic features have been extracted within the most informative slices for all segmented and tracked nuclei. To provide ground truth, all nuclei have been classified manually into the seven phases of mitosis. We split the available samples for each class randomly into training data and test data at a ratio of 2:1. The number of available samples and example images for each class are given in Figure 11.5. The feature values were standardized, and a support vector machine classifier was trained as described earlier. For the different phases (classes), we obtain between 80.0% and 98.1% correct classifications and an average accuracy of 90.1%. To check the reliability of the result we repeated the classification step, applying a

						
Inter	Pro	Prometa	Meta	Ana 1	Ana 2	Telo
1143	79	56	120	17	89	263

**Figure 11.5** Mitotic classes. Example images of the different mitotic phases and number of available samples.

**Table 11.1** Confusion Matrix and Accuracies for the Experiment with Five-Fold Cross Validation, Including Dynamic Features; Overall Accuracy: 94.6%

<i>True Class</i>	<i>Classifier Output</i>							<i>Accur.</i> [%]
	<i>Inter</i>	<i>Pro</i>	<i>Prometa</i>	<i>Meta</i>	<i>Ana1</i>	<i>Ana2</i>	<i>Telo</i>	
Inter	<b>1114</b>	6	0	1	0	0	22	<b>97.5</b>
Pro	5	<b>72</b>	2	0	0	0	0	<b>91.1</b>
Prometa	0	0	<b>51</b>	5	0	0	0	<b>91.1</b>
Meta	0	0	2	<b>114</b>	1	1	2	<b>95.0</b>
Ana1	1	0	2	2	<b>11</b>	1	0	<b>64.7</b>
Ana2	0	0	0	0	1	<b>84</b>	4	<b>94.4</b>
Telo	33	0	0	1	1	3	<b>225</b>	<b>85.6</b>

five-fold outer cross-validation on the whole data set. As shown in Table 11.1, we obtain classification accuracies of 64.7% to 97.5% for the different phases and an average accuracy of 88.5%. Thus, both average accuracies correspond well and we can draw the conclusion that we can rely on an average classification accuracy of around 89%. If we do not just average the accuracies for the different classes but take into account the number of samples per class, we obtain an overall accuracy of 94.6%.

To examine the effect of including dynamic features, we removed all dynamic features and repeated the classification experiments. In this case, we obtained an average accuracy of 79.1% and an overall accuracy of 92.9% for the experiment with five-fold cross-validation (see Table 11.2). It turns out that by *including* dynamic features we can improve the result significantly. The improvement becomes even more obvious when we compare the accuracies for the single phases of both experiments as listed in Tables 11.2 and 11.1: If dynamic features are included, the accuracies are significantly higher for all phases, except for *Telophase*. The largest improvement can be observed for *Anaphase1* with an increase from 29.4% to 64.7% and for *Prometaphase* with an increase from 78.6% to 91.1%. Since the three phases *Prometa*-, *Meta*-, and *Anaphase1* are characterized by large changes of the chromosomal structures, they have high within-class variabilities and also high between-class similarities. This is the reason for the misclassifications between these classes that can be observed in the confusion matrices in Tables 11.1

**Table 11.2** Confusion Matrix and Accuracies for the Experiment with Five-Fold Cross Validation; Dynamic Features Have Not Been Included; Overall Accuracy: 92.9%

<i>True Class</i>	<i>Classifier Output</i>							<i>Accur.</i> [%]
	<i>Inter</i>	<i>Pro</i>	<i>Prometa</i>	<i>Meta</i>	<i>Ana1</i>	<i>Ana2</i>	<i>Telo</i>	
Inter	<b>1109</b>	8	0	1	0	0	26	<b>97.0</b>
Pro	11	<b>66</b>	1	0	1	0	0	<b>83.5</b>
Prometa	0	0	<b>44</b>	6	6	0	0	<b>78.6</b>
Meta	1	0	5	<b>110</b>	0	0	4	<b>91.7</b>
Ana1	1	0	5	3	<b>5</b>	2	1	<b>29.4</b>
Ana2	0	0	0	0	1	<b>76</b>	12	<b>85.4</b>
Telo	21	0	0	1	2	8	<b>231</b>	<b>87.8</b>

and 11.2. Especially for these three classes, the incorporation of dynamic features results in a major improvement.

## 11.4 Discussion and Conclusion

We have presented an approach for automated analysis of the duration of mitotic phases in 3-D confocal microscopy image sequences. Our approach segments and tracks splitting cells throughout the sequences and thus determines cell pedigrees. By using static and dynamic features, our scheme classifies the cells with high accuracy into seven mitotic phases. Based on the sequence of phases that have been computed in subsequent frames, the duration of each phase can be determined. The computed phase durations can be compared to control experiments to automatically identify experiments that show delays in mitotic phases.

Although our approach already produces promising results, we are still working on further improvements. In the tracking step, the achieved mitosis detection rate should be further improved. To this end, we plan to include more features in the mitosis-detection criterion. Furthermore we are working on improving the classification accuracy, especially for the problematic classes *Prometa-*, *Meta-*, and *Anaphase1*, by investigating more appropriate image features. Another issue is to include feature selection methods. By reducing the number of features that have to be computed for each cell nucleus, the computation time of the overall approach could be reduced. Finally, we will apply our approach for the analysis of a much larger number of image sequences and evaluate its performance.

### Acknowledgments

This chapter has been supported by the EU project MitoCheck.

## References

- [1] Huang, K., and R. Murphy, "Boosting Accuracy of Automated Classification of Fluorescence Microscope Images for Location Proteomics," *BMC Bioinformatics*, Vol. 5, June 2004, p. 78.
- [2] Conrad, C., H. Erfle, P. Warnat, N. Daigle, T. Löch, J. Ellenberg, R. Pepperkok, and R. Eils, "Automatic Identification of Subcellular Phenotypes on Human Cell Arrays," *Genome Research*, Vol. 14, 2004, pp. 1130–1136.
- [3] Chen, X., and R. Murphy, "Robust Classification of Subcellular Location Patterns in High Resolution 3D Fluorescence Microscope Images," *Proc. 26th Annu. Int. Conf. IEEE Engineering in Medicine and Biology Society*, San Francisco, CA, 2004, pp. 1632–1635.
- [4] Lindblad, J., C. Wählby, E. Bengtsson, and A. Zaltsman, "Image Analysis for Automatic Segmentation of Cytoplasm and Classification of Rac1 Activation," *Cytometry Part A*, Vol. 57A, 2003, pp. 22–33.
- [5] Yang, F., M. Mackey, F. Ianzini, G. Gallardo, and M. Sonka, "Cell Segmentation, Tracking, and Mitosis Detection Using Temporal Context," *Proc. 8th Internat. Conf. on Medical Image Computing and Computer-Assisted Intervention (MICCAI'2005)* J. Duncan and G. Gering, (eds.), vol. 3749 of *Lecture Notes in Computer Science*, Palm Springs, CA, Springer-Verlag Berlin Heidelberg, October 2005, pp. 302–309.

- [6] Perlman, Z., M. Slack, Y. Feng, T. Mitchison, L. Wu, and S. Altschuler, "Multi-dimensional Drug Profiling by Automated Microscopy," *Science*, Vol. 306, 2004, pp. 1194-1198.
- [7] Zhou, X., K.-Y. Liu, P. Bradley, N. Perrimon, and S. T. Wong, "Towards Automated Cellular Image Segmentation for RNAi Genome-Wide Screening," *Proc. 8th Internat. Conf. on Medical Image Computing and Computer-Assisted Intervention (MICCAI'2005)*, J. Duncan and G. Gering, (eds.), Vol. 3749 of *Lecture Notes in Computer Science*, Palm Springs, CA, Berlin Heidelberg: Springer-Verlag, October 2005, pp. 302-309.
- [8] Harder, N., B. Neumann, M. Held, U. Liebel, H. Erfle, J. Ellenberg, R. Eils, and K. Rohr, "Automated Recognition of Mitotic Patterns in Fluorescence Microscopy Images of Human Cells," *Proc. IEEE Internat. Symposium on Biomedical Imaging: From Nano to Macro (ISBI2006)*, J. Kovačević and E. Meijering, (eds.), Arlington, VA, April 2006, pp. 1016-1019.
- [9] Li, K., E. Miller, L. Weiss, P. Campbell, and T. Kanade, "Online Tracking of Migrating and Proliferating Cells Imaged with Phase-Contrast Microscopy," *Proc. IEEE Workshop on Math. Methods in Biomed. Image Analysis (MMBIA'2006)*, New York, June 2006, pp. 65-72.
- [10] Padfield, D., J. Rittscher, T. Sebastian, N. Thomas, and B. Roysam, "Spatio-Temporal Cell Cycle Analysis Using 3D Level Set Segmentation of Unstained Nuclei in Line Scan Confocal Fluorescence Images," *Proc. IEEE Internat. Symposium on Biomedical Imaging: From Nano to Macro (ISBI'2006)*, J. Kovačević and E. Meijering, eds., Arlington, VA, April 2006, pp. 1036-1039.
- [11] Gonzalez, R., and R. Woods, *Digital Image Processing*, 2nd ed., Upper Saddle River, NJ Prentice-Hall, 2002.
- [12] Otsu, N., "A Threshold Selection Method from Grey Level Histograms," *IEEE Transactions on Systems, Man and Cybernetics*, Vol. 9, 1979, pp. 62-66.
- [13] Kittler, J., and J. Illingworth, "Minimum Error Thresholding," *Pattern Recognition*, Vol. 19, No. 1, 1986, pp. 41-47.
- [14] Chetverikov, D., and J. Verestoy, "Tracking Feature Points: A New Algorithm," *Proc. 14th Int. Conf. Pattern Recognition*, Vol. 2, Brisbane, Qld., Australia, August 1998, pp. 1436-1438.
- [15] Withers, J., "Tracking Cell Splits and Merges," *Proc. IEEE Southwest Symposium on Image Analysis and Interpretation*, San Antonio, TX, April 1996, pp. 117-122.
- [16] Chang, T., and C. Kuo, "Texture Analysis and Classification with Tree-Structured Wavelet Transform," *IEEE Trans. Image Processing*, Vol. 2, No. 4, 1993, pp. 429-441.
- [17] Haralick, R. M., "Statistical and Structural Approaches to Texture," *Proceedings of the IEEE*, Vol. 67, No. 5, 1979, pp. 768-804.
- [18] Burkhardt, H., and S. Siggelkow, *Invariant Features in Pattern Recognition: Fundamentals and Applications*, New York: John Wiley & Sons, 2001.
- [19] Zernike, F., "Beugungstheorie des Schneidenverfahrens und seiner verbesserten Form, der Phasenkontrastmethode," *Physika*, Vol. 1, 1934, pp. 689-704.
- [20] Vapnik, V., *Statistical Learning Theory*, New York: John Wiley & Sons, 1998.
- [21] Burges, C., "A Tutorial on Support Vector Machines for Pattern Recognition," *Data Mining and Knowledge Discovery*, Vol. 2, 1998, pp. 121-167.
- [22] Chang, C.-C., and C.-J. Lin, *LIBSVM: A Library for Support Vector Machines*, 2001, <http://www.csie.ntu.edu.tw/~cjlin/libsvm>.



# Automated Spatio-Temporal Cell Cycle Phase Analysis Based on Covert GFP Sensors

Dirk Padfield, Jens Rittscher, Nick Thomas, and Badrinath Roysam

## 12.1 Introduction

The concept of “fail-safe” is standard practice in engineering design. Systems with multiple mechanical and electrical safeguards are designed every day in many technologies and industries. The fact that all of these engineers are alive and healthy to carry on making better and safer nuclear power plants, airplanes, cars, espresso machines, and all the other potentially lethal essentials of modern life, is in large part thanks to a biological “fail-safe”—a true essential of life: the cell cycle.

Cell cycle control and its links with cancer and biological responses to DNA damage represent one of the most dynamic areas of contemporary biomedical research [1]. To effectively study the progression, pausing, or stalling of cells through the cell cycle, methods of identifying where individual cells are in the cycle are required. Among other applications, this is necessary for studying the effect of inhibitor compounds that are designed to block the replication of cancerous cells. Mitotic cells are easily recognized under the microscope as the cells become rounded in preparation for cell division, but microscopy does not readily discriminate between cells in interphase (between mitoses) in G1, S, or G2.

The ability to automatically follow the movement of cells and capture events such as mitosis and apoptosis as addressed by many researchers have had important implications on biological research. We expand upon this by enabling the study of the cell cycle in greater detail by applying automatic image analysis algorithms to extract information on cell cycle progression through the four phases of each cell using a cell cycle phase marker (CCPM) that does not alter the cell cycle behavior of the cells. We thus extend the capability of other automatic cell segmentation and tracking approaches by enabling the ability to capture cell phase information. This opens new possibilities for biological research in diagnosis and treatment focused on the cell cycle.

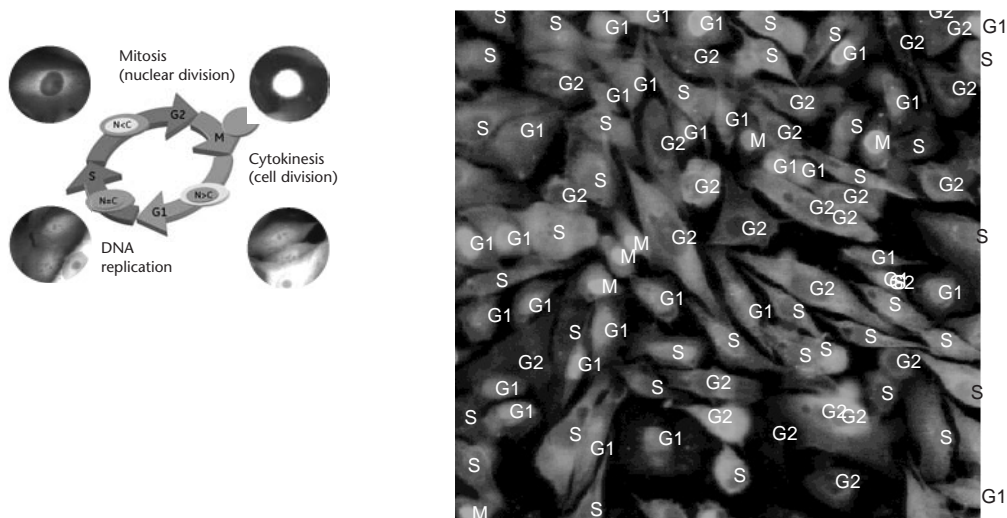
In Section 12.2, we present a high-level overview of the main biological elements related to our work. In Section 12.3, we describe the state of the art along with a summary of our approach and contributions. An overview of the mathematical framework is given in Section 12.4, and we present our approach to the problem of segmenting and tracking cells in CCPM datasets in Section 12.5. Our experimental results and their validation are presented in Section 12.6. We present a prototype analysis tool for cell cycle research in Section 12.7. Finally, we present our conclusions and ideas for future research in Section 12.8.

## 12.2 Biological Background

What follows is a high-level overview of the biological topics related to our particular problem. Further details of these topics can be found in [2, 3]. We conclude this section with a description of the problem statement.

### 12.2.1 Cell Cycle Phases

The cell cycle is comprised of four phases, G1 (gap 1), S (synthesis), G2 (gap 2), and M (mitosis), each of which comprises an ordered series of processes and events designed to ensure error-free cell replication (Figure 12.1). In G1, the cell carries out DNA repair and other checks and preparations in readiness for S phase. In S, complex mechanisms achieve the impressive task of faithfully copying 3 billion bits of genetic information carried on 2 meters of tightly wound DNA constrained in a volume of one-thousandth of a trillionth of a cubic meter. In G2, all of the organelles, macromolecules, and other structural and functional components of the cell are replicated to double the mass of the cell in preparation for division. Finally, in M phase a series of biomechanical processes break down the nuclear envelope, separate the chromosomes, form the nuclear walls of daughter nuclei, and segregate all the organelles and other cytoplasmic components before pinching in the cytoplasmic membrane to complete the formation of two identical daughter cells.



**Figure 12.1** Phases of the cell cycle indicated by a cell cycle phase marker. The phases are marked as G1, S, G2, and M. The left side shows a schematic of the cell cycle along with a representation of the relative brightness of the nucleus (inner oval) and cytoplasm (outer oval) in each phase. N represents the nuclear brightness, and C represents the cytoplasmic brightness. The surrounding four images show real examples of each of these phases, where the bottom two show the two daughter cells resulting from mitosis. A cropped region of a typical cell cycle phase marker with color-coded phase classifications overlaid slightly to the right of the nucleus centers is shown on the right side of the figure.



### 12.2.2 Cell Cycle Checkpoints

At key points in the cell cycle, the cell decides whether to proceed to the next phase, to pause to allow more time to prepare, or to abort the cell cycle. These checkpoints exist at specific points in the cell cycle to prevent cells from progressing to the next phase in the event of DNA damage or other conditions that would make cell division dangerous for the cell [4]. Checkpoints are especially important as points in the cell cycle where the control system can monitor its internal state and environment and can be regulated by signals from other cells. Some of these signals promote progress through the cell cycle, whereas others inhibit it [2]. These checkpoints ensure the “fail-safe” operation of the cell cycle; put simply, the cell is designed to self-destruct unless all checkpoints are satisfied. In cancer, these checks and balances are removed or short-circuited, leading to uncontrolled cell proliferation.

Many of the main checkpoints in the cell cycle are in the G1 and G2 gap phases. The G1 checkpoint allows the cell to confirm that the environment is favorable for cell proliferation and that the cell’s DNA is intact before committing to S phase. The G2 checkpoint ensures that cells do not enter mitosis until any damaged DNA is repaired and DNA replication is fully completed [2].

Fully understanding the mechanisms of the cell cycle and particularly the operation of key checkpoints is fundamental to devising more effective cancer treatments. Detailed understanding of the operation and failure of cell cycle checkpoints brings with it the potential to design therapies to restore defective functions or to inhibit short circuits. Understanding the differences in the cell cycle between normal and cancer cells also brings the opportunity to exploit these differences in targeting therapy specifically to tumor cells, minimizing effects on normal cells.

Despite extensive investigation of the cell cycle over a period of more than 100 years, the gaps in our understanding of the molecular mechanisms involved in cell cycle checkpoints remain significant. Consequently, further detailed study of the G1, S, and G2 phases is necessary in pursuit of cell cycle mechanisms and checkpoints that can serve as targets in drug discovery for the treatment of cancer [1]. Many thousands of compounds targeting different classes of proteins could potentially form the basis of new cell cycle directed therapies, and efficient methods for determining their modes of action and effectiveness are required.

Several challenges exist for the study of checkpoints. In general, traditional biochemical studies of the cell cycle require populations of cultured cells that proceed synchronously through the cell cycle in order to measure an averaged response that would otherwise be indiscernible in an asynchronous culture. Synchronization methods rely on treatment with drugs that block specific steps in the cell cycle in order to arrest all the cells at a particular point in the cycle. Removing the block allows the arrested cells to proceed relatively synchronously through the cell cycle. This approach brings with it two drawbacks for testing the effects of new drugs. First, cells are already exposed to one drug before the test begins, raising the potential for interacting effects between drugs, complicating or obscuring the findings; second, synchronization is short lived and decays rapidly as cells pass through the cell cycle [3], limiting the ability to perform long-term contiguous studies of cells exposed to test drugs.

More importantly, while the cell cycle is typically represented as an internal clock within cells, in any population, each cell's clock runs at a slightly different speed, depending, among other things, on the sequential operation of the checkpoints discussed earlier. Consequently, the duration of the cell cycle varies considerably within any population of cells, with some cells progressing smoothly like a Swiss chronograph while other cells pause and stutter like a cheap quartz watch with a failing battery. Encompassing this diversity in studying the cell cycle as a target for cancer therapy is essential. Drugs designed to target a specific process or checkpoint will only be acting on a subpopulation of cells that are in the relevant position in the cell cycle, and thus different doses or duration of treatment will have widely different effects on cell survival. Studying individual cells in a statistically meaningful population over several generations by live cell imaging, with the ability to determine individual cell responses in terms of cell cycle phase duration and progression, is an effective means of monitoring the effects of a new therapeutic.

### 12.2.3 Cell Staining

Image analysis of fluorescent cellular images typically requires staining with a dye to identify cell nuclei. This requirement presents a problem for long-term cellular imaging, since all fluorescent DNA binding dyes inhibit DNA replication to a greater or lesser extent with inevitable toxicity, the biological equivalent of trying to copy data on magnetic tape coated in glue.

An alternative method to mark nuclei and keep cells alive through more than one cell cycle is to genetically engineer the cell to express a fluorescent protein such as green fluorescent protein (GFP) coupled with a nuclear localization sequence or as a fusion to a histone so the protein is resident in the nuclei of all cells [5]. However this approach requires additional genetic manipulation of the cells and brings with it the associated risk of unknowingly modifying the process being studied, since there is no means of comparing cell cycle progression in the presence and absence of the nuclear marker to determine the effect, if any, of the marker. Also, although the nuclei are marked, nuclear fluorescence is not related to DNA content, and hence the G1, S, and G2 phases of interphase cannot be distinguished, and the various subphases of mitosis can only be distinguished by morphological analysis. For the study of phase-specific cell cycle inhibitors such as Roscovitine and Nocodazole [6], which block the cell in G1 and G2, respectively, it is necessary to be able to identify and discriminate these phases.

The most common technique used for studying all four phases of the cell cycle, flow cytometry, measures the amount of DNA in each cell of a population. A population of cells is treated with a fluorescent DNA binding dye and passed one cell at a time through a laser and detector that measures the amount of dye bound in each cell and hence the amount of DNA present. The DNA content of a cell reveals its position in the cell cycle; the DNA content of G2 cells is exactly twice that of G1 cells, and cells in S phase have an intermediate DNA content that increases with the extent of replication [3]. This method, however, only reveals overall statistics for the entire population of the number of cells in each of the phases and thus the approximate duration of each phase of the cell

cycle. Furthermore, flow cytometry is a destructive process; once cells are analyzed, they are no longer part of the population and can no longer be studied. Thus, to study the phases of individual cells over time, a method is required whereby the cells can be measured without removing them from the population.

Following cell cycle progression in living cells can be achieved by the use of dynamic cell cycle sensors based on expression of fluorescent proteins linked to key cell cycle control elements. In this work, a nontoxic dynamic cell cycle phase marker (CCPM) [6, 7] is used that follows the cell cycle progression in living cells based on expression of a fluorescent protein linked to key cell cycle control elements. A CCPM enables imaging live cell assays for time periods lasting as long as several days. In this study we have used a cell line that stably expresses a fusion protein comprising GFP fused to the C-terminal PSLD domain of DNA Helicase B, which reports cell cycle position in living cells via movement between nucleus and cytoplasm during cell cycle progression. Sensor distribution through the cell cycle for a CCPM dataset is illustrated in Figure 12.1, where a cell is shown in each of the phases. This cell cycle sensor is unique in that it enables the identification of the four main phases of the cell cycle for live cells. It thus enables the study of the effect in live cells of inhibitor compounds that block the replication of cancer cells by stopping them in one of the phases of the cell cycle. The analysis of this type of data can contribute significantly to the study of cell cycle inhibitors and the diagnosis and treatment of cancer.

#### 12.2.4 Problem Statement

Each CCPM cell culture assay well comprises several hundred cells, and they need to be monitored several times per hour over several days. In addition, for each compound studied, several wells need to be prepared to give statistically significant results encompassing different concentrations of the test compound in replicates. When the number of compounds is large, it becomes evident that manually outlining every cell in each well for all time frames for many compounds is intractable. Therefore, it is necessary to employ automatic analysis algorithms.

Several factors make this problem particularly challenging. The cell cycle phase marker changes the fluorescent signature of each individual cell as a function of the cell phase, as illustrated in Figure 12.1. A large number of cells can be packed very densely, which makes visual tracking of even a single cell difficult. Also, the image intensity of the whole cell changes throughout the phases. To complicate matters, the cell is able to move more freely and quickly during mitosis because the cell rounds up and partially or completely detaches from the substrate, so the speed of the cell also varies based on the phase.

The specification of the problem is that of a high-throughput, high-content analysis where large numbers of compounds need to be screened and each cell should be studied individually to address the problem of a lack of cell synchronization. Analysis methods should be capable of automatically segmenting the various phases of the nuclei and generating simple and meaningful representations of the results. Meaningful representations of the data need to be extracted to facilitate the effective screening of different cell cycle inhibitors.

## 12.3 State of the Art

Great progress has been made to characterize cell motility, migration, shape, the dynamics of cell populations, and other such measures. Several research groups such as [8–11] have built cell tracking systems that enable the study of various biological processes such as cell growth, fertilization, embryonic development, tissue repair and wound healing, differentiation, and immune response.

Many of these approaches make use of a technology commonly known as visual tracking. It should be noted that especially within the past decade, a number of algorithms were developed in the computer vision community that allow the tracking of fast-moving objects under complex dynamics as well as the simultaneous tracking of multiple objects. Standard tracking approaches generally handle effects such as changes in lighting or scale and assume that the appearance of the objects remains constant. Visual tracking approaches that utilize stochastic filters for estimating the position and shape of every object require stochastic models of the biological system for each individual object. Bayesian inference is then applied to estimate the motion and shape of each cell.

In the case of CCPM images, both the appearance and the trajectory of the objects change with time. Therefore, it is difficult to approach the problem using standard tracking techniques. In addition to estimating the motion trajectory and shape deformation of each cell, determining the state of each cell with respect to its cell cycle is a key challenge.

Many researchers have used level sets for segmenting images of cells. In [12], Solorzano et al. use competing 2-D level sets to segment multiple cells. In [13], Mukherjee, Ray, and Acton use 2-D level sets to track leukocyte cells in transillumination images over time, and in [14], for validating these tracks, Ray and Acton use 2-D level sets in 2-D *spatio-temporal images*, which are defined in [15]. In [16], Feghali directly uses 3-D level sets for segmenting the tracks in 2-D slices taken over time as a *spatio-temporal volume* (although not for the application of cell segmentation). Three-dimensional level sets are also used by Sarti et al. in [17], in this case applied to 3-D volumes of nuclei in confocal microscopy images.

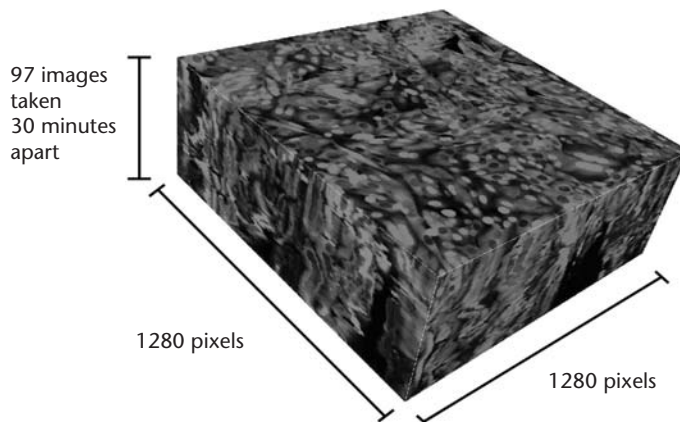
Existing cell tracking methods can roughly be divided into two main classes [18, 19]. The first is composed of independent frame cell detection, followed by linking based on minimizing the distances between detected cells according to some criteria. The second is based on first detecting the cells in one frame and then evolving them in time to keep track of cell movements and deformations. In [11], Li et al. use a multitarget tracking system using level sets and a stochastic motion filter to segment hundreds of cells in phase contrast images. In [20], Al-Kofahi et al. generate lineage trees for cells segmented and tracked in phase contrast images. In [18], Debeir et al. use the mean shift algorithm for tracking cells in phase-contrast images. They are not interested in segmenting the cells, only tracking them over time. In [21], Dzyubachyk et al. present a fusion of the standard variational method described in [22], with the Chan and Vese model [23] for segmenting and tracking cells in microscopy images using level sets. In [24], Bunyak et al. use level set segmentation to segment cells and multihypothesis tracking to track cells for tissue repair applications using phase contrast imaging. In [25], Yang et al.

track cells by using 2-D level set segmentation along with mitosis detection and marker-controlled watershed cell separation. In [9], Dufour et al. present a method for segmenting and tracking cells using one level set for each cell to enable quantitative analyses of cellular shape and motion from dynamic 3-D microscopy images.

Segmenting images of live cells into the four phases has not previously been attempted, but researchers have developed analysis algorithms for studying the phases of mitosis that are characterized by different morphological properties. In [26], Harder et al. classify cells with fluorescently marked nuclei into interphase and several phases of mitosis using feature extraction and feature classification. In [8], Chen et al. segment and track large numbers of cells marked with a nuclear stain and classify them into several stages of mitosis.

The related literature demonstrates that a wide range of effective approaches have been applied to the problem of cell segmentation and tracking. We expand upon the state of the art by approaching the individual study of the four phases of the cell cycle. As opposed to many other tracking tasks, all temporal information is available at the time of analysis. We can use this fact to formulate the problem as a spatio-temporal volume segmentation task where the sequence of 2-D images are stacked to form a 3-D volume, as illustrated in Figure 12.2. One particular advantage of formulating the problem as a spatio-temporal segmentation task is that it enables the possibility for segmenting the different phases independently. This approach is also motivated by the nonuniformity of the cell cycle and the fact that in certain phases of the cell cycle cells are easier to track than in others.

Dividing the segmentation task into different steps is a key aspect of our approach. The speed at which the appearance of each cell changes depends on its phase in the cell cycle, and, as a result, the difficulty of the segmentation task varies drastically. During the G2 and S phases, nuclei carve out dark “tunnels” of the 3-D volume. The nuclei are dark, while the surrounding cytoplasm is



**Figure 12.2** Representation of the 2-D images taken over time as a 3-D volume. The 97 images of size  $1,280 \times 1,280$  were taken 30 minutes apart. The G2 and S phase nuclei can be seen as dark tunnels that carve through the volume.

relatively bright. The M phase cells are almost uniformly bright and relatively easy to segment. In contrast, the G1 phase is difficult to segment because the fluorescence is evenly distributed between the nucleus and the cytoplasm, and no clear boundaries are present.

We first apply 3-D segmentation techniques to extract all cells in the G2 and S phases, separately segment the M phase cells, and then use a track linking approach to track the cells through the G1 phase. Our main contribution is the design of a model-based speed function coupled with a fast marching path planning approach that enables the tracking of cells across the difficult-to-segment G1 phase. To constrain the evolution of a level set for segmenting the S and G2 phase cells, we developed a shape and size constraint that exploits the location of the seeds and models the cell characteristics. We also designed a seed placement algorithm based on a model of S and G2 nuclei. These seeds are used as inputs to the level set segmentation algorithm for segmenting the nuclei.

## 12.4 Mathematical Framework: Level Sets

Active contours have been used extensively for image segmentation. The basic idea in active contour models is to evolve a curve, subject to constraints from a given image, in order to detect objects in the image. Since original work by Kass [27], extensive research has been done on “snakes” or active contour models for boundary detection. The classical approach is based on deforming an initial contour  $C_0$  toward the boundary of the object to be detected. The deformation is obtained by minimizing a functional designed so that its (local) minimum is obtained at the boundary of the object. The classical snakes approach associates the curve  $C$  with an energy given by

$$E(C) = \alpha \int_0^1 |C'(q)|^2 dq + \beta \int_0^1 |C''(q)|^2 dq - \lambda \int_0^1 |\nabla I(C(q))| dq \quad (12.1)$$

where  $\alpha$ ,  $\beta$ , and  $\lambda$  are real positive constants. The first two terms control the smoothness of the contours to be detected, and the third term is responsible for attracting the contour toward the object in the image (external energy). This approach is nonintrinsic, since the energy depends on the parameterization of the curve and is not directly related to the object geometry. The model is also not capable of easily handling changes in topology.

To avoid the limitations inherent in the snakes model, level sets can be used, which give an implicit representation of the curve. The main advantages of using level sets are that arbitrarily complex shapes can be modeled and topological changes such as merging and splitting are handled implicitly. The theory and many examples of applications of level sets are given in [28–30]. Instead of manipulating the contour in an image directly, the contour is embedded as the zero level set of a higher dimensional function called the level set function  $\phi(\mathbf{x}, t)$ . The surface intersects the image at the location of the curve. As the curve is at height 0, it is called the zero level set of the surface. The higher-dimensional level set function is then evolved under the control of a differential equation instead of the original curve. The zero level set remains identified with the curve during evolution of the



surface; at any time, the evolving contour can be obtained by extracting the zero level set  $\phi(\mathbf{x}, \mathbf{t}) = 0$  from the output.

Level set methods can roughly be divided into two classes: those that rely on edges to stop the evolution of the level set (i.e., with edges), and those that rely on breaking the image into regions based on intensity and other region characteristics (i.e., without edges). The level set paradigm has been applied to image segmentation using both of these methods.

### 12.4.1 Active Contours with Edges

In [31], Malladi et al. first used the level set equations for segmentation, and in [32], Caselles et al. added an edge attracting force to the formulation, resulting in the geodesic active contour equation for the update of the level set function. The Euler-Lagrange equation for the update of the level set related to the snakes model from (12.1) is given by

$$\frac{\partial \phi}{\partial t} = -g |\nabla \phi| + \gamma g \kappa |\nabla \phi| - \eta \nabla g \cdot \nabla \phi \quad (12.2)$$

The first term on the right acts as a propagation term, the second as a regularization term, and the third as an edge attracting term. The scalars  $\gamma$  and  $\eta$  give relative weights to the terms of the equation.  $\kappa$  is the mean curvature of the evolving contour

$$\kappa = \nabla \cdot \frac{\nabla \phi}{|\nabla \phi|} = \frac{\phi_{xx}\phi_y^2 - 2\phi_x\phi_y\phi_{xy} + \phi_x^2\phi_{yy}}{(\phi_x^2 + \phi_y^2)^{3/2}} \quad (12.3)$$

where  $\phi_x, \phi_y$  are the first derivatives and  $\phi_{xx}$  and  $\phi_{yy}$  are the second derivatives.

The function  $g$  is a monotonically decreasing function from 1 to 0 of the image gradient. Two common selections of the function  $g$  are

$$g(|\nabla I|) = \frac{1}{1 + |\nabla G_\sigma * I|^p} \quad (12.4)$$

$$g(|\nabla I|) = e^{-|\nabla G_\sigma * I|} \quad (12.5)$$

where  $G_\sigma$  is a Gaussian kernel convolved with the image  $I$  to smooth it, and  $p$  can be varied to change the influence of the edges. The function  $g$  results in a speed image that is close to 1 in areas of low gradient and close to 0 in areas of high gradient so that the level set slows down at the edges.

### 12.4.2 Active Contours Without Edges

In [23], Chan and Vese present a model that can detect contours both with and without gradient such as, for instance, objects with very smooth boundaries or even



with discontinuous boundaries. In addition, interior contours are automatically detected, and the initial curve can be anywhere in the image.

The form of the regularized functional to minimize is:

$$\begin{aligned}
 F_{\varepsilon}(c_1, c_2, \phi) = & \mu \int_{\Omega} \delta_{\varepsilon}(\phi(x, y)) |\nabla \phi(x, y)| dx dy \\
 & + v \int_{\Omega} H_{\varepsilon}(\phi(x, y)) dx dy \\
 & + \lambda_1 \int_{\Omega} |u_0(x, y) - c_1|^2 H_{\varepsilon}(\phi(x, y)) dx dy \\
 & + \lambda_2 \int_{\Omega} |u_0(x, y) - c_2|^2 (1 - H_{\varepsilon}(\phi(x, y))) dx dy \quad (12.6)
 \end{aligned}$$

The first term in (12.6) represents the length of the contour, the second the area, the third the consistency of the interior intensity, and the last the consistency of the exterior intensity. Here  $\mu$ ,  $v$ ,  $\lambda_1$ , and  $\lambda_2$  are variable weights for the terms.

$H$  is the Heaviside function, and  $H_{\varepsilon}$  is the regularized Heaviside function  $H_{\varepsilon}(z) = \frac{1}{2} \left( 1 + \frac{2}{\pi} \arctan\left(\frac{z}{\varepsilon}\right) \right)$ . This function is close to unity inside the contour and close to zero outside. The  $c_1$  and  $c_2$  variables are the averages of the values inside and outside of the contour, respectively, and are defined as

$$c_1(\phi) = \frac{\int_{\Omega} u_0(x, y) H(\phi(x, y)) dx dy}{\int_{\Omega} H(\phi(x, y)) dx dy} \quad (12.7)$$

$$c_2(\phi) = \frac{\int_{\Omega} u_0(x, y) (1 - H(\phi(x, y))) dx dy}{\int_{\Omega} (1 - H(\phi(x, y))) dx dy} \quad (12.8)$$

The associated Euler-Lagrange equation for  $\phi$  is

$$\frac{\partial \phi}{\partial t} = \delta_{\varepsilon}(\phi) \left[ \mu \nabla \cdot \left( \frac{\nabla \phi}{|\nabla \phi|} \right) - v - \lambda_1 (u_0 - c_1)^2 + \lambda_2 (u_0 - c_2)^2 \right] = 0 \quad (12.9)$$

where  $u_0$  is the original image. Notice that  $\lambda_1$  and  $\lambda_2$  have different signs.

Such methods segment the image based on the homogeneity of the image region, but they can fail if this assumption is not valid. For example, if cells in various phases have different appearances, they cannot be represented collectively as a homogeneous region.

## 12.5 Spatio-Temporal Cell Cycle Phase Analysis

In order to automatically generate a meaningful description of the cell cycle in images with a CCPM, it is necessary to track nuclei over time. We have developed a set of algorithms for automatically segmenting and tracking cells in CCPM datasets. The images are first preprocessed using a smoothing algorithm [33] and employing flat-field correction, which iteratively fits a quadratic surface to the image similar to [34–37]. Using the preprocessed images, we introduce a seed placement and classification method, a shape and size constraint for level set evolution, and a

tracking method based on fast marching path planning. Many of the algorithms were developed using algorithms from the Insight Toolkit [38].

### 12.5.1 Automatic Seed Placement

In order to evolve a level set, initial seeds need first to be defined. We take a two-step approach to seed placement within nuclei: multiresolution normalized cross correlation with a ring-like kernel followed by point classification.

We designed a ring kernel that is positive inside the ring band, negative inside, and zero outside. This yields high correlation values for G2 and S nuclei, since they are dark structures surrounded by bright cytoplasm. We run the correlation step with different sized kernels to detect various nucleus sizes. Nonmaximum suppression of the correlation image can thus effectively detect nuclei.

This step also yields several detections in the background, since background segments surrounded by the cytoplasm of nearby cells look similar to nuclei. To correct for this, the seed placement step is followed by a seed classification step using edge curvature measures. The Canny edges are separated into those having positive curvature, negative curvature, and zero curvature, where curvature  $\kappa$  is defined as the divergence of the normalized image gradient as in 12.3 with  $\phi$  substituted with the image intensities.

A training phase is employed to determine what feature values characterize a cell. In this phase, a set of seed points are manually classified into the categories of nucleus or background from a representative image. Around each training point, a region of interest representative of the typical size of a nucleus is considered, and three properties are measured: (1) the image intensity, (2) the number of edges with positive curvature, and (3) the magnitude of those edges. These measures are good discriminators because the nuclei are generally brighter than the background, and the nuclei are surrounded by many strong edges with positive curvature. On the other hand, edges around the background are generally fewer in number and magnitude.

A Fisher linear discriminant [39] classifier is used to separate the seed points into the classes of nucleus versus background. Using the classification surface, the automatically generated seeds from the normalized cross-correlation step for testing images are classified. The signed distance of these seeds is used as the initial level set for the segmentation step.

### 12.5.2 Shape/Size Constraint for Level Set Segmentation

Using the preprocessed images and the seeds, we segment the cells using level sets. Referring to Section 12.4, we approach the segmentation using the active contours *with edges*. The active contours without edges approach is difficult to use for these datasets because the appearance of the nuclei changes continuously such that there are not well-defined classes. It is conceivable that multiple level sets could be used as in [9], but there are too many cells for this to be computationally feasible.

Using the active contours with edges approach, we set the curvature and edge attracting terms high so as to keep the evolution within the nucleus. We set the

function  $g$  based on a sigmoid function to give more control over the mapping of the edge strength than those given in (12.4),

$$g(|\nabla I|) = \frac{1}{1 + e^{-\frac{|\nabla G_\sigma * I| - \beta_e}{\alpha_e}}} \quad (12.10)$$

Here  $|\nabla G_\sigma * I|$  represents the gradient magnitude of the convolution of the image  $I$  with a Gaussian function parameterized by  $\sigma$ . The variable  $\alpha_e$  controls the slope of the curve and should be between 0 and  $\infty$  to map the low gradient magnitudes to high speeds and vice versa. The variable  $\beta_e$  shifts the curve left to right and should be between the min and max of  $|\nabla G_\sigma * I|$ . The  $e$  subscripts of  $\alpha_e$  and  $\beta_e$  signify that these parameters are related to edges.

Since this formulation is based on edges, if the level set leaks, it will proceed rapidly in the background as illustrated in the supplementary video. The video illustrates that weak gradients are particularly problematic. If the level set leaks, it will proceed rapidly in the background, and, if allowed to propagate, the level set from these weak-edge nuclei can eventually join with other nuclei and result in unusable segmentations. One approach to stop the leaking is to increase the advection force, which attracts the level set to edges. However, the constantly changing intensity profile of the dynamic cell cycle sensor frequently yields gradients inside the nucleus. Therefore, a high advection force can cause the level set to become stuck in local minima inside of the nucleus. In addition, there is often no edge present at the border of the nucleus, and the advection force cannot constrain the level set in this case. An alternative is the implementation of a size constraint such as that proposed in [40]. However, size alone is not sufficient since the resulting constrained level set will not necessarily correspond to the shape of the cell.

Instead of using a purely model-driven approach, we propose to incorporate prior knowledge of the nuclei locations. The seed placement step ensures that the seed points are placed near the medial axis of a cell. Based on this observation, we can construct a model of the location of the nuclear edge from a mapping of the distance function from the seeds that will affect the speed of the level set function. This mapping should give positive speed for distances less than the expected cell size and negative speed for values outside. We designed a mapping function that results in smoothly varying speed values,

$$s(\tau) = 2 \left( \frac{1}{1 + \exp\left(-\frac{\tau - \beta_s}{\alpha_s}\right)} \right) - 1 \quad (12.11)$$

and we set the parameters so that the zero crossing of the speed function occurs at the expected nuclear size. Here  $s(\tau)$  is the speed that depends on the distance  $\tau$ ,  $\beta_s$  is set to the expected cell size, and  $\alpha_s$  controls the slope of the curve. The  $s$  subscripts of  $\alpha_s$  and  $\beta_s$  signify that these parameters are related to the curve speed. The scalar multiplication and subtraction factors lead to a function that yields speeds from 1 to  $-1$ . Note that this function is calculated only once for every pixel in the image. Thus, rather than updating the model at every iteration as some other methods do, this method is very computationally efficient.

The  $s(\tau)$  function can be applied to the propagation term of the level set equation to slow down this term as the level set expands. To incorporate this constraint into the level set equation, we balance it against the  $g$  edge function that is already multiplied by the propagation term. The level set equation updated from (12.2) is thus represented as

$$\begin{aligned} \frac{\partial \phi}{\partial t} = & -(\lambda g + (1 - \lambda)s(\tau)) |\nabla \phi| \\ & + \gamma g \kappa |\nabla \phi| - \eta \nabla g \cdot \nabla \phi \end{aligned} \quad (12.12)$$

where we use a variable  $\lambda$  that controls the relative weight of these edge and distance forces.

Since the curvature and advection terms have not been affected, they are still free to continue to regularize the curve and attract it to edges, respectively. Thus, in the presence of strong gradients, the advection force will take over as the level set evolves and lock onto the edges as before. However, in the presence of weak edges, the shape/size constraint will keep the level set from growing without bound.

Using the shape/size constraint, the level sets inside nuclei with strong gradients are still able to move to these edges, while those in nuclei with weak gradients are constrained not to leak into the background. By the last frame of the video, the evolution has already reached steady state and stopped at the configuration shown, as opposed to the evolution without this constraint, which continues to evolve outside of the cells.

The result of the level set segmentation step is a set of 3-D tubes corresponding to the S and G2 phases of the cells. These cells can then be associated with the corresponding M phase cells. The M phase cells are round and bright, and they are segmented using hysteresis thresholding combined with marker-controlled watershed segmentation. To obtain a full 3-D tree structure, a tracking step is needed to connect across the G1 phase.

### 12.5.3 Model-Based Fast Marching Cell Phase Tracking

We here describe a novel method for tracking across the G1 phase of the cell cycle using the segmentations of the G2, S, and M phases. Our approach uses the fast marching algorithm as a path planning tool, where we define a speed map based on a model of the phase transition. Our model is based on the appearance change of the nuclei from internally bright in the M phase to gradually dark at the end of the S phase and into the G2 phase (see Figure 12.1). This can be viewed as a path planning problem where the cost function is defined to vary according to the model, and it can be solved using the fast marching method [41]. The fast marching method, described in [29], is a method for solving a time arrival equation described by the Eikonal equation

$$|\nabla T| F = \sqrt{\left(\frac{\partial T}{\partial x}\right)^2 + \left(\frac{\partial T}{\partial y}\right)^2 + \left(\frac{\partial T}{\partial z}\right)^2} F(x, y, z) = 1 \quad (12.13)$$

in 3-D where  $F(x,y,z)$  is the speed map or cost function and  $T$  is the resulting time-crossing map for every point in the domain. Given a starting point, the fast marching method builds the solution outwards throughout the domain without iteration, choosing the smallest time at each step of its evolution. Then, given any point in the domain, the shortest path is constructed by propagating from that point to the fast marching starting point using gradient descent by solving the ordinary differential equation  $\frac{dx}{dt} = -\nabla T$ .

In the path planning problem, the most important part is to define an appropriate cost function  $F$ . In our model, the cost function switches from emphasizing bright nuclei to dark nuclei along the tracks. In other words, the cost is low (fast moving) in bright nuclei and high in dark areas at the beginning of the track and gradually switches to a low cost for dark nuclei and high cost for bright areas. Because the function should range between 0 and 1, we define it by

$$F(x,y,n) = f(I(x,y,n)) = \frac{1}{1 + \exp\left(-\frac{I(x,y,n) - \beta}{\alpha(n)}\right)} \quad (12.14)$$

$$0 < F(x,y,n) < 1$$

where the speed function  $F$  is a function of the intensity  $I(x,y,n)$  at a given image point  $(x,y,n)$ , and  $z$  has been substituted with  $n$  to represent the  $z$  distance relative to the starting point.  $\beta$  controls the shift of the function, which can be set experimentally and remain fixed.  $\alpha(n)$  controls the slope of the curve, which varies depending on the distance from the starting point. Changing the sign of  $\alpha$  flips the function around the horizontal axis at 1/2. To generate a cost function to move quickly in bright nuclei,  $\alpha$  should be positive; to move quickly in dark nuclei, it should be negative, and it should change gradually between these stages. To generate a smooth transition from bright to dark nuclei, we solve for  $\alpha$  for varying speed given a fixed  $\beta$  and a fixed starting intensity. The speed should vary in equal increments between 0 and 1, and the number of steps  $N$  depends on the expected amount of time taken for the transition. The fixed minimum intensity  $I_t$  is set to be the lowest intensity corresponding to a cell, or, equivalently, the background threshold. Solving for  $\alpha$  in (12.14) for a speed varying from 0 to 1 gives

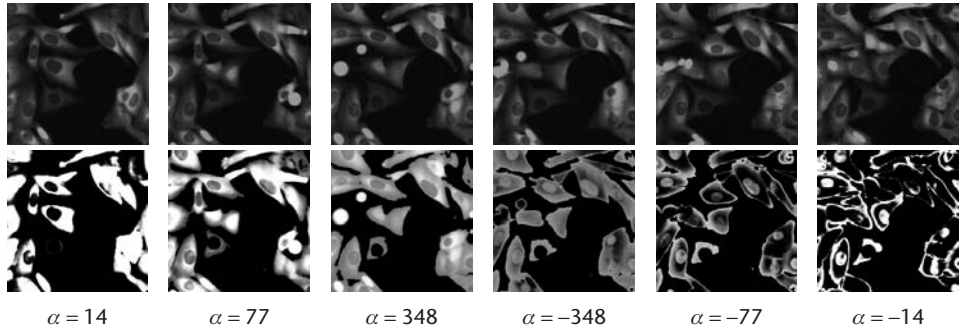
$$\alpha(n) = -\frac{I_t - \beta}{\ln\left(\frac{1}{F_t(n)} - 1\right)} \quad (12.15)$$

$$n = 0, \dots, N - 1$$

$$F_t(0) = \varepsilon, F_t(N - 1) = 1 - \varepsilon$$

Here  $F_t(n)$  is the speed corresponding to the minimum intensity  $I_t$  at position  $n$ , and  $\varepsilon$  is a small number that avoids computational errors at speeds of 0 and 1.

To implement this model, a starting point is chosen at the end of the M phase of each parent cell. A time-dimension distance function is generated from this point, where all points in the same x-y plane as the starting point have distance zero, all those at the next time plane have distance 1, and so on for the entire volume. These distances correspond to  $n$  in (12.15), and an  $\alpha$  can be calculated



**Figure 12.3** Speed images for the fast marching algorithm. The top row shows the original images, and the bottom row shows the cost function calculated for each image. The cost function is built separately for each parent cell with the end of the M phase as the starting point. In this example, the tracked cell is the circled one undergoing mitosis. With increasing  $n$ , or distance, from the starting point, the alpha increases to move the speed from 0 towards  $1/2$  and then flips sign and decreases as the speed moves towards 1. A nonlinear alpha is required to give a smooth speed transition in equal increments according to (12.15). This gives more speed to bright nuclei in the beginning and changes to gradually more speed for dark nuclei towards the end, where brighter parts of the cost function image indicate higher speeds.

for each one (note that if the distance is larger than  $N - 1$ , the  $\alpha(N - 1)$  value is used). Using these alpha values that vary throughout the volume along with the intensity at each voxel, (12.14) can be used to calculate the speed mapping for each point in the image.

Some example images of the resulting speed function can be seen on the bottom row of Figure 12.3, and the original images from which the speed images were calculated are shown on the top row. These cost functions are used for the fast marching algorithm.

This fast marching tracking algorithm is run on all parent cells to find their daughter cells. The overall algorithm is given in Algorithm 12.1. Note that for each parent, the fast marching algorithm is run for the entire domain, which can be computationally expensive if the volume is large and there are many parent cells. We obtain a significant speedup by enabling the setting of targets which, once reached, cause the fast marching algorithm to terminate. The beginning points of

---

**Algorithm 12.1** Fast Marching Tracking Algorithm

---

- 1: for each parent cell do
  - 2: Using (12.14) and (12.15), find the speed image  $F(x, y, n)$  to the entire domain from the parent cell.
  - 3: Solve  $|\nabla T|F = 1$  to find  $T$ .
  - 4: Choose as the two daughters the two targets that have the smallest  $T$ .
  - 5: Extract the paths to the daughter cells using gradient descent  $\frac{dx}{dt} = -\nabla T$  from the daughters to the parent.
  - 6: end for
-

the daughter cells are specified as the target points. Once two of the targets have been reached, the algorithm terminates since it has found the daughters.

## 12.6 Results

The algorithms were tested on 22 sets of series of 97 images of size  $1,280 \times 1,280$  with pixels representing  $750 \mu\text{m} \times 750 \mu\text{m}$  on the specimen. The algorithms were run on a  $400 \times 400 \times 97$  pixel region cropped out of the same location in each of the full volumes for computational efficiency. Images were acquired on an IN Cell Analyzer 3000 laser line scanning confocal imager (GE Healthcare, Milwaukee, Wisconsin) using 488-nm excitation and a 535-nm–545-nm emission filter. The IN Cell 3000 uses a 40x objective with an effective magnification at the camera of 32x. The cells were grown in a well plate and maintained on the instrument throughout the duration of imaging under standard culture conditions ( $37^\circ\text{C}/5\% \text{CO}_2$ ). Each of the 97 images was taken 30 minutes apart for a total time of 48 hours.

### 12.6.1 Large-Scale Toxicological Study

The 22 wells consist of 6 control wells and 16 wells treated with varying concentrations of cell cycle inhibitors: 8 with Roscovitine and 8 with Nocodazole, which arrest cells in the G1 and G2 phases, respectively. The biological expectation for the treated wells is that, for larger concentrations, the cell cycle will be arrested earlier and the cells will either die or remain in the final phase until the end of the experiment.

The quantitative results found that, while the phase durations of the control datasets had similar lengths, cells treated with Roscovitine and Nocodazole were arrested and prevented from splitting. This gives a clear indication that both Roscovitine and Nocodazole suppress proliferation compared to the control datasets. To visualize this, Color Plate 17 shows a representative control cell tree and Nocodazole cell tree. The control tree splits as usual, whereas the inhibited cell attempts to split but gets arrested in mitosis.

To evaluate the proposed tracking approach, a number of mitosis events were tracked using both a Euclidean distance metric as well as the fast marching method. The evaluation demonstrated that, while the Euclidean distance generates a linear interpolation between the points, the fast marching method extracts a path that more accurately characterizes the track of the cell. Because the fast marching method models cell transition, it moves quickly in the beginning to follow the bright M phase and follows much more closely the center of the cell throughout the transition (see Section 12.7.2).

### 12.6.2 Algorithmic Validation

The seed placement and classification steps, which are necessary to initialize the level set segmentation, occupy an important role in the processing because seeds should be placed in the nuclei and not in the background to enable the correct



nuclear segmentation. To validate these algorithms, a dataset is used that includes the CCPM along with a nuclear stain. This nuclear stain cannot be used for the time-lapse experiments because it is toxic and kills the cells over time. But it can be used to yield a ground truth map for the location of nuclei at one time frame.

Our approach is to segment the nuclei in the nuclear channel and use this as a mask for determining whether the seeds were placed correctly in the CCPM channel. This segmentation consists of adaptive thresholding, followed by watershed segmentation from the extended maxima of the binary image distance map to separate the touching nuclei. The seed placement algorithms are run on the CCPM channel as usual, and each of the seeds that was placed is compared to the nuclear mask.

To validate the seed placement and seed classification steps, images from 96 wells with nuclear stains were used. For the initial seeds and the classified seeds, the accuracy score was calculated as the ratio of seeds placed in nuclei to all seeds, and the classification step demonstrated an increase in accuracy from 20% to 70%. This number indicates that some seeds are still placed in the background, but many such seeds are removed by the segmentation evolution, since seeds in the nuclei are merged together due to spatial connectivity, while those in the background tend to shrink. This number also appears low because the space occupied by the nuclei is much less than the background. It does, however, provide a quantitative measure that can be used to improve the seed placement since new algorithms can be easily tested and compared against previous methods.

To validate the tracks and phases, a system was developed for facilitating manual generation of ground truth data. This system loads a series of 2-D images taken over time and allows the user to track a particular cell through mitosis by marking the centroid of the cell on each image by its phase (G1, S, G2, or M). Each cell cycle is sequentially numbered beginning at the G1 stage after mitosis, and the parent and child relationships are stored for each tracked cell cycle. This ground truth system was used to generate tracks and phases for more than 20 cell cycles, and the accuracy of this ground truth data was confirmed by an expert biologist. The automatic tracking results were automatically compared with the manual results, and the cells demonstrated correct phase tracking, meaning that the parents were associated with the correct daughters. The next step is to validate the boundaries of the segmentation of the cells and generate ground truth for more cells to further validate the automatic results. We are also investigating the use of a dataset with a CCPM and nuclear marker taken over a short period of time to validate the algorithms.

## 12.7 A Tool for Cell Cycle Research

The results of our initial study are encouraging and hold the promise of having significant impact on cell cycle research. While the automatic extraction of quantitative data is a core requirement, the visualization of the underlying data will be equally important. In order to study certain phenomena, biologists will need to

review the original image data, but the automatic analysis methods can also lead to new ways of visualizing the data in an intuitive and helpful manner. We envision that the automatic quantification will, for example, lead to the identification of certain abnormal events.

### 12.7.1 Research Prototype

The manual review of spatio-temporal image data is inherently time consuming. The user first needs to localize salient events, and then he/she needs to inspect the surrounding neighborhood. In Color Plate 18 we show a screenshot of a first research prototype that addresses some of these issues. The schematic on the lower left gives an overview of the mitosis events the system has found. As the user selects specific events, the other views show (clockwise from top left) the corresponding 2-D image slice, a schematic of the ancestor tree related to the event, and spatio-temporal images of the cell tracks (spatio-temporal images will be described in Section 12.7.2). Such an interactive setup allows the biologist to view the events of interest in a schematic form and to look for abnormal trends and then effectively review the original data corresponding to those regions.

For studying the effects of antiproliferative drugs, tree and branch representation of high complexity data such as those in Color Plates 17 and 18 enable visualization of variations in many parameters that characterize drug action. Such variations may include intralinear and interlinear changes in duration of cell cycle phases (length of color on branch), cell cycle blocks (extended tree branch in single color), accelerated or delayed mitosis (distance between branch nodes), nuclear morphology (branch thickness), DNA endoreduplication or nuclear fragmentation (splitting of branches to twigs), and cell death (branch termination).

Abstracting this type of information from time-lapse video could give researchers great insight into what is happening to cells when they are treated with a drug or when a gene is knocked out or overexpressed. This representation of data would allow them to study such conditions as whether particular cell cycle phases were extended or shortened, whether this effect was the same or different across the cell population, whether shortening of one phase was compensated for by extension in another, whether cells were more or less motile during these changes, and whether mitosis occurred correctly and on time.

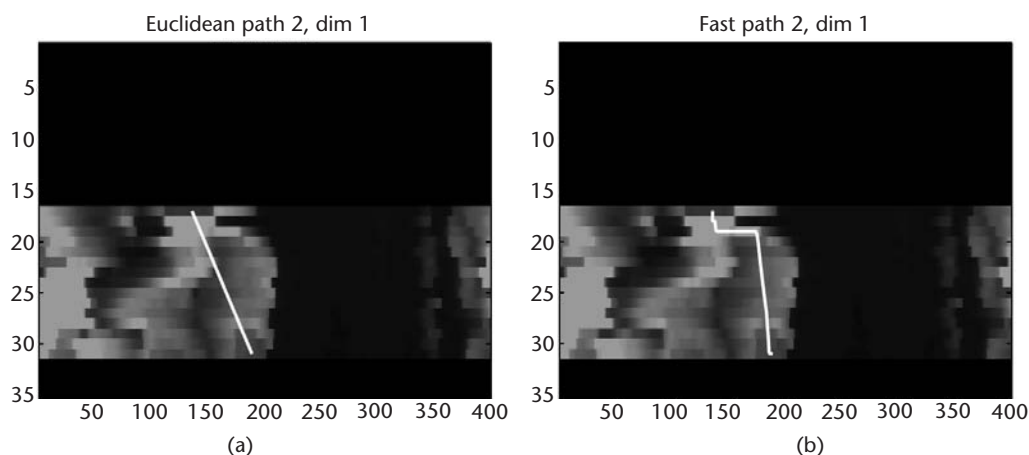
With regard to phase classification, the exact locations of the phase transitions are not well defined since the appearance of the cell through the cycle changes continuously as the fluorescent marker moves between the cytoplasm and nucleus. For this reason, we are currently working to expand this interface to include a continuous phase appearance model. These transitions can be based on thresholds that act as parameters for the phase classification, and these can be interactively set by biologists to help them study the effect of cell cycle phase. We are constructing a database of images of cells that are automatically extracted and ordered by their location in the cell cycle based on appearance. The combination of such images is leading to a continuous appearance model for the cell cycle where the phases are not necessarily restricted to the four G1, S, G2, and M phases.

### 12.7.2 Visualization

One effective way to represent cell tracks uses spatio-temporal images. The idea of a spatio-temporal image [15] is for every 2-D plane of the original volume to extract either the row or column that passes through the track. Using one line for the image, the lines can be stacked over time to generate an image. Such an image displays the track surrounded by the pixels of the image that it passed through. It therefore gives an intuitive representation of the path of the track.

In Figure 12.4, we show a spatio-temporal image of the tracks in the horizontal direction for both Euclidean and fast marching methods for the rightmost tracks (the left tracks do not move very far, so they are not as illustrative). The figure shows that, while both methods end up at the same place, the fast marching method, starting from the top of the spatio-temporal image, moves quickly in the bright regions and then gradually moves to the end point, whereas the Euclidean method follows a straight line between the points. In the image, the two daughter cells can be seen as the two bright regions on either side of the image separated by the darker background region, and the fast marching method avoids moving through the background.

Although a spatio-temporal image is an effective way of viewing the background surrounding a tracked path, by definition it is limited by only enabling the visualization of one track at a time. In our experiments, we are interested in tracks that branch as the cells undergo mitosis, so it is more useful to define a representation that can show two tracks simultaneously. For this purpose, we developed a representation that we call a *dual track spatio-temporal image*. Once a cell splits,



**Figure 12.4** (a, b) Spatio-temporal images for the Euclidean and fast marching methods. (a) The spatio-temporal image [15] of the Euclidean method and (b) shows the spatio-temporal image for the fast marching method. This representation shows that the fast marching method better tracks the actual trajectory of the cell, whereas the Euclidean method simply interpolates. The parent cell is shown at the start of the track at the top of the figure, and the two daughter cells show up as the two bright regions separated by a darker background region moving vertically through the image. By the nature of spatio-temporal images, only one track can be shown per image.

the subsequent images will contain two daughters of the parent cell. The tracking step already identified these tracks, so we can fit a line to the centroids of the daughter cells and observe the intensities intersected by this line. The pixels under this line define the background for the tracks, and these can be built up over the time dimension.

Such track visualizations can provide useful visual feedback of the nature of the cell track and can be used to provide meaningful measurements to biologists of the characteristics of the cell along the path.

## 12.8 Summary and Future Work

This chapter introduces a framework for tracking cells in space and time in conjunction with measuring the output from a cell cycle phase marker using segmentation and tracking methods. These methods facilitate the automatic analysis of the phases of the cell cycle over extended periods of time without manipulating the genetic makeup of the cells.

We introduced a speed function that models the appearance change of the cells through the phases coupled with the use of fast marching for tracking that enables accurate tracking of the parent cells to daughter cells and closely follows the path of the cell. The experimental results indicate that this model-based tracking method holds the promise of reliably tracking cells through mitosis events. We introduced a model-based shape/size constraint for the level set segmentation step that avoids the problem of leaking as well as methods for automatic seed placement. We also introduced methods for validation and visualization of the data for effective analysis of the results and use by biologists.

Future work includes using the output of these methods to measure such quantitative cell characteristics on large control and toxicological datasets to generate statistically meaningful results that correspond with and yield insight into biologically relevant phenomena. Since the manual validation of these algorithms is cumbersome, an edit-based validation framework is being developed that will provide a semiautomatic method of analyzing the results.

Future work also includes the further development of the research prototype to make available to biologists more tools for the analysis of cell phase. Our continuous phase model described in Section 12.7 combined with the ability to set thresholds in areas of interest of this continuous range may lead to new insights into the response of cells to various inhibitor compounds.

## References

- [1] Blagosklonny, M. V., ed., *Cell Cycle Checkpoints and Cancer*, Georgetown, TX: Landes Bioscience, 2001.
- [2] Alberts, B., D. Bray, A. Johnson, J. Lewis, M. Raff, K. Roberts, and F. Walter, *Essential Cell Biology*, 2nd ed., Garland Publishing, 2004.
- [3] Murray, A., and T. Hunt, *The Cell Cycle: An Introduction*, Oxford: Oxford University Press, 1993.

- [4] Karp, G., *Cell and Molecular Biology: Concepts and Experiments*, 4th ed., New York: John Wiley & Sons, 2005.
- [5] Kanda, T., K. Sullivan, and G. Wahl, "Histone-gfp Fusion Protein Enables Sensitive Analysis of Chromosome Dynamics in Living Mammalian Cells," *Current Biology* 8, 1998, pp. 377-385.
- [6] Stubbs, S., and N. Thomas, "Dynamic Green Fluorescent Protein Sensors for High-Content Analysis of the Cell Cycle," *Methods in Enzymology*, Vol. 414C, 2006, pp. 1-21.
- [7] Thomas, N., "Lighting the Circle of Life: Fluorescent Sensors for Covert Surveillance of the Cell Cycle," *Cell Cycle*, Vol. 2, November-December 2003, pp. 545-549.
- [8] Chen, X., X. Zhou, and S. T. Wong, "Automated Segmentaton, Classification, and Tracking of Cancer Cell Nuclei in Time-Lapse Microscopy," *IEEE Transactions on Biomedical Engineering*, Vol. 53, April 2006, pp. 762-766.
- [9] Dufour, A., V. Shinin, S. Tajbakhsh, N. Guillen-Aghion, J.-C. Olivo-Marin, and C. Zimmer, "Segmenting and Tracking Fluorescent Cells in Dynamic 3-d Microscopy with Coupled Active Surfaces," *IEEE Transactions on Image Processing*, Vol. 14, No. 9, 2005, pp. 1396-1410.
- [10] Wang, X., W. He, D. Metaxas, R. Mathew, and E. White, "Cell Segmentation and Tracking using Texture-Adaptive Snakes," *IEEE ISBI*, 2007.
- [11] Li, K., E. Miller, L. Weiss, P. Campbell, and T. Kanade, "Online Tracking of Migrating and Proliferating Cells Imaged with Phase-Contrast Microscopy," *Proceedings of CVPRW*, 2006, pp. 65-72.
- [12] de Solorzano, C. O., R. Malladi, S. Lelievre, and S. Lockett, "Segmentation of Cell and Nuclei Using Membrane Related Proteins," *Journal of Microscopy*, Vol. 201, 2001, pp. 1-13.
- [13] Mukherjee, D., N. Ray, and S. Acton, "Level Set Analysis of Leukocyte Detection and Tracking," *IEEE Transactions on Image Processing*, Vol. 13, April 2004.
- [14] Ray, N., and S. T. Acton, "Data Acceptance for Automated Leukocyte Tracking Through Segmentation of Spatiotemporal Images," *IEEE Trans. Biomed. Eng.*, Vol. 52, October 2005.
- [15] Sato, Y., J. Chen, R. Zoroofi, N. Harada, S. Tamura, and T. Shiga, "Automatic Extraction and Measurement of Leukocyte Motion in Microvessels Using Spatiotemporal Image Analysis," *IEEE Trans. Biomed. Eng.*, Vol. 44, No. 4, 1997, pp. 225-236.
- [16] Feghali, R., "Multi-Frame Simultaneous Motion Estimation and Segmentation," *IEEE Trans. Consumer Electronics*, Vol. 51, No. 1, 2005, pp. 245-248.
- [17] Sarti, A., C. O. de Solorzano, S. Lockett, and R. Malladi, "A Geometric Model for 3-D Confocal Image Analysis," *IEEE Trans. Biomed. Eng.*, Vol. 47, 2000, pp. 1600-1609.
- [18] Debeir, O., P. V. Ham, R. Kiss, and C. Decaestecker, "Tracking of Migrating Cells Under Phase-Contrast Video Microscopy with Combined Mean-Shift Processes," *IEEE Trans. Med. Imaging*, Vol. 24, No. 6, 2005, pp. 697-711.
- [19] Yang, X., H. Li, and X. Zhou, "Nuclei Segmentation Using Marker-Controlled Watershed, Tracking Using Mean-Shift, and Kalman Filter in Time-Lapse Microscopy," *IEEE Trans. Circuits Syst. I-Regul. Pap.*, Vol. 53, No. 11, 2006, pp. 2405-2414.
- [20] Al-Kofahi, O., R. Radke, S. Goderie, Q. Shen, S. Temple, and B. Roysam, "Automated Cell Lineage Construction: A Rapid Method to Analyze Clonal Development Established with Murine Neural Progenitor Cells," *Cell Cycle*, Vol. 5, 2006, pp. 327-335.
- [21] Dzyubachyk, O., W. Niessen, and E. Meijering, "A Variational Model for Level-Set Based Cell Tracking in Time-Lapse Fluorescence Microscopy Images," *IEEE ISBI*, 2007.
- [22] Rousson, M., and R. Deriche, "A Variational Framework for Active and Adaptive Segmentation of Vector Valued Images," *Proc. of IEEE Workshop on Motion and Video Computing*, 2003.

- [23] Chan, T., and L. Vese, "Active Contours Without Edges," *IEEE Trans. Image Processing*, Vol. 10, February 2001, pp. 266–277.
- [24] Bunyak, F., K. Palaniappan, S. K. Nath, T. L. Baskin, and G. Dong, "Quantitative Cell Motility for In Vitro Wound Healing Using Level Set-Based Active Contour Tracking," *IEEE ISBI*, 2006, pp. 1040–1043.
- [25] Yang, F., M. Mackey, F. Ianzini, G. Gallardo, and M. Sonka, "Cell Segmentation, Tracking, and Mitosis Detection Using Temporal Context," *MICCAI '05*, J. Duncan and G. Gerig, (eds.), No. 3749 in LNCS, 2005, pp. 302–309.
- [26] Harder, N., F. Bermúdez, W. Godinez, J. Ellenberg, R. Eils, and K. Rohr, "Automated Analysis of the Mitotic Phases of Human Cells in 3D Fluorescence Microscopy Image Sequences," *MICCAI '06*, R. Larsen, M. Nielsen, and J. Sporring, (eds.), LNCS, 2006, pp. 840–848.
- [27] Kass, M., A. Witkin, and D. Terzopoulos, "Snakes: Active Contour Models," *Int. Journal of Computer Vision*, Vol. 1, January 1988, pp. 312–331.
- [28] Osher, S. J., and J. A. Sethian, "Fronts Propagating with Curvature-Dependent Speed: Algorithms Based on Hamilton–Jacobi Formulations," *Journal of Computational Physics*, Vol. 79, 1988, pp. 12–49.
- [29] Sethian, J. A., *Level Set Methods and Fast Marching Methods*, Cambridge: Cambridge University Press, 1996.
- [30] Osher, S. J., and R. P. Fedkiw, *Level Set Methods and Dynamic Implicit Surfaces*, New York: Springer, 2002.
- [31] Malladi, R., J. Sethian, and B. Vemuri, "Shape Modeling with Front Propagation: A Level Set Approach," *IEEE Trans. on PAMI*, Vol. 17, 1995, pp. 158–175.
- [32] Caselles, V., R. Kimmel, and G. Sapiro, "Geodesic Active Contours," *Proc. ICCV 1995*, Cambridge, MA, 1995.
- [33] Whitaker, R., and X. Xue, "Variable-Conductance, Level-Set Curvature for Image Denoising," *Proc. IEEE International Conference on Image Processing*, 2001, pp. 142–145.
- [34] Gilles, S., M. Brady, J. Declerck, J.-P. Thirion, and N. Ayache, "Bias Field Correction of Breast MR Images," *VBC*, 1996, pp. 153–158.
- [35] Lindblad, J., and E. Bengtsson, "A Comparison of Methods for Estimation of Intensity Nonuniformities in 2-D and 3-D Microscope Images of Fluorescence Stained Cells," *Scandinavian Conference on Image Analysis 2001*, 2001, pp. P-W4A.
- [36] Wahlby, C., J. Lindblad, M. Vondrus, E. Bengtsson, and L. Björkstén, "Algorithms for Cytoplasm Segmentation of Fluorescence Labeled Cells," *Analytical Cellular Pathology*, Vol. 24(2,3), 2002, pp. 101–111.
- [37] Narasimha-Iyer, H., A. Can, B. Roysam, C. Stewart, H. Tanenbaum, A. Majerovics, and H. Singh, "Robust Detection and Classification of Longitudinal Changes in Color Retinal Fundus Images for Monitoring Diabetic Retinopathy," *IEEE Trans Biomed Eng*, Vol. 53, No. 6, 2006, pp. 1084–1098.
- [38] Ibanez, L., W. Schroeder, L. Ng, and J. Cates, *The ITK Software Guide*, 2nd ed., Kitware, Inc., 2005, [www.itk.org/ItkSoftwareGuide.pdf](http://www.itk.org/ItkSoftwareGuide.pdf).
- [39] Fisher, R. A., "The Use of Multiple Measurements in Taxonomic Problems," *Annals of Eugenics*, Vol. 7, No. II, 1936, pp. 179–188.
- [40] Zhao, H.-K., T. Chan, B. Merriman, and S. Osher, "A Variational Level Set Approach to Multiphase Motion," *Journal of Computational Physics*, Vol. 127, 1996, pp. 179–195.
- [41] Kimmel, R., and J. Sethian, "Fast Marching Methods for Robotic Navigation with Constraints," *Center for Pure and Applied Mathematics Report*, May 1996.



# Cell Segmentation for Division Rate Estimation in Computerized Video Time-Lapse Microscopy

Xiaoxu Wang, Weijun He, Zhen Qian, Dimitris Metaxas, Robin Mathew, and Eileen White

## 13.1 Introduction

The automated estimation of cell division rate plays an important role in the evaluation of a gene function in high-throughput biomedical research. Automatic segmentation and cell counting of phase contrast images is a challenging task due to low-contrast membrane boundaries and similar intensities inside and outside the cell. Phase contrast images are widely used when high magnifications are needed and the specimen is colorless or the details are so fine that color does not show up well. Under these conditions, bright field microscopy images show too little contrast between structures with similar transparency, and fluorescent imaging and confocal microscopes are far more expensive. Cilia and flagella, for example, are nearly invisible in bright field but show up in sharp contrast in phase contrast images. Most previous cellular microscopy image analyses are carried on synthetic images or fluorescence images. To make fluorescence images, certain fluorescent proteins are introduced into cells by genetical modification. This procedure is tedious, time-consuming, and may interfere with the original proteins under study. It is a challengeable task to segment cells in phase contrast images. Edge detection methods suffer from low-contrast boundaries, and intensity thresholding does not work well due to similar intensities between inside areas and outside areas of cell membranes.

It is necessary to determine cell concentration in microbiology, cell culture, and many applications that require the use of suspensions of cells. The traditional device used for determining the number of cells per unit volume of a suspension is a counting chamber. Suspensions should be diluted enough so that cells do not overlap on the surface and are introduced into one of the V-shaped wells in a counting chamber with a pasteur or other type of pipet. A counting grid on the coverslip is brought into focus under the microscope. The number of cells is counted manually, the area is measured approximately by the grid, and the concentration is calculated. For time-lapse microscopy images with high throughput, manual counting and area measurements require a large amount of effort and time. A counting chamber cannot be used in every frame of microscopy images because the grids on coverslips block the view of cells. A large volume of data generated from cancer cell research calls for automatic processing in a quick and accurate manner. In many cell images the cell to cell contacts are very common in a high-density population. Thus, tracking an individual cell [1,2] in such situations is very difficult.

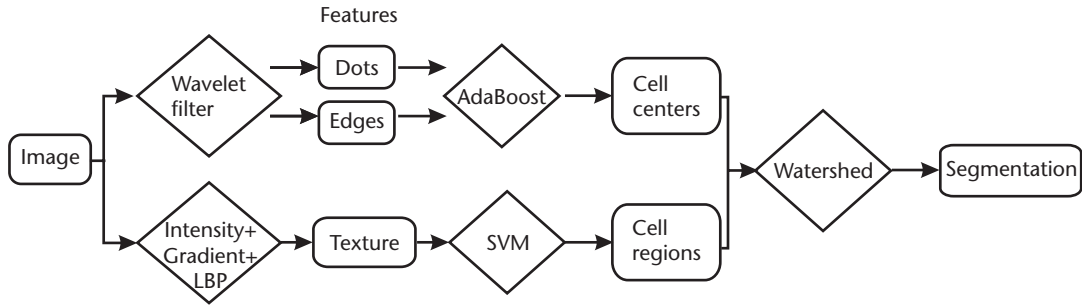


Segmentation of individual cells in cell clusters will give accurate cell counts for division rate estimation and provide a good observation model for cell tracking systems.

Parametric active contour [3–6] and level-set methods [7–9] are among the most popular segmentation approaches. These methods use internal smoothness forces and external image forces to iteratively approximate the object boundary starting from an initial user-supplied boundary. Texture can be included as one of the external image forces in these models, such as the work in MetaMorph [10]. In processing the temporal sequences, the initialization is manually done only for the first frame. The segmentation result of one frame is provided as the initialization of the next frame because the change is small between two consecutive frames. These methods have been successfully applied to cell segmentation in 2D+t data sets [1, 2]. In these methods, one model is built for each individual cell; therefore, the image features of neighboring cells are difficult to incorporate together to yield a better result. Full consideration of the interaction between each of the two cells will raise the complexity into  $O(n^2)$  and dramatically slow down the convergence. As a completely different approach, we segment cell clusters first and then separate cells in the same cluster. The segmentation of a single cell benefits from the segmentation procedure of all its surrounding neighbors, and the time complexity is kept as  $O(n)$ .

We use a learning method to find an initial boundary of cells and cell clusters. The curve evolution techniques are applied to adjust the boundary based on edges. The training phase in our learning method involves very modest user interaction by indicating several typical positive pixels (cells) and negative pixels (background). We use a novel feature representation that combines both the intensity distribution and gradient magnitude distribution in a small subwindow around the pixel. The size of the subwindow is supplied by the user. We show that the  $\mathcal{L}^1$  distance between such two feature vectors corresponds to the Earth mover's distance [11]. The training phase is also dynamic. The user feedback can help improve the classifier rapidly. After several iterations of classification and feedback, an accurate classifier is developed for automatic segmentation for new images. Our learning to segment approach is general and can be applied to other foreground/background segmentation problems.

The watershed algorithm is applied on the foreground segmentation results to further separate cells in one cluster. Due to the nature of the watershed algorithm to oversegment, regions are merged after segmentation based on rules that different regions with separating ridges lower than a level are merged together. To ensure that one segmented region contains exactly one cell, we set the cell centers as seeds and merge all regions without seeds to their neighboring regions. In the application of the watershed algorithm to the fluorescent cell images [12], nuclei are taken as seeds. For phase contrast images, cells are detected by the votes of multiple sets of features. The AdaBoost algorithm has been successfully used in human face detection [13]. A strong classifier is generated by sorting the performance of weak learners built on Harr wavelet responses respectively, while searching for an optimal combination of them. In cell images, texture with high intensity variation in cell nuclei and the halo around cell membranes cause high responses of the



**Figure 13.1** Flow chart of cell segmentation.

Maxican hat wavelet (MHW) filters. We apply the MHW filter to cell images and take the raw responses as potential weak learners to be selected by AdaBoost. The approximate locations of cells are detected by classifying small subwindows into positive and negative sets.

The flow chart of cell segmentation procedure is shown in Figure 13.1. Cell centers and cell regions are detected by different methods and put into the watershed algorithm to yield an accurate segmentation of individual cells. In cell center detection, subwindows about cell size are classified into cells and noncells with features like dots and edges. In cell region segmentation, small-size subwindows are classified into cell regions and background by the histogram of their texture features.

Detection and segmentation methods are introduced in Section 13.2. Experimental results and interpretations are presented in the Section 13.3. In order to estimate the cell division rate, it is sufficient to process frames with a large time step. Thus the number of frames to be processed can be reduced from hundreds to tens. Conclusions are drawn in Section 13.4.

## 13.2 Methodology

We detect cells with AdaBoost, and features are extracted by the Mexican hat wavelet, including dots in nuclei and abstracted boundary lines. Meanwhile we segment the foreground of cell images by classifying texture histograms of small window bins with support vector machines. The different cells inside a cell cluster are separated by the watershed algorithm with nuclei seeds detected with AdaBoost.

### 13.2.1 Cell Detection with AdaBoost

Cell detection is the first step of accurate cell segmentation. It provides the number of cells and the locations of cells, and it groups the weak edge and intensity information extracted from the image into different cells. Two sets of features help people to detect cells and also facilitate automatic cell detection. Proteins in cell nuclei show dark dots in the image, and membrane boundaries show white

halo in phase contrast images. We detect these dots and white boundaries by Mexican hat wavelet, extract feature vectors, and train an AdaBoost classifier on them. AdaBoost selects good features that can be combined to form an effective strong classifier for cell detection.

### 13.2.1.1 Feature Representation

The nuclei in cells show up as dotted areas darkly against the surrounding cytoplasm. Due to the halo around cells and the shading inside cells, the areas with the lowest density from a uniform threshold are not necessary nuclei. Wavelet techniques have shown very good performance in detecting texture in local scale. To detect dotted areas with high contrast, we convolve the Mexican hat wavelet filter to the cell image and get areas with high-intensity gradient.

The wavelet transformation is the decomposition of a function  $f(x)$  on a basis that incorporates the local and scaling behavior of the function. In the time domain, the continuous transform involves translations and dilations

$$w(R, b) = \frac{1}{\sqrt{R}} \int f(x) \psi\left(\frac{x-b}{R}\right) dx, f(x, y) \in L_2(x, y) \quad (13.1)$$

where  $\psi$  is the mother wavelet and  $R$  is the scale of this isotropic wavelet.

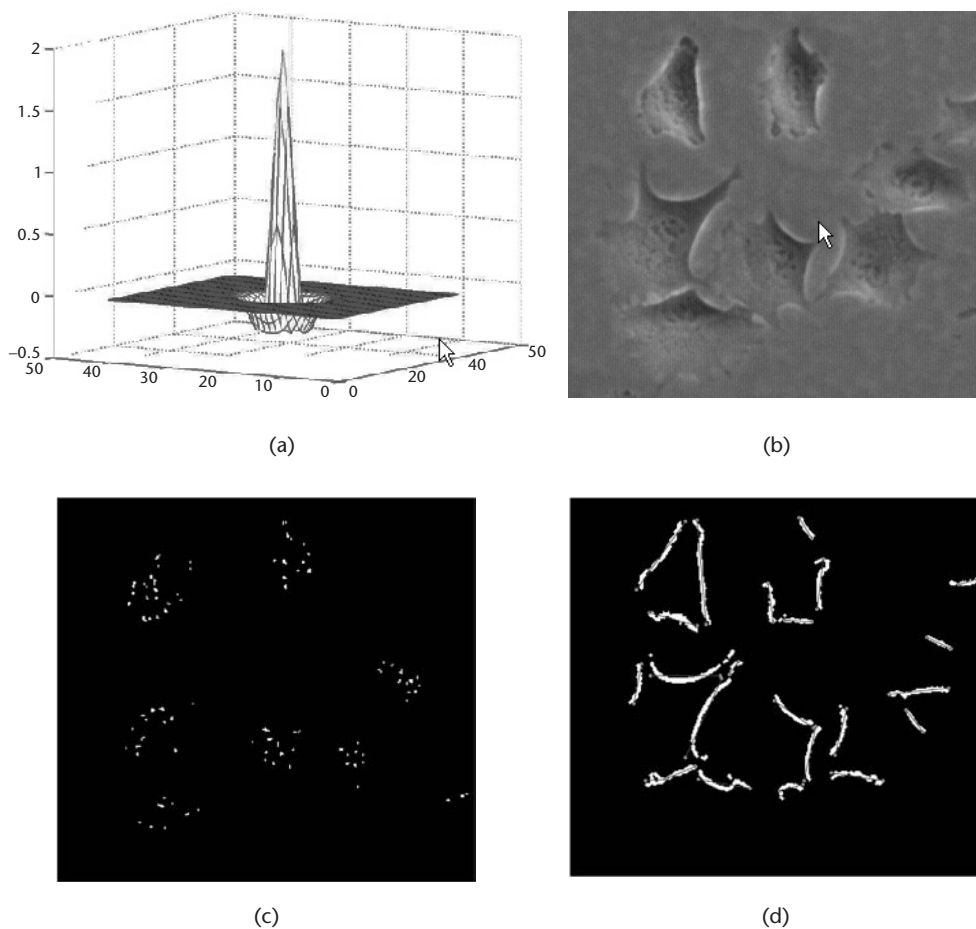
The 2-D Mexican hat wavelet is generated by applying a Laplacian calculator on the 2-D Gaussian filter, as defined in the following equation

$$\psi(x, y) \propto \Delta\phi(x, y) \propto (x^2 + y^2 - 2)e^{-\frac{1}{2}(x^2+y^2)} \quad (13.2)$$

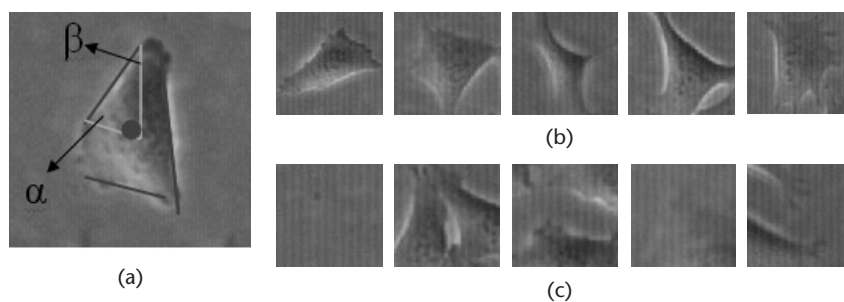
has been used to detect point sources in cosmic microwave background (CMB) maps in astrophysics.

The areas with high response to negative MHW include dots in nuclei and dark edges on the membrane. After removing the edges, which have larger areas, the rest areas are dotted nuclei, as shown in Figure 13.2. We use the response of a negative MHW filter directly as one of our feature sets. The other feature set includes the white edges caused by the halo around the membranes of cells. After removing small components, the convolving results show the main white edges. We fit long curves with Hough transform. Four values of each line are put into feature vectors: the distance from the center of the detecting window to the edge lines, the length of the edge lines, and the two angles formed by the center and the two ends of the edge, as shown in Figure 13.3(a). Since the number of edge lines in a detecting windows varies, we set this feature set with large enough constant length and fill null into the rest of the space. Both the number of edge lines around a cell and the characteristics of the edge lines are selected by boosting methods.

As shown in Figure 13.2(a), by convolving the Mexican hat filter, the intensity of central area will be subtracted by surrounding area. We use a Mexican hat to detect white boundaries and use an upside-down MHW to detect black points. Figure 13.2(c) shows the pixels with the responses higher than a threshold, after applying an upside-down MHW on the cell image shown in Figure 13.2(b) and removing large areas. Figure 13.2(d) shows the responses of the MHW after removing



**Figure 13.2** (a) 2-D Mexican Hat wavelet. (b) Cell image. (c) Responses from negative MHW after removing large areas. (d) Responses from MHW after removing small areas and applying Hough Transform.



**Figure 13.3** (a) Features extracted from edge lines. (b) Sample images in positive feature set. (c) Sample images in negative feature set.

small areas. The boundary curves are broken at high curvature points, and the red lines are detected by Hough transform.

### 13.2.1.2 AdaBoost Algorithm

From a large set of features with significant variation, the AdaBoost algorithm (see Algorithm 13.1) can select the representative ones that can distinguish positive instances and negative instances. A thresholding function on each feature, called a weak learner, is trained in different iterations. The final strong classifier is the weighted expectation of the votes of the weak learners with good performance. The features that can separate cells and noncells better have higher weights than irrelevant features in the final voting. Due to the correlation of different features, a combination of top features might not be the best combination. Therefore, the features are not evaluated independently. To get the best combination of features, AdaBoost employs a greedy strategy. It selects the best feature first, then reweighs the training instances along such an order that the instances classified better by already selected weak learners have lower priority. It selects the next best feature based on the error rate calculated with the updated weights. The most likely feature to be selected next is the one that can achieve best classification performance on the difficult cases left by the already selected features. In practice, no single feature can perform the classification task with low error. Features that are selected early in the process yield error rates between 0.1 and 0.3. Features selected in later rounds, as the task becomes more difficult, yield error rates between 0.4 and 0.5. This searching method guarantees finding one of the optimal combinations of representative features. Freund and Schapire [14] proved that the training error of the strong classifier approaches zero exponentially in the number of rounds.

A weak learner votes for the cell detection result by a thresholding function, consisting of a feature ( $f_j$ ), a threshold ( $\theta_j$ ), and a parity ( $p_j$ ) indicating the direction of the inequality sign:

$$h_j(x) = \begin{cases} 1 & \text{if } p_j f_j(x) < p_j \theta_j \\ 0 & \text{otherwise} \end{cases} \quad (13.3)$$

We select a set of single cells in small subwindows, normalize them into the same window size, and set them as the positive set. The negative set is constructed by some randomly selected subwindows, showing the background or the space between cells. The criteria is that in the positive set there is a cell with its nucleus centered in the image, and in the negative set there is no cell in the center of the image. Multiple partial cells could be in a corner in a negative instance.

We trained on a training set with 1,000 cell images marked by biologists, and 1,000 noncell images from the randomly cropped set after removing a few cell images. During the testing procedure, we search subwindows of cell images in a certain size range. Each subwindow is classified by the learned strong classifier into positive and negative categories. A real cell can have multiple positive subwindows around it. Instead of trying to determine which positive responses are caused by one cell and should be merged into one, we map the centers of all positive subwindows onto a black background.

**Algorithm 13.1** AdaBoost Algorithm

Boosting procedure on cell features:

- In the training set, given feature vectors  $x$  and class attribute  $y$  as instances  $(x_1, y_1), \dots, (x_n, y_n)$ , where  $y_i = 0, 1$  for negative and positive examples, respectively.
- Initialize weights  $w_{1,i} = \frac{1}{2m}, \frac{1}{2l}$  for  $y_i = 0, 1$ , respectively, where  $m$  and  $l$  are the number of negatives and positives, respectively.
- For  $t=1, \dots, T$ :
  1. Normalize the weights,  $w_{t,i} \leftarrow \frac{w_{t,i}}{\sum_{j=1}^n w_{t,j}}$ .
  2. For each feature, train a thresholding classifier. The error rate is evaluated as  $\epsilon_j = \sum_i w_{t,i} |h_j(x_i) - y_i|$ .
  3. Choose the classifier  $h_t$  with the lowest error rate  $\epsilon_t$ .
  4. Update the weights:  $w_{t+1,i} = w_{t,i} \beta_t^{1-e_i}$ , where  $e_i = 0$  if example  $x_i$  is classified correctly,  $e_i = 1$  otherwise, and  $\beta_t = \frac{\epsilon_t}{1-\epsilon_t}$ .
- The final strong classifier is

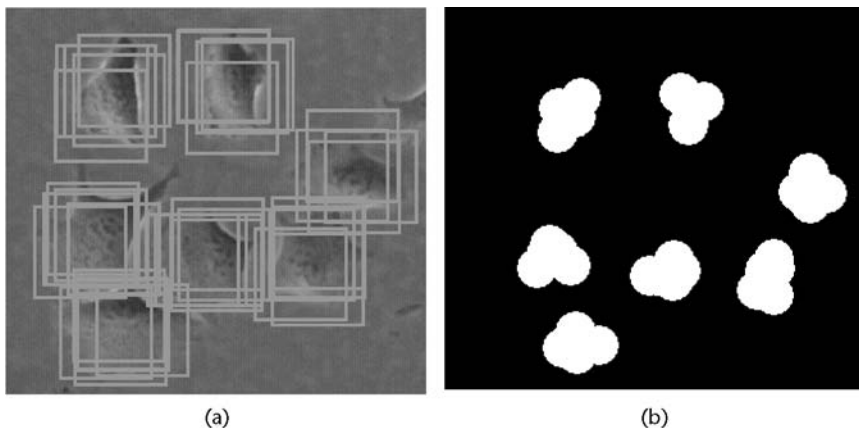
$$h(x) = \begin{cases} 1 & \sum_{t=1}^T \alpha_t h_t(x) \geq \frac{1}{2} \sum_{t=1}^T \alpha_t \\ 0 & \text{otherwise} \end{cases}$$

$$\text{where } \alpha_t = \log \frac{1}{\beta_t}$$

As shown in Figure 13.4, the centers of nearby positive responses merge into one area.

**13.2.2 Foreground Segmentation**

In this work cell clusters are segmented with learning-based methods, by classifying the region features based on a few user-selected training samples. Since both cell nucleus and cytoplasm are translucent in phase contrast images, it is impossible to segment the interested region with a threshold of intensity only. We utilize the



**Figure 13.4** (a) AdaBoost detecting results. (b) Detected cell centers.

variation pattern in intensities, such as gradient and local binary pattern (LBP), to distinguish cell areas from the background. The statistics of local features are obtained from small-size windows and put into a support vector machine (SVM) for training and classification. The difference of their histograms are measured with the Earth Mover's Distance (EMD). The SVM project the feature vectors into a kernel space and separate different clusters in the training set with a hyperplane. Then the whole image is divided into small bins and classified into two categories by the SVM.

### 13.2.2.1 Feature Vectors and Earth Mover's Distance

We use three sets of feature vectors for classification: the intensity, the magnitude of gradient, and the local binary pattern (LBP). Each feature set can be shown in an image with the same size as the original image. The intensity and the magnitude of gradient are obviously orientation invariant features. The LBP is derived from a general definition of texture in a local neighborhood. The comparison results of a pixel and its neighbors are binary coded and turned into a binary number. For a pixel  $(x_c, y_c)$ , the LBP code characterizes the local image texture around  $(x_c, y_c)$ :

$$LBP_{P,R}(x_c, y_c) = \sum_{p=0}^{P-1} \text{sign}(I_p - I_c) 2^p \quad (13.4)$$

where  $I_p$  are the intensity of  $P$  neighbors of pixel  $c$ . The rotation invariant code is produced by circularly rotating the original code until its minimum value is attained.

In each feature image, we characterize the histogram of a  $n \times n$  subwindow around a pixel with a feature vector. We sort all values in the subwindow and get

$$I(i), i = 1 \dots n^2, \text{ where } I(i) \leq I(j), 1 \leq i \leq j \leq n^2$$

Then the distribution feature vector is represented as

$$I(i), i = [n/2], [3n/2], \dots, [(2n-1)n/2]$$

The length of the distribution feature is  $n$ , which is reasonably short without loss of much representation accuracy. Compared to histogram representation, this representation of distribution does not require a fixed bin size and thus is more accurate. We will show later the  $\mathcal{L}^1$  distance between two distributions in our representation scheme corresponds to EMD.

### 13.2.2.2 Segmentation with Classification and Curve Evolution

Our learning-based segmentation framework is outlined in Algorithm 13.2. In the training phase, the user begins by indicating several positive/negative pixels inside/outside the cells and provides the size of the subwindow. The corresponding intensity/gradient magnitude distributions in the subwindows are then computed as the feature vectors. These feature vectors along with their labels are served as the initial training examples. An RBF kernel-based SVM [15] classifier is learned using this training set.



**Algorithm 13.2** Learning-Based Segmentation Framework

Training:

1. Input: a training image and the size of the subwindow
2. Do until satisfied:
3.     Indicate several typical positive and negative pixels
4.     Add these examples to the training set
5.     Train a radial basis function (RBF) SVM classifier
6.     For each nonoverlap subwindow:
7.         Compute the feature vector and classify
8.     Iterative refinement by classifying boundary subwindows
9.     Foreground/background curve evolution in the boundary band
10.    Smoothing

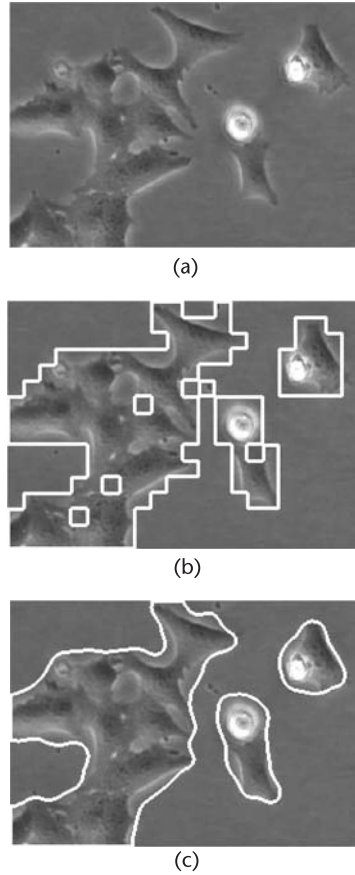
Classification and Segmentation: Step 6–10

Instead of classifying every pixel in an image, which is time-consuming, our strategy is to focus the attention on the object boundary. The classification is iterative. In the first step we only classify nonoverlapping subwindows in the image. With high probability, the classification errors are located near the classification boundary between the positive and negative subwindows. Those most ambiguous boundary pixels (typically, the corners) are automatically located. We apply the classifier to the subwindows around them. This boundary refinement classification step repeats several times depending on the size of the subwindow. The final classification result is the weighted sum of each classification. The weight of each classification for a pixel in a subwindow is the Gaussian weight according to its spatial position. In this way we avoid classifying every pixel and only look into those ambiguous boundary points. This step results in a rough boundary between cells and background.

To accurately determine the boundary, we also need to consider the edge information. A boundary band is defined by dilating the rough boundary with the size of the subwindow. Then both the cell and background regions dilate with the same speed into this band and claim pixels except the edge pixels, which are determined by Canny edge-detection method [16]. Thus both cell and background regions can not pass through the edges. However, the false edges can be circumvented since they tend to be short in length. In each dilating step, we also consider the smoothness condition (i.e., those points with high curvature should move faster). This curve evolution is finished until the boundary band is completely divided as cell region or background region. The cell boundary is smoothed as the last step.

In the training phase, the user can give feedback by correcting the typical segmentation errors. The corrected examples are included in the training set. We retrain the classifier and generate a new segmentation result through the same procedure of classification and curve evolution. This feedback/refinement procedure iterates until the user is satisfied with the segmentation result. The final classifier (support vectors and the parameters) is saved for automatic segmentation of cell images.

After the final classifier is resulted, we can use it to automatically segment out cells or cell clusters. Figure 13.5 shows step by step the automatic segmentation procedure with classification and curve evolution. Figure 13.5(a) is a cropped cell image. Figure 13.5(b) shows the result after applying the classifier on nonover-



**Figure 13.5** Segmentation procedure; (a) original image, (b) initial classification, and (c) refined boundary.

lapping subwindows. The classifier is trained on five positive and five negative examples. The white lines are the rough boundary between cells and the background. Figure 13.5(c) is the final segmentation result after smoothing the final cell region. The total cell area can then be calculated.

### 13.2.3 Cytoplasm Segmentation Using the Watershed Algorithm

In a high-density population, cells are clustered together with attaching borders. The watershed algorithm with seeds is applied here to separate individual cells. The watershed algorithm originally suggested by Digabel and Lantuejoul [17] has proven to be very useful in many areas. Considering the intensities of an image as elevation in a landscape, the watershed methods immerse the surface with water and find the boundaries of basins. The water first produces a local minimum of the surface. When the water level increases along the surface, water in adjacent areas will meet at a ridge of the landscape. A dam is built at the place where two areas of water meet two separate and different areas.

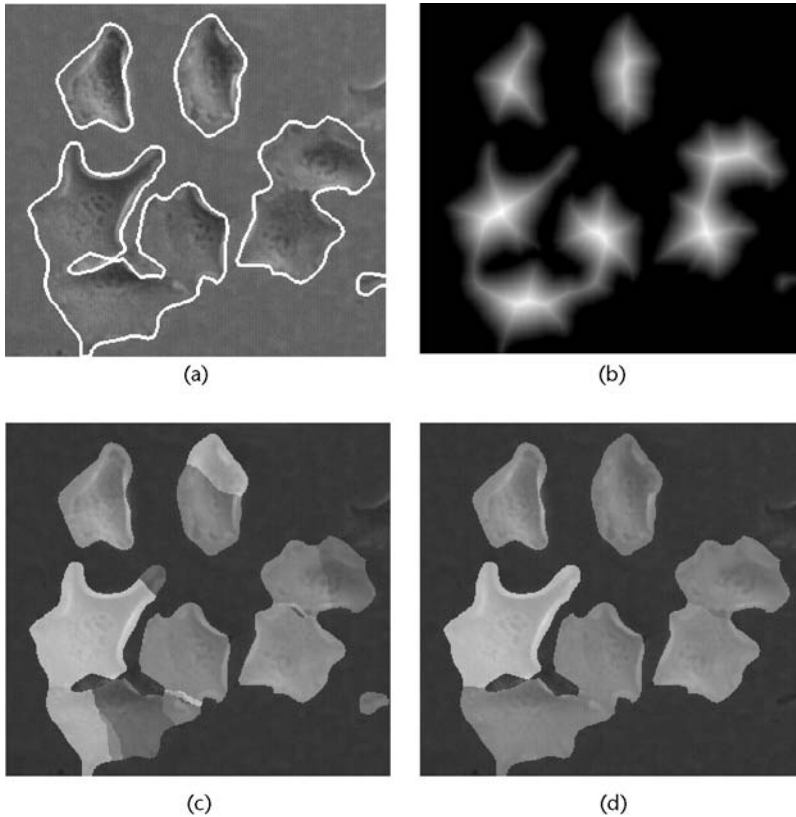
Watershed is a robust cell segmentation algorithm for fluorescent images. In fluorescent cell image applications [12], the nuclei image was thresholded first, and the watershed algorithm is applied to the distance map of the thresholding results. Because the watershed method tends to over-segment, areas with the border lower than a threshold are merged together afterwards. In fluorescent images, nuclei images and cytoplasm images can be taken from the different channels of the same image setting. The watershed method has also been applied to cytoplasm segmentation with nuclei as seeds to avoid oversegmentation.

In this work, we take a similar approach as proposed in [10] and illustrated in Figure 13.6. A distance transform is put onto the foreground segmentation results. The cell detections results, obtained using the AdaBoost algorithm, are now taken as seeds of the watershed algorithm. Regions without seeds are either merged to its neighbors with seeds or removed from the image.

### 13.2.4 Cell Division Rate Estimation

The cell division can be modeled as

$$N_t = N_0 2^{\alpha t} \quad (13.5)$$



**Figure 13.6** (a) Cell cluster segmentation results. (b) Distance map. (c) Segmentation results without seeds. (d) Segmentation results with cell detection seeds.

where  $\alpha$  is the division rate we would like to estimate,  $N_0$  and  $N_t$  are the cell counts at time 0 and  $t$ . The cell division rate  $\alpha$  can be expressed as:

$$\log_2(N_t) = \log_2(N_0) + \alpha t \quad (13.6)$$

After segmentation on a few images, we get several  $(t, N_t)$  pairs. Then the cell division rate can be estimated through a linear fitting for (13.6).

### 13.3 Experiments

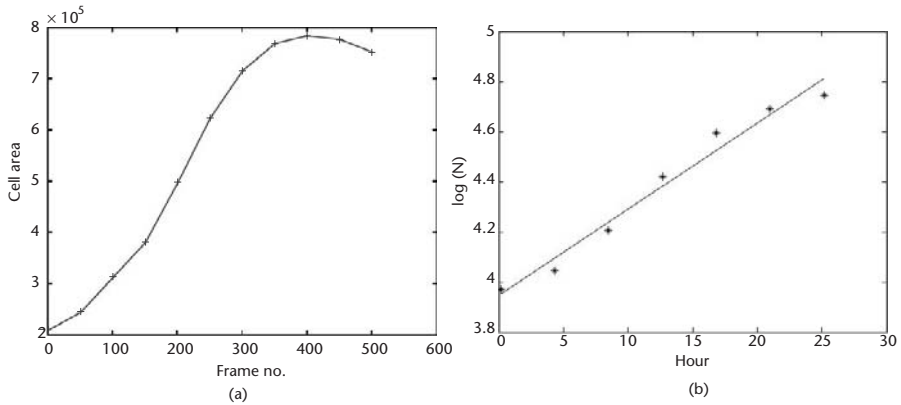
Time-lapse movies of several cell types with different genotypes were generated using computerized video time-lapse microscopy (CVTL) microscopy. CVTL microscopy consisted of an Olympus IX71 inverted microscope fitted with high resolution X,Y and Z motorized scanning stage and a temperature, humidity, and nutrition controlled environmental chamber. Autophagy, also called self-cannibalism, is a process in which organelles and proteins inside of cells are delivered to lysosomes for proteolysis when cells are deprived of nutrition. Autophagy is one way for cells to tolerate metabolic stress and avoid apoptotic or necrotic pathways of cell death, although completely consuming nutrition of themselves will also lead to autophagic death. During autophagy, cells exhibit different appearances and behaviors that interest biologists [18]. The images are phase contrast images of the cells captured at 10-minute intervals, same as the normal cells, for 3–5 days. This enabled us to follow several cell lineages and cellular events in multiple fields for long periods of time.

In this experiment, we segment out cells or cell clusters and then estimate the division rate for one time-lapse movie consisting of around 500 frames. The size of each frame is  $870 \times 1164$  pixels. The chosen subwindow size is  $13 \times 13$  pixels. Cells or cell clusters are automatically segmented for every other 25 frames (i.e., 250 minutes apart). Color Plate 19 shows the segmentation result for frame 1, 26, 51, and 76. We compare our automatic segmentation result  $A$  with manual segmentation result  $M$  in Table 13.1. Both recall  $(A \cap M)/M$  and precision  $(A \cap M)/A$  are above 95% for all four frames. In order to validate our results, we manually count the numbers of cells in these four frames.

In Figure 13.7(a), the total cell number versus frame number plot shows an exponential cell growing pattern at the beginning, but the growth rate drops when the field is very highly populated. The growth rate decrease can be explained by the cell-to-cell interaction when the population is very dense. Our division rate estimation is for the initial phase when the population is not so dense. Thus, we

**Table 13.1** Segmentation Accuracy and Average Cell Size Estimation

Frame#	$(A \cap M)/M$	$(A \cap M)/A$	TotalCellArea( $M$ )	Count ( $N$ )	AvgCellArea
1	97.72%	98.69%	107,484	53	2028
26	95.31%	98.81%	115,254	57	2022
51	97.48%	98.42%	137,149	67	2047
76	96.70%	96.11%	166,830	83	2010



**Figure 13.7** (a, b) Cell division rate estimation.

consider seven frames (frame 1, 26, 51, 76, 101, 126, and 151) to compute the cell division rate. By fitting a line for (13.6) using least squares (Figure 13.7(b)), we have  $\alpha = 0.0344$  (1/hour) (i.e., the autophagy cell divides every  $1/0.0344 \approx 29.07$  hours in this time-lapse movie). The experiments show that the proliferation rate slows down because cell metabolism is suppressed when cells are deprived of nutrition during autophagy.

## 13.4 Conclusions

The main contributions of this work are two-fold. First, we presented a novel cell detection method that incorporates low-level image features and AdaBoost learning method in the same framework. Second, we applied a robust segmentation method that can estimate individual cell boundaries accurately by texture classification and the watershed algorithm. The segmentation methods enable us to estimate automatically the cell division rate in CVTL microscopy, which paves the way for future high-throutput biological image analysis. Finally, the learning phase is very efficient and involves very modest user interaction.

## References

- [1] Zimmer, C., E. Labruyere, V. Meas-Yedid, N. Guillen, and J.-C. Olivo-Marin, "Segmentation and Tracking of Migrating Cells in Videomicroscopy with Parametric Active Contours: A Tool for Cell-Based Drug Testing," *IEEE Trans. Med. Imaging*, Vol. 21, No. 10, 2002, pp. 1212–1221.
- [2] Yang, F., M. A. Mackey, F. Ianzini, G. Gallardo, and M. Sonka, "Cell Segmentation, Tracking, and Mitosis Detection Using Temporal Context," *MICCAI*, 2005, pp. 302–309.
- [3] Kass, M., A. Witkin, and D. Terzopoulos, "Snakes: Active Contour Models," *Intl. Journal of Computer Vision*, Vol. 1, No. 4, 1988, pp. 321–331.

- [4] Staib, L. H., and J. S. Duncan, "Boundary Finding with Parametrically Deformable Models," *IEEE Trans. Pattern Anal. Mach. Intell.*, Vol. 14, No. 11, 1992, pp. 1061-1075.
- [5] Caselles, V., R. Kimmel, and G. Sapiro, "Geodesic Active Contours," *ICCV*, 1995, pp. 694-699.
- [6] Xu, C., and J. Prince, "Snakes, Shapes, and Gradient Vector Flow," *IEEE Trans. Image Proc.*, 1998, pp. 359-369.
- [7] Malladi, R., J. A. Sethian, and B. C. Vemuri, "Shape Modeling with Front Propagation: A Level Set Approach," *IEEE Trans. on Pattern Anal. and Mach. Intell.*, Vol. 17, No. 2, 1995, pp. 158-175.
- [8] Sethian, J. A., *Level Set Methods and Fast Marching Methods*, Cambridge: Cambridge University Press, 1999.
- [9] Li, K., E. D. Miller, L. E. Weiss, P. G. Campbell, and T. Kanade, "Online Tracking of Migrating and Proliferating Cells Imaged with Phase-Contrast Microscopy," *Cancer Cell*, 2005.
- [10] Huang, X., D. N. Metaxas, and T. Chen, "Metamorphs: Deformable Shape and Texture Models," *CVPR (1)*, 2004, pp. 496-503.
- [11] Rubner, Y., C. Tomasi, and L. J. Guibas, "The Earth Mover's Distance as a Metric for Image Retrieval," *Intl. Journal Computer Vision*, Vol. 40, No. 2, 2000, pp. 99-121.
- [12] Joakim, L., W. Carolina, B. Ewert, and Z. Alla, "Image Analysis for Automatic Segmentation of Cytoplasm and Classification of rac1 Activation," *Cytometry*, Vol. 57A, No. 1, 2004, pp. 22-33.
- [13] Viola, P., and M. Jones, "Robust Real-Time Object Detection," *International Journal of Computer Vision*, Vol. 57, 2004, pp. 137-154.
- [14] Schapire, R. E., "A Brief Introduction to Boosting," *Proc. of the 16th Intl. Joint Conf. on Artificial Intelligence*, 1999, pp. 1401-1406.
- [15] Cristianini, N., and J. Shawe-Taylor, *Support Vector Machines and Other Kernel-Based Methods*, Cambridge: Cambridge University Press, 2000.
- [16] Canny, J., "A Computational Approach to Edge Detection," *IEEE Trans. Pattern Anal. Mach. Intell.*, Vol. 8, No. 6, 1986, pp. 679-698.
- [17] Digabel, H., and C. Lantuejoul, "Iterative Algorithms," *European Symp. Quantitative Analysis of Microstructures in Materials Sciences, Biology and Medicine*, 1977, pp. 85-99.
- [18] Degenhardt, K., R. Mathew, B. Beaudoin, K. Bray, D. Anderson, G. Chen, C. Mukherjee, Y. Shi, C. Gelinas, Y. Fan, D. A. Nelson, S. Jin, and E. White, "Autophagy Promotes Tumor Cell Survival and Restricts Necrosis, Inflammation, and Tumorigenesis," *Cancer Cell*, Vol. 1, 2006, pp. 51-64.

# Systems Biology and the Digital Fish Project: A Vast New Frontier for Image Analysis

Sean G. Megason

## 14.1 Introduction

With the completion of the genome projects and the advent of many high-throughput technologies, it is now possible to take a systems-based approach to many questions in biology. In this chapter we argue why imaging-based approaches to systems biology will play a very important role in this emerging field, and more importantly what challenges imaging-based systems biology poses to the image analysis community. We discuss the types of image data that are generated, the goals of the image analysis, and the current progress and future challenges in meeting these image analysis goals. These topics are discussed in the context of our software application GoFigure and an effort we have underway to digitize embryonic development called the Digital Fish project.

## 14.2 Imaging-Based Systems Biology

New opportunities in the field of image analysis have always been spawned by both new imaging technologies and new scientific applications. This is certainly the case today with the development of a number of new approaches in microscopy and the emergence of the field of systems biology. The widespread adoption of confocal and multiphoton microscopy along with the tremendous developments of fluorescent proteins such as GFP have created a renaissance in optical microscopy. A number of forces have also converged, including genomics, proteomics, and high-throughput screening, along with these new approaches in microscopy to create the field of systems biology. These technologies generate new kinds of image sets and allow biologists to ask new kinds of questions, but in so doing they create many new challenges in image analysis. These developments have together opened up a vast new frontier of challenges and opportunities in image analysis.

### 14.2.1 What Is Systems Biology?

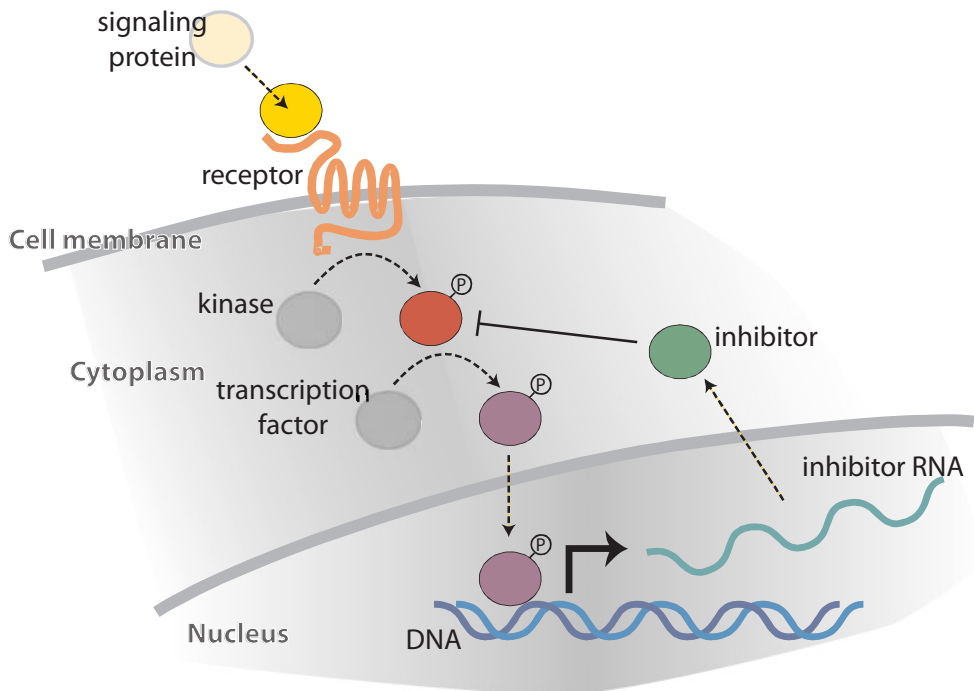
*Systems biology* quite simply refers to investigating how multiple components of a biological system interact to give rise to the function of that system. These components can be anything from metabolites to genes, proteins, cells, and even whole organisms. And likewise the system can be a single biochemical pathway, a cell, a whole organism, or even an ecosystem. Note that this definition of systems biology



does not exclude many other areas of biology, such as biochemistry, cell biology, genetics, and embryology, and indeed these other areas of biology partially overlap with systems biology as well as each other. What characterizes systems biology is an emphasis on looking at the systems level, on being quantitative, and the use of mathematical and computer modeling. In many ways systems biology is the logical progression of these other areas of research. In order to characterize a system, it is first necessary to characterize its components. This has been accomplished to a large extent through decades of research in biochemistry and molecular biology and more recently through genomics and proteomics. It is only through the success of these reductionist approaches in defining the pieces that we can now try to put the pieces back together to understand the system.

Genes and proteins are of particular interest in systems biology because it is the interaction of these components that does much of the “computation” to guide biological processes. A typical animal genome contains 15,000 to 30,000 genes [1] and a corresponding number of proteins (the number of proteins is actually higher due to alternative sites for splicing, promoters, and polyadenylation). However, not all of these genes are turned on in any given cell. Different types of cells express different subsets of genes, and to a large extent it is this difference in gene expression that gives rise to the different functional properties of cells. Some genes encode for proteins directly involved in the properties of a cell. For example, the *hemoglobin* gene encodes for the protein that lets your red blood cells carry oxygen, while the *myosin* and *actin* genes allow your muscles to contract. Other types of genes do not encode for proteins with direct structural or phenotypic functions but instead encode proteins involved in information processing: secreted signaling proteins can transfer information between cells; receptors can transfer information from outside a cell to inside a cell; numerous signal transduction components including kinases, phosphatases, proteases, GTPases, and ubiquitin ligases can transmit and process information inside a cell; and perhaps most importantly transcription factors can regulate the expression of other genes (Figure 14.1). These different types of proteins can interact with each other physically to transmit information. For example, a secreted signaling protein can physically bind to its receptor, causing a change in the conformation of the receptor. This change in conformation could activate the enzymatic activity of the receptor, causing it to phosphorylate a target such as another kinase. This kinase could phosphorylate a transcription factor, allowing it to move from the cytoplasm to the nucleus, where it can bind to specific sites of DNA to regulate the expression of some subset of genes (Figure 14.1). Such a set of proteins from signaling molecule to transcription factor is called a signal transduction pathway. Interestingly, the subset of genes regulated by this signal transduction pathway could include the secreted signaling molecule itself and other positive and negative regulators of the pathway, setting up feedback loops. Such feedback loops are thought to play important roles in regulating genetic circuits [2].

Thanks to the genome projects, we now have a fairly complete picture of the genetic makeup of most organisms used in experimental biology [1, 3–6]. The genome projects gave us the sequences (the order of all the A’s, G’s, C’s, and T’s) of the DNA that comprises these genomes. Implicit within the genomic sequence



**Figure 14.1** Signal transduction pathways transmit and process information. In this example, a secreted signaling protein is released from one cell and binds a receptor on another cell. This causes a conformational change that activates the kinase activity of the receptor, allowing a downstream kinase to be phosphorylated. This phosphorylation activates the kinase, causing it to phosphorylate a transcription factor. This phosphorylation allows the transcription factor to enter the nucleus, where it can bind specific targets of DNA to turn on a set of genes. Some of these genes may be inhibitors to produce feedback loops.

of an organism is a set of instructions for creating that organism. The genome can be thought of as a program that when executed creates an organism through the process of embryonic development and then maintains that organism through growth and homeostasis so that the organism can reproduce and pass on this program across time. Defects in this program caused by genetic mutations lead to many diseases such as cancer. Although we now have the complete program for a number of organisms, we are very far from understanding how that program works. This is in large part because we can only understand a fraction of the code contained within the genome. What we can read fairly easily in genomic sequences are *coding regions*. There are good computational and experimental approaches for determining which parts of the genome are transcribed to make mRNA, which is then translated to make protein. But only a small fraction of the genome is coding sequence. Embedded within the noncoding sequence is information that helps determine which genes get expressed when and where in an organism. For example, transcription factors bind specific sequences of noncoding DNA and can regulate the expression of nearby genes. However, these sequences are fairly short and degenerate, making it very difficult to predict the targets of a transcription

factor. Another problem is that although we can accurately predict which parts of the genome will be made into proteins, we cannot predict the function of that protein just based on its sequence. Taken together, although the genome projects have given us the complete code for constructing organisms, all we can really read is the parts list—the genes, RNAs, and proteins. The big challenge ahead is to understand how these parts fit together to form networks, how these networks function as circuits, and how these circuits function to orchestrate biological processes. This is the goal of systems biology. This goal must be accomplished in large part through experimental work because there are many things in biology that we simply cannot predict due to its complexity. Theory, modeling, and computer simulation will play an essential role in systems biology, but they need to be data driven.

An essential first step in systems biology is understanding how the individual components can interact to form networks. Traditionally, geneticists can look for functional interactions between two genes by creating double mutants and looking for nonadditive phenotypes. Biochemists can look for physical interactions between two proteins by seeing if they “stick” to each other—for example, you can use an antibody specific to one protein to precipitate it from a solution and then use an antibody specific to the other protein to see if it was also precipitated. These approaches have been quite informative, but they are low throughput. Recently there have been several approaches to address molecular interactions on a systematic fashion. Approaches including the yeast two-hybrid system, co-immunoprecipitation of epitope tagged proteins, protein microarrays, and systematic epistasis have been used to define thousands of molecular interactions [7, 8]. An often-used approach for representing these interactions is graphs (network diagrams) in which the nodes of the graph represent proteins and edges represent interactions between two proteins. There is currently a great deal of activity termed *interactomics* to construct graphs that represent all possible protein-protein interactions and even all protein-DNA interactions [7, 8].

The next step in systems biology is to go from having a network diagram to understanding how that network functions as a circuit. There are a few problems with the previous simple graph-based representation for taking this step. One is that not all proteins are expressed in all cells, so the actual network present in any given cell is a subgraph of the graph of all possible interactions. And to make things more complicated, it typically isn’t a binary “present or absent” value that matters; rather, the actual concentration of the protein is important. Another problem is that proteins can have different functional states, and this information is not captured in the earlier representation. The function of a protein can be changed through phosphorylation, ubiquitination, differential subcellular localization, or through allosteric regulation caused by binding to another protein or small molecule. All these changes can alter a protein’s ability to interact with another protein. What we want to understand is information flow through a network, and information is often carried through networks by changing the concentration of proteins or by changing their functional state. It is thus essential: (1) to experimentally measure these differences in concentration and functional state for

all the different cells, and (2) to incorporate this information into the network representation.

Once all the essential components and interactions of a circuit have been defined, it is possible to try to understand how the circuit functions. Function typically implies a temporal dimension, and thus going from understanding the structure of a network to the function of the network means going from a static to a dynamic view. A temporal understanding is important because molecular circuits function by changing “something” over time, such as the concentration or functional state of one or more proteins in the circuit. There is an input, some kind of computation, and then an output just as in any computer program but typically much slower. To understand this process, we need to trace the computation by “stepping through” the code as it is executing over time like you do during debugging. There are a variety of techniques to experimentally monitor a circuit as it is functioning over time. Biochemical approaches can be used to measure changes in protein concentration or phosphorylation over time. “Omic” approaches such as microarrays or mass-spectrometry can be used to measure how the levels of many RNAs or proteins vary over time. Imaging can also be used to monitor the dynamics of a circuit. For example, different color fluorescent proteins such as GFP can be used to mark the essential nodes of a circuit, and then these nodes can be followed over time using time-lapse imaging. We feel that this imaging-based approach to functional systems biology is quite powerful, so it will be the focus of this chapter.

Once a rough idea of the structure of a circuit and how its components change over time is established, it is often important to use modeling to investigate the dynamics of the circuit and how changes to individual aspects of the circuit are manifest at the systems level. Even simple circuits of only a few components can have quite complex dynamics that cannot be predicted by simple intuition. There are a number of types of models used in systems biology [9]. The classical approach is chemical reaction rate kinetics. In this approach all the chemical components and the chemical reactions that can convert between components are modeled. The rate that one component is converted into another component can be represented by a differential equation, and the entire system can be represented by a set of differential equations. There are two problems with this approach. One is that the reaction rate constants are difficult to measure and usually unknown. The other is that differential calculus assumes a continuous, infinitely divisible space. This assumption is fine in a large, well-stirred beaker but can break down in a cell where the number of individual molecules can be quite small, leading to random fluctuations in their numbers. For this reason, other modeling approaches are also used that try to account for the discrete nature of molecules such as stochastic simulation algorithms. It is also possible to hide some of the biochemical details, since they are often not known and use agent-based models that provide much more flexibility.

### 14.2.2 Imaging in Systems Biology

Although systems biology largely sprung out of the fields of genomics and proteomics, we feel imaging will play a very central role in the future of systems

biology [10]. At a practical level, the omics revolution of the last decade set the stage for systems biology by providing us with the complete list of all the parts of the system. Omics was also important in that it provided a fresh paradigm for biological research. The very essence of an omic approach is to gather complete, comprehensive, systematic knowledge: genomics aims to get complete genome sequences, microarrays try to monitor the expression of all genes, and proteomic approaches strive to measure all the proteins involved in a biological process. Omics also places more emphasis on standardization and quantitation to allow close comparison between different experiments. And finally computation plays a very important role in omics. Large databases are used to store all the genomic sequence and expression data, and a myriad of bioinformatic approaches are used to mine these data (e.g., to find related sequences, sort microarray data based on similarity of expression patterns, or to predict regulatory elements that control gene expression). Omics brought about an increased reliance on novel computational approaches for biological research, which in turn caused increased interactions between biologists and computer scientists. This important shift in both paradigm and culture brought on by omics continues strong in systems biology.

Despite omics playing the central role in the birth of systems biology, we feel microscopic imaging will play an increasingly important role in its future. This is because imaging can uniquely provide data that is single cell, longitudinal, quantitative, and anatomical—all of which are essential for understanding genetic circuits [10]. Cells are the basic building blocks of organisms, as well as a fundamental unit of computation. Most components of biological circuits are unable to cross cell membranes, and thus biological circuits are clustered within single cells. Even genetically identical, neighboring cells grown in the same environment can have very different phenotypes. This is due either to the effect of noise in circuits as the cells grow or to very small initial differences in the components of the cells [11]. Since they are *in vitro*, the first step of most omic approaches is to grind up a large number of cells to extract their DNA, RNA, or protein, which effectively blurs together all these important differences. Imaging provides high spatial resolution such that single cells within a population can easily be assayed. The spatial resolution of optical imaging is in fact high enough that subcellular data can be readily obtained.

The second important advantage of imaging is that it provides data that is longitudinal over time. As discussed earlier, understanding the function of biological circuits means understanding what they do over time—their dynamics. It is thus essential to have an assay that can collect measurements over time in an actively functioning system. *In vitro* omic approaches require the biological sample to be ground up to extract the molecules of interest, which effectively “kills” the system so it cannot be studied over time. The standard way around this problem is to do a time-course study in which aliquots of cells from an actively growing culture are taken at different time points after an experimental manipulation. This does provide longitudinal data, but it is not necessarily single-cell resolution. Any assay that requires cells to be killed in order to be measured cannot provide both single-cell and longitudinal data. Imaging, on the other hand, is noninvasive,

allowing time-lapse imaging to assay single cells over time as biological circuits are functioning within them.

The third advantage of imaging is that it can be quantitative at the protein level. When constructing models of biological circuits, it is often not sufficient to have “on” or “off” data about gene expression. Rather it is important to know the actual concentration of biological molecules at different places within a cell and different times. Most omic approaches are at least semi-quantitative, but the number they give can usually only be used for comparing different experiments made with the same assay (i.e., a relative measure). For example, there are elaborate statistical methods for measuring gene expression using microarrays [12]. These numbers can be used to say an RNA is present at three-fold higher levels at one condition versus another condition, but ideally you would say this RNA is present at 50 molecules per cell. With fluorescent imaging it is possible to get absolute quantitation, and it is possible to do this at the level of protein rather than just RNA [13, 14]. Most omic approaches such as microarrays work with RNA rather than protein because RNA is much easier to work with *in vitro* due to its uniform biochemical properties and ability to hybridize to complementary nucleic acid probes. However, it is protein rather than RNA that does most of the work in biological circuits. The use of GFP fusion proteins allows quantitative imaging to be done at the protein level. Importantly, the amount of fluorescence given off by a fluorophore is directly proportional to the concentration of the fluorophore. Thus, with the proper controls, it is possible to use fluorescent imaging to measure the actual number of molecules of a fluorescent fusion protein inside a living cell.

The final advantage of imaging over omics for doing systems biology is that imaging can provide data from spatially/anatomically intact organisms. Organisms vary over space. There are different kinds of cells in one part of an organism than in another part. It is in fact how these differences are patterned that is one of the main subjects of developmental biology. From a systems biology perspective, these differences over space mean that different cells receive different inputs from their environment, have different computations occurring inside them, and generate different outputs. It is important to capture these differences with reference to a spatial framework. *In vivo* imaging can be done on intact tissues and even whole organisms, allowing biological data to be digitized with reference to anatomical location. With omic approaches, the sample is ground up, which destroys any anatomical reference for the data. This problem can be partially overcome for omic approaches by carefully plucking cells from precise locations, but this is limited by the surgical skill of the investigator and the lack of clear morphological landmarks for many tissues even when there are underlying molecular or cellular differences.

In addition to these advantages, which are already well established for imaging, I am bullish that future technological advances in the field of microscopy will further open up the frontier of imaging-based systems biology. There have been tremendous technological advances in imaging in the last decade, and there is no reason to think this rate of progress will slow down. The last decade has seen the widespread adoption of confocal and two-photon microscopy, which along with GFP technology has created an impact on biomedical research whose importance cannot be overstated. More recently there have been a number of other advances.



Fluorescent proteins have been created with numerous colors from blue to far red, which can change color and which can mark the functional state of a protein [15] (see Chapter 2). On the microscopy side, there has recently been a number of advances that have shattered the long-held resolution limit of optical microscopy set by the wavelength of light imposed by diffraction. A number of techniques have been published in the last few years that increase the resolution of optical microscopy by greater than ten-fold [16]. These are only just now becoming commercialized, but once they are they could have a profound impact on biological research. All of these new imaging techniques will create new needs in image analysis.

## 14.3 Example: The Digital Fish Project

Imaging is now being used for a number of projects in systems biology, ranging from high-content screening in cell culture [17, 18] to using imaging of FP transgenics to monitor biological circuits in organisms including bacteria, yeast, plants, and animals [19–21]. Although the difficulty and details of image analysis will vary depending on the experimental setup, the goals of image analysis for many of these applications are similar—namely, to extract quantitative, cell-based data. Rather than touch lightly on a number of different biological applications of imaging, we will delve more deeply into a single application, the Digital Fish project, which we are involved with and feel illustrates many of the image analysis challenges in the field of systems biology.

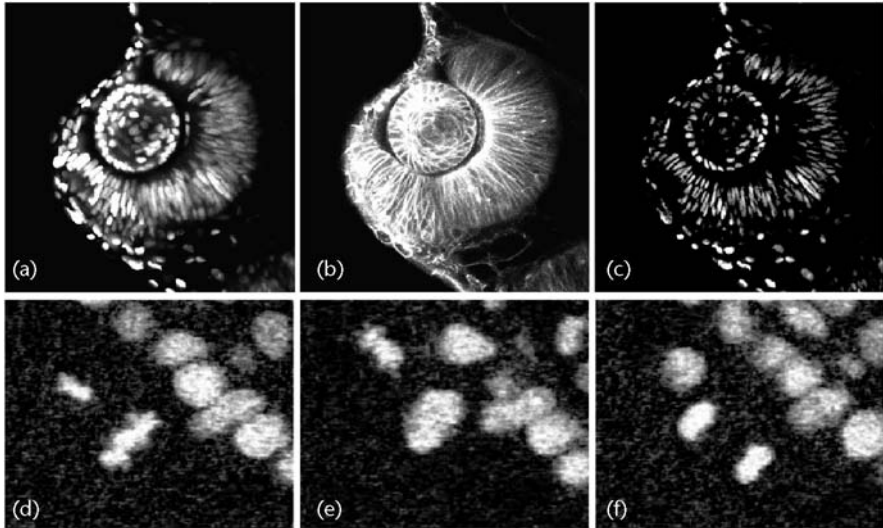
### 14.3.1 Goals of Project

Embryonic development can be thought of as the execution of a program encoded in the genome. But unlike with digital software, the execution of this genetic code is opaque. Biologists do not have a debugger or integrated development environment for their model animals that allows them track the execution of the code, monitor the status of the variables, or edit and recompile the code to see what changes. The goal of the Digital Fish project is just that—we seek to develop all the tools necessary to allow us to trace the execution, monitor the variables, and edit and recompile the code both in real biological fish as well as in a digital recreation through the use of imaging, genetics, and computer simulation.

We are developing several technologies toward this goal. The principal technology is called *in toto* imaging [22]. The goal of *in toto* imaging is to image every single cell in a tissue and eventually the whole embryo over time as it develops. Image analysis software is then used to track all the cell movements, divisions, and deaths that form tissues; to quantitate the levels of fluorescence inside each cell and within different subcellular compartments; to annotate cell type and tissue type to the segmented cells; to register and compare data from different embryos; and to visualize and analyze the data. *In toto* imaging is thus the main tool for digitizing and uploading data from live embryos in a quantitative, single-cell, and systematic fashion.

Another technology we are developing is a genetic approach called FlipTraps. FlipTraps are generated by randomly integrating a DNA cassette (Figure 14.2) into





**Figure 14.2** Segmentation labels used in the Digital Fish project. Confocal sections showing the green channel (a) and red channel (b) of the eye of a zebrafish embryo labeled with histone-EGFP and membrane localized mCherry. (c) Result of subtracting (b) from (a) to better resolve nuclei for segmentation. Histone-EGFP also marks mitosis as shown in three consecutive frames of a dividing cell, 4 minutes between frames (d-f).

the genome. If this cassette integrates into an intron in the proper orientation and frame, then splicing will cause a fluorescent protein to be fused to the endogenous protein. These FP fusions generally do not disrupt the function of the “trapped” protein and thus allow us to watch the protein in whole, living embryos with fluorescent imaging. The fluorescence allows us to see what tissues and cells a protein is expressed in at different times of development, which is important in determining a protein’s function. Since the FP is fused to the protein of interest, we can also image the subcellular localization of the trapped protein. Different proteins localize to different compartments within a cell, and this localization is often indicative of the protein’s function. For example, transcription factors must be in the nucleus to function and receptors for signaling proteins are on the membrane. Many proteins actually change localization depending on their functional state, so FP fusions can be used as functional reporters. The FlipTrap cassette is also designed such that when Cre recombinase is added (e.g., with a tissue-specific transgene), the cassette flips around such that it no longer generates a functional FP fusion protein but now generates a mutant allele marked with a different color FP. These “flipped” FlipTraps can be used to study the phenotype of mutating a gene, which is also critical for determining its function. And finally, FlipTraps contain sites for a site-specific integrase, which allows exogenous pieces of DNA to replace the FlipTrap cassette in order to reprogram the genetic code at the FlipTrap locus.

Coming back to the aforementioned goals of the Digital Fish project, we can use these technologies in the following ways. One is that in toto imaging allows us to watch the execution of the program. Often in biology a perturbation is done at one time point and then its effect is measured at a later time point, but what

happened in the intervening time that caused the effect to be manifest is unknown. In toto imaging allows us to monitor the cells involved in a biological process continuously and quantitatively, and FlipTrap fluorescent fusion proteins allow us to fluorescently label the essential nodes of the network such that the program can be monitored during execution. This approach can also be thought of as providing a spyglass on the memory of a computer during the execution of a program. In a digital computer program, the state of the execution of a program is stored in variables. In a biological program, the state of the execution of the program is stored in physical changes to the molecules of the program. These changes are often simply a change in the number of molecules of a certain protein but can also be changes in phosphorylation or subcellular localization. In toto imaging and FlipTraps allow us to monitor many such “variable states.” And finally by either flipping FlipTraps or integrating exogenous DNA into FlipTraps, we can alter the code, recompile it, and see the phenotype to try to understand how the code controls a biological process.

### 14.3.2 Why Fish?

The subject of the Digital Fish project is a small, fresh water, tropical fish called zebrafish (*Danio rerio*). Zebrafish are commonly kept as pets and found in many pet stores as “zebra Danios.” Zebrafish have emerged as one of the standard model organisms for genetics in the last few decades to join the ranks of the fruit fly *Drosophila*, the roundworm *C. elegans*, and the house mouse *Mus musculus* [23]. Zebrafish, like the other model systems, are easy to raise and breed in a laboratory setting and have a fairly short generation time (2–3 months), making them suitable for genetics. Since zebrafish are vertebrates, their organs, tissues, cell types, and genetic pathways are much more similar to human than is the case with *Drosophila* or *C. elegans*, so what we learn is more relevant to human health. Zebrafish are also excellent for imaging. The embryos and larvae are transparent, allowing the entire embryo to be imaged with optical microscopy (Color Plate 20). Much of the tissues in fruit fly, mouse, and other models such as *Xenopus* (frog) are not accessible to optical microscopy at many important stages of development because the tissue scatters highly and absorbs light. Zebrafish embryos are also small (600  $\mu\text{m}$ ), allowing short working distance, high numerical aperture (NA) objectives to be used. High NA objectives are essential for maximizing the amount of light that is captured and thus improving the signal-to-noise ratio, which is always an issue with fluorescent imaging. High NA objectives are also important for capturing thin optical sections with confocal and 2-photon imaging. And, finally, zebrafish embryos develop freely outside the mother in water. This makes it much easier to culture fish embryos during time-lapse imaging than embryos such as mouse which develop in utero.

### 14.3.3 Imaging

We will first discuss imaging because it is essential for the people analyzing the images to fully understand the entire process of obtaining the images. Often a

problem that might take six months to address using image analysis can be fixed easily at the time of image acquisition. Likewise, the biologist might spend six months trying to optimize the imaging, when the images are already sufficient to answer the biological question given the right image analysis algorithm. But for this to happen, it is essential for the biologist to understand the image analysis problems, for the computer scientist to understand the imaging process, and for the two to communicate closely.

#### 14.3.3.1 Microscopes

There are a variety of methods for generating contrast in optical microscopy, but the most important mechanism by far is fluorescence. Fluorescent microscopy relies on the process of fluorescence in which a molecule termed a *fluorophore* absorbs a photon of light causing an excited electron state. This energy is held on to for a short amount of time (typically 1–20 nanoseconds), during which some of the energy is lost to molecular vibrations/rotations. The excited electronic state then relaxes to the ground state and loses the energy by emitting a photon. Since some of the energy has been lost, the emitted photon has less energy than the absorbed photon, and thus the emitted photon is red-shifted (has a longer wavelength) relative to the excitation photon. This difference in wavelength (Stokes shift) can be used to separate the excitation light from the emission light through the use of filters and dichroic mirrors, resulting in an image with high signal (fluorescent emission photons) to background (reflected excitation photons). Another advantage of fluorescent microscopy is that there are fluorescent dyes covering the entire visible and near-infrared spectrum, which allows multiple fluorescent markers to be used simultaneously and their signals separated into different channels of the image based on their color. Fluorophores can be localized within a biological specimen in different ways. Some organic dyes naturally bind to DNA or membranes because of their structure, allowing for fluorescent labeling of nuclei and membranes, for example. Fluorescent dyes can also be attached to antibodies (either directly or through a secondary antibody) that recognize a particular biological structure. One of the most important breakthroughs in fluorescent microscopy is the development of genetically encoded fluorescent proteins such as green fluorescent protein (GFP) [24]. GFP is a protein originally isolated from jellyfish that allows them to “glow” by emitting green light. In jellyfish the energy to excite GFP comes from a bioluminescent protein called aequorin, but in fluorescent microscopy this energy can be supplied simply by shining blue light on the sample. GFP-like proteins with different spectra have now been isolated from a number of other marine organisms. These variants, along with laboratory-engineered enhancements of these proteins, cover the spectrum from blue to near-infrared in their emission, allowing several different FPs to be imaged simultaneously.

In addition to FPs, the other significant development in fluorescent microscopy is confocal and 2-photon microscopy [9]. These are both types of fluorescent microscopy that allow volumetric imaging of tissue to be performed through the acquisition of stacks of “optical sections” taken at sequential focal planes. The main advance in both forms of microscopy is the ability to eliminate out-of-focus light

such that the focal plane is selectively imaged. Confocal and 2-photon microscopy achieve optical sectioning using different principles. In confocal microscopy, a “pin-hole” aperture is placed conjugate to the focal plane and serves to physically block most out-of-focus light. Two-photon microscopy relies on the principle of 2-photon excitation in which 2 photons, each of half the normal excitation energy (and thus in the near-infrared), are absorbed by a fluorophore nearly simultaneously, causing the fluorophore to be excited to the same electronic state as if a single more energetic photon had been absorbed. The chances of 2 photons being simultaneously absorbed is proportional to the square of the concentration of photons, and the concentration of photons is proportional to the inverse square of the distance from the focal plane (imagine a cone of light with its tip at the focal plane). The chances of 2-photon excitation thus fall off as the fourth power of the distance from the focal plane, so with the proper amount of excitation light, fluorescence is practically limited to the focal plane. It is also possible to achieve 3-photon or greater fluorescent excitation, so this approach is sometimes generically called multiphoton fluorescence microscopy. Since both approaches achieve the same goal of optical sectioning, and they are often both implemented on the same microscope, they are commonly referred to collectively. In the Digital Fish project, we are using both confocal and 2-photon microscopy. Confocal has better resolution, and the lasers used for excitation are cheaper and cover a wider spectral range. Two-photon imaging has better depth penetration and less phototoxicity.

#### 14.3.3.2 Labeling

In order to generate an image with fluorescent microscopy, it is necessary to “label” the sample with a fluorophore. Fluorescent organic dyes can be used, but it is difficult to target them to specific structures, difficult for the dyes to penetrate tissue, and they can be toxic. Antibodies can be used to direct fluorescent dyes to very specific targets, but generally only in fixed (dead) tissue. The most powerful method of labeling specimens and the principal method used in the Digital Fish project is using fluorescent proteins (FPs). Since FPs are genetically encoded, the specimen itself can be made to produce the label. This avoids problems with label penetration, and importantly the specimen does not need to be killed in order to be labeled, allowing for *in vivo*, time-lapse imaging. Genetic encoding also permits a great deal of power in engineering fluorescent protein labels, since standard techniques in molecular biology allow for routine and precise alteration of DNA. The FP itself can be engineered to be brighter, different colors, switch colors in response to light, or even alter its output based on  $\text{Ca}^{++}$  concentration, voltage, or binding to other proteins [15]. When and where the fluorescent protein is produced can also be genetically programmed. Pieces of DNA called enhancers that control what tissues genes are expressed in can be isolated and used to express an FP only in a specific tissue. This process involves connecting the piece of DNA that contains the enhancer to the piece of DNA that encodes the fluorescent protein and then inserting this construct into an organism to generate a “transgenic” organism. It is also possible to use FPs to label not only specific tissues, but also specific regions of a cell. Since FPs are genetically encoded, the gene encoding the FP can be placed “in

frame” with the gene encoding a protein of interest such that now a single protein is produced. Such FP fusion proteins often retain the function and subcellular localization of the protein of interest but are now fluorescent. Transgenic organisms can be made using both an enhancer to drive tissue-specific expression and a fusion protein to direct subcellular localization. Such a transgenic organism allows both expression and localization to be read out in a living organism.

In the Digital Fish project we are making wide use of a type of transgenic zebrafish called a FlipTrap as discussed earlier. FlipTraps express FPs with both tissue specificity and subcellular localization, but they do so using a slightly different approach (Color Plate 21). Rather than using an extra copy of an enhancer and protein-coding region, FlipTraps “trap” the endogenous elements of DNA to generate a fluorescent fusion protein. This approach is advantageous because it ensures that all of the necessary regulatory elements are present, which can be difficult with an isolated enhancer. It also allows the FP fusion protein to be expressed at the same levels as the endogenous protein, since the FP fusion protein is expressed from the endogenous gene rather than an extra copy. As a result, the number of molecules of the trapped protein can in principle be measured using fluorescent imaging. A disadvantage of FlipTraps is that they are made by randomly inserting a DNA vector into the genome and then screening for expression. We intend to generate a large collection of FlipTraps as part of the Digital Fish project, but if a particular gene wants to be studied and is not in this collection, then the former transgenic approach must be used. Since FlipTraps are expressed at endogenous levels that can be low, signal to noise is also a concern.

FlipTraps mark the expression of a single protein in yellow. This protein may only be expressed in a small subset of cells. In order to stain the rest of the embryo and provide segmentation markers for tracking cells, we routinely use other colors of fluorescent proteins to mark the nuclei and membranes. We use a fusion protein of histone H2B with a fluorescent protein such as cerulean to mark the nuclei cyan and a membrane localized fluorescent protein such as mCherry to mark the membranes red [23] (Figure 14.2). This dual color strategy for segmentation labels is useful for several reasons. The histone-FP marks the nuclei, which can be used for tracking. However, in some tissues there is very little cytoplasm, causing adjacent nuclei to appear to touch—making segmentation difficult. By subtracting out the signal from the membrane-FP, the nuclei are much better resolved and easier to segment (Figure 14.2). The membrane-FP also shows tissue morphology very nicely and the histone-FP allows cell divisions to be tracked (Figure 14.2).

#### 14.3.3.3 Image Acquisition

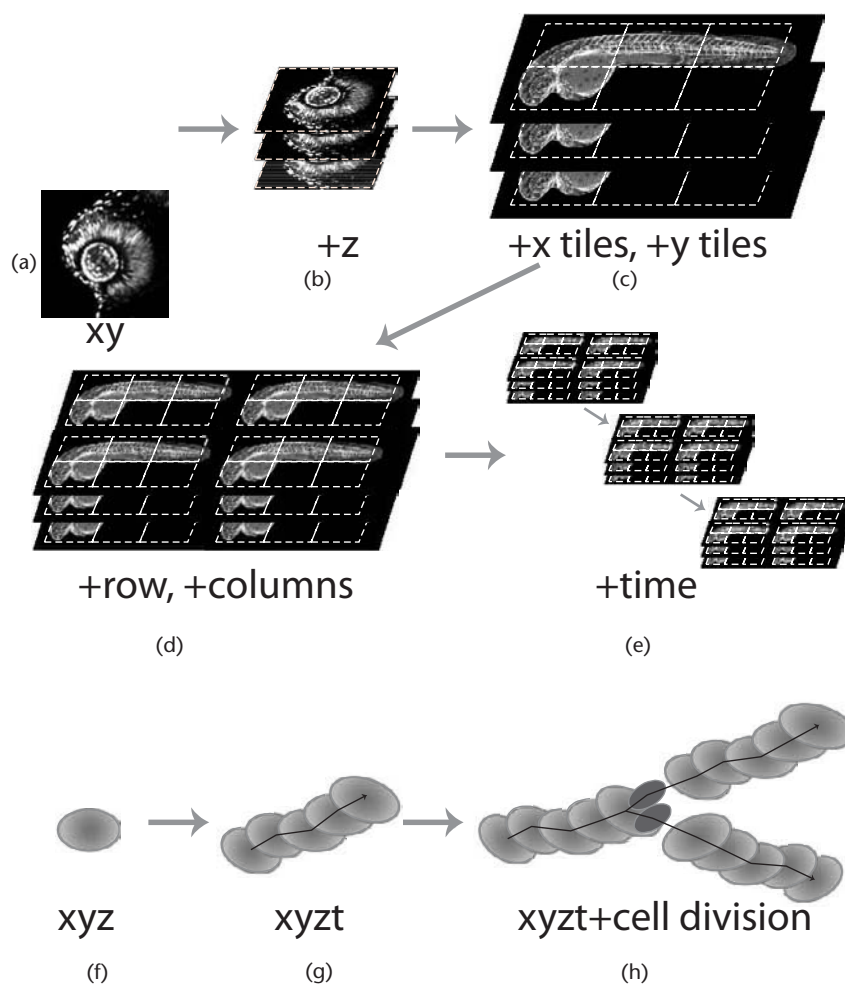
After choosing a microscope and labeling the specimen, the next step is to actually acquire the images. A number of dimensions must be acquired. Since biological circuits function over time, many questions in systems biology require the use of time-lapse imaging in which the specimen is repeatedly imaged over time as a biological process occurs. This requires successfully culturing the specimen while it is being imaged, which isn’t easy but can be done for bacteria, cell culture, and zebrafish embryos, for example. The time scales will vary depending on the

biological problem, but a frame rate on the order of minutes over a period of several hours is required to study things such as cell movement and biological circuits involving transcription/translation. Faster imaging is required for signaling involving  $\text{Ca}^{++}$  or phosphorylation changes. For studying single cells in a dish, wide-field (i.e., not confocal/2-photon) imaging can be used resulting in *xyt* images. However, for tissue or embryos, it is essential to use confocal/2-photon imaging to remove out-of-focus light. The thickness of the optical section depends on the numerical aperture of the objective, but for a high-quality objective ( $>1.0$  NA) optical sections can be  $<1.0\ \mu\text{m}$ . However, optical sections get thicker quickly as the NA of the objective lens drops or the confocal pinhole is widened. By capturing an image at a number of adjacent focal planes, a stack of optical sections can be captured that represents the volume of the sample. By convention, the plane parallel to the focal plane is referred to with the coordinates  $x$  and  $y$ , while the axis perpendicular to the focal plane (parallel to the optical axis) is termed the  $z$ -axis. A single image stack is thus an *xyz* image.  $Z$ -stacks can also be captured repeatedly over time to create an *xyzt* image. An important consideration about confocal/2-photon imaging is that the resolution along the optical axis is poorer (half as good at best in practice) than the resolution in the focal plane, so the *xyz* images are anisotropic. Since several different fluorophores can be used to label a specimen, images can also contain multiple channels corresponding to the different color labels. These colors can also be thought of as an extra dimension of the image. Thus, a typical image set for studying systems biology in embryos will have a few colors, tens to hundreds of  $z$ -sections, and a few hundred time-points.

One goal of the Digital Fish project is to be able to image entire zebrafish embryos at single-cell resolution. Currently the objectives that provide sufficient resolution for single-cell imaging cannot image the entire embryo in one field of view. However, through the use of a motorized stage, we can tile across the embryo to generate a montage that does capture the whole embryo at high resolution, and this can be repeated over the  $z$ -axis and time. We also eventually want to scan in the embryonic expression patterns of thousands of FlipTraps. To achieve the throughput necessary for this goal, we can image arrays of embryos arranged in a row/column format (embryo arrays) all at the same time. In summary, the dimensions of our images can include any of the following:  $x$ ,  $y$ ,  $z$ , time, color,  $x$ -tile,  $y$ -tile, row, and column (Figure 14.3).

Another goal of the Digital Fish project is to achieve “systematic” imaging. Microscopy is often done by imaging different embryos from different orientations, at different stages of development, with different microscope settings, and different labeling conditions. These differences make it very hard to compare results between experiments. Biological imaging also typically only covers a subset of developmental time and space (whatever tissue or developmental stage the biologist is interested in). This makes it difficult to extend results obtained from one tissue to another tissue. It also makes it impossible to look for higher-level patterns. There are several aspects to achieving systematic imaging. One is standardization. We have developed techniques (e.g., embryo arrays) that allow zebrafish embryos to be mounted in a standardized, reproducible method yet still develop normally such that they can be continuously imaged from the same orientation. Thus, images at





**Figure 14.3** Dimensions for image analysis. Raw images in the Digital Fish project can span across a number of dimensions (a–e). (a) Laser scanning microscopes capture 2-D optical sections. (b) A series of optical sections can be captured at different focal planes to make a z-stack. (c) A motorized stage can be used to tile across specimens that are larger than the field of view, such as a whole zebrafish embryo. (d) A motorized stage can also be used to capture embryos arrayed in a row column format to increase throughput. (e) Time-lapse imaging is done to watch embryos as they develop. Segmented cells also span several dimensions (f–h). (f) A single cell’s nucleus or whole membrane is in xyz. (g) The track that a cell moves across over time is in xyzt, and (h) the lineage that is formed by cells dividing is in xyzt+cell division.

the same coordinate (z, time, and so on) from one embryo are very nearly the same part of the body as in another embryo. Another aspect of systematic imaging is achieving comprehensive data. Embryo arrays allow us to tile across zebrafish embryos to image the entire embryo (all of space) and allow for continuous imaging for all of embryonic development (all of time). By imaging a large number of FlipTraps, we also hope to achieve fair coverage across the genomic dimension. An important goal of the Digital Fish project is to fill in our knowledge of the “molecular data universe,” which describes the expression levels of all proteins



as a function of developmental time, anatomical place, and subcellular localization. High-resolution knowledge of this universe would tremendously facilitate understanding biological computation by allowing systems biologists to discover the functions that relate the expression of each protein to other proteins. As Flip-Traps can also be used to generate genetic mutations, we want to take this same systematic approach to phenotype.

Image acquisition also raises some practical issues. One is the large size of the image sets. As an example, a typical in toto image set today might contain  $1,024 \times 1,024$  pixels, three colors, 100 z-sections, and 500 time-points, making for 150 GB at 8 bits/pixel. This size will continue to increase when embryos are tiled or multiple embryos are imaged. For example, when microscopes become fast and sensitive enough to image an entire embryo throughout embryogenesis at single cell resolution, this data set will be  $\sim 2$  TB uncompressed. The large size of these image sets makes them difficult to store, process, and visualize. Another practical issue is that time-lapse imaging of living embryos must be done in a limited amount of time, creating what can be thought of as “envelope.” Using a microscope of a given sensitivity (detected photons per unit time), the user must choose how to use the available photons: how far apart to make the z-sections, how many z-sections to capture, how far apart to make the time points, how many pixels wide should the images be, how long to integrate the signal at each pixel (this determines signal-to-noise ratio), and color separation. Improving any one of these attributes must come at a cost for one or more of the others. From an information theoretical perspective, there is only a certain bit rate of information that the microscope can provide, and the user must choose how to use this information—to get better signal-to-noise  $xy$  images, better  $z$  resolution, and so on. The bit rate can be improved by turning up the laser power, but this can cause photobleaching of the fluorophore and phototoxicity to the embryo. It is important for the person doing the image analysis to understand these tradeoffs, because the imager can easily redistribute how the bits are used if they are not needed in one area and would be more useful elsewhere.

#### 14.3.3.4 Images in the Real World

Images in the real world of fluorescent imaging are very different from the starting point of much image analysis theory. Image analysis and signal processing theory often starts with the idea that “ground truth” is a continuous signal that is then “corrupted” by the sampling process of digital imaging. Subsequent steps in image processing rely on this assumption to try to reconstruct the underlying information in the image. In the real world, both matter and light are discrete. Images are formed by measuring a discrete number of photons from a discrete number of fluorophores. This number is often quite low with fluorescent imaging, and in the extreme it can be 1. Various approaches in fluorescent imaging allow single molecules to be imaged, although tricks must be used to overcome the inherent noise [24]. The quantum nature of fluorophores can even be used to advantage to spatially localize a signal with much greater resolution [16] than the diffraction limit given by Abbe’s law, which treats light as a continuous wave. The quantum

nature of light can also be used to improve signal to noise using a technique called *photon counting*, which basically assumes that the signal must be an integer multiple of some quanta. The discrete nature of matter in fluorescent imaging is most important when it comes to understanding signal to noise. Fluorescent imaging is almost always photon starved. Each pixel in an image corresponds to a small number of fluorophores giving off a small number of photons, leading to what is called Poisson noise or shot noise. Poisson noise refers to the fact that as a smaller number of events are observed, random fluctuations in the occurrence or detection of those events become a larger proportion of the number of events detected. This noise is proportional to the square root of the signal, so when the signal is small the signal-to-noise ratio can be quite poor. The presence of Poisson noise in fluorescent images is fundamental and generally unavoidable, and thus should not be ignored in any image reconstruction theory such as deconvolution, spectral unmixing, or image restoration. It is also a fact of life for segmentation and registration, and one of the critical variables that must be tested to measure the performance of these algorithms.

#### 14.3.4 Image Analysis

The image analysis goals of the Digital Fish Project touch on many of the commonly studied problems in the image analysis community, although with some added twists that make things both more interesting and more challenging. These include image montaging; deinterlacing/denoising; segmentation and tracking of cells as they move and divide; quantitation of the geometry and topology of tissues, cells, and subcellular compartments; quantitation of fluorescence levels and number of molecules within cells and subcellular compartments; and automated annotation of cell type/tissue type/subcellular distribution. In addition to these pure image analysis goals, there are also strong needs for visualization, data analysis, and data registration/integration, which we will discuss separately.

##### 14.3.4.1 GoFigure

We are developing a software application called GoFigure [26] to address the image analysis needs of the Digital Fish Project. The goal of GoFigure is to be an application that is easy enough for biologists to use yet powerful enough for analysis of complex microscopy data for doing systems biology. To achieve these goals it is important not only for GoFigure to utilize the most advanced image analysis algorithms, but to implement these algorithms in a user-friendly way. This means exposing all the parameters critical for “tuning” an algorithm such that the users can adapt it to their images; implementing the algorithms in an efficient, stable, and well-engineered manner; and providing a way for the user to visualize, interact, and eventually enhance the results of the automated algorithms. All this, of course, should be provided as an integrated and easy-to-use application.

GoFigure has been under development for a few years. It is currently based on Windows MFC for the GUI, the Visualization Toolkit (VTK) for visualization,

MySQL for data management, and custom developed segmentation code. We are currently transitioning GoFigure away from MFC, making it cross-platform. We intend to leverage the NA-MIC kits (VTK for visualization, KWWidgets for the GUI, and the Insight Segmentation and Registration toolkit (ITK) for segmentation/registration) to help that transition, keeping other core features, such as remote-database access and storage and practical user interactions, to meet our specific goals. These software libraries as well as GoFigure itself are all open-source with BSD-style licenses.

We intend GoFigure to be usable by most biologists “out of the box,” as an integrated application, but we also anticipate that there will be a number of users who wish to add their own modules to meet their specific needs. We also think that some features of GoFigure could be of interest for other researchers who would not require a full application, or whose goals could be quite different from what GoFigure is made for. We have thus decided to provide all of GoFigure’s features separately as components of the NA-MIC kits, for other researchers to use them as building blocks of their own problem’s solution or to use the GoFigure application as a framework for incorporating their own modules. For other users who will request it, we will provide data access, a developer mailing list, a Web site, and email support to encourage community-based software development. We hope this “tapered” approach will benefit as many users as possible at all levels of expertise.

#### 14.3.4.2 Montaging

One image analysis challenge we face in the Digital Fish project is stitching together images from adjacent tiles to create one large montage image. Capturing high-resolution images requires the use of objectives with a high numerical aperture. Such objectives typically have a high magnification and small field of view. If the object of interest does not fit within the field of view, then a motorized stage on the microscope can be programmed to tile across the specimen. For example, to image the entire zebrafish embryo with a 40X objective, it is necessary to use a  $2 \times 3$  to  $4 \times 6$  array of tiles. Each tile would typically be a z-stack of tens to hundreds of images, which is captured before moving to the next tile. Several sources of image artifacts can make montaging difficult. One is that the focal plane of many microscope objectives is not perfectly flat—rather it curves up at the edges—leading to problems with rigid montaging. It is also useful to minimize the required amount of overlap between images to allow the use of fewer tiles and faster image acquisition times. Another issue is that there can be bleaching during image acquisition, especially at the overlapped regions, leading to nonuniformities in image intensity. The biggest challenge in montaging z-stacks of developing embryos is that since adjacent tiles are captured a few minutes apart during which time the embryo has been developing, the actual image content of the overlapping regions can differ. There are two basic types of movement that can occur—tissue movement and cell movement. With tissue movement, all of the cells move coherently due to normal forces of morphogenesis. With cell movement, individual cells can migrate in different directions and speeds from each other and the surrounding tissue. Typically cells might be moving at a few micrometers per

minute, and each image might be 250 micrometers on a side captured every few minutes.

#### 14.3.4.3 Deinterlacing/Denoising

Confocal and 2-photon are both forms of *laser-scanning microscopy*, which refers to the fact that the images are formed by raster scanning a focused laser across the specimen to form an image pixel by pixel. Laser scanning is typically accomplished using tip and tilt mirrors attached to two galvanometers to perform x and y scanning. The y mirror must be driven at a frequency equal to the imaging rate ( $\sim 1$  Hz), while the x mirror must be driven at a rate equal to the y scan rate divided by the number of lines across the y dimension ( $\sim 1$  kHz), which is near the physical limit of the galvanometer. In order to increase the imaging rate, bidirectional scanning can be used in which image data is captured on both forward and backward passes of the laser. However, hysteresis in the travel of the mirror and lags in the data acquisition electronics can cause a misalignment of the lines.

Noise is also a fundamental problem, as discussed earlier. Poisson (shot) noise is present in many fluorescent images due to the small number of photons that contribute to each pixel. There is also noise introduced by the detectors (e.g., photomultiplier tubes), amplifiers, and analog-to-digital converters used to detect fluorescent photons. Taken together, it is often important to perform deinterlacing and denoising or image reconstruction as a prefiltering step before further steps in image analysis.

#### 14.3.4.4 Cell Tracking/Segmentation

One of the most important tasks in image analysis for in toto imaging and the Digital Fish project is tracking cells as they move around and divide to form the developing embryo. Cell tracking is essential for a number of types of analysis in biology. In the area of cell and developmental biology, cell tracking is important because it can be used to determine cell lineage patterns. Understanding cell lineage trees can be quite informative for understanding how various cell types form and for defining stem cells. For systems biology applications, cell tracking is essential for performing longitudinal analysis. If you want to understand what a biological circuit is doing over time at the single cell level, then you have to be able to track cells (e.g., with fluorescently marked circuit components) over time, as discussed in Chapter 10. The timescale of biological computation is often slow enough that it is necessary to track cells over multiple rounds of cell division to watch the circuit function.

Cell tracking is basically a challenge in segmentation but at multiple (and linked) dimensions. For the Digital Fish project, there are three important dimensions—3-D (xyz), 4-D (xyzt), and 4-D + cell-division. At the level of 3-D, the goal is to uniquely and individually segment every cell in a volume of tissue such that each cell is recognized as separate from all other cells. Segmentation can be done using the nucleus of each cell rather than the whole cell. Nuclear segmentation tends to be easier, since nuclei have a simpler and more uniform shape (ellipsoid) than whole cells. Nuclei are also further apart from each other compared to whole

cells, since nuclei are separated by cytoplasm and cell membranes whereas whole cells are adjacent to each other. The level of 4-D is for tracking the path that cells (or nuclei) move over time. Four-dimensional segmentation can be accomplished by first segmenting the cells in 3-D and then linking these segmented objects over time. Alternatively, the segmentation can be done directly in 4-D, which should be able to better handle noisy images. And finally to form lineage trees, it is necessary to segment cells across cell division (mitosis). Again, this can be done by linking 4-D segmented objects across cell division or through direct segmentation at the level of 4-D + cell-division. The histone-FP label we use generates characteristic “bar-shape” nuclei at mitosis, which should facilitate tracking over cell divisions (Figure 14.2). Since cell division always converts one mother cell into two daughter cells, cell lineage trees take the form of a binary tree. In addition to a cell dividing to form two cells, a cell can differentiate (and thus become postmitotic) or die. Cell death (apoptosis) is a normal process in the development of many tissues. As a result of cell differentiation and death, different branches of cell lineage trees can have different depths.

#### 14.3.4.5 Discrete Geometry and Topology

The geometry and topology of cells and subcellular compartments is important for several aspects of the Digital Fish project. Some segmentation algorithms (e.g., discrete active contours) require a discrete representation of the surface of the objects to be segmented. For such algorithms, it is important to have a robust and efficient data structure for representing and processing the geometry and the topology of the surfaces [27, 28]. Even when not required for segmentation, it is necessary to convert segmented objects to a discrete representation for many downstream steps. Discrete representations are important for storage and transmission of segmented objects. GoFigure stores segmented objects in a MySQL database that can be accessed over a local network (and the Internet in the future), so compact methods to represent geometry and topology are beneficial. Once cells are defined by a discrete surface, they are also easier to visualize relative to volume rendering the raw images because of noise and uneven intensities in the raw data and faster processing of surfaces. Geometry and topology are also important for modeling. For mechanical modeling of tissue, it is important to use a representation that supports the method being used, such as finite element analysis. Cell geometry and topology will also be important in the next generation of models of cell signaling. Some signaling can only occur between juxtaposed cells, and other signals have a limited range of diffusion. To understand the computation occurring in a tissue, it will be important to model the shape of individual cells and their relative amounts of cell membrane and neighbor relationships. Ideally, the representation of cells for the Digital Fish project would also take into account the linkage of cells across 3-D, 4-D, and 4-D + cell-division as described earlier. Going from 3-D to 4-D is still a matter of ambient space, but taking into account cell subdivision modifies the topology of the object. Such a representation has the potential to be more compact and perform better on tasks such as data retrieval, data traversal, and discrete surface processing altogether. An ideal representation will also allow rapid calculation of

geometrical and topological properties of each cell, such as volume, surface area, curvature, Euler characteristics, speed, displacement, and cell cycle rate.

#### 14.3.4.6 Quantitation of Fluorescence/Localization

A major goal of the Digital Fish project is to quantitate the expression of a large number of proteins ( $>1,000$ ) at cellular resolution across the space and time of embryogenesis. As discussed earlier, FlipTraps produce endogenously expressed fluorescent fusion proteins that can theoretically be used to measure the number of molecules of the protein in each cell and even in different subcellular compartments. This has been done successfully in yeast [29], but to move it up to zebrafish a number of potential caveats must be understood (and perhaps modeled), including shot noise, bleaching, scattering, and absorption. Segmentation of cells and subcellular compartments is the preferred method for quantitating where a signal is coming from, but there are also approaches that do not rely on a previous segmentation. For example, with the membrane/nuclear labels we are using, the nucleus, cell membrane, and cytoplasm of a cell can be segmented, and these masks are used to quantitate the level of fluorescence within each of these subcellular regions (Figure 14.2). However there are many additional organelles and regions of a cell. Fluorescent proteins can label these regions and can be used to measure subcellular localization by colocalization, but their routine use for in toto imaging is impractical due to limits on the number of colors that can be simultaneously used. An alternative approach is to use image content directly to quantitate the subcellular localization pattern by looking at sets of texture features from intensity to spatial frequency and higher order moments [30].

#### 14.3.4.7 Annotation of Cell/Tissue Type

Once cells have been segmented and fluorescence levels quantitated, it would also be useful to know the identities of the cells and tissues. Different tissues and different types of cells have characteristic shapes, positions, cell movements, and lineages. For the Digital Fish project, the challenge is to accurately and automatically annotate cells and tissues with their proper type (e.g., motor neuron, photoreceptor cell) using the information that is available. This information is principally the results of the cell segmentation/tracking using the membrane and nuclear labels. Automatic annotation is important for both describing expression patterns (e.g., FlipTrap fluorescent fusion proteins) as well as for describing phenotype (e.g., FlipTrap conditional alleles). Annotation of expression patterns should be simpler, since the anatomy/morphology marked by the membrane and nuclear labels is consistent and normal (wild type). Automatic annotation of phenotype is also wanted but more challenging, since the anatomy will vary between mutant and wild type embryos. However, if we are able to capture a complete timelapse of the development of a mutant embryo using in toto imaging, then we can roll back the clock until the mutant embryo is anatomically wild type. The difference between wild type and mutant as the



timelapse is then played forward can be used to quantitate and annotate the phenotype.

#### **14.3.5 Visualization**

Visualization is key to the Digital Fish project simply because of the huge amount of data that is being dealt with. Image sets can have 100,000 or more images spread across x, y, z, time, multiple tiles, and multiple embryos. And segmented cells can number even higher in numbers and are also spread across multiple dimensions including 3-D, 4-D, and 4-D + cell-division. Visualizing such large, multidimensional data sets is difficult yet essential for not drowning in the data. Ideally visualization would allow raw images to be volume rendered and explored across different higher dimensions at varying levels of resolution from the whole embryo to single cells. Segmented data can then be overlaid on top of the raw data, which is essential for verifying the quality of the segmentation and for providing biological context to the processed data. It is also important to link data across multiple dimensions and multiple views. For example, if a cell in 3-D is selected, then its corresponding track and lineage over time should also be highlighted in the render window, and the cell's properties should be displayed textually in another window [26, 31].

#### **14.3.6 Data Analysis**

There is also a lot of possibility for higher-level data visualization and analysis in the Digital Fish project, since we hope to produce data with unprecedented resolution and coverage. Just as the genome projects opened up a new frontier in the bioinformatics of genome-wide sequence analysis, we hope that the Digital Fish project will create new opportunities for the bioinformatics of embryo-wide expression and phenotype analysis. For gene expression, it will be important to develop quantitative approaches to see how expression of a gene changes over time, how protein subcellular localization varies over time and space, how expression differs between different genes, and how all of this relates to the development of the embryo and the underlying genomic sequence. Likewise for phenotype, it will be important to get a quantitative metric of morphology for comparing two different 4-D digital embryos, for relating phenotype to the expression of the mutated gene, and for linking phenotype to the underlying genetic circuit. These challenges are in many ways more bioinformatics than pure image processing, but since the underlying data have a well-defined spatial and temporal ordering like image data, we anticipate that this aspect of the Digital Fish project will also benefit from insights from the image analysis community.

#### **14.3.7 Registration/Integration, Reference Atlas**

The ultimate goal of the Digital Fish project is to produce a digital fish. The digital fish will be both an anatomically organized warehouse of molecular data as well as a platform for developing computer models on. The warehouse aspect of the digital fish will incorporate expression patterns and phenotypes from a large number



of genes (perhaps thousands). Since we are limited to imaging only a few colors at a time, we will scan in expression patterns and phenotypes basically one gene at a time. This means we will need to integrate data from thousands of embryos onto a standard framework to allow for comparison. There are several ways to integrate the data. The integration problem can be approached as an image registration problem. Since we will attempt to capture all the raw images in a standardized fashion, each *xyzt* in toto image set of a developing embryo should be sufficiently similar that the nuclear and membrane channels can be used for 4-D registration. It may also be possible to perform the registration on the segmented data. This can be done simply by treating the segmented data as a 4-D image, but better yet it would also incorporate knowledge of the lineage tree and knowledge of cell type/tissue type annotation to do the registration. Importantly, the exact number and position of cells varies from embryo to embryo, so integration techniques must be robust to this noise. Ultimately, all of the expression and phenotype data should be incorporated onto a standardized “reference fish” that also incorporates anatomy and links to other bioinformatic resources and atlases. Interfaces to the data warehouse must be provided to allow others to develop models of developmental processes based on data in the digital fish.

## 14.4 Bridging the Gap

### 14.4.1 Open Source

There exists a large gap between the image analysis community and the cell, developmental, and systems biology communities. Making code open source is important not only because it is ethically responsible scientific practice, but also because it helps bridge this gap. Open source code is essential to scientific publishing, so that others can review, repeat, and build upon the work. Publish means “to make public,” so without the code it’s not really publishing. Some will argue that as long as the algorithms are adequately described in the paper, then that should allow for others to reproduce the work and is thus sufficient for publishing. That may have been true once upon a time but is not in line with current realities for several reasons. One is that for many algorithms the details are very important—without tweaking the parameters just right, the algorithm won’t work. The same is true in the “wet” world of biology, where many papers publish very abbreviated protocols that leave others to waste countless hours and money working out the details that could have easily been provided by the biologists attaching their protocol as supplementary data. Another reason is that current research is very complex. People using work from a paper are unlikely to be using just that single algorithm. They will likely be pulling together many different algorithms to do something useful. Hand coding every algorithm from scratch would greatly slow down progress. A third reason is that current research is more and more multidisciplinary. People from outside your narrow field of research might be interested in your algorithm. Having a working example greatly simplifies this interdisciplinary connection. And the final reason is selfish. If you want your ideas to live on and be used, then make your code open. If you want your ideas to die in a dusty journal on a library

shelf, then don't. Given the choice between two similarly performing algorithms, the first of which is in a journal only and the second of which is well-engineered, well-documented, well-supported open source code, the user is always going to choose the latter. It is important to keep in mind the point of research in image analysis. Is it to come up with yet another "novel" [32] method using the same toy images to solve a problem that has already been solved for those images, or is to analyze real images in some way that practically benefits research?

There is more to open source than just making the source code available. It is not enough to just dump your poorly designed, poorly engineered, undocumented spaghetti code onto a Web site. The goal of open source code is to be readable, reusable, and extensible by others, so all of those good software engineering practices really do matter (descriptive variables, modular design, clean interfaces, clearly commented, properly formatted, thoroughly debugged, and so on). Your code should be written with other users in mind from the beginning, just as a lab notebook should be written such that is readable and repeatable by other scientists.

#### 14.4.2 Traversing the Gap

Systems biology and image analysis are two complex, difficult-to-master fields on their own. Becoming an expert in one leaves little time to master the other. The available training programs and mentorship for these two fields also overlaps very little. As a result, there is a large gap between these communities. Although the metaphor most commonly used is "building a bridge" across this gap, I think the more accurate image is "trekking across the traverse." These two communities are well established in their own right, but the best connections between these fields are not yet known and are a matter for future research to figure out. Long before a bridge is built in the real world, numerous possible routes are explored by pioneers. The wilderness must first be conquered, then trails established and slowly improved to roads over the preferable routes, and only then can a bridge be designed and built. Once the bridge is built, it is easy for the masses to cross it, but I think there is a lot of pioneering research to be done before that point is reached. What this means is that we cannot all sit back and wait for the bridge to be built. Those of us who are interested must go out and forge routes through the jungle between these communities. It will not be easy or straightforward, especially done alone. I think the best way forward is to send expedition parties ahead comprised of people with a mix of backgrounds in computer science and biology such that they compositely have the skills to navigate this unexplored territory. It is only by trekking together that biologists and computer scientists can traverse the gap across this vast and exciting frontier.

### 14.5 Conclusions

It is an exciting time to be doing biology. The knowledge we have accumulated through decades of research in molecular and cellular biology now promises to be united into a systematic understanding of how the genome programs the formation and function of embryos and organisms. New approaches using GFP transgenics

and microscopic imaging are poised to play a key role in achieving this goal. However, realizing the full potential of microscopic imaging for doing systems biology will require significant progress in image analysis. We are quite hopeful that through cooperation between the image analysis and systems biology communities, these interesting challenges can be overcome and the promise of imaging-based systems biology can be realized.

### Acknowledgments

I thank Alexandre Gouaillard for comments on the manuscript. This work is supported by the National Human Genome Research Institute.

### References

- [1] International Human Genome Sequencing Consortium, "Finishing the Euchromatic Sequence of the Human Genome," *Nature*, Vol. 431, 2004, pp. 931–945.
- [2] Kaufman, M., and R. Thomas, "Emergence of Complex Behaviour from Simple Circuit Structures," *C. R. Biol.*, Vol. 326, 2003, pp. 205–214.
- [3] Adams, M. D., et al., "The Genome Sequence of *Drosophila Melanogaster*," *Science*, Vol. 287, 2000, pp. 2185–2195.
- [4] Venter, J. C., et al., "The Sequence of the Human Genome," *Science*, Vol. 291, 2001, pp. 1304–1351.
- [5] Mouse Genome Sequencing Consortium, "Initial Sequencing and Comparative Analysis of the Mouse Genome," *Nature*, Vol. 420, 2002, pp. 520–562.
- [6] International Human Genome Sequencing Consortium, "Initial Sequencing and Analysis of the Human Genome," *Nature*, Vol. 409, 2001, pp. 860–921.
- [7] Cusick, M. E., et al., "Interactome: Gateway into Systems Biology," *Hum. Mol. Genet.*, Vol. 14, 2005, pp. R171–R181.
- [8] Harbison, C. T., et al., "Transcriptional Regulatory Code of a Eukaryotic Genome," *Nature*, Vol. 431, 2004, pp. 99–104.
- [9] Williams, R. M., D. W. Piston, and W. W. Webb, "Two-Photon Molecular Excitation Provides Intrinsic 3-Dimensional Resolution for Laser Based Microscopy and Microphotochemistry," *FASEB J.*, Vol. 8, 1994, pp. 804–813.
- [10] Megason, S. G., and S. E. Fraser, "Imaging in Systems Biology," *Cell*, Vol. 130, 2007, pp. 784–795.
- [11] Elowitz, M. B., et al., "Stochastic Gene Expression in a Single Cell," *Science*, Vol. 297, 2002, pp. 1183–1186.
- [12] Breitling, R., "Biological Microarray Interpretation: The Rules of Engagement," *Biochim. Biophys. Acta*, Vol. 1759, 2006, pp. 319–327.
- [13] Wolkenhauer, O., et al., "Modeling and Simulation of Intracellular Dynamics: Choosing an Appropriate Framework," *IEEE Trans. on Nanobioscience*, Vol. 3, 2004, pp. 200–207.
- [14] Joglekar, A. P., E. D. Salmon, and K. S. Bloom, "Counting Kinetochore Protein Numbers in Budding Yeast Using Genetically Encoded Fluorescent Proteins," *Methods Cell Biol.*, Vol. 85, 2008, pp. 127–151.
- [15] Giepmans, B. N., et al., "The Fluorescent Toolbox for Assessing Protein Location and Function," *Science*, Vol. 312, 2006, pp. 217–224.
- [16] Hell, S. W., "Far-Field Optical Nanoscopy," *Science*, Vol. 316, 2007, pp. 1153–1158.

- [17] Perrimon, N., and B. Mathey-Prevot, "Applications of High Throughput RNA Interference Screens to Problems in Cell and Developmental Biology," *Genetics*, Vol. 175, 2007, pp. 7–16.
- [18] Mitchison, T. J., "Small-Molecule Screening and Profiling by Using Automated Microscopy," *ChemBioChem*, Vol. 6, 2005, pp. 33–39.
- [19] Rosenfeld, N., et al., "Gene Regulation at the Single-Cell Level," *Science*, Vol. 307, 2005, pp. 1962–1965.
- [20] Colman-Lerner, A., et al., "Regulated Cell-to-Cell Variation in a Cell-Fate Decision System," *Nature*, Vol. 437, 2005, pp. 699–706.
- [21] Jonsson, H., et al., "An Auxin-Driven Polarized Transport Model for Phyllotaxis," *Proc. Natl. Acad. Sci. USA*, Vol. 103, 2006, pp. 1633–1638.
- [22] Megason, S. G., and S. E. Fraser, "Digitizing Life at the Level of the Cell: High-Performance Laser-Scanning Microscopy and Image Analysis for In Toto Imaging of Development," *Mech Dev.*, Vol. 120, 2003, pp. 1407–1420.
- [23] Link, B. A., and S. G. Megason, "Zebrafish as a Model for Development," in *Sourcebook of Models for Biomedical Research*, P. M. Conn, (ed.), Totowa, NJ: Humana Press, 2007.
- [24] Chalfie M., et al., "Green Fluorescent Protein as a Marker for Gene Expression," *Science*, Vol. 263, 1994, pp. 802–805.
- [25] Sako, Y., "Imaging Single Molecules in Living Cells for Systems Biology," *Mol. Syst. Biol.*, Vol. 2, 2006, p. 56.
- [26] Gouaillard, A., et al., "GoFigure and The Digital Fish Project: Open Tools and Open Data for an Imaging Based Approach to System Biology," *Insight Journal*, special edition "2007 MICCAI Open Science Workshop," 2007.
- [27] Gelas, A., et al., "Compactly Supported Radial Basis Functions Collocation Method for Image Segmentation," *IEEE Trans. on Image Processing*, Vol. 16, No. 7, 2007, pp. 1873–1887.
- [28] Gouaillard, A., et al., "Remeshing Algorithm for Multiresolution Prior Model in Segmentation," *Proc. of International Conference on Image Processing*, October 2003, IEEE ICIP, 2004, p. 2753.
- [29] Wu, J. Q., and T. D. Pollard, "Counting Cytokinesis Proteins Globally and Locally in Fission Yeast," *Science*, Vol. 310, 2005, pp. 310–314.
- [30] Glory, E., and R. F. Murphy, "Automated Subcellular Location Determination and High-Throughput Microscopy," *Dev Cell.*, Vol. 12, 2007, pp. 7–16.
- [31] Cedilnik, A., et al., "Integration of Information and Volume Visualization for Analysis of Cell Lineage and Gene Expression During Embryogenesis," *Proc. of SPIE*, Vol. 6809, 2007.
- [32] Ibanez, L., "Principles and Practices of Scientific Originology," *Insight Journal: ISC/NA-MIC Workshop on Open Science at MICCAI*, 2007.

# Quantitative Phenotyping Using Microscopic Images

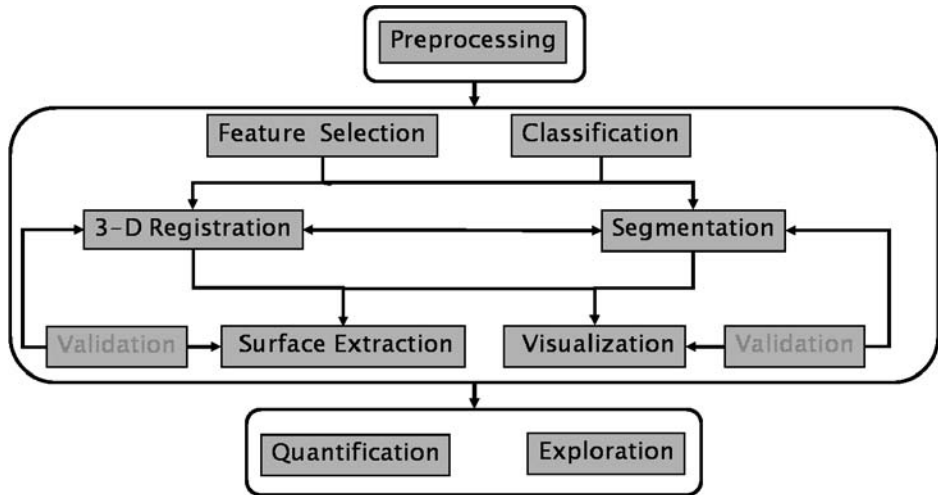
Kun Huang, Kishore R. Mosaliganti, Lee Cooper, Raghu Machiraju, Gustavo Leone, and Joel Saltz

## 15.1 Introduction

One of the major challenges in modern biology is to quantitatively characterize microscopic features in 3-D space with high resolution and elucidate the relationship between the morphology of these features with specific phenotypes. This spatial resolution is crucial for a complete description of the cellular and tissue morphology, which is essential for understanding genetic functions, as observed in many areas such as cell and cancer biology. At this microscopic scale, phenomena are numerous: cancer initiates in the tumor microenvironment based on complicated interactions among epithelial cells, immune cells, fibroblasts, and extracellular matrix; organs develop in the embryo involving extensive signaling and transformation of different types of cells; and the change of neuron spine morphology is associated with the process of learning.

With advancement in imaging techniques and computer sciences, such as image analysis and computer vision, it is now possible to characterize these features at micron resolution. While the current microscopic imaging technology provide only 2-D images, techniques such as confocal and multiphoton microscopy can capture the 3-D structures of the specimens by yielding a stack of serial 2-D images. In addition, there is a long history of using 2-D histological sections to reconstruct 3-D structures using various image registration and segmentation algorithms in the bioengineering and pathology communities [1–21]. Nevertheless, given that structures of biomedical samples are heterogeneous, and anisotropic, we are still facing challenges for not only aligning 2-D images but also clearly annotating and elucidating the 3-D anatomical structures and cellular (even molecular) distributions. In this chapter, we present an algorithmic framework for 3-D visualization and reconstruction of cellular data from microscopy images. Our goals require us to achieve reconstruction at a cellular level in the presence of serious under-sampling.

Previously, in [22], we described a pipeline to visualize histological stacks derived from the mice placenta organ. The emphasis therein was not on reconstructing the cellular geometry. However, we exploit the same workflow as shown in Figure 15.1 for that study with extensions in almost every step. As we will discuss in the rest part of this chapter, obtaining 3-D cellular reconstruction is not only about image registration, which aligns 2-D images in 3-D space. It requires new algorithms for image segmentation, registration, visualization, and quantification. Moreover, interactions between image segmentation and registration steps are essential for the success of our framework. While the reconstruction of cells depends



**Figure 15.1** The image processing workflow for reconstructing and quantitative morphometric analysis of serial microscopic images.

on accurate registration between consecutive images, image registration also relies on segmentation of features including tissues and cells.

As shown in Figure 15.1, in this chapter we will introduce our work in four major areas: *segmentation*, *registration*, *visualization of cellular structures in 3-D*, and *quantification*. Relevant application context is described in Section 15.2. In Section 15.3, we introduce a novel image segmentation framework for biomedical tissues. The key for this technique is to treat different types of tissues as different biomaterials and then distinguish them using stereoscopic features for characterization of microstructures such as  $N$ -point correlation functions. This framework, which is derived from material sciences, has been shown to be highly successful in segmenting challenging microscopic images. With the segmentation of the tissue or structure of interest, we need to further segment individual cells. Currently, the segmentation of overlapping nuclei in a biologically consistent manner is an active topic of research. There is a plethora of reported work that uses morphological operators and application/modality-specific features. These approaches are not often generalizable. In Section 15.4, we describe our algorithm, which contains a level set-based coarse segmentation followed by an extensive view of the centroidal Voronoi tessellations (CVTs) scheme. Then in Section 15.5, we discuss the problem of image registration in several scenarios, including both rigid and nonrigid cases. With accurate image registration and cellular segmentation results, we still face big challenges in rendering the 3-D atlas of the cellular distributions. A 3-D visualization/reconstruction algorithm may only be deployed when the dataset is registered, has sufficient sampling resolutions in all the dimensions, and presents sufficient continuity in colors, gradients, and illumination. Hence, direct volume rendering using transfer functions has limited scope of application. We describe our volumetric rendering schemes in Section 15.6 for all the applications. Finally, since the ultimate goal for 3-D reconstruction is to carry out quantitative analysis

on the samples, in Section 15.7, we present the quantitative analysis and results for our applications.

Since our work is motivated by and developed for three large-scale biomedical studies, the algorithms will be presented in the context of these applications. Nevertheless, the theory and algorithms are generalizable, since our applications are very representative in many aspects that cover both histological images and confocal microscopy. For all the sections, the related work will be reviewed in each relevant section.

## 15.2 Relevant Biomedical Applications

The focus of this chapter is to present algorithms and solutions for several key technical issues in developing 3-D models for quantification purposes. The biological applications include a 3-D morphometry study on the role of the retinoblastoma gene (Rb) in mouse development, the role of the tumor suppressor gene PTEN in the development of breast cancer, and the 3-D reconstruction of cellular structure of zebrafish embryo. Here we briefly describe these applications.

### 15.2.1 Mouse Model Phenotyping Study: Role of the Rb Gene

The goal of this project is to examine the morphological effects of inactivating the retinoblastoma (Rb) tumor suppressor gene in mouse placental tissue. The Rb tumor suppressor gene was identified more than two decades ago as the gene responsible for causing retinal cancer (retinoblastoma) but has also been found to be mutated in numerous other human cancers. Unexpectedly, recent studies of Rb-deficient (Rb<sup>-/-</sup>) embryos suggest that Rb plays a critical role in regulating development of the placenta and that loss of Rb in placental lineages causes many of the fetal abnormalities found in Rb<sup>-/-</sup> fetuses. Our previous work suggested that deletion of Rb leads to extensive morphological changes in the mouse placenta, including possible reduction of total volume and vasculature of the placental labyrinth, increased infiltration from the spongiotrophoblast layer to the labyrinth layer, and clustering of labyrinthic trophoblasts. However, these observations are based solely on the qualitative inspection of a small number of histological slices from each specimen alone. In order to fully and objectively evaluate the role of Rb deletion, detailed characterization of the morphological attributes of the mouse placenta at cellular and tissue levels is essential. This capability would allow for direct correlation of cellular and tissue phenotype with Rb<sup>-/-</sup> genotype.

### 15.2.2 Mouse Model Phenotyping Study: The PTEN Gene and Cancer

In this work, our collaborator is interested in understanding the role of the *PTEN* tumor suppressor gene in the regulation of normal cellular processes. Phenotyping experiments on mouse mammary models have revealed that suppression of *PTEN* gene leads to abnormal cellular transformations. It is the stated goal to understand the orchestrated sequence of events leading to tumor initiation and progression at a cellular as well as a molecular scale. In this context, a full-fledged spatial

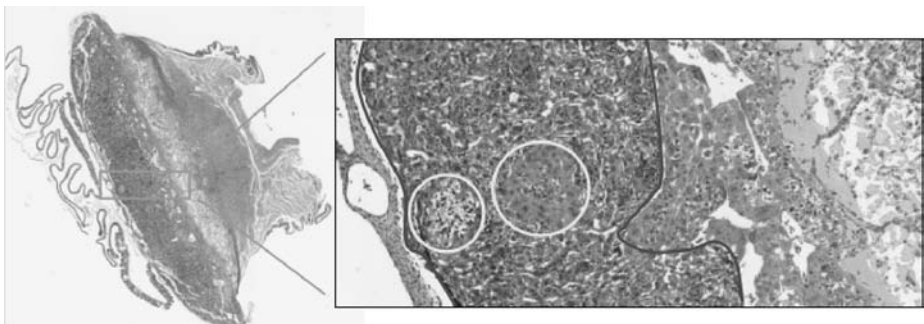


reconstruction of the ductal tissue can significantly reduce the time required to generate new hypotheses regarding the cellular mechanisms. A pair of *wild-type* mouse mammary glands were harvested and prepared using a standard histological protocol. They were fixed in formalin, embedded in paraffin, and sectioned at 5- $\mu\text{m}$  thickness using a microtome to yield about 1,000 sections per dataset. Serial sections were mounted on glass slides and scanned at  $200\times$  magnification (0.46- $\mu\text{m}$  interpixel spacing) using a light microscope. The image dimensions on average were (22K $\times$ 65K) in RGB format. Mammary ductal tissue is composed of concentric layers of epithelial in a matrix of extracellular material. The ducts are identified on each section as a distinct conic or quadric projection of a complex tortuous 3-D object (Figure 15.2(a)).

### 15.2.3 3-D Reconstruction of Cellular Structure of Zebrafish Embryo

Our collaborators at the Center of Excellence in Genomic Science at California Institute of Technology (Caltech) (Alexandre Gouaillard, Titus Brown, Marianne Bronner-Fraser, Scott E. Fraser, and Sean Megason) have initiated the Digital Fish Project, which is also reviewed in Chapter 14. Their goal is to use in toto imaging of developing transgenic zebrafish embryos to acquire digital, quantitative, cell-based, molecular data suitable for modeling the biological circuits that turn an egg into an embryo. In toto imaging uses confocal microscopy to capture the entire volume of organs and eventually whole embryos at cellular resolution every few minutes in living specimens throughout their development. 4-D image sets ( $x - y - z - t$ ) with dimensions 1,024 $\times$ 1,024 $\times$ 80 $\times$ 60 are generated. The plan is to use in toto imaging to digitize the complete expression and subcellular localization patterns of thousands of proteins throughout zebrafish embryogenesis. We provide 3-D results from applying our methods at select time-points chosen at  $t = 0$  (beginning) and 60 (ending). More details and a comprehensive of this application can be found in Chapter 9.

A common property shared by the three biomedical applications is that they all require the capacity for 3-D reconstruction of a large number of microscopic images. The first two studies mainly involve light microscopic images containing hundred of millions or even billions of cells. The last study uses confocal micro-



**Figure 15.2** A 2-D slice of a histology-stained mouse placenta is shown. A zoomed region of interest reveals several different tissue layers that have characteristic microstructural component packing distributions.

scopic images, and the goal is to trace the 3-D cellular distribution over time. These challenging problems motivate us to develop a universal framework for processing and reconstructing the high-resolution 3-D model of biomedical samples.

## 15.3 Tissue Segmentation Using $N$ -Point Correlation Functions

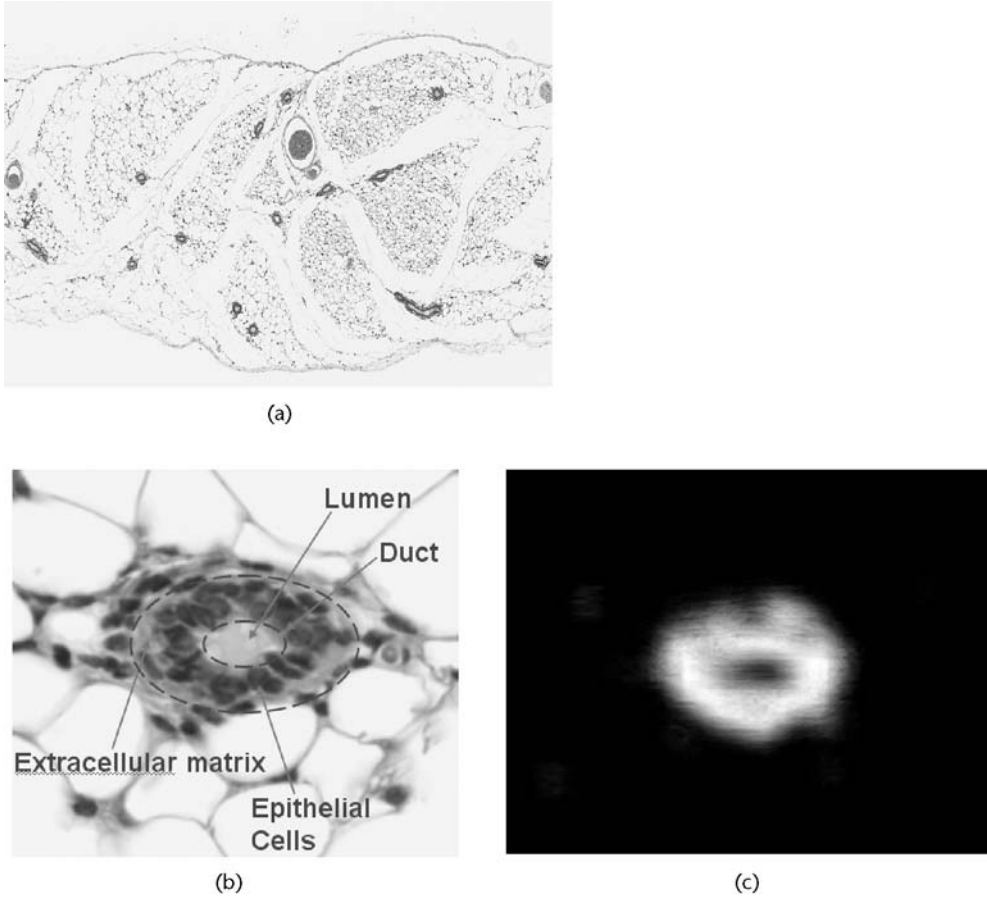
Tissue layers differ mainly in the spatial distributions and packing of microstructure components, such as the red blood cells (RBCs), nuclei, extracellular matrix, and background material. We algorithmically process high-resolution datasets to determine these distributions. Robust segmentation involves the discovery of feature spaces that estimate and spatially delineate component distributions, wherein the tissue layers naturally appear as salient clusters. The clusters can then be suitably classified.

Figure 15.2 shows a typical mouse placenta section that we encounter in our work. The interface between two tissue types at full resolution is marked out using a red boundary. Note the lack of a clear well-defined boundary between the two tissue types. Instead, the change is better perceived by noting the subtle changes in microstructure properties (texture) that manifests within each tissue region. Figure 15.3 shows another histology-stained section of the mouse mammary tissue that was used in our experiments. The epithelial cell lining surrounding a duct has a characteristic packing arrangement. The material surrounding the duct consists of fat cells arranged in honeycomb-like cellular matrices. Our examples serve to illustrate that the tissues are best identified by the relative packing densities and spatial distributions of nuclei, RBCs, extracellular material, and background microstructural components. We propose the use of  $N$ -point correlation functions ( $N$ -pcfs) borrowed from the material science literature [23] for image segmentation. These functions efficiently characterize the microstructure in a heterogeneous substrate [24–26].

### 15.3.1 Introduction to $N$ -Point Correlation Functions

To simplify the presentation, assume the presence of only two phases in the microstructure, namely, *phase 0* and *phase 1*. Let  $p \in \Omega$  be any point in the microstructure  $C : \Omega \rightarrow \{0,1\}$ . Further, let  $\Omega_p \subset \Omega$  be a suitable neighborhood of  $p$ . Consider placing an  $N$ -sided regular polyhedron with edge length  $k$  and orientation  $(\theta, \phi)$  in  $\Omega_p$ . The probability that all the  $N$ -vertices lie in *phase 0* is defined as an  $N$ -point correlation function ( $N$ -pcf),  $P_{i_1 i_2 \dots i_N}^k(p, \theta, \phi)$ , where  $i_m = 0$  for  $m \in 1, 2, \dots, N$ . The subscript  $i_m$  denotes the phase of the  $m$ th polyhedron vertex. The  $N$ -pcf for a regular polyhedron of edge length  $k$  depends on its orientation  $(\theta, \phi)$  and location  $p$  in the microstructure. In a similar manner, other forms of the point correlation function (with auto and cross-correlation phases at the vertices) may be defined. The orientation averaged  $N$ -pcf  $P_{ij}^k$ , which are of interest in this work, can be computed from the corresponding direction-dependent functions  $\tilde{P}_{ij}^k(\theta, \phi)$  as follows:

$$\langle P_{i_1 i_2 \dots i_N}^k(p) \rangle = \frac{1}{2\pi} \int_0^{2\pi} \int_0^{\frac{\pi}{2}} \tilde{P}_{i_1 i_2 \dots i_N}^k(p, \theta, \phi) d\theta d\phi \quad (15.1)$$



**Figure 15.3** Component arrangements. (a) A histology section of the mouse mammary gland showing several duct cross-sections. (b) A zoomed duct section reveals the characteristic packing arrangement of epithelial cell linings. (c) Mapped 2-*pcf* feature values.

We now provide some insight into the probability measures captured by these functions. Consider the simple case of a 1-*pcf*, say,  $P_0$ . It represents the probability that a point  $p$  is in *phase 0*. This quantity measures the volume fraction of *phase 0* in the microstructure. Similarly,  $P_1$  is the volume fraction of *phase 1*, and we have  $P_0 + P_1 = 1$ .

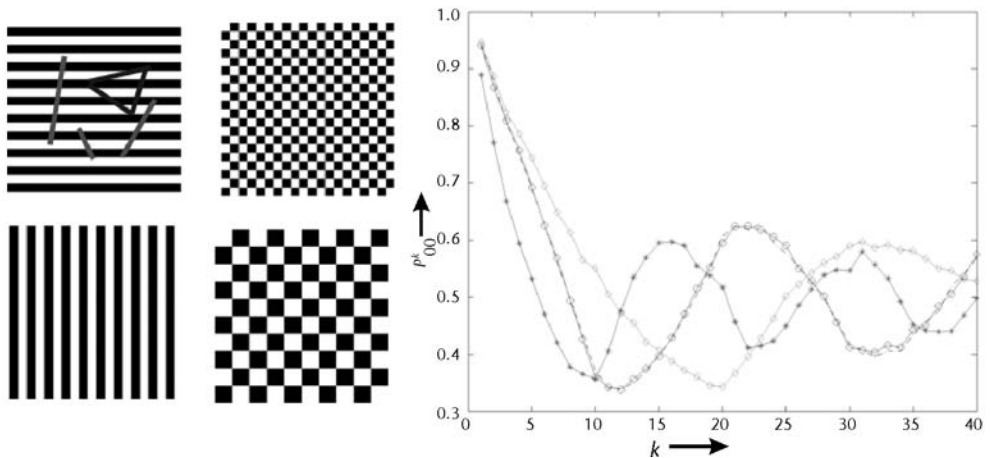
A 2-*pcf* is the probability of a straight line segment of length  $k$  randomly placed in the microstructure such that one end is in phase  $i_1 \in \{0,1\}$  and the other end is in phase  $i_2 \in \{0,1\}$ . For a two-phase microstructure, there are four possible two-*pcfs*—namely,  $P_{00}^k$ ,  $P_{01}^k$ ,  $P_{10}^k$  and  $P_{11}^k$  and:

$$\begin{aligned}
 P_{00}^k + P_{01}^k + P_{10}^k + P_{11}^k &= 1 & P_{01}^k &= P_{10}^k; \\
 P_{00}^k + P_{01}^k &= P_0; & P_{10}^k + P_{11}^k &= P_1
 \end{aligned} \tag{15.2}$$

Please refer to Figure 15.4 wherein four different microstructures composed of black (0) and white (1) phases are considered. Note that each individual texture class in the image provides a unique or characteristic  $2\text{-pcf}$  feature measure for a certain value of the separation distance  $k$ . Figure 15.4 (right), a plot of the  $P_{11}$  measure for the four textures as a function of  $k$ , is plotted. We observe that the four textures present characteristic signatures that enable their identification. For a given image, it is not known a priori what the values of  $k$  are. Hence, in practice, a range of values needs to be explored while estimating these functions, or, alternatively, the given image needs to be inspected for suitable separation distances among components. The set of possible integral values that  $k$  may assume is represented by the discrete set  $K \subset \mathbb{Z}$ . The  $N\text{-pcf}$  feature descriptor for a tissue region represented by  $P_{i_1 i_2 \dots i_N}^{(k)} \in \mathbb{R}^{K \times Q^N}$  is an  $N + 1$  mode tensor.

Essentially, a  $N\text{-pcf}$  is a multivariate distribution function. To estimate this function, we resort to using Monte Carlo sampling of the material components distribution using a sliding window ( $\Omega_p$ ). Conceptually, for a given separation length  $k$ , one needs to create auto- and cross-histograms at every point  $p$  in the discrete image plane. To estimate the functions at  $p$ , the number of samples ( $S$ ) and window sizes ( $\Omega_p$ ) need to be specified. The minimum window size is proportional to the maximum separation distance that the functions will be evaluated for, and the sample size is chosen to keep the variance of the measured result to a desired range.

To evaluate the  $2\text{-pcf}$  for separation distance  $k$  and phases  $i, j$  in a region containing  $m$ -phases, we place a number of randomly oriented and positioned lines. We then count the fraction of line segments that have an end point in phase  $i$  and the other in  $j$  to give an estimate of the  $2\text{-pcf}$   $P_{ij}^k$ .



**Figure 15.4** The figure shows four different microstructure ensembles composed of two-phase components, namely, phase 0 (black) and phase 1 (white). A plot of the orientation-averaged function  $P_{00}^k$  for varying  $k$  reveals different characteristic signatures.

### 15.3.2 Segmentation of Microscopic Images Using $N$ -pcfs

We now list some salient aspects of our segmentation framework.

1. Identifying homogeneous phase components: At the outset, we identify the microstructural components from the RGB images using a Gaussian maximum likelihood estimation (MLE) framework.
2. Estimating component distributions: Algorithms that utilize color/image space techniques (e.g., clustering, watershed, level-set methods) for region segmentation are appropriate only when the image regions are easily separated. Texture classification algorithms are more relevant to our problem. In our datasets, tissue regions present signature packing and ensemble distributions. We treat a slice as a multiphase material wherein each tissue layer can be independently analyzed for the ensemble properties.

In Section 15.3.1, the  $N$ -pcfs are estimated using a sliding window strategy that is applied throughout the image to yield a feature tensor at each pixel location. The tensor encodes information relevant to the spatial proximity of different components relative to each other.

3. Tensor Classification: The  $N$ -pcf features of a tissue sample are naturally expressed as  $N + 1$  mode (order  $N + 1$ ) tensors. We decompose the tensor feature space for a given tissue type using the higher-order singular value decomposition [27] method to identify the fundamental descriptors that best explain the unique distributions spanned by that tissue type in a large functional space.

## 15.4 Segmentation of Individual Cells

### 15.4.1 Modality-Dependent Segmentation: Active Contour Models

Three-dimensional segmentation algorithms will incorrectly delineate complete cells, given the problems of undersampling that exist in the image data. We use the active contour models with a level-set implementation for obtaining an initial 2-D segmentation of the nuclei. The two key steps for the level-set method are as follows:

1. Embedding the surface: we represent a given nucleus contour  $\Gamma(t)$  as the zero level-set of the signed distance function  $\psi(\mathbf{x}, t)$ . Formally,  $\Gamma(t) = \{\mathbf{x} : \psi(\mathbf{x}, t) = 0\}$ .
2. Embedding the motion: we derive the update equation (15.3) such that the motion of the zero level set has certain desired properties described later. For this purpose, we use the active contour formulation with shape priors developed by Leventon et al. [28]:

$$\frac{\partial \psi}{\partial t} = f(I)(\alpha c + \beta \kappa)|\nabla \psi| + \gamma \nabla f \cdot \nabla \psi + \delta \gamma(\psi^* - \psi) \quad (15.3)$$

The function  $f$  refers to the image-based feature function that is minimized at a nucleus boundary and remains high elsewhere. The function  $f$  involves information

drawn from the image gradients and *neck* artifacts. We will return to it later in the discussion.

The first speed term  $(c + \kappa)|\nabla\psi|$  consists of the curvature-dependent and propagation-dependent speed terms. The parameter  $c$  is a balloon force that is added to evolve the curve outwards, and  $\kappa$  is the curvature along the normal to the level-set contour. Since the boundary is characterized by a local minimum in  $f$ , the term  $\nabla f \cdot \nabla\psi$  constitutes the boundary attraction term. This ensures that the contour lies on the nucleus boundary upon convergence. The final term  $(\psi^* - \psi)$  is a recent addition by Leventon et al. [28], wherein they incorporated principal components of the segmentation shape model to drive the update equation. The surface  $\psi^*$  is the maximum a posteriori shape given the current segmentation and image information. The parameters  $\alpha$ ,  $\beta$ ,  $\gamma$  and  $\delta$  are user-defined settings for the relative scaling of the three speeds and the model-driven update.

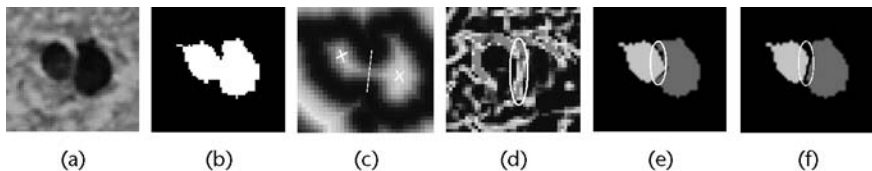
We incorporate three ideas from techniques that were developed independently—namely, (1) shape models (already described in the third speed term), (2) inter-nuclear boundary gradients, and (3) *neck* shape cues.

Training data consisting of manually segmented nuclei from 2-D images was used in estimating a PCA-based *shape model* with three modes of variation in a manner similar to that described in [28]. The advantage of using this model is that a good number of cells within a phenotype share similar sizes, shapes, and even orientations. Hence this information is incorporated as the MAP shape  $\psi^*$  in guiding the evolution in (15.3).

Please refer to Figure 15.5 for an illustration of the associated concepts of *image feature function*  $f$ . Let  $I$  represent a typical image with well-contrasted nuclei that needs to be segmented (Figure 15.5(a)). A threshold is applied to separate the nucleus foreground ( $I_f$ ) from the background ( $I_b$ ) (Figure 15.5(b)). Formally:

$$I_f(x,y) = \begin{cases} 0, & \text{if } I(x,y) > T \\ 1, & \text{if } I(x,y) \leq T \end{cases} \quad (15.4)$$

Let  $D(I_f)$  and  $D(I_b)$  represent the unsigned distance fields emanating from the threshold contour that exist outside and within the contour, respectively. Consider the image formed by  $P = D(I_f) + D(I_b)$ , shown in Figure 15.5(c).  $D(I_b)$  causes the



**Figure 15.5** Nuclei segmentation using geodesic active contours. (a) A pair of overlapping nuclei. (b) Applying a threshold  $T = 100$  on the red channel of the color image provides the nuclei foreground  $I_f$  and background  $I_b$ . (c) Unsigned distance field  $P$  of the nuclear contour. The nuclei centers ("x") are located at maxima and the neck region is in a directional minimum (white line segment). (d) High gradient magnitudes  $|\nabla I|$  typically exist in the neck region although this is not guaranteed. (e) Segmentation obtained using geodesic active contours. (f) Improving the segmentation by using linear tessellations.



appearance of a directional minimum in the neck region as represented by a white line segment. The appearance of a directional minimum is a direct consequence of the *neck* shape resulting in lower magnitudes of the distance field. At the same time, the nucleus-background boundary is marked by a 0 isovalue in  $P$  by definition, and positive elsewhere. Both these reasons contribute in *halting* the evolution that results in nuclei segmentation. While the presentation so far accounts for the neck cues, we also observe that some nuclei exhibit high gradients at the site of overlap, as shown in Figure 15.5(d). As in standard practice, we take the gradient information,  $g(I)$ , into account. Our feature function is therefore defined as:

$$f = \frac{g(I) + \eta(D(I_f) + D(I_b))}{1 + \eta} \quad (15.5)$$

$$g(I) = \frac{1}{1 + |\nabla G_\sigma * I|^2} \quad (15.6)$$

The gradient information  $g(I)$  is the reciprocal function of the image gradient magnitudes. The image gradients are computed using a standard derivative-of-Gaussian (doG) filter with an appropriate  $\sigma$ . The parameter  $\eta$  represents a scaling factor ranging from  $[0, \infty)$ . For large values, the neck cues are assigned more weight than the internuclear gradients  $g(I)$  and vice versa. The level-set initialization needs to occur inside each nucleus. Hence we apply a threshold on image  $P$  and choose the resulting iso-contour lying within the nucleus foreground as our initialization.

#### 15.4.2 Modality-Independent Segmentation: Using Tessellations

We observe that the level-set segmentation procedure described earlier does not produce consistent boundaries when separating nuclei clusters, as shown in Figure 15.5(e). This is because the feature function is defined using distance maps that are, in turn, sensitive to noisy contours. Furthermore, the standard level-set parameter settings do not effectively capture the variations in nuclear shape and internuclear gradients. This leads to inconsistent segmentations, especially at boundaries.

While it may be argued that this is a consequence of using the level-set methodology, related work shows that this problem has been a recurring one as far as microscopic datasets are concerned. As we noted earlier in Section 15.1, the staining protocol, the slicing methods, and so on take a heavy toll on the quality of the images generated. The variations are ubiquitous to microscopy datasets and prove to be an Achilles' heel for standard segmentation algorithms. For example, Adiga et al. [29] reported on an advanced watershed segmentation with a postprocessing mechanism to correct the oversegmentations. A rule-based merging scheme based on heuristics was set up. Unfortunately, these heuristics are application-specific and lack a rigorous framework of implementation. In a similar vein, Raman et al. [30] reported on the use of morphological operators and connected components to obtain a coarse segmentation. A set of heuristics were applied that naturally led to an approach similar to one based upon tessellations. Their groupings required placing



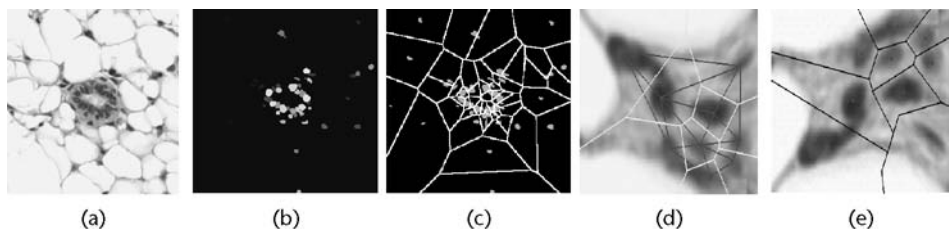
lines across novel contour points of positive curvature and enforcing constraints such as the nonintersection of separating line segments, convexity, and average area of the partitioned nuclei.

We now describe a rigorous, novel postprocessing technique that seeks to correct the boundaries. Our work makes a logical and significant extension of the previous attempts. We make use of the naturally occurring Voronoi tessellations to generate our line segments. These segments are altered using a *Bayesian probabilistic framework*. As a result, new heuristics that may occur in specific applications are naturally incorporated into the model. It marks a significant shift in philosophy—isolate image regions having a salient nucleus rather than extracting individual nucleus from a large image.

#### 15.4.2.1 Algorithm Overview

The algorithmic intuition is best explained as a sequence of steps along with a running example drawn from the mammary duct dataset. Please refer to Figure 15.6. We deploy the geodesic active contours algorithm on the given data to obtain coarse nuclei segmentations (Figure 15.6(b)). To correct, we do as follows:

1. The Voronoi tessellation of the image (Figure 15.6(c)) is constructed using the centroid of the identified nuclei as the generator set. The nucleus that is housed in a Voronoi cell may infiltrate into neighboring Voronoi cells and vice versa (Figure 15.6(d)). We now rectify the tessellation to correctly separate nuclei.
2. The set of Delaunay triangles dual to the Voronoi map is used in modulating the tessellations. We obtain the parameterized barycentric representation of the Voronoi tessellation line using a local Delaunay triangle, as outlined in Section 15.4.2.3.
3. We determine the maximum a posteriori (MAP) line parameters given image information, preliminary segmentations, and a set of heuristic rules. As a result, more viable tessellation lines are chosen for the final segmentation, as shown in Figure 15.6(d). Now, the nuclei are deemed to be separated and used in the interpolation framework.



**Figure 15.6** Cellular segmentation pipeline. (a) An example image of a duct cross-section formed by epithelial nuclei. (b) Segmentation of nuclei using level sets. (c) Voronoi tessellation of the image plane. (d) Zoomed version of the Voronoi tessellations. (e) Optimal tessellation placement with nuclei well separated.

### 15.4.2.2 Voronoi Tessellations—Step 1

Given a set of generating points  $V_i \in \mathbb{R}^2$ , the Voronoi map is a partitioning of  $\mathbb{R}^2$  using line segments into salient regions. Each region  $Z_i$  corresponding to the generator  $V_i$  is defined by:

$$Z_i = \{V \in \Omega \mid |V - V_i| < |V - V_j| \forall j \wedge i \neq j\} \quad (15.7)$$

Please refer to Figure 15.6(c). Having obtained preliminary nuclei segmentations using active contours, Voronoi partitioning of the image is accomplished using the nuclei centroid as generating points. Ideally, each individual nucleus lies within a corresponding Voronoi cell. In reality, this is not the case. A nucleus is anisotropic in shape, and tends to overlap and stray across the Voronoi cell boundaries. Figure 15.6(d) provides one such example. Our methods interactively alter the Voronoi tessellations to provide better nuclei separation by accounting for the overlap in various regions. The output from this stage is shown in Figure 15.6(e).

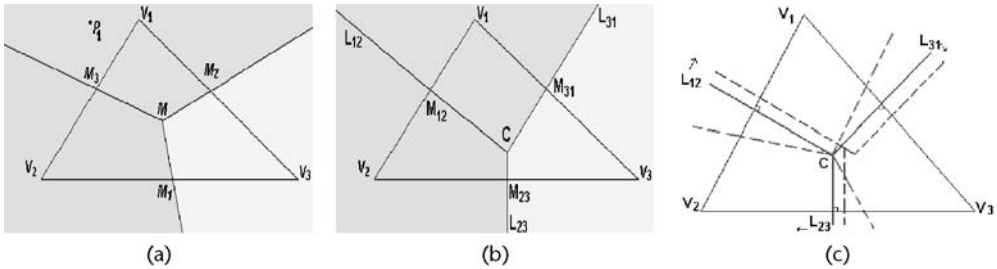
Note that the Voronoi representation of the tessellations given by (15.7) is implicit and not parameterized. We instead use a framework that explicitly represents the Voronoi tessellations using parameters that in turn, can be suitably modified.

### 15.4.2.3 Barycentric Representation of Tessellations—Step 2

We review some basic aspects of barycentric coordinates with the help of Figure 15.7(a). Given the vertices  $V = \{V_1, V_2, V_3\}$  of a Delaunay triangle  $T$ , any point  $P(x, y)$  can be parameterized in terms of the barycentric coordinates  $c = (c_1, c_2, c_3)$ . The following equation when solved for  $c$  gives us this representation:

$$\begin{bmatrix} V_{1x} & V_{2x} & V_{3x} \\ V_{1y} & V_{2y} & V_{3y} \\ 1 & 1 & 1 \end{bmatrix} \begin{bmatrix} c_1 \\ c_2 \\ c_3 \end{bmatrix} = \begin{bmatrix} x \\ y \\ 1 \end{bmatrix} \quad (15.8)$$

Note that the barycentric coordinates form a partition of unity (i.e.,  $c_1 + c_2 + c_3 = 1$ ). By definition, the vertices  $V$  have barycentric coordinates of  $(1, 0, 0)$ ,



**Figure 15.7** (a) Barycentric coordinates-based subdivision. (b) Tessellations unique to a Delaunay triangle  $T$  are shown. The lines meet at Voronoi vertex  $C$  and are perpendicular bisectors of the triangle formed from the associated nuclei centroid. (c) Possible tessellation movements are shown with translated and rotated edges starting from the Voronoi tessellation.

(0,1,0), and (0,0,1), respectively. Using the barycentric variables  $(c_1, c_2, c_3)$ , the equation of a general line is given by:

$$L^T : c_i - \lambda c_j = \delta \quad i, j \in \{1, 2, 3\}, i \neq j \quad (15.9)$$

The parameters  $(\lambda, \delta)$  represent the two degrees of freedom that are afforded in an equation describing a line. For example, setting  $(\lambda, \delta)$  as (1,0) in (15.9) results in three equations for the triangle medians, which meet at the centroid  $M$  (Figure 15.7(a)).

In Figure 15.7(b), we show a Voronoi cell vertex  $C$  as local to a Delaunay triangle  $T$  and common to three tessellation line segments  $L_{12}$ ,  $L_{23}$ , and  $L_{31}$  (solid lines). Using the barycentric representation, the equation of each tessellation line is:

$$L_{ij}^T : c_i - \lambda_{ij}^v c_j = \delta_{ij}^v \quad \forall i, j \in \{1, 2, 3\}, i \neq j \quad (15.10)$$

The Voronoi parameters  $(\lambda_{ij}^v, \delta_{ij}^v)$  are uniquely solved by invoking the property that the tessellation line segments pass through mid-points  $M_{ij}$  and  $C$  (circumcenter of Delaunay triangle  $T$ ). Mosaliganti et al. in [31] present the solution in detail.

By changing the Voronoi parameters  $(\lambda_{ij}^v, \delta_{ij}^v) \rightarrow (\lambda_{ij}, \delta_{ij})$ , the slope and intercept of each tessellation line  $L_{ij}$  is adapted to achieve better nuclei separation. An example of the resulting line placements obtained by translating and rotating the Voronoi boundaries is shown by the dashed lines in Figure 15.7(c).

Changing the Voronoi tessellations in each Delaunay triangle and repeating this process over all triangles leads to better descriptions of the overall Voronoi tessellation (Figure 15.6(d, e)). The new tessellations optimally house the nuclei and are more representative of the extent of nuclei infiltration.

#### 15.4.2.4 Estimating $(\lambda, \delta)$ —Step 3

We automate the procedure of changing tessellation line parameters using a Bayesian probabilistic model of nuclei separation. This procedure is novel and allays the hesitancy in using global partitions like the Voronoi tessellations. For each line segment, we seek to estimate the maximum a posteriori parameters  $(\lambda^*, \delta^*)$ .

$$(\lambda^*, \delta^*) = \arg \max_{\lambda, \delta} P(\lambda, \delta | S, I_f, f(I)) \quad (15.11)$$

In this equation,  $S$  is the initial coarse segmentation (Section 15.3),  $I_f$  is the nuclei foreground, and  $f(I)$  is as defined in (15.5). Using Bayes rule,

$$\begin{aligned} P(\lambda, \delta | S, I_f, f(I)) &= \frac{P(S, I_f, f(I) | \lambda, \delta) P(\lambda, \delta)}{P(S, I_f, f(I))} \\ &= \frac{P(S | \lambda, \delta) P(I_f | \lambda, \delta, S) P(f(I) | \lambda, \delta, S, I_f) P(\lambda, \delta)}{P(S, I_f, f(I))} \end{aligned} \quad (15.12)$$

We discard the normalization term in the denominator, as it does not influence  $\lambda$  or  $\delta$  and explain the remaining terms in turn.

- **Similarity term:** The first term  $P(S|\lambda, \delta)$  denotes the posteriori conditional probability of achieving the coarse segmentation,  $S$ , given the parameters  $\lambda$  and  $\delta$  of the final optimal tessellation. Consider the illustration in Figure 15.8(a). We denote  $(\tilde{\lambda}, \tilde{\delta})$  as the parameters of the least-squares fitted line separating the coarse segmentation boundary. Therefore, we write:

$$P(S|\lambda, \delta) = P(\tilde{\lambda}, \tilde{\delta}|\lambda, \delta) \quad (15.13)$$

Now, it is reasonable to assume that line parameters  $(\tilde{\lambda}, \tilde{\delta})$  when similar to the optimal case results in a high probability of better segmentation as depicted in the figure. Again, dissimilar parameters means a displaced tessellation from the optimal case and therefore has a low probability. Hence, we model this term as a Laplacian density function over the squared difference in parameters:

$$P(S|\lambda, \delta) = e^{-[(\tilde{\lambda}-\lambda)^2 + (\tilde{\delta}-\delta)^2]} \quad (15.14)$$

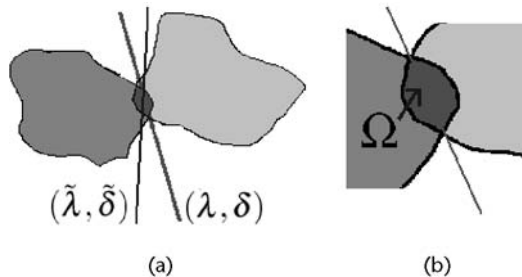
- **Overlap term:** The neck region is defined as  $\Omega = I_f \cap L(\lambda, \delta)$  (i.e., the intersection of the nuclei foreground and the tessellation line). For an illustration, refer to Figure 15.8(b). Typically, the neck region is optimally narrow at the point of nuclei separation (see Figure 15.2(b) and Figure 15.5(c)). Hence, we model this term as:

$$P(I_f|\lambda, \delta, S) = e^{-|\Omega|} \quad (15.15)$$

- **Gradient term:** The third term  $P(f(I)|\lambda, \delta, S, I_f)$  computes the conditional probability of the observed feature function  $f(I)$  given the segmentation ( $S$ ) and optimal tessellation line  $(\lambda, \delta)$ . Typically, the function was designed in (15.5) to have low values in  $\Omega$ . Hence, we write:

$$P(f(I)|\lambda, \delta, S, I_f) = e^{-\int_{\Omega} f(I) d\Omega} \quad (15.16)$$

- **Parameter priors:** The last term is the Voronoi tessellation  $(\lambda^v, \delta^v)$  applied as a prior. Recall that the tessellation is initialized as a Voronoi tessellation



**Figure 15.8** (a) Illustration showing the optimal and segmented lines in the similarity term. (b)  $\Omega$  shown as the intersection of nuclei foreground and the tessellation line

and hence in the absence of any information, we would like to maintain status quo.

$$P(\lambda, \delta) = e^{-[(\lambda - \lambda^v)^2 + (\delta - \delta^v)^2]} \quad (15.17)$$

A gradient descent optimization is applied on (15.11) to guide us to an optimal set of parameters  $(\lambda^*, \delta^*)$ . The barycentric parametrization serves to normalize all the tessellation lines to have the same optimal step lengths of the line parameters and convergence criterion. Normally, a Cartesian representation ( $y = mx + c$ ) of the lines would have different slope ( $m$ ) and intercept ( $c$ ) values. This causes the setting of initial parameters in the optimizer and in the MAP formulation to be line-specific, thereby making the problem intractable. The optimization procedure is repeated over all the tessellation line segments, leading to new partitioning of the image space. In Table 15.4, we have listed parameter settings of our optimizer in our experiments. We have now obtained final nuclei segmentations on 2-D serial section images.

## 15.5 Registration of Large Microscopic Images

Image registration is essential for 3-D reconstruction from serial microscopic images. There is a long history of using 2-D histological sections to reconstruct 3-D structures using various image registration algorithms in the bioengineering and pathology communities [1–21]. Johnson and Christensen [32] present a hybrid landmark/intensity-based deformable registration technique. The approach uses an iterative process of first registering landmarks independently of intensity, then attempts to minimize image intensity differences independent of landmarks. In Chui et al. [33], manually extracted sulcal points, located on the outer cortical surface, were spatially normalized via a robust point matching algorithm, thus achieving nonlinear matching of the brains. In spite of all these works, a major challenge is how to register large microscopic image datasets with billions of pixels in each image.

Here we present our work toward developing a scalable image registration framework for large microscopic images. In our study, registration is a two-step process that employs rigid and nonrigid registration algorithms. Rigid registration provides the rotation and translation needed to align adjacent images. It also provides an initialization for the deformable registration algorithm. Nonrigid registration compensates for local distortions in an image caused by tissue stretching, bending, and shearing.

### 15.5.1 Rigid Registration

We present two algorithms for rigid registration. The first algorithm is used for reconstructing low-resolution mouse placenta images. The second algorithm is optimized for higher resolution images.

#### 15.5.1.1 Rigid Registration Via Maximization of Mutual Information

This algorithm exploits the fact that the placenta tissue has an elongated oval shape. We carry out a principal component analysis of the foreground region to estimate the orientation of the placenta tissue. This orientation information is used to initialize an estimate of the rotation angle and centroid translation. After the images are transformed into a common coordinate reference frame, a maximum mutual information-based registration algorithm is carried out to refine the matching [6, 7]. In order to avoid suboptimal configurations, multiple initial configurations (rotational and translational) are used. Due to its high computational cost, this algorithm is performed on images downsampled by a factor of 20. The details of the implementation can be found in [7].

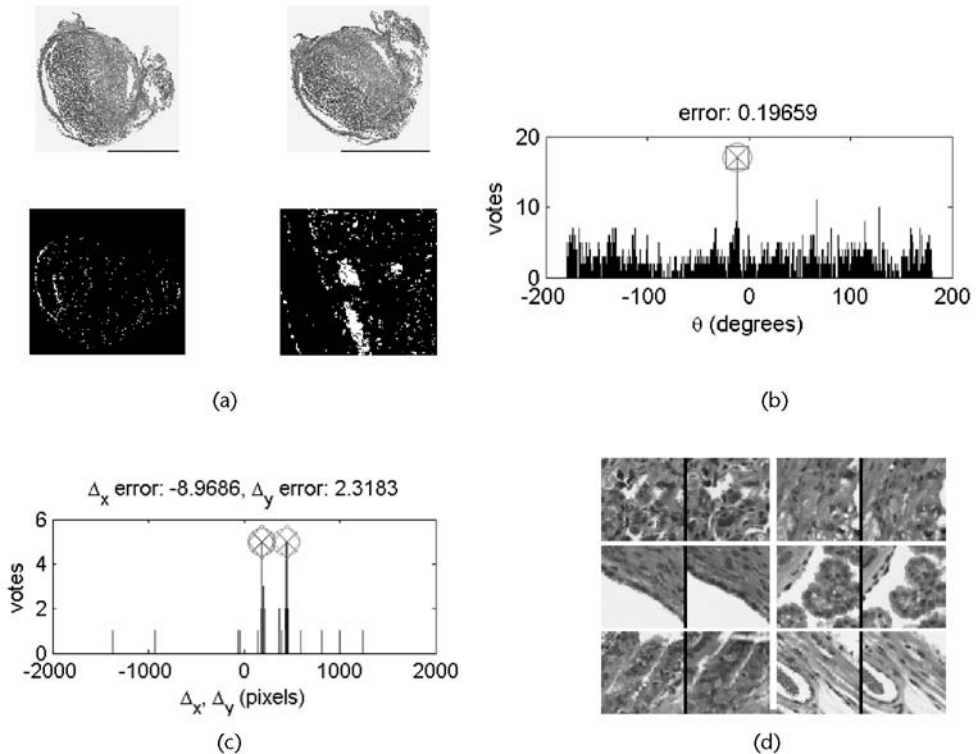
#### 15.5.1.2 Fast Rigid Registration Using High-Level Features

We propose the use of high level features (i.e., the regions corresponding to specific anatomical structures, for matching and registration). For example, in our work on the 3-D reconstruction of mouse placenta specimens, we specifically use regions of red blood pixels that correspond to cross-sections of blood vessels. There are several major advantages to using such features. First, these features are easy to segment, as they often correspond to large regions of pixels with similar colors. Second, even in large images, the number of such features is usually limited. Finally, these features are “global” and can be matched based on their morphology. Therefore the matching process is not limited to local search and can accommodate any significant misalignment between the images. The key issue in using such high-level features is how to automatically detect and discard mismatches. To this end, we have developed two approaches. There is a necessary condition such that two pairs of matched features can generate a purported rigid transformation specified by the rotation angle  $\theta$  and translational vector  $T$ . It can be conceived that a large portion of the computed transformations should concentrate around the true one in the transformation space. Therefore, a fast *voting* process can be adopted to select the optimal rigid transformations and also get rid of the mismatches. An example of this process is shown in Figure 15.9. If the number of features are small (e.g., fewer than 10), we developed a graph theoretical approach for feature matching [20].

This rigid registration process is usually very fast. When implemented in Matlab, for the example in Figure 15.9, it takes only 115 seconds to the rigid transformation (rotation and translation). The rigid (global) transformation provides an excellent initialization for the nonrigid registration, which requires a large amount of matched features as control points (shown in Figure 15.9(d)). An important note is that for the nonrigid registration, we only use the computed rotation and translation values and we do *not* need to transform the image based on the rigid transformation.

#### 15.5.2 Nonrigid Registration

Our nonrigid registration procedure includes two main steps. The first step is to identify a large number of feature points in the image. Unlike traditional methods,

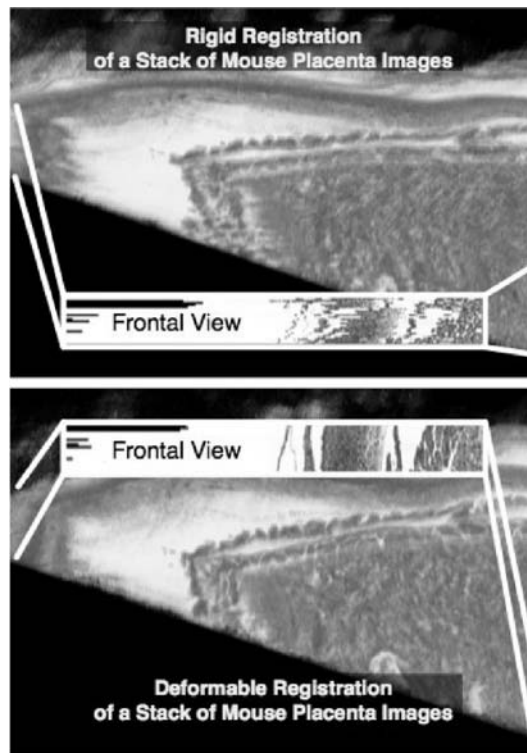


**Figure 15.9** (a) Extraction of the region features for fast rigid registration. The left two images are examples of microscopy images approximately  $4,000 \times 4,000$  pixels to be registered. The right binary images show the extracted regions of pixels for the left image at different resolutions. Only 50–70 such regions are selected from the large images. (b) Voting histogram on the rotation angle. The difference between the voting result and the manual result is less than  $0.2^\circ$ . (c) Histogram for the translation components  $x$  and  $y$ . The difference between the voting results and the manual results are less than 10 pixels. (d) Randomly selected matched points with the image patches around them between the two images.

wherein feature points are selected based on their prominence, we select points uniformly. For instance, we choose points that are 200 pixels apart both vertically and horizontally. Then the variation in a  $31 \times 31$  pixel window centering at each selected point is analyzed. The selection of the window size depends on the resolution of the image so that the window can capture a reasonable amount of cells. If the selected point belongs to the foreground, the neighboring window around it is transformed into the grayscale color space. Then the variance of pixel intensity values is computed. We retain the selected point as a feature point only when the variance of the neighboring window pixel intensity value is large enough (which implies a complex neighborhood). A complex neighborhood around a pixel in one image allows more accurate matching with the unique region in the next image that is the true correspondence for the original region. Regions with small intensity variance tend to generate mismatches. An extreme example is that a block of white space can be matched with many other blocks' white spaces without knowing which one is the correct match. This step usually yields about 200 features



points that are uniformly distributed across the foreground of each image. In the second step, we rotate the window around the feature point by the angle that is already computed in the rigid registration procedure. This gives a template patch for initialization in the next image. In the next image, a much larger neighborhood (e.g.,  $100 \times 100$  pixels) is selected. The best patch in this larger neighborhood is defined as the patch that has the largest cross correlation with the template patch, and the center of this patch is designated as the corresponding feature point. The two steps together usually generate more than 100 matched feature points between the two images. These points are then used as control points to compute the nonlinear transformation such as thin-plate splines or polynomial transformations [7, 8]. In this project, we tested both six-degree polynomial transformations and piecewise affine transformations. The 3-D reconstructions are similar in both schemes, while the piecewise affine transformation is easier to compute and propagate across a stack of images. Figure 15.10 shows renderings of the placenta that were reconstructed using the rigid and deformable registration algorithms.



**Figure 15.10** Comparison of rigid and deformable registration algorithms. A stack of 25 images were registered using rigid registration algorithm (top) and nonrigid registration algorithm (bottom) and the 3-D reconstruction results are rendered. The frontal views show the cross-sections of the reconstructed model. The benefits of using deformable registration algorithms are clearly visible in the frontal view of the image stack cross-section. In the top frontal view, which is the cross section of the rigid registered images, the structures are jaggy and discontinuous. In the bottom frontal view, the results from the nonrigid (deformable) registration algorithm display smooth and continuous structures.

## 15.6 3-D Visualization

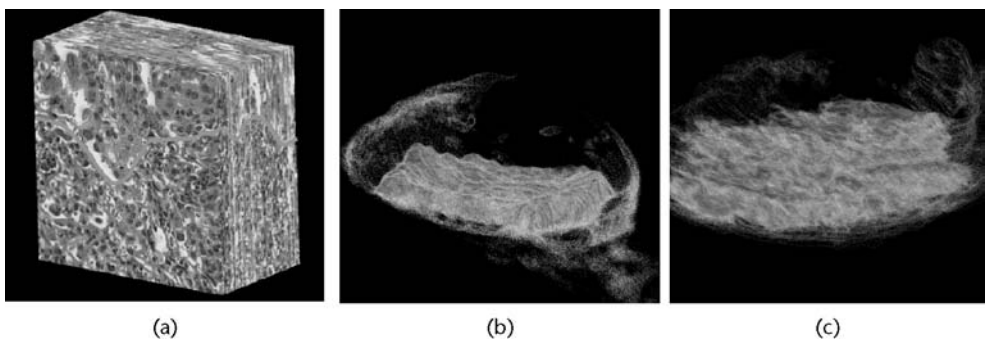
In this section, we describe our results in 3-D reconstruction and visualization of serial-section image stacks from light and confocal microscopy. We applied our methods in three different experimental studies involving genetic phenotyping and drug discovery applications. Our methods are easily applied with changes in parameter settings to each of the data sets obtained from very different sources.

### 15.6.1 Mouse Model Phenotyping Study: Role of the *Rb* Gene

In this project, as described in Section 15.2.1, we are interested in visualizing the tissue intermixing that occurs on the labyrinth-spongiotrophoblast tissue interface of the mouse placenta organ. A recent study has revealed that with the knockout of the *Rb* gene, the surface interdigitation wildly increases and clumps together with poor infiltration depth [34]. We are interested in visualizing this phenotype difference [16].

Two pairs of wild-type and mutant (*Rb*<sup>−</sup>) placenta were harvested at 13.5 days of gestation and prepared using a standard histological protocol. They were fixed in formalin, embedded in paraffin, and sectioned at 5- $\mu$ m thickness using a microtome. Serial sections were mounted on glass slides and scanned at 200 $\times$  magnification using a light microscope. The image dimensions on average were (15K  $\times$  15K  $\times$  3). Each placenta data-set produced approximately 600–800 color images, ranging in size from 300 GB to 500 GB. The images are extremely noisy and require preprocessing, down-sampling, image registration, and tissue segmentation prior to the visualization stage.

Figure 15.11(a) shows the a high-resolution RGB rendering of a small physical volume. The contrasting microstructure on either side of the interface is clear. In particular, there is a intense presence of dark nuclei and RBCs on the labyrinth side. The spongiotrophoblast region is marked by an absence of RBCs and has more vacuoles. After preliminary investigations on sample images, we concluded that using a 2-*pcf* with  $k \in [5, 25]$  for vacuoles (phase 0), nuclei (phase 1), and



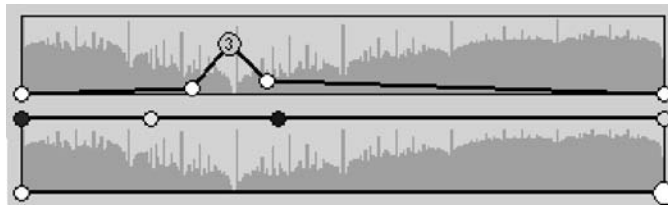
**Figure 15.11** (a) A normal cutaway section of mouse placenta with manually marked tissue layers. Visualizations showing the tissue layer intermixing in the labyrinth-spongiotrophoblast interface of (b) normal and (c) mutant mice placenta.

RBC components (phase 2) will well differentiate the tissue regions. The labyrinth region registered high values of  $P_{12}$ . Meanwhile, the spongiotrophoblast region was marked by a moderate value in  $P_{01}$  and low values in  $P_{12}$ . These probabilities were linearly combined to provide a scalar volume  $P = P_{12} + |P_{01} - 0.5| + |P_{12} - 0.5|$  for rendering using a simple transfer function.

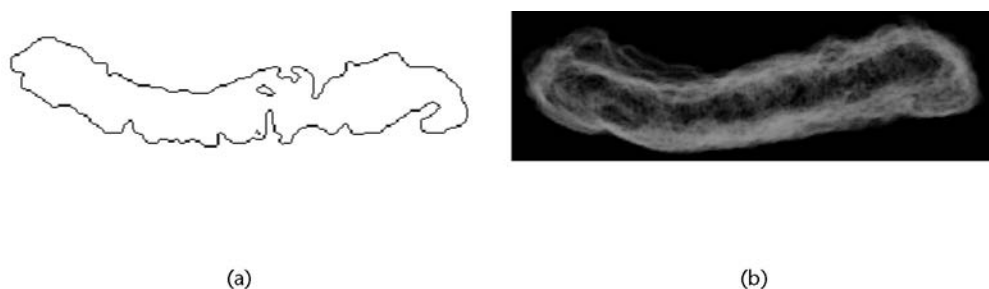
Figure 15.12 shows our transfer function setting to highlight interface between the two regions. The histogram indicates the presence of the labyrinth and spongiotrophoblast layers. At the valley region between the bimodal peaks, the opacity function is spiked and reduced elsewhere. Now, it is easy to notice the genetic phenotyping difference in the two placenta samples. The mutant shows a higher degree of intermixing as compared to the normal placenta.

We then realize the final goal of visualizing and quantifying the infiltration in the labyrinth-spongiotrophoblast interface by detecting surface pockets. The image shown in Figure 15.13(a) shows a 2-D contour of a cross section of the segmented labyrinth layer. We are interested in examining the infiltrations and extrusions that exist in 3-D. However, when the entire volume is rendered in 3-D, the infiltrations and extrusions can be occluded by the rest of the labyrinth surface. The presence of the infiltrations is not obvious in the 3-D rendering until a large portion of the placenta is cropped away and rendered as in Figure 15.13(b).

Figure 15.14 shows the results of highlighting infiltrations and extrusions on the labyrinth surface in wild-type (05-977) and mutant ( $Rb^-$ ) (05-1904) mouse placenta. Specifically, Figure 15.14(a, d) shows the entire original surface of the labyrinth. No infiltrations or extrusions are obvious in the image. The image in Figure 15.14(b, e) highlights infiltrations using an outward marching level-set to obtain feature size information. Similarly, the image in Figure 15.14(c, f) uses an inward marching level set to highlight extrusions on the data. Color Plate 22 provides a more distinct phenotyping difference in the interface topology. The following observations can be readily made: (1) The wild-type placenta seems to have well-developed infiltrations/extrusions that run deep into the other tissue. The mutant placenta is however marked by their absence. Instead there is random interdigitation that is clumped together at different sites. (2) It also can be seen that the wild-type labyrinth has more uniformly distributed features than the mutant placenta.



**Figure 15.12** Opacity and color transfer function applied on the probabilistic volume  $P$  to highlight the interface region. Note the presence of bimodal peaks in the histogram from the labyrinth and spongiotrophoblast layers.

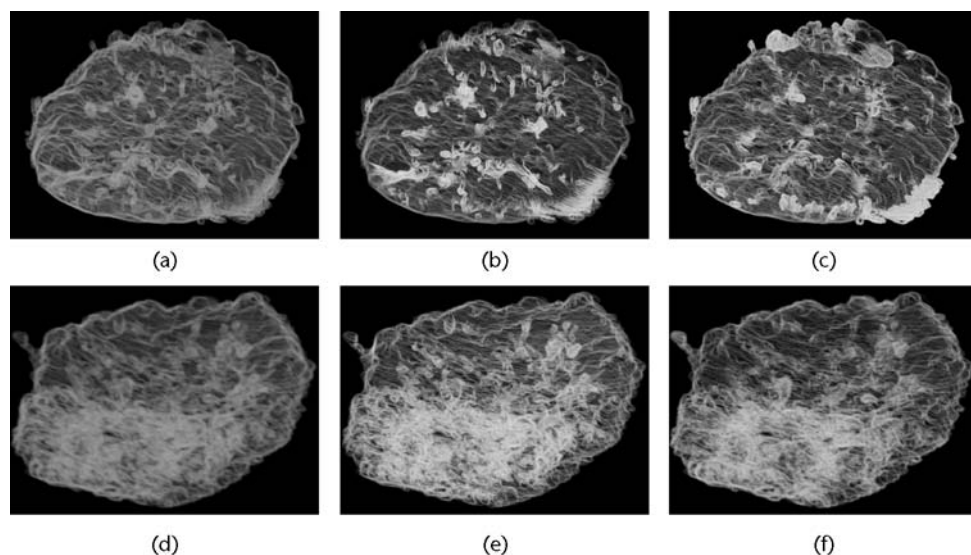


**Figure 15.13** (a) 2-D contour of a cross section of the labyrinth layer. (b) 3-D rendering of many consecutive labyrinth tissue contours with a constant opacity.

### 15.6.2 Mouse Model Phenotyping Study: Role of the PTEN Gene in Cancer

As we have discussed in the Section 15.2.2, we seek to understand the orchestrated sequence of events leading to tumor initiation and progression at a cellular as well as a molecular scale, which is induced by the deletion of the PTEN gene in the fibroblasts. The focus of the study is the mammary gland ducts, which are potential sites for tumor initiation.

Mammary ductal tissue is composed of concentric layers of epithelial in a matrix of extracellular material. The ducts are identified on each section as a distinct conic or quadric projection of a complex tortuous 3-D object [Figure 15.2(a)]. We used the  $N$ -point correlation functions as feature vectors to classify ductal tissue

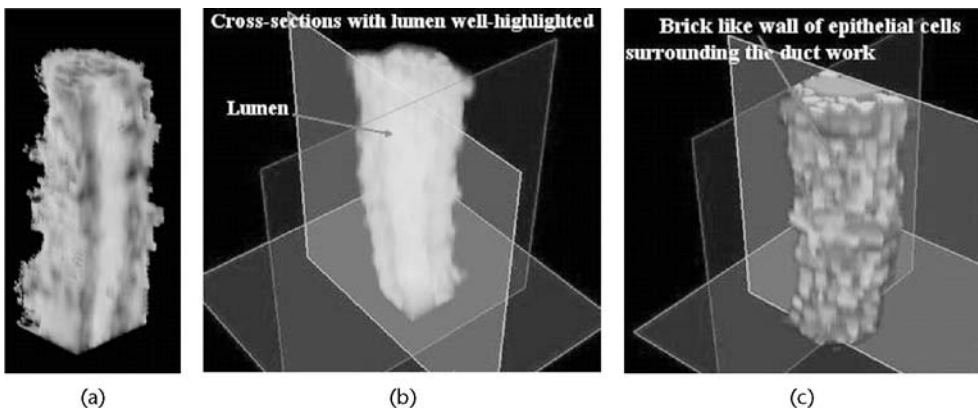


**Figure 15.14** The top row contains images of normal mouse placenta labyrinth while the bottom row shows mutant ( $Rb^-$ ) placentas. The left column (a, d) shows images of the overall mouse labyrinth layers; no specific infiltrations or extrusions in the tissue can be seen. The middle column (b, e) highlights the infiltrations in increasing intensity. The right column (c, f) shows the result of highlighting extrusions in increasing intensity.

regions [35, 36]. These functions measure the packing of the cells and are shown to provide robust classification. Rigid registration was accomplished using a global alignment procedure [37], followed by a refined local matching of individual ductal areas [38]. Three-dimensional profiles of the ducts were extracted from the large dataset to yield smaller volumes of  $300 \times 300 \times 34$  per duct for processing. We then apply the tools described in this work to the problem of providing duct reconstructions at a cellular scale.

Mammary tumors often arise in close vicinity to the ductal tissue. Earlier, we had described the morphology of a duct as a concentric arrangement of epithelial cells embedded in extracellular material. The remainder of the tissue consists of fat cells with sparse populations of the nuclei and little or no extracellular material. From 2-D images, we inferred that a 2-*pcf* for the background (phase 0), nuclei (phase 1), and extracellular material (phase 2) was sufficient to outline duct profiles. The average separation ( $k$ ) between nuclei was found to be 30 pixel units. Clearly, the ductal tissues have closely packed nuclei and present high values of the function  $P_{11}$  and  $P_{12}$  simultaneously. In contrast, other regions in the volume may have high values of  $P_{11}$  or  $P_{12}$  but never simultaneously. Therefore, we once again linearly combine both the functions to provide a scalar volume for exploration. A stacking of the 2-*pcf* features computed on 2-D images provided the following visualizations in 3-D. Figure 15.3(c) shows the generated feature values on the mammary slice in Figure 15.3(b). Figure 15.15(b) is an axial section of the duct revealing the lumen that lies trapped in the duct. Figure 15.15(c) shows the wall of the epithelial cell lining that is akin to a brick chimney wall.

Individual nuclei were the identified in 2-D images and overlapping nuclei clusters were split consistently using the two successive segmentation stages based on active geodesic contours and tessellations. We then performed interpolation of intermediate slice locations using an elliptic shape model to reconstruct 3-D



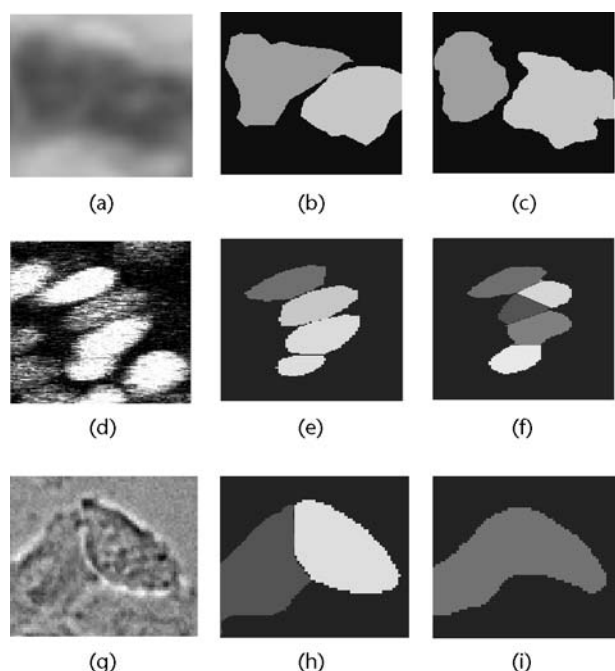
**Figure 15.15** (a) Raw RGB data showing a duct that manually assembled from 3-D slices. (b) The same duct was automatically highlighted by using a transfer function. (c) The outer isosurface of the ductal tissue.

ductal volumes for visualization. A total of 18 contiguous duct sequences were reconstructed using this automated procedure.

Color Plate 23 provides examples of four such sequences. Panel A is a transfer function volume rendering of a segmented duct using a cutting plane parallel to the duct axis. The elliptic nuclei profiles are visible in the ductal wall. Panel B is the true color rendering with interpolated textures of the ductal tissue. It is easy to notice the lack of any cellular descriptions in the rendering. Panel C shows yet another branching duct with nuclei and lumen alone. A hemi-cylindrical cut-away section was used to reveal the underlying lumen. Panel D is a top view of the duct revealing a constellation of cells along the duct akin to a brick chimney wall.

### 15.6.3 Zebrafish Phenotyping Studies

As described in Section 15.2.3, our goal is to use in toto imaging of developing transgenic zebrafish embryos to acquire digital, quantitative, cell-based, molecular data suitable for modeling the biological circuits that transform an egg into an embryo. In toto imaging uses confocal microscopy to capture the entire volume of organs and eventually whole embryos at cellular resolution every few minutes in living specimens throughout their development. Four-dimensional image sets ( $x - y - z - t$ ) with dimensions  $1,024 \times 1,024 \times 80 \times 60$  are generated. The



**Figure 15.16** Instances of outliers in the segmentation process with the top row showing a mammary duct sample with an inconsistent split, the middle row showing a zebrafish image with oversegmentation and the bottom row from a clonal colony with undersegmentation. (a, d, g) Original images; (b, e, h) manual masks; and (c, f, i) segmentations.



**Table 15.1** Sensitivity and Specificity Values for Pocket Detection

<i>Dataset</i>	<i>Depth</i>	<i>Diameter</i>	<i>Sens.</i>	<i>Spec.</i>	<i>Error</i>
05-829	$\geq 14$	$\leq 8$	0.9223	0.8253	0.0324
	$\geq 12$	$\leq 8$	<b>0.9134</b>	<b>0.8527</b>	<b>0.0215</b>
	$\geq 12$	$\leq 10$	0.9690	0.8041	0.0785
05-1904	$\geq 14$	$\leq 8$	0.9021	0.8475	0.0542
	$\geq 12$	$\leq 8$	<b>0.8907</b>	<b>0.8822</b>	<b>0.0433</b>
	$\geq 12$	$\leq 10$	1.000	0.8173	0.0851
05-977	$\geq 14$	$\leq 8$	0.9853	0.8238	0.0662
	$\geq 12$	$\leq 8$	<b>0.8594</b>	<b>0.8735</b>	<b>0.0544</b>
	$\geq 12$	$\leq 10$	0.9637	0.7835	0.0951
05-1903	$\geq 14$	$\leq 8$	0.9522	0.8325	0.0483
	$\geq 12$	$\leq 8$	<b>0.9162</b>	<b>0.8756</b>	<b>0.0357</b>
	$\geq 12$	$\leq 10$	1.000	0.5281	0.0642

plan is to use in toto imaging to digitize the complete expression and subcellular localization patterns of thousands of proteins throughout zebrafish embryogenesis. We provide 3-D results from applying our methods at select time-points chosen at  $t = 0$  (beginning) and 60 (ending).

Figure 15.16(a–c), Figure 15.16(d–f), and Figure 15.16(g–i) represent sequences from the three time points. The columns depict the rendering of original raw data, the foreground, and cell segmentations, respectively. Note that once again the repetition in colors is owing to the large number of cells. Fewer cells in the first time-point increase in the later time-point with the formation of salient structures.

## 15.7 Quantitative Validation

### 15.7.1 Mouse Placenta Phenotyping Studies

We validate our results using manually segmented surface pockets that are present in a contiguous section of the 3-D stack of images. The contiguous section is selected approximately from the center of the stack. The central section is usually associated with better consistency in staining, section thickness, and reduced deformations of the tissue. This usually results in better segmentation and higher registration accuracy. Surface pockets were then identified in sections that were drawn from each placenta dataset. Each detected pocket in this stack can be placed in four categories: (1)  $a$  counts the number of pockets that are marked in the ground-truth and fit our model (true positives); (2)  $b$  counts the pockets that are not marked in

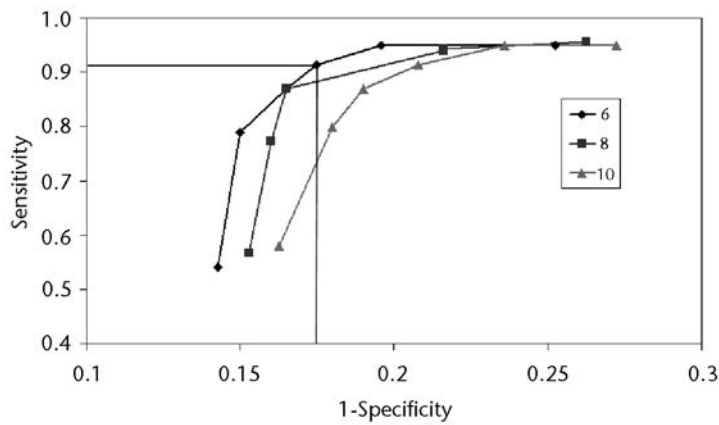
**Table 15.2** Execution Time in Seconds for the Three Metrics

<i>Dataset</i>	<i>Euclidean</i>	<i>Evolution</i>	<i>Combined</i>
05-829	23	221	<b>41</b>
05-1904	19	215	<b>42</b>
05-977	26	274	<b>41</b>
05-1903	21	225	<b>38</b>

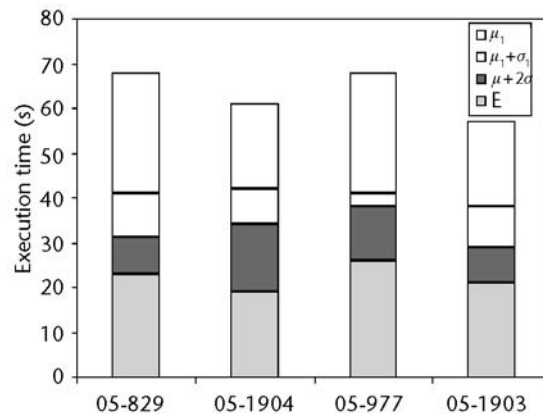


ground-truth but fit our model (false positives); (3)  $c$  counts the pockets that are marked up but do not fit our model (false negatives); and (4)  $d$  counts the pixels that are neither marked nor fit our model (true negatives). Note that a high value of specificity ( $\frac{d}{b+d}$ ) indicates that it is easy for the algorithm to rule out a spurious pocket with a high probability. On the other hand, a value of high sensitivity ( $\frac{a}{a+c}$ ) can identify a bona fide pocket with a high probability of success. The error may be defined as  $\frac{b+c}{a+b+c+d}$ .

Table 15.1 tabulates the sensitivity, specificity, and error rates observed for different settings of the minimum allowable pocket depth ( $\Pi_{depth}$ ) and the max-



(a)



(b)

**Figure 15.17** (a) ROC family of curves for different  $\Pi_{depth}$  settings with  $\Pi_{CS} = 6, 8$ , and  $10$  respectively. An optimal setting is given by  $\Pi_{CS} = 8$  and  $\Pi_{depth} = 12$  with sensitivity and specificity values at  $(0.9134, 0.8527)$ . (b) Effect of different settings of the  $\tau$  parameter on the time-performance while using the combined distance metric accumulated over the Euclidean metric (denoted by  $E$  when  $\tau = \infty$ ).

imum allowable cross-sectional base diameter ( $\Pi_{cs}$ ). The execution times for the different metrics are listed in Table 15.2. The following observations are made:

1. Within every placenta category, as the range of allowable pocket sizes widens ( $\Pi_{depth} = 14$ ) or ( $\Pi_{cs} = 10$ ), the sensitivity increases and the specificity decreases as compared to the highlighted case when ( $\Pi_{depth} = 12$  and ( $\Pi_{cs} = 8$ ). This is an expected trend since nonpocket features now fit our constraints, thereby lowering specificity. Simultaneously, all true pockets also readily fit the model, thereby increasing the sensitivity.
2. Across the placentas, we always obtain a good sensitivity with moderate specificities. Error rates are maintained below 0.10. The wild-type placentas (05-829 and 05-1903) have well-developed fingers and therefore have better detection rates as compared to the mutants (05-977 and 05-1904).
3. Figure 15.17(a) plots the family of ROC iso-contour curves of the  $\Pi_{cs}$  parameter in the 05-829 dataset for different settings of the  $\Pi_{depth}$  parameter. A step-size of 0.5 was considered while varying the  $\Pi_{depth}$  parameter in the ranges (12–14) while  $\Pi_{cs}$  was varied as 6, 8, and 10. The ROC curve indicate stability in the observed results and validates the choice of their settings.

### 15.7.2 Mouse Mammary Gland Phenotyping Study

We evaluate the utility of the segmentation framework in effectively segmenting nuclei that appear as clusters. Validation studies are performed with manually marked nuclei areas. It is very difficult to manually identify all the valid nuclei in a dataset. Typically, the number of nuclei can be in the order of several thousands. Therefore, we sample 10 regions of dimensions  $100 \times 100$  in a unbiased fashion from each dataset. All the nuclei in these windowed regions are marked out to obtain classified masks that serve as ground-truth. The matched pair of nuclei can be separated and counted in three categories: (1) *a* counts the number of *true-positive* results. (2) *b* counts the number of *false-negative* results. (3) *c* counts the number of *false-positive* results. Note that false-negative results cannot be determined since we have no a priori information on where a nuclei should not have existed. Thus, one can define the *sensitivity* and *positive predictive value* (PPV) of our framework as follows:

$$\text{sensitivity} = \frac{a}{a + b} \quad \text{PPV} = \frac{a}{a + c} \quad (15.18)$$

**Table 15.3** Test Datasets Chosen for Validation Studies

<i>Dataset</i>	<i>Dimension</i>	<i>Cells</i>
Clonal 1	$1,024 \times 1,024$	378
Clonal 2	$1,024 \times 1,024$	610
Clonal 3	$1,024 \times 1,024$	794
Ducts	$300 \times 300 \times 34$	1,710
Zebrafish	$1,024 \times 1,024 \times 80$	4,130

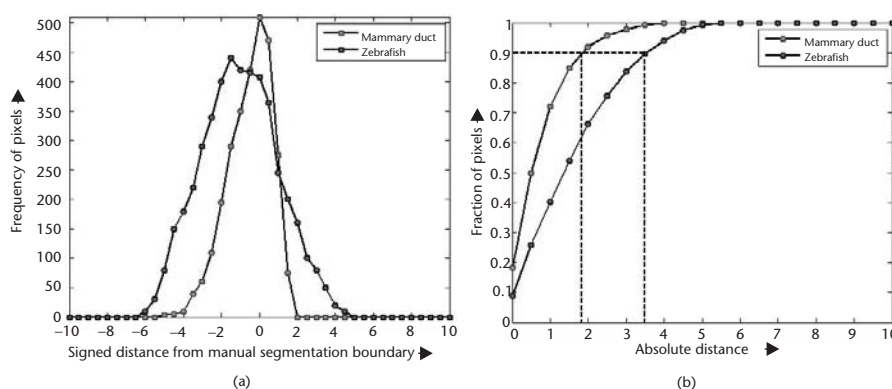
**Table 15.4** Sensitivity and PPV Values for Cell Segmentation

Dataset	Cells	Sens.	PPV
Clonal 1	74	0.9324	0.9452
Clonal 2	117	0.8547	0.9259
Clonal 3	174	0.8996	0.9455
Ducts	217	0.9724	1
Zebrafish	252	0.8968	0.9826

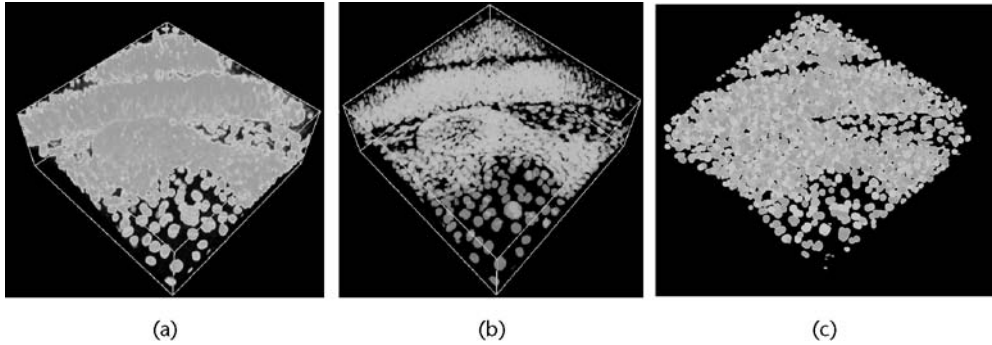
Table 15.3 lists our test datasets with dimensions and the total number of nuclei actually segmented throughout the dataset. The test datasets include a clonal assay dataset consisting of three temporal frames, a mammary duct dataset containing of 34 slices, and a zebrafish confocal dataset having 80 slices.

From Table 15.4, we observe that our methods yield an average values of 94% and 96% for sensitivity and PPV, respectively. Sensitivity measures the effectiveness of the algorithm in detecting the true-positives. A high value indicates that it is easy for the algorithm to rule out a spurious match with a high probability. On the other hand, the positive predictive value estimates the proportion of segmented nuclei that are *bona fide* ones. The false-positives are mostly due to *undersegmentation*—the true cell region is found to be grouped in a single larger segmented region. Similarly, the true-negatives are due to *oversegmentation*—the true cell region is found to have multiple segmentations.

Validation studies were also performed using the same protocol as described in [39]. In this case, a histogram of signed distances of the nucleus contour with respect to the ground-truth contour is computed for all the true-positive results generated from the previous study. In Figure 15.18, we plot the distribution of distance of the segmentation boundary pixels from the manual boundary. We observe that in the case of the mammary ducts, 90% of the boundary pixels in the automatic segmentation are within 3 pixels in distance from the corresponding manual boundary. Similarly, 75% of the boundary pixels are within 2 pixel dis-



**Figure 15.18** (a) Combined histogram for the signed distances found in the mammary and confocal datasets, and (b) cumulative distribution of absolute distances from automatic segmentation to manual segmentation.



**Figure 15.19** 3-D cellular reconstructions from confocal images of the zebrafish embryo at  $t = 60$ . (a) Raw data renderings, (b) foreground extractions, and (c) cell segmentations.

tances. Figure 15.19 also shows that similar trends were observed in the case of the confocal images of the zebrafish.

## 15.8 Summary

In this chapter, we presented a series of algorithms for quantitatively characterizing the 3-D structure of biomedical samples at the microscopic scale. While the traditional approaches focus on the image registration algorithms for generating 3-D structures from 2-D images, we have shown that a realistic visualization and modeling requires extensive development in not only image registration, but also in image segmentation, cell segmentation, visualization, and quantification algorithms. Based on a comprehensive workflow, we demonstrate our novel algorithms in all these aspects, which are motivated by several large-scale biomedical studies in developmental biology and cancer biology. These algorithms, along with the workflow, provide a universal framework for quantitative phenotyping studies in the microscopic scale.

## References

- [1] Levinthal, C., and R. Ware, "Three-Dimensional Reconstruction from Serial Sections," *Nature*, Vol. 236, 1972, pp. 207–210.
- [2] Capowski, J., "Computer-Aided Reconstruction of Neuron Trees from Several Sections," *Computational Biomedical Research*, Vol. 10, No. 6, 1977, pp. 617–629.
- [3] Johnson, E., and J. Capowski, "A System for the Three-Dimensional Reconstruction of Biological Structures," *Computational Biomedical Research*, Vol. 16, No. 1, 1983, pp. 79–87.
- [4] Huijismans, D., W. Lamers, J. Los, and J. Strackee, "Toward Computerized Morphometric Facilities: A Review of 58 Software Packages for Computer-Aided Three-Dimensional Reconstruction, Quantification, and Picture Generation from Parallel Serial Sections," *The Anatomical Record*, Vol. 216, No. 4, 1986, pp. 449–470.
- [5] Moss, V., "The Computation of 3-Dimensional Morphology from Serial Sections," *European Journal of Cell Biology*, Vol. 48, 1989, pp. 61–64.

- [6] Brandt, R., T. Rohlfing, J. Rybak, S. Krofczik, A. Maye, M. Westerhoff, H.-C. Hege, and R. Menzel, "A Three-Dimensional Average-Shape Atlas of the Honeybee Brain and its Applications," *The Journal of Comparative Neurology*, Vol. 492, No. 1, 2005, pp. 1-19.
- [7] Hajnal, J., H. Derek, and D. Hawkes, *Medical Image Registration*, Boca Raton, FL: CRC Press, 2001.
- [8] Goshtasby, A., *2-D and 3-D Image Registration: For Medical, Remote Sensing, and Industrial Applications*, New York: Wiley-Interscience, 2005.
- [9] Streicher, J., D. Markus, S. Bernhard, R. Sporle, K. Schughart, and G. Muller, "Computer-Based Three-Dimensional Visualization of Developmental Gene Expression," *Nature Genetics*, Vol. 25, 2000, pp. 147-152.
- [10] Braumann, U., J. Kuska, J. Eienkel, L. Horn, M. Luffler, and M. Huckel, "Three-Dimensional Reconstruction and Quantification of Cervical Carcinoma Invasion Fronts from Histological Serial Sections," *IEEE Transactions on Medical Imaging*, Vol. 24, No. 10, 2005, pp. 1286-1307.
- [11] Crum, W., T. Hartkens, and D. Hill, "Non-Rigid Image Registration: Theory and Practice," *The British Journal of Radiology*, Vol. 77, 2004, pp. S140-S153.
- [12] Hill, W., and R. Baldock, "The Constrained Distance Transform: Interactive Atlas Registration with Large Deformations Through Constrained Distance," *Proceedings of the Workshop on Image Registration in Deformable Environments*, 2003.
- [13] Yoo, T., *Insight into Images: Principles and Practice for Segmentation, Registration, and Image Analysis*, Wellesley, MA: AK Peters, 2004.
- [14] Sarma, S., J. Kerwin, L. Puelles, M. Scott, T. Strachan, G. Feng, J. Sharpe, D. Davidson, R. Baldock, and S. Lindsay, "3d Modelling, Gene Expression Mapping and Post-Mapping Image Analysis in the Developing Human Brain," *Brain Research Bulletin*, Vol. 66, Nos. 4-6, 2005, pp. 449-453.
- [15] Jenett, A., J. Schindelin, and M. Heisenberg, "The Virtual Insect Brain Protocol: Creating and Comparing Standardized Neuroanatomy," *BMC Bioinformatics*, Vol. 7, 2006, p. 544.
- [16] Wenzel, P., L. Wu, R. Sharp, A. de Bruin, J. Chong, W. Chen, G. Dureska, E. Sites, T. Pan, A. Sharma, K. Huang, R. Ridgway, K. Mosaliganti, R. Machuraju, J. Saltz, H. Yamamoto, J. Cross, M. Robinson, and G. Leone, "Rb Is Critical in a Mammalian Tissue Stem Cell Population," *Genes & Development*, Vol. 21, No. 1, 2007, pp. 85-97.
- [17] Cooper, L., K. Huang, A. Sharma, K. Mosaliganti, and T. Pan, "Registration Vs. Reconstruction: Building 3-D Models from 2-D Microscopy Images," *Proceedings of the Workshop on Multiscale Biological Imaging, Data Mining and Informatics*, 2006, pp. 57-58.
- [18] Huang, K., L. Cooper, A. Sharma, and T. Pan, "Fast Automatic Registration Algorithm for Large Microscopy Images," *Proceedings of the IEEE NLML Life Science Systems & Applications Workshop*, 2006, pp. 1-2.
- [19] Koshevov, P.A., T. Tasdizen, and R.T. Whitaker, *Implementation of an Automatic Slice-to-Slice Registration Tool*, SCI Institute Technical Report UUSCI-2006-018, University of Utah, 2006.
- [20] Prescott, J., M. Clary, G. Wiet, T. Pan, and K. Huang, "Automatic Registration of Large Set of Microscopic Images Using High-Level," *Proceedings of the IEEE International Symposium on Medical Imaging*, 2006, pp. 1284-1287.
- [21] Mosaliganti, R., T. Pan, R. Sharp, R. Ridgway, S. Iyengar, A. Gulacy, P. Wenzel, A. de Bruin, R. Machiraju, K. Huang, G. Leone, and J. Saltz, "Registration and 3D Visualization of Large Microscopy Images," *Proceedings of the SPIE Medical Imaging Meeting*, Vol. 6144, 2006, pp. 923-934.

- [22] Sharp, R., R. Ridgway, P. Mosaliganti, K. Wenzel, P. Pan, A. Bruin, R. Machiraju, K. Huang, G. Leone, and J. Saltz, "Volume Rendering Phenotype Differences in Mouse Placenta Microscopy Data," *Special Issue on Anatomic Rendering and Visualization, Computing in Science and Engineering*, Vol. 9, No. 1, 2007, pp. 38–47.
- [23] Torquato, S., *Random Heterogenous Material*, New York: Springer-Verlag, 2004.
- [24] Gokhale, A., "Experimental Measurements and Interpretation of Microstructural N-Point Correlation Functions," *Microscopy and Microanalysis*, Vol. 10, 2004, pp. 736–737.
- [25] Gokhale, A., A. Tewari, and H. Garmestani, "Constraints on Microstructural Two-Point Correlation Functions," *Scripta Materialia*, Vol. 53, 2005, pp. 989–993.
- [26] Singh, H., Y. Mao, A. Sreeranganathan, and A. Gokhale, "Application of Digital Image Processing for Implementation of Complex Realistic Particle Shapes/Morphologies in Computer Simulated Heterogeneous Microstructures," *Modeling and Simulation in Material Science and Engineering*, Vol. 14, 2006, pp. 351–363.
- [27] de Lathauwer, L., B. de Moor, and J. Vandewalle, "A Multilinear Singular Value Decomposition," *SIAM Journal of Matrix Analysis and Applications*, Vol. 21, No. 4, 2000, pp. 1253–1278.
- [28] Leventon, M., W. Grimson, and O. Faugeras, "Statistical Shape Influences in Geodesic Active Contours," *Proceedings of the IEEE Conference on Computer Vision and Pattern Recognition*, 2000, pp. 316–232.
- [29] Adiga, U., and B. Chaudhuri, "An Efficient Method Based on Watershed and Rule-Based Merging for Segmentation of 3-D Histo-Pathological Images," *Pattern Recognition*, Vol. 34, No. 7, 2001, pp. 1449–1458.
- [30] Raman, S., B. Parvin, C. Maxwell, and M. Barcellos-Hoff, "3D Segmentation of Mammospheres for Localization Studies," *International Symposium on Visual Computing*, 2005, pp. 427–436.
- [31] Mosaliganti, K., R. Machiraju, J. Heverhagen, J. Saltz, and M. Knopp, "Exploratory Segmentation Using Geometric Tessellations," *Proceedings of Tenth International Fall Workshop on Vision, Modeling and Visualization*, 2005, pp. 1–8.
- [32] Johnson, H., and G. Christensen, "Consistent Landmark and Intensity Based Image Registration," *IEEE Transactions on Medical Imaging*, Vol. 21, 2002, pp. 450–461.
- [33] Chui, H., J. Rambo, J. S. Duncan, R. Schultz, and A. Rangarajan, "Registration of Cortical Anatomical Structures Via Robust 3D Point Matching," *IPMI '99: Proceedings of the 16th International Conference on Information Processing in Medical Imaging*, 1999, pp. 168–181.
- [34] Wu, L., A. de Bruin, H. I. Saavedra, M. Starovic, A. Trimboli, Y. Yang, J. Opavska, P. Wilson, J. Thompson, M. Ostrowski, T. Rosol, L. Woollett, M. Weinstein, J. Cross, M. Robinson, and G. Leone, "Extra-Embryonic Function of Rb is Essential for Embryonic Development and Viability," *Nature*, Vol. 421, 2003, pp. 942–947.
- [35] Ridgway, R., O. Irfanoglu, R. Machiraju, and K. Huang, "Image Segmentation with Tensor-Based Classification of N-Point Correlation Functions," *MICCAI Workshop on Medical Image Analysis with Applications in Biology*, 2006.
- [36] Janoos, F., O. Irfanoglu, K. Mosaliganti, R. Machiraju, K. Huang, P. Wenzel, A. de-Bruin, and G. Leone, "Multi-Resolution Image Segmentation Using the 2-Point Correlation Functions," *IEEE International Symposium of Biomedical Imaging*, 2007, pp. 300–303.
- [37] Mosaliganti, K., T. Pan, R. Sharp, R. Ridgway, A. Gulacy, S. Iyengar, P. Wenzel, A. de-Bruin, R. Machiraju, K. Huang, G. Leone, and J. Saltz, "Registration and 3-D Visualization of Large Microscopy Images," *SPIE Conference on Medical Imaging*, 2006, pp. 923–934.

- [38] Cooper, L., K. Huang, A. Sharma, K. Mosaliganti, and T. Pan, "Registration vs. Reconstruction: Building 3-D Models from 2-D Microscopy Images," *Proceedings of Workshop on Multiscale Biological Imaging, Data Mining and Informatics*, 2006, pp. 57-58.
- [39] Carpenter, A., T. Jones, M. Lamprecht, C. Clarke, T. Kang, O. Friman, D. Guertin, J. Chang, R. Lindquist, J. Moffat, P. Golland, and D. Sabatini, "Cellprofiler: Image Analysis Software for Identifying and Quantifying Cell Phenotypes," *Cell Biology*, Vol. 7(R100), 2006.





# Automatic 3-D Morphological Reconstruction of Neuron Cells from Multiphoton Images

Ioannis A. Kakadiaris, Alberto Santamaría-Pang, Costa M. Colbert, and Peter Saggau

## 16.1 Introduction

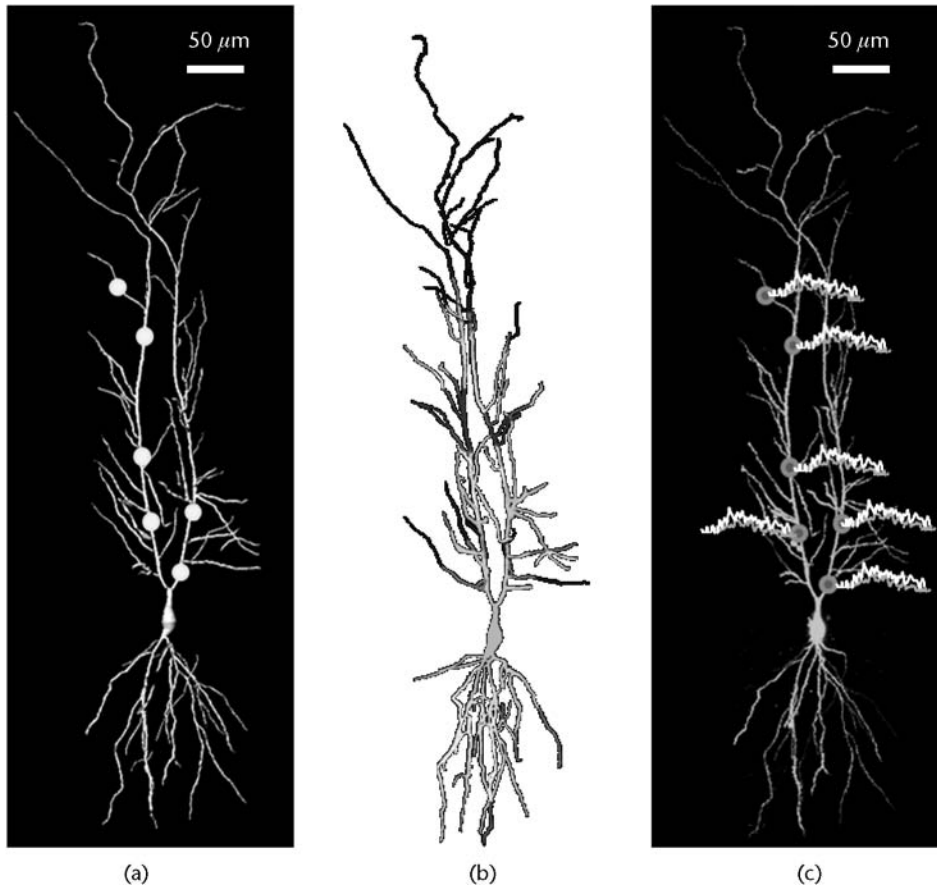
Neuronal morphologies are broadly affected by age, genetic diseases such as Down's Syndrome, and degenerative diseases such as Alzheimer's disease. Nonetheless, neuronal computation in general, and the role of morphology in particular, remain poorly understood and active areas of research.

A major obstacle to this research is the lack of automated methods to produce morphological reconstructions of neurons during the very limited time span of an acute experiment. These methods would allow real-time mapping of functional imaging data (e.g., spatio-temporal patterns of dendritic voltages or intracellular ions) to neuronal structure. Such protocol would be as follows: (1) perform structural imaging of the living cell; (2) obtain a morphological model (Figure 16.1(a)); (3) perform a simulation based on the morphological model (Figure 16.1(b)); and (4) obtain functional imaging data at locations indicated as significant by the simulation (Figure 16.1(c)).

The approaches outlined in this chapter are developed with the goals of enabling fully automated reconstructions of neuronal morphologies from multiphoton microscopy data to (1) to enable morphological-guided functional imaging, and (2) to create libraries of neurons morphologies.

Semiautomatic methods for neuron morphology reconstruction can be categorized in (1) skeletonization-based methods [1–4], where the neuron morphology is reconstructed from a centerline model; and (2) cylindrical extraction-based methods [5–9], where the morphology of the neuron is extracted assuming a cylindrical model. Both approaches, cylindrical-based and skeleton-based, have their respective advantages and limitations. Cylindrical-based approaches assume a tubular-like, smooth shape of dendrites, although dendrites have a highly irregular shape. Skeleton-based approaches assume the object of interest has already been segmented, but in reality segmentation is one of the most challenging steps in morphological reconstruction.

Dendrite centerline extraction can also be posed as a general problem of centerline extraction. In this case, the methods that have been explored focus mainly in the extraction of blood vessels (smooth tubular structures). In Deschamps et al. [10], centerline extraction of segmented tubular objects is accomplished by evolving monotonic fronts, where the cost function is a distance function from the edges of the binary object of interest. Likewise, Hossouna et al. [11] propose



**Figure 16.1** Guided functional imaging of neurons: (a) morphological reconstruction obtained from structural imaging, (b) computational model, and (c) guided functional imaging.

centerline extraction from monotonic front evolution, where the centerline follows the maximal distance from the boundary of the binary object. Recently, Bouix et al. [12] used the average outward flux through a Jordan curve. In this case, the gradient vector field of the Euclidean distance to the boundary was exploited to approximate the centerlines. Vasilevskiy and Siddiqi [13] and Nain et al. [14] developed a geometric flow framework to perform 2-D and 3-D vessel segmentation using prior knowledge of the vessel shape. Kimmel [15] offers a review of different geometric measures in variational methods. Complementary, elegant statistical methods for vessel segmentation have been proposed by Florin et al. [16], where shape variations of the vessel are learned online during the segmentation. All the previous approaches extract the centerline of regular or irregular objects. However, most of these methods are designed to extract centerlines of smooth structures assuming prior segmentation, while other methods of centerline extraction are performed without estimating the diameter of the tubular structure.

In this chapter, we present a new method to automatically reconstruct the morphology of neuron cells, which extends our previous work [17]—specifically,

simultaneously estimating centerlines of an irregular tubular object, as well as dendritic diameter. Our latest work in this area can be found at [18].

## 16.2 Materials and Methods

### 16.2.1 Experimental Data

Neurons were loaded with Alexa Fluor 594 dye and images acquired with a customized multiphoton microscope. We collected 12 data sets, each consisting of seven or more partially overlapping stacks, approximately  $640 \times 480 \times 150$  voxels, with  $0.3 \mu\text{m}$  in the  $x$ - $y$ -axis and  $1.0 \mu\text{m}$  in the  $z$ -axis. Excitation wavelength was set to  $810 \text{ nm}$ , while the lens and index of refraction both correspond to water. We assume that the mathematical model of an acquired image  $I$  is the following:

$$I(x, y, z) = (P * O)(x, y, z) + N(x, y, z) \quad (16.1)$$

where  $P$  is the point spread function (PSF) of the optical microscope,  $O$  is the true image, and  $N$  is a source of noise.

Our proposed approach for morphological reconstruction consists of the following steps:

- Step 1: deconvolution;
- Step 2: frame-shrinkage denoising;
- Step 3: registration;
- Step 4: dendrite segmentation;
- Step 5: morphological reconstruction.

#### 16.2.1.1 Step 1—Deconvolution

The major challenges of analyzing fluorescent neuronal images are related to the 3-D point-spread-function (PSF) imposed by the optics of the microscope and the imaging conditions. These factors include (1) sample composition (tissue or agarose specimen); (2) variable contrast due to uneven dye distribution within the cell; (3) intensity decay along the  $z$ -axis; (4) different sources of noise (thermal noise, photon shot noise); and (5) the fact that many features of interest (i.e., thin dendrites) are at the limit of imaging resolution. To enhance the acquired data, we have obtained an experimental PSF using a number of latex beads of approximate diameter  $0.2 \mu\text{m}$ . Then, deconvolution is performed by using the Huygens software and the quick maximum-likelihood estimation method.

#### 16.2.1.2 Step 2—Frame-Shrinkage Denoising

In most applications, denoising is a preprocessing step for different image analysis tasks such as segmentation, skeletonization, and spine detection. The challenges to effectively removing noise can be summarized as: (1) preserving fine details, (e.g., spines and small dendrites), which can be confused with noise; (2) maintaining the structural integrity (e.g., not producing gaps); and (3) maintaining generality with respect to different noise distributions (e.g., Gaussian and Poisson) and

sensors [19]. We can classify two major regions in which noise is present. The first is the *background region* where noise is homogeneous and relatively “weak.” The second is the *foreground region*, where noise is not homogeneous, but it is rather more pronounced near the dendrites as compared with the rest of the background.

Different approaches of noise removal in 3-D optical imaging toward morphological reconstruction are based on the separable wavelet transform (Dima et al. [2]) or anisotropic diffusion (Broser et al. [20]). The separable wavelet transform uses a multiscale scheme derived from the downsample-upsample operators. This imposes difficulties in analyzing dendrites of less than a micron in width, the equivalent of two or three voxels. Although anisotropic diffusion enhances the semitubular structure of the cell, it may not preserve important structures such as spines, which are attached to the dendrites. In this section, we provide the basic concepts of the construction and implementation of an efficient frame-shrinkage denoising algorithm. For more details, see Santamaría-Pang et al. [21]. In general, frame-shrinkage denoising is performed as follows:

Input Volume  $\longrightarrow$  Analysis  $\longrightarrow$  Frame-shrinkage  $\longrightarrow$  Synthesis  $\longrightarrow$  Output

A *Parseval frame* in the Hilbert space  $l^2(\mathbb{Z}^3)$  is a countable collection of vectors  $\{v_i\}_{i \in I}$  that satisfy the perfect reconstruction property:

$$x = \sum_{i \in I} \langle x, v_i \rangle v_i \text{ for all } x \in l^2(\mathbb{Z}^3) \quad (16.2)$$

Note that  $\{v_i\}$  is not a basis, and the same frame elements  $\{v_i\}$  used in the analysis are also used in synthesis, similar to orthogonal wavelets.

The construction is based on three 1-D filters that generate a 1-D Parseval frame [22]:  $K_0 = (1/4)[1, 2, 1]$ ,  $K_1 = (1/4)[\sqrt{2}, 0, -\sqrt{2}]$  and  $K_2 = (1/4)[-1, 2, -1]$ .  $K_0$  is an average operator, while  $K_1$  and  $K_2$  are first and second derivative operators, respectively.

The triple tensor product of these filters induces a *separable* Parseval frame, denoted by:

$$K_{p \cdot 3^2 + q \cdot 3 + r}(\omega_1, \omega_2, \omega_3) = K_p(\omega_1)K_q(\omega_2)K_r(\omega_3) \quad (16.3)$$

Using a result that allows us to lift this separable frame, we produce a *nonseparable* Parseval frame that incorporates directional filters along the main diagonal of the unitary cube. The modified and added filters are (1) scaling of the edge detectors along the coordinate axes:  $F_1 = \frac{\sqrt{3}}{2}K_1$ ,  $F_3 = \frac{\sqrt{3}}{2}K_3$ ,  $F_9 = \frac{\sqrt{3}}{3}K_9$ , and (2) new edge detectors along the main diagonals in 3-D:  $F_{27} = \frac{1}{4}(K_9 + K_3 + K_1)$ ,  $F_{28} = \frac{1}{4}(K_9 - K_3 + K_1)$ ,  $F_{29} = \frac{1}{4}(K_9 + K_3 - K_1)$ ,  $F_{30} = \frac{1}{4}(K_9 - K_3 - K_1)$ .

In order to shrink the frame coefficients associated with noise down to zero, we define filter-adaptive threshold bounds as being used to implement an affine hysteresis thresholding scheme by integrating an ensemble threshold operator with thresholds: (1) high ( $T_r^H = 0.75 \cdot \max(I * F_r)$ ); and (2) low ( $T_r^L = 0.5 \cdot$

$\max(I * F_r)$ ). The function that implements the affine thresholding is given by ( $T_2 > T_1 > 0$ ):

$$\rho_{T_1, T_2}(x) = \begin{cases} x, & \text{if } |x| > T_2 \\ \frac{T_2}{T_2 - T_1}(x - \text{sign}(x)T_1), & \text{if } T_1 < |x| \leq T_2 \\ 0, & \text{otherwise} \end{cases} \quad (16.4)$$

In summary, our denoising algorithm operates as follows:

Input: The noisy data  $X$  and the number of decomposition levels  $L$

2.1: Recursively decompose the volume  $X$  up to level  $L$  using the filter bank to obtain  $Y_{\tilde{F}}$ .

2.2: Compute  $\tilde{Y}_r = \text{Threshold}_r(I * \tilde{F}_r)$  by applying the ensemble approach.

2.3: Reconstruct  $\tilde{X}$  from  $\tilde{Y}_r$  using the same filter bank.

### 16.2.1.3 Step 3—Registration

Many dendrites are larger than the usual field of view of the average laser-scanning microscopes. Multiple image volumes are therefore necessary to fully capture the neuron structure. We are thus required to merge and align the multiple data sets to a single volume. The experimentalist supplies estimated  $x$ ,  $y$ ,  $z$  offsets between each stack, which are obtainable when moving the microscope from one area of interest to the next. To measure similarity during registration, we use the sum of mean-squared differences for each voxel in the two images. This measure is then minimized using limited-memory Broyden Fletcher Goldfarb Shannon minimization with simple bounds.

### 16.2.1.4 Step 4—Dendrite Segmentation

In order to morphologically reconstruct a neuron cell, dendrites must be detected. The shape of a typical dendrite is that of an irregular tubular structure. Our approach is based on *local structure analysis* derived from a structure tensor field. For a fixed  $\sigma$ , we compute the gradient of a 3-D image  $I$  as  $\Delta I_\sigma(\mathbf{x})$ :

$$J_\sigma = [\Delta I_\sigma(\mathbf{x}) \Delta I_\sigma(\mathbf{x})^\top] = \begin{pmatrix} I_{xx} & I_{xy} & I_{xz} \\ I_{yx} & I_{yy} & I_{yz} \\ I_{zx} & I_{zy} & I_{zz} \end{pmatrix} \quad (16.5)$$

We observe that the eigenvalues  $\lambda_1, \lambda_2, \lambda_3$  of  $J_\sigma$  are real and positive since the tensor  $J_\sigma$  is symmetric and positive definite. The information derived from the eigenvalues of  $J_\sigma$  encodes structural information in a local neighborhood controlled by the parameter  $\sigma$ . If we order the eigenvalues  $\lambda_1 \leq \lambda_2 \leq \lambda_3$ , then different combinations reveal structural information. For example, if  $\lambda_1 \approx \lambda_2 \approx \lambda_3 \approx 0$ , then there is no structure present; if  $\lambda_1 \approx 0$ ,  $\lambda_1 \ll \lambda_2$ , and  $\lambda_2 \approx \lambda_3$ , then the structure resembles that of an *ideal tubular structure* [23], and if  $\lambda_1 > 0$  and  $\lambda_1 \approx \lambda_2 \approx \lambda_3$ , then the structure resembles a blob. From these configurations of the eigenvalues, analytical functions to enhance structural shapes can be derived [24, 25]. However,

analytical expressions are limited to ideal models, as they represent an ideal point in a geometrical model.

We derive a structural measure by learning an association rule between a known centerline and the eigenvalues of the structure tensor for a given tubular object. For details, see Santamaría-Pang et al. [17].

Support vector machines (SVMs) estimate a decision function  $f(\mathbf{x})$ :

$$f(\mathbf{x}) = \sum_{i=1}^l y_i \alpha_i K(\mathbf{x}_i, \mathbf{x}) + b \quad (16.6)$$

where  $\mathbf{x} \in \mathbb{R}^n$ ,  $\mathbf{x}_i \in \mathbb{R}^n$ ,  $i = 1, \dots, l$  are the support vectors,  $K$  is a kernel function,  $y_i \in \{-1, 1\}$ , with  $\alpha_i > 0$ , such that  $\sum_{i=1}^l y_i \alpha_i = 1$ , and  $b$  is a learned constant. For classification problems, class prediction is performed by finding a threshold value for the function  $f$  and by assigning a penalty value.

Instead of using SVMs for classification, we use them to robustly estimate a posterior probability density function using the approach proposed by Platt [26]. The posterior probability  $P(y = 1|f)$  is approximated by fitting a parametric sigmoid function as:

$$P(y = 1|f) = \frac{1}{1 + e^{(Af(\mathbf{x})+B)}} \quad (16.7)$$

where the parameters  $A$  and  $B$  are computed by defining a new training set  $(f_i, t_i)$ , with  $t_i = \frac{(y_i+1)}{2}$  and using a maximum likelihood estimation:

$$\min_{Z=(A,B)} F(Z) = - \sum_{i=1}^l [t_i \log(p_i) + (1 - t_i) \log(1 - p_i)] \quad (16.8)$$

where  $p_i = \frac{1}{1 + e^{(Af_i+B)}}$  and  $f_i = f(\mathbf{x}_i)$ .

During the training phase, the parameters estimated are  $A$  and  $B$  (16.8) and the support vectors  $\alpha_i$ ,  $b$  (16.6). Figure 16.2 presents the results of applying two different shape models to one 3-D image stack. Model A represents a “smooth and regular” tubular model, whereas model B represents an “irregular” tubular model. Note the difference when predicting tubular structure: the predicted model A is in fact considerably smoother than the predicted model B. This is evident since spines are enhanced in model B as opposed to model A.

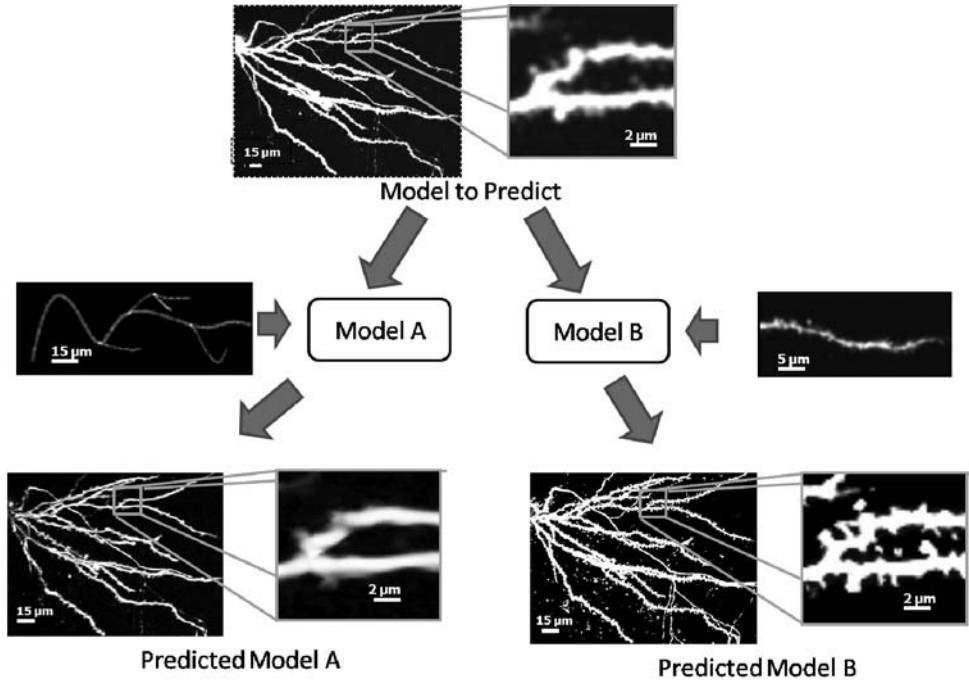
#### 16.2.1.5 Step 5—Morphological Reconstruction

Morphological reconstruction is posed into a level set framework (for more details, see [18]). Since morphological reconstruction needs to estimate dendrite lengths and diameters, the method described here is based on enhancing 3-D dendritic structures (from step 4) and using the distance transform to obtain an estimate of the dendrite diameters.

The proposed energy function to robustly extract dendritic paths is given by the following form of the Eikonal equation:

$$[g(D_n(H(\mathbf{x}))) \|\nabla T(\mathbf{x})\| = 1 \quad (16.9)$$





**Figure 16.2** Schematic of shape learning from two models.

with  $T(p_0) = 0$  and  $p_0$  as the voxel corresponding to the soma center point. The term  $g(D_n(H(\mathbf{x})))$  is composed of a morphological operator  $H$  and the normalized distance transform operator  $D_n$ . The morphological operator  $H(\mathbf{x})$  is defined as  $H(\mathbf{x}) = f_1(P(\mathbf{x}|f)) \cup f_2(V(\mathbf{x}))$ , where the term  $f_1(P(\mathbf{x}|f))$  is a probabilistic morphological operator, composed of the posterior probability  $P$ , that a voxel belongs to the centerline (16.7), and it is equal to 1 in regions greater than or equal to a given probability value. The second term  $f_2(V(\mathbf{x}))$  is a threshold operator that is equal to 1 in regions greater than or equal to a given intensity value.

For the specific application, morphological reconstruction is performed in four substeps. The first substep involves propagating a front with low curvature from the center point of the soma, the point  $p_0$ . The volume used for this propagation is the binary volume obtained by  $H$ . The surface evolution produces a distance map that captures the distance of every voxel from the soma center point  $p_0$ . The second substep is finding the terminating voxels. We compute the maximum distance  $d_{\max}$  from  $p_0$ , and then we create a number of connected component subvolumes  $S_i^j$ ,  $1 \leq i \leq N$ ,  $1 \leq j \leq K_i$ , where  $K_i$  is the number of connected components for each  $S_i$  region, according to:

$$S_i = \{\mathbf{x} | d_i \leq d(\mathbf{x}) \leq d_{i+1} + \varepsilon\} \quad (16.10)$$

where  $d(\mathbf{x})$  is the distance from  $\mathbf{x}$  to  $p_0$ ,  $d_i = \frac{i \cdot d_{\max}}{N}$ ,  $\varepsilon = \frac{d_{\max}}{r \cdot N}$ , and  $r > 1$ . Termination voxels are those voxels for which one of the following conditions apply: (1)  $\max(d(S_i^j))$ , with  $i = N$ , or (2) the set of voxels with  $\max(d(S_i^j))$ ,  $1 \leq i \leq N - 1$ , which are not in  $S_{i+1}$ . Subsequently, a 3-D front starting from the initial voxel is

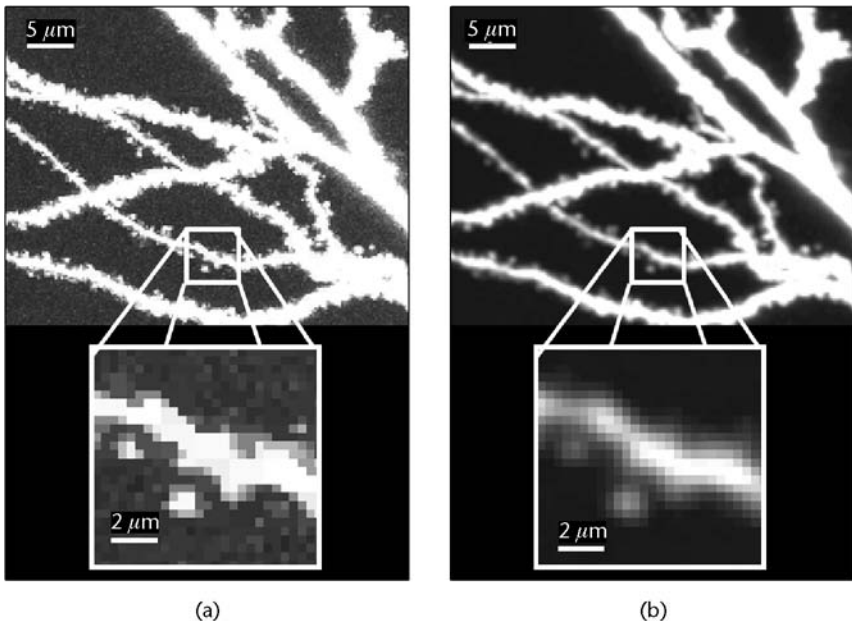
initiated according to (16.9), and centerlines are extracted by marching along the gradient from the ending voxels to the initial voxel  $p_0$ .

Dendritic diameters are estimated for each voxel along each segment. A function  $R$  to approximate the diameter of a dendrite is defined as a function of the distance transform volume as  $R(\mathbf{x}) = 2 \cdot k \cdot D_m(H(\mathbf{x}_i^j))$ , where  $k$  is a penalty value and the function  $D_m$  is the average distance from the voxel  $i$  defined as

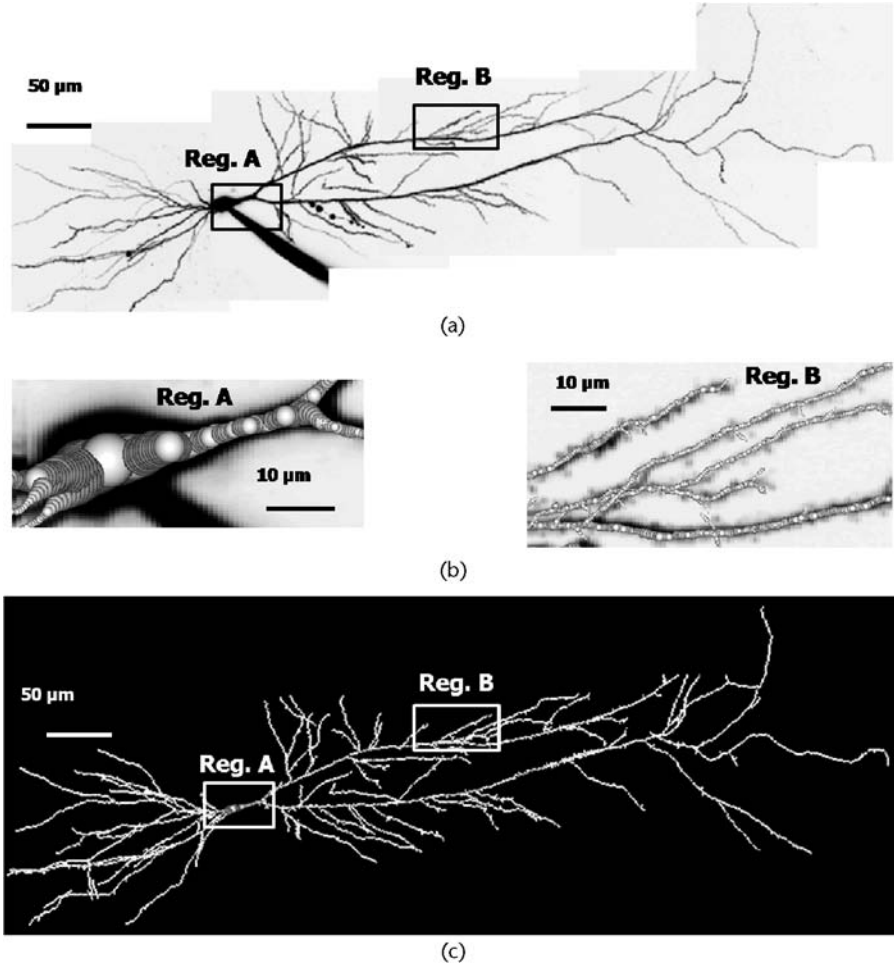
$$D_m(H(\mathbf{x}_i^j)) = \frac{1}{3} \cdot \sum_{z=\{-1,0,1\}} D(H(\mathbf{x}_i^{j+z})) \quad (16.11)$$

### 16.3 Results

We have morphologically reconstructed 12 CA1 pyramidal neuron cells. For each cell, first we apply our denoising algorithm to each image stack (Figure 16.3). Next, we register all the individual image stacks to produce a single volume per cell. Figure 16.4(a) depicts a typical dataset with dimensions  $2,546 \times 912 \times 121$ , consisting of six overlapping image stacks. Then, we perform dendrite segmentation by learning the shape variations of a dendrite segment. To avoid overestimation, the dendrite diameter, we have selected a penalty value of  $k = 0.9$  (evident in the soma region (region A, Figure 16.4(b))). Figure 16.4(c) depicts the reconstruction obtained with the proposed method, and Figure 16.4(a) depicts the minimum intensity projection along the  $x - y$  axis of the denoised volume. In Figure 16.4(b),



**Figure 16.3** Volume denoising: (a) original volume, and (b) denoised with frame shrinkage.



**Figure 16.4** Morphological reconstruction: (a) minimum intensity projection of the denoised volume, (b) reconstruction (white color) overlaid with the minimum intensity projection in two regions of interest, and (c) morphological model.

region A depicts a detail in the soma region, while region B depicts the detail of typical dendrites of average diameter.

It is important to mention that simulations are highly sensitive to dendritic diameter estimation.<sup>1</sup> The larger the diameter, the larger the surface area, and therefore the resistance.

## 16.4 Conclusions

We have presented a computational and experimental framework toward real-time functional imaging of neuronal cells. The key points of the proposed approach are

1. Membrane resistance (MR) is defined as  $MR = \frac{MR_0}{2\pi r_d}$ , where  $MR_0$  is the specific resistance of the membrane and  $r_d$  is the dendrite diameter.

(1) a centerline extraction formulation in terms of 3-D structural offline learning, and (2) a robust energy function used to extract dendrite centerlines and express them as a single connected tree representation. Our proposed method is general, since no assumptions about the shape of tubular objects are being made.

### Acknowledgments

We would like to thank B. Losavio and Y. Liang for their valuable assistance. This work was supported in part by NIH 1R01AG027577, NSF IIS-0431144, and NSF IIS-0638875. Any opinions, findings, conclusions, or recommendations expressed in this material are the authors' and may not reflect the views of the NIH or NSF.

### References

- [1] Koh, I., W. Lindquist, K. Zito, E. Nimchinsky, and K. Svoboda, "An Image Analysis Algorithm for Dendritic Spines," *Neural Computation*, Vol. 14, 2002, pp. 1283-1310.
- [2] Dima, A., M. Scholz, and K. Obermayer, "Automatic Segmentation and Skeletonization of Neurons from Confocal Microscopy Images Based on the 3-D Wavelet Transform," *IEEE Transactions Image Processing*, Vol. 11, July 2002, pp. 790-801.
- [3] Schmitt, S., J. Evers, C. Duch, M. Scholz, and K. Obermayer, "New Methods for the Computer-Assisted 3D Reconstruction of Neurons from Confocal Image Stacks," *NeuroImage*, Vol. 23, 2004, pp. 1283-1298.
- [4] Evers, J., S. Schmitt, M. Sibila, and C. Duch, "Progress in Functional Neuroanatomy: Precise Automatic Geometric Reconstruction of Neuronal Morphology from Confocal Image Stacks," *Journal of Neurophysiology*, Vol. 93, 2005, pp. 2331-2342.
- [5] Al-Kofahi, K. A., S. Lasek, D. H. Szarowski, C. J. Pace, and G. Nagy, "Rapid Automated Three-Dimensional Tracing of Neurons from Confocal Image Stacks," *IEEE Trans. Inform. Technol. Biomed.*, Vol. 6, June 2002, pp. 171-187.
- [6] Rodriguez, A., D. Ehlenberger, K. Kelliher, M. Einstein, S. Henderson, J. Morrison, P. Hof, and S. Wearne, "Automated Reconstruction of Three-Dimensional Neuronal Morphology from Laser Scanning Microscopy Images," *Methods*, Vol. 30, No. 1, 2003, pp. 94-105.
- [7] Weaver, C., P. Hof, S. Wearne, and W. Lindquist, "Automated Algorithms for Multi-scale Morphometry of Neuronal Dendrites," *Neural Computation*, Vol. 16, July 2004, pp. 1353-1383.
- [8] Wearne, S., A. Rodriguez, D. Ehlenrger, A. Rocher, S. Henderson, and P. Hof, "New Techniques for Imaging, Digitization and Analysis of Tree-Dimensional Neural Morphology on Multiple Scales," *Neuroscience*, Vol. 136, No. 3, 2005, pp. 661-680.
- [9] Broser, P., R. Schulte, A. Roth, F. Helmchen, S. Lang, G. Wittum, and B. Sakmann, "Nonlinear Anisotropic Diffusion Filtering of Three-Dimensional Image Data from Two-Photon Microscopy," *J. Biomedical Optics*, Vol. 9, November 2004, pp. 1253-1264.
- [10] Deschamps, T., and L. D. Cohen, "Fast Extraction of Tubular and Tree 3D Surfaces with Front Propagation Methods," *Proc. International Conference on Pattern Recognition*, Vol. 1, (Quebec, Canada), 2002, pp. 731-734.
- [11] Hassouna, M. S., A. A. Farag, and R. Falk, "Differential Fly-Throughs (DFT): A General Framework for Computing Flight Paths," *Proc. Medical Image Computing and Computer Assisted Intervention*, Vol. 1, Palm Springs, FL, 2005, pp. 654-661.
- [12] Bouix, S., K. Siddiqi, and A. Tannenbaum, "Flux Driven Automatic Centerline Extraction," *Medical Image Analysis*, Vol. 9, No. 3, 2005, pp. 209-221.

- [13] Vasilevskiy, A., and K. Siddiqi, "Flux Maximizing Geometric Flows," *IEEE Transactions on Pattern Analysis and Machine Intelligence*, Vol. 24, No. 12, 2002, pp. 1565–1578.
- [14] Nain, D., A. J. Yezzi, and G. Turk, "Vessel Segmentation Using a Shape Driven Flow," *Proc. Medical Image Computing and Computer Assisted Intervention*, Vol. 1, Saint-Malo, France, 2004, pp. 51–59.
- [15] Kimmel, R., "Fast Edge Integration," in *Level Set Methods and Their Applications in Computer Vision*, New York: Springer-Verlag, 2003.
- [16] Florin, C., N. Paragios, and J. Williams, "Globally Optimal Active Contours, Sequential Monte Carlo and On-Line Learning for Vessel Segmentation," *Proc. European Conference on Computer Vision*, No. 3, Graz, Austria, 2006, pp. 476–489.
- [17] Santamaría-Pang, A., T. S. Bildea, C. M. Colbert, P. Saggau, and I. A. Kakadiaris, "Towards Segmentation of Irregular Tubular Structures in 3D Confocal Microscope Images," *Proc. MICCAI International Workshop in Microscopic Image Analysis and Applications in Biology*, Copenhagen, Denmark, 2006, pp. 78–85.
- [18] Santamaría-Pang, A., "Automatic Three-Dimensional Morphological Reconstruction of Neurons," Ph.D. thesis, University of Houston, Houston, TX, December 2007.
- [19] Pawley, J. B., *Handbook of Biological Confocal Microscopy*, New York: Plenum, 1995.
- [20] Broser, P. J., R. Schulte, A. Roth, F. Helmchen, S. Lang, G. Wittum, and B. Sakmann, "Nonlinear Anisotropic Diffusion Filtering of Three Dimensional Image Data from Two-Photon Microscopy," *Journal of Biomedical Optics*, Vol. 9, No. 6, 2004, pp. 1253–1264.
- [21] Santamaría-Pang, A., T. S. Bildea, S. Tan, and I. Kakadiaris, "Denoising for 3D Photon-Limited Imaging Data Using Non-Separable Filterbanks," *IEEE Transactions on Image Processing*, 2008.
- [22] Ron, A., and Z. Shen, "Affine System in  $L^2(\mathbf{R}^d)$ : The Analysis of the Analysis Operator," *Journal of Functional Analysis*, Vol. 148, 1997, pp. 408–447.
- [23] Frangi, A., W. Niessen, K. Vincken, and M. Viergever, "Multiscale Vessel Enhancement Filtering," *Proc. First Medical Image Computing and Computer Assisted Intervention*, Vol. 1496, October 1998, pp. 130–137.
- [24] Sato, Y., S. Nakajima, H. Atsumi, T. Koller, G. Gerig, S. Yoshida, and R. Kikinis, "3-D Multi-Scale Line Filter for Segmentation and Visualization of Curvilinear Structures in Medical Images," *Medical Image Analysis*, Vol. 2, No. 2, 1998, pp. 143–168.
- [25] Streekstra, G., and J. Pelt, "Analysis of Tubular Structures in Three-Dimensional Confocal Images," *Network: Comput. Neural Syst.*, No. 13, 2002, pp. 381–391.
- [26] Platt, J., "Probabilistic Outputs for Support Vector Machines and Comparison to Regularize Likelihood Methods," *Adv. in Large Margin Classifiers*, 2000, pp. 61–74.



# Robust 3-D Reconstruction and Identification of Dendritic Spines

Firdaus Janoos, Raghu Machiraju, Xiaoyin Xu, and Stephen T. C. Wong

## 17.1 Introduction

In neurobiology, 3-D reconstruction of neuronal structures such as dendrites and spines is essential for understanding the relationship between their morphology and functions [1] and helps understand neuronal circuitry and behavior in neurodegenerative diseases. Dendrites are the tree-like structures of a neuronal cell, and spines are small protrusions formed on the surface of a dendrite. The shape and number of spines on a dendrite can change over time [2], and their morphological changes are associated with synaptic plasticity [3].

The quantitative morphology and analysis of the linear branching structures in neurons is of broad interest [4–10] and is used to study neurological diseases, such as Alzheimers disease (AD) and *fragile X syndrome* [11,12]. Important aspects of cognitive function, such as experience-based learning [13], attention, and memory [14] are correlated with variations in dendritic arborescence and with spine density and distribution [15,16]. It is hypothesized that the dendritic spine structure affects the physiological properties of synapses located on them [17–19]. The structure of neuronal dendrites and their spines underlie the connectivity of neural networks and may therefore be important predictors of their function [20].

Jacobsen et al. [12] created a mouse model of AD and tracked how spine density changed in the mouse brain. Their quantitative analysis showed that there is a decrease in spine density in the outer molecular layer of the dentate gyrus of the mouse brain. This study identifies an early reflection of pathology at an age and with a level of quantification that can be exploited as a potential indicator of therapeutic interventions. Quantitative analysis has also been used in studying fragile X syndrome on impairment that can range from learning disabilities to more severe cognitive or intellectual disabilities and that affects 1 in 3,600 males and 1 in 4,000 to 6,000 females. Lack of expression of the *fragile X mental retardation protein* (FMRP) is seen as the major cause of the disease. In 2001 Irwin et al. examined human brain autopsy materials and found that fragile X patients exhibit abnormal dendritic spine lengths and shapes [11]. Compared with normal age-matched controls, quantitative analysis shows that fragile X patients have more long dendritic spines and fewer short dendritic spines in both temporal and visual cortical areas. In 2002, the same group of researchers studied the dendritic spines on layer V pyramidal cells of visual cortices, taken from fragile-X knockout and wild-type control mice and found similar quantitative results that fragile-X mice exhibited significantly more long dendritic spines and significantly fewer short dendritic spines than control mice [21]. As a step toward understanding the function of FMRP, and its homologous, transgenic mice were generated that carried the entire



FMRP, and those mice displayed reduced symptoms of fragile X. These findings have significant implications for gene therapy for fragile X syndrome [22]. From this example, we can see that quantitative analysis of spine morphology identifies the differences between patients of fragile X and normal control.

There has been extensive research in the field of neuron reconstruction, dendrite tracing, and spine identification from light microscopy images. Three-dimensional light microscopy images of neurons lose a significant amount of information when projecting to 2-D (Figure 17.1), and the preferred method for detailed measurement and study of internal cell structure is from 3-D reconstructions [23,24]. Automatic reconstruction aids in the analysis of a large number of neurons and the mapping of the spatial relationships between different tracts and neuropiles, such that detailed mathematical and physical models can be constructed to estimate those physiological parameters that can not be otherwise measured easily [25]. Graph models (*dendrograms*) of the neuron, which concisely capture the neuron geometry and topology, are extremely valuable for analyzing the structure of the neuron backbone and the dendritic spines [26] and elucidating their synaptic and neurological function [16]. However, most methods for spine detection suffer from low reliability and poor accuracy and have heavy requirements of manual supervision. Robust methods for 3-D reconstruction and detection of dendritic spines, and spine morphometry are needed in order to predict whether changes in their dimensions could alter their biophysical properties.

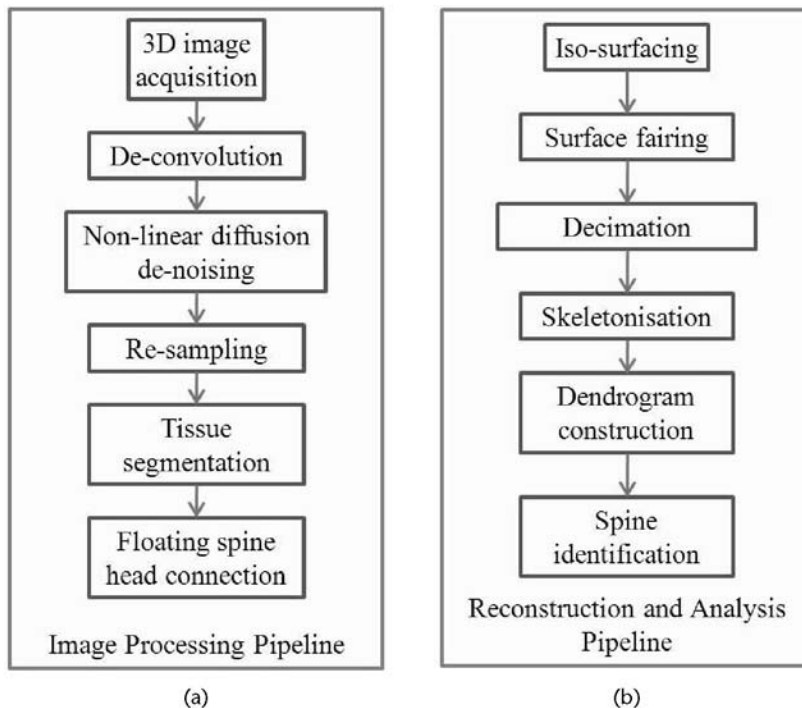
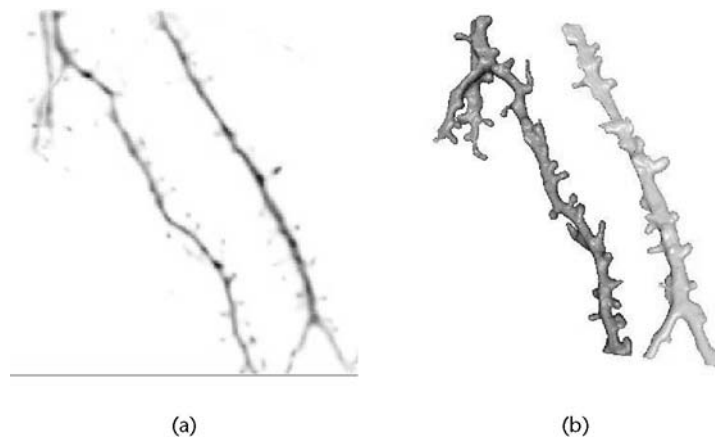


Figure 17.1 (a, b) Algorithm overview.

Whereas most methods for neuron reconstruction treat the neuron as a volume, we represent the dendrite and the spines as a surface (2-manifold). The advantages of a surface representation are that it allows enforcing of physically plausible smoothness constraints on the shape of the neuron, and it facilitates the extraction of the neuronal skeleton. There are a large number of algorithms and heuristics in the literature for skeletonization, each of which produce different results and do not provide guarantees of correctness [27,28]. We use a geometric skeletonization method by [29] based on the *medial geodesic function*. This algorithm has prove to be well posed and robust against noise, and it produces curve-skeletons that preserve the topology of the original object (homotopic equivalence). The surface model of the dendrite, along with the information computed by the skeletonizing procedure, allows for the accurate identification of spines and for morphological measurements like the diameter, eccentricity, length, and volume. The parameters in the spine identification procedure are intuitive, easy to understand, robust, and motivated by the biology of the neuron being studied.

It should be noted, that while the proposed approach may not be the most viable, it does provide a robust method of constructing 3-D geometric models of spines. This chapter is organized as follows: In Section 17.2, we review some important contributions in neuron reconstruction, tracing, dendrogram construction, and spine identification. We describe the dataset, image acquisition, and processing methods in Section 17.3 (see Figure 17.2(a)). The surface extraction, neuron reconstruction, skeletonization, and spine identification pipeline is explained in Section 17.4 (see Figure 17.2(b)). In Section 17.5, results of the method applied on the data-set are shown. We also explore the implications of the various parameters in detail and make recommendations for selecting their values. Finally, in Section 17.6 we conclude by discussing some thoughts on our current method and directions of future work.



**Figure 17.2** (a) The 2-D maximum intensity projection of a 3-D neuron image. (b) The full 3-D reconstruction. The 3-D reconstruction captures the branching structure and the morphology of the dendrites with much greater accuracy and is used as the basis for spine identification.

## 17.2 Related Work

Capowski [30] gives a plenary and in-depth survey of neuron reconstruction and analysis methods. Most of the current methods of reconstruction are semi-automatic and require user guidance to identify salient structures and deal with ambiguities in each confocal microscopy data-set independently [31–33]. These techniques demand several weeks of a specialist’s time for one neuronal reconstruction and do not have the objectivity of automated methods. The goal of decreasing the expense of user interaction often acts contrary to that of ensuring the accuracy and the topological correctness of the result. Consequently, a few recent methods (e.g., [34]) seek for an optimal compromise between automatic segmentation and manual reconstruction.

Some reconstruction methods represent neuronal (and other tubular branching) structures as a tree of connected cylinders or similar mathematical objects [9, 35–40], which detracts from the capability of the model to provide accurate quantitative measurement of the underlying cellular morphology, and require strong assumptions about the objects of interest. Due to the morphologic complexity and variety of neuronal cell types, no general models are suggested in the literature.

Other methods [1, 10, 41–47] employ curve-skeleton methods to build a linear graph representation of dendritic structures. These methods conform to a weak model; however, the curve-skeletonization algorithms employed tend to be very sensitive to small changes in the object shape and do not provide topological guarantees about the resulting 1-D skeleton. We discuss this more in Section 17.4.2.

The analysis of dendritic structure and morphology is largely accomplished manually, and it is extremely time consuming, it is not reproducible, and its accuracy is dependent on the skill of the user. A few spine identification and quantification techniques of varying degrees of automation have been suggested to reduce manual labor and improve the accuracy and reproducibility of the result. Some authors [48–50] use the medial axis to identify spines in 2-D as protrusions relative to dendritic skeleton. Significant information in the 3-D image is lost when projecting to 2-D, and the accuracy of such methods is therefore limited.

Others [51–53] use 3-D medial axis-based strategies to extract a skeleton and identify “spurs” as potential spines. Medial axis-based methods suffer from the general problems of sensitivity to noise and spurious spine detections, and have to use heuristics to eliminate false positives. Model-based spine identification techniques [36, 40] have trouble detecting thin-necked and short spines and have to be manually supervised. In [20], the authors devise a 3-D technique in which spines are not detected using the medial axis branches emerging from the backbone, but instead, as geometric protrusions relative to the backbone.

## 17.3 Image Acquisition and Processing

In this section we describe the data-set (Section 17.3.1), followed by the image processing pipeline that corrects for the anisotropy in the sampling resolution

(Section 17.3.2) and segments out the neuronal cytoplasm from the background phase (Section 17.3.3). This is followed by a step to join the floating spine heads and remove spurious tissue fragments in the sample (Section 17.3.4).

### 17.3.1 Data-Set

Three-dimensional images of pyramidal neurons in rat hippocampi expressing green fluorescent protein (GFP) were acquired by the digitization of neuronal cultures using a 2-photon laser scanning microscopy (2PLSM) with a 40 $\times$  objective and 0.8 NA [16]. The image stacks have dimension 512 $\times$ 512 $\times$ 12 voxels at 0.07  $\mu\text{m}$   $\times$  0.07  $\mu\text{m}$   $\times$  1  $\mu\text{m}$  resolution. For high-content neuron screening, GFP is used to mark neurons in vitro. GFP absorbs blue light and converts it to green light, which is of lower energy. The emitted green light is then captured by an optical microscope such as a 2PLSM.

To correct the images for the microscope's point spread function (PSF), which causes out-of-focus objects to appear in the optical slices, we use the deconvolution package AutoDeblur<sup>1</sup> to restore the image. Figure 17.3(a, b) shows volume renderings of the deblurred images after 10 iterations. The parameters of the deconvolution algorithm depend on the setup of the microscopy.

The nature of the image acquisition process and photobleaching effects introduces the following types of artifacts:

- *Shot noise*: Fluorescence detection in image acquisition is performed by photomultiplier tubes (PMTs). PMTs are high-gain, low-sensitivity devices that combined with the low number of photons emitted by small structures, such as dendritic spines, produce *photon shot noise*.
- *Photo-bleaching effects*: Heterogenous photobleaching of fluorescence emission is induced by differences in exposure rates and times at different  $z$ -planes orthogonal to the optical axis.
- *Unrelated structures*: Often, the region being scanned consists of a portion of another dendrite or unrelated tissue structure. Floating tissue fragments may also be present on the slide at the time of scanning.
- *Floating spine heads*: Owing to the photobleaching effect, spine heads may be seen as detached from the main dendrite structure with a leading protrusion in the direction of the spine head.

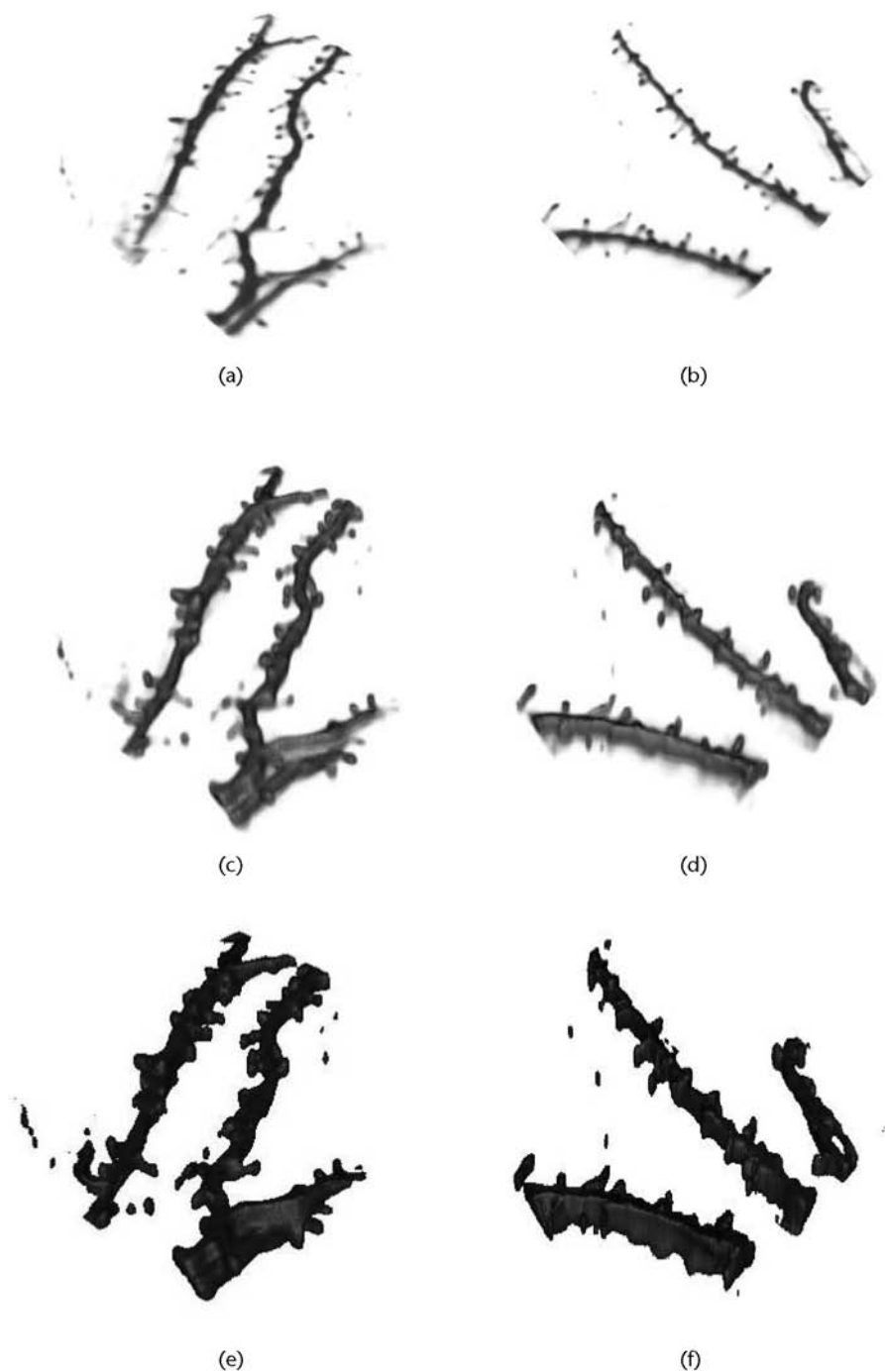
These artifacts require the additional processing steps described next.

### 17.3.2 Denoising and Resampling

The image intensity in neuronal regions exhibits noise and sharp variations.

This lack of smoothness in the intensity field prevents meaningful analysis of the data such as segmentation and identification of the dendritic edges.

1. AutoDeblur is a product of AutoQuant Image, Inc.



**Figure 17.3** Volume renderings of two GFP stained pyramidal neuron images from rat hippocampi. (a, b): After deconvolution. (c, d): After denoising and resampling (Section 17.3.2) to 1:1:1 voxel aspect ratio. (e, f): After segmentation (Section 17.3.3).

We use nonlinear diffusion filtering [54], which removes high-frequency noise while avoiding the blurring and localization problems of linear Gaussian smoothing [55]. It is a nonuniform process that has reduced diffusivity at those locations having a larger likelihood to be edges. If  $\Omega$  denotes the domain of the image  $g(\mathbf{x}) : \Omega \rightarrow \mathbb{R}$ , then the filtered image  $u(\mathbf{x}, t)$  is a solution to the nonlinear diffusion equation:

$$\frac{\partial u}{\partial t} = \text{div}(\mathbf{D}(|\nabla u|^2) \nabla u) \quad \text{on } \Omega \times (0, \infty) \quad (17.1)$$

$$\text{where } \mathbf{D}(|\nabla u|^2) = \frac{1}{1 + |\nabla u|^2 / \lambda_{nl}^2} \quad (\lambda_{nl} > 0) \quad (17.2)$$

with the original image as the initial condition  $u(\mathbf{x}, 0) = g(\mathbf{x})$  on  $\Omega$ , reflecting boundary conditions<sup>2</sup>  $\partial_n u = 0$  on  $\partial\Omega \times (0, \infty)$ . Here  $\lambda_{nl}$  plays the role of a contrast parameter [56] smoothing low-contrast areas ( $|\nabla u| \leq \lambda_{nl}$ ) and enhancing high-contrast areas ( $|\nabla u| > \lambda_{nl}$ ).

Unfortunately, this diffusion equation is numerically unstable [57]. By convolving  $u$  with a Gaussian  $K_\sigma$  when computing the gradient  $\nabla u_\sigma$ , a regularization is obtained that has a unique solution, is infinitely differentiable, and is more robust to noise. To account for the  $\approx 1:1:10$  anisotropy in the imaging resolution, we modify the regularized filter to use an anisotropic Gaussian  $K_\Sigma$  with a 10:10:1 ratio of scales  $\sigma_x, \sigma_y, \sigma_z$ .

The nonlinear diffusion equation with anisotropic regularization has the form:

$$\frac{\partial u}{\partial t} = \text{div}(\mathbf{D}(|\nabla u_\Sigma|^2) \nabla u_\Sigma) \quad \text{on } \Omega \times (0, \infty) \quad (17.3)$$

where,<sup>3</sup>

$$\Sigma = \sigma \begin{bmatrix} 1 & 0 & 0 \\ 0 & 1 & 0 \\ 0 & 0 & \frac{1}{10} \end{bmatrix} \quad u_\Sigma = K_\Sigma \star u \quad (17.4)$$

After smoothing, the image is resampled to 1:1:1 resolution with quartic (fourth order) B-spline interpolation. Figure 17.3(c, d) shows the results at the end of the denoising and resampling stage.

### 17.3.3 Segmenting the Neuron

Thanks to the edge-enhancing property of nonlinear diffusion, global thresholding of the intensity field gives a reliable and accurate segmentation of the neuron. This is because the variations in the intensity field outside the neuron are almost zero, and hence a threshold  $\Omega$  of just above zero is very effective in isolating the neuron. At the same time, the filter sharpens edges at the boundaries of the neuronal

2.  $\partial_n$  denotes the derivative normal to the image boundary.
3.  $\star$  represents convolution in (17.4).

objects, thereby making the segmentation more robust to variations in the threshold parameter  $\Omega$ . The conditioning of the thresholding operation is quantified by the relative change in the size of the segmented object with respect to a change in  $\Omega$ . Assuming that the neurons are approximately cylindrical objects, the condition number  $\text{cond}(\Omega)$  is given by

$$\text{cond}(\Omega) = \frac{\delta r/r}{\delta \Omega/\Omega} \quad (17.5)$$

where  $r$  is the radius of the cylinder. The value of  $\delta r/r$  is approximated by

$$\frac{\delta r}{r} \approx \sqrt{\frac{\delta V}{V}} \quad (17.6)$$

where  $V$  is the volume of the segmented dendritic tissue. We present our investigation into the sensitivity of  $\Omega$  in Section 17.5. Figure 17.3(e, f) shows volume renderings of segmented neuronal objects from two data-sets.

#### 17.3.4 Floating Spine Heads

The neuron images contain floating spine heads, separated from the main dendritic backbone, due to photobleaching effects and limited microscope resolution. The neuron sample also contains unrelated tissue fragments that show up as disconnected blobs during imaging. While the spurious fragments need to be removed, the floating spine heads should be identified and connected back to the main dendrite.

It has been observed that the floating spine heads tend to point toward the dendrite, while the dendrite too has a protrusion pointing toward the spine, and both are in close proximity of each other. Color Plate 24 shows a 2-D projection of a segmented neuron image with three detached spine heads and a few spurious fragments. For spine heads 1 and 3, locating the closest point on the main backbone is sufficient to determine the connection between the two. However, for case 2, a join to the closest point is incorrect. Here, along with the orientation of the spine head itself, the protuberance in the dendrite should be used to guide the connection. This suggests a method of connecting floating spine heads by growing the spine and the dendrite along the directions in which they protrude. If a join occurs within a certain number of time steps, it is a valid spine; else, it is spurious fragment.

Active contour shape models [58] are a level-set approach that enables us to achieve these goals by using shape information to control the evolution of iso-contours. The boundary  $\zeta(t) = \{\mathbf{x} | \psi(\mathbf{x}, t) = 0\}$  of the neuron at time  $t$  is encoded as the zero level-set of the field  $\psi(\mathbf{x}, t)$ . The update equation of the level-set is given by

$$\frac{\partial \psi}{\partial t} = g(\psi)(c + \kappa)|\nabla \psi| \quad \text{where,} \quad g(\psi) = \frac{1}{1 + |\psi|^2} \quad (17.7)$$

The parameter  $\kappa$  is the curvature along the normal to the level-set contour, and  $c$  is a balloon force that evolves the level-set front outward. The term  $\kappa|\nabla \psi|$  guides the evolution of the front using the local curvature.



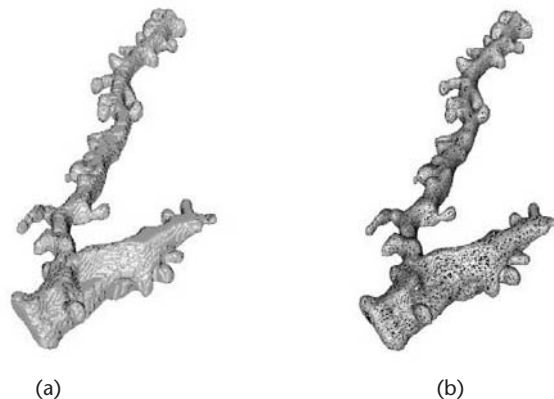
Therefore, the complete algorithm to connect floating spine heads and discard fragments is as follows:

1. From the segmented image  $I$ , identify dendrites and potential floating spines by thresholding the volume of the connected components with respect to a reference volume  $\vartheta$  (see Section 17.5 for more details).
2. Set the signed distance map  $D(I)$  of the neuron image as the level-set function  $\psi(\mathbf{x}, 0)$ .
3. Evolve the level-set (17.7) to move in the directions of high curvature for a specified number of time steps  $\tau_{gac}$  (Figure 17.4).
4. If the level-sets originating from spine heads and dendritic backbones meet within  $\tau_{gac}$ , then determine the location of their join point and connect them up at that point (Figure 17.4).
5. Tag all remaining fragments as spurious and discard them.

Because of the proximity constraint, the level-set needs to be evolved over only a very few number of time steps ( $\tau_{gac} \approx 5$ ) for a valid join to occur. The distance transform, too, needs to be computed only in the close vicinity of the edges and can be done very efficiently in linear time [59]. Therefore, the overall computation cost of this procedure is relatively low.

## 17.4 Neuron Reconstruction and Analysis

After the image processing pipeline, the connected components are identified as separate dendrites and are analyzed independently. Existing neuron reconstruction methods use signal processing and image processing techniques, followed either by model fitting or skeletonization for neuron reconstruction (Section 17.2). We represent the dendrite by a surface model because: (1) it allows us to control

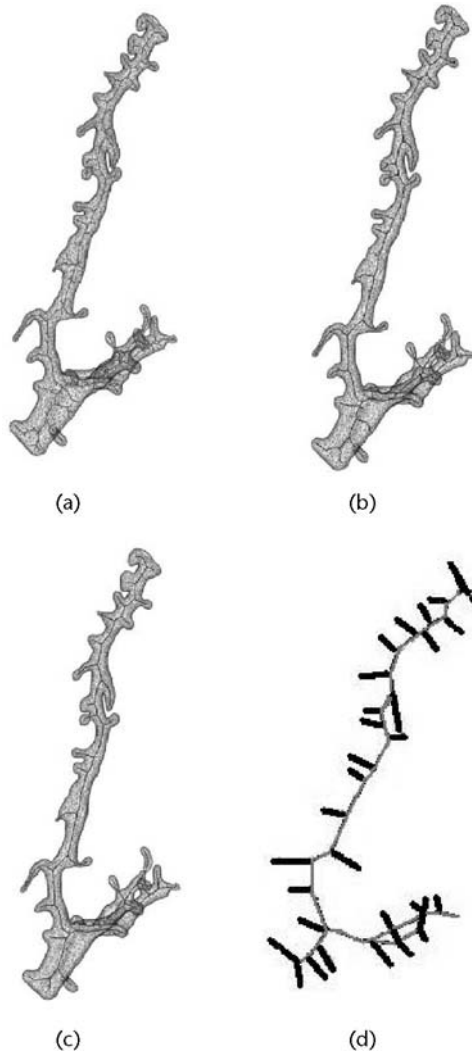


**Figure 17.4** Surface model of dendrite. (a) The original isosurface of the segmented neuron object. (b) The surface after lowpass filtering and quadric error decimation.

the smoothness of the neuron surface, thereby imposing a physically plausible constraint on the reconstruction, and (2) it lets us perform detailed morphological measurements.

#### 17.4.1 Surfacing and Surface Fairing

The surface of the segmented dendrite is obtained by iso-surfacing at any value between (0,1), using extended marching cubes [60]. This surface is over tessellated and suffers from artifacts of staircase noise (Figure 17.5(a)). We first low-pass filter the surface to remove the high-frequency noise, and then down-sample it to a sufficient resolution.



**Figure 17.5** (a–c) The curve-skeletons for  $\theta = 0.0$ ,  $-0.2$ , and  $-0.5$ , respectively. (d) The dendrite graph (before pruning) for the skeleton in (b). The thin gray lines indicate backbone edge chains, and the thick black lines are branch chains: (a)  $SK_s^\theta$  for  $\theta = 0.0$ ; (b)  $SK_s^\theta$  for  $\theta = -0.2$ ; (c)  $SK_s^\theta$  for  $\theta = -0.5$ ; and (d) dendrite graph for  $SK_s^{(-0.2)}$ .

Lowpass filtering is effected using the two-step surface fairing method described by Taubin [61]. Let  $\mathbf{x} = (x_1, x_2, x_3)^T$  be the 3-D coordinates defined at the vertices of a polyhedral surface. The Laplacian of the point  $\mathbf{x}_i$  on the surface is defined by the weighted average over its neighborhood  $\mathbb{N}_i$  as

$$\Delta \mathbf{x}_i = \frac{1}{|\mathbb{N}_i|} \sum_{j \in \mathbb{N}_i} w_{ij} (\mathbf{x}_i - \mathbf{x}_j) \quad (17.8)$$

The fairing process is a smoothing step that also causes surface shrinkage (17.9) followed by an expansion step (17.10), applied iteratively  $N$  times:

$$\mathbf{x}'_i = \mathbf{x}_i + \alpha \Delta \mathbf{x}_i \quad \text{for } 0 < \alpha < 1 \quad (17.9)$$

$$\mathbf{x}''_i = \mathbf{x}'_i + \mu \Delta \mathbf{x}_i \quad \text{where } \mu < -\alpha \quad (17.10)$$

The transfer function  $f(k)$  of the filter, with respect to surface frequency  $k$ , has the following property:

$$\lim_{N \rightarrow \infty} f^{(N)}(k) = \begin{cases} 1 & 0 \leq k \leq \frac{1}{\alpha} + \frac{1}{\mu} \\ 0 & \frac{1}{\alpha} + \frac{1}{\mu} \leq k \leq 2 \end{cases} \quad (17.11)$$

Here  $(1/\alpha + 1/\mu) > 0$  is the cutoff frequency, and  $N$ , the number of iterations, controls the rate of decrease in the stop band. This algorithm is fast (linear time), produces smoothing without shrinkage, and quickly achieves a stable solution with respect to  $N$ .

Next, the tessellation density is reduced by decimating the mesh using the quadric error metric [62]. Here, every edge is assigned a cost function—namely, the error resulting from its contraction, and the lowest cost edges are iteratively selected and collapsed. Each vertex is associated with a set of planes, and the error at the vertex is defined to be the sum of squared distances from it to all the planes in its set. Each set is initialized with the faces incident to the vertex in the original surface. When an edge is contracted into a single vertex, the resulting set is the union of the two sets associated with the endpoints. The cost of contracting an edge  $(v_1, v_2)$  to a single vertex  $\bar{v}$  is now the error at  $\bar{v}$ . This decimation technique does not prevent changes of topology in the mesh, and it suffers from small inaccuracies. However, given the simple topology of a dendrite, and the speed and simplicity of the algorithm, this method is very appropriate for our application. Figure 17.5(b) shows the result of this decimation step.

Increasing the surface decimation factor  $\rho$  has two benefits: (1) it simplifies the model and makes further computations more efficient, and (2) it allows us to impose smoothness constraints on the model.

The smoothness of the surface is measured by the average dihedral angle  $(\bar{\phi}_M)$  of the edges in the mesh. This is further elaborated upon in Section 17.5.

### 17.4.2 Curve Skeletonization

A curve-skeleton is a 1-D curve, possibly with branches, in the “center” of the shape. A related and much more well-defined concept is the medial axis, which is also referred to as the skeleton. For a 3-D shape, however, the medial axis has two-dimensional components (*medial surface*). Therefore, the medial axis cannot be a substitute for a 1-D skeleton. Another disadvantage of the medial surface (axis) is its intrinsic sensitivity to small changes in the objects surface [63]. Essentially, any curve-skeleton should satisfy the following basic properties [27]:

1. Homotopic to the original object (topology preservation);
2. Invariant under isometric transformations;
3. Allows recovery of the original object (reconstruction);
4. 1-D (thin);
5. Centered within the object;
6. Visibility of every boundary point on the object from at least one curve-skeleton location (reliable);
7. Ability to distinguish different components of the original object, reflecting its part/component structure (junction detection);
8. Preservation of the connectedness of the original object;
9. Small changes in the skeleton for small changes in object surface (robust).

We use the definition of curve skeletons based on the *medial geodesic function* by Dey and Sun [29], which combines the intrinsic property of the surface (the geodesic distances) along with its embedding in  $\mathbb{R}^3$  (the medial axis), thereby capturing the shape information comprehensively. The medial geodesic function gives the shortest geodesic distances between the points where the maximal balls centered at the medial axis touch the surface. Formally, if  $O \subset \mathbb{R}^3$  is a space called *shape* bounded by a connected 2-manifold surface  $S$ , then the medial axis  $M \subset O$  is the set of centers of the maximal balls inscribed in  $O$ . Let  $M_2 \subset M$  be the set of points on the medial axis whose maximal balls touch the surface  $S$  at two distinct points. It can be shown that  $M_2$  is also a 2-manifold and covers most of  $M$  (i.e.,  $M \setminus M_2$  has measure 0). For a point  $x \in M_2$ , let  $B_x$  be the maximal inscribed ball centered at  $x$  and  $a_x$  and  $b_x$  be the two touching points where  $B_x$  meets  $S$ . Then  $f(x)$ , the length of the geodesic path on  $S$  between  $a_x$  and  $b_x$ , is the medial geodesic function (MGF). The curve-skeleton is defined as the singular set (maxima or saddle points) of  $f(x)$  for  $x \in M_2$ .

It is mathematically shown that this definition of a curve-skeleton has properties of homotopic equivalence, isometric invariance, thinness (1-D), centeredness, junction detection, stability (robustness), and connectedness. The MGF values at each point on the skeleton give the size information of the shape. Also the ratio  $\varepsilon$  between the geodesic and Euclidean circles passing through the touching points quantify how different the shape is from a tubular one (*eccentricity*).

The algorithm has one parameter  $-1.1 \leq \theta \leq 0.0$  that controls the strictness for selecting points from the medial axis  $M_2$  as being skeleton points. As  $\theta$  decreases, the curve skeleton becomes less detailed. Formally, if  $SK_S^\theta$  is the curve

skeleton for surface  $S$  extracted with parameter  $\theta$ , then  $SK_S^{\theta_1} \subseteq SK_S^{\theta_2}$  if  $\theta_1 < \theta_2$ . The selection of this parameter is explained in Section 17.5. Color Plate 25(a–c) show the results of curve-skeleton extraction for a few values of  $\theta$ .

### 17.4.3 Dendrite Tree Model

The curve-skeleton  $SK_S^\theta$  of the neuron is represented by an attributed tree structure  $\mathcal{D} \equiv \{\mathcal{V}, \mathcal{E}\}$ , which compactly encodes the geometry and topology of the dendrite. The set of vertices is

$$\mathcal{V} = \{v_i | v \equiv (\mathbf{x}, d)\} \quad (17.12)$$

where  $\mathbf{x} \in \mathbb{R}^3$  are the spatial coordinates, and  $d \in \mathbb{N}$  is the degree of the vertex. The set of edges is

$$\mathcal{E} = \{e | e \equiv ([v_i, v_j], \gamma[\mathbf{a}, \mathbf{b}], r, f, \varepsilon)\} \quad (17.13)$$

where  $v_i, v_j \in \mathcal{V}$  are its vertices,  $\gamma$  is the length of the edge,  $[\mathbf{a}, \mathbf{b}] \in \mathbb{R}^3$  are the touching points of medial ball with the surface,  $r$  is the radius of the medial ball,  $f \in \mathbb{R}$  is the medial geodesic length for the edge, and  $\varepsilon$  is the eccentricity.

The dendrite tree has two types of chains of edges  $\{e_1(v_1, v_2), e_2(v_2, v_3) \dots e_n(v_n, v_{n+1})\}$ :

1. Branch chains that start at leaf node ( $v_1 | d(v_1) = 1$ ) and end at a branch node ( $v_{n+1} | d(v_{n+1}) > 2$ );
2. Backbone chains that run between two branch nodes.

Color Plate 25(d) shows the graph of the dendrite in Color Plate 25(b). The dendrite tree is pruned of those branch chains whose cumulative length  $\sum_{i=1}^n \gamma_i$  is less than a threshold length  $\Gamma_{\min}$ . This step eliminates spurious branches in the curve-skeleton by imposing restrictions on the minimum length of potential spines in the dendrite.

### 17.4.4 Morphometry and Spine Identification

For each branch  $\beta$  in the dendrogram model we compute the following morphological features:

- $\gamma^\beta$  as the cumulative lengths  $\sum_{i=1}^n \gamma_i$  of the edges  $e_1 \dots e_n$  from the base (branch nodes) to the apex (leaf nodes);
- Radius  $r_0^\beta$  of the medial ball and eccentricity  $\varepsilon_1^\beta$  at the base of the branch;
- Radius  $r_n^\beta$  and eccentricity  $\varepsilon_n^\beta$  at the apex;
- Average weighted radius  $r^\beta = (1/\gamma_i^\beta) \sum_{i=1}^n \gamma_i r_i$ ;
- Volume  $V^\beta$  as the cumulative volume of the edges  $\sum_{i=1}^n \pi r_i^2 \gamma_i$  (approximating each edge by a cylinder);
- The angle  $\phi^\beta$  the branch chain makes with the backbone edge at the base;
- The curvature  $\kappa^\beta$  of the backbone at the base of the branch chain.

To distinguishing between branch chains that belong to end segments of the dendritic backbone and those that belong to the spines (see Color Plate 25(d)) in the pruned dendrite tree, we use the following decision sequence:

1. If  $\beta$  is a branch chain of cumulative length  $\gamma^\beta$  greater than a threshold length  $\Gamma_{\max}$ , then mark it as dendritic backbone.
2. Else:
  - a. If the average weighted radius  $r^\beta$  is greater than a threshold  $R_{\max}$ , mark it as a backbone chain  $\beta_{bb}$ .
  - b. Else mark it as spine chain  $\beta_s$ .

The threshold  $\Gamma_{\max}$  enforces a maximum length constraint on valid spines, while  $R_{\max}$  enforces a maximum radius constraint. While our frameworks allow for more sophisticated morphological models when checking for spines, we find that this model performs well for our data-sets. Some results are presented in the next section.

## 17.5 Results

The results of the spine-identification procedure were validated on a data-set of 20 image stacks of pyramidal neuron cultures. Each 3-D image contains multiple independent dendritic backbones with branching topology (Color Plate 26(a, b)). Comparison with ground truth was done by overlaying the extracted skeleton and the identified spines on to the denoised neuron image, projecting into 2-D along the  $z$ -axis, and manually checking the results. Color Plate 26(c, d) shows this projection.

Our method was implemented in a combination of MATLAB,<sup>4</sup> C++, ITK<sup>5</sup> and VTK.<sup>6</sup> We used the CurveSkel software package<sup>7</sup> to calculate the curve skeleton of the dendrites. Our algorithm was deployed on a PC with an Intel Core2 Duo 1.8-GHz processor and 2-GB RAM. The running time to process one neuron image is approximately 12 minutes.

Table 17.1 gives a list of the parameters in the pipeline, their optimal values, and the conditions under which they need to be tuned. Parameters of type *Setup* depend upon either the properties of the image acquisition process or the digitization process and would need to be changed only if this setup were to change. The parameters of type *Data-set* depend on the characteristics of the neurons being analyzed and can be kept the same for the entire data-set.

Edges with gradient value less than the diffusion conductance parameter  $\lambda_m$  are smoothed, while those above it are enhanced. Given the nature of the intensity

4. MATLAB® is a product of The MathWorks, Inc.

5. Insight Segmentation and Registration Toolkit from the National Library of Medicine (NIH/NLM) ([www.itk.org](http://www.itk.org)).

6. Visualization Toolkit from Kitware, Inc. ([www.vtk.org](http://www.vtk.org)).

7. CurveSkel Software by T. K. Dey and J. Sun ([www.cse.ohio-state.edu/~tamaldehy/cskel.html](http://www.cse.ohio-state.edu/~tamaldehy/cskel.html)).

**Table 17.1** List of Parameters and Their Optimal Values

<i>Parameter</i>	<i>Explanation</i>	<i>Values</i>	<i>Type</i>
$\lambda_{nl}$	Nonlinear diffusion conductance (17.2)	0.5 to 1.5	–
$N_{nl}$	Nonlinear diffusion number of time-steps	15	–
$\sigma$	Regularization scale (17.3)	2 to 5	Setup
$\Omega$	Segmentation threshold (Section 17.3.3)	20 to 200	–
$\tau_{gac}$	Level-set time-steps	5 to 10	Setup
$\vartheta$	Floating fragment max volume ( $\times 10^3$ ) (Section 17.3.4)	5 to 1000	–
$\alpha$	Surface fairing smoothing (17.9)	0.3 to 0.7	–
$\mu$	Surface fairing expansion (17.10)	–0.1 to –0.4	–
$N$	Surface fairing steps (17.11)	20 to 80	–
$\rho$	Surface decimation factor	0.90 to 0.96	Data-set
$\theta$	Skeletonization strictness (Section 17.4.2)	0.0 to –0.2	Data-set
$\Gamma_{\min}$	Minimum spine length (Section 17.4.3)	$12 \pm 3$	Data-set
$\Gamma_{\max}$	Maximum spine length (Section 17.4.4)	$38 \pm 5$	Data-set
$R_{\max}$	Maximum spine radius (Section 17.4.4)	$17 \pm 5$	Data-set

field in a neuron image, we find a large difference between the gradients of valid edges and noise edges, and the smoothing step is not sensitive to the selection of  $\lambda_{nl}$ . Reference [54] has shown that edges remain stable over a long period of time in the nonlinear diffusion process, while the solution gradually converges to a steady state. We too observe that after 10 iterations, most of the noise is removed, and the edges remain stable up to 200 iterations (Figure 17.6). Consequently, the number of time steps  $N_{nl}$  is fixed at 15 for all data-sets. The regularization scale  $\sigma$  depends upon the physical spacing between the voxels. For our microscopy setup, a value  $\sigma$  between 2 to 5 was found to be satisfactory.

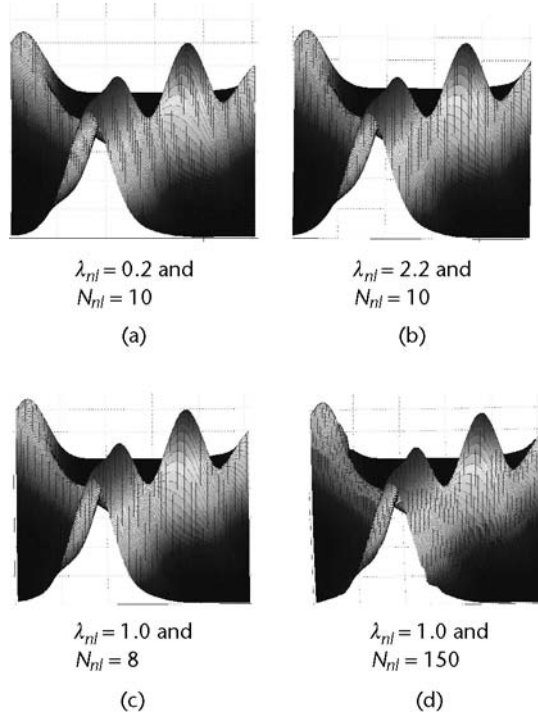
The condition number  $\text{cond}(\Omega)$  (17.5) quantifies the sensitivity of the segmentation threshold  $\Omega$  (Section 17.3.3). As seen in Figure 17.7(a), the condition number is low for  $\Omega < 300$ , and once the background tissue is segmented out ( $\Omega > 10$ ), the approximate radius (in voxels) of the segmented neuron stabilizes (Figure 17.7(b)). As a result of this large range in acceptable values of  $\Omega$ , the algorithm is robust with respect to it and it does not have to be fine tuned.

The  $\tau_{gac}$  parameter enforces a proximity constraint (Section 17.3.4) between valid floating spine head and the dendritic backbone and depends upon the characteristics of the imaging process and the underlying tissue, which are responsible for this disconnect. We find that  $\tau_{gac} \approx 5$  is appropriate for all cases in our dataset. The volumes of the smallest dendrite ( $>120,000$  voxels) and the largest floating tissue fragment ( $\ll 5,000$  voxels) differ by two orders of magnitude, and therefore the volume threshold  $\vartheta$  has a lot of slack in its selection.

The two parameters  $\alpha$  and  $\mu$  of the surface fairing step affect the pass-band and stop-band of the surface frequencies (Section 17.4.1). The parameter  $N$  controls the sharpness of the cutoff frequency. Their value can be kept fixed and does not have to be tuned. This is because the scale of the noise in the iso-surface is many orders of magnitude smaller than the scale of the features (spines) in the neurons, as can be clearly seen from Figure 17.4(a).

To select the best quadric error decimation factor  $\rho$ , we use the average dihedral angle  $\bar{\phi}_{\mathbb{M}}$  of the surface mesh  $\mathbb{M}$  to quantify smoothness. Figure 17.7(c) shows



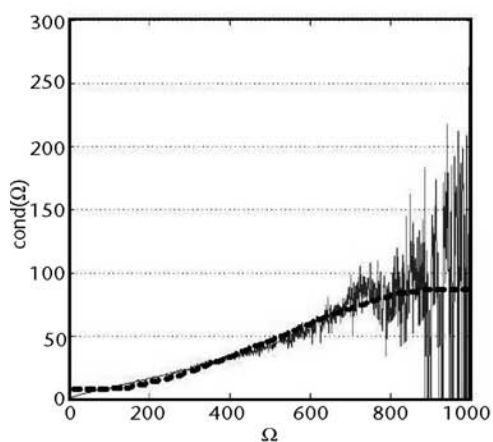


**Figure 17.6** The effect of conductance  $\lambda_{nl}$  and number of time steps  $N_{nl}$  on nonlinear diffusion filtering of the neuron images. (a–d) Intensity map for a 2-D section of the 3-D volume for varying values of  $\lambda_{nl}$  and  $N_{nl}$ .

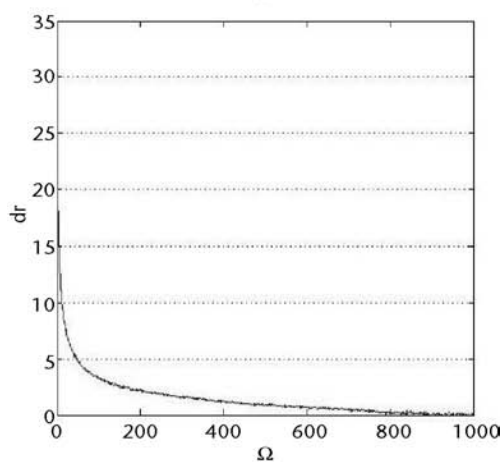
the value of  $\bar{\phi}_M$  with respect to the decimation factor  $\rho$ . Initially, as number of polygons in the original mesh starts reducing,  $\bar{\phi}_M$  of the remains fairly constant. However, after a certain percentage of the faces are removed, the surface begins to develop sharp edges, and  $\bar{\phi}_M$  begins to rise sharply. The optimal value of  $\rho$  is in the region where the knee point occurs. We have found a factor of 0.8 to 0.95 to produce good results.

The skeletonization strictness parameter  $\theta$  (Section 17.4.2), the spine length thresholds  $\Gamma_{\min}$  (Section 17.4.3),  $\Gamma_{\max}$  and maximum spine radius threshold  $R_{\max}$  (Section 17.4.4) work in conjunction to directly influence the sensitivity<sup>8</sup> and specificity<sup>9</sup> of the spine identification process. The values of  $\Gamma_{\min}$ ,  $\Gamma_{\max}$ , and  $R_{\max}$  serve to impose biologically meaningful constraints on the size of the spines and are known a priori, while  $\theta$  is set constant for the entire dataset. From the receiver operating characteristic (ROC) curves (Figure 17.8) we observe the effect of variations in  $\Gamma_{\min}$ ,  $\Gamma_{\max}$ , and  $R_{\max}$  on the accuracy of the algorithm. We obtained optimal sensitivity (0.953) and specificity (0.901) at  $\theta = 0.05$ ,  $\Gamma_{\min} = 12$ ,  $\Gamma_{\max} = 38$ , and  $R_{\max} = 17$  for our dataset.

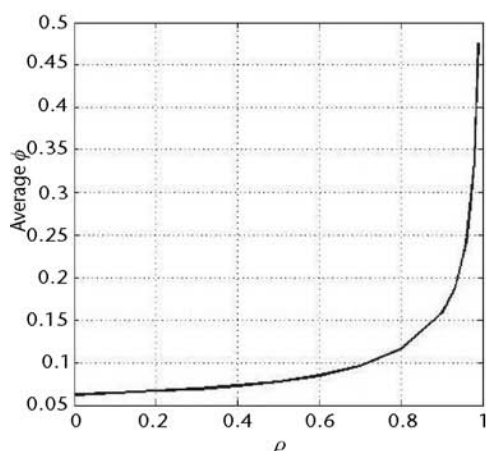
8. Defined as  $TP/(TP + FN)$ , where  $TP$ : count of true positives,  $TN$ : count of true negatives,  $FP$ : count of false positives, and  $FN$ : count of false negatives.
9. Defined as  $TN/(TN + FP)$ .



(a)

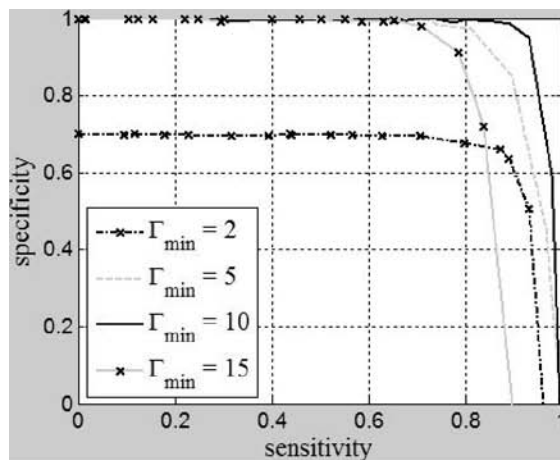


(b)

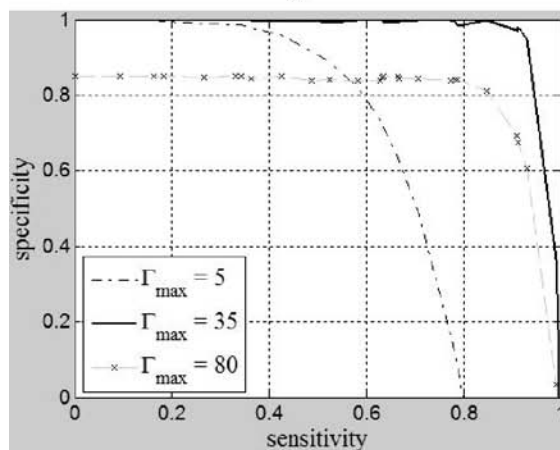


(c)

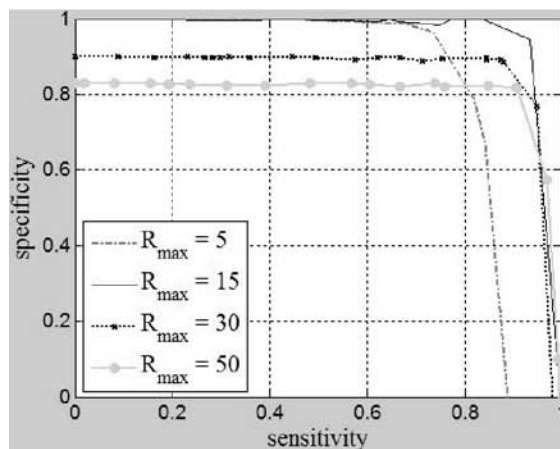
**Figure 17.7** (a) The condition number with respect to  $\Omega$ . The dashed line is a least-squares fit of the data. (b) the approximate radius (in voxels) of the segmented volume with respect to  $\Omega$ . (c) The average dihedral angle  $\bar{\phi}_{\mathcal{M}}$  of dendrite surface mesh  $\mathcal{M}$  versus decimation factor  $\rho$ .



(a)



(b)



(c)

**Figure 17.8** ROC curves with respect to  $\theta$ . (a) The ROC curve for different values of  $\Gamma_{\min}$ . (b) The ROC curve for different values of  $\Gamma_{\max}$ . (c) The ROC curve for different values of  $R_{\max}$ .

## 17.6 Conclusion

In this chapter we have presented a method to robustly reconstruct neuronal dendrites in 3-D and to accurately identify spines on the dendrites. We developed a surface representation of the neuron that is compact and allows us control over the smoothness of the reconstructed surface. The curve-skeleton of the neuron was extracted using a procedure based on the medial geodesic function, which is robust to noise and correct in the sense of topological preservation. Based on the surface representation and the curve-skeleton, we could accurately detect spines and measure spine length, volume, area, basal angle, and other morphological features. Such features, in combination with other experimental information, may help researchers to delineate the mechanisms and pathways of neurological conditions such as Alzheimer's disease and tuberous sclerosis complex syndrome. The parameters of our method are easy to understand and biologically motivated. We also presented a detailed study of the effect of the various parameters on the image processing, reconstruction, and spine identification procedures that shows the robustness of this approach to parameter selection.

We are investigating methods to use the rich description of neuronal structure presented here to track dendrites and spines over time and study their morphological changes. By combining the 3-D reconstruction algorithm with image registration, we plan to study the relationship between the changes in spines and their synaptic formations dynamically in order to uncover potentially new mechanisms of neuronal networks and functions. We also believe that the processing time for one neuron image can be reduced by a factor of  $2\times$  by optimizing our algorithm and implementing it entirely in C/C++.

### Acknowledgments

We thank Professor Karen Zito, UC-Davis, for providing the neuron image datasets. We also thank Professor T. K. Dey, The Ohio State University, for inspiring this approach and for the use of their software. This work is partially supported by NIH-BISTI grant (P20 EB000591-02). The work of X. Xu and S. T. C. Wong was supported in part by the Harvard Center for Neurodegeneration and Repair, Harvard Medical School, and Functional and Molecular Imaging Center, Brigham and Women's Hospital.

### References

- [1] Dima, A., M. Scholz, and K. Obermayer, "Automatic Generation of 3D-Graph Representations of Nerve Cells from Confocal Microscope Scans," *Göttingen Neurobiology Conference, German Neuroscience Society*, Vol. 2, 2001, p. 1041.
- [2] Hering, H., and M. Sheng, "Dendritic Spine: Structure, Dynamics and Regulation," *Neuron*, Vol. 2, 2001, pp. 880–888.
- [3] Yuste, R., and T. Bonhoeffer, "Morphological Changes in Dendritic Spines Associated with Long-Term Synaptic Plasticity," *Annual Reviews in Neuroscience*, Vol. 24, 2001, pp. 1071–1089.
- [4] Turner, J. N., J. W. Swann, D. H. Szarowski, K. L. Smith, M. Marko, and A. Leith, "Confocal Microscopy and Three-Dimensional Reconstruction of Electrophysiologically

- Identified Neurons in Thick Brain Slices,” *Journal of Electron Microscopy Technique*, Vol. 18, No. 1, 1991, pp. 11–23.
- [5] Willis, B., B. Roysam, J. N. Turner, and T. J. Holmes, “Iterative, Constrained 3-D Image Reconstruction of Transmitted Light Bright-Field Micrographs Based on Maximum-Likelihood Reconstruction,” *Journal of Microscopy*, Vol. 169, March 1993, pp. 347–361.
  - [6] Turner, J. N., W. Shain, D. H. Szarowski, S. Lasek, B. Sipple, C. J. Pace, K. A. Al-Kofahi, A. Can, and B. Roysam, “Confocal Light Microscopy of Brain Cells and Tissue: Image Analysis & Quantitation,” *Acta Histochemica et Cytochemica*, Vol. 32, No. 1, 1999, pp. 5–11.
  - [7] Clements, J. D., and S. J. Redman, “Cable Properties of Cat Spinal Motoneurons Measured by Combining Voltage Clamp, Current Clamp and Intracellular Staining,” *Journal of Physiology*, Vol. 409, 1989, pp. 63–87.
  - [8] Cullheim, S., J. Fleshman, L. L. Glenn, and R. E. Burke, “Membrane Area and Dendritic Structure in Type-Identified Triceps Surae Alpha Motoneurons,” *Journal of Computational Neurology*, Vol. 255, 1987, pp. 68–81.
  - [9] Schmitt, S., A. Dima, M. Scholz, and K. Obermayer, “Automatic Three-Dimensional Reconstruction of Neurons from Confocal Images,” *Göttingen Neurobiology Conference*, 2001.
  - [10] He, W., T. A. Hamilton, A. R. Cohen, T. J. Holmes, J. N. Turner, and B. Roysam, “Automated Three-Dimensional Tracing of HRP Stained Neurons from a Stack of Brightfield Optical Slices,” *Microscopy and Microanalysis*, Vol. 9, 2003, pp. 296–310.
  - [11] Irwin, S., B. Patel, M. Idupulapati, J. Harris, R. Crisostomo, B. Larsen, F. Kooy, P. Willems, P. Cras, P. Kozlowski, R. Swain, I. Weiler, and W. Greenough, “Abnormal Dendritic Spine Characteristics in the Temporal and Visual Cortices of Patients with Fragile-X Syndrome: A Quantitative Examination,” *Am. J. Med. Genet.*, Vol. 98, No. 2, 2001, pp. 161–167.
  - [12] Jacobsen, J., C. Wu, J. Redwine, T. Comery, R. Arias, M. Bowlby, R. Martone, J. Morrison, M. Pangalos, P. Reinhart, and F. Bloom, “Early-Onset Behavioral and Synaptic Deficits in a Mouse Model of Alzheimer’s Disease,” *Proc. Natl Acad Sci USA*, Vol. 103, No. 13, 2006, pp. 5161–5166.
  - [13] Engert, F., and T. Bonhoeffer, “Dendritic Spine Changes Associated with Hippocampal Long-Term Synaptic Plasticity,” *Nature*, Vol. 399, 1999, pp. 66–70.
  - [14] Moser, M. B., M. Trommald, and P. Anderson, “An Increase in Dendritic Spine Density on Hippocampal CA1 Pyramidal Cells Following Spatial Learning in Adult Rats Suggests the Formation of New Synapses,” *National Academy of Science*, Vol. 91, 1994, pp. 12673–12675.
  - [15] Glantz, L. A., and D. A. Lewis, “Decreased Dendritic Spine Density on Prefrontal Cortical Pyramidal Neurons in Schizophrenia,” *Archives of General Psychiatry*, Vol. 57, No. 1, 2000, pp. 65–73.
  - [16] Zito, K., G. Knott, G. Shepherd, S. Shenolikar, and K. Svoboda, “Induction of Spine Growth and Synapse Formation by Regulation of the Spine Actin Cytoskeleton,” *Neuron*, Vol. 44, No. 2, 2004, pp. 321–334.
  - [17] Harris, K. M., F. E. Jensen, and B. Tsao, “Three-Dimensional Structure of Dendritic Spines and Synapses in Rat Hippocampus (CA1) at Postnatal Day 15 and Adult Ages: Implications for the Maturation of Synaptic Physiology and Long-Term Potentiation,” *Journal of Neuroscience*, Vol. 12, 1992, pp. 2685–2705.
  - [18] Benshalom, G., and E. L. White, “Dendritic Spines are Susceptible to Structural Alterations Induced by Degeneration of their Presynaptic Afferents,” *Brain Res*, Vol. 443, 1988, pp. 377–382.
  - [19] Harris, K. M., and J. Stevens, “Tstudy of Dendritic Spines by Serial Electron Microscopy

- and Three-Dimensional Reconstructions,” *Neurology and Neurobiology*, Vol. 37, 1988, pp. 179–199.
- [20] Koh, I. Y. Y., W. B. Lindquist, K. Zito, E. A. Nimchinsky, and K. Svoboda, “An Image Analysis Algorithm for Dendritic Spines,” *Neural Computation*, Vol. 14, No. 6, 2002, pp. 1283–1310.
  - [21] Irwin, S., M. Idupulapati, M. Gilbert, J. Harris, A. Chakravarti, E. Rogers, R. Crisostomando, B. Larsen, A. Mehta, C. Alcantara, B. Patel, R. Swain, I. Weiler, B. Oostra, and W. Greenough, “Dendritic Spine and Dendritic Field Characteristics of Layer V Pyramidal Neurons in the Visual Cortex of Fragile-X Knockout Mice,” *Am. J. Med. Genet.*, Vol. 111, No. 2, 2002, pp. 140–146.
  - [22] Peier, A., K. McIlwain, A. Kenneson, S. Warren, R. Paylor, and D. Nelson, “(Over)correction of FMR1 Deficiency with YAC Transgenics: Behavioral and Physical Features,” *Hum. Mol. Genet.*, Vol. 9, No. 8, 2000, pp. 1145–1159.
  - [23] Stevens, J. K., and J. Trogadis, “Computer-Assisted Reconstruction from Serial Electron Micrographs: A Tool for the Systematic Study of Neuronal Form and Function,” *Advances in Cellular Neurobiology*, Vol. 5, 1984, pp. 341–369.
  - [24] Wilson, C. J., F. Murakami, H. Katsumaru, and N. Tsukahara, “Dendritic and Somatic Appendages of Identified Rubrospinal Neurons of the Cat,” *Neuroscience*, Vol. 22, 1987, pp. 113–130.
  - [25] Dima, A., “Computer Aided Image Segmentation and Graph Construction of Nerve Cells from 3-D Confocal Microscopy Scans,” Ph.D. thesis, Technical University Berlin, Berlin, Germany, 2002.
  - [26] Weaver, C. M., P. R. Hof, S. L. Wearne, and W. B. Lindquist, “Automated Algorithms for Multiscale Morphometry of Neuronal Dendrites,” *Neural Computation*, Vol. 16, No. 7, 2004, pp. 1353–1383.
  - [27] Cornea, N., D. Silver, and P. Min, “Curveskeleton Applications,” *IEEE Conference on Visualization*, 2005, pp. 95–102.
  - [28] Ma, W., F. Wu, and M. Ouhyoung, “Skeleton Extraction of 3D Objects with Radial Basis Functions,” *IEEE SMA*, 2003.
  - [29] Dey, T. K., and J. Sun, “Defining and Computing Curve-Skeletons with Medial Geodesic Function,” *Eurographics Symposium on Geometry Processing*, 2006, pp. 143–152.
  - [30] Capowski, J. J., *Computer Techniques in Neuroanatomy*, New York: Plenum, 1989.
  - [31] Glaser, J. R., and E. Glaser, “Neuron Imaging with Neurolucida—A PC-Based System for Image Combining Microscopy,” *Computerized Medical Imaging and Graphics*, Vol. 14, 1990, pp. 307–317.
  - [32] Garvey, C., J. Young, W. Simon, and P. Coleman, “Automated Three-Dimensional Dendrite Tracking System,” *Electroencephalogr. Clinical Neurophysiology*, Vol. 35, 1973, pp. 199–204.
  - [33] Carlbom, I., D. Terzopoulos, and K. M. Harris, “Computer-Assisted Registration, Segmentation, and 3D Reconstruction from Images of Neuronal Tissue Sections,” *IEEE Transactions on Medical Imaging*, Vol. 13, June 1994, pp. 351–361.
  - [34] Schmitt, S., J.-F. Evers, C. D. M. Scholz, and K. Obermayer, “New Methods for the Computer-Assisted 3D Reconstruction of Neurons from Confocal Image Stacks,” *Neuro-Image*, 2004.
  - [35] Urban, E. S., S. M. O’Malley, B. Walsh, A. Santamaría-Pang, P. Saggau, C. Colbert, and I. A. Kakadiaris, “Automatic Reconstruction of Dendrite Morphology from Optical Section Stacks,” *Workshop on Computer Vision Approaches to Medical Image Analysis*, 2006, pp. 190–201.
  - [36] Al-Kofahi, K. A., S. Lasek, D. H. Szarowski, C. J. Pace, G. Nagy, J. N. Turner, and B. Roysam, “Rapid Automated Three-Dimensional Tracing of Neurons from Confocal

- Image Stacks,” *IEEE Transactions on Information Technology in Biomedicine*, Vol. 6, No. 2, 2002, pp. 171–187.
- [37] Uehara, C., C. Colbert, P. Saggau, and I. A. Kakadiaris, “Towards Automatic Reconstruction of Dendrite Morphology from Live Neurons,” *IEEE Conference of the Engineering in Medicine and Biology Society*, 2004.
  - [38] Tyrrell, J., B. Roysam, E. di Tomaso, R. Tong, E. Brown, and R. Jain, “Robust 3-D Modeling of Tumor Microvasculature Using Superellipsoid,” *IEEE International Symposium on Biomedical Imaging: Macro to Nano*, Vol. 6, 2006, pp. 185–188.
  - [39] Herzog, A., G. Krell, B. Michaelis, J. Wang, W. Zuschratter, and K. Braun, “Restoration of Three-Dimensional Quasi-Binary Images from Confocal Microscopy and Its Application to Dendritic Trees,” *SPIE Three-Dimensional Microscopy: Image Acquisition and Processing IV*, 1997, pp. 146–157.
  - [40] Herzog, A., G. Krell, B. Michaelis, and W. Zuschratter, “Tracking on Tree-Like Structures in 3-D Confocal Images,” *3-D and Multidimensional Microscopy: Image Acquisition and Processing*, Vol. 3261, 1998, pp. 165–176.
  - [41] Cohen, A. R., B. Roysam, and J. N. Turner, “Automated Tracing and Volume Measurements of Neurons from 3-D Confocal Fluorescence Microscopy Data,” *Journal of Microscopy*, Vol. 173, No. 2, 1994, pp. 103–114.
  - [42] Goldbaum, M. H., N. Katz, S. Chaudhuri, M. Nelson, and P. Kube, “Digital Image Processing for Ocular Fundus Images,” *Ophthalmology Clinics North America*, Vol. 3, No. 3, 1990, pp. 447–466.
  - [43] Goldbaum, M. H., V. Kouznetsova, W. E. H. B. L. Cote, and M. Nelson, “Digital Image Processing for Ocular Fundus Images,” *Ophthalmology Clinics North America*, Vol. 3, No. 3, 1990, pp. 447–466.
  - [44] Clark, T. M., W. R. Freeman, and M. H. Goldbaum, “Digital Overlay of Fluorescein Angiograms and Fundus Images for Treatment of Subretinal Neovascularization,” *Journal of Retinal Vitreous Diseases*, Vol. 2, No. 12, 1992, pp. 118–126.
  - [45] Chaudhuri, S., S. Chatterjee, N. Katz, M. Nelson, and M. Goldbaum, “Detection of Blood Vessels in Retinal Images Using Two-Dimensional Matched Filters,” *IEEE Transactions Medical Imaging*, Vol. 8, 1989, pp. 263–269.
  - [46] Can, A., H. Shen, J. Turner, H. Tanenbaum, and B. Roysam, “Rapid Automated Tracing and Feature Extraction From Live High-Resolution Retinal Fundus Images Using Direct Exploratory Algorithms,” *IEEE Transactions on Information Technology in Biomedicine*, Vol. 3, 1999, pp. 125–138.
  - [47] Gerig, G., T. Koller, G. Székely, C. Brechbühler, and O. Kübler, “Symbolic Description of 3-D Structures Applied to Cerebral Vessel Tree Obtained from MR Angiography Volume Data,” *Processing in Medical Imaging*, No. 687, 1993, pp. 94–111.
  - [48] Rusakov, D. A., and M. G. Stewart, “Quantification of Dendritic Spine Populations Using Image Analysis and a Tilting Disector,” *Journal of Neuroscience Methods*, Vol. 60, 1995, pp. 11–21.
  - [49] Mosaliganti, K., F. Janoos, X. Xu, R. Machiraju, K. Huang, and S. Wong, “Temporal Matching of Dendritic Spines in Confocal Microscopy Images of Neuronal Tissue Sections,” *MICCAI Workshop on Medical Image Analysis with Applications in Biology*, 2006, pp. 106–113.
  - [50] Bai, W., X. Zhou, L. Ji, J. Cheng, and S. Wong, “Automatic Dendritic Spine Analysis in Two-Photon Laser Scanning Microscopy Images,” *Cytometry A*, Vol. 71, No. 10, 2007, pp. 818–826.
  - [51] Watzel, R., K. Braun, A. Hess, H. Scheich, and W. Zuschratter, “Detection of Dendritic Spines in 3-Dimensional Images,” *Deutsche Arbeitsgemeinschaft für Mustererkennung Symposium*, 1995, pp. 160–167.



- [52] Koh, I. Y. Y., “Automated Recognition Algorithms for Neural Studies,” Ph.D. thesis, Stony Brook University, 2001.
- [53] Cheng, J., X. Zhou, E. Miller, R. Witt, J. Zhu, B. Sabatini, and S. Wong, “A Novel Computational Approach for Automatic Dendrite Spines Detection in Two-Photon Laser Scan Microscopy,” *Neuroinformatics*, Vol. 165, No. 1, 2007, pp. 122–134.
- [54] Perona, P., and J. Malik, “Scale-Space and Edge Detection Using Anisotropic Diffusion,” *IEEE Transactions on Pattern Analysis and Machine Intelligence*, Vol. 12, No. 7, 1990, pp. 629–639.
- [55] Witkin, A., “Scale-Space Filtering,” *International Joint Conference on Artificial Intelligence*, Karlsruhe, West Germany, 1983, pp. 1019–1021.
- [56] Weickert, J., “Anisotropic Diffusion in Image Processing,” Ph.D. thesis, Universität Kaiserslautern, 1996.
- [57] Catté, F., P.-L. Lions, J.-M. Morel, and T. Coll, “Image Selective Smoothing and Edge Detection by Nonlinear Diffusion,” *SIAM Journal of Numerical Analysis*, Vol. 29, No. 1, 1992, pp. 182–193.
- [58] Caselles, V., R. Kimmel, and G. Sapiro, “Geodesic Active Contours,” *International Journal on Computer Vision*, Vol. 22, No. 1, 1997, pp. 61–97.
- [59] Breu, H., J. Gil, D. Kirkpatrick, and M. Werman, “Linear Time Euclidean Distance Transform Algorithms,” *IEEE Transactions on Pattern Analysis and Machine Intelligence*, Vol. 17, May 1997, pp. 529–533.
- [60] Nielson, G. M., and B. Hamann, “The Asymptotic Decider: Resolving the Ambiguity in Marching Cubes,” *IEEE Conference on Visualization*, 1991, pp. 83–91.
- [61] Taubin, G., “A Signal Processing Approach to Fair Surface Design,” *SIGGRAPH Conference on Computer Graphics and Interactive Techniques*, 1995, pp. 351–358.
- [62] Garland, M., and P. S. Heckbert, “Simplifying Surfaces with Color and Texture Using Quadric Error Metrics,” *IEEE Conference on Visualization*, 1998, pp. 263–269.
- [63] Choi, S. W., and H.-P. Seidel, “Linear One-Sided Stability of Mat for Weakly Injective Domain,” *Journal of Math Imaging Vis.*, Vol. 17, No. 3, 2002, pp. 237–247.



# Small Critter Imaging

Zheng Zia, Xiaobo Zhou, Youxian Sun, and Stephen T. C. Wong

Small animals represent vital model systems for the study of organism development and human disease [1]. In vivo imaging technologies prove to be extremely valuable tools for such studies. Recent advances in small animal imaging have yielded techniques such as positron emission tomography (PET), magnetic resonance imaging (MRI), x-ray computed tomography (CT), and optical imaging. Since individual modalities offers their own unique advantages, it would be beneficial be able to fuse them together in order to gain richer multidimensional physiologic information. In this chapter, we introduce small animal in vivo optical imaging methods and discuss our approach to register 3-D fluorescence molecular tomography (FMT) and CT images of rodents.

## 18.1 In Vivo Molecular Small Animal Imaging

Small animal models are often used as surrogates for humans in the study of normal and disease states. It is now possible to introduce genetic mutations identical to those commonly found in human cancer tissue into the endogenous murine gene locus, improving the physiological relevance of small animal studies [2]. Growing opportunities to apply methods of molecular and cellular biology to the study and treatment of human diseases have increased the demand of such animal models with more human-like diseases. This has led to the desire to devise a technique to image animals in order to track disease progression without requiring a biopsy or euthanasia of the animal. In vivo imaging can improve our ability to probe complex biologic interactions dynamically and to study disease and treatment responses over time in the same animal, thus offering the potential to accelerate basic research and drug discovery [2].

Among animal imaging modalities, optical imaging is unequivocally one of the most exciting visualization tools, since it offers several advantages such as high sensitivity, nonionizing radiation utilization, and optical probe stability. Hence, the discussion of this chapter focuses on optical animal imaging techniques.

### 18.1.1 Fluorescence Microscopic Imaging

Fluorescence imaging has become an increasingly versatile and powerful tool for biologists over the last decade. Recently, the invention of two new imaging modalities, confocal, and 2-photon microscopy together with the creation of an array of fluorescent protein reporters have triggered an explosion in fluorescence imaging techniques in biological investigation.

Confocal microscopy was first developed by Marvin Minsky in the 1950s. In traditional optical microscopy techniques based on 1-photon absorption processes,

penetration depth and resolution are limited. During the past two decades, new optical microscopy techniques have utilized nonlinear light-matter interactions to generate signal contrast. Two-photon fluorescence microscopy [3], which uses a 2-photon absorption technique to excite fluorescence, has changed fluorescence microscopy greatly. This technique has two major advantages [4]. Multiphoton absorption occurs in the near-infrared wavelength range and has deeper penetration and less phototoxicity, whereas emission occurs in the visible spectral range. In addition, the signal has nonlinear relationship with the density of photons. As a result, the absorption of photons is confined near the focal plane and results in reduced photobleaching [4].

In order to provide the ability to image molecular contrast *in vivo* in whole animals or tissue, macroscopic visualization methods have been developed. One of the recent technological evolutions, the fluorescence molecular tomography (FMT) proposed by V. Ntziachristos [5], is discussed in detail in the next section.

### 18.1.2 Bioluminescence Imaging

Bioluminescence is light produced by a chemical reaction within an organism through a biochemical reaction. The light is generated when the oxidation of a compound called “Luciferin” reacts with a catalyst enzyme called “Luciferase.” For *in vivo* bioluminescence imaging, biological entities or process components are labeled with a luciferase gene inserted into the DNA of a cell, which gives the cell bioluminescent properties. It will generate light in the presence of luciferin, which in turns can be imaged with a sensitive detector. Compared to fluorescence imaging, which uses an external light source, there is no inherent background bioluminescence in most normal tissue, yielding a higher image contrast [6].

Bioluminescence tomography is being actively researched currently. For example, Kok [7] created a 3-D reconstruction of the approximate location of the original light sources from a number of multiangle 2-D bioluminescence images.

### 18.1.3 Coherent Anti-Stokes Raman Scattering Imaging

Fluorescence and bioluminescence imaging methods both require staining tissues. However, many specimens in biology and medicine such as biochemical species or cellular components will not fluoresce or tolerate labeling. In these cases, other contrast mechanisms with molecular specificity are needed.

Coherent anti-Stokes Raman scattering (CARS) microscopy [8] is a highly sensitive [9] vibrationally selective imaging modality capable of rapid *in vivo* molecular imaging [10], based on the contrast in CARS microscopy arising from the intrinsic molecular vibrations in a specimen. CARS microscopy is capable of providing molecular information with submicron spatial resolution, allowing the production of images depicting intact tissue and cellular architecture *in situ*. In CARS, a pump beam, at frequency  $\omega_p$ , and a Stokes beam, at frequency  $\omega_s$ , interact with a sample through a four-wave mixing process. When the beat frequency  $\omega_p - \omega_s$  is tuned to match the frequency of a Raman active molecular vibration, resonant molecules are coherently driven with the excitation fields, resulting in the generation of a strong

“anti-Stokes” signal at  $\omega_{as} = 2\omega_p - \omega_s$ . Due to the nonlinear nature of the CARS process, the anti-Stokes signal is generated only at a small focal spot that can be scanned in space, allowing the acquisition of high-resolution, three-dimensional image volumes. In thick, turbid tissue such as brain matter, a large percentage of the CARS signal is redirected through multiple scattering events into the backwards (EPI) direction and can be easily collected by a large-area point detector. With a signal strength that is orders of magnitude greater than conventional Raman scattering, and spatial resolutions far better than infrared imaging, CARS microscopy has been noted to be useful in a variety of applications. Recently, it was used to image tissue in a living organism at the video rate [10], allowing for real-time, chemically selective imaging *in vivo*.

#### 18.1.4 Fibered In Vivo Imaging

A major disadvantage of optical imaging in *in vivo* biomedical applications is its low penetration depth. Most optical imaging methods cannot access tissues or cell types deep within solid organs or hollow tissue. Recently, fiber optic-based endoscope imaging has become increasingly versatile by reducing the size and expanding the functionality of optical fiber-based devices, making it possible for optical systems to image deep tissue. Many fiber optic-imaging systems have designs based on confocal [11–16], 2-photon absorption [16], second harmonic generation, and CARS [12]. Additionally, a fiber-optic device may be implanted within live animal subjects for long-term imaging studies, which would lead to new *in vivo* assays for the testing of drugs and other therapies [13, 14].

As an example, Mauna Kea Technologies (Paris, France) has some fiber-optics products that are commercially available (see Chapter 19). Their products use flexible fiber bundles to guide and collect light. One of their products has a lateral and axial resolution of 1.8  $\mu\text{m}$  and 10  $\mu\text{m}$ , respectively. Another product, which is suitable for minimally invasive animal experiments, has a tip with only 0.3-mm diameter.

## 18.2 Fluorescence Molecular Imaging (FMT)

Fluorescence has been a potent tool in small animal imaging. However, *in vivo* confocal or multiphoton microscopy can image just superficial structures. Imaging and quantification of fluorochrome reporters in deep structures ( $> 1$  mm) are very elusive [15]. V. Ntziachristos and R. Weissleder proposed and implemented a novel, volumetric imaging technique (FMT) [16] that accounts for the diffusive propagation of photons in tissue. The technique is capable of resolving and quantifying pico- to femtomole quantities of fluorochromes in whole animals and can achieve several centimeters of tissue penetration.

#### 18.2.1 Fluorescence Scanning

The FMT system is showcased in Color Plate 27. The near infrared 670 nm from a laser diode (a) is split by a silica coupler, (b) to the reference branch, (c) and to the optical switch (d). The light is switched sequentially to 24 outputs and directed

onto the optical bore (f) using 24 multimode optical fibers (e). Thirty-six optical fiber bundles, which are used for light detection and transmission, are arranged in a  $6 \times 6$  array onto a flat plate (h). Three rings of 12 detector fibers are interlaced with two rings of 12 source fibers. The distance between rings is 0.5 cm.

### 18.2.2 FMT Data Processing

The fluorescence is measured with a three-cavity bandpass interference filter. Intrinsic light is detected without the filter. For every source-detector pair, the normalized fluorescence measurement  $U_N(\vec{r}_s, \vec{r}_b)$  can be calculated [5].  $U_N(\vec{r}_s, \vec{r}_b)$  is a function of the medium's fluorochrome distribution.

$$U_N(\vec{r}_s, \vec{r}_b) = \frac{1}{U_0(\vec{r}_s - \vec{r}_d, k^{\lambda_1})} \cdot \int d^3r \cdot U_0(\vec{r}_s - \vec{r}, k^{\lambda_1}) \cdot \frac{n(\vec{r})}{1 - i\omega\tau(\vec{r})} \frac{v}{D^{\lambda_2}} G(\vec{r}_d - \vec{r}, k^{\lambda_2}) \quad (18.1)$$

where  $D^{\lambda_2}$  is the diffusion coefficient at  $\lambda_2$ ,  $v$  is the speed of light into the medium, and  $n(\vec{r})$  is the position-dependent product of the fluorochrome absorption coefficient  $\mu_a(\vec{r})$  and fluorescence quantum yield  $\gamma$ . The parameters  $k^{\lambda_1}, k^{\lambda_2}$  are the wave propagation vectors at wavelengths  $\lambda_1, \lambda_2$ , respectively, and  $\tau(\vec{r})$  is the fluorescence lifetime of the fluorochrome at position  $\vec{r}$ . Equation (18.1) is written for the general case where the source term is light of modulated intensity  $\omega$ . The function  $U_0(\vec{r}_s - \vec{r}, k^{\lambda_2})$  describes the established photon field into the diffuse medium at position  $\vec{r}$  due to a source at position  $\vec{r}_s$ , and  $G(\vec{r}_d - \vec{r}, k^{\lambda_2})$  is the Greens function solution to the diffusion equation that describes the propagation of the emission photon wave from the fluorochrome at position  $\vec{r}$  to the detector at  $\vec{r}_d$  [5]. Equation (18.1) can be discretized into a number of coupled linear equations in order to perform reconstruction. The final fluorochrome concentration is given by  $[F(\vec{r})] = n(\vec{r})/\gamma \cdot \epsilon$ , where  $\epsilon$  is the fluorochrome's extinction coefficient. Recently N. Deliolanis and colleagues have improved the system using CCD camera-based technology to perform noncontact, 360-degree projection fluorescence tomography, which yields a superior information content compared with fiber-based implementations [24].

### 18.2.3 Multimodality

FMT has been used for 3-D imaging and visualization of gene expression and cell traffic in whole animals. However, fluorescence contrast is mainly functional or molecular and carries little anatomical information. So combining FMT and modalities with high-resolution complementing anatomical features such as CT and MRI is an attractive strategy. J. Grimm et al. [2] exemplified how gene expression profiles can be used to select innovative imaging approaches for cancer with the

combination of functional and anatomical imaging. Importantly, the anatomical modality can guide the inversion problem by offering a priori information, which is helpful in finding a better solution. The following section introduces a method to coregister FMT and CT animal images in order to gain functional and anatomical information [17].

## 18.3 Registration of 3-D FMT and MicroCT Images

### 18.3.1 Introduction

Most optical molecular animal imaging methods provide high-resolution functional information, but carry little anatomical information. In biomedical applications, however, investigators require accurate structural information for clear interpretation. In this work, we describe our approaches used to register 3-D FMT and microCT images for fusing fine anatomical structures and functional information. This work has contributed to the registration of the 2-D flat image and the 3-D microCT image of the mouse to bridge the gap between the 3-D FMT image and 3-D microCT image of the animal.

Images acquired from FMT and microCT have different intensities and spatial resolutions. To solve the registration problem of multimodal images, the maximization of mutual information of voxel intensities has been proposed and demonstrated to be a powerful method, allowing fully automated robust and accurate registration of multimodal images in a variety of applications without the need for segmentation or other preprocessing of the images. As for registration of 3-D FMT and microCT images of the mouse, 3-D FMT reveals only specific tumors without much anatomical information, as its maximum diameter is only a couple of millimeters in length and is much smaller than microCT image of the whole animal, which is about 10 cm long. This results in a challenging problem of directly aligning both images efficiently and precisely. More information is needed in order to facilitate registration. Fortunately, 2-D flat images (photography) and 3-D FMT images can be acquired in series using the planar fluorescence reflectance imaging/FMT system without moving the subject [2]. Therefore, their spatial relationship is known after acquisition, and FMT images can be superimposed onto the surface anatomical features to create a rough context. Our observation is that 2-D flat images can be employed to bridge the gap between small 3-D FMT images and large microCT images of the same animal. Thus, we are facing a 2-D/3-D registration problem, which has been investigated in the literature for various applications [18]. The registration of 2-D flat and 3-D images is a novel task because the 2-D flat image is a surface projection image of the 3-D object, which is totally different from other medical image modalities such as x-rays, reconstructed radiographs (DRR), digital subtraction angiography (DSA), fluoroscopic images, positron emission tomography (PET), and single photon emission computed tomography (SPECT). Although many papers address the registration between 2-D images and 3-D images, they are different from our work because this work deals with boundary-based registration. Image registration methods can be categorized in two distinct groups: intensity-based and feature-based techniques [18]. Because only boundary information can be used to register 2-D flat and 3-D microCT



images, the feature-based matching method rather than the intensity-based method is employed, which allows registering images of completely different nature and can handle complex between-image distortions.

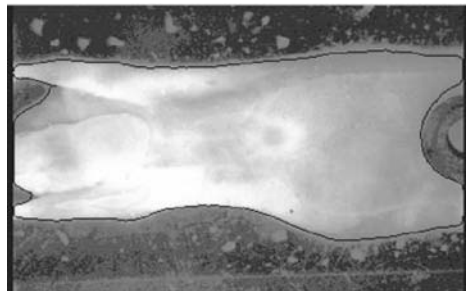
### 18.3.2 Problem Statement and Formulation

Since 3-D FMT images contain only tumor information in the mouse and carry little anatomical information, it is difficult to coregister 3-D FMT and 3-D microCT images directly. Fortunately, while 3-D FMT images are acquired, flat images can be generated and matched with 3-D FMT images to give an anatomical context of the mouse in 2-D. If we register 2-D flat images with 3-D microCT images, we can roughly align 3-D FMT and microCT images in 2-D. The resultant transformation can then be employed as a starting point for further alignment in all three dimensions. A 2-D flat image is basically a photograph (i.e., a surface projection image) of the mouse. We project 3-D microCT images to obtain a 2-D projection image that is similar to the flat image. Only the boundary information in both 2-D images is the same and can be used for registration.

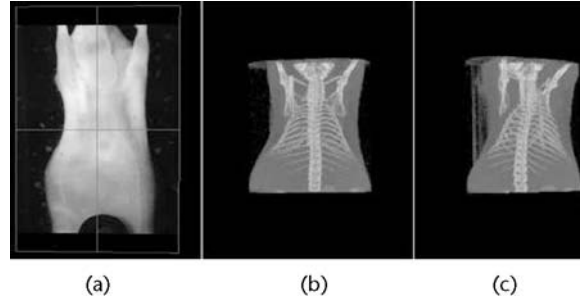
The first step is to segment the 2-D flat image, shown in Figure 18.1. The boundary of the mouse, denoted by  $C_r$ , is obtained by segmenting the 2-D flat image by gradient vector flow snake model.

The second step is to project the 3-D microCT images to obtain a projected 2-D microCT images corresponding to the flat image. The projected image is denoted by  $P(\theta, I)$ , where  $I$  is the 3-D microCT image,  $\theta = (\theta_1, \theta_2)$  is the adjustable projection parameters (two rotation angles about axes in the coronal plane of microCT images), and  $P(\theta, I)$  is the projection operation on 3-D microCT image  $I$ . The proper  $\theta$  is used to make the projected microCT image as similar as possible to the flat image, as shown in Figure 18.2. Figure 18.2(b) resembles the 2-D flat image more than Figure 18.2(c). After projection, the microCT image  $P(\theta, I)$  is then segmented to obtain the boundary of the mouse for registration, denoted by  $C_m(\theta)$ .

The third step is to register the two 2-D images by the two point sets  $C_r$  and  $C_m(\theta)$ . We denote the two point sets by reference point set and moving point set with their elements denoted in  $C_r = \{r_i | i = 1, \dots, N_r\}$  and  $C_m(\theta) = \{m(\theta)_j | j =$



**Figure 18.1** Segmentation of the flat image with GVF snake.



**Figure 18.2** (a) 2-D flat image, (b) projection of the 3-D CT image with a  $\theta$ , and (c) projection of the 3-D CT image with another  $\theta$ .

$1, \dots, N_m\}$ , where  $r_i$  and  $\mathbf{m}(\theta)_j$  are the pixel position vectors. During different imaging sessions such as microCT and flat/FMT imaging, The positioning of the mouse is different, which would cause some deformation of the mouse. We believe that affine transformation can be employed to model this deformation. Therefore, we assume that the relationship between the two point sets is 2-D Euclidean affine transformation, comprising of six parameters. That is, for  $s \in \mathbb{R}^2$  and  $s \in C_m(\theta)$  we define:

$$T(\lambda; s) = \begin{bmatrix} \lambda_1 & \lambda_2 \\ \lambda_3 & \lambda_4 \end{bmatrix} s + \begin{bmatrix} \lambda_5 \\ \lambda_6 \end{bmatrix} \quad (18.2)$$

where  $\lambda = [\lambda_1, \lambda_2, \lambda_3, \lambda_4, \lambda_5, \lambda_6]$  are the affine parameters, among which  $\lambda_5, \lambda_6$  are translation parameters and  $T(\lambda; s)$  is the pixel position vector. The task of the registration is to determine the parameters of transformation  $\lambda = [\lambda_1, \lambda_2, \lambda_3, \lambda_4, \lambda_5, \lambda_6]$  and the previous adjustable projection parameters  $\theta$ , which best align the moving point set and reference point set.

Registration is evaluated by a disparity function  $\varepsilon(s) = \|s\|_2$ . To compute  $\varepsilon(s)$ , we require the specification of the correspondence between the reference and moving point sets. This correspondence is denoted by the function  $\xi(j)$  where  $j = 1, \dots, N_m$ , which finds the corresponding reference point index for each moving point after affine transformation  $T(\lambda; \mathbf{m}(\theta)_j)$ . The index of the closest point correspondence  $\xi(j)$  for every moving point is computed as follows:

$$\xi(j) = \arg \min_{k \in \{1, \dots, N_r\}} \varepsilon(r_k - T(\lambda; \mathbf{m}(\theta)_j)) \quad (18.3)$$

Thus, the disparity function can be defined as:

$$J(\lambda, \theta) = \frac{1}{N_m} \sum_{j=1}^{N_m} \varepsilon(r_{\xi(j)} - T(\lambda; \mathbf{m}(\theta)_j)) \quad (18.4)$$

The optimal solution is given by:

$$(\lambda^*, \theta^*) = \arg \min_{\lambda, \theta} J(\lambda, \theta) \quad (18.5)$$

Finally, the estimate of the optimal registration is given by minimizing  $J(\lambda, \theta)$  over  $(\lambda, \theta)$ . With the obtained projection and affine parameters, we can align 3-D FMT and microCT images in 2-D space.

Iteration is used to optimize our problem. For each iteration, the 3-D microCT image should be automatically projected according to the adjustable projection parameter  $\theta$ . This poses another problem of automatically segmenting the projected microCT image during iteration. In order to get a good initial contour, we first convert the gray projected microCT image to a binary image with the global image threshold, which is computed automatically using Otsu's method [19]. Then, morphological operations including opening and closing are performed on the binary version of the projected microCT image. The boundary of the binary image is employed as the starting position of the GVF snake model.

### 18.3.3 Combined Differential Evolution and Simplex Method Optimization

A novel algorithm combining differential evolution (DE) and improved simplex method for solving (18.5) is introduced and validated with simulated images and real images of mice [20].

The two additional projection parameters and noncorresponding points in the two point sets create many local minima in the optimization problem. We turn to certain global optimization methods, among which the differential evolution [21] is a simple and efficient adaptive scheme for global optimization over continuous spaces. But the population size of DE is proportional to the parameter number, and the evaluation of the objective function contains a projection operation on the 3-D CT image that would overburden the computation. So in our studies, using the DE method with all the parameters is very time consuming. As we mentioned previously, the simplex method is accurate and efficient to estimate the affine transformation parameters, and it is the adjustable projection parameters that make the optimization problem have many local minima. So we can combine both DE and simplex methods to optimize the problem. That is, for every specified  $\theta$  the two point sets can be extracted. Then the simplex method is used to minimize

$$J_{\theta}(\lambda) = \frac{1}{N_m} \sum_{j=1}^{N_m} \varepsilon(r_{\xi(j)} - T(\lambda; \mathbf{m}(\theta)_j)) \quad (18.6)$$

where  $\theta$  is specified. The optimal  $J_{\theta}(\lambda^*)$  is regarded as the value of the objective function of DE with the specified  $\theta$ .

In the six-dimensional search spaces of vectors  $\lambda$ , a simplex with seven vertices is deformed and moved to a descending direction inferred in terms of distribution of sampled objective function at the vertices. The three motions such as reflection, expansion, and contraction are prepared for the simplex to scan over the search space. Provided with an initial parameter vector  $\lambda_0^{(0)}$  at the first iteration, an alignment of the simplex vertices is given by  $\lambda_0^{(0)}$  and  $\{\lambda_k^{(0)} = \lambda_0^{(0)} + \gamma \mathbf{e}_k\}_{k=1}^6$  ( $\gamma > 0$ ), where  $\mathbf{e}_k$  is the normal basis vector. The simplex method requires only function evaluations, not derivatives. The method has a geometrical naturalness about it, which makes it delightful to describe or work through.

Another problem with the simplex method we have to consider is estimating the global initial values of  $\lambda_0^{(0)}$ , one component of which is the translation parameters. Since our algorithm is based on iterative calculation, the initial alignment of  $\{\mathbf{m}(\theta)_j\}_{j=1}^{N_m}$  and  $\{\mathbf{r}_i\}_{i=1}^{N_r}$  affects its convergence rates and precision. Registration of the geometric centers of both the data solves their initial shift such that

$$[\lambda_5^{(0)}, \lambda_6^{(0)}] = \frac{1}{N_r} \sum_{i=1}^{N_r} \mathbf{r}_i - \frac{1}{N_m} \sum_{j=1}^{N_m} \mathbf{m}(\theta)_j \quad (18.7)$$

The other initial affine parameters  $[\lambda_1^{(0)}, \lambda_2^{(0)}, \lambda_3^{(0)}, \lambda_4^{(0)}]$  are set to  $[1 \ 0 \ 0 \ 1]$ .

The simplex method has only three motions: reflection, expansion, and contraction, to search for a better solution. To improve the search we introduce a least square step as an additional searching method during the evaluation of the objective function. With  $\theta$  fixed, given  $\lambda$  we can get the corresponding closest point set  $Q = \{\mathbf{q}(j) | j = 1, \dots, N_m\}$  using (18.3). We denote  $\mathbf{q}_k$  as the  $k$ th point of  $Q$ , which has two elements  $\mathbf{q}_k = [\mathbf{q}_{k1}, \mathbf{q}_{k2}]$ . The affine transformation model between the two point sets can be written as

$$\mathbf{Y} = \chi \tilde{\lambda} \quad (18.8)$$

where  $\mathbf{m}(\theta)_k = [\mathbf{m}(\theta)_{k1}, \mathbf{m}(\theta)_{k2}]$  and

$$\mathbf{Y} = \begin{bmatrix} \mathbf{q}_{11} & \mathbf{q}_{12} \\ \vdots & \vdots \\ \mathbf{q}_{N_m1} & \mathbf{q}_{N_m2} \end{bmatrix} \quad (18.9)$$

$$\chi = \begin{bmatrix} 1 & \mathbf{m}(\theta)_{11} & \mathbf{m}(\theta)_{12} \\ \vdots & \vdots & \vdots \\ 1 & \mathbf{m}(\theta)_{N_m1} & \mathbf{m}(\theta)_{N_m2} \end{bmatrix} \quad (18.10)$$

$$\tilde{\lambda} = \begin{bmatrix} \tilde{\lambda}_5 & \tilde{\lambda}_6 \\ \tilde{\lambda}_1 & \tilde{\lambda}_3 \\ \tilde{\lambda}_2 & \tilde{\lambda}_4 \end{bmatrix} \quad (18.11)$$

Parameter  $\tilde{\lambda}$  is the affine parameters between the moving point set  $C_m(\theta)$  and its corresponding closest point set  $Q$ . A least squares estimation of  $\tilde{\lambda}$  can be obtained by

$$\tilde{\lambda} = [\chi^T \chi]^{-1} \chi^T \mathbf{Y} \quad (18.12)$$

Consequently, with  $\theta$  fixed,  $\lambda$  can be updated by (18.12). A better solution will be found while evaluating the objective function.

### 18.3.3.1 Summary of the Algorithm

The components of our proposed optimization is summarized as follows:

- Use the DE method over  $\theta$  with the simplex method as its objective function.
- Utilize the simplex method to optimize the affine transformation problem with specified  $\theta$ .
- Evaluate the objective function of the simplex method over the affine parameters  $\lambda$ .
  - Project the 3-D microCT image according to the adjustable projection  $\theta$  parameter and then segment the projected image to get the moving point set  $\{\mathbf{m}(\theta)_j\}_{j=1}^{N_m}$ .
  - Compute the moving point set after affine transformation with the current estimate  $\lambda^*:\{T(\lambda^*, \mathbf{m}(\theta)_j)|j = 1, \dots, N_m\}$  and the corresponding closest point set  $\{\mathbf{q}(j)|j = 1, \dots, N_m\}$ . Thus, the objective function value is computed  $J_\theta(\lambda^*)$  with (18.4).
  - Update parameters using the least squares method.

A flowchart is shown in Figure 18.3.

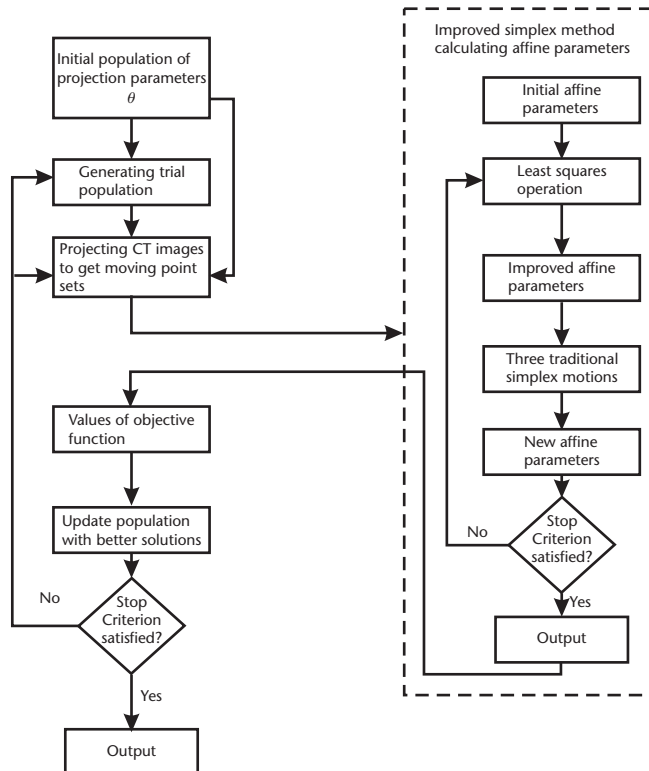
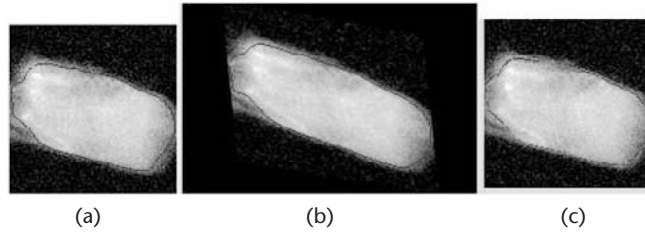


Figure 18.3 Flowchart of the combined DE and simplex method.



**Figure 18.4** (a) The projected image, (b) simulated flat image, and (c) corresponding registration result.

#### 18.3.3.2 Experiment with Simulated Image Data

First, a synthetic flat image and the 3-D microCT image are registered. The synthetic flat image is generated as follows:

1. Project a 3-D microCT image after rotating about two axes according to the adjustable projection parameters  $\theta$ .
2. Transform the projected 2-D image with affine transformation parameters.
3. Add random noise (zero mean normally distributed with standard deviations  $\delta$ ) to the transformed 2-D image to get “practical” simulated flat images.

More than 20 experiments with different parameters were executed. Results were considered acceptable if the optimal objective function was lower than 0.7 pixel. Figure 18.4 exemplifies a registration result.

#### 18.3.3.3 Experiment with Real Data

We have two mice datasets. The size of each real flat image is  $231 \times 341$  with a pixel spacing of  $0.0185 \times 0.0185$  cm. The size of the 3-D microCT images of the mouse thorax covering tumors is  $512 \times 512 \times 512$ , and its voxel spacing is  $0.0072 \times 0.0072 \times 0.0072$  cm. The sizes of the 3-D FMT images of the two mice are  $20 \times 20 \times 21$  and  $30 \times 30 \times 30$  with voxel spacing of  $0.12 \times 0.12 \times 0.057$  cm and  $0.15 \times 0.15 \times 0.041$  cm, respectively. The relative 2-D position of the flat and the 3-D FMT image is known, since they are acquired in series using the planar fluorescence reflectance imaging/FMT system without moving the subject. Accordingly, we can register the 3-D microCT and 3-D FMT images in 2-D space by registering the flat image and the projected microCT image. The real data is registered with physical coordinate.

We illustrate the registration results of the real data in Color Plate 28. The first column shows the fusion of the flat image and the projected 3-D FMT image, which is known by the FMT system. The registration result of the flat and 3-D microCT images with proposed algorithm is shown in the second column. Then, we can fuse the 3-D FMT and microCT images in the x-y plane with the 2-D registration result. The fusion of 3-D FMT and microCT images can significantly

improve the interpretation of functional FMT images, along with the clear anatomical structures provided by high-quality microCT images, and this multimodality registration technique has a great potential to facilitate drug discovery and cancer research.

### 18.3.4 A Novel Optimization Method Based on Sequential Monte Carlo

This section introduces a novel optimization method based on sequential Monte Carlo to resolve (18.5). In [22] a sequential Monte Carlo technique—condensation (conditional density propagation), is used for visual tracking. Herein we denote  $\mathbf{x} = \lambda \times \theta$ . Condensation uses dynamical models, together with visual observation, to propagate the random set over time. The state at time  $t$  is  $\mathbf{x}_t$  and its history  $\mathbf{X}_t = \{\mathbf{x}_1, \dots, \mathbf{x}_t\}$ . Similarly, the observation at time  $t$  is  $\mathbf{z}_t$  with history  $\mathbf{Z}_t = \{\mathbf{z}_1, \dots, \mathbf{z}_t\}$ .

#### 18.3.4.1 Condensation (Conditional Density Propagation)

Consider the following dynamic system modeled in a state-space form:

$$\text{State model : } \mathbf{x}_t = f_t(\mathbf{x}_{t-1}, \mathbf{u}_{t-1}) \quad (18.13)$$

$$\text{Observation model : } \mathbf{z}_t = g_t(\mathbf{x}_t, \mathbf{v}_t) \quad (18.14)$$

where  $\mathbf{u}_t$  and  $\mathbf{v}_t$  are the state noise and observation noise at time  $t$ . We need to estimate all information about the state at time  $t$  that is deduced from observation history  $\mathbf{Z}_t : p(\mathbf{x}_t | \mathbf{Z}_t)$ . In [23] it was mentioned that in practice, the exact computation of the posterior density is impossible. Inevitably, the problem has to be approximated.

Condensation is a sequential Monte Carlo technique employed to estimate the posterior probability density function with a set of samples [22, 23]. In terms of a mathematical formulation, such a method approximates the posterior probability density function by random samples  $\{\mathbf{x}_t^m | m = 1, \dots, N\}$  corresponding with weights  $\{w_t^m | m = 1, \dots, N\}$ , such that

$$p(\mathbf{x}_t | \mathbf{Z}_t) \approx \sum_{m=1}^N w_t^m \delta(\mathbf{x}_t - \mathbf{x}_t^m) \quad (18.15)$$

To propagate the probability density over time, condensation uses “factored sampling” [22] iteratively. A weighted sample set  $\{\mathbf{x}_{t-1}^m, w_{t-1}^m | m = 1, \dots, N\}$  is generated from the previous iteration. We sample (with replacement)  $N$  times from the set by choosing an index  $n \in \{1, \dots, N\}$  with probability  $w_{t-1}^n$ . The new samples then undergo the given state model (18.13). The weights associated with these states are computed as

$$w_t^n = \frac{p(\mathbf{z}_t | \mathbf{x}_t^n)}{\sum_{j=1}^N p(\mathbf{z}_t | \mathbf{x}_t^j)} \quad (18.16)$$



where  $p(\mathbf{z}_t|\mathbf{x}_t^n)$  is the conditional observation density. The elements with high weights may be chosen several times, whereas others with relatively low weights may not be chosen at all. At this stage, the sample set  $\{\mathbf{x}_t^m, w_t^m | m = 1, \dots, N\}$  is generated to represent the posterior probability density at time  $t$ .

#### 18.3.4.2 Dynamic Model for Registration

Since we would like to estimate six affine transformation parameters and two adjustable projection parameters, the dynamic model can be defined as

$$\mathbf{x}_t = \mathbf{x}_{t-1} + \mathcal{N}(0, \mathbf{U}) \quad (18.17)$$

where  $\mathbf{x}_t = [\lambda_1, \lambda_2, \lambda_3, \lambda_4, \lambda_5, \lambda_6, \theta_1, \theta_2]^T$  and  $\mathbf{U}$  is the covariance matrix of the zero-mean Gaussian random vector [24]. To generate better samples, a local search is performed to decrease the sample size. Though traditional ICP methods often converge to local minimum, each iteration makes  $J(\mathbf{x}_t)$  decrease. So we can incorporate least squares of the affine parameters into the dynamic model as a local search operation to generate better samples. With  $\theta$  fixed, given  $\lambda$ , we can get the corresponding closest point set  $\mathcal{Q} = \{\mathbf{q}(j) | j = 1, \dots, N_m\}$  using (18.3), just as in previous optimization method. We denote  $\mathbf{q}_k$  as the  $k$ th point of  $\mathcal{Q}$ , which has two elements  $\mathbf{q}_k = [\mathbf{q}_{k1}, \mathbf{q}_{k2}]$ . The affine transformation model between the two point sets can be written as:

$$\mathbf{Y} = \chi \tilde{\lambda} + v \quad (18.18)$$

where  $v$  is a noise vector, and  $\mathbf{Y}, \chi$  and  $\tilde{\lambda}$  are defined in (18.9–18.11), respectively. Parameter  $\tilde{\lambda}$  is the affine parameters between the moving point set  $C_m(\theta)$  and its corresponding closest point set  $\mathcal{Q}$ . A least squares estimation of  $\tilde{\lambda}$  can be obtained by:

$$\tilde{\lambda} = [\chi^T \chi]^{-1} \chi^T \mathbf{Y} \quad (18.19)$$

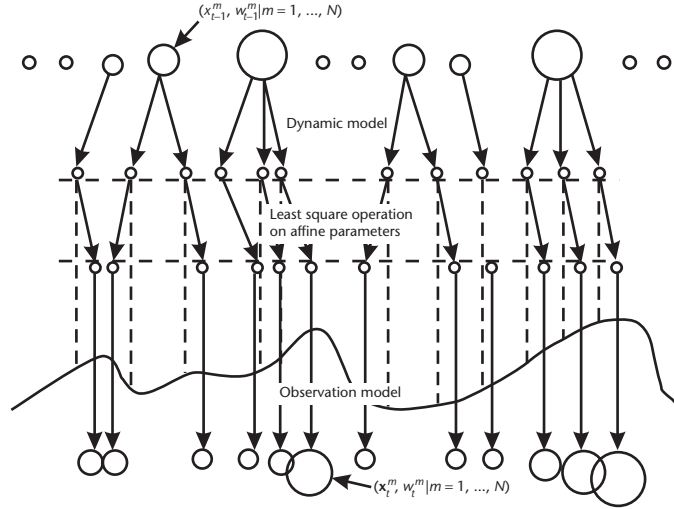
Accordingly, with  $\theta$  fixed,  $\lambda$  can be updated by (18.19). We denote this operation as  $\lambda^{\text{new}} = \vartheta(\lambda)$ . Now parameters in the dynamic model (18.17) can be rewritten as

$$\lambda_t = \vartheta(\lambda_{t-1} + \mathcal{N}(0, \mathbf{U}_\lambda)) \quad (18.20)$$

$$\theta_t = \theta_{t-1} + \mathcal{N}(0, \mathbf{U}_\theta) \quad (18.21)$$

where  $\mathbf{U}_\lambda$  and  $\mathbf{U}_\theta$  is the covariance matrix of the zero-mean Gaussian random vector.

Condensation requires sufficient sample size to approximate  $p(\mathbf{x}_t|\mathbf{Z}_t)$ , which will burden the computation. Figure 18.5 shows that least square operation performs a local search to find better samples. Our experiments have demonstrated that this combination can reduce the sample size considerably.



**Figure 18.5** One-time step in our proposed algorithm: least square operation performs as a local search.

#### 18.3.4.3 Observation Model for Registration

The observation model is defined as

$$\mathbf{z}_t = [T(\lambda_t; \mathbf{m}(\theta_t))_1, \dots, T(\lambda_t; \mathbf{m}(\theta_t))_{N_m}]^T + \zeta \quad (18.22)$$

where  $\zeta$  is the unknown noise. We need to minimize  $J(\lambda, \theta)$  over  $(\lambda, \theta)$ . Herein,  $p(\mathbf{z}_t | \mathbf{x}_t)$  is regarded as the quality of the projection and affine transformation. Samples with less  $J(\lambda, \theta)$  will be arranged with larger weights. In the case described earlier,  $p(\mathbf{z}_t | \mathbf{x}_t)$  is inversely proportional to  $J(\mathbf{x}_t)$  (the less, the merrier). Accordingly,  $p(\mathbf{z}_t | \mathbf{x}_t) \propto \frac{1}{J(\mathbf{x}_t)}$ , which can be substituted into (18.16) to arrive at

$$w_n^t = \frac{1/J(\mathbf{x}_t^n)}{\sum_{j=1}^N 1/J(\mathbf{x}_t^j)} \quad (18.23)$$

The lesser the  $J(\mathbf{x}_t^n)$  is, the more likely the  $\mathbf{x}_t^n$  will be chosen. Thus, we can minimize  $J(\mathbf{x})$ .

## 18.4 Conclusions

New animal imaging modalities, especially those for in vivo molecular imaging, are emerging as powerful tools to accelerate biomedical discovery and preclinical studies. With animal models now widely used, finding more accurate and robust ways to conduct and interpret animal experiments noninvasively becomes a key factor in the basic and preclinical science. In this work, we introduce major optical imaging methods for small animal studies and illustrate a new multimodality fusion method that combines 3-D FMT and microCT images to improve the

information content. The coregistration of molecular biology and high-resolution anatomical images will provide an accurate interpretation and noninvasive means of investigating animal models.

### Acknowledgments

The authors would like to acknowledge the excellent collaboration with their molecular imaging collaborators in this research effort, and, in particular, Dr. Vasilis Ntziachristos, Department of Radiology, Massachusetts General Hospital. This research is supported by The Bioinformatics Program, the Methodist Hospital Research Institute, Weill Cornell Medical College, Houston, Texas, and NIH R01 LM008696, R01LM009161, R01 AG028928 grants to STCW.

### References

- [1] Weissleder, R., "Scaling Down Imaging: Molecular Mapping of Cancer in Mice," *Nat. Rev. Cancer*, Vol. 2, 2002, pp. 11–18.
- [2] Grimm, J., D. G. Kirsch, S. D. Windsor, C. F. Kim, P. M. Santiago, V. Ntziachristos, T. Jacks, and R. Weissleder, "Use of Gene Expression Profiling to Direct *In Vivo* Molecular Imaging of Lung Cancer," *PNAS*, Vol. 102, No. 40, October 2005.
- [3] Denk, W., J. H. Strickler, and W. W. Webb, "Two-Photon Laser Scanning Fluorescence Microscopy," *Science*, 248, 1990, pp. 73–76.
- [4] Helmchen, F., and W. Denk, "Deep Tissue Two-Photon Microscopy," *Nature Methods*, 2005.
- [5] Ntziachristos, V., and R. Weissleder, "Charge-Coupled-Device Based Scanner for Tomography of Fluorescent Near-Infrared Probes in Turbid Media," *Med. Phys.*, Vol. 29, No. 5, 2002, pp. 803–809.
- [6] Contag, C. H., and M. H. Bachmann, "Advances in *In Vivo* Bioluminescence Imaging of Gene Expression," *Annu. Rev. Biomed. Eng.*, 2002.
- [7] Kok, P., "Multiple Modality Registration, Fusion and Visualization for Bioluminescence Imaging," Master Thesis, Delft University of Technology, 2006.
- [8] Sunney, X. X., J. X. Cheng, and E. O. Potma, "Coherent Anti-Stokes Raman Scattering Microscopy," in *Handbook of Biological Confocal Microscopy*, 3rd ed., J. Pawley, (ed.), New York: Springer Science, 2006, pp. 595–606.
- [9] Saar, G., and X. S. Xie, "High Sensitivity Vibrational Imaging with Frequency Modulation Coherent Anti-Stokes Raman Scattering (FM CARS) Microscopy," *Opt. Lett.* 31, 2006, pp. 1872–1874.
- [10] Evans, C. L., E. O. Potma, M. P. Haag, D. Côté, C. P. Lin, and X. S. Xie, "Chemical Imaging of Tissue *In Vivo* with Video-Rate Coherent Anti-Stokes Raman Scattering Microscopy," *PNAS*, Vol. 102, No. 46, 2005.
- [11] Shin, H. J., M. C. Pierce, D. Lee, H. Ra, O. Solgaard, and R. R. Kortum, "Fiber-Optic Confocal Microscope Using a MEMS Scanner and Miniature Objective Lens," *Optics Express*, Vol. 15, No. 15, 2007.
- [12] Légaré, F., C. L. Evans, F. Ganikhanov, and X. S. Xie, "Towards CARS Endoscopy," *Opt. Express*, 2006.
- [13] Flusberg, B. A., E. D. Cocker, W. Piyawattanametha, J. C. Jung, E. L. M. Cheung, and M. J. Schnitzer, "Fiber-Optic Fluorescence Imaging," *Nature Methods*, Vol. 2, No. 2, 2005, pp. 941–950.

- [14] Flusberg, B. A., J. C. Jung, E. D. Cocker, E. P. Anderson, and M. J. Schnitzer, "In Vivo Brain Imaging Using a Portable 3.9 Gram Two-Photon Fluorescence Microendoscope," *Optics Letters*, Vol. 30, No. 17, 2005.
- [15] Ntziachristos, V., C. H. Tung, C. Bremer, and R. Weissleder, "Fluorescence Molecular Tomography Resolves Protease Activity *In Vivo*," *Nature Medicine*, Vol. 8, No. 7, 2002.
- [16] Ntziachristos, V., and R. Weissleder, "Experimental Three-Dimensional Fluorescence Reconstruction of Diffuse Media Using a Normalized Born Approximation," *Opt. Lett.*, Vol. 26, 2001, pp. 893–895.
- [17] Deliolanis, N., T. Lasser, D. Hyde, A. Soubret, J. Ripoll and V. Ntziachristos, "Free-Space Fluorescence Molecular Tomography Utilizing 360 Degrees Geometry Projections," *Optical Letters*, Vol. 32, No. 4, 2007.
- [18] McLaughlin, R. A., J. Hipwell, G. P. Penney, K. Rhlde, A. Chung, J. A. Noble, and D. J. Hawkes, "Intensity-Based Registration Versus Feature-Based Registration for Neurointerventions," *Proc. Medical Image Understanding and Analysis*, 2001, pp. 69–72.
- [19] Otsu, N., "A Threshold Selection Method from Gray-Level Histograms," *IEEE Transactions on Systems, Man, and Cybernetics*, Vol. 9, 1979, pp. 62–66.
- [20] Xia, Z., X. Huang, X. Zhou, Y. Sun, V. Ntziachristos, and S. T. C. Wong, "Registration of 3-D CT and 2-D Flat Images of Mouse Via Affine Transformation," *IEEE Transactions on Information Technology in Biomedicine*, 2007.
- [21] Storn, R., and K. Price, *Differential Evolution—A simple and Efficient Adaptive Scheme for Global Optimization over Continuous Spaces*, ICSI TECHNICAL Report, TR-95-012, March 1995.
- [22] Isard, M., and A. Blake, "Condensation-Conditional Density Propagation for Visual Tracking," *International Journal of Computer Vision*, Vol. 29, No. 1, 1998, pp. 5–28.
- [23] Florin, C., J. Williams, A. Khamene, and N. Paragios, "Registration of 3-D Angiographic and X-Ray Images Using Sequential Monte Carlo Sampling," *Proc. ICCV Workshop on Computer Vision for Biomedical Image Applications*, 2005.
- [24] Moghari, M. H., and P. Abolmaesumi, "A Novel Incremental Technique for Ultrasound to CT Bone Surface Registration Using Unscented Kalman Filtering," *MICCAI*, 2005, pp. 197–204.

# Processing of In Vivo Fibered Confocal Microscopy Video Sequences

Tom Vercauteren, Nicholas Ayache, Nicolas Savoie, Grégoire Malandain, and Aymeric Perchant

New imaging technologies allow the acquisition of in vivo and in situ microscopic images at the cellular resolution in any part of the living body. The automated analysis of these images raises specific issues that require the development of new image processing techniques. In this chapter, we present some of these issues and describe some recent advances in the field of microscopic image processing, in particular the automatic construction of very large mosaics from times series of microscopic images to enlarge the field of view. This is also a step to bridge the gap between microscopic and higher resolution images like magnetic resonance imaging (MRI), position emission tomography (PET), single photon emission computed tomography (SPECT), or ultrasound (US). This chapter is illustrated with relevant examples for biological or clinical applications.

## 19.1 Motivations

Cancer is a group of diseases characterized by uncontrolled growth and spread of abnormal cells and is the second leading cause of death worldwide. This simple definition of cancer makes it quite clear that cells play a key role in the different stages of cancer development. Some 90% of cancers are preceded by a curable, precancerous, and noninvasive stage that progresses without symptoms over a period of years before reaching a cancerous and invasive stage. In the very first step of epithelial cancer, anomalous cells first appear in the deepest layer of the epithelium, directly above the basal membrane. The basal membrane separates the epithelium from the deeper layers of the tissue and provides a very strong and effective protection. It is approximately located at 100  $\mu\text{m}$  deep from the tissue surface for malpighian epithelium, such as cervix epithelium, and 300  $\mu\text{m}$  for glandular epithelium (i.e., tissue that contains secretion glands such as colon, pancreas, and thyroid). Because there are no blood vessels in the epithelium, epithelial cells cannot spread to other parts of the body. It is thus important to detect anomalies at a very early stage before the cancer becomes invasive (i.e., before the basal membrane is broken).

Since cancer is a disease that affects cells and starts below the surface of the tissue, its early diagnosis requires a subsurface visualization of the tissue at the cellular level. Current in vivo imaging technologies such as MRI, CT, PET, cytometrics, bioluminescence, fluorescence tomography, high-resolution ultrasound,

or SPECT are only capable of producing images at resolutions between  $30\text{ }\mu\text{m}$  and  $3\text{ mm}$ . This range of resolution, while largely acceptable for a vast array of applications, is insufficient for cellular level imaging. On the other side of the resolution range, we find several types of microscopy. The vast majority of microscopes, whether conventional or confocal, are limited for use with cell cultures or ex vivo tissue samples. The tiny fraction of microscopes that are dedicated to in vivo use, and that can function inside the living organism, are called intravital microscopes. These apparatuses are cumbersome, difficult to put into use and restricted to research use, on small animals. They also require a very delicate and specific preparation of the animal that includes installing a window on the animal body whereby the microscope can look through it into the body.

Since these conventional imaging techniques do not allow for a subsurface cellular visualization of the tissue during a clinical procedure, standard cancer detection protocols are not straightforward. For epithelial cancers (i.e., most cancers affecting solid organs), the current medical diagnosis procedure is to take a tissue sample, or biopsy, and to have it examined under the microscope by a pathologist. Most of these biopsy procedures are performed via endoscopy. An endoscope allows for the visualization of the tissue's surface at the macroscopic level. It can neither see below the surface nor provide a microscopic view of the tissue. Because of this drawback, biopsies have to be performed without a relevant visual guide.

Several systems today are under study to help the endoscopist make an informed decision during the diagnostic endoscopic procedure. Fluorescence spectroscopy can be used to detect dysplasia and early carcinoma based on the analysis of fluorescence spectra [1]. Drawbacks of fluorescence spectroscopy lie in the lack of morphological information (i.e., no cell architecture is available from this modality), and the important rate of false positives due to inflammatory processes. Chromoendoscopy combined with magnification endoscopy has become popular as a diagnostic enhancement tool in endoscopy [2]. In particular, in vivo prediction of histological characteristics by crypt or pit pattern analysis can be performed using high-magnification chromoendoscopy [3]. One drawback of this technique is that it cannot provide at the same time the macroscopic view for global localization and the zoomed image. Further innovations for better differentiation and characterization of suspicious lesions, such as autofluorescence endoscopy and narrow band imaging, are currently under investigation. However for targeting both biopsies and endoscopic resection and improving patient care, the ideal situation is to characterize tissues completely in vivo, and thus to visualize cellular architecture. This implies the availability of microscopic imaging during endoscopic examination.

A promising tool to fill this gap is given by fibered confocal microscopy (FCM). The confocal nature of this technology makes it possible to observe subsurface cellular structure, which is of particular interest for early detection of cancer. This technology can serve as a guide during the biopsy and can potentially perform optical biopsies (i.e., a high resolution noninvasive optical sectioning within a thick transparent or translucent tissue) [4].

## 19.2 Principles of Fibered Confocal Microscopy

The ideal characteristics or specifications of a system dedicated to optical biopsies are numerous. The resolution should not exceed a few microns to make it possible to distinguish individual cells and possibly subcellular structures. Above all, the system should be easy to operate, in complete adequateness with the current clinical practice. It should not modify the clinician's procedure and practice. Following a short learning curve due to the manipulation of a new instrument and to the interpretation of images never obtained before in such conditions, no more adaptation should be needed in the clinical setting. In particular, the parts of the system meant to be in contact with the patient should be easily disinfected, using standard existing procedures. Such characteristics are crucial for the development of a system designed to be used in routine practice and not only for clinical research purposes.

### 19.2.1 Confocal Microscopy

Confocal microscopy enables microscopic imaging of untreated tissue without previous fixation and preparation of slices and thus meets some of the operational ease requirements as well as the resolution requirement. The technical principle is based on point-by-point imaging. In a laser scanning confocal microscope, a laser beam is focused by the objective lens into a small focal volume within the imaged sample. A mixture of emitted fluorescence light as well as reflected laser light from the illuminated spot is then recollected by the objective lens. The detector aperture obstructs the light that is not coming from the focal point. This suppresses the effect of out-of-focus points. Depending on the imaging mode, the detector either measures the fluorescence light or the reflected light. The measured signal represents only 1 pixel in the resulting image. In order to get a complete image and perform dynamic imaging, the imaged sample has to be scanned in the horizontal plane for 2-D imaging as well as the vertical plane for 3-D imaging.

Confocal microscopy can be adapted for *in vivo* and *in situ* imaging by schematically inserting a fiber optics link between the laser source and the objective lens.

### 19.2.2 Distal Scanning Fibered Confocal Microscopy

First attempts for developing fibered confocal microscopes (FCM) have historically been made by teams coming from the world of microscopy. The well-known constraints of confocal microscopy were directly transposed to specific architectures for new *endomicroscopes*. With a similar technological core, these designs were in majority based on distal scanning schemes where one fiber serves at the same time as a point source and a point detector. Different architectures have been investigated by several academic groups and commercial companies: distal fiber scanning, distal optical scanning, and MEMs distal scanning. The great advantage of this technology is illustrated by its very good lateral resolution: almost that of

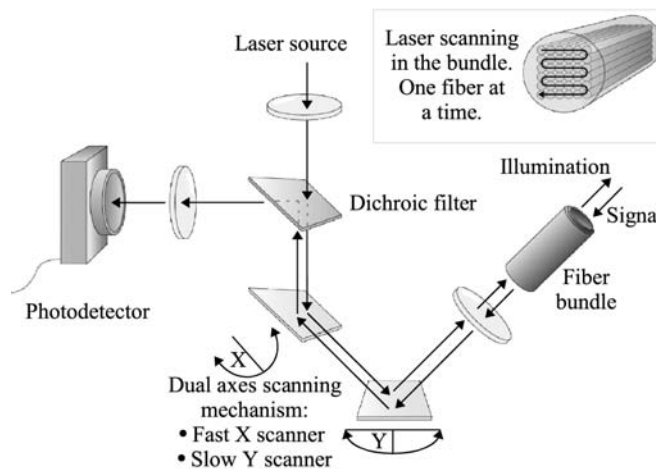


nonfibered systems. The systems developed by Optiscan [5], Olympus [6], Stanford University [7], and others produce very crisp images through only one optical fiber. These systems have first been driven by technological solutions already existing in the microscopy field. Their ability to obtain high-resolution images is one of their strengths. However, image quality is just one clinical requirement among many different needs absolutely necessary for performing in vivo microscopic imaging. Other needs include miniaturization, ease of use, and real-time imaging. One can point out that distal scanning solutions are not able to meet all the demands of a clinical routine examination. Even if they are considered very good imaging solutions, they are often relatively invasive, do not allow for real-time imaging, and are not fully integrated within the current medical routine.

### 19.2.3 Proximal Scanning Fibered Confocal Microscopy

To circumvent the problems of distal scanning FCM, a number of teams have tried to use a proximal scanning architecture [8,9]. In this work, we use a second generation confocal endoscopy system called Cellvizio developed by Mauna Kea Technologies (MKT), Paris, France. MKT's adaptation of a confocal microscope for in situ and in vivo imaging in the context of endoscopy can be viewed as replacing the microscope's objective by a flexible optical microprobe of length and diameter compatible with the working channel of any flexible endoscope (see Color Plate 29). For such purpose, a fiber bundle made of tens of thousands of fiber optics is used as the link between the proximal scanning unit and the microscope objective, remotely placed at the tip of the flexible optical microprobe. The schematic principle of fibered confocal microscopy is shown in Figure 19.1, and typical images are shown in Color Plate 30.

Such a choice has many advantages on the application side [10,11]. Decoupling the scanning function from the imaging one allows the optimization of both functions independently. The distal optics can thus be miniaturized down to a

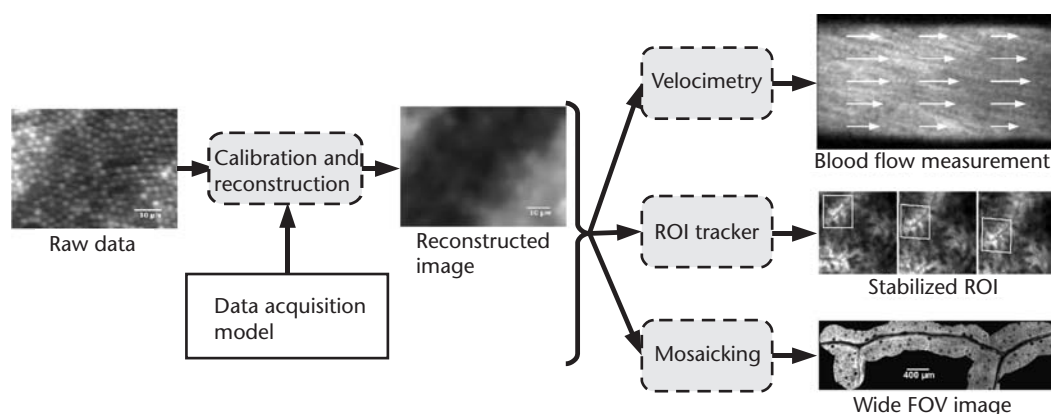


**Figure 19.1** Schematic principle of fibered confocal microscopy.

volume much smaller than what distal scanners can reach now, with very little compromise between optical quality and size. Since the scanner can be allocated an arbitrary volume, well-known and reliable rapid scanning solutions such as resonant or galvanometric mirrors can be used. A purely passive optical microprobe is also more compatible with any cleaning or decontamination procedure that regular clinical use requires. Last but not least, fiber bundles are already existing products, available on the market under different designs and specifications, with no need for specific developments for their use in medical devices. Their association with simplified distal ends enable their manufacturing at a relatively low cost, opening the way to the production of disposable items.

Cellvizio makes it possible to observe subsurface cellular structures with an optical section parallel to the tissue surface at a depth between 0 and 100  $\mu\text{m}$ . The imaging depth cannot be controlled on a single optical microprobe but depends on the specific optical microprobe used. Therefore, the physician will be using different optical microprobes, with different technical specifications, for different applications. Confocal image data is collected at a frame rate of 12 frames per second. Smallest lateral and axial resolutions are 1  $\mu\text{m}$  and 3  $\mu\text{m}$ , respectively. Fields of view ranging from  $130 \times 130 \mu\text{m}$  to  $600 \times 600 \mu\text{m}$  can be obtained thanks to a set of flexible optical microprobes with diameters varying from 0.16 to 1.5 mm. These microprobes can be inserted through the working channel of any endoscope. Note that since the FCM is typically used in conjunction with an endoscope, both macroscopic (endoscope image) and microscopic view (FCM image) can be obtained at the same time. This is illustrated in Figure 19.2. This dual-view facilitates the selection of the area to be biopsied.

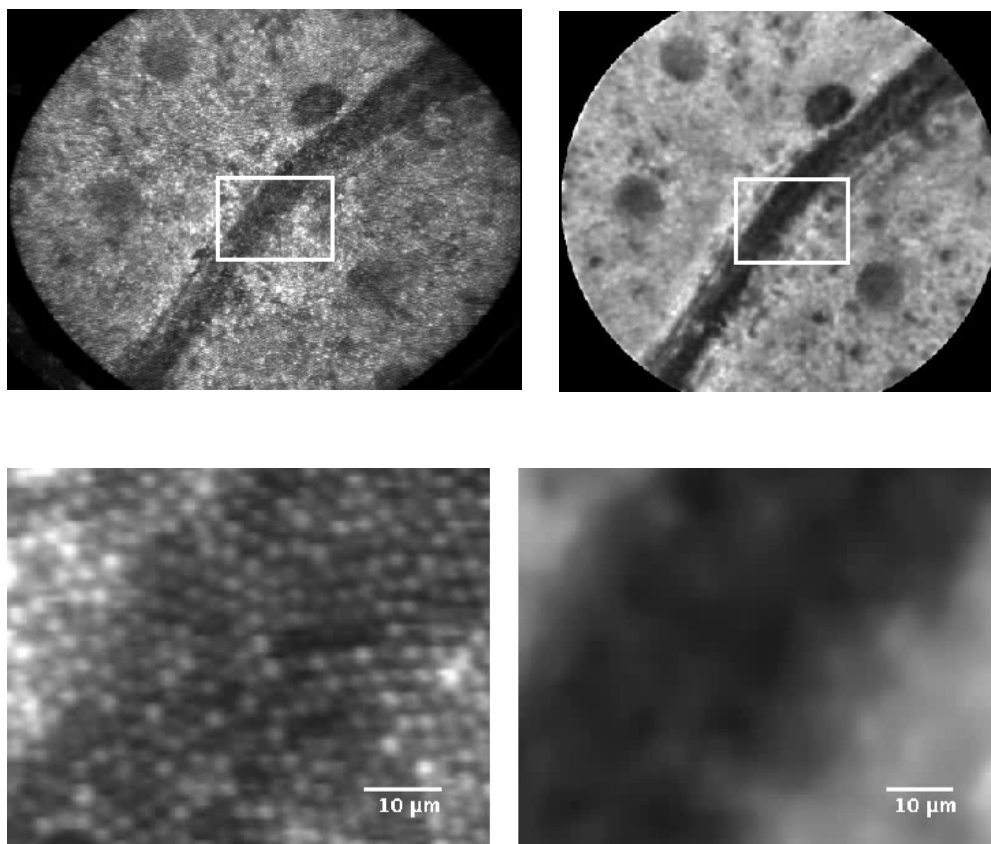
Of course, this approach has well-known drawbacks. Proper light focusing and collection at the distal end of the probe is simplified by the absence of distal scanning means but remains a critical issue. This is particularly true when reaching very small optics dimensions. Because of the passivity of the fiber optics bundle, the system also suffers from some loss of resolution and is limited to 2-D imaging. However, the most widely reported problem of this approach is certainly related



**Figure 19.2** Some of the challenges involved in the processing of in vivo fibered confocal microscopy video sequences.

to the image itself. It often suffers from artifacts and aliasing effects, and, most importantly, always shows a strongly visible honeycomb pattern.

In the sequel, we show that specific image processing schemes can be designed to cope with these artifacts in real time. The control and acquisition software that comes with the Cellvizio is thus an inherent part of the imaging device and helps it move toward a true optical biopsy system. Such a real-time reconstruction algorithm provides smooth-motion video sequences that can be used for more advanced image processing tasks. Figure 19.3 illustrates some of the image processing challenges we address in this chapter. After the presentation of our real-time fiber pattern rejection scheme in Section 19.3, we will focus on three advanced image processing tasks: the measurement of blood flow from single images, the stabilization of a specific region of interest, and the construction of wide-field-of-view image mosaics.



**Figure 19.3** Autofluorescence FCM images of a *Ficus Benjamina* leaf. Left: Raw data. Right: Reconstructed images. Top: Complete images. Bottom: Zoom on rectangle. Note that the nonuniform honeycomb modulation and the geometric distortions on the raw data have been corrected in the reconstructed image.

## 19.3 Real-Time Fiber Pattern Rejection

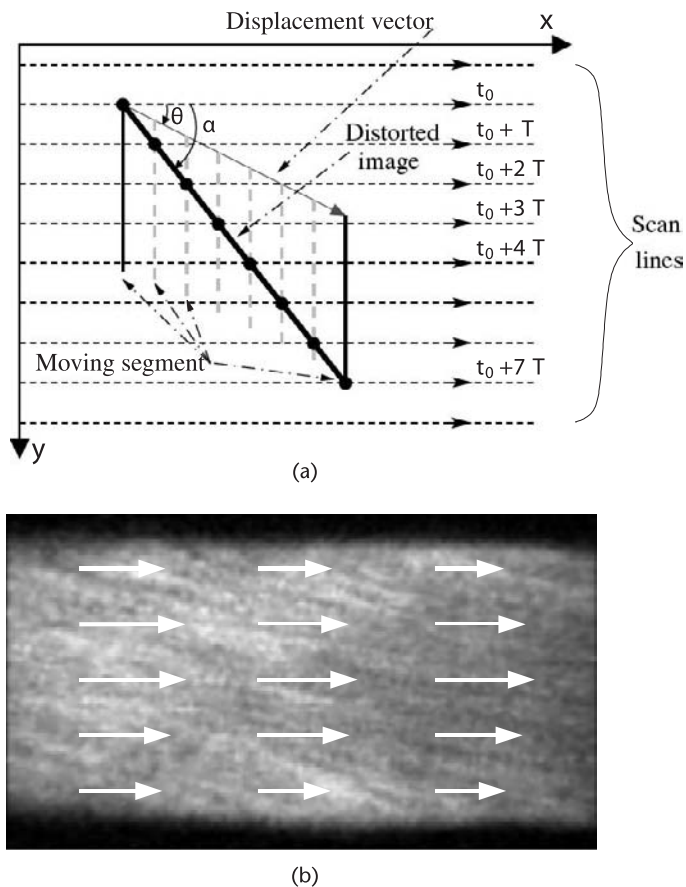
The specific imaging modality we focus on raises specific image processing problems. The nonuniform honeycomb pattern and the geometric distortions that appear on the raw data make it impracticable for user interpretation or for automated analysis if left untreated. Algorithms that take on the image reconstruction task in real time have thus been developed. They provide users with high-quality, smooth-motion video sequences. These are effortlessly interpretable by the professionals who rely on them for diagnosis and readily usable for further automated image processing and analysis. Most of the available methods are only focused on the removal of the honeycomb pattern [12,13] and often only imply performing a simple low pass filtering. Our approach in [14] not only removes the honeycomb pattern but also recovers the true signal that comes back from the tissue and removes the geometric distortions.

### 19.3.1 Calibrated Raw Data Acquisition

Proximal implementation of the scanning function enables the use of very robust and reliable solutions for a fast and accurate scanning. The laser scanning unit performs a scanning of the proximal surface of the flexible optical microprobe with the laser source by using two mirrors. Horizontal line scanning is done using a 4-kHz oscillating mirror, while a galvanometric mirror handles frame scanning at 12 Hz. A custom synchronization hardware controls the mirrors and digitizes, synchronously with the scanning, the signal coming back from the tissue using a mono-pixel photodetector. Cellvizio scanning reproducibility is better than one-half of a fiber diameter. This performance first enables the calibration of the continuous motion of the illuminating spot. It allows us to compensate for the sine-wave shape of the field distortion due to the resonant mirror (fisheye-like effect) and permits a comprehensive rectangular mapping of the field of view. This is mandatory for any further interpretation of the metrics of the images, or any complex combination of individual frames. Second, the proximal scanning is associated with optimized optics that guarantee a very good injection of the laser within the fibers.

When organized according to the scanning, the output of the FCM can be viewed as a raw image of the surface of the flexible optical microprobe. Scanning amplitude and signal sampling frequency have been adjusted to perform a spatial oversampling of the fiber bundle. This is clearly visible on the raw image in Figure 19.4 where one can see the individual fibers composing the bundle. Such an oversampling is needed to distinguish the signal coming from each individual fiber. A typical fiber bundle is composed of 30,000 fiber optics, with a fiber inter-core distance  $d_{ic}$  of 3.3  $\mu\text{m}$  and a fiber core diameter of 1.9  $\mu\text{m}$ . Fiber arrangement is locally quasi-hexagonal but does not show any particular order at larger scales.

Critical elements in the raw image formation process lie in a correct spatial sampling of the flexible optical microprobe but also in the adjustment of the point spread function (PSF) of the system with this spatial sampling. We indeed want to avoid aliasing on the tissue side. When analyzing the system from the point of view of the sampling theory, the PSF corresponds to the lowpass filter and the



**Figure 19.4** Blood flow velocimetry. (a) Imaging of a moving vertical segment by a scanning laser. The segment has a translation movement from the upper left corner to the lower right corner of the image. The segment is first intersected by a scan line at instant  $t_0$  (black disks represent imaged points). The following scan lines image the segment at different positions (dotted segments). The resulting shape is the slanting segment of angle  $\alpha$ . (b) In vivo mouse cremaster microvessel. The arrows are proportional to the estimated velocities computed on a block in the image. Note that, as expected, the velocity does not change along the direction of the microvessel and is maximal at the center.

fiber-optics bundle to the sampling grid. The Nyquist frequency is then given by  $(M/d_{ic})/2$ , where  $M$  is the magnification of the optical head and typically ranges from 1.0 to 2.5. The PSF of the system must therefore satisfy this frequency. As a general rule, the PSF width should approximately be the Nyquist period. The resulting lateral resolution of such a system is then given by  $2 * d_{ic}/M$ . For a user to benefit from the full spatial resolution allowed by the sampling theorem, an optimal fiber pattern rejection and geometric distortion compensation scheme is needed.

### 19.3.2 Real-Time Processing

The task of the on-the-fly image reconstruction module is to restore, at a rate of 12 frames per second, the true physical signal from the raw data by removing the

fiber bundle honeycomb modulation and the scanning distortion. Each fiber of the bundle provides one and only one sampling point on the tissue. Associated with these sampling points comes a signal that depends on the imaged tissue and on the single-fiber characteristics. The role of the image processing is first to build a mapping between the FCM raw image and the fibers composing the flexible optical microprobe. Once this mapping is obtained, characteristics of each fiber are measured and the effective signal coming back from the tissue is estimated. We then have nonuniformly sampled frames, where each sampling point corresponds to a center of a fiber in the flexible optical microprobe. An interpolation algorithm is then used to provide the user with smooth images. Let us now provide some details for each of these steps.

- *Calibration:* As a preliminary step, we build a mapping between the FCM raw image and the fibers composing the flexible optical microprobe. This is achieved by using a segmentation algorithm specifically designed for our fiber-optics bundle. Since we now have access to the position of the fibers within the raw image and to the scanning distortion, it becomes possible to get a point set with the exact, distortion-free, positions of the fibers in the bundle.

This mapping allows us to compute the signal measured by a single-fiber. When combined and averaged together, the almost 15 to 50 pixels corresponding to one single fiber lead to a signal  $I$  with a much better SNR.

Since the signal that is measured by a single fiber depends on the imaged biological sample fluorescence  $\alpha_{flu}$  and on the fiber itself, we need to estimate some characteristics of each single fiber such as its gain and autofluorescence. For this purpose, we acquire an image of a nonfluorescent sample,  $\alpha_{flu} = 0$ , and compute the background signal  $I_b$  measured by each fiber. We also acquire an image of a sample of constant fluorescence,  $\alpha_{flu} = \text{cst}$ , and compute the signal  $I_s$  associated to each fiber.

- *Imaging model:* To represent the relationship between the actual biological sample fluorescence of interest  $\alpha_{flu}$  and the raw signal  $I$  measured by each fiber of the flexible optical microprobe, we use the following model from [14]:

$$I = I_0 \cdot (a \cdot \tau_{inj} \cdot \tau_{col} \cdot \alpha_{flu} + b \cdot \tau_{inj} \cdot \alpha_{autoflu}) \quad (19.1)$$

where  $a$  and  $b$  are constants,  $\tau_{inj}$  and  $\tau_{col}$  are the injection rate and collection rate of the fiber,  $\alpha_{autoflu}$  is the intrinsic auto-fluorescence of the fiber, and  $I_0$  is the intensity of the laser source.

Given the raw signal and the calibration data, the true physical measure  $\alpha_{flu}$  we would like to have cannot be directly estimated. It is however possible to recover it up to a scaling factor with the following equation:

$$I_{restored} = \frac{I - I_b}{I_s - I_b} = K \cdot \alpha_{flu} \quad (19.2)$$

where  $K$  is a constant independent of the considered fiber.



- *Reconstruction*: At this step, we have a restored intensity  $I_{restored}$  for each fiber composing the image bundle. The final process is the interpolation or approximation of this point set into an image on a square grid. The simplest method uses a nearest-neighbor scheme, where all pixels within the area of one fiber are assigned a common value. Other usual algorithms for scattered data interpolation or approximation, such as triangulation-based methods, kriging methods, radial basis functions interpolations, B-spline approximations, natural neighbors, or moving least squares methods (see, for example, [15–17] and references therein) can also be used depending on the required smoothness, approximation order, efficiency, and other numerical issues. We found that for real-time applications, a linear interpolation on triangles provided a good compromise between visual appearance and computational requirements.

## 19.4 Blood Flow Velocimetry Using Motion Artifacts

The analysis of the behavior of blood cells and vessels is a very important topic of physiology research. As such, in vivo measurements made, for example, by intravital fluorescence microscopy have proved since the early 1970s to be crucial to the understanding of the physiology and pathophysiology of microcirculation. More recently, fibered confocal microscopy has been shown to allow for the observation and measurement of several characteristics of microcirculation with the clear benefit of reducing the invasiveness to its bare minimum [18].

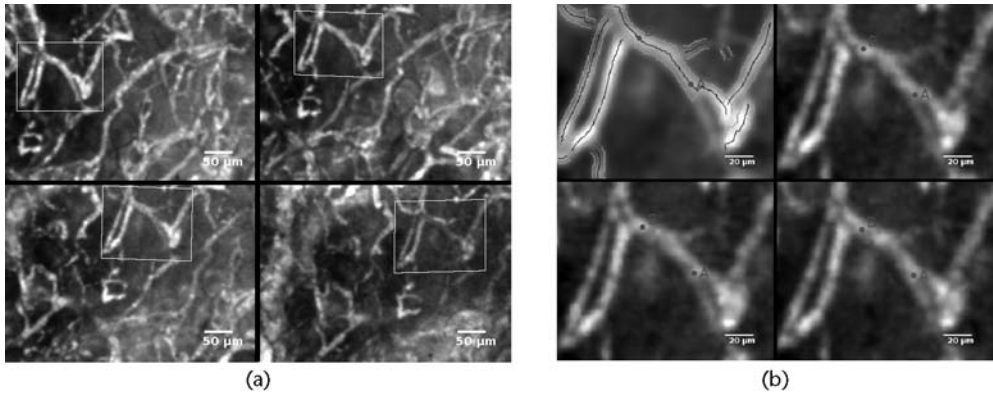
However, as for any quantitative measurement from images, the automated analysis of the data poses a number of new challenges that need to be addressed with specific solutions. In this section we show an image processing algorithm proposed in [19] dedicated to the velocimetry of blood flow imaged with FCM.

### 19.4.1 Imaging of Moving Objects

An interesting point of scanning imaging devices is that the output image is not a representation of a given instant, but a juxtaposition of points acquired at different times [19]. Consequently, if objects in the field of view are moving with respect to the flexible optical microprobe, what we observe is not a frozen picture of these objects, but a skewed image of them. Each scan line indeed relates to a different instant, and the objects move between each scan line.

From the analysis of the laser scanning in Section 19.3.1, it is seen that the scanning movement can be decomposed into a fast horizontal sinusoidal component and a slow linear uniform vertical component. Horizontally, the imaging is done only on the central part of the trajectory, where the spot velocity is maximal and nearly constant. Since in this part, the spot horizontal velocity  $V_x$  ( $> 5$  m/s) is several orders of magnitude higher than both the spot vertical velocity  $V_y$  ( $\sim 2$  mm/s) and the velocity  $V_c$  of observed red blood cells (RBCs) ( $< 50$  mm/s), two approximations can be made: the scan lines are horizontal and the time needed by the spot to cross the imaged part is negligible, meaning that the objects are consid-





**Figure 19.5** (a) ROI tracking using affine transformations: 4 frames (index 1, 51, 101, 151) from the same sequence are displayed with the registered ROI. Complete sequence includes 237 frames. (b) Upper-left: vessel detection on the temporal mean frame after stabilization. Other images: three contiguous frames of the stabilized sequence (12 Hz). Blood velocity was acquired on the medial axis segment.

ered motionless during a scan line. This amounts to assuming that the horizontal spot velocity is infinite.

Let us consider a standard 2-D+t volume  $V(x, y, t)$ . Without scanning, this volume will be imaged by 2-D slices  $V(x, y, t_0)$  at different instants  $t_0$ . With scanning, the process of image formation comes down to imaging the plane  $V(x, y, t_0 + y/V_y)$ . Figure 19.5(a) presents what will be observed when imaging a vertical segment moving horizontally with respect to the flexible optical microprobe.

### 19.4.2 Velocimetry Algorithm

Classical methods for velocity measurements of blood cells in microvessels are often based on the processing of 2-D temporal image sequences obtained in the field of intravital microscopy. Line shift diagram, spatio-temporal analysis, or blood cell tracking are used in such setting to process the sequences generated by CCD-based video microscopes [20].

In contrast, the method presented in [19] uses very specific information about the imaging device. By the combination of its own movement and the laser scanning, a red blood cell should appear almost as a slanting segment, whose length and orientation with respect to the scanning and the microvessel are dictated by its velocity. This specificity can be used to measure the velocity of blood cells in microvessels from single images. The method exploits the motion artifacts produced by the laser scanning. Although velocity can be estimated from a single image, temporal sequences can then be exploited to increase the robustness and accuracy of the estimation.

To get an idea of how the algorithm works, we model a imaged red blood cell as a disk of radius  $R$ . This assumption is rather realistic since the diameter of a typical mammal RBC is 5–9  $\mu\text{m}$  and can thus only be seen by a few fibers in the flexible optical microprobe. Let us assume that the RBC has a linear uniform

movement described by a velocity  $V_c$  and a trajectory angle  $\theta$ . Let us also assume that the RBC is imaged by a scanning laser whose horizontal velocity is infinite and vertical velocity is  $V_y$  so that the disk will be distorted by the scanning imaging.

Let us look at the equation of the distorted envelope (i.e., the intersection between the disk envelope and the scanning spot). The points  $(x_c, y_c)$  of the envelope of the disk at the instant  $t$  verify the equation:

$$\frac{(x_c - V_c \cdot t \cdot \cos\theta)^2}{R^2} + \frac{(y_c - V_c \cdot t \cdot \sin\theta)^2}{R^2} = 1 \quad (19.3)$$

The vertical position  $y_s$  of the spot is given by  $y_s = V_y t$ . The horizontal spot velocity is supposed infinite, which is why the intersections of the spot trajectory and the envelope are the intersections of the envelope with the line of ordinate  $y_s$ . Using  $t = y_s/V_y$  in (19.3), we see that the distorted envelope is in fact an ellipse. The moving disk will thus appear as an ellipse in the output image. The angle  $\alpha$  (modulo  $\pi/2$ ) and length  $L$  of the major ellipse axis are given by:

$$\tan 2\alpha = \frac{2\cos\theta}{V_r - 2\sin\theta} \quad (19.4)$$

$$L = \frac{2R\sqrt{2}}{\sqrt{V_r^2 - 2V_r \cdot \sin\theta + 2 - V_r \sqrt{V_r^2 - 4V_r \cdot \sin\theta + 4}}} \quad (19.5)$$

with  $V_r = V_c/V_y$ .

Equations (19.4) and (19.5) link the velocity and angle  $\theta$  of the moving disk to the observed values  $L$  and  $\alpha$ . Given  $L$  and  $\alpha$ , the inversion of the relations gives two possible solutions for  $V_c$  and  $\theta$ . This implies that a single output image only allows us to retrieve the velocity and trajectory angle of the disk with an ambiguity between two possibilities. The ambiguity could be removed by considering two scans, one top-down and another bottom-up, for example.

One difficulty lies in using  $L$  because extracting individual shapes in images like the ones of Figure 19.5(b) seems unlikely. Only the orientation  $\alpha$  can be retrieved, which forbids the use of (19.5). The solution is to suppose that the angle of trajectory  $\theta$  is known (for example, in Figure 19.5(b), the trajectory of the RBCs is supposed colinear to the edges of the vessel). With this hypothesis, (19.4) allows for the determination of the disk velocity.

From the images, it is clear that the segmentation of individual traces is not possible. In fact, in Figure 19.5(b) as the plasma is marked by a fluorescent dye, distorted RBC shapes are expected to appear as dark trails. But what we observe seem to be bright trails. Our explanation is that there are so many dark trails that it induces a contrast inversion. Given the RBC blood concentration (i.e., 4–5 million per microliter of blood), about 1,000 RBCs should be in this image. What we see are thus the bright interstices between the dark trails. It is the slope of these white ridges that we extract from the images in order to estimate the velocity through the orientation of the ridges. The extraction algorithm itself is based on a combination of ridge detection and robust estimators.

Our algorithm assumes that the ridges are tubular-like structures with a Gaussian profile of standard deviation  $\sigma_0$ . It proceeds in four steps. First, we enhance the horizontal edges by computing the vertical gradient component  $I_y(x,y)$  of the image  $I$ . Since ridges are composed of points that are at equal distance of a positive gradient response and a negative gradient response, the medialness response  $R(x,y) = I_y(x,y + \sqrt{\sigma_0^2}) - I_y(x,y - \sqrt{\sigma_0^2})$  of [21] should be maximal on the ridges. Our second step uses a high threshold on  $R(x,y)$  to compute regional maxima on each connected component of the thresholded image. In the third step, regional maxima are used as seeds to extend the ridges. This extension is done by following the local maxima of  $R(x,y)$  until a low threshold is reached. This approach is similar to doing a hysteresis thresholding in a privileged direction. Finally, a line is robustly fitted on each extracted ridge to measure the slope.

### 19.4.3 Results and Evaluation

In the field of biomedical imaging, the issue of validation for image processing tasks is essential but is often a difficult problem that needs very specific approaches in order to be addressed. In this work, several experiments have been conducted to estimate the correctness of the method. First, a numerical simulator was developed. It models the acquisition of the Cellvizio and simulates a simple laminar flow of RBCs where RBCs are represented by a realistic 3-D model that departs from the disk model we used for the theoretical part. RBC velocities are randomly set according to a normal distribution. Applying the proposed method and taking the median of the estimated velocities leads to a velocity estimation within a 6% margin error. Second, we applied our method to a sequence of 40 images obtained on real acquisitions of mouse cremaster microvessel. For each image, we computed the median of estimated velocities. Since the actual velocity of RBCs in the vessel is unknown, we cannot estimate the correctness of the estimation; nevertheless, this allows us to test the stability and robustness of the method. For the whole sequence, the mean of the median velocity of each image is 7.18 mm/s and the standard deviation is 0.7 mm/s. This result tends to prove that our velocity estimation is robust and stable along the sequence. Our most advanced validation experiment uses an inhouse-built hydraulic circuit. Water with fluorescent balls, whose size is comparable to an RBC, flows in this circuit and the flow velocity is adjustable. This system lets us compare our velocity estimations with the velocity computed from the rate of flow of the circuit. This serves as a validation of our method. We do not have access to the precision of the velocity computed from the rate of flow, but both methods agree with a mean relative error of 16%.

Our velocimetry method has been applied, in Figure 19.5(b), to a real acquisition of mouse cremaster microvessel. The image is divided into a set of blocks. For each block, a robust estimation of the velocity is computed. We can see that our method is able to recover the red blood cell velocity profile within the microvessel. As expected, the velocity does not change along the direction of the microvessel and is maximal at the center.

As this approach is based on a line scan interaction between the laser scanning and the moving cells, higher velocity can be measured than with methods based

on analysis of successive temporal frames. When most systems are limited to the measurement of red blood cell velocity inferior to 2 or 5 mm/s, the presented method allows the measurement of velocities up to 30 mm/s.

## 19.5 Region Tracking for Kinetic Analysis

The high-resolution images provided by Cellvizio are mostly acquired on living organs; therefore, specific image processing tools are required to cope with the natural movements of the tissues being imaged. Moreover, if the images of a sequence were stabilized, measurements of various image parameters would become possible or easier and could be carried out for many applications, such as gene expression monitoring, drug biodistribution, or pharmacokinetics.

Due to the very specific type of images generated by Cellvizio, classical image stabilization and registration techniques could not be applied here. As a result, we have developed a dedicated region of interest (ROI) tracking tool that takes into account the characteristics of Cellvizio and enables an automatic registration, analysis, and quantification on sequences of images [22].

In Section 19.4, we have shown that the motion of the imaged objects with respect to the optical microprobe led to some motion artifacts. The velocimetry took advantage of these artifacts to enable blood flow measurement. However, in most cases motion artifacts would simply induce possible misquantifications. A high frame rate can sometimes compensate for the resulting distortions, but when the frame rate cannot be increased, motion artifacts can in general not be avoided. We show here that the knowledge we have about the motion distortion can also be used to get an efficient motion compensation algorithm. We address the case where a user wants to focus on a small region of the living tissue that is difficult to stabilize mechanically. For instance, in vivo and in situ acquisition on the liver, the bladder, or even the heart can be unstable. Such organs receive a growing interest among biologists to assess pharmacokinetics parameters of molecules, to screen the changing morphology of the anatomy, or to measure biodistribution parameters.

### 19.5.1 Motion Compensation Algorithm

Let us suppose that the motion of the imaged object with respect to the optical microprobe between two contiguous frames is a simple translation at speed  $\tilde{\eta} = [\tilde{\eta}^x, \tilde{\eta}^y]$ . A scanned line with vertical position  $y$ , will be sampled at the time  $t(y) = t(0) + \frac{y}{V_y}$ . During the scanning, a point  $p = [x, y] \in I$  in the image coordinate system will be sampled at position  $p_d = [x_d, y_d]$  in the object coordinate system. We note  $\eta = \frac{\tilde{\eta}}{V_y}$  the normalized speed for the frame scanning. The position  $p_d$  of the imaged object point is given by

$$\begin{aligned} x_d &= x + (t(x) - t(0))\tilde{\eta}^x = x + \frac{y}{V_y}\tilde{\eta}^x = x + \eta^x y \\ y_d &= y + (t(y) - t(0))\tilde{\eta}^y = y + \frac{y}{V_y}\tilde{\eta}^y = (1 + \eta^y)y \end{aligned}$$

For the  $k$ th frame, this linear transformation between the image coordinate system and the object coordinate system is noted  $v_k$ . Each point  $p$  of a frame  $I_k$  is mapped to a reference space coordinate system by the transformation  $f_k : p \rightarrow p_{ref}$  such that

$$f_k(p) = r_k \circ v_k(p)$$

where  $r_k$  is a rigid body transformation, and  $\circ$  denotes the composition of spatial transformations. Between two frames  $j$  and  $k$ , the spatial transformation is thus given by

$$f_{j,k}(p) = v_j^{-1} \circ r_j^{-1} \circ r_k \circ v_k = v_j^{-1} \circ r_{j,k} \circ v_k \quad (19.6)$$

In order to recover the alignment between the images and the motion distortions, one could try to register the frames using the complete transformation model. However, this would imply ignoring the relationship between positions and velocities and would thus not really be robust. We therefore choose to compute the velocities using the displacements information only. Using finite difference equations, we can relate the global positioning and the velocity  $\eta$ . The estimation of the velocities is done using only the translation part of  $r_{j,k}$ . This velocity is used in the following algorithm to compensate for the scanning distortions. For each contiguous frames the following steps are performed:

1. Estimate the translation using a 2-D normalized cross correlation.
2. Estimate the velocity from the translation.
3. Compute the distortion transformation.
4. Optimize the rigid transformation.

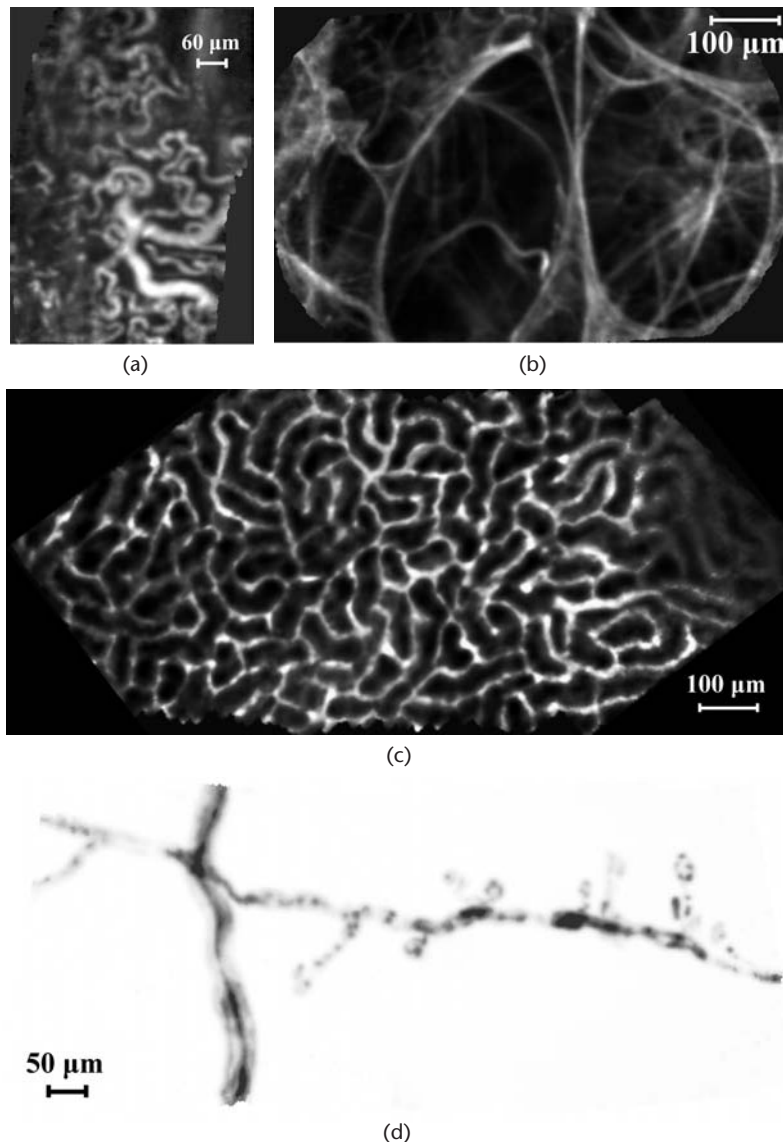
### 19.5.2 Affine Registration Algorithm

Using Cellvizio, the handheld optical microprobe can freely glide along the soft tissue while keeping contact with it. The spatial transformation between two frames will thus be composed of a translation, a possible rotation, and even a little scaling if the tissues are compressed. Another representation of the frame-to-frame spatial transformation is thus given by an affine transformation model, which is a generalization of the model in (19.6).

The image registration scheme we use is based on a minimization of the sum of squared differences between the intensities of the current image  $I_k$  and a reference image  $I$ :  $\sum_p |I(p) - I_k(f_k(p))|^2$ , with  $f_k$  being an affine transformation. To ensure a fast convergence in the optimization procedure, we initialized each transformation by the best translation found by a normalized cross correlation and use a fast and efficient optimizer. The efficient second-order minimization (ESM) scheme of [23] provides excellent results for real-time robotic applications. We have adapted it to use an affine transformation instead of a projective one [24]. The main advantage of this algorithm is to provide a true second-order optimization scheme with the complexity of a first-order optimization scheme such as Gauss-Newton. Of course, other optimizers could be used.

### 19.5.3 Application to Cell Trafficking

In [22], this ROI tracking was used to assess cell trafficking in a capillary. The aim is to measure a slow blood velocity in a capillary. For this range of blood velocity and this size of capillary (as small as a single RBC), the previous velocimetry



**Figure 19.6** Mosaics using different types of images acquired with Cellvizio. (a) In vivo tumoral angiogenesis in mouse with FITC-Dextran high MW (21 input frames). (Courtesy of A. Duconseille and O. Clément, Université Paris V, Paris, France.) (b) Ex vivo autofluorescence imaging in human lung (15 input frames). (Courtesy of Dr. P. Validire, Institut Mutualiste Monsouris, Paris, France.) (c) Microcirculation of the peritubular capillaries of a live mouse kidney with FITC-Dextran high MW (31 input frames). (d) Dendritic receptors in a live Thy1-YFP mouse (70 input frames). Courtesy of I. Charvet, P. Meda, CMU, Geneva, Switzerland and L. Stoppini, Biocell Interface, Geneva, Switzerland.)



algorithm could not be used since single RBCs can be seen on the images. On the other hand, more conventional methods using temporal image sequences could not directly be used because of the unstable nature of many imaged tissues, such as tumoral grafts. This is why we choose to first track a given region of interest and then use a cross-correlation scheme on the stabilized sequence. The user can select manually a rectangular ROI on the image. Figure 19.6(a) shows the tracking of this region on a sequence acquired with a handheld probe on a tumoral skin xenograft. Vessels were stained using dextran fluorescein from Invitrogen.

On the temporal mean frame of the stabilized sequence, we have segmented the vessels using a 2-D adaptation of the multiscale tubular vessel detection algorithm of [21]. We used this same adaptation on the same type of images in [25] to perform morphometric analysis of the vascular network. The upper-left image of Figure 19.6(b) shows the result of the detection: the medial axis and the vessel borders. The medial axis of the vessel in the ROI was used to extract the vessel intensity in the center line. The normalized cross correlation of these two lines allows for the estimation of the velocity of the blood in the capillary.

The range of velocities that can be addressed depends on the scanning period and amplitude. We here give some typical values for Cellvizio. The velocity precision is given by the minimum translation observable between two frames:  $\delta v = 0.02$  mm/s. The velocity interval computed using a maximum detectable translation of half the horizontal field of view is  $[0, 7.2]$  mm/s.

An additional interesting feature of this tracker is that it also enables the reconstruction of images on the region of interest with an enhanced resolution. This is made possible when the kinetic of the signal is slow enough, thanks to the noise reduction provided by the processing of several registered noisy images of the same region and to a small remaining aliasing of the input images.

## 19.6 Mosaicking: Bridging the Gap Between Microscopic and Macroscopic Scales

We demonstrated that fibered confocal microscopy can unveil in real time the cellular structure of the observed tissue. However, as interesting as dynamic sequences may be during the time of the medical procedure or biological experiment, there is a need for the expert to get an efficient and complete representation of the entire imaged region. A physician needs, for example, to actually add still images in the patient's medical record.

Image sequence mosaicking techniques are used to provide this efficient and complete representation and widen the field of view (FOV). Several possible applications are targeted. First of all, the rendering of wide-field microarchitectural information on a single image will help experts to interpret the acquired data. This representation will also make quantitative and statistical analysis possible on a wide field of view. Moreover, mosaicking for microscopic images is a means of filling the gap between microscopic and macroscopic scales. It allows mul-



timodality and multiscale information fusion for the positioning of the optical microprobe.

Classical mosaicking algorithms do not take into account the characteristics of fibered confocal microscopy—namely, motion distortions, irregularly sampled frames, and nonrigid deformations of the imaged tissue. In this section, we present some key points of the algorithms we developed in [26,27] to address this problem.

### 19.6.1 Overview of the Algorithm

Our approach in [27] is based on a hierarchical framework that is able to recover a globally consistent alignment of the input frames onto a reference coordinate system, to compensate for the motion-induced distortion of the input frames and to capture the nonrigid deformations of the tissue. Similarly to address the velocimetry problem and the region of interest tracking problems presented earlier, we use the specificity of FCM to model and use the relationship between the motion distortions and the motion of the optical microprobe. As in (19.6), the displacement of the optical microprobe across the tissue can be described by a rigid shift denoted by  $r_n$ . The motion distortion can be modeled by a linear transformation  $v_n$ . Finally, due to the interaction of the contact optical microprobe with the soft tissue, a small nonrigid deformation  $b_n$  appears. The frame-to-reference mappings are thus modeled by

$$f_n(p) = b_n \circ r_n \circ v_n(p) \quad (19.7)$$

The goal of the mosaicking algorithm is to recover these transformations for each frame.

A typical approach for dealing with the estimation of such complex models is to have a hierarchical, coarse-to-fine approach. We therefore focus on a method that iteratively refines the model while always keeping the global consistency of the estimated frame-to-reference transformations.

#### 19.6.1.1 From Local to Global Alignment

We start by assuming that the motion distortions as well as the nonrigid tissue deformations can be ignored. By making the reasonable assumption that consecutive frames are overlapping, an initial estimate of the global rigid mappings can be obtained by using a rigid registration technique to estimate the motion between the consecutive frames. Global alignment is then obtained by composing the local motions. This initial estimate suffers from a well-known accumulation of error problem that needs to be taken into account.

The first loop of our algorithm alternates between three steps. The first step of this loop assumes that the motion distortions have been correctly estimated and registers pairs of distortion-compensated frames under a rigid body transformation assumption. The second step of the loop uses these local pairwise registration results to make a globally consistent estimation of the rigid mappings  $r_n$ . The third step uses the relationship between the motion and the motion distortions to provide an updated and consistent set of rigid mappings and motion compensations.

Let us focus on the second step of the first loop. During this local-to-global alignment scheme, we use all available pairwise rigid registration results to estimate a set of globally consistent transformations. A sound choice is to consider a least-square approach. However the space of rigid body transformations is not a vector space but rather a Lie group that can be considered as a Riemannian manifold. Classical notions using distances are therefore not trivial to generalize. In our work, we propose to cast this problem into an estimation problem on a Lie group.

By using the log map, we can define the (geodesic) distance between two rigid body transformations  $r$  and  $s$  as

$$\text{dist}(r, s) = \text{dist}\left(\text{Id}, r^{-1} \circ s\right) = \|\log_{\text{Id}}(r^{-1} \circ s)\| \quad (19.8)$$

In order to estimate the true rigid body transformations  $[r_1, \dots, r_N]$ , we choose to minimize the distance between the observations  $r_{j,i}^{(\text{obs})} \in \Theta$  and the transformations  $r_j^{-1} \circ r_i$  predicted by our model:

$$[r_1^*, \dots, r_N^*] = \arg \min_{[r_1, \dots, r_N]} \frac{1}{2} \sum_{(i,j) \in \Theta} \text{dist}(r_j^{-1} \circ r_i, r_{j,i}^{(\text{obs})}) \quad (19.9)$$

Note that further improvements to this formulation can be made. Mahalanobis distance and robust statistics can be used. It is also possible to weight the different registration results. An efficient optimization scheme is proposed in [26] to solve this estimation problem.

#### 19.6.1.2 Mosaic Construction and Tissue Deformation Compensation

Once a globally consistent set of transformations is found, the algorithm constructs a point cloud by mapping all observed sampling points onto a common reference coordinate system. An efficient scattered data fitting technique is then used on this point cloud to construct an initial mosaic. The residual nonrigid deformations are finally taken into account by a second loop in our algorithm that iteratively registers an input frame to the mosaic and updates the mosaic based on the new estimate of the frame-to-mosaic mapping. The nonrigid registration can typically use the diffeomorphic registration scheme we present in [28].

Let us now get some insight into the efficient scattered data fitting technique we developed. Let  $\{(p_k, i_k) \in \Omega \times \mathbb{R}\}$  be the set of sampling points and their associated signal. Our goal is to get an approximation of the underlying function on a regular grid  $\Gamma$  defined in  $\Omega$ . The main idea is to use a method close to Shepard's interpolation. The value associated with a point in  $\Gamma$  is a weighted average of the nearby sampled values,

$$\hat{I}(p) = \sum_k w_k(p) i_k = \sum_k \frac{h_k(p)}{\sum_l h_l(p)} i_k \quad (19.10)$$

The usual choice is to take weights that are the inverse of the distance,  $h_k(p) = \text{dist}(p, p_k)^{-1}$ . In such a case we get a true interpolation [16]. An approximation is obtained if a bounded weighting function  $h_k(p)$  is chosen. We choose a Gaus-

sian weight  $h_k(p) = G(p - p_k) \propto \exp(-||p - p_k||^2/2\sigma_a^2)$  and (19.10) can thus be rewritten as

$$\hat{I}(p) = \frac{\sum_k i_k G(p - p_k)}{\sum_k G(p - p_k)} = \frac{\left[ G \star \sum_k i_k \delta_{p_k} \right](p)}{\left[ G \star \sum_k \delta_{p_k} \right](p)} \quad (19.11)$$

where  $\delta_{p_k}$  is a Dirac distribution centered at  $p_k$ , and  $\star$  denotes a spatial convolution. We can see from this formulation that our reconstruction method thus only needs two convolutions (Gaussian smoothing) and one division, which makes it very efficient.

### 19.6.2 Results and Evaluation

As mentioned earlier, the issue of algorithm validation is critical in the field of biomedical imaging and usually requires dedicated and sophisticated approaches. In order to evaluate our global positioning and motion distortion-compensation framework, image sequences of a rigid object were acquired in [27]. The object needs to have structures that can be seen with the fibered confocal microscope. For the mosaicking to be of interest, we also need to see shapes whose sizes are larger than the field of view of our imaging device. We therefore choose to image a silicon wafer.

A fair evaluation can only be made by comparing the output of the algorithm with independent information. Apart from simulated data, a ground truth of the imaged region is very difficult to get. Even with a standard microscope having a comparable resolution but a greater FOV, it is not easy to see on the wafer whether the exact same region is being imaged or not. However, in addition to the mosaic, our algorithm also provides an estimation of the motion of the flexible microprobe. The evaluation framework we designed compares this estimation with a gold standard given by a computer numerical control (CNC) milling machine. The CNC milling machine is used to hold the flexible microprobe and prescribe, with respect to the silicon wafer, a motion whose accuracy is of the order of magnitude of the apparent fiber intercore distance  $d_{ic}$ . We find that the motion recovered by our algorithm agrees with the prescribed one within a 3% error margin.

From the application point of view, mosaicking for fibered confocal microscopy provides a step to bridge the gap between microscopic and macroscopic scales. Cellvizio offers a new way to image and characterize several types of tissue. In many cases, mosaicking can help move beyond the limitations of FCM by offering an extended field of view. Our method has been successfully applied to many types of sequences acquired in both small animal and human tissue. We provide some insight of this by showing the result of our algorithm on some typical images.

Figure 19.6(a) shows a mosaic constructed from 21 input frames, each with a FOV of  $417 \mu\text{m} \times 297 \mu\text{m}$ . On this figure, we can see mouse tumoral angiogenesis. The need for in vivo imaging is urgent in this field. It can indeed help assess the efficiency of angiogenesis therapy [29]. Mosaicking techniques can further help in getting objective quantitative measurements. The result shown in Figure 19.6(b) is of much clinical interest, since it proves that obtaining a microscopic image of hu-

man lung tissue without any staining is feasible. Our mosaicking algorithm pushes this interest one step further by showing multiple alveolar structures in a single image. The mosaic in Figure 19.6(c), arising from 31 input frames, shows the tubular architecture of the kidney. In this setting, mosaicking could help getting trustful statistical shape measurements. Figure 19.6(d) shows the ability of Cellvizio to image nervous tissue down to the dendritic endings and shows how mosaicking can help see many of those dendritic endings simultaneously. Seventy input frames all with a FOV of  $397 \mu\text{m} \times 283 \mu\text{m}$  were used to produce the mosaic.

## 19.7 Conclusions

New imaging technologies such as fibered confocal microscopy raise several new image processing and image analysis challenges that cannot readily be addressed by using classical approaches. In this chapter, several dedicated tools were presented. By taking into account the specificity of this imaging modality, the automated algorithms we developed lead to more physiologically relevant data and easier interpretation by the experts, and provide an important step to bridging the gap between microscopic and higher resolution images like MRI, PET, SPECT, or US.

## References

- [1] Bourg-Heckly, G., J. Blais, J. J. Padilla, O. Bourdon, J. Etienne, F. Guillemain, and L. Lafay, "Endoscopic Ultraviolet-Induced Autofluorescence Spectroscopy of the Esophagus: Tissue Characterization and Potential for Early Cancer Diagnosis," *Endoscopy*, Vol. 32, No. 10, 2000, pp. 756–765.
- [2] Sharma, P., A. P. Weston, M. Topalovski, R. Cherian, A. Bhattacharyya, and R. E. Sampliner, "Magnification Chromoendoscopy for the Detection of Intestinal Metaplasia and Dysplasia in Barrett's Oesophagus," *Gut*, Vol. 52, January 2003, pp. 24–27.
- [3] Kudo, S.-E., C. A. Rubio, C. R. Teixeira, H. Kashida, and E. Kogure, "Pit Pattern in Colorectal Neoplasia: Endoscopic Magnifying View," *Endoscopy*, Vol. 33, 2001, pp. 367–373.
- [4] Meining, A., M. Bajbouj, S. Delius, and C. Prinz, "Confocal Laser Scanning Microscopy for In Vivo Histopathology of the Gastrointestinal Tract," *Arab Journal of Gastroenterology*, Vol. 8, March 2007, pp. 1–4.
- [5] Hoffman, A., M. Goetz, M. Vieth, P. R. Galle, M. F. Neurath, and R. Kiesslich, "Confocal Laser Endomicroscopy: Technical Status and Current Indications," *Endoscopy*, Vol. 38, December 2006, pp. 1275–1283.
- [6] Inoue, H., S. ei Kudo, and A. Shiokawa, "Technology Insight: Laser-Scanning Confocal Microscopy and Endocytoscopy for Cellular Observation of the Gastrointestinal Tract," *Nature Clinical Practice: Gastroenterology & Hepatology*, Vol. 2, January 2005, pp. 31–37.
- [7] Wang, T. D., M. J. Mandella, C. H. Contag, and G. S. Kino, "Dual-Axis Confocal Microscope for High-Resolution In Vivo Imaging," *Optics Letter*, Vol. 28, March 2003, pp. 414–416.
- [8] Sokolov, K., J. Aaron, B. Hsu, D. Nida, A. Gillenwater, M. Follen, C. MacAulay, K. Adler-Storthz, B. Korgel, M. Descour, R. Pasqualini, W. Arap, W. Lam, and

- R. Richards-Kortum, "Optical Systems for In Vivo Molecular Imaging of Cancer," *Technology in Cancer Research & Treatment*, Vol. 2, December 2003, pp. 491-504.
- [9] Sung, K.-B., C. Liang, M. Descour, T. Collier, M. Follen, and R. Richards-Kortum, "Fiber-Optic Confocal Reflectance Microscope with Miniature Objective for In Vivo Imaging of Human Tissues," *IEEE Transactions on Biomedical Engineering*, Vol. 49, October 2002, pp. 1168-1172.
  - [10] Flusberg, B. A., E. D. Cocker, W. Piyawattanametha, J. C. Jung, E. L. M. Cheung, and S. M. J., "Fiber-Optic Fluorescence Imaging," *Nature Methods*, Vol. 2, December 2005, pp. 941-950.
  - [11] Helmchen, F., "Miniaturization of Fluorescence Microscopes Using Fibre Optics," *Experimental Physiology*, Vol. 87, November 2002, pp. 737-745.
  - [12] Winter, C., S. Rupp, M. Elter, C. Münzenmayer, H. Gerhäuser, and T. Wittenberg, "Automatic Adaptive Enhancement for Images Obtained with Fiberscopic Endoscopes," *IEEE Transactions on Biomedical Engineering*, Vol. 53, October 2006, pp. 2035-2046.
  - [13] Elter, M., S. Rupp, and C. Winter, "Physically Motivated Reconstruction of Fiberscopic Images," in *Proceedings of the 18th International Conference on Pattern Recognition (ICPR'06)*, (Hong Kong), August 2006, pp. 599-602.
  - [14] Le Goualher, G., A. Perchant, M. Genet, C. Cavé, B. Viellerobe, F. Berier, B. Abrat, and N. Ayache, "Towards Optical Biopsies with an Integrated Fibered Confocal Fluorescence Microscope," *Proceedings of the 7th International Conference on Medical Image Computing and Computer Assisted Intervention (MICCAI'04)* (C. Barillot, D. R. Haynor, and P. Hellier, eds.), Vol. 3217 of *Lecture Notes in Computer Science*, 2004, pp. 761-768.
  - [15] Lodha, S. K., and R. Franke, "Scattered Data Techniques for Surfaces," in *Dagstuhl '97, Scientific Visualization*, Washington, D.C., pp. 181-222, IEEE Computer Society, 1999.
  - [16] Amidror, I., "Scattered Data Interpolation Methods for Electronic Imaging Systems: A Survey," *Journal of Electronic Imaging*, Vol. 11, April 2002, pp. 157-176.
  - [17] Lee, S., G. Wolberg, and S. Y. Shin, "Scattered Data Interpolation with Multilevel B-Splines," *IEEE Transactions on Visualization and Computer Graphics*, Vol. 3, No. 3, 1997, pp. 228-244.
  - [18] Laemmel, E., M. Genet, G. Le Goualher, A. Perchant, J.-F. Le Gargasson, and E. Vicaut, "Fibered Confocal Fluorescence Microscopy (Cell-viZio™) Facilitates Extended Imaging in the Field of Microcirculation," *Journal of Vascular Research*, Vol. 41, No. 5, 2004, pp. 400-411.
  - [19] Savoie, N., G. Le Goualher, A. Perchant, F. Lacombe, G. Malandain, and N. Ayache, "Measuring Blood Cells Velocity in Microvessels from a Single Image: Application to *in vivo* and *in situ* Confocal Microscopy," *Proceedings of the IEEE International Symposium on Biomedical Imaging: From Nano to Macro (ISBI'04)*, April 2004, pp. 456-459.
  - [20] Sato, Y., J. Chen, R. A. Zoroofi, N. Harada, S. Tamura, and T. Shiga, "Automatic Extraction and Measurement of Leukocyte Motion in Microvessels Using Spatiotemporal Image Analysis," *IEEE Transactions on Biomedical Engineering*, Vol. 44, April 1997, pp. 225-236.
  - [21] Krissian, K., G. Malandain, N. Ayache, R. Vaillant, and Y. Troussel, "Model-Based Detection of Tubular Structures in 3D Images," *Computer Vision and Image Understanding*, Vol. 80, November 2000, pp. 130-171.
  - [22] Perchant, A., T. Vercauteren, F. Oberrietter, N. Savoie, and N. Ayache, "Region Tracking Algorithms on Laser Scanning Devices Applied to Cell Traffic Analysis," *Proceedings of the IEEE International Symposium on Biomedical Imaging: From Nano to Macro (ISBI'07)*, Arlington, VA, April 2007, pp. 260-263.

- [23] Benhimane, S., and E. Malis, "Homography-Based 2D Visual Tracking and Servoing," *International Journal of Robotics Research*, Vol. 26, July 2007, pp. 661-676.
- [24] Vercauteren, T., X. Pennec, E. Malis, A. Perchant, and N. Ayache, "Insight Into Efficient Image Registration Techniques and the Demons Algorithm," *Proceedings of Information Processing in Medical Imaging (IPMI'07)* (N. Karssemeijer and B. P. F. Lelieveldt, eds.), Vol. 4584 of *Lecture Notes in Computer Science*, Kerkraade, The Netherlands, July 2007, pp. 495-506.
- [25] Lin, K. Y., M. A. Maricevich, A. Perchant, S. Loiseau, R. Weissleder, and U. Mahmood, "Novel Imaging Method and Morphometric Analyses of Microvasculature in Live Mice Using a Fiber-Optic Confocal Laser Microprobe," *Proceedings of the Radiological Society of North America (RSNA'06)*, Chicago, IL, 2006.
- [26] Vercauteren, T., A. Perchant, X. Pennec, and N. Ayache, "Mosaicing of Confocal Microscopic *In Vivo* Soft Tissue Video Sequences," *Proceedings of the 8th International Conference on Medical Image Computing and Computer Assisted Intervention (MICCAI'05)* (J. S. Duncan and G. Gerig, eds.), Vol. 3749 of *Lecture Notes in Computer Science*, 2005, pp. 753-760.
- [27] Vercauteren, T., A. Perchant, G. Malandain, X. Pennec, and N. Ayache, "Robust Mosaicking with Correction of Motion Distortions and Tissue Deformation for *In Vivo* Fibered Microscopy," *Medical Image Analysis*, Vol. 10, No. 5, 2006, pp. 673-692.
- [28] Vercauteren, T., X. Pennec, A. Perchant, and N. Ayache, "Non-Parametric Diffeomorphic Image Registration with the Demons Algorithm," *Proceedings of the 10th International Conference on Medical Image Computing and Computer Assisted Intervention (MICCAI'07)* (N. Ayache, S. Ourselin, and A. J. Maeder, eds.), Vol. 4792 of *Lecture Notes in Computer Science*, Brisbane, Australia, October 2007, pp. 319-326.
- [29] McDonald, D. M., and P. L. Choyke, "Imaging of Angiogenesis: From Microscope to Clinic," *Nature Medicine*, Vol. 9, June 2003, pp. 713-725.





# About the Editors

**Jens Rittscher** is a staff scientist at GE Global Research, Niskayuna, New York. His primary research interests are in biomedical image analysis and computer vision. As a member of the Visualization and Computer Vision Laboratory, he collaborates very closely with biologists within GE as well as biotechnology companies and academic research laboratories. The current focus of his research is the automated analysis of multichannel confocal image data, computerized time-lapse microscopy, and small animal imaging. In addition to working on biomedical applications, Dr. Rittscher has worked extensively on the automatic annotation of video data, algorithms for visual tracking, and methods for model-based segmentation. In 2006 he also held an adjunct assistant professorship in the Department of Computer Science at the Rensselaer Polytechnic Institute. Dr. Rittscher is a coorganizer of the workshop series on Microscopic Image Analysis with Applications in Biology and has served on the program committees of various international computer vision and medical imaging conferences. In 2000 he completed his doctoral studies, supported by a Marie Curie Fellowship of the European Union, at the Department of Engineering Science at the University of Oxford; he also holds a degree in mathematics from the University of Bonn, Germany.

**Raghu Machiraju** is an associate professor in the Department of Computer Science and Engineering at The Ohio State University (OSU). He also holds appointments in the College of Medicine at OSU. Professor Machiraju collaborates closely with faculty in biomedical informatics, human cancer genetics, and radiology. His interests are in visualization and image analysis, especially as they apply to problems in the physical and biomedical sciences. His current projects include the development of algorithms for microscopy data acquired to support various phenotyping studies and for change detection in images from multiple modalities. Before coming to OSU, Professor Machiraju was on the faculty at the NSF Engineering Research Center, Mississippi State University, where he contributed to feature detection algorithms for a variety of flow problems. His research has been supported by NIH, NSF, General Electric, and Mitsubishi Electric Research Laboratories. Additionally, he has served on the program committees of several conferences on visualization and computer graphics and is currently serving as the cochair of the Visualization 2008 conference.

**Stephen T. C. Wong** is the vice chair of research and the chief of medical physics in the Department of Radiology at The Methodist Hospital at Houston. He is also a professor of bioengineering and computer science in radiology at the Weill Medical College of Cornell University and the director of The Center for Biotechnology and Informatics at the Methodist Hospital Research Institute at Houston. In addition, Professor Wong is an adjunct professor of bioengineering at Rice University,

an adjunct professor of mechanical engineering at the University of Houston, an adjunct professor of health information science at the University of Texas Health Science Center at Houston, and an adjunct professor of systems biology at Shanghai University, China. Before joining Methodist-Cornell in 2007, Professor Wong was the founding director of the HCNR Center for Bioinformatics at Harvard Medical School, the founding executive director of the Functional and Molecular Imaging Center at the Brigham and Womens Hospital, and an associate professor of radiology at Harvard University. He has more than two decades of research and leadership experience in academia, medicine, and private industry, including at HP, AT & T Bell Labs, Japanese Fifth Generation Computing Project, Royal Philips Electronics, Charles Schwab, UCSF, and Harvard. Professor Wong has made original contributions to the fields of picture archiving and communication systems (PACS), neuroinformatics, VLSI automation, and optoelectronics. He has published more than 300 peer-reviewed scientific papers, 8 patents, 4 books, and review grants for NIH and NSF. His research center investigates multiscale imaging, image guidance, and systems biology methods in understanding the mechanisms of neurobiology and cancer biology and in developing personalized diagnostic and therapeutic solutions for neurologic disorders and cancer.

## List of Contributors

**Gunjan Agarwal**

312 Biomedical Research Tower  
460 West 12th Avenue  
Columbus, OH 43210  
United States  
e-mail: agarwal.60@osu.edu

**François Aguet**

EPFL IOA STI LIB  
BM 4.141 Station 17  
1015 Lausanne  
Switzerland  
e-mail: francois.aguet@epfl.ch

**Yousef Al-Kofahi**

Rensselaer Polytechnic Institute  
Department of Electrical, Computer,  
and Systems Engineering  
110 8th Street  
Troy, NY 12180-3590  
United States  
e-mail: alkofo@ecse.rpi.edu

**Nicholas Ayache**

INRIA Sophia Antipolis  
Asclepios Research Group  
2004 route des Lucioles  
06902 Sophia Antipolis  
France  
e-mail: nicholas.ayache@sophia.inria.fr

**Carol Barnes**

Neural Systems, Memory, and Aging Division  
Life Sciences North Bldg.  
Rm. 384  
University of Arizona  
Tucson, AZ 85724  
United States  
e-mail: carol@nsma.arizona.edu

**Musodiq Bello**

GE Global Research  
Visualization and Computer Vision Laboratory  
KW C 220A  
One Research Circle  
Niskayuna, NY 12309  
United States  
e-mail: mosodiq.bello@research.ge.com

**Christopher Bjornsson**

Rensselaer Polytechnic Institute  
Center for Biotechnology and Interdisciplinary Studies  
110 8th Street  
Troy, NY 12180-3590  
United States  
e-mail: bjornc@rpi.edu

**Jérôme Boulanger**

UMR 144  
Institut Curie  
26 rue d'Ulm  
F-75005 Paris  
France  
e-mail: jerome.boulanger@curie.fr

**Patrick Bouthemy**

IRISA  
Campus de Beaulieu  
F-35042 Rennes  
France  
e-mail: patrick.bouthemy@irisa.fr

**Ali Can**

GE Global Research  
Visualization and Computer Vision Laboratory  
KW C 307  
One Research Circle  
Niskayuna, NY 12309  
United States  
e-mail: ali.can@research.ge.com

**Anne E. Carpenter**

The Broad Institute of MIT and Harvard  
7 Cambridge Center  
Cambridge, MA 02142  
United States  
e-mail: anne@broad.mit.edu

**Ying Chen**

Rensselaer Polytechnic Institute  
Department of Electrical, Computer,  
and Systems Engineering  
110 8th Street  
Troy, NY 12180-3590  
United States  
e-mail: chen9@rpi.edu

**Costa M. Colbert**

Biology and Biochemistry  
University of Houston  
Houston, Texas 77204-5001  
United States  
e-mail: ccolbert@uh.edu

**Lee Cooper**

The Ohio State University  
205 Dreese Laboratories  
Department of Electrical and  
Computer Engineering  
2015 Neil Avenue Mall  
Columbus, OH 43210  
United States  
e-mail: cooperle@bmi.ohio-state.edu

**Michael W. Davidson**

Florida State University  
Department of Biological Science  
National High Magnetic Field Laboratory  
1800 E. Paul Dirac Drive  
Tallahassee, FL 32310-3706  
United States  
e-mail: davidson@magnet.fsu.edu

**Roland Eils**

German Cancer Research Center  
INF 267  
Heidelberg, 69120 Germany  
e-mail: r.eils@dkfz-heidelberg.de

**Jan Ellenberg**

European Molecular Biology Laboratory  
Meyerhofstrasse 1  
69117 Heidelberg  
Germany  
e-mail: jan.ellenberg@embl-heidelberg.de

**Auguste Genovesio**

Image Mining Group  
Institut Pasteur Korea  
Seongbuk-gu  
136-791 Seoul  
South Korea  
e-mail: agenoves@ip-korea.org

**Michael Gerdes**

GE Global Research  
Molecular and Cell Biology Laboratory  
K1 5D 44B  
One Research Circle  
Niskayuna, NY 12309  
United States  
e-mail: michael.gerdes@research.ge.com

**Fiona Ginty**

GE Global Research  
Computation and Biostatistics Laboratory  
K1 5B 39A  
One Research Circle  
Niskayuna, NY 12309  
United States  
e-mail: fiona.ginty@research.ge.com

**William J. Godinez**

German Cancer Research Center  
INF 267  
69120 Heidelberg  
Germany  
e-mail: w.godinez-navarro@dkfz-heidelberg.de

**Polina Golland**

MIT Computer Science and  
Artificial Intelligence Laboratory  
32 Vassar Street 32-D470  
Cambridge, MA 02139  
United States  
e-mail: polina@csail.mit.edu

**Nathalie Harder**

German Cancer Research Center  
INF 267  
69120 Heidelberg  
Germany  
e-mail: n.harder@dkfz-heidelberg.de

**Kristin L. Hazelwood**

Florida State University  
National High Magnetic Field Laboratory  
1800 E. Paul Dirac Drive  
Tallahassee, FL 32310-3706  
United States  
e-mail: hazelwood@magnet.fsu.edu

**Weijun He**

Center for Computational Biomedicine Imaging  
and Modeling  
Rutgers University  
110 Frelinghuysen Road  
Piscataway NJ 08854  
United States  
e-mail: weijunhe@cs.rutgers.edu

**Kun Huang**

The Ohio State University  
Rm.3170B  
Graves Hall  
Department of Biomedical Informatics  
333 West 10th Avenue  
Columbus, OH 43210  
United States  
e-mail: khuang@bmi.osu.edu

**Firdaus Janoos**

The Ohio State University  
395 Drees Laboratories  
Department of Computer Science  
and Engineering  
2015 Neil Avenue  
Columbus, OH-43210  
United States  
e-mail: firdaus@ieee.org

**Thouis R. Jones**

The Broad Institute of MIT and Harvard  
7 Cambridge Center  
Cambridge, MA 02142  
United States  
e-mail: thouis@broad.mit.edu

**Ioannis A. Kakadiaris**

University of Houston  
Computational Biomedicine Lab  
Department of Computer Science  
4800 Calhoun  
Houston, TX 77204-3010  
United States  
e-mail: ioannisk@uh.edu

**Charles Kervrann**

IRISA  
Campus de Beaulieu  
F-35042 Rennes  
France  
e-mail: charles.kervrann@irisa.fr

**Jelena Kovacevic**

Departments of BME and ECE  
Center for Bioimage Informatics  
Carnegie Mellon University  
Pittsburgh PA 15213  
United States  
e-mail: jelenak@cmu.edu

**Gustavo Leone**

The Ohio State University  
808 Biomedical Research Tower  
460 W. 12th Avenue  
Columbus, OH 43210  
United States  
e-mail: gustavo.leone@osumc.edu

**Gang Lin**

Rensselaer Polytechnic Institute  
Department of Electrical, Computer,  
and Systems Engineering  
110, 8th Street  
Troy, NY 12180-3590  
United States  
e-mail: ling@ecse.rpi.edu

**Raghu Machiraju**

The Ohio State University  
395 Drees Laboratories  
Department of Computer Science  
and Engineering  
2015 Neil Avenue  
Columbus, OH-43210  
United States  
e-mail: machiraju.1@osu.edu

**Grégoire Malandain**

INRIA Sophia Antipolis  
Asclepios Research Group  
2004 route des Lucioles  
06902 Sophia Antipolis  
France  
e-mail: gregoire.malandain@sophia.inria.fr

**Robin Mathew**

Center for Advanced Biotechnology  
and Medicine  
679 Hoes Lane  
Room 140  
Piscataway, NJ 08854-5638  
United States  
e-mail: mathew@cabm.rutgers.edu

**Sean G. Megason**

Department of Systems Biology  
Harvard Medical School  
200 Longwood Avenue  
Boston, MA 02115  
United States  
e-mail: megason@hms.harvard.edu

**Dimitris Metaxas**

Center for Computational Biomedicine Imaging  
and Modeling  
Rutgers University  
110 Frelinghuysen Road  
Piscataway, NJ 08854  
United States  
e-mail: dnm@cs.rutgers.edu

**William Mohler**

Department of Genetics & Developmental Biology  
University of Connecticut Health Center  
263 Farmington Avenue  
Farmington, CT 06030  
United States  
e-mail: wmohler@uchc.edu

**Michael C. Montalto**

Omnyx  
800 Centennial Drive  
Building 4  
Piscataway, NJ 08855-1327  
United States  
e-mail: michael.montalto@omnyxpath.com

**Felipe Mora-Bermúdez**

European Molecular Biology Laboratory  
Meyerhofstrasse 1  
69117 Heidelberg  
Germany  
e-mail: mora@embl-heidelberg.de

**Kishore R. Mosaliganti**

Department of Systems Biology  
Harvard Medical School  
200 Longwood Avenue  
Boston, MA 02115  
United States  
e-mail: kishore\_mosaliganti@hms.harvard.edu

**Christopher S. Murphy**

Florida State University  
National High Magnetic Field Laboratory  
1800 E. Paul Dirac Drive  
Tallahassee, FL 32310-3706  
United States  
e-mail: csmurphy8885@yahoo.com

**Arunachalam Narayanaswamy**

Rensselaer Polytechnic Institute  
Department of Electrical, Computer,  
and Systems Engineering  
216 13th Street  
Troy, NY 12180-3590  
United States  
e-mail: naraya3@rpi.edu

**Scott G. Olenych**

Florida State University  
National High Magnetic Field Laboratory  
1800 E. Paul Dirac Drive  
Tallahassee, FL 32310-3706  
United States  
e-mail: olenych@magnet.fsu.edu

**Jean-Christophe Olivo-Marin**

Unité Analyse d'Images Quantitative  
Institut Pasteur  
F-75724 Paris  
France  
e-mail: jcolivo@pasteur.fr

**Dirk Padfield**

GE Global Research  
Visualization and Computer Vision Laboratory  
KW C 223B  
One Research Circle  
Niskayuna, NY 12309  
United States  
e-mail: padfield@research.ge.com

**Thierry Pécot**

IRISA  
Campus de Beaulieu  
F-35042 Rennes  
France  
e-mail: Thierry.Pecot@irisa.fr

**Hanchuan Peng**

Janelia Farm Research Campus  
Howard Hughes Medical Institute  
19700 Helix Drive  
Ashburn, VA 20147  
United States  
e-mail: pengh@janelia.hhmi.org

**Aymeric Perchant**

Mauna Kea Technologies  
9 rue d'Enghien  
75010 Paris  
France  
e-mail: aymeric.perchant@maunakeatech.com

**Zhen Qian**

Center for Computational Biomedicine Imaging  
and Modeling  
Rutgers University  
110 Frelinghuysen Road  
Piscataway, NJ 08854  
United States  
e-mail: zqian@research.rutgers.edu

**Jens Rittscher**

GE Global Research  
Visualization and Computer Vision Laboratory  
KW C 214  
One Research Circle  
Niskayuna, NY 12309  
United States  
e-mail: jens.rittscher@research.ge.com

**Gustavo K. Rohde**

Department of BME and  
Center for Bioimage Informatics  
Carnegie Mellon University  
Pittsburgh, PA 15213  
United States  
e-mail: gustavor@cmu.edu

**Karl Rohr**

German Cancer Research Center  
INF 267  
69120 Heidelberg  
Germany  
e-mail: k.rohr@dkfz-heidelberg.de

**Badrinath Roysam**

Rensselaer Polytechnic Institute  
Department of Electrical, Computer,  
and Systems Engineering  
110 8th Street  
Troy, NY 12180  
United States  
e-mail: roysam@ecse.rpi.edu

**David M. Sabatini**

The Whitehead Institute for Biomedical Research  
Nine Cambridge Center  
Cambridge, MA 02142  
United States  
e-mail: sabatini@wi.mit.edu

**Peter Saggau**

One Baylor Plaza  
Baylor College of Medicine  
Houston, TX 77030  
United States  
e-mail: psaggau@bcm.edu

**Jean Salamero**

UMR 144  
Institut Curie  
26 rue d'Ulm  
F-75005 Paris  
France  
e-mail: Jean.Salamero@curie.fr

**Joel Saltz**

The Ohio State University  
3190-F Graves Hall  
333 W. 10th Avenue  
Columbus, OH 43210  
United States  
e-mail: joel.Saltz@osumc.edu

**Alberto Santamaría-Pang**

Computational Biomedicine Lab  
Department of Computer Science  
University of Houston  
4800 Calhoun  
Houston, TX 77204-3010  
United States  
e-mail: asantama@central.uh.edu

**Nicolas Savoie**

Mauna Kea Technologies  
9 rue d'Enghien  
75010 Paris  
France  
e-mail: nicolas.savoie@maunakeatech.com

**William Shain**

Wadsworth Center  
NYS Department of Health  
Empire State Plaza  
P.O. Box 509  
Albany, NY 12201-0509  
United States  
e-mail: shain@wadsworth.org

**Jean-Baptiste Sibarita**

UMR 144  
Institut Curie  
26 rue d'Ulm  
F-75005 Paris  
France  
e-mail: Jean-Baptiste.Sibarita@curie.fr

**Anup Sood**

GE Global Research  
Biological and Organic Chemistry Laboratory  
K1 4D 55  
One Research Circle  
Niskayuna, NY 12309  
United States  
e-mail: anup.sood@research.ge.com

**Youxian Sun**

The State Key Laboratory  
of Industrial Control Technology  
Zhejiang University  
38 Zheda Road  
Hangzhou 310027  
China  
e-mail: yxsun@iipc.zju.edu.cn

**Xiaodong Tao**

GE Global Research  
Visualization and Computer Vision Laboratory  
KW C 223A  
One Research Circle  
Niskayuna, NY 12309  
United States  
e-mail: xiaodong.tao@research.ge.com

**Nick Thomas**

GE Healthcare  
Maynard Centre  
Cardiff CF147YT  
United Kingdom  
e-mail: Nick.Thomas@ge.com

**Michael Unser**

EPFL IOA STI LIB  
BM 4.127 Station 17  
1015 Lausanne  
Switzerland  
e-mail: michael.unser@epfl.ch

**Tom Vercauteren**

INRIA Sophia Antipolis  
Asclepios Research Group  
2004 route des Lucioles  
06902 Sophia Antipolis  
France  
e-mail: tom.vercauteren@sophia.inria.fr

**Cédric Vonesch**

EPFL IOA STI LIB  
BM 4.138 Station 17  
1015 Lausanne  
Switzerland  
e-mail: cedric.vonesch@epfl.ch

**Jean-Luc Vonesch**

Institut de Gntique et de Biologie Molculaire et Cellulaire  
B.P. 10142  
67404 ILLKIRCH CEDEX  
France  
e-mail: jlv@igbmc.u-strasbg.fr

**Xiaoxu Wang**

Center for Computational Biomedicine Imaging  
and Modeling  
Rutgers University  
110 Frelinghuysen Road  
Piscataway, NJ 08854  
United States  
e-mail: xiwang@cs.rutgers.edu

**Eileen White**

Center for Advanced Biotechnology and Medicine  
679 Hoes Lane  
Room 140  
Piscataway, NJ 08854-5638  
United States  
e-mail: ewhite@cabm.rutgers.edu

**Stephen T. C. Wong**

The Methodist Hospital Research Institute  
and Department of Radiology  
The Methodist Hospital  
Weill Cornell Medical College  
6565 Fannin, B5-022  
Houston, TX 77030-2707  
United States  
e-mail: stwong@tmhs.org

**Zheng Xia**

The Methodist Hospital Research Institute  
and Department of Radiology  
The Methodist Hospital  
Weill Cornell Medical College  
6565 Fannin, B5-022  
Houston, TX 77030-2707  
United States  
e-mail: ZXia@tmhs.org

**Xiaoyin Xu**

Department of Radiology  
Brigham and Womens Hospital  
75 Francis Street  
Boston, MA 02115  
United States  
e-mail: xxu@bwh.harvard.edu

**Xiaobo Zhou**

The Methodist Hospital Research Institute  
and Department of Radiology  
The Methodist Hospital  
Weill Cornell Medical College  
6565 Fannin, B5-022  
Houston, TX 77030-2707  
United States  
e-mail: xzhou@tmhs.org



# Index

## A

Abbe's law, 346–47  
Acridine dyes, 25–26  
Active contours  
  with edges, 303, 305  
  parametric, 318  
  segmentation methods, 75–76  
  without edges, 303–4  
AdaBoost  
  algorithm, 322–23  
  boosting procedure on cell features, 323  
  cell detection with, 319–23  
  detecting results, 323  
  in human face detection, 318  
Adaptive validation gate, 261–64  
Affine registration algorithm, 455  
Airy units (AU), 93  
Alexa Fluor dyes, 26–28  
  defined, 26  
  digital images, 27  
  fluorescence excitation, 27  
  photobleaching resistance, 26–27  
  as reactive intermediates, 28  
  *See also* Fluorescent dyes  
Alzheimer's disease (AD), 401  
Analog-to-digital (A/D) conversion, 51, 54–55  
Annotation, of cell/tissue type, 351–52  
Approximated filter based on grid, 242–45  
  description, 242  
  example, 243–45  
  pseudocode, 276–77  
  *See also* Bayesian filters  
Artifacts, in microscopic images, 14–15  
Associative measurements, 124, 131  
  defined, 131  
  distance-based, 132–34

  graph-theoretic interpretation, 136  
  relationships, 131  
  *See also* Image-based measurements

Autocorrelation methods, 225–26

Automated image analysis strategies, 121

Automated segmentation  
  edit-based validation protocol, 144–45  
  ground truth data, 142  
  intersubject variations, 143  
  intrasubject variations, 143  
  multiobserver validation, 144  
  results validation, 142–45  
  *See also* Segmentation  
Automatic seed placement, 305  
Auto regressive moving average (ARMA)  
  model, 78

## B

Background estimation, 178–81  
  example, 181  
  pixel-wise, 178–79  
  spatial coherence for, 179–81  
Background noise, 98  
Background region, 392  
Barycentric coordinates-based subdivision, 368  
Bases, 57  
  defined, 57  
  orthonormal (ONBs), 58  
Bayesian filters  
  analysis, 229–50  
  approximated, based on a grid, 242–45  
  based on grid, 234–35  
  conceptual, 229–31  
  IMM, 238–42  
  importance, 229  
  Kalman, 231–34  
  particle, 245–50  
  use of, 229

- Bayesian probabilistic framework, 367
- Bayesian tracking, 227–28
  - components, 227–28
  - diagram, 228
  - drawbacks, 228
  - stages, 228
  - See also* Particle tracking
- Bayes rule, 369
- Berkeley Drosophila Genome Project (BDGP), 158, 166
- Bernoulli random variables, 217
- Bias-variance tradeoff, 179, 181
  - defined, 181
  - framework, 179
  - statistical test, 181
- Biological imaging, 258–69
  - adaptive validation gate, 261–64
  - association, 264–65
  - IMM dynamic models, 259–60
- Biological specimens, imaging techniques, 13
- Bioluminescence imaging, 426
- Biomarkers, 191–204
  - subcellular, 203–4
  - tissue-based, 191–92
- Blobs, 123
  - intensity features, 125
  - modeling, 125
  - morphological features, 125
  - segmentation algorithms, 124
  - segmentation flowchart, 125
- Blood flow velocimetry, 450–54
  - algorithm, 451–53
  - imaging of moving objects, 450–51
  - results and evaluation, 453–54
- Blooming, 96
- Blue fluorescent protein (BFP), 38
- Branch points, 128
- C
- Calcium ion flux, 30–31
- Calibration, 449
- Canny edge-detection method, 325
- C. elegans*, 137, 140
- Cell cycle checkpoints, 297–98
- Cell cycle phase analysis, 295–314
  - algorithmic validation, 310–11
  - biological background, 296–300
  - cell staining, 298–99
  - checkpoints, 297–98
  - introduction, 295
  - large-scale toxicology study, 310
  - level sets, 302–4
  - phases, 296
  - problem statement, 299
  - results, 310–11
  - spatio-temporal, 304–10
  - state of the art, 300–302
  - tool, 311–14
- Cell cycle phase marker (CCPM), 295
  - cell cultures, 299
  - channel, 311
  - datasets, 304, 311
  - dynamic, 299
- Cell cycle research tool, 311–14
  - research prototype, 312
  - visualization, 313–14
- Cell detection
  - with AdaBoost, 319–23
  - feature representation, 320–22
- Cell division, 138
  - modeling, 327–28
  - rate estimation, 328, 329
- Cell geometry, 350
- Cell lineage, 140, 141
- Cell migration, 138
- CellProfiler, 209, 218
- Cell screening, 209–19
  - challenges, 210
  - exploration and inference, 215–18
  - illumination and staining correction, 210–12
  - image-based high-content, 210
  - introduction, 209
  - measurements, 214
  - methods, 210–18
  - segmentation, 212–14
  - spatial bias correction, 214–15
- Cell segmentation, 130
  - accuracy, 328

- average cell size estimation, 328
  - cell detection, 319–23
  - conclusions, 329
  - cytoplasm, 326–27
  - Digital Fish project, 349–50
  - division rate estimation, 327–28
  - experiments, 328–29
  - flow chart, 319
  - foreground, 323–26
  - individual cells, 364–71
  - introduction, 317–19
  - learning-based framework, 325
  - methodology, 319–28
  - modality-dependent, 364–66
  - modality-independent, 366–71
  - nuclei, 365
  - pipeline, 367
  - See also* Segmentation
  - Cell staining, 298–99
  - CellVisualizer, 218
  - Centroidal Voronoi tessellations (CVTs), 358
  - Chapman-Kolmogorov equations, 230
  - Charge coupled devices (CCDs), 96, 193
  - Chemical dimensions, 115–16
  - Chromoendoscopy, 442
  - Chromosome morphology, 290
  - Circular convolution, 55
  - Classification, 77–78, 107
    - boundary refinement, 325
    - per-cell, 216–18
  - Cloud segmentation algorithms, 128–29
  - Clustering, 77–78
  - Coding regions, 333
  - Coherent anti-Stokes Raman scattering (CARS) microscopy, 426–27
  - Compartments, 123
  - Compound microscope
    - conjugate planes, 2
    - elements, 2
    - element schematic, 3
    - objective lens, 3
  - Computed tomography (CT), 425
  - Computer numerical control (CNC), 460
  - Conceptual filter, 229–31
  - Condensation, 436–37
    - algorithm. *See* Particle filter
    - defined, 436
    - sample size, 437
  - Confocal microscopy, 93–94
    - incoherent point spread function, 93–94
    - irradiation of fluorophores, 23
    - optical sectioning, 93
    - quantum dots in, 36
  - Confusion matrix, 291
  - Continuous-domain image processing, 51–53
    - deterministic versus stochastic description, 52
    - Fourier view, 52–53
    - framework, 51–52
    - linear-shift invariant systems, 52
    - point spread functions (PSF), 52
  - Contrast, in transmitted light microscopy, 6–7
  - Contributors, this book, 467–71
  - Cooling, 96
  - Coregulated gene detection, 163–66
  - Cross correlation, 225
  - Curve-skeletonization algorithms, 404, 412–13
  - CurveSkel software package, 414
  - Cyan fluorescent protein (CFP), 38, 88
  - Cyanine dyes, 28–29
    - Cy5 derivatives, 29
    - defined, 28
    - digital images, 29
    - as reactive dyes, 28
    - See also* Fluorescent dyes
  - Cytoplasm
    - segmentation of, 202
    - segmentation with watershed algorithm, 326–27
- ## D
- DAPI
    - images, 199
    - in nuclei identification, 204
  - Dark current, 98
  - Dark field microscopy, 8
  - Data-driven modeling, 172
  - Data preprocessing, 106

- Deconvolution, 69–72, 104–5
- Deinterlacing/denoising, 349
- Delaunay triangles, 367
- Dendrite segmentation, 393–94
- Dendrite tree model, 413
- Dendritic spines, 401–19
  - conclusion, 419
  - data set, 405
  - denoising, 405–7
  - floating spine heads, 408–9
  - image acquisition and processing, 404–9
  - medial axis-based methods, 404
  - morphometry, 402
  - neuron reconstruction and analysis, 409–14
  - neuron segmentation, 407–8
  - parameters and optimal values, 415
  - quadric error decimation factor, 415–16
  - reconstruction methods, 404
  - related work, 404
  - resampling, 405–7
  - results, 414–18
  - ROC curves, 416, 418
  - skeletonization strictness parameter, 416
  - structure analysis, 404
- Dendrograms, 402
- Denoising, 69–72, 104
  - dendritic spines, 405–7
  - Digital Fish project, 349
  - frame-shrinkage, 391–93
  - as imaging task, 69–72
  - volume, 396
- Detectors, 95–98
  - characteristic parameters, 95–96
  - intensity, 95
  - operating temperature, 96
  - photomultiplier tubes (PMTs), 96–98
  - semiconductor, 96
  - spatial resolution, 95
  - technologies, 96–98
  - temporal resolution, 95–96
  - wavelength, 95
- Deterministic methods, 226
- DiaTrack, 266
- Differential evolution (DE), 432
- Differential interference contrast (DIC)
  - defined, 9
  - images, 10
  - microscopy, 9–10
  - optical path length gradients, 9
  - prisms, 16
  - video-enhanced, 13
- Diffraction planes, 2
- Digital Fish project, 338–53
  - annotation of cell/tissue type, 351–52
  - cell tracking/segmentation, 349–50
  - data analysis, 352
  - defined, 338
  - deinterlacing/denoising, 349
  - dimensions for image analysis, 345
  - discrete geometry and topology, 350–51
  - FlipTraps, 339, 340, 343–45, 351
  - fluorescent proteins, 342
  - goals, 338–40, 344
  - image acquisition, 343–46
  - image analysis, 347–52
  - imaging, 340–47
  - labeling, 342–43
  - microscopes, 341–42
  - montaging, 348–49
  - quantitation of fluorescence/localization, 351
  - real world images, 346–47
  - registration/integration, 352–53
  - subject, 340
  - systematic imaging, 344
  - visualization, 352
- Digital subtraction angiography (DSA), 429
- Discrete-domain image processing, 55–56
  - Fourier view, 56
  - framework, 55
  - LSI systems, 55
- Discrete Fourier Transform (DFT), 56
  - matrix, 61
  - as signal expansion, 60
  - tiles, 59–60
- Discrete-Time Fourier Transform (DTFT), 56
- Discrete wavelet transform (DWT), 63
- Disparity function, 431

- Distance-based associative measurements, 132–34
- Distance maps, 133
  - signed, 134
  - zones, 133
- Divide-and-conquer strategy, 122–31
  - biological entities, 123
  - illustrated, 124
  - operational interpretations, 124
- D. melanogaster*, 216
- DNA
  - cassette integration, 338–39
  - enhancers, 342
  - noncoding, 333
  - protein interactions, 334
- Drosophila melanogaster*, 210
- DsRed fluorescent protein, 39
- Dual track spatio-temporal images, 313
- Dynamic features, 288–89, 291
- E
  - Earth Mover's Distance (EMD), 324
  - Edit-based validation protocol, 144–45
  - Efficient second-order minimization (ESM) scheme, 455
  - Eikonal equation, 307
  - Electronic noise, 14
  - Embryonic image clustering, 157–60
    - eigen-embryo feature vectors, 158–59
    - performance measurement, 160
  - Emergent behaviors, 119
  - Endomicroscopes, 443
  - Enhanced green fluorescent protein (EGFP), 38
  - Enhanced yellow fluorescent protein (EYFP), 39
  - Environmental probes, 29–32
  - Euclidean distance metric, 310
  - Euler-Lagrange equation, 304
  - Extended-depth-of-field algorithm, 105
  - Extended Kalman filter (EKF), 230, 235–38
    - description, 235–36
    - estimator of, 248
    - example, 236–38
    - idea, 235
    - nonlinear signal estimate, 237
    - parameters, 238
    - pseudocode, 277
- F
  - False-positive results, 382
  - FARSIGHT, 115–46
    - core blob algorithms, 125
    - divide-and-conquer segmentation strategy, 122–31
    - framework illustration, 145
    - image analysis results validation, 142–45
    - image-based measurements, 131–34
    - introduction, 115–22
    - spatio-temporal associations, 135–42
    - summary, 145–46
  - Fast marching tracking, 307–10
    - algorithm, 309
    - defined, 307
    - spatio-temporal images, 313
    - speed images for, 309
  - Feature detection, 104
  - Fibered confocal microscopy (FCM), 441–61
    - blood flow velocimetry with motion artifacts, 450–54
    - conclusions, 461
    - defined, 442
    - distal scanning, 443–44
    - mosaicking, 457–62
    - motivations, 441–42
    - output, 447
    - principles, 443–46
    - processing, 441–61
    - proximal scanning, 444–46
    - real-time fiber pattern rejection, 447–50
    - region tracking for kinetic analysis, 454–57
    - schematic principle, 444
  - Fibered in vivo imaging, 427
  - Field planes, 2
  - Filter cube, 12
  - First-order linear extrapolation (FLE), 259, 260
  - Fisher distribution, 181

- Fisher linear discriminant classifier, 305
- FLAsH, 40
- FlipTraps, 339, 340, 343
  - conditional alleles, 351
  - disadvantage of, 343
  - embryonic expression patterns, 344
  - endogenously expressed fluorescent fusion proteins, 351
  - FP expression, 343
  - imaging, 345
  - See also* Digital Fish project
- Floating spine heads, 405, 408–9
- Fluorescein isothiocyanate (FITC), 23
- Fluorescence
  - defined, 86–87
  - limiting factors, 98–99
  - noise sources, 98
  - physical principles, 86–88
  - related phenomena, 87–88
- Fluorescence in situ hybridization (FISH), 191
- Fluorescence lifetime imaging microscopy (FLIM), 16, 102–3
  - defined, 102
  - experiment, 102
  - uses, 103
  - using, 115
- Fluorescence microscopy, 12
  - advanced experimental techniques, 99–103
  - advanced systems, 108–9
  - current and future trends, 107–10
  - defined, 12
  - early history, 89
  - excitation of sample, 12
  - introduction to, 85–110
  - microtubules by, 13
  - modern history, 90
  - molecular probes, 19–43
  - multiphoton, 342
  - multiplexing, 192–93
  - super-resolution, 109–10
  - two-photon, 426
  - video-enhanced, 13
  - See also* Microscopy
- Fluorescence molecular tomography (FMT), 425, 427–29
  - data processing, 428
  - fluorescence scanning, 427–29
  - image registration, 429–38
  - multimodality, 428–29
- Fluorescence polarization (FP) in FRET (FP-FRET), 16
- Fluorescence recovery after photobleaching (FRAP), 16, 42, 101–2
  - defined, 101–2
  - diffusion coefficients, 107
- Fluorescence resonance energy transfer (FRET), 16, 38, 100–101
  - as conformational change indicator, 101
  - efficiency, 100
  - experiment images, 101
  - principle, 100
- Fluorescence scanning, 427–28
- Fluorescent dyes, 19
  - acridine, 25–26
  - Alexa Fluor, 26–28
  - cyanine, 28–29
  - DNA binding, 298
  - MitoTracker, 32, 33
  - multiplexing, 193
  - propidium iodide, 26
  - synthesis, 21
  - traditional, 25–26
- Fluorescent labels, 107–8, 116
- Fluorescent probes, 19–43
  - for endoplasmic reticulum fluorescence, 34
  - environmental, 29–32
  - fluorescent proteins, 36–39
  - hybrid systems, 39–40
  - introduction, 19–21
  - organelle, 32–34
  - synthetic, 19
  - in widefield fluorescence, 25
- Fluorescent proteins, 36–39
  - advantages, 37
  - blue (BFP), 38
  - cyan (CFP), 38, 88
  - defined, 36–37
  - Digital Fish project, 342

- DsRed, 39
- enhanced green (EGFP), 38
- enhanced yellow (EYFP), 39
- fusion, 91
- green (GFP), 37–38, 85, 88
- optical highlighter, 39
- photocontrolable, 108
- recombinant, 107–8
- yellow (YFP), 38, 91
- Fluorophores, 20
  - absorption, 21
  - brightness level, 22
  - calcium response, 30
  - characteristics, 21–25
  - conclusions, 43
  - defined, 86, 341
  - fluorescence properties, 21
  - genetically encoded, 21
  - irradiation, 23
  - localization, 341
  - spectral profiles, 21
  - using in fluorescence microscopy, 21
- Foreground region, 392
- Foreground segmentation, 323–26
  - classification and curve evolution, 324–26
  - Earth Mover's Distance, 324
  - See also* Segmentation
- Fourier analysis, 60–61
- Fourier bases, 60–61
- Fourier frames, 61
- Fourier transform (FT), 52–53, 56
- Fragile X mental retardation protein (FMRP), 401–2
- Fragile X syndrome, 401, 402
- Frames
  - defined, 57
  - Fourier, 61
  - harmonic tight (HTFs), 61
  - Parseval tight (PTFs), 59
- Fraunhofer diffraction, 4
- Fusion protein, 91
- G**
- Gabor analysis, 61–62
- Gabor transform (GT), 62
- Gene expression patterns, 161
- Generalized PCA (GPCA), 65, 66
- Gene regulation
  - known relationships, 164
  - motifs, 163–66
- Genome projects, 332–33
- Geometric skeletonization method, 403
- Gimbal lock, 127
- Global thresholding, 286
- GoFigure, 347–48, 350
- Golgi apparatus, 33, 34, 169, 171
- Gradient-based estimators, 68
- Green fluorescent protein (GFP), 20, 37–38, 39, 85, 171
  - discovery, 88
  - first experiments, 88
  - See also* Fluorescent proteins
- Grid-based filter, 242–45
  - description, 242
  - example, 243–45
  - pseudocode, 276–77
- H**
- Harmonic tight frames (HTFs), 61
- Hematoxylin-Eosin (H&E), 191
- Hessian matrix, 200
- Hierarchical merging tree, 126
- High-content cell screening, 210–18
  - challenges, 210
  - exploration and inference, 215–18
  - illumination correction, 210–12
  - measurements, 214
  - methods, 210–18
  - segmentation, 212–14
  - spatial bias correction, 214–15
  - staining correction, 210–12
- High-content experimentation, 120, 121
- High-throughput experimentation, 120, 121
- HIV-1 complexes
  - docking of, 267–68
  - motility of, 267–69
  - vibratory movements, 269
- Hybrid systems, 39–40



## I

- Ideal tabular structure, 393
- Illumination and staining
  - correction, 210–12
  - variation, 211
- Image analysis, 194–202
  - cell tracking/segmentation, 349–50
  - deinterlacing/denoising, 349
  - Digital Fish project, 347–52
  - framework, 50–56
  - montaging, 348–49
  - preprocessing, 195–96
  - registration, 197–99
  - segmentation, 199–200
  - segmentation of cytoplasm and epithelial regions, 202
  - unified segmentation algorithm, 200–202
  - workflow, 284–85
- Image analysis tools, 56–68
  - Fourier analysis, 60–61
  - Gabor analysis, 61–62
  - multiresolution analysis, 62–64
  - signal and image representations, 57–60
  - statistical estimation, 67–68
  - unsupervised, data driven representation and analysis methods, 64–66
- Image-based measurements
  - associative, 124, 131
  - computing and representing, 131–34
  - intrinsic, 124, 131
- Image calibration, 103
- Image classification and recognition, 153
- Image clustering, 153
- Image feature function, 365
- Image preprocessing, 195–96
- Image registration, 153, 197–99
- Image retrieval, 153
- Image simplification, 104
- Imaging
  - bioluminescence, 426
  - CARS, 426–27
  - Digital Fish project, 340–47
  - fiber in vivo, 427
  - fluorescent, 346, 425–27
  - FMT, 427–29
  - of moving objects, 450–51
  - omics versus, 336–37
  - small critter, 425–39
  - systematic, 344
  - in systems biology, 335–38
- Imaging framework, 50–56
  - A/D conversion, 54–55
  - continuous-domain image processing, 51–53
  - discrete-domain image processing, 55–56
- Imaging tasks, 68–79
  - classification, 77–78
  - clustering, 77–78
  - deconvolution, denoising and restoration, 69–72
  - intelligent acquisition, 68–69
  - modeling, 78–79
  - mosaicking, 74
  - registration, 72–73
  - segmentation, 74–76
  - tracing, 77
  - tracking, 77
- Importance sampling, 246
- Incoherent point spread function
  - confocal microscope, 93–94
  - defined, 93
- Independent component analysis (ICA), 65
- Insight Segmentation and Registration toolkit (ITK), 348
- Integrative systems biology, 119
- Intelligent acquisition, 68–69
- Interacting multiple models (IMM) filter, 229, 231, 238–42, 248–49
  - defined, 238
  - description, 238–41
  - dynamic models, 259–60
  - estimator, 239
  - example, 241–42
  - first-order linear extrapolation (FLE), 259, 260
  - pseudocode, 277–78
  - random walk (RW), 259
  - second-order linear extrapolation (SLE), 259, 260
  - use of, 258

Interscene dynamic range, 95  
Intersubject variations, 143  
Intracellular trafficking  
  background modeling, 172–74  
  background simulation, 175  
  controllable simulation methods, 175  
  data-driven modeling, 172  
  example, 177–78  
  introduction to, 170–71  
  membrane modeling, 174  
  membrane simulation, 175–77  
  models in video-microscopy, 172–74  
  physics-based modeling, 172  
  simulation, 174–77  
Intrascene dynamic range, 95  
Intrasubject variations, 143  
Intrinsic measurements, 124, 131  
  defined, 131  
  storage, 131  
  *See also* Image-based measurements  
In vivo molecular small animal imaging,  
  425–27  
ISOMAP algorithm, 66

## J

Joint PDAF, 257–58  
  defined, 257  
  feasible joint association event, 257, 258  
  joint association event, 257  
  pseudocode, 282  
  search window, 258  
  *See also* Probabilistic data association  
    filter (PDAF)

## K

Kalman filter (KF), 230, 231–34  
  extended, 235–38, 277  
  with parameters, 232  
  pseudocode, 276  
  signal estimate by, 234  
  transition matrix, 233  
Kernel PCA, 65  
Kinetic analysis, 454–57  
Kruskal's algorithm, 157  
Kullback-Leibler divergence, 216  
K-way clustering, 155

## L

Labeling, 342–43  
Learning-based segmentation framework,  
  325  
Least-squares approximation, 59  
Lens aberrations, 7  
Level sets, 302–4  
  active contours with edges, 303  
  active contours without edges, 303–4  
  classes, 303  
  paradigm, 303  
  shape/size constraint, 305–7  
  use advantage, 302  
Light microscopy. *See* Microscopy  
Linear shift-invariant (LSI) systems, 52  
Living cell microscopy  
  image processing methods, 172  
  introduction to, 171–72  
Local adaptive thresholding, 286  
Local binary pattern (LBP), 324  
Local embedding (LLE) algorithm, 66  
Local structure analysis, 393  
LysoSensor, 33  
LysoTracker, 33

## M

Magnetic resonance imaging (MRI), 425,  
  441  
Magnification, in microscopy, 6  
Mahalanobis distance, 262  
Manifold learning, 153  
Manmade objects, 123, 131  
MAP estimation, 70–72  
  minimization function modeling, 71  
  prior modeling, 71–72  
Markov process, 241  
Mass-spectrometry, 335  
Mexican hat wavelet (MHW) filters, 319,  
  320  
  illustrated, 321  
  upside-down, 320  
Maximize likelihood (ML), 252–54  
Maximum a posteriori (MAP) estimators,  
  67–68  
Maximum-entropy criterion, 288  
Maximum-intensity criterion, 288

- Maximum intensity projection (MIP), 182, 285
- Maximum likelihood estimation (MLE), 364
- Mean squared error (MSE) estimators, 67, 70
- Measurement(s)
  - associative, 124, 131, 132–34, 136
  - cell screening, 214
  - high-content cell screening, 214
  - intrinsic, 124, 131
  - network tomography, 184–85
  - per-cell, 214
  - per-gene, 216
- Medial geodesic function, 403, 412
- Membrane trafficking simulation, 175–77
  - network extraction, 176
  - path computation, 177
  - photometric rendering, 177
  - selection of origin-destination pairs, 176–77

*See also* Intracellular trafficking
- Messenger RNA (mRNA), 118, 160
- Metal-oxide-semiconductor (MOS)
  - photocapacitor, 96
- MetaMorph, 318
- Microarrays, 335
- MicroCT images
  - alignment, 432
  - boundary information, 429–30
  - fusion, 435–36
  - projecting, 430
  - registration of, 429–38
- Microscopes
  - confocal scanning, 93–94
  - Digital Fish project, 341–42
  - image formation and, 91–95
  - images, 14–15, 51
  - polarization, 9
  - selective plane illumination (SPIM), 110
  - widefield, 91–93
- Microscopy, 1–16
  - in biology, 12–14
  - CARS, 426–27
  - confocal, 23
  - contrast, 6–7
  - dark field, 8
  - differential interference contrast, 9–10
  - fibered confocal, 441–61
  - fluorescence, 12, 19–43, 85–110
  - image analysis tools, 56–68
  - image formation, 2–5
  - imaging tasks, 68–79
  - light, trends, 16
  - living cell, 171–72
  - magnification, 6
  - need for, 1–2
  - phase contrast, 7–8
  - photoactivated localization (PALM), 16, 109
  - polarization, 8–9
  - reflected light, 10–12
  - resolution, 5
  - scanning probe (SPM), 1
  - STED, 109
  - stochastic optical reconstruction (STORM), 109
  - techniques, 2
  - total internal reflection, 13
  - transmitted light, 2–5
  - video, 178–81
- Minimum error thresholding, 287
- Minimum spanning tree (MST), 154
  - clustering methods, 157
  - partition method, 157
- Mitochondrial probes, 32, 33
- Mitotic cell nuclei tracking, 287–88
- Mitotic phases
  - automated analysis, 283–92
  - classification results, 290–92
  - different, 284
  - duration, 284
  - experimental results, 290–92
  - image analysis workflow, 284–85
  - image data, 290
- MitoTracker dyes, 32, 33
- Modality-dependent segmentation, 364–66
- Modality-independent segmentation, 366–71
- Model-based segmentation algorithms, 124–25
- Model fitting, 106–7

- Modeling, 78–79
  - blobs, 125
  - cell division, 327–28
  - data-driven, 172
  - error, 119
  - MAP estimation, 71–72
  - physics-based, 172
- Molecular pathology, 191
- Molecular species, 119
- Montaging, 348–49
- Morphological reconstruction, 394–96
- Mosaicking, 74, 105, 457–61
  - algorithm overview, 458–60
  - construction and tissue deformation compensation, 459–60
  - goal, 458
  - local to global alignment, 458–59
  - results and evaluation, 460–61
  - techniques, 460–61
- Motion compensation algorithm, 454–55
- Mouse model phenotyping study, 359–60
  - PTEN gene and cancer, 359–60, 377–79
  - Rb gene role, 359, 375–77
- Mouse placenta phenotyping studies, 380–82
- MST-Cut, 154–66
  - algorithm, 155–57
  - for clustering of coexpressed/coregulated genes, 154–60
  - defined, 154, 155
  - detection of coregulated genes and regulatory motifs, 163–66
  - eigen-embryo, 161, 163
  - embryonic image clustering, 157–60
  - experiments, 160–66
  - F-measure scores, 162
  - related algorithms, 157
  - on synthetic datasets, 160–63
- Multicell image segmentation, 285–87
- Multichannel segmentation techniques, 202–3
- Multihypothesis tracking (MHT), 251, 254–55
  - defined, 254
  - indicators, 254
  - probabilistic version, 255
  - pseudocode, 281
- Multimodality, 428–29
- Multiphoton excitation, 88
- Multiphoton microscopy, 109, 342
- Multiple-based object merging, 127
- Multiple objective imaging, 109
- Multiple particle tracking (MPT), 226–27
- Multiplexing, 192–94
  - fluorescence microscopy, 192–93
  - fluorescent dyes, 193
  - photobleaching, 194
  - quantum dots, 193–94
- Multiresolution analysis, 62–64
  - discrete wavelet transform (DWT), 63
  - implementing, 62
  - recommendations, 63–64
  - wavelet packets (WPs), 63
  - wavelet transform (WT), 62
- Multiscale active contours (MSAC), 76
- N
- NA-MIC kits, 348
- Nearest neighbor (NN), 250
  - association (NNA), 227
  - illustrated example, 253
  - pseudocode, 280
- Network extraction, 176
- Network tomography, 181–87
  - application, 184
  - concept, 182–84
  - constraints and a priori knowledge, 186–87
  - experiments, 187
  - general case, 186
  - measurements, 184–85
  - partitioning cell region, 182
  - principle, 182–84
  - problem optimization, 185–87
- Neuronal morphology reconstruction, 389–98
  - conclusions, 397–98
  - deconvolution, 391
  - dendrite centerline extraction, 389
  - dendrite segmentation, 393–94
  - dendritic diameters, 396

## Neuronal morphology reconstruction (*cont.*)

- experimental data, 391
- frame-shrinkage denoising, 391–93
- illustrated, 397
- introduction, 389–91
- materials and methods, 391–96
- obstacle, 389
- registration, 393
- results, 396–97
- semiautomatic methods, 389
- vessel segmentation, 390

## Neuron reconstruction, 409–14

- curve skeletonization, 412–13
- dendrite tree model, 413
- morphometry and spine
  - identification, 413–14
- skeletonization for, 409
- surface fairing, 410–11
- surfacing, 410–11

## Neurons

- graph models, 402
- guided functional imaging of, 390
- linear branching structures, 401
- segmentation, 407–8

## Nipkow-disk system, 108

## Nissl-positive neurons (Nissl), 117

## *N. meningitidis*, 269

## Noise

- background, 98
- in microscopic images, 14–15
- photon shot, 98
- Poisson, 347, 349
- shot, 347, 349, 405
- sources, 98

## Nonlinear diffusion equation, 407

## Nonrigid registration, 372–74

- steps, 372–73
- uses, 371

*See also* Registration

## N-point correlation functions,

- 361–64

- introduction to, 361–63
- microscopic image segmentation with, 364

- as multivariate distribution functions, 363

- tissue segmentation with, 361–64

## Nuclei

- dark tunnels, 301
- identification, 204
- segmentation, 365
- tracking, 287–88

## Numerical aperture (NA), 7

- defined, 3
- high, 7
- widefield microscope, 92

## Nyquist frequency, 448

## O

### Omics, 335, 336

### Open source code, 353–54

### Optical highlighter fluorescent proteins, 39

### Optical sectioning, 93

### Organelle probes, 32–34

- mitochondrial, 32, 33
- uses, 32

*See also* Fluorescent probes

### Origin-destination pairs, 176–77

### Orthonormal bases (ONBs), 58

### Otsu thresholding, 287

### Oversegmentation, 383

## P

### Parametric active contours, 318

### Parseval frames, 392

### Parseval's equality, 58

### Parseval tight frames (PTFs), 59

### Particle filter, 245–50

- defined, 245
- description, 245–47
- example, 248–50
- Gaussian, 246
- pseudocode, 278–79
- with resampling, 248, 279–80
- signal estimate, 247

### Particle tracking, 223–70

- adaptive validation gate, 261–64
- algorithm robustness, 265Imaris, 266
- applications, 265–69

- applications to cell biology, 267–69
- association, 264–65
- autocorrelation methods, 225–26
- Bayesian filters analysis, 229–50
- Bayesian methods, 227–28
- biological imaging methods, 258–65
- conclusions, 269–70
- deterministic methods, 226
- introduction, 223–25
- joint probabilistic data association filter (JPDAF), 257–58
- main association methods, 250–58
- methods, 225–28
- multihypothesis (MHT), 251, 254–55
- multiple methods, 226–27
- nearest neighbor (NN), 250, 252–54
- performances for multiple objects, 270
- probabilistic data association filter (PDAF), 255–57
- quality of, 266
- validation on synthetic data, 265–67
- See also* Tracking
- Path computation, 177
- Pattern recognition, 107
- Phase contrast microscopy, 7–8
- Phenotypes, 217
- Photoactivated localization microscopy (PALM), 16, 109
- Photobleaching
  - consequences, 40
  - defined, 41
  - dendrite spine, 405
  - differential, 42
  - events, 41
  - fluorescence recovery after (FRAP), 42
  - multiplexing, 194
- Photocontrolable proteins, 108
- Photometric rendering, 177
- Photomultiplier tubes (PMTs), 22, 96–98, 405
- Photon counting, 347
- Photon shot noise, 98
- Physics-based modeling, 172
- Pixel-wise estimation, 178–79
- Plates
  - defined, 123
  - segmentation methods for, 129–30
- Point spread functions (PSF), 391, 447
  - incoherent, 92–93, 93–94
  - LSI system, 52
- Poisson noise, 347, 349
- Polarization microscopy, 8–9
- Polarizer, 9
- Positive predictive value (PPV), 382
- Positron emission tomography (PET), 425, 429, 441
- Prima facie, 135
- Principal component analysis (PCA), 64–65, 158
- Probabilistic data association filter (PDAF), 255–57
  - covariance update, 256–57
  - defined, 255
  - joint, 257–58
  - pseudocode, 281
  - search window, 256
  - state update, 256
- Probability distribution function (PDF), 204
- Propidium iodide, 26
- Proteins, 333, 334
- Proximal scanning FCM, 444–46
- Pseudocodes, 276–82
  - extended Kalman filter, 277
  - grid-based filter, 276–77
  - IMM filter, 277–78
  - JPDAF, 282
  - Kalman filter, 276
  - MHT association, 281
  - particle filter SIS, 278–79
  - particle filter with resampling, 279–80
  - probabilistic data association, 281
  - resampling, 279
  - suboptimal NNA, 280
- Pseudo-residuals, 179
- Pupil function, 93
- Q
  - Quadric error decimation factor, 415–16
  - Quantitation of biomarkers, 191–204

- Quantitation of biomarkers (*cont.*)
  - image analysis, 194–202
  - multichannel segmentation techniques, 202–3
  - multiplexing, 192–94
  - subcellular, 203–4
  - summary, 204
- Quantitative analysis, 106–7
  - data preprocessing, 106
  - model fitting, 106–7
  - motion assessment and tracking, 107
  - pattern recognition and classification, 107
- Quantitative phenotyping, 357–84
  - biomedical applications, 359–61
  - introduction, 357–59
  - with microscopic images, 357–84
  - mouse mammary gland phenotyping study, 382–84
  - mouse model study, 359–60
  - mouse placenta phenotyping studies, 380–82
  - segmentation of individual cells, 364–74
  - segmentation with  $N$ -point correlation functions, 361–64
  - summary, 384
  - 3-D visualization, 375–80
  - validation, 380–84
  - workflow, 358
  - zebrafish embryo, 360–61
- Quantization precision, 95
- Quantum dots, 20, 34–36
  - anatomy, 35
  - in confocal microscopy, 36
  - defined, 34, 107
  - illumination, 34
  - multiplexing, 193–94
  - photostability, 36
  - spectral profiles, 35
  - in widefield fluorescence microscopy, 36
- Quantum efficiency, 95
- Quenching
  - collisional agents, 41
  - common example, 41
  - consequences, 40
  - defined, 40–41
  - static (complex), 41
- R**
  - Rab-GTPases, 170, 171
  - Radial basis function (RBF), 289
  - Random walk (RW), 259
  - Real intermediate image plane (RIIP), 5
  - Real-time fiber pattern rejection, 447–50
    - calibrated raw data acquisition, 447–48
    - calibration, 449
    - imaging model, 449
    - real-time processing, 448–50
    - reconstruction, 450
  - Real-time focusing algorithm, 106
  - ReAsH, 40
  - Receiver operating characteristic (ROC)
    - curves, 416, 418
  - Recombinant proteins, 107–8
  - Red blood cells (RBCs), 451–53
  - Reflected light microscopy, 10–12
    - contrast mechanisms, 11–12
    - defined, 10
    - schematic diagram, 10
    - See also* Microscopy
  - Region adjacency graph, 126
  - Region-based segmentation, 200
  - Regions of interest (ROI), 285
    - rectangular, 457
    - tracking, 454, 456
  - Region tracking, 454–57
    - affine registration algorithm, 455
    - application to cell trafficking, 456–57
    - motion compensation algorithm, 454–55
  - Registration, 72–73
    - disparity function evaluation, 431
    - dynamic model for, 437
    - elastic, 106
    - image, 197–99
    - importance, 371
    - of large microscopic images, 371–74
    - of MicroCT images, 429–38
    - neuron morphology reconstruction, 394
    - nonrigid, 372–74
    - observation model for, 438



- rigid, 105, 371–72
  - of 3-D FMT, 429–38
- Resampling
  - dendritic spines, 405–7
  - particle filter with, 248, 279–80
  - pseudocode, 279
  - sequential importance (SIR), 247
- Resolution
  - Rayleigh's criterion, 5
  - spatial, 95
  - super, 109–10
  - temporal, 95–96
- Restoration, 69–72
- Rigid registration, 371–72
  - deformable registration comparison, 374
  - global alignment procedure, 378
  - high-level features, 372
  - maximization of mutual information, 372
  - region feature extraction, 373
  - uses, 371
  - See also* Registration
- RNA in situ hybridization, 153
- RNA interference (RNAi), 283–84
  - large-scale screens, 284
  - secondary screens, 283
- RNAs, 334, 335, 337
- Rule-based merging scheme, 366
- S**
- Scanning probe microscopy (SPM), 1
- Screening, 107
- Secondary geometric models, 128
- Second-harmonic imaging microscopy (SHIM), 16
- Second-order linear extrapolation (SLE), 259, 260
- Segmentation, 74–76
  - active-contour, 75–76
  - automated, results validation, 142–45
  - blob algorithms, 124
  - cell, 317–29
  - cloud algorithms, 128–29
  - of cytoplasm and epithelial regions, 202
  - defined, 122
  - dendrite, 393–94
  - divide-and-conquer strategy, 122–31
  - for division rate estimation, 317–29
  - foreground, 323–26
  - high-content cell screening, 212–14
  - image, 199–202
  - learning-based framework, 325
  - methods for foci/punctae, 129
  - methods for hollow shells, 129–30
  - methods for manmade objects, 131
  - methods for plates, 129–30
  - modality-dependent, 364–66
  - modality-independent, 366–71
  - model-based algorithms, 124–25
  - of multicell images, 285–87
  - multichannel techniques, 202–3
  - neurons, 407–8
  - nuclei, 365
  - outliers in, 379
  - oversegmentation, 383
  - region-based, 200
  - steps, 301
  - subcellular, 199
  - thresholding, 74
  - tissue, 361–64
  - undersegmentation, 383
  - unified, 200–202
  - validation, 123
  - Voronoi-based, 75
  - watershed, 75
- Selective plane illumination microscopy (SPIM), 110
- Semiconductor detectors, 96
- Sequential importance resampling (SIR), 247
- Sequential importance sampling (SIS), 247
- Sequential Monte Carlo, 436–38
  - condensation, 436–37
  - dynamic model for registration, 437
  - observation model for registration, 438
- Shannon sampling theorem, 54
- Shift invariant, 52
- Short-time Fourier transform (STFT), 62
- Shot noise, 347, 349, 405
- Sickle-cell hemoglobin, 13
- Signal and image representations, 57–60

- Signal and image representations (*cont.*)
  - matrix view, 57–58
  - orthonormal bases, 58–59
  - tight frames, 59
  - time-frequency considerations, 59–60
- Signal/image processing, 103–7
  - data size, 103
  - dimensionality, 103
  - image preparation, 103–4
  - quantitative analysis, 106–7
  - registration, 105–6
  - restoration, 104–5
  - segmentation, 106
- Signals, 123
- Signal-to-noise ratio (SNR), 95
- Simplex method, 433
- Single photon emission computed tomography (SPECT), 429, 441
- Small critter imaging, 425–39
  - bioluminescence, 426
  - coherent anti-Stokes Raman scattering (CARS), 426–27
  - conclusions, 438–39
  - fibered in vivo, 427
  - fluorescence microscopic, 425–26
  - image registration, 429–38
  - in vivo molecular, 425–27
- Snakes model, 302
- SNARF-1, 31, 32
- Spatial bias correction, 214–15
- Spatial dimensions, 115
- Spatial filtering, 4
- Spatial resolution, 95
- Spatio-temporal associations, 135–42
- Spatio-temporal cell cycle phase analysis, 304–10
  - automatic seed placement, 305
  - fast marching cell phase tracking, 307–10
  - shape/size constraint, 305–7
  - See also* Cell cycle phase analysis
- Spatio-temporal images, 300
  - dual track, 313
  - for Euclidean method, 313
  - for fast marching method, 313
- Spatio-temporal volume, 300
- Spectrally sensitive indicators, 30
- Spectral sensitivity, 95
- Spine morphometry, 402
- STACS algorithm, 76
- Static (complex) quenching, 41
- Statistical estimation, 67–68
  - gradient-based estimators, 68
  - MAP estimators, 67–68
  - MSE estimators, 67, 70
- STED microscopy, 109
- Stereomicroscope, 11–12
- Stereoscopic vision, 11
- Stimulated emission, 87
- Stimulated emission depletion (STED), 16
- Stochastic optical reconstruction microscopy (STORM), 109
- Subcellular biomarkers, 203–4
- Subcellular segmentation, 199
- Superposition, 3
- Super-resolution, 109–10
- Support vector machine (SVM), 324, 394
- Support vector machine (SVM) classifier, 289, 324
- Surfaces, 123
- Synthetic fluorescent probes, 19, 20
- Systems biology, 331–38
  - defined, 331–35
  - Digital Fish project, 338–53
  - gap, bridging, 353–54
  - genes in, 332
  - imaging in, 335–38
  - open source code and, 353–54
  - proteins in, 332
- T**
  - Temporal dimension, 117
  - Temporal resolution, 95–96
  - Tessellations, 366–71
    - barycentric representation, 368–69
    - gradient term, 370
    - line parameters, 369
    - overlap term, 370
    - parameter priors, 370–71
    - similarity term, 370
    - Voronoi, 367, 368
  - 3-D FMT images

- alignment, 432
- fusing, 435
- interpretation of, 436
- 3-D regions of interest (ROI), 285
- 3-D visualization, 375–80
- Thresholding, 74, 285–86
  - global, 286
  - local adaptive, 286
  - minimum error, 287
  - Otsu, 287
- TIKAL, 266
- Time-frequency plane, 59
- Tissue microarrays (TMAs), 194
- Tissue segmentation, 361–64
- Total internal reflectance fluorescence (TIRF), 16
- Total internal reflection microscopy, 13
- Tracing, 77
- Tracking, 77
  - Bayesian, 227–28
  - cell, 300, 349–50
  - Digital Fish project, 349–50
  - fast marching cell phase, 307–10
  - imaging task, 77
  - mitotic cell nuclei, 287–88
  - multihypothesis (MHT), 254–55, 281
  - multiple particle (MPT), 226–27
  - particle, 223–70
  - region, 454–57
  - ROI, 454, 456
  - visual approaches, 300
- Transmitted light microscopy, 2–5
- True-positive results, 382
- Trunk mesoderm anlage (TMA), 166
- Tubes, 123
- U
- Ultrasound (US), 441
- Unbiased line detection algorithm, 178
- Undersegmentation, 383
- Unmixing problems, 106
- Unsupervised, data driven representation and analysis methods, 64–66
  - GPCA, 66
  - ICA, 65
  - ISOMAP, 66
  - KPCA, 65
  - LLE, 66
  - PCA, 64–65
- V
- Velocimetry algorithm, 451–53
- Ventral nerve cord primordium (VNCP), 166
- Video-enhanced DIC, 13
- Video-microscopy
  - background estimation, 178–81
  - intracellular trafficking models in, 172–74
- Visualization
  - cell cycle research tool, 313–14
  - Digital Fish project, 352
  - 3-D, 375–80
- Visualization Toolkit (VTK), 347
- Voronoi-based segmentation, 75
- Voronoi tessellation, 367, 368
- W
- Watershed algorithm, 318
  - cytoplasm segmentation with, 326–27
  - defined, 327
- Watershed segmentation, 75
- Wavelet packets (WPs), 63
- Wavelet transform (WT), 62
- Widefield microscope, 91–93
  - components for fluorescence imaging, 92
  - incoherent point spread function, 92–93
  - principle, 91–92
- Y
- Yellow fluorescent protein (YFP), 38, 91
- Z
- Zebrafish, 340
  - cellular structure reconstruction, 360–61, 384
  - phenotyping studies, 379–80
- Zone integrals, 133



## Related Titles from Artech House

*Advances in Diagnostic and Therapeutic Ultrasound Imaging*, Jasjit S. Suri, Chirinjeev Kathuria, Ruey-Feng Chang, Filippo Molinari, and Aaron Fenster, editors

*Biomolecular Computation for Bionanotechnology*, Jian-Qin Liu and Katsunori Shimohara

*Electrotherapeutic Devices: Principles, Design, and Applications*, George D. O'Clock

*Fundamentals and Applications of Microfluidics, Second Edition*, Nam-Truong and Steven T. Wereley

*Matching Pursuit and Unification in EEG Analysis*, Piotr Durka

*Micro and Nano Manipulations for Biomedical Applications*, Tachung C. Yih and Ilie Talpasanu, editors

*Microfluidics for Biotechnology*, Jean Berthier and Pascal Silberzan

For further information on these and other Artech House titles, including previously considered out-of-print books now available through our In-Print-Forever® (IPF®) program, contact:

Artech House  
685 Canton Street  
Norwood, MA 02062  
Phone: 781-769-9750  
Fax: 781-769-6334  
e-mail: [artech@artechhouse.com](mailto:artech@artechhouse.com)

Artech House  
46 Gillingham Street  
London SW1V 1AH UK  
Phone: +44 (0)20 7596-8750  
Fax: +44 (0)20 7630-0166  
e-mail: [artech-uk@artechhouse.com](mailto:artech-uk@artechhouse.com)

Find us on the World Wide Web at: [www.artechhouse.com](http://www.artechhouse.com)